Lev M. Blinov

Structure and Properties of Liquid Crystals

Springer

Structure and Properties of Liquid Crystals

Lev M. Blinov

Structure and Properties of Liquid Crystals

Springer

Dr. Lev M. Blinov
Russian Academy of Sciences
Inst. Crystallography
Leninskii prospect 69
119333 Moscow
Russia
lev39blinov@gmail.com

ISBN 978-90-481-8828-4 e-ISBN 978-90-481-8829-1
DOI 10.1007/978-90-481-8829-1
Springer Dordrecht Heidelberg London New York

Library of Congress Control Number: 2010937563

Cover design: eStudio Calamar S.L.

Printed on acid-free paper

Springer is part of Springer Science+Business Media (www.springer.com)

To my family: Galina, Anastasia and Timothy

Epigraph

Ego plus quam feci, facere non possum
Marcus Tillius Cicero
English, translation close to the original
More than I have done, I cannot do
or maybe it better sounds like this in standard English
I cannot do more than I have done

Foreword

Liquid crystals have found an important place in modern life. Just look around: we see them in our clocks, computer displays, TV screens, telephones and calculators, car dashboards, photo-cameras, etc. Other applications include slide projection systems, spatial light modulators, temperature sensors and even liquid crystal lasers. In all these technical innovations, which appeared over the life of only a single generation, liquid crystals occupy a key position. This is because they consume a barely perceptible amount of energy when they change their state under external influences such as temperature, electric field, mechanical stress or whatever. In addition, there are very important biological aspects of liquid crystals.

The army of people working in the liquid crystal field continues to grow. The first conferences held during the early part of the last century involved only tens of participants; then, later, a few hundreds. More recently a wide river of principal liquid crystal conferences has given rise to several subsidiary, but also quite broad streams of meetings: Worldwide Conferences, European conferences, conferences of National Liquid Crystal societies, separate conferences on chemistry (sometimes only on chirality problems), optics, photonics and ferroelectricity of liquid crystals. Each of such meetings attracts hundreds of participants, but of different profiles: chemists, physicists, engineers for radio- and optoelectronics, biologists and physicians.

In recent years a group of several excellent top-level books have been published on the physics of liquid crystals and many others, dealing with particular problems related to physics of liquid crystals. Popular books on liquid crystals are very scarce; only three of them are mentioned in the list presented in Chapter 1. Evidently, there is a huge gap between the first group of books and the second. The monographs have been written by theoreticians at a very high level using the advanced mathematical apparatus of modern physics. The popular books are written vividly without a single formula. If we consider the books as training devices, the second group is designed for children's school sports, the first for Olympians. But what about the intermediate levels?

This is the gap I would like to try to fill. The book proposed to bridge the gap has been written by an experimentalist who, through all his life, has tried to understand and explain to his students the complexity of liquid crystal physics using either simple analogies or going back to the very first principles we have studied in middle and high schools. In this book there is no sentence starting with "It is easy to show. . .."; either it has been shown, or explained by simple analogy. In fact I only use mathematics at the level of engineering high school. In those cases when I need something more (for example, the Fourier transform, tensor algebra or variation calculus) I carefully explain all the details. In addition there are about 300 drawings clarifying the text. The aim of the book is modest: it is to introduce to a reader the most important ideas related to the structure and physical properties of liquid crystals, including some of the theoretical aspects. The book is intended for a wide spectrum of scientists, including experimental physicists, physical chemists, engineers, and especially, for undergraduate students and Ph.D. students.

The book consists of three parts: Structure, Physical Properties, and Electro-Optics of liquid crystals. Of course, I am aware that electro-optical properties may be regarded as physical properties. However they are particularly relevant for modern technology and correspond more to the author's own interests. For these reasons, electro-optic properties deserve a more honorable position. In the Part I, after a brief introduction, there is a short first chapter devoted to symmetry, the concept used throughout the book. In Chapter 2 we discuss the molecular aspects and the fundamental issue for all liquid crystal phases (or mesophases), the problem of the orientational distribution of molecules. In Chapter 3 there is a general description of the most important liquid crystal phases, beginning with the nematic phase and ending with chiral and achiral ferroelectric phases. After reading that chapter, the reader who only wishes to make a slight acquaintance with liquid crystals may quit or, at least, have a rest.

Chapter 4 will introduce the reader to the basic concepts of the X-ray analysis of crystals and its applications to particular liquid crystal phases. It should be noted that in the present literature this problem is not adequately dealt with anywhere, and this chapter attempts to rectify this deficiency. Chapter 5 covers phase transitions, one of the key problems of the liquid crystal physics, and which has been widely discussed in other texts at very different levels. In this chapter I give only a detailed explanation of the basic concepts of the phase transitions between most important mesophases.

Chapter 6 heralds the second part of the book and introduces the reader to anisotropy of the magnetic and electric properties of mesophases. Following in Chapter 7 there is a focus on the anisotropy of transport properties, especially of electrical conductivity. Without these two chapters (Chapters 6 and 7), it would be impossible to discuss electro-optical properties in the third section of the book. Further, Chapters 7 and 8 deal with the anisotropy of the properties of elasticity and viscosity. Chapter 8 is more difficult than the others, and in order to present the theoretical results as clearly as possible, the focus is on the experimental methods for the determination of Leslie viscosity coefficients from the viscous stress tensor of the nematic phase. Chapter 9 terminates the discussion of the anisotropy of

physical properties. Here, the case in point is the interaction of liquid crystals, mostly nematics, with a solid substrate. The problems of interfaces, especially, surface polarization and anchoring conditions occupies the central place here and the chapter is, in fact, a bridge between the second and third parts of the book.

Finally the three remaining Chapters 10–12 are devoted to optics and electro-optics of, respectively, nematic, cholesteric and smectic (ferroelectric and antiferro-electric) phases. In contrast to my earlier book published by Wiley in 1983, only the most principal effects have been considered and the discussion of the underlying principles is much more detailed.

Throughout the book the Gauss system of units is used, although all numerical estimates of quantities have been made in both systems, Gauss and International (SI). The referenced bibliography is rather small, because I deliberately included only books, review articles and the seminal papers that paved the way for further investigations. All these literature sources are presented with their titles.

This book was written over a long period of 10 years before and during my teaching course (2003–2009) of liquid crystal physics to Ph.D. students in Calabria University (CU) (Italy). Among the students there were not only physicists but chemists and engineers and even biologists. I have tried to make my course serious, simple and interesting, but it is for others to decide if I have succeeded. I am indebted to Prof. Roberto Bartolino for his invitation to work in Italy and to his co-workers (Profs. G. Cipparrone, R. Barberi, C. Umeton, C. Versace, G. Strangi and Drs. M. de Santo, A. Mazzulla, P. Pagliusi, F. Ciuchi, M. Giocondo and many others) who were always friendly and attentive to any of my problems and from whom I learned a lot of new things concerning both science and life. I would like to express also many thanks to my coworkers from the Institute of Crystallography, Russian Academy of Sciences Drs. M.I. Barnik, V.V. Lazarev, S.P. Palto, B.I. Ostrovsky, N.M. Shtykov, B.A. Umansky, S.V. Yablonsky and S.G. Yudin with whom I had the pleasure to work on liquid crystals for many years and have this pleasure now. I am always thankful to my friends-colleagues Guram Chilaya, Dietrich Demus, Elizabeth Dubois-Violette, George Durand, David Dunmur, George Gray, Etienne Guyon, Wolfgang Haase, Wim de Jeu, Efim Kats, Mikhail Osipov, Alexander Petrov, Sergei Pikin, Ludwig Pohl, Jacques Prost, and Katsumi Yoshino for fruitful discussions of many topics related and more frequently not related to liquid crystals but making our life in science more colorful.

Contents

Part I
Structure of Liquid Crystals

Chapter 1
Introductory Notes

First my middle school teachers and then my high school teachers told me that substances could be in the form of gases, liquids and crystalline solids, between which, on cooling, transitions could occur in the following sequence: gas → liquid → crystal. And I believed them, although even then liquid crystals had already been around for a respectable time. Today we tell students that if an organic substance consists of rod-like molecules, it may, on cooling, change from a gas to a normal (isotropic) liquid, then into a strange anisotropic liquid (called a nematic liquid crystal), see Fig. 1.1.

Further cooling may cause the anisotropic liquid to change into a lamellar structure, like a stack of paper, but with thin liquid sheets. Something that is a one-dimensional crystal, but within the stack is a two-dimensional liquid. This is the smectic A phase with molecules standing upright within the layer. Such layers easily slide on each other. These three phases have been identified by Friedel [1]. On further cooling the molecules may decide to tilt a little giving rise to the smectic C phase, the tilt angle of which increases with decreasing temperature.

But this is not all. In other substances, further cooling the smectic A phase results in the layers breaking up into hexagons but still sliding easily over each other; this is the smectic B_{hex} phase. Only at even lower temperatures does the sample acquire a normal crystalline structure. Thus instead of two phase transitions gas-liquid and liquid–crystal we have found four or five transitions between different phases.

Other substances manifest other sequences. For instance, in organic compounds having disc-like molecules we find a columnar phase built of liquid molecular columns packed in a two-dimensional crystalline structure. It is a one-dimensional liquid along the columns, and, at the same time, a two-dimensional crystal. An ancient Greek temple with liquid columns would be a good model of the columnar phase. Today we define liquid crystals as fluids with a certain long-range order in their molecular arrangement (i.e. they are anisotropic liquids). Each mesophase is a macroscopically uniform intermediate state between an isotropic liquid and a crystalline solid. The history of liquid crystals began with the observation by Reinitzer [2] of a strange phase intermediate between the liquid melt and the crystalline phase upon heating and cooling cholesteryl benzoate. The samples of this compound were sent by Reinitzer to O. Lehmann (Karlsruhe) who was an expert in polarizing microscopy. In Fig. 1.2 we can see the nice photos of the two

L.M. Blinov, *Structure and Properties of Liquid Crystals*,
DOI 10.1007/978-90-481-8829-1_1,

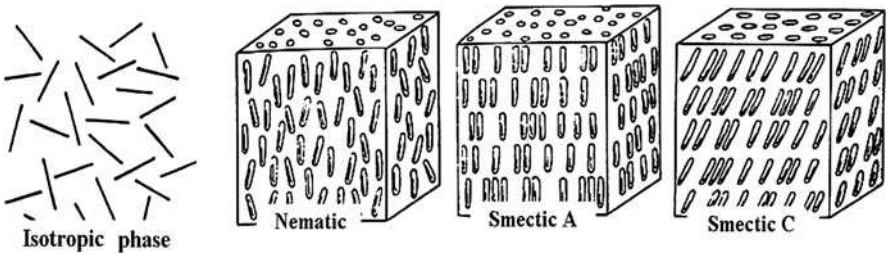

Fig. 1.1 From *left* to *right*: molecular structure of isotropic, nematic, smectic A and smectic C phases

Fig. 1.2 Photos of Friedrich Reinitzer (*left*) and Otto Lehmann (*right*)

founding-fathers of the liquid crystal community taken from the book on liquid crystal history written by Prof. Sonin [3].

It was Lehmann who, having investigated the gift of Reinitzer, understood that he was dealing with a new state of matter. Lehmann also observed such intermediate phases in other substances and, at first, gave them the name *fließende Kristalle* (crystals showing fluidity) [4]. Later he decided that the term *flüssige Kristalle* (liquid crystals) corresponds better to the essence of mesophases and used it as a title of the very first book on liquid crystals [5] (for more details about history of liquid crystals see [6, 7]).

Today we know that the cholesterol esters consist of helical (chiral) molecules, and on cooling from the isotropic phase they undergo a transition into another phase called a *cholesteric phase*. This shows unique optical properties. In Fig. 1.3a we see a photo-image of a 20 μm thick polycrystalline layer of cholesteryl acetate viewed in a polarizing microscope. Upon heating the substance melts, that is it becomes

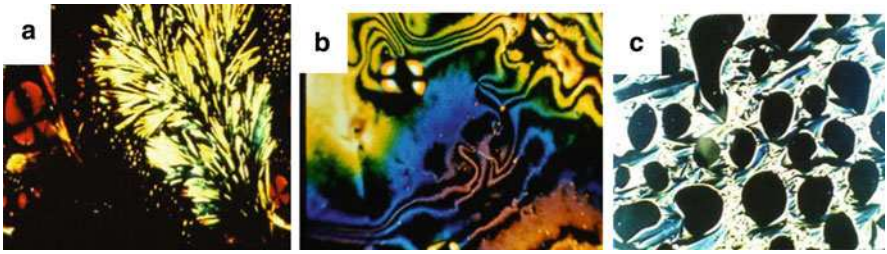

Fig. 1.3 Photo-image of a 20 μm thick polycrystalline layer of cholesteryl acetate placed between two cover glasses in crystalline phase (**a**), cholesteric phase (**b**) and at the transition from the cholesteric to isotropic phase (**c**)

fluid but optically anisotropic and shows bright diffraction colours, Fig. 1.3b. With increasing temperature we observe a phase transition to the isotropic phase. The latter is not birefringent, and therefore looks black between crossed polarizers. In Fig. 1.3c we see black drops on the bright background of the superheated cholesteric phase.

It should be noted that the appearance of the "cholesteric" phase of Reinitzer was different from the appearance of the classical cholesteric phase shown in Fig. 1.3b. The phase was opaque and had blue tint. It took a century to decipher its structure: it appears to be a *blue phase* (see Chapter 4) with a structure of liquid lattice consisting exclusively of defects of an initially ideal helical structure. This phase is periodic and shows Bragg diffraction of light in all the three principal directions. Therefore, Reinitzer has discovered the first generic photonic crystal! At present, a study of photonic crystals, mostly artificial, is one of the hot topics in physics [8].

The timing of the discovery of liquid crystals was unlucky. It coincided with the period when the beautiful foundations of modern physics were being laid, but the stone with the mark "liquid crystals" was somehow lost in controversy. Only now, through the enormous efforts of several generations of scientists, has the missing stone of liquid crystals been inserted in its legitimate place in the foundation of Science. And among those who put liquid crystals into the mainstream of physics there were such giants as F. Leslie, A. Saupe and especially P.G. de Gennes (The Nobel Prize in Physics, 1991).

The early book of de Gennes [9] and the subsequent one written together with Prost [10] may be highly recommended to physicists. During the work on the present book I used them frequently as well as the other excellent books on liquid crystal physics [11–14]. The reader can also find a great deal of interesting information on particular problems related to the physical properties of mesophases in monographs [15–21]. For newcomers I would recommend a nice, philosophically tinted book by P. Collings [22], a piece of art prepared by A.S. Sonin in Russian [23], and a slightly more scientific book written for schoolboys by S.A. Pikin and myself [24] (in Russian and Spanish). The literature for further reading is given at the ends of relevant chapters.

References

1. Friedel, G.: Les états mesomorphic da la matiér. Ann. Phys. **18**, 273–474 (1922)
2. Reinitzer, F.: Beiträge zur Kenntniss des Cholesterins. Monathefte für Chemie **9**, 421 (1888)
3. Sonin, A.S.: The Road a Century Long. Nauka, Moscow (1988) (in Russian)
4. Lehmann, O.: Über fließende Kristalle. Zs. Phys. Chem. **4**, 510–514 (1889)
5. Lehmann, O.: Die Flüssige Kristalle. Leipzig, Wilhelm Engelmann (1904)
6. Kelker, H.: History of liquid crystals. Mol. Cryst. Liq. Cryst. **21**, 1–48 (1973)
7. Sluckin, T.J., Dunmur, D.A., Stegemeyer, H.: Crystals That Flow: Classic Papers in the History of Liquid Crystals. Taylor & Francis, London (2004)
8. Joannopoulos, J.D., Meade, R.D., Winn, J.N.: Photonic Crystals: Molding the Flow of Light. Princeton University Press, Princeton, NJ (1995)
9. De Gennes, P.G.: The Physics of Liquid Crystals. Clarendon, Oxford (1975)
10. de Gennes, P.G., Prost, J.: The Physics of Liquid Crystals, 2nd edn. Oxford, Science Publications (1995)
11. Chandrasekhar, S.: Liquid Crystals, 2nd edn. Cambridge University Press, Cambridge (1992)
12. Vertogen, G., de Jeu, V.H.: Thermotropic Liquid Crystals. Fundamentals. Springer-Verlag, Berlin (1987)
13. Demus, D., Goodby, J., Gray, G.W., Spiess H.-W., Vill V. (eds): Physical Properties of Liquid Crystals. Wiley-VCH, Weinheim (1999)
14. Dunmur, D., Fukuda A., Luckhurst, G. (eds): Physical Properties of Liquid crystals: Nematics. INSPEC, London (2001)
15. Priestley, E.B., Wojtowicz, P., Sheng, P. (eds): Introduction to Liquid Crystals. Plenum Press, New York (1975)
16. Blinov, L.M.: Electro-Optical and Magneto-Optical Properties of Liquid Crystals. Wiley, Chichester (1983); Blinov, L.M., Chigrinov, V.G.: Electrooptic Effects in Liquid Crystal Materials. Springer-Verlag, New York (1993)
17. Pikin, S.A.: Structural Transformations in Liquid Crystals. Gordon & Breach, New York (1991)
18. Kats, E.I., Lebedev, V.V.: Fluctuation effects in the Dynamics of Liquid Crystals. Springer-Verlag, New York (1993)
19. Kleman, M., Lavrentovich, O.: Soft Matter Physics. Springer-Verlag, New York (2003)
20. Lagerwall, S.T.: Ferroelectric and Antiferroelectric Liquid Crystals. Wiley-VCH, Weinheim, NY (1999)
21. Muševič, I., Blinc, R., Žekš, B.: The Physics of Ferroelectric and Antiferroelectric Liquid Crystals. World Scientific, Singapore (2000)
22. Collings, P.: Liquid Crystals: Nature's Delicate Phase of Matter. Princeton University Press, Princeton, NJ (1990)
23. Sonin, A.S.: Centaurs of Nature. Atomizdat, Moscow (1980) (in Russian)
24. Pikin, S.A., Blinov, L.M.: Liquid Crystals, Kvant Series 20. Nauka, Moscow, (1982) (in Russian); Spanish translation "Cristales Liquidos", Mir, Moscow, 1985

Chapter 2
Symmetry

The concept of symmetry is equally important for understanding properties of individual molecules, crystals and liquid crystals [1]. The symmetry is of special importance in physics of liquid crystal because it allows us to distinguish numerous liquid crystalline phases from each other. In fact, all properties of mesophases are determined by their symmetry [2]. In the first section we consider the so-called *point group* symmetry very often used for discussion of the most important liquid crystalline phases. A brief discussion of the *space group* symmetry will be presented in Section 2.2.

2.1 Point Group Symmetry

2.1.1 Symmetry Elements and Operations

There are only few symmetry elements, which generates a number of symmetry operations [3, 4]. We may illustrate them by their applications to simple geometrical objects.

(a) *Proper rotation axis of n*th-*order*, C_n

Consider first *rotational symmetry*. Let us take an equilateral triangle and rotate it clockwise about its center by $360°/3 = 120°$, Fig. 2.1a. The new triangle would be undistinguishable from the original one (but not identical). The symmetry *element* we used is the proper rotation *axis* of order 3 (C_3-axis). The same triangle can be rotated by a half of the full turn about one of the three other axes (medians going out of each vertex), Fig. 2.1b. The corresponding symmetry element is a C_2 axis (rotation angle $360°/2$, $n = 2$). For a square, we can find one C_4 axis and four C_2 axes, for a hexagonal benzene molecule one C_6 axis and six C_2 axes.

The symmetry element C_3 may generate two other symmetry operations. For instance, applying C_3 rotation twice we again obtain an indistinguishable triangle. Symbolically, C_3^2 means rotation by $2 \times 2\pi/3 = 240°$. The same C_3 rotation applied three times result in the exactly the same triangle. Therefore C_3^3 is one of

L.M. Blinov, *Structure and Properties of Liquid Crystals*,
DOI 10.1007/978-90-481-8829-1_2,

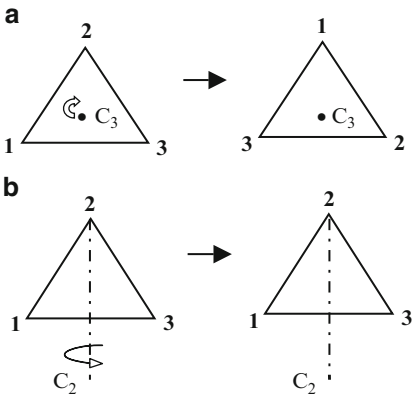

Fig. 2.1 Rotational symmetry. The illustration of operations made by proper rotation axes of third (**a**) and second (**b**) order

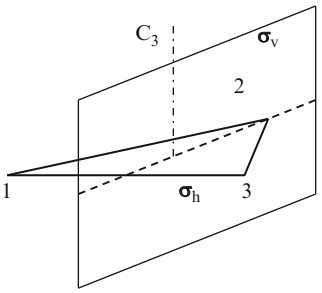

Fig. 2.2 Bilateral symmetry. Plane σ_v (*vertical*) is plane of reflection that contains the axis of the highest order C_3 for the equilateral triangle. After applying this element points 1 and 3 exchange their positions. Plane of the triangle is reflection plane σ_h (*horizontal*) perpendicular to C_3

the *identity operations*, ${C_3}^3 = E$. Generally, the identity operation corresponds to doing nothing with any figure and can also be obtained with C_2 or C_4 axes or with any axis of order n: ${C_2}^2 = {C_4}^4 = {C_n}^n = E$.

(b) *A plane of symmetry*, σ

This element generates only one operation, a reflection in the plane as in a mirror, Fig.2.2. Repeated twice this operation results in the initial structure that is $\sigma^2 = E$. Taking again our triangle we can see that plane σ interchanges points 1 and 3 leaving point 2 at the same place. Such symmetry is called *bilateral symmetry*. There may be several symmetry planes and they designated either as σ_h (the plane perpendicular to the axis C_n with highest number n) or σ_v (plane containing the C_n axis). By convention, the C_n axis with highest number n is taken as a vertical, therefore, indices h and v mean "horizontal" and "vertical". In our figure we see the σ_v plane, and the plane of the triangle is σ_h. Note that a chiral object, for instance a hand, has no mirror plane (however, two hands in praying position have a mirror plane between them [4]).

(c) *Inversion center, I*

This symmetry element *I* generates an operation of inversion through a point called the inversion center, Fig. 2.3. Therefore now we deal with *inversion symmetry*. We can take any point of an object and connect it by a straight line with the center O. Then, along the same line behind the center and at the equal distance from it we must find the point equivalent to the first one. A good example is a parallelogram. Note, that two inversions result in the identical object, $I^2 = E$.

(d) *Improper rotation*, S_n

This element is also called a rotation–reflection axis or mirror–rotation axis. It consists of two steps, a rotation through $1/n$ of the full turn followed by reflection in a plane perpendicular to the rotation axis, Fig. 2.4. A molecule of ethane in the staggered configuration is a good illustration of S_6 rotation–reflection axis, see the figure. Note, that this object has neither C_6 axis nor σ plane on their own. But after combined operations C_6 (60° clockwise) and σ we obtain an indistinguishable object with interchanged positions of all hydrogen atoms. Therefore S_6, and, more generally, S_n is independent symmetry operation. Like element C_n, element S_6 may generate several operations, for instance, ${S_6}^2 = C_3$ because this operation consists of rotation by $2 \times 2\pi/6 = 120° = 2\pi/3$ and identity operation $\sigma^2 = E$. Totally, ${S_6}^2 = C_3E$. Other examples are: ${S_3}^2 = {C_3}^2$; ${S_3}^3 = \sigma$; ${S_3}^4 = C_3$; ${S_3}^6 = E$.

Finally, we have five independent symmetry elements: identity *E*, proper rotation axis C_n, symmetry plane σ, inversion center *I* and rotation–reflection axis S_n, generating single (elements *E*, σ, *I*) or multiple (elements C_n, S_n) symmetry operations.

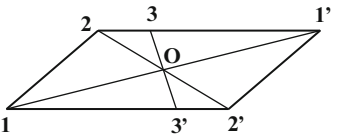

Fig. 2.3 Inversion symmetry. Point O is inversion center and the inversion operation exchanges positions of points 1–1′, 2–2′, 3–3′ etc.

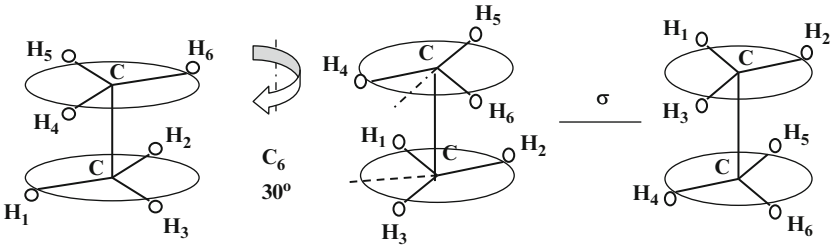

Fig. 2.4 Improper rotation. Axis connecting points C–C is a rotation–reflection axis S_6. An ethane molecule has a symmetry element including two subsequent operations, the rotation of the whole structure through an angle of 30° with a subsequent reflection by plane σ. After this the left and right sketch become identical

2.1.2 Groups

Now, for each geometrical object or a molecule we can write a *set of symmetry operations*, which transform the object into its equivalent formal representation. Let consider three examples.

(i) Water molecule, Fig. 2.5a. It has the C_2 axis, two symmetry planes and together with identity element we have a full set of symmetry operations E, C_2, σ, σ'. As we shall see soon this set corresponds to symmetry group C_{2v}.
(ii) The next is an ion $[Co(NH_3)_4ClBr]^{+3}$ shown in Fig. 2.5b. Its set of symmetry operations is E, C_4, C_4^2, C_4^3, $4\sigma_v$ (group C_{4v}).
(iii) Finally we take a flat borate molecule BCl_3 having the symmetry of an equilateral triangle, therefore allowing the following operations: E, C_3, C_3^2, C_2, C_2', C_2'', σ_h, S_3, S_3^2, σ_v, σ_v', σ_v'' (group D_{3h}).

Some operations belong to the same classes (see below), therefore we may write the set in a more compact way: E, $2C_3$, $3C_2$, σ_h, $3S_3$, $3\sigma_v$.

It is essential that any element of each set of operations can be obtained by a combination of other elements from the same set. Application of the subsequent symmetry operations is called *multiplication*. For a water molecule we can write the corresponding *multiplication table*, Table 2.1. For instance, the multiplication of operations C_2 from the first row and the first column corresponds to the identity operation, $C_2 \cdot C_2 = E$, shown in the table. Further, $C_2\sigma = \sigma'$ and $\sigma C_2 = \sigma'$, so these operations commute in our particular case. Generally they may not commute and the order of operations is important (by convention, multiplication operation $C_2\sigma$ means that first we apply operation σ and then C_2).

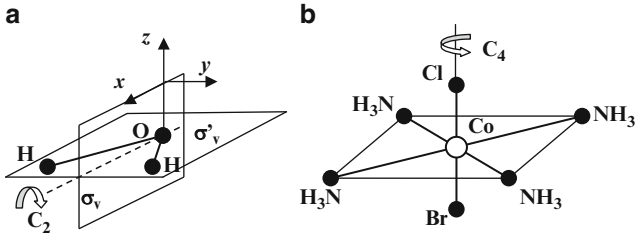

Fig. 2.5 Set of symmetry operations and the structure for water molecule belonging to group C_{2v} (**a**) and the structure of ion $Co(NH_3)_4ClBr]^{+3}$ belonging to group C_{4v} (**b**)

Table 2.1 Multiplication table for symmetry elements of water molecule

	E	C_2	σ	σ'
E	E	C_2	σ	σ'
C_2	C_2	E	σ'	σ
σ	σ	σ'	E	C_2
σ'	σ'	σ	C_2	E

In the mathematical sense, each set of the operations shown above and, more generally, characterizing the symmetry of objects of different shape forms a *group*. So, what is a group? A set of elements A, B, C, etc. form a group if there is a rule for combining any two elements to form their "product" AB (or $A \cdot B$) such that:

- Every "product" of two elements is an element of the same set.
- There is a unit element E such that $EA = AE = A$.
- The associative law is valid, that is $A(BC) = (AB)C$, etc.
- Each element A has its inverse element A^{-1} belonging to the same set such that $AA^{-1} = A^{-1}A = E$.

The group "product" might be different (multiplication, addition, permutation, space rotation, etc).

For example, a set of integers including negative, zero and positive numbers $-\infty, \ldots, -n, \ldots, -3, -2, -1, 0, 1, 2, 3, \ldots, n, \ldots, \infty$ form a group under *addition* as a group operation. Indeed, all the group rules are fulfilled:

$A + B = C$ (e.g. $2 + 18 = 20$) belongs to the same set,
evidently $A + (B + C) = (A + B) + C$
$E = 0$ (e.g., $0 + A = A$, that is addition of zero changes nothing)
$A + (-A) = 0 = E$ (under *addition* as group operation $(-A)$ symbolically means A^{-1})

This group contains infinite number of elements, therefore it is an *infinite group* or group of infinite order.

Another example is a set of four 2×2 matrices that form a *finite* group of order 4 (because we have four elements in the group) under *multiplication* operation (it may directly be checked using the rule for matrix multiplication):

$$A = \begin{bmatrix} 1 & 0 \\ 0 & 1 \end{bmatrix}, B = \begin{bmatrix} 0 & 1 \\ -1 & 0 \end{bmatrix}, C = \begin{bmatrix} -1 & 0 \\ 0 & -1 \end{bmatrix}, D = \begin{bmatrix} 0 & -1 \\ 1 & 0 \end{bmatrix} \tag{2.1}$$

Here the identity element is matrix A, the associative law for matrices is always valid, the inverse matrices are B for D and vice versa ($BD = DB = A$), elements A and C are inverses on their own ($AA = A$, $CC = A$). It is interesting that there is a one-to-one correspondence between the elements of the group of our four matrices and the elements of the group of complex numbers 1, i, -1, $-i$. The two groups have the same multiplication table. For example, the product of the elements of the first group (matrices) $B_1C_1 = D_1$ corresponds to the product $B_2C_2 = D_2$ of the second group (numbers). Therefore, we say that these two groups are *isomorphic*.

The concept of isomorphism is very important. Here, we are interested in the groups of elements whose products are symmetry operations. Each set of symmetry operations is a group, which may be *represented* by a group of matrices isomorphic to our group. To demonstrate this, let us go back to group C_{2v} in Fig. 2.5a and pay attention to the coordinate system: this is the *basis* for representation of the selected group in the matrix form. Since the water molecule is two-dimensional the group will be represented by 4×4 matrices. We shall consider the hydrogen–oxygen

bonds as vectors x, y and the symmetry operation will transform them into vectors $x'$and y'. The identity operation E does not change anything, and this operation is represented by the unit matrix E:

$$E = \begin{bmatrix} 1 & 0 \\ 0 & 1 \end{bmatrix}; C_2 = \begin{bmatrix} 1 & 0 \\ 0 & -1 \end{bmatrix}; \sigma_v = \begin{bmatrix} 1 & 0 \\ 0 & -1 \end{bmatrix}; \sigma_v' = \begin{bmatrix} 1 & 0 \\ 0 & 1 \end{bmatrix} \tag{2.2}$$

The C_2 operation exchanges only y-projections of the two vectors, and this is given by matrix C_2. In our particular case, the result of σ_v operation is the same and the corresponding matrices C_2 and σ_v are equal. Operation σ_v' does not change positions of the two vectors and is matrices E and σ_v' are identical. The sums of the diagonal elements of a matrix is a trace or a character of the matrix. Our matrices have the following characters 2, 0, 0, 2 corresponding to one of possible representations of group C_{2v}.

Therefore, we can operate with the matrices using a powerful apparatus of modern mathematics and obtain important results not at all evident from the beginning. Such a *theory of group representations* will not be considered here although that theory is very powerful and widely used not only in crystallography [2] but in many areas of physics [1, 5, 6]. In this section we shall only list the sets of symmetry operations corresponding to the most important *point symmetry groups*. The term "point" reflects the fact, that under any operation of the groups listed, at least, one point of the object is not changed. For comparison, when an object is translated in space we should discussed its translational symmetry and corresponding *space symmetry groups* [7].

2.1.3 Point Groups

Generally, there is infinite number of point groups, but not all of them correspond to real physical objects such as molecules or crystals. For example, only 32 point groups are compatible with crystal lattices. Each of them is labeled by a certain symbol according to Schönflies or according to the International classifications. The Schönflies symbols are vivid and more often used in scientific literature. Here we present only those point groups we may encounter in the literature on liquid crystals.

In the Table 2.2 the Schönflies symbols are given on the left side, symmetry operations (not symmetry elements) are given on the right side. As we see a number of symmetry operations increases from top to bottom. Therefore, we say that D_{6h} is more symmetric phase than, say, C_{2h}. The capital letter D (with index $n = 2, 3, 6, \ldots$) is used when n number of C_2 axes appear, which are perpendicular to the principal C_n axis. All symmetry operations except σ_d have been discussed above. The operation σ_d appears in D_{4h}, D_{6h} etc. to distinguish between vertical reflection planes σ_v containing the C_2 axes and additional planes (also vertical) passing along bisectors between already available pairs of the C_2 axes.

Table 2.2 Some point groups with Schönflies and international symbols

Schönflies symbol	International	Symmetry operations
C_1	1	E
C_s or C_{1h}	*m*	E, σ_h
C_i or S_2	$\bar{1}$	E, I
C_2	2	E, C_2
C_{2h}	2/*m*	E, C_2, I, σ_h
C_{2v}	*mm*	E, C_2, σ_v, σ_v'
C_{3v}	3*m*	E, $2C_3$, $3\sigma_v$
D_{2h}	*mmm*	E, $3C_2$, I, σ_h, σ_v, σ_v'
D_{3h}	$\bar{6}m2$	E, $2C_3$, $3C_2$, σ_h, $2S_3$, $3\sigma_v$
D_{6h}	6/*mmm*	E, $2C_6$, $2C_3$, C_2, $3C_2'$, $3C_2''$, I, $2S_3$, $2S_6$, σ_h, $3\sigma_d$, $3\sigma_v$

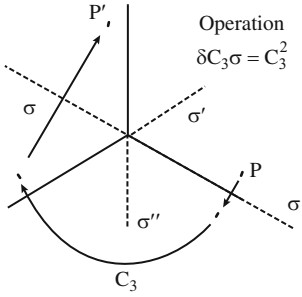

Fig. 2.6 The procedure illustrating that, in NH_3 molecule (group C_{3v}), operations C_3 and ${C_3}^2$, belong to the same class and operations σ, σ′, σ″ belong to another class

For the sake of brevity, some operations form *classes* consisted of conjugate symmetry operations. For example, consider the C_{3v} group: operation $2C_3$ includes two conjugate operations C_3 and ${C_3}^2$ (not two C_3 axes!). The definition of the conjugate elements of a group is as follows: we say operations A and B of a group are conjugate and belong to the same class if $XAX^{-1} = B$ where X is any of the same group operations and X^{-1} is its inverse operation. Therefore, B is similarity transform of A (note, that $XX^{-1} = E$). Note that single operation E forms the class on its own because, for any X, $XEX^{-1} = EXX^{-1} = E$.

Since operation σ is equal to its own inverse, it is convenient to use it as X and analyze whether operations C_n. form a class or not. For example, consider NH_3 molecule (group C_{3v}) whose projection along the C_3 axis is shown in Fig. 2.6. Let us take point P and, at first, make twice C_3 operation to arrive at point P′. Then, we start again from point P and, guided by arrows in the figure, make operation $\sigma C_3 \sigma^{-1}$. We again arrive at point P′. Therefore $\sigma C_3 \sigma^{-1} = {C_3}^2$, and operations C_3 and ${C_3}^2$ belong to the same class. Now, since from the C_3 symmetry is evident that C_3 is inverse of ${C_3}^2$, we may find a conjugate of σ: $C_3 \sigma {C_3}^2 = \sigma''$. Finally, all symmetry operations for the C_{3v} group, i.e. E, C_3, ${C_3}^2$, σ, σ′, σ″ can be combined in three classes E, $2C_3$, 3σ, as shown in Table 2.2.

2.1.4 Continuous Point Groups

There are also so-called *continuous point groups*, which include rotations of objects (or coordinate systems) by infinitesimal angles. Therefore the number of their elements tends to a limit that is infinity and the groups themselves are infinite. The continuous point groups were introduced by P. Curie and can be represented by physical objects [3]. Totally there are seven continuous groups. They are important for description of very symmetric liquid crystalline phases such as nematic, smectic A and polar nematic phase the existence of which is still under discussion. There are also continuous space groups describing helical (chiral) phases, see below. For the beginning consider the groups of cones. The symmetry of an immobile cone, see Fig. 2.7a, is $C_{\infty v}$ (or ∞m according to the International classification). It includes an infinite order axis C_∞, an infinite number of symmetry planes σ_v like the ABC plane but has no σ_h plane. Therefore, the C_∞-axis has properties of a genuine vector. We say this axis is a *polar axis* and the phase is also polar, in particular, it may possess spontaneous polarization. In the liquid crystal physics this group would describe the *polar nematic phase*, the very existence of which is still questionable. The rotating cone, see Fig. 2.7b, has polar symmetry reduced to $\mathbf{C}_\infty$ (or ∞) because the only symmetry element is a rotation axis C_n with $n = \infty$. Due to rotation there is no symmetry plane. The cone may rotate either clockwise or anti-clockwise and we can say that it has two enantiomorphic modifications.

The next is a series of cylinders. The immobile cylinder has symmetry elements shown in Fig. 2.8a: a rotation axis of infinite order C_∞, an infinite number of C_2 axes perpendicular to C_∞, a horizontal symmetry plane σ_h and infinite number of vertical symmetry planes σ_v. Its point group $D_{\infty h}$ (or ∞/mm) corresponds to symmetry of the conventional (non-chiral) nematic or smectic A phase. A rotating cylinder, Fig. 2.8b, has no C_2 axis perpendicular to the C_∞ rotation axis but has a horizontal symmetry plane σ_h (no chirality). Its point group symmetry is $C_{\infty h}$ (or ∞/m). A twisted cylinder, Fig. 2.8c, is chiral therefore has lost all symmetry planes but still has the C_∞ axis and infinite number of C_2 axes perpendicular to C_∞. Therefore, according to Schönflies, it keeps the D letter and its symmetry group is D_∞ (or $\infty 2$) corresponding to chiral cholesteric or chiral smectic A* phase. Both the twisted and rotating cylinders may be encountered in

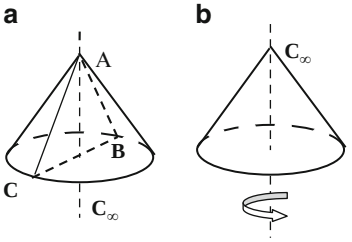

Fig. 2.7 Continuous groups of cones: symmetry elements of an immobile cone $C_{\infty v}$ (**a**) and group of a rotating cone C_∞ (**b**)

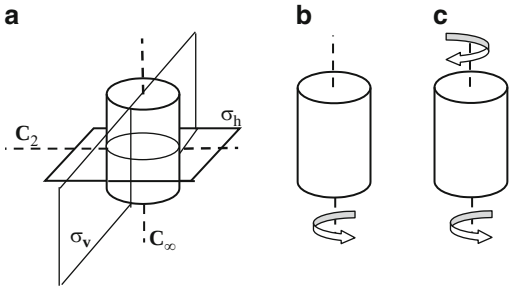

Fig. 2.8 Continuous groups of cylinders: symmetry elements of an immobile cylinder, group $D_{\infty h}$ (**a**), the group of a rotating cylinder $C_{\infty h}$ (**b**) and chiral group of a twisted cylinder D_{∞} (**c**)

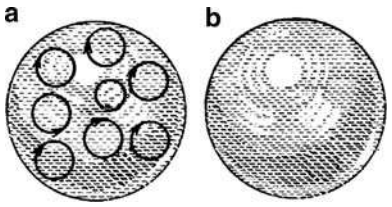

Fig. 2.9 Continuous groups of spheres: group of a chiral sphere K or R (**a**) and group of achiral (having mirror symmetry) sphere K_h or O (**b**)

two enantiomorphic modifications. Note that all cylinders and cones are optically uniaxial.

The two objects shown in Fig. 2.9 are spheres made of different materials. The sphere (b) is made of non-chiral material. Such a sphere has full orthogonal symmetry group O(3) or K_h (i.e. $\infty\infty m$): infinite number of C_∞ axes, infinite number of reflection planes passing through the center of the sphere, an inversion center. Any isotropic achiral liquid has this point symmetry group. However, liquids consisting of chiral molecules, which rotate the light polarization plane (like some sugar solutions), have lower symmetry, Fig. 2.9a; they belong to the full rotational group R(3) or K (or $\infty\infty$) because they have lost all symmetry planes and the inversion center. To conclude, the full list of seven continuous point groups includes (in the order of reducing symmetry): spheres (K_h, K), cylinders ($D_{\infty h}$, $C_{\infty h}$, D_{∞},), and cones ($C_{\infty v}$ and C_{∞}).

2.2 Translational Symmetry

(a) *Crystals made of atoms with spherical symmetry*

Such crystals have only *translational* (i.e., *positional*) order and no orientational order. Their structure is characterized by (i) the point group symmetry of an elementary cell which includes rotations, reflections and inversion as group operation and (ii) the group of translations which includes vectors with their addition as a group operation. The translation vector is $\mathbf{T} = n_1\mathbf{a} + n_2\mathbf{b} + n_3\mathbf{c}$ where **a, b, c** are unit

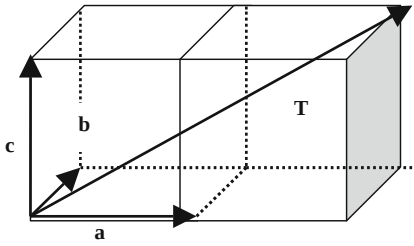

Fig. 2.10 The translation vector $\mathbf{T} = n_1\mathbf{a} + n_2\mathbf{b} + n_3\mathbf{c}$ with $n_1 = 2$, $n_2 = 1$, $n_3 = 1$; (**a**), (**b**) and (**c**) are unit basis vectors

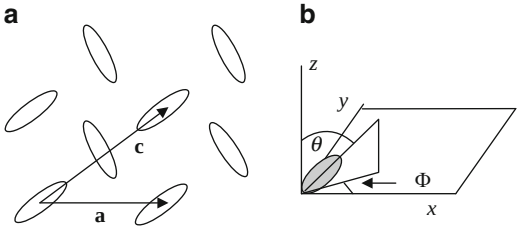

Fig. 2.11 Molecular crystal with rigidly fixed molecules (a) and Euler angles ϑ and Φ (b) for a particular molecule

vectors and n_i are integers. For example, $n_1 = 2$, $n_2 = 1$, $n_3 = 1$, see Fig. 2.10. The overall symmetry (the crystal group) is determined by combination of all these elements.

(b) *Molecular crystals*

Due to anisometric (particularly elongated) shape of molecules, these crystals possess both the *translational* and *orientational* order. The latter is determined by Euler angles ϑ, Φ such molecules form with respect to selected coordinate frame as shown in the right part of Fig. 2.11. The third Euler angle Ψ describing rotation of a molecule about its longest axis is not shown for simplicity. The point group symmetry includes this orientational order.

(c) *Plastic crystals and liquid crystals*

A loss of the orientational order of a molecular crystal due to free rotation of molecules around x, y and z-axes with the positional order remained results in *plastic crystals*. The point group symmetry increases to that characteristic of crystals with spherical atoms. However, such crystals are much softer. An example is solid methane CH_4 at low temperature.

A loss of the translational order (at least, partially) results in *liquid crystals* of different rotational and translational symmetry. On heating, one can observe step-by-step melting and separate phase transitions to less ordered phases of enhanced symmetry. On cooling, correspondingly one observes step-by-step "crystallization". An isotropic liquid is the most symmetric phase, it has full translational and orientational freedom, and this can be written as a product of group multiplication, O(3) $\times$ T(3), where O(3) is the full orthogonal symmetry (infinite and

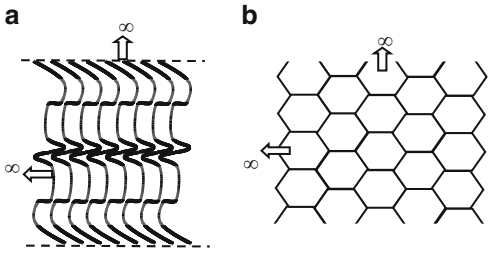

Fig. 2.12 One-dimensional (**a**) and two-dimensional (**b**) periodicity in the three-dimensional space

continuous) group and T is the full infinite continuous group of translations [8]. Upon cooling, a series of phase transitions occurs, and each time the symmetry is reduced. Each new point symmetry group is a subgroup of O(3) and a new group of translations is a subgroup of T(3). For example, on transition to the nematic phase the translational freedom is not confined but the rotational symmetry is lowered and the full symmetry is reduced to $D_{\infty h} \times T(3)$.

In Fig. 2.12a one-dimensional periodic structure is shown in the three-dimensional space. The curve line having point group C_{1h} (or C_s) is repeated with a certain period along the horizontal axis. Such translation may be symbolically written as $T_1{}^3$. It is the same space group the smectic A phase has, see Fig. Int.1 in Chapter 1. In Fig. 2.12b the two-dimensional hexagonal lattice in the three-dimensional space ($T_2{}^3$) is presented. We shall discuss later the smectic B phase having this type of the hexagonal order of molecules.

It should be noted that cholesteric liquid crystals (chiral nematics) having point group symmetry D_∞ are also periodic with the pitch considerably exceeding a molecular size. The preferable direction of the local molecular orientation, i.e. the director oriented along the C_∞ axis, rotates additionally through subsequent infinitesimal angles in the direction perpendicular to that axis. Hence a helical structure forms with a screw axis and continuous translation group.

(d) *Classification of liquid crystals*

Liquid crystals can be classified according to

(i) Their mean of formation: thermotropic (change of temperature and pressure), lyotropic (change of the molecular concentration in water and some other solvents), carbonized (change of polymerization degree), some rare special mechanisms (e.g., formation of chain structures in some inorganic substances).
(ii) Molecular shape, as discussed in Chapter 2, like rod-like or calamitic (from Greek καλαμοζ that means "cane"), discotic, banana- or bent-like, dendrites, etc.
(iii) Optical properties (uniaxial, biaxial, helical).
(iv) Chemical classes (biphenyls, Schiff bases, pyrimidines, tolanes, etc).
(v) The symmetry of a liquid crystalline phase which determines physical properties of the phase. This classification is a generalization of the earlier one suggested by G. Friedel. In Chapter 3 we consider symmetry and structure of the most important liquid crystalline phases.

References

1. Landau, L.D., Lifshits, E.M.: Quantum Mechanics, 3rd edn. Nauka, Moscow (1974). Ch.12 (in Russian)
2. Pikin, S.A.: Structural Transformations in Liquid Crystals. Gordon & Breach, New York (1991)
3. Sonin, A.S.: Besedy o kristallofizike (Talks on Crystal Physics). Atomizdat, Moscow (1976) (in Russian)
4. Hargittai I., Hargittai, M.: Symmetry Through the Eyes of a Chemist. VCH Verlaggesellschaft, New York (1986)
5. Bhagavantam, S., Venkatarayudu, T.: Theory of Groups and Its Applications to Physical Problems, 2nd edn. Andhra University, Waltair (1951)
6. Weyl H.: Symmetry. Princeton University Press, Princeton (1952)
7. Kittel, Ch: Introduction to Solid State Physics, 4th edn. Wiley, New York (1971)
8. Kats, E.I.: New types of ordering in liquid crystals. Uspekhi Fis. Nauk **142**, 99–129 (1984)

Chapter 3
Mesogenic Molecules and Orientational Order

3.1 Molecular Shape and Properties

A great variety of organic molecules can form liquid crystalline phases. They are called mesogenic molecules and belong to different chemical classes, see the comprehensive book by G. Gray on chemical aspects [1] and his review articles [2, 3]. The discussion of more recent achievements in the chemistry of liquid crystals may be found in beautifully illustrated article by Hall et al. [4].

3.1.1 Shape, Conformational Mobility and Isomerization

Figure 3.1 represents the characteristic types of mesogenic molecules. Among them are rods, laths, discs, helices which are more popular for physical investigations and technological applications and also main-chain and side-chain polymers. We may add to this list banana- or bent-shape molecules and dendrimers [4] that recently become very popular.

Rigid rods (a), laths (b) and disks (c) have no conformational degree of freedom. They are very convenient for theoretical discussions and computer simulations of the mesophase structure. Closer to reality are rods (or disks) with flexible tails (hydrocarbon chains) shown in Fig. 3.2a, which facilitate formation of layered liquid crystal phases. As an example of conformational degrees of freedom of flexible molecular fragments is the *trans–cis* isomerization. In sketch 3.2b *trans*-form is on the left, *cis*-form in the middle, a combination of the two on the right. The rotational isomerization is another example: in sketch 3.2c the internal rotation of phenyl rings about the single bond in a biphenyl moiety is sketched.

A molecule having the same chemical structure can exist in different atomic configurations [5]. It forms different stereoisomers either mesogenic or not. One important example is a molecule of cyclohexane (CH in Fig. 3.3) having all the bonds single. The cyclohexane can acquire a form of either chair or trough to be compared with a flat form of the benzene molecule having conjugated single and double bonds. Moreover, the cyclohexane molecule reveals another type of

L.M. Blinov, *Structure and Properties of Liquid Crystals*,
DOI 10.1007/978-90-481-8829-1_3,

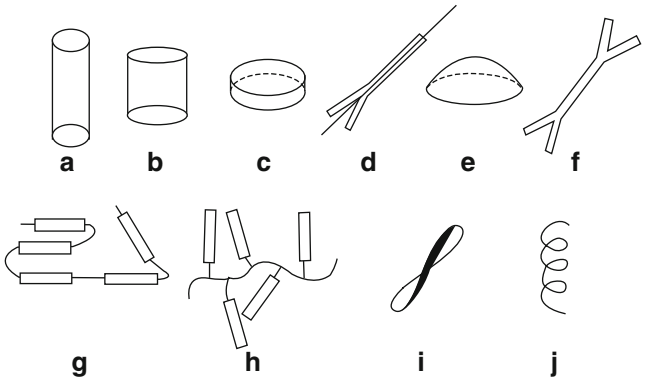

Fig. 3.1 Different forms of mesogenic molecules: rods (**a**), lath-like (**b**), discs (**c**), swallow-tail (**d**), bowls (**e**) double swallow-tails (**f**), main-chain (**g**) and comb-like (**h**) polymers, propellers (**i**) and spirals (**j**)

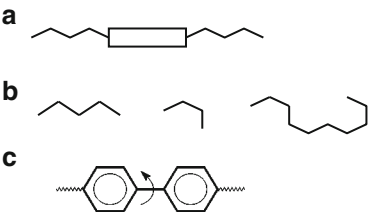

Fig. 3.2 Different degrees of freedom for non-rigid mesogenic molecules: molecules with flexible tails (**a**), *trans*-, *cis*- and combined *trans-cis* isomerisation of the flexible chains (**b**); rotational isomerism of biphenyl moiety (**c**)

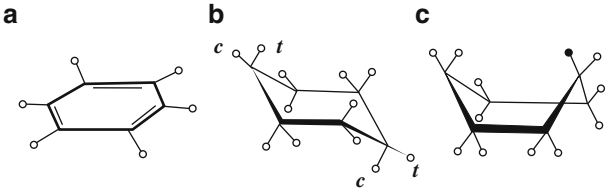

Fig. 3.3 Rigid benzene molecule (**a**) and chair (**b**) and trough (**c**) isomeric forms of a cyclohexane molecule

isomerization. The hydrogen atoms marked by *t* and *c* letters are in nonequivalent positions with respect to the longest molecular axes: only the *trans*-position is compatible with that axis. It is known that atoms in different positions have different chemical reactivity. For instance, the –COOH group can be attached to the cyclohexane moiety in the *trans*-position. Then, a combination of the chair CH structure with the *trans*-position of that group, due to a chemical reaction, results in an elongated overall structure of the new-synthesized molecule, which is more appropriate for liquid crystal formation. In addition, elongated dimers can form due to H-bonds between –COOH groups, see below.

3.1.2 Symmetry and Chirality

The word *chirality* originates from Greek χιροσ (hand). Chiral objects (and molecules) have no mirror symmetry (no one mirror plane). Examples of such objects are spirals, propellers, screws, hands. Note that the symmetry of a liquid crystal phase is not the same as the symmetry of constituent molecules but they often share some symmetry elements. As an example let us look at the symmetry of a "brick" and a "building" in Fig. 3.4. They are different although it is not a convincing example, because our tower has not been erected by self-assembling of bricks.

Chiral molecules, only left or only right, form chiral phases, left and right chiral molecules in equal amount form achiral (enantiomorphic) phases [6]. Consider a chiral molecule of a popular compound DOBAMBC (D(or L)-*p*-decyloxybenzylidene-*p*′-amino-2methylbutyl cinnamate). It has an asymmetric carbon in its tail and form a chiral SmC* phase in the range of 95–117°C, Fig. 3.5a. A molecule with a chiral tail looks like an ice-hockey stick and forms a helical liquid crystal phase. Left and right forms of a chiral tail result in the left and right handedness of a molecule Fig. 3.6. On the other hand, chirality of cholesterol esters is exclusively due to a curvature of the molecular skeleton Fig. 3.5b.

The synthesis of chiral molecules is a real challenge. There are, at least, three different approaches.

(i) A chemist needs simple chiral molecules as initial or intermediary reagents. They can be found among natural substances because the Nature selects left or right forms. For example, left (or right) amino acids can be used. Then the synthesis can be continued until the left (or right) form of the final chiral product is obtained.

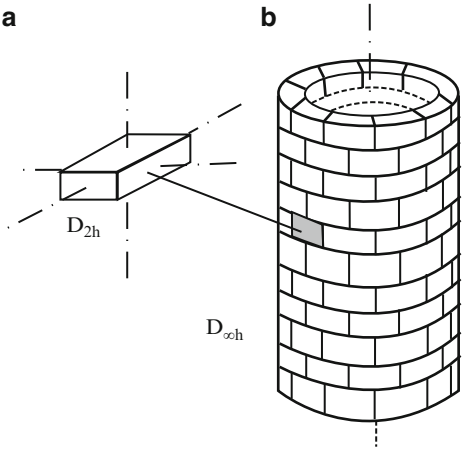

Fig. 3.4 Illustration of different symmetry (D_{2h} and $D_{\infty h}$) of a brick (**a**) and an architectural "masterpiece" made from the same bricks (**b**)

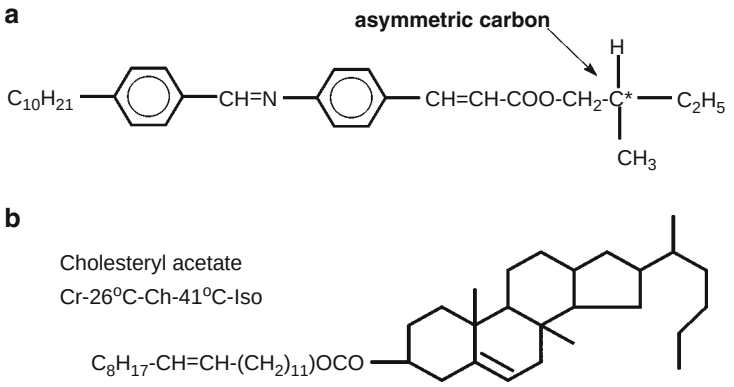

Fig. 3.5 Chemical formulas of two important chiral molecules: DOBAMBC (**a**) and cholesteryl acetate (**b**)

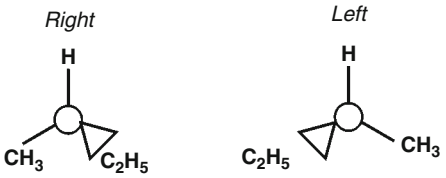

Fig. 3.6 Asymmetric carbon and its left or right surrounding

(ii) As shown by Pasteur, chiral solutes can crystallize from a solution in the form of left and right optically active crystals and left and right chiral isomers can be separated.
(iii) The synthesis can be made in the chiral conditions (e.g., in a chiral solution, like a cholesteric liquid crystal, or on special substrates, or using a chiral, one directional stirring, etc.).
(iv) Chirality can be created optically by circularly polarized light.

3.1.3 Electric and Magnetic Properties

(a) *Polarizability*

All atoms and molecules can be polarized by an electric field. The polarization (induced dipole of a unit volume) is $\mathbf{P} = \alpha\mathbf{E}$ where α is molecular polarizability. For spherically symmetric atoms or molecules (like C60 fullerenes) the polarizability is a scalar quantity (tensor of zero rank) and $\mathbf{P}\|\mathbf{E}$. In general case of lath-like molecules, α_{ij} is a second rank tensor (9 components) and $\mathbf{P}_j = \alpha_{ij}\mathbf{E}_i$. By a proper choice of the reference frame the tensor can be diagonalized

$$\alpha_{ij} = \begin{vmatrix} \alpha_{xx} & 0 & 0 \\ 0 & \alpha_{yy} & 0 \\ 0 & 0 & \alpha_{zz} \end{vmatrix}$$

and components α_{xx}, α_{yy} and α_{zz} represent three principal molecular polarizabilities. For molecules having cylindrical symmetry (rods or disks) with the symmetry axis z, only two different components remain $\alpha_{xx} = \alpha_{yy} = \alpha_{\perp}$ and $\alpha_{zz} = \alpha_{\parallel}$.

(b) *Permanent dipole moments*

If a molecule has an *inversion center* it is non-polar and its dipole moment (a vector, i.e., a tensor of rank 1) $\mathbf{p}_e = 0$. In a less symmetric case $\mathbf{p}_e$ is finite. It is measured in units Debye and in the Gauss system $1D = 10^{-18}$ CGSQ·cm ($3.3 \cdot 10^{-30}$ C·m in SI system). More vividly, 1D corresponds to one electron positive and one electron negative charges separated by a distance of ≈0.2 Å. The dipole moment of a complex molecule can be estimated as a vector sum of the moments of all intramolecular chemical bonds, $\mathbf{p}_e = \Sigma\, \mathbf{p}_i$. Consider two classical examples shown in Fig. 3.7.

(i) A molecule of 5CB (4-pentyl-4′-cyanobiphenyl) has a longitudinal electric dipole moment about 3D due to a triple –C≡N bond.
(ii) A molecule of MBBA (4-methoxy-benzylidene-4′-butylaniline) has a transverse dipole moment due to the methoxy-group and, of course, both molecules have anisotropic polarizabilities.

The vector of a permanent dipole moment $\mathbf{p}_e$ and polarizability tensor α_{ij} describe the linear (in field) electric and optical properties. The nonlinear properties are described by tensors of higher ranks (this depends on the number of fields included). For instance, the efficiency of mixing two optical waves of frequencies ω_1 and ω_2 is determined by polarization $\mathbf{P}_k(\omega_3) = \gamma_{ijk}\, \mathbf{E}_i(\omega_1) \cdot \mathbf{E}_j(\omega_2)$ where $\mathbf{E}_i(\omega_1)$ and $\mathbf{E}_j(\omega_2)_j$ are amplitudes of two interacting fields. Here γ_{ijk} is a third rank tensor of the electric hyperpolarizability.

(c) *Magnetic moments*

A magnetic field induces magnetic moments in a molecule: $p_{mi} = m_{ik} H_k$. The diamagnetic susceptibility tensor m_{ik} has the same structure as the tensor of

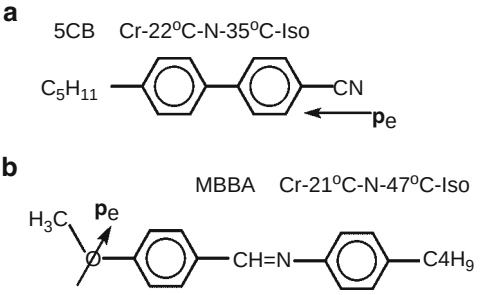

Fig. 3.7 The most popular among physicists molecules 5CB (**a**) and MBBA (**b**) forming liquid crystals at room temperature. Note strictly longitudinal and almost transverse direction of the dipole moments of the two molecules with respect to their long molecular axes

molecular polarizability with three or two different principal components. Some molecules possess permanent magnetic moments. For instance, the moments originate from unpaired electron spins in the inner shells of such metal atoms as M = Ni, Co, Fe, etc. in metal-mesogenic compounds (Fig. 3.8).

Another case is free radicals with permanent magnetic moments of such molecular groups as –NO, in which unpaired electron spins are located on oxygen atoms. Stability of such radicals is provided by sterical screening of a reaction center from the surrounding medium by bulky chemical groups (like methyl one). Such a radical can be a fragment of an elongated mesogenic molecule. It should be noted, however, that the field orientation of spin moments is almost decoupled from the molecular skeleton motion (in contrast to electric moments of molecular groups). The simultaneous orientation of spins and molecular skeletons by a magnetic field takes place only if the so-called spin-orbital interaction is significant.

3.2 Intermolecular Interactions

Atoms in an organic molecule are mostly bound by covalent bonds with high intramolecular interaction energy $W \sim 10^{12}$ erg/M (or 100 kJ/M in SI units). In units more convenient for a physicist: $W = 10^5$ J/$(1.6 \cdot 10^{-19} \cdot 6.02 \cdot 10^{23}) \approx 1$ eV/molecule. Intermolecular interactions are essentially weaker, of the order of 0.01–0.1 eV. Their nature can be quite different. A good example is 5CB forming molecular dimers, Fig. 3.9, due to interaction between two dipoles located on the two cyano-groups. Below we shall briefly consider the most important mechanisms of interactions between liquid crystal molecules. For the more advanced discussion of intermolecular potentials see [7].

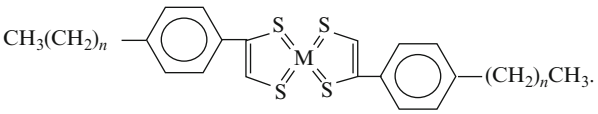

Fig. 3.8 An example of a molecule of metal-mesogenic compounds

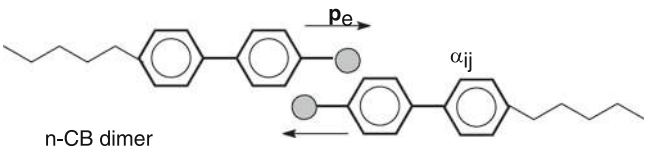

Fig. 3.9 A structure of a dimer formed by two molecules of compound 5CB due to dipole-dipole interaction. $\mathbf{P}_e$ and α_{ij} are molecular dipole and polarizability

(a) *Electrostatic interaction*

At a large distance from a system of charges, the electric field around the system can be expanded in a series of multipoles, see Fig. 3.10. Correspondingly the electrostatic molecular interactions can be classified by interaction energy as follows [8]:

Monopole (q) – monopole (q) (Coulomb energy):	$W \sim q^2/r$	
Monopole (q) – electric dipole (p_e):	qp_e/r^2	(Fixed dipole)
	$q^2{p_e}^2/r^4$	(Free rotating dipole)
Dipole (p_e) – dipole (p_e) (Keesom energy):	p_1p_2/r^3	(Fixed dipoles)
	${p_1}^2{p_2}^2/kTr^6$	(Free rotating dipoles)
Monopole (q) – induced dipole:	$q^2\alpha/r^4$	
Dipole (p_e) – induced dipole (Debye energy):	${p_1}^2\alpha/r^6$	
Dipole–quadrupole, quadrupole–quadrupole, etc.		

These general formulas can be used in the molecular theory of formation of mesophases.

(b) *Dispersion interaction*

This is also dipole–dipole interaction but between oscillating, not permanent dipoles. It is a pure quantum-mechanical effect of oscillatory motion of electrons in the ground state. It is described by the London formula (here ν is a frequency of a single oscillator considered):

$$U_{1,2} = -\frac{3(h\nu)\alpha^2}{4r^6}$$

In a more general case one has a sum of different oscillators. The dispersion interactions are partially responsible for the well known attractive term a/V^2 between neutral molecules in the Van der Waals equation of state $(p + a/V^2)(V - b) = RT$. The corresponding energy is of the order of 0.1 kJ/M or 10^{-4} eV/mol. By the way, the repulsive term $(V - b)$ in the same equation that takes into account the excluded volume effect b is due to the steric interaction discussed next.

(c) *Steric interaction and intermolecular potential*

Classically, one can consider atoms or molecules as non-penetrable for other atoms or molecules, Fig. 3.11. In fact it is a quantum-mechanical effect related to the Pauli principle. For spherical molecules, the Lennard-Jones (or 6–12) potential is often used [8, 9]:

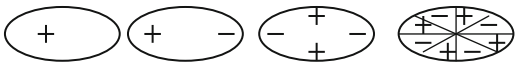

Fig. 3.10 Structures of different molecular multipoles, which could be responsible for the interaction of mesogenic molecules

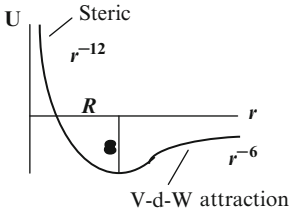

Fig. 3.11 The form of the Lennard-Jones potential for interaction of two spherical molecules located at a distance r from each other

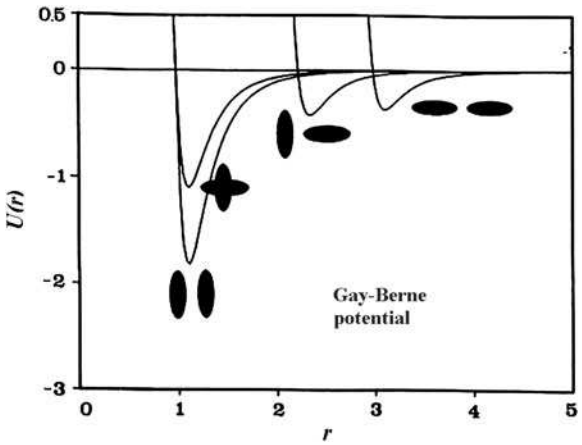

Fig. 3.12 Gay–Berne potential $U(r)$ as a function of intermolecular distance r between elongated molecules. Black ellipsoids mimic the pairs of interacting molecules in different geometry of interaction. Both scales are arbitrary

$$U(x) = \varepsilon(x^{-12} - x^{-6})$$

where $x = r/R$, R and ε are the equilibrium distance and interaction energy shown in the figure. For elongated molecules consisting of several atoms, the Gay–Berne potential shown in Fig. 3.12 is more realistic. This potential takes into account a mutual orientation of elongated molecules. From the same figure one may see how the equilibrium distance and the depth of the energy minimum differ for differently oriented molecules.

(d) *Hydrogen bonds*

This either intra- or intermolecular bond arises between strongly electro-negative atoms, such as oxygen or nitrogen, chlorine and fluorine. These atoms can be bound by a mediator, a proton that is partially forms a covalent bond with one of such atoms but also strongly interacts with the other electronegative atom. In this situation, an electrostatic interaction plays the dominant role but with some admixture of the covalent bond. To some extent, a proton has common orbital for the two connected atoms. A well-known example is water where oxygen atoms form

a network using the hydrogen atoms as bridges between them. A typical energy of the hydrogen bond is rather high, 10–50 kJ/M, i.e. 0.1–0.5 eV/molecule.

Hydrogen bonds can be responsible for formation of molecular dimers which, in turn, become building blocks for liquid crystal phases as shown Fig. 3.13a. Without O. . .H bonding, short molecules of benzoic acids would never form the nematic or SmC phases as they, in fact, do. Another example is the derivative of the cyclohexane-carboxylic acid (CHCA) shown in Fig. 3.13b Such cyclohexane-type dimers form the nematic phase with very low optical anisotropy. In the molecule (monomer) the cyclohexane moiety is in the chair-form and the $–C_4H_9$ and –COOH groups are in the *trans*-positions (*t*) as explained in Fig. 3.3. Such a dimer (*trans*-isomer) may be considered as rod-like. The corresponding *cis*-isomer would have a strongly bent-shape structure hardly compatible with liquid crystal phase. By the way, similar but reversible *trans–cis–trans* photo-isomerization is observed in compounds with azo-(–N=N–) or azoxy-(–N=NO–) bridges between phenyl rings. Such compounds may be used for the light control of the liquid crystal structure and properties.

(e) *Hydrophilic and hydrophobic interactions*

These interaction, although very important, are not as fundamental as the others. They are related to the affinity to water. Hydrophilic interactions include the same electrostatic, steric and H-bond interactions and all of them are, generally speaking, electromagnetic. The hydrophobic "interaction" is an entropy effect; there is no special repulsive force. For example, oil and water are immiscible. Merely water molecules feel more comfortable among the same neighbors, to which they form a network of H-bonds. If an oil molecule with its long hydrocarbon tail were incorporated into water, it would destroy the network and reduce the entropy of the mixture.

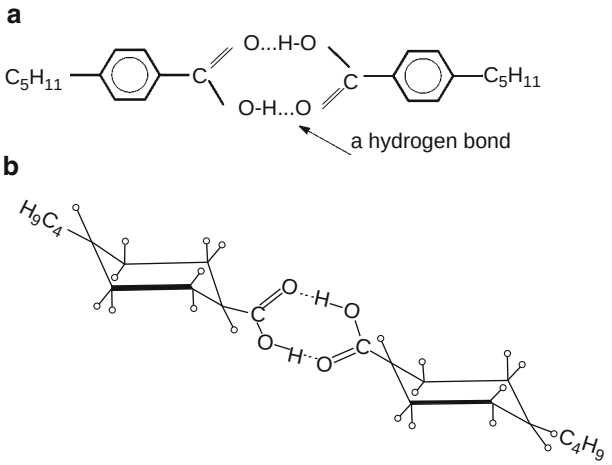

Fig. 3.13 The role of the hydrogen bond in formation of dimers of benzoic acid molecules (**a**) and cyclohexane-carboxylic acid molecules (**b**)

3.3 Orientational Distribution Functions for Molecules

The translational and orientational degrees of freedom can be treated separately (this follows from fundamentals of group theory which states that groups of translations and rotations are subgroups of the crystalline space groups: $P(\mathbf{r}, \Omega) = P(\mathbf{r}) \times P(\Omega)$. Here $\times$ is a symbol of the *group product*. In particular case of the isotropic liquid or nematic phase (no positional order) $P(\mathbf{r}, \Omega) = \rho P(\Omega)$ where $\rho = constant$ is density.

Generally, a one-particle distribution function $P(\mathbf{r}, \Omega)$ represents a probability to find a molecule with orientation Ω at position $\mathbf{r}$. Here Ω includes three Euler angles Ψ, Φ and ϑ as shown in Fig. 3.14. This probability is assumed to be independent of other particles. In the figure, x, y, z is a Cartesian laboratory frame, the z-axis is taken as a reference: usually it coincides with one of the symmetry axis of a *molecular system*. For a nematic phase discussed in this chapter, such a symmetry axis coincides with the preferable axis of orientation of molecules. This axis is called the *director*, a unit axial vector with head and tail indistinguishable, $\mathbf{n} = -\mathbf{n}$. We say the director has head-to-tail symmetry. If there is no interaction with surrounding, the director may take any direction and its realignment cost no energy (no energy gap to overcome). Such a gapless orientational motion that restores the spherical symmetry of the isotropic phase is called a Goldstone mode. Evidently, that the direction of the director may be fixed by a weak magnetic field or by interaction with the surfaces, and our z-axis is assumed to be fixed by some external factor.

The frame ξ, η, ζ is attached to a *molecule*. Then Euler angles correspond to

- Deflection of the longitudinal molecular ζ-axis from axis z (angle ϑ)
- Rotation of the molecular shortest η- axis about its own longitudinal ζ-axis (angle Ψ)
- Precession of the longitudinal ζ-axis within a cone surface around z (angle Φ)

In this chapter we consider only an *orientational distribution function f*(Ω) [10, 11]. Why do we need it? Because it is a kind of a bridge between the microscopic and macroscopic descriptions of the nematic phase. We define a value

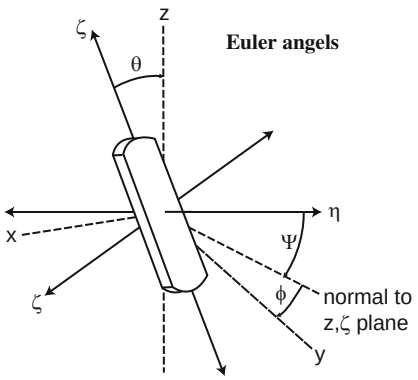

Fig. 3.14 Euler angles of the molecular frame ξ, η, ζ with respect to the Cartesian laboratory frame x, y, z

$$f(\Omega)d\Omega = f(\Phi, \vartheta, \Psi)\ \sin\vartheta\, d\Phi\, d\vartheta\, d\Psi \tag{3.1}$$

as a fraction of molecules in the "angular volume" with Euler angles between Φ and $d\Phi$, ϑ and $d\vartheta$, Ψ and $d\Psi$. Function $f(\Omega)$ is a single-particle function because molecules are considered to be independent, i.e. any correlation in their motion is disregarded. The total probability to find a molecule with any orientation equals 1:

$$\int f(\Omega)d\Omega = \int_0^{2\pi} d\Phi \int_0^{\pi} \sin\vartheta \mathrm{d}\vartheta \int_0^{2\pi} d\Psi \cdot f(\Phi, \vartheta, \Psi) = 1 \tag{3.2}$$

We can use this normalization condition to find the $f(\Omega)$ function, at least, for the isotropic liquid or isotropic liquid crystal phase. Indeed, in this case there is no angular dependence of $f(\Omega)$ i.e. $f(\Phi,\vartheta,\Psi)$ = const. After integrating we find: $f(\Phi,\vartheta,\Psi)_{\mathrm{iso}} = 1/8\pi^2$.

And what about optically uniaxial phases? In the case of a nematic, the molecular distribution is independent of the precession angle (Φ = const) but may depend on angle Ψ. For a smectic A, in the first approximation, the orientational distribution function is the same as for the nematic. However, there is some interaction between the translational and orientational degrees of freedom that can be taken into account as a correction to $f(\vartheta,\Phi)$. At first, consider a distribution function for a uniaxial phase consisting of axially symmetric molecules [12].

3.3.1 Molecules with Axial Symmetry

The molecules either have a generic infinite rotation axis (cones, rods, rotational ellipsoids, spherocylinders or discs) or acquire this average uniaxial form due to free rotation around the longitudinal molecular axis ζ. Then $f(\Omega)$ becomes Ψ-independent [13]: $f = f(\vartheta)/4\pi^2$ with $f(\vartheta) = f(\pi - \vartheta)$, see Fig. 3.15. This figure shows that angle 0 and π are equally and the most populated by molecules and these two angles correspond to the condition $\mathbf{n} = -\mathbf{n}$. The angles close to $\pi/2$ are the less populated. Now our task is to find the form of $f(\vartheta)$ and relate it to experimentally measured parameters.

As any axially symmetric function, $f(\vartheta)$ can be expanded in series of the Legendre polynomials $P_i(\cos\vartheta)$

$$f(\vartheta) = (1/2)[1 + a_1P_1(\cos\vartheta) + a_2P_2(\cos\vartheta) + a_3P_3(\cos\vartheta) + a_4P_4(\cos\vartheta) + ...] \tag{3.3}$$

Recall that the Legendre polynomials of general formula $P(x) = \dfrac{1}{2^n n!} \cdot \dfrac{d^n[(x^2-1)^n]}{dx^n}$, $n = 0, 1, 2, \ldots$ are solutions of the Legendre equation $(1-x^2)y'' - 2xy' + n(n+1)y = 0$, which are orthogonal to each other. The condition for orthogonality reads:

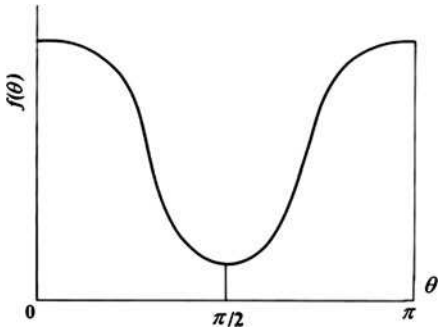

Fig. 3.15 Form of the molecular distribution function over the polar Euler angles ϑ

$$\int_{-1}^{1} P_m(x)P_n(x)dx = 0 \text{ for } m \neq n \quad \text{and} \quad \int_{-1}^{1} [P_m(x)]^2 dx = \frac{2}{2m+1} \tag{3.4}$$

The Legendre polynomials $P_m(x)$ are tabulated for $x = 0$–1. In our case, the polynomials depend on angle ϑ with $x = \cos\vartheta$ and the integration should be made from π to 0. For even or odd m the polynomials are even or odd functions of $\cos\vartheta$, respectively:

$P_0(\cos\vartheta) = 1$
$P_1(\cos\vartheta) = \cos\vartheta$
$P_2(\cos\vartheta) = (1/2)(3\cos^2\vartheta - 1)$
$P_3(\cos\vartheta) = (1/2)(5\cos^3\vartheta - 3\cos\vartheta)$
$P_4(\cos\vartheta) = (1/8)(35\cos^4\vartheta - 30\cos^2\vartheta + 3)$, etc.

Each function has a particular symmetry (like electron shells in atoms have their own symmetry *s*, *p*, *d*, etc.). The angular dependencies of the first two polynomials are plotted in Fig. 3.16.

In order to find numerical coefficients a_L we multiply both sides of Eq. (3.3) by $P_L(\cos\vartheta)$ and integrate over ϑ, using the orthogonality of Legendre polynomials, Eq.(3.4):

$$\int_{\pi}^{0} P_L(\cos\vartheta)f(\vartheta)d(\cos\vartheta) = \frac{1}{2}\int_{\pi}^{0} a_L[P_L(\cos\vartheta)]^2 d(\cos\vartheta) = \frac{a_L}{2L+1} L = 0, 1, 2, \ldots$$

Now we obtain

$$a_L = (2L+1)\frac{\int_{\pi}^{0} P_L(\cos\vartheta)f(\vartheta)\sin\vartheta d\vartheta}{\int_{\pi}^{0} f(\vartheta)d\cos\vartheta} \tag{3.5}$$

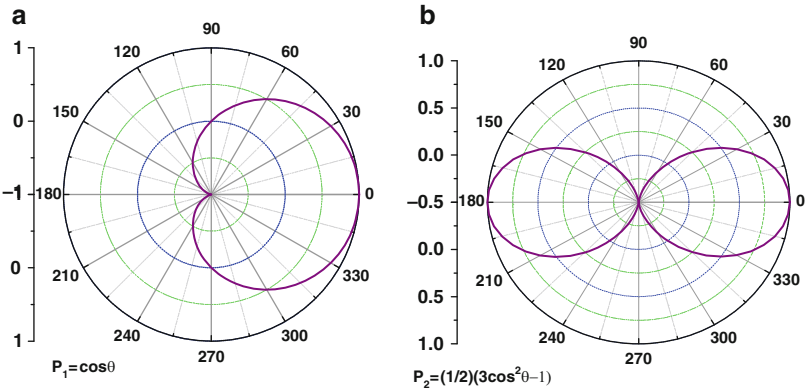

Fig. 3.16 Angular dependencies of the first two Legendre polynomials in polar coordinates

with the normalization condition (3.2) in denominator. As to the numerator, it is just the average value of polynomial $P_L(\cos\vartheta)$ written in the form of the *theorem of average*. Finally we obtain numerical coefficients:

$$a_L = (2L+1)\cdot\langle P_L(\cos\vartheta)\rangle \tag{3.6}$$

Note that $<P_L(\cos\vartheta)>$ are ϑ-dependent numbers, not functions. Finally we can write the orientational distribution function *for a uniaxial medium composed of uniaxial molecules*:

$$f(\vartheta) = (1/2)\left[\begin{array}{c} 1+3\langle P_1(\cos\vartheta)\rangle P_1(\cos\vartheta)+5\langle P_2(\cos\vartheta)\rangle P_2(\cos\vartheta)+ \\ 7\langle P_3(\cos\vartheta)\rangle P_3(\cos\vartheta)+9\langle P_4(\cos\vartheta)\rangle P_4(\cos\vartheta)+\ldots \end{array}\right] \tag{3.7}$$

The set of amplitudes a_L may be considered as a set of order parameters for the medium discussed. All of them together provide a complete description of $f(\vartheta)$.

For uniaxial molecules *with inversion center* (i.e. having head-to tail symmetry of a cylinder) the odd terms disappear:

$$f(\vartheta) = (1/2)[1+5\langle P_2(\cos\vartheta)\rangle P_2(\cos\vartheta)+9\langle P_4(\cos\vartheta)\rangle P_4(\cos\vartheta)+\ldots] \tag{3.8}$$

or briefly:

$$f(\vartheta) = f(\cos\vartheta) = \sum_0^\infty \frac{1}{2}(4l+1)S_{2l}P_{2l}(\cos\vartheta) \text{ with } l = 0,1,2\ldots \tag{3.9}$$

As mentioned above, coefficients S_{2L} are unknown numbers: $S_0 \equiv 1$, $S_1 = <P_1(\cos\vartheta)> = <\cos\vartheta>$, $S_2 = <P_2(\cos\vartheta)> \equiv (1/2)\ <3\cos^2\vartheta - 1>$, $S_4 = <P_4(\cos\vartheta)> \equiv (1/8)<35\cos^4\vartheta - 30\cos^2\vartheta + 3>$, etc. Therefore, instead of

unknown function $f(\vartheta)$ we can operate with unknown numbers that can easier be found from experiment.

3.3.2 Lath-Like Molecules

The phase is still uniaxial with head-to-tail symmetry, i.e., its distribution function is independent of the precession angle Φ that is $f(\Omega) = f(\vartheta, \Psi)/2\pi$. However, nuclear magnetic resonance (NMR) shows that the free rotation of molecules about their long axes (angle Ψ) is, to some extent, hindered as shown in Fig. 3.17a. In the figure the preferable direction of the longest molecular axes (director) is parallel to z. Then we can distinguish among two different cases of local molecular orientation with two projections S_z of a short molecular axis onto the director, either large as in Fig. 3.17b or, in fact, zero (Fig. 3.17c).

As a consequence, the refraction index component perpendicular to the director $n_\perp$ is larger in case b than in case c, and the component $n_\parallel$ is smaller. Therefore, the optical anisotropy $\Delta n = n_\parallel - n_\perp$ in case b is smaller. To take the new situation into account, two *local* order parameters are introduced for the *uniaxial nematic phase*, one is the same as discussed above for the longitudinal molecular axes ($S = S_{\zeta\zeta}$), and the other describes the *local order* of the shortest molecular axes that is *local biaxiality* (D):

$$\begin{aligned} S_{\varsigma\varsigma} &= \frac{1}{2}\left\langle 3\cos^2\vartheta - 1\right\rangle \\ D = S_{\xi\xi} - S_{\eta\eta} &= \frac{3}{2}\left\langle \sin^2\vartheta \cos 2\Psi\right\rangle \end{aligned} \tag{3.10}$$

For the ideal nematic with $\sin\vartheta = 0$ and $S_{\zeta\zeta} = 1$ there is no difference between cases b and c. The locally (microscopically) biaxial nematic phase should not be confused with *macroscopically biaxial phases* to be discussed in the next section.

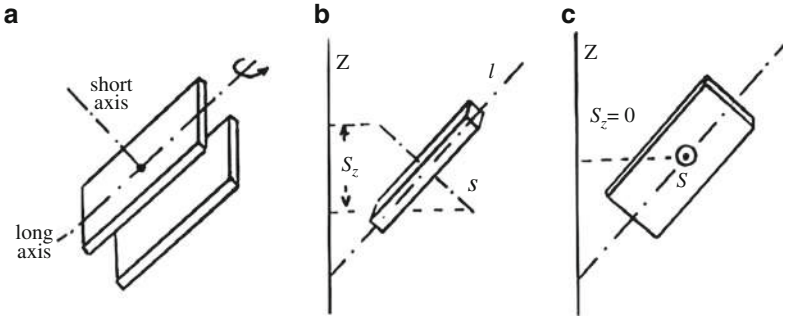

Fig. 3.17 Local packing of lath-like molecules that hinders rotation of individual molecules about their longest axes (**a**) and illustration of a large (**b**) or zero (**c**) projections S_z of a short molecular axis onto the director axis z. s and l are the shortest and longest axes of a lath-like molecule

3.4 Principal Orientational Order Parameter (Microscopic Approach)

We discuss nematics, therefore $\mathbf{n} = -\mathbf{n}$ (no polarity) and $f(\vartheta)$ is cylindrically symmetric function (point group $D_{\infty h}$). We would like to know this function for each particular substance at variable temperature but, unfortunately, $f(\vartheta)$ (that is all amplitudes S_{2l} in expansion (3.9)) is difficult to measure. We may, however, limit ourselves with one or few leading terms of the expansion and find approximate form of $f(\vartheta)$.

For instance, why not to take S_0 or S_1? For conventional nematics they are useless because S_0 is angle independent and $S_1 = <\cos\vartheta>$ is an odd function incompatible with $\mathbf{n} = -\mathbf{n}$ condition. By the way, S_1 is very useful for discussion of phases with polar order, in which the head-to-tail molecular symmetry is broken (e.g., in phases with the conical symmetry $C_{\infty v}$ instead of cylindrical symmetry $D_{\infty h}$).

The next is coefficient $S_2 = (1/2) <3\cos^2\vartheta - 1>$ introduced by Tsvetkov [14] that describes the *quadrupolar order*. It looks suitable, at least, when we consider important particular cases:

(i) For the ideal nematic with all rod-like molecules parallel to each other $<\cos^2\vartheta> = 1$ and $S_2 = 1$.
(ii) For complete orientational disorder $<\cos^2\vartheta> = 1/3$, $S_2 = 0$ and this corresponds to the isotropic phase.
(iii) There is another possible molecular orientation also corresponding to $<\cos^2\vartheta> = 1/3$ and $S_2 = 0$: it is a "magic" orientation (see below), that would correspond to the nematic phase with finite higher S_{2l} coefficients.
(iv) One can put all molecules in the plane perpendicular to the principal axis and then everywhere $\vartheta = \pi/2$, $<\cos^2\vartheta> = 0$ and $S_2 = -1/2$. The phase with $S_2 = -1/2$ would still be conventional nematic phase, but such nematics have not been found yet. However, by evaporation of organic compounds consisted of rod-like molecules onto a solid substrate, one can prepare amorphous solid films of the $D_{\infty h}$ symmetry which would mimic the nematic phase with $S_2 \approx -1/2$, see Fig. 3.18.

From (i) to (iv) we conclude that, as the first approximation to the microscopic orientational distribution function of a nematic, we can take from Eq. (3.9) only one term with $l = 1$ and $S_2 = (1/2) <3\cos^2\vartheta - 1>$:

$$f(\vartheta) = f(\cos\vartheta) \approx (1/2)(4L+1)S_2P_2(\cos\vartheta) = (5/2)S_2P_2(\cos\vartheta) \qquad (3.11)$$

The function (3.11) with coefficient 5/2 ignored is shown in Fig. 3.19 for two different values of S_2. The curves marked as $S_2 = 1$ and $S_2 = 0.6$ correspond to the ideal and typical nematics, respectively. For the isotropic phase the corresponding curve would coincide with zero line.

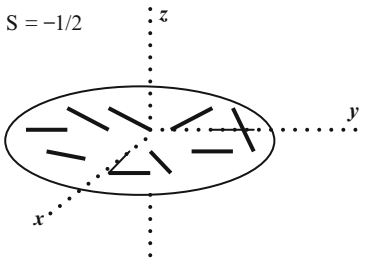

Fig. 3.18 Illustration of a virtual nematic phase with order parameter $S = -1/2$

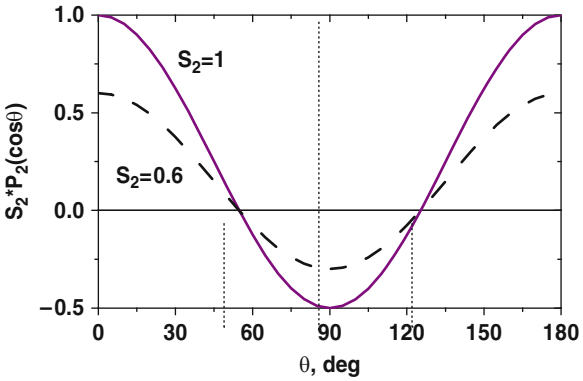

Fig. 3.19 Orientational distribution function of molecules for two different values of order parameter S_2

Parameter S_2 can be found from the anisotropy of magnetic susceptibility, optical dichroism and birefringence, NMR, etc. The determination of higher order parameters requires for more sophisticated techniques. For instance, S_4 can be found from Raman light scattering [15], luminescence or other two-wave interaction optical experiments. Data on S_6, S_8 are not available at present. In some cases, the X-ray scattering can even provide $f(\vartheta)$ as a whole but with limited accuracy.

To illustrate the importance of higher order terms, particularly S_4, consider two molecular distributions shown in Fig. 3.20. On the left side, all molecules of a virtual nematic phase are at the same angle $\vartheta = 54.73$ deg, therefore $f(\vartheta) \propto \delta(\vartheta - 54.73)$. For this "magic" orientation, $\cos^2\vartheta = 1/3$, $\cos^4\vartheta = 1/9$ and $S_2 = 0$, $S_4 = -7/18$ (see Legendre polynomials P_2 and P_4 written above). On the right side, the molecules of another virtual nematic are scattered over angles around $\vartheta = 54.73$ deg in such a special way that the average $<\cos^2\vartheta>$ calculated with new $f(\vartheta)$ function is again equal to 1/3 and, as before, $S_2 = 0$. However, $<\cos^4\vartheta>$ calculated with new $f(\vartheta)$ and new S_4 is different from $-7/18$. Therefore to distinguish between

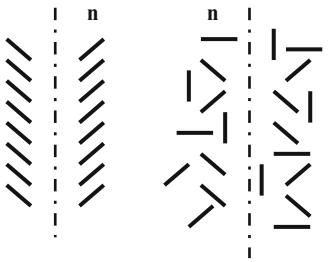

Fig. 3.20 Illustration of importance of higher order terms: the two very different, virtual molecular distributions have the same S_2 order parameter but differ by the values of higher order parameters S_4, S_6, etc.

two molecular distributions we have to take into account at least S_4 or as many S_{2l} coefficients as possible.

3.5 Macroscopic Definition of the Orientational Order Parameter

3.5.1 Tensor Properties

Generally, properties of liquid crystals depend on direction, they are tensorial. Some of them (like density in nematics) may be scalar. A scalar is a tensor of rank 0. It has one component in a space of any dimensionality, $1^0 = 2^0 = 3^0 \ldots = 1$. Other properties, like spontaneous polarization **P** (e.g., in chiral smectic C*) are vectors, i.e., the tensors of rank 1. In the two-dimensional space they have $2^1 = 2$ components, in the 3D space there are $3^1 = 3$ components. For instance in the Cartesian system $\mathbf{P} = \mathbf{i}P_x + \mathbf{j}P_y + \mathbf{k}P_z$. Such a vector can be written as a row (P_x, P_y, P_z) or as a column. Properties described by tensor of rank 2 have $2^2 = 4$ components in 2D space and $3^2 = 9$ components in the 3D-space. They relate two vector quantities, such as magnetization **M** and magnetic induction **B**, $\mathbf{M} = \chi\mathbf{B}$, where χ is magnetic susceptibility. Each of the two vectors has three components and, generally, each component (projection) M_α ($\alpha = x,y,z$) may depend on each of B_β components ($\beta = x,y,z$):

$M_x = \chi_{xx}B_x + \chi_{xy}B_y + \chi_{xz}B_z$; $M_y = \chi_{yx}B_x + \chi_{yy}B_y + \chi_{yz}B_z$; $M_z = \chi_{zx}B_x + \chi_{zy}B_y + \chi_{zz}B_z$ or in the matrix form:

$$\begin{vmatrix} M_1 \\ M_2 \\ M_3 \end{vmatrix} = \begin{vmatrix} \chi_{11} & \chi_{12} & \chi_{13} \\ \chi_{21} & \chi_{22} & \chi_{23} \\ \chi_{31} & \chi_{32} & \chi_{33} \end{vmatrix} \cdot \begin{vmatrix} B_1 \\ B_2 \\ B_3 \end{vmatrix}$$

The matrix representation can be written in a more compact form

$$M_\alpha = \sum_\beta \chi_{\alpha\beta}B_\beta = \chi_{\alpha\beta}B_\beta. \tag{3.12}$$

Here α, $\beta = 1, 2, 3$ and, following Einstein, the repeated index β means summation over β.

The magnetization was only taken as an example. Many other properties (dielectric susceptibility, electric and thermal conductivity, molecular diffusion, etc.) are also described by second rank tensors of the same (quadrupolar) type $\chi_{\alpha\beta}$. Microscopically, such properties can be described by single-particle distribution functions, when intermolecular interaction is neglected. There are also properties described by tensors of rank 3 with $3^3 = 27$ components (e.g., molecular hyperpolarizability γ_{ijk}) and even of rank 4 (e.g., elasticity in nematics, K_{ijkl}) with $3^4 = 81$ components. Microscopically, such elastic properties must be described by many-particle distribution functions.

As physical properties of the matter are independent of the chosen frame, suffixes α and β can be interchanged. Therefore, $\chi_{\alpha\beta} = \chi_{\beta\alpha}$ and only 6 components of $\chi_{\alpha\beta}$ are different, three diagonal and the other three off-diagonal. Such a symmetric tensor (or matrix) can always be diagonalized by a proper choice of the Cartesian frame whose axes would coincide with the symmetry axes of the LC phase. In that reference system only three diagonal components χ_{11}, χ_{22} and χ_{33} are finite.

3.5.2 Uniaxial Order

For a uniaxial phase (nematic, discotic nematic, SmA, SmB, etc.) with the symmetry axis along z, all properties along x and y are the same and $\chi_{11} = \chi_{22} \neq \chi_{33}$. The corresponding matrix

$$\chi_{\alpha\beta} = \begin{vmatrix} \chi_\perp & 0 & 0 \\ 0 & \chi_\perp & 0 \\ 0 & 0 & \chi_{II} \end{vmatrix} \tag{3.13}$$

has only two different components and the relevant physical quantity can be decomposed into two parts, the mean value $<\chi> = (1/3)(\chi_{\parallel} + 2\chi_\perp)$ and the anisotropic part $\Delta\chi = \chi_a = \chi_{\parallel} - \chi_\perp$.

The anisotropic part of tensor (3.13) is

$$\chi^{(a)}_{\alpha\beta} = \chi_{\alpha\beta} - \langle\chi\rangle\delta_{\alpha\beta}$$

where $\delta_{\alpha\beta}$ is second rank unit tensor with trace $\delta_{xx} + \delta_{yy} + \delta_{zz} = 3$. Hence, the *anisotropy tensor* is traceless, has dimension of the χ value and becomes zero in the isotropic phase:

$$\chi^a_{\alpha\beta} = \begin{vmatrix} \chi_\perp & 0 & 0 \\ 0 & \chi_\perp & 0 \\ 0 & 0 & \chi_{II} \end{vmatrix} - \begin{vmatrix} \langle\chi\rangle & 0 & 0 \\ 0 & \langle\chi\rangle & 0 \\ 0 & 0 & \langle\chi\rangle \end{vmatrix} = \begin{vmatrix} -1/3\chi_a & 0 & 0 \\ 0 & -1/3\chi_a & 0 \\ 0 & 0 & 2/3\chi_a \end{vmatrix}$$

In principle, this tensor might be used as orientational order parameter for a uniaxial phase, however, its dimensionless form would be more preferable. Therefore, we normalize anisotropy χ_a to the maximum possible anisotropy corresponding to the ideal molecular alignment as in a solid crystal at absolute zero temperature. Then we arrive at the *order parameter tensor* [16]*:*

$$Q_{\alpha\beta} = \frac{\chi_{\alpha\beta}^{(a)}}{\chi_{\alpha\beta}^{\max}} = \frac{\chi_a}{\chi_a^{\max}} \cdot \begin{vmatrix} -1/3 & 0 & 0 \\ 0 & -1/3 & 0 \\ 0 & 0 & 2/3 \end{vmatrix} \tag{3.14}$$

Here $S = \chi_a/\chi_a^{\max}$ is a scalar modulus of the order parameter dependent on the degree of molecular (statistical) order whereas the tensor shows the orientational part of the order parameter. With such an approach, the macroscopic and microscopic definitions of the order parameter would coincide if we assume

$$S = \chi_a/\chi_a^{\max} = S_2 = <P_2(\cos\vartheta)> = \frac{1}{2}\left\langle 3\cos^2\vartheta - 1\right\rangle \tag{3.15}$$

The experimental values of the orientational order parameter found macroscopically for conventional nematics from the magnetic or optical anisotropy are in good agreement with those calculated from microscopic data (NMR, Raman spectroscopy).

Order parameter tensor can be written using the director components n_α (α=x,y,z).

$$Q_{\alpha\beta} = \frac{\chi_a}{\chi_a^{\max}}\left(n_\alpha n_\beta - \frac{1}{3}\delta_{\alpha\beta}\right) = S\left(n_\alpha n_\beta - \frac{1}{3}\delta_{\alpha\beta}\right) \tag{3.16}$$

For example, for $\mathbf{n}\|z$ the director components are (0, 0, 1) and from (3.16) we immediately get the form (3.14). Here we clearly see the two components of the order parameter, the scalar amplitude S and the orientational part (in parentheses).

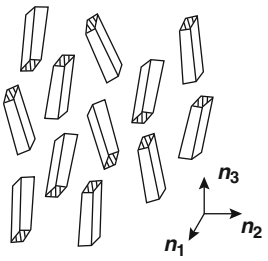

Fig. 3.21 Packing of molecules in a macroscopic nematic biaxial phase of symmetry D_{2h}

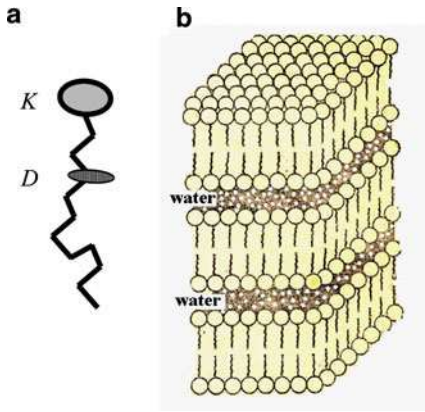

Fig. 3.22 A molecule of potassium (K) laurate with deuterium (D) label (**a**) and a structure of the lyotropic lamellar phase (**b**)

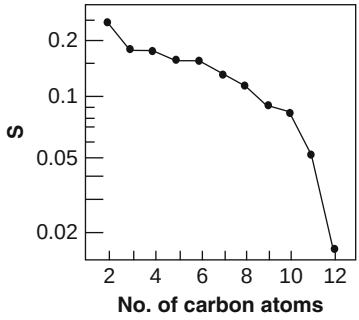

Fig. 3.23 Lamellar lyotropic phase of potassium laurate: orientational order parameter for individual links of the molecular chain as a function of the distance of the link from the potassium atom

3.5.3 Macroscopic Biaxiality

In contrast to quite common microscopically biaxial nematics belonging to point group $D_{\infty h}$ and discussed in the previous section, the macroscopically biaxial phase (group D_{2h}) shown in Fig. 3.21 has unequivocally been found only in lyotropic nematics [17] formed by some biphilic (or amphiphilic) molecules in water solutions [18]. Some other cases are still under discussion (nematics formed by metallomesogens, banana-like [19] or polymer molecules [20]). Strictly speaking, cholesteric liquid crystals (or, more generally, chiral nematics) may be regarded as weakly biaxial. Less symmetric phases such as smectic C, smectic E, etc. are, of course, macroscopically biaxial.

In macroscopically biaxial phase all the three components of a physical property are different, e.g., $\chi_{11} \neq \chi_{22} \neq \chi_{33}$, the trace of tensor $\chi_{\alpha\beta}$ is $\chi_{11} + \chi_{22} + \chi_{33} = 3<\chi>$ and the tensor itself can be written as $\chi_{\alpha\beta} = 3<\chi>Q_{\alpha\beta}$ with the traceless order parameter tensor

$$Q_{\alpha\beta} = \begin{vmatrix} -(1/3)(Q_1 - Q_2) & 0 & 0 \\ 0 & -(1/3)(Q_1 + Q_2) & 0 \\ 0 & 0 & (2/3)Q_1 \end{vmatrix} \tag{3.17}$$

Now the biaxial nematic phase has two order parameters Q_1 and Q_2 and, in general, three different phases can be distinguished, namely, isotropic ($Q_1 = Q_2 = 0$), uniaxial nematic (Q_1,$Q_2 = 0$) and biaxial nematic (Q_1,Q_2) phases. Note that biaxial molecules may form both biaxial and uniaxial phases; the latter appear due, for instance, to free rotation of biaxial molecules around their long molecular axes. As to the uniaxial molecules, they may also form either uniaxial (as a rule) or biaxial phases; the latter may be formed by biaxial dimers or other "building blocks" formed by uniaxial molecules.

3.6 Apparent Order Parameters for Flexible Chains

When molecules are not so simple as rigid rods or discs, one may introduce apparent partial order parameters different for different molecular moieties. This is especially evident for lyotropic liquid crystals [21], such as, for instance, the lamellar phase formed by surfactants in water, see Fig. 3.22b. A good example is a water solution of potassium laurate. A flexible hydrocarbon chain K–CH_2–CH_2–$\mathbf{CD_2}$–CH_2–... can be deuterated with a position of deuterium label varied along the chain, as shown by in Fig. 3.22a. Then, by the NMR technique sensitive only to deuterium nuclei, the apparent order parameter of the corresponding chain link can be determined. As shown in Fig. 3.23, it decreases with increasing the distance from the potassium atom due to flexibility of the hydrocarbon chain. Thus, we can say that the hydrocarbon tail is "solid" at the left end and "liquid" at the right one [22].

References

1. Gray, G.W.: Molecular Structure and the Properties of Liquid Crystals. Academic, London (1962)
2. Gray, G.W.: Liquid crystals and molecular structure: nematics and cholesterics. In: Luckhurst, G.R., Gray, G.W. (eds.) The Molecular Physics of Liquid Crystals, pp. 1–29. Academic, London (1979). Chapter 1
3. Gray, G.W.: Liquid crystals and molecular structure: smectics. In: Luckhurst, G.R., Gray, G.W. (eds.) The Molecular Physics of Liquid Crystals, pp. 263–284. Academic, London (1979). Chapter 12
4. Hall, A.W., Hollinghurst, J., Goodby, J.W.: Chiral and achiral calamitic liquid crystals for display applications. In: Collings, P., Patel, J. (eds.) Handbook of Liquid Crystal Research, pp. 17–71. Oxford University Press, New York (1997)
5. Blinov, L.M., Chigrinov, V.G.: Electrooptic Effects in Liquid Crystal Materials. Springer-Verlag, New York (1993)
6. Kuball, H.-G.: From chiral molecules to chiral phases: comment on the chirality of liquid crystal phases. Liquid Crystals Today **9**(1), 1–7 (1999)
7. Osipov, M.A.: Molecular theories of liquid crystals. In: Demus, D., Goodby, J., Gray, G.W., Spiess, H.-W., Vill, V. (eds.) Physical Properties of Liquid Crystals, pp. 40–71. Wiley-VCH, Weinheim (1999)

8. Israelachvili, J.N.: Intermolecular and Surface Forces, 2nd edn. Academic Press, London (1992)
9. Stone, A.J.: Intermolecular forces. In: Luckhurst, G.R., Gray, G.W. (eds.) The Molecular Physics of Liquid Crystals, pp. 31–50. Academic, London (1979). Chapter 2
10. Zannoni, C.: Distribution functions and order parameters. In: Luckhurst, G.R., Gray, G.W. (eds.) The Molecular Physics of Liquid Crystals, pp. 51–84. Academic, London (1979). Chapter 3
11. Vertogen, G., de Jeu, V.H.: Thermotropic Liquid Crystals. Fundamentals. Springer-Verlag, Berlin (1987)
12. Wojtowicz, P.: Introduction to molecular theory of liquid crystals. In: Priestley, E.B., Wojtowicz, P., Sheng, P. (eds.) Introduction to Liquid Crystals, pp. 31–44. Plenum Press, N-Y (1975)
13. de Gennes, P.G., Prost, J.: The Physics of Liquid Crystals, 2nd edn. Oxford Publishers University Press, Oxford (1995)
14. Zwetkoff, W.: Über die Molecülanordnung in der anisotrop-flüssigen phase. Acta Physicochim. URSS **16**, 132 (1942)
15. Pershan, P.S.: Raman studies of orientational order in liquid crystals. In: Luckhurst, G.R., Gray, G.W. (eds.) The Molecular Physics of Liquid Crystals, pp. 385–410. Academic, London (1979). Chapter 17
16. de Gennes, P.G.: Short range order effects in the isotropic phase of nematics and cholesterics. Mol. Cryst. Liq. Cryst. **12**, 193–314 (1971)
17. Sonin, A.S.: Lyotropic nematics. Usp. Fiz. Nauk. **153**, 273–310 (1987). in Russian
18. Yu, L.J., Saupe, A.: Observation of a biaxial nematic phase in potassium-laurate -1-decanol-water mixtures. Phys. Rev. Lett. **45**, 1000 (1980)
19. Acharya, B.R., Primak, A., Kumar, S.: Biaxial nematic phase in bent-core thermotropic mesogens. Phys. Rev. Lett. **92**(14), 145506 (2004)
20. Severing, K., Saalwächter, K.: Biaxial nematic phase in a thermotropic liquid-crystalline side-chain polymers. Phys. Rev. Lett. **92**(14), 125501 (2004)
21. Pershan, P.S.: Lyotropic Liquid crystals, pp. 34–39. Physics Today, May (1982)
22. Charvolin, J., Tardieu, A.: Lyotropic liquid crystals; structures and molecular motions. In: Liebert, L., Ehrenreich, H., Seitz, F., Turnbull, D. (eds.) Liquid Crystals. Solid State Physics, pp. 209–258. Academic, New York (1978)

Chapter 4
Liquid Crystal Phases

This chapter presents a review of different liquid crystal phases. The main attention is paid to the thermotropic liquid crystals, which manifest rich polymorphism upon variation of temperature. Moreover, the thermotropic phases are subdivided into rod-like or calamitic and discotic ones; the latter are discussed only briefly. At first, we discuss achiral media with lyotropic phases included and then consider the role of chirality.

4.1 Polymorphism Studies

The polymorphic transformations can be studied by different techniques that are illustrated below by some characteristic examples.

4.1.1 Polarized Light Microscopy

It is very simple and vivid method [1]. One can observe characteristic streaks (Schlieren-textures) showing particular macroscopic defects, e.g., disclinations and establish the phase symmetry. In Fig. 4.1a the characteristic defects of the nematic phase (disclinations), are well seen. Fan-shape texture of the smectic C phase is shown in Fig. 4.1b. One can also distinguish between different types of uniform molecular orientation in different liquid crystal preparations using a conoscopy technique (microscopic observations in the convergent light beam): in this case symmetry of the pattern corresponds to the texture symmetry.

A very useful technique is a study of *miscibility* of different substances [2]. As a rule, only identical phases are mixed with each other (nematic with nematic, smectic A (SmA) with SmA, SmC with SmC etc.). Therefore, using a well investigated substance as a reference, one can make a preliminary conclusion about a structure of a new compound not doing X-ray and other cumbersome structural studies. For instance, by mixing with a reference liquid crystal, it was concluded

L.M. Blinov, *Structure and Properties of Liquid Crystals*,
DOI 10.1007/978-90-481-8829-1_4,

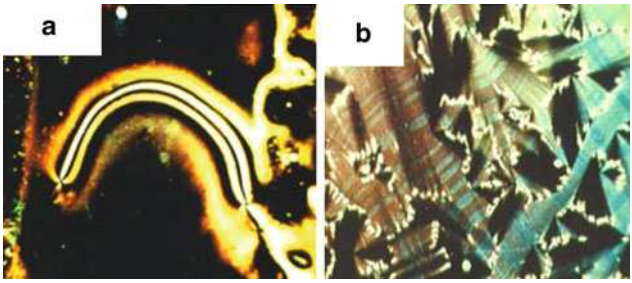

Fig. 4.1 Textures of the nematic (**a**) and smectic C (**b**) phases observed with a polarization microscope

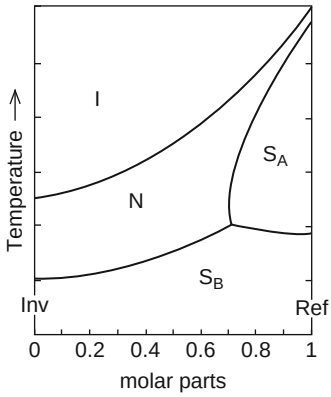

Fig. 4.2 Miscibility diagram: **Ref** and **Inv** mean the reference compound with well known phase sequence and unknown compound to be investigated. Starting with molar content $c = 1$ and proceeding to the left while measuring phase transition temperatures one finally arrives at $c = 0$ with complete phase diagram, therefore, having information about the unknown compound

that substance p-methoxy-p′-pentylstilbene (MOPS), see Fig. 4.2, has the SmB (below 110°C), Nematic (110–125°C) and Isotropic (above 125°C) phases.

4.1.2 Differential Scanning and Adiabatic Calorimetry (DSC and AC)

These techniques are widely used in investigations of phase transitions. DSC allows the express measurements of the transition enthalpy and determination of the phase transition type. For example, at the SmB-Cr (crystal) transition a great amount of enthalpy is released as evident from Fig. 4.3. Therefore, with high probability, this transition is of strong first order, the others shown in the figure (Isotropic phase-SmA and SmA–SmB) are not as strong and may be referred to as weak first order transitions. True second order transitions may not be seen in DSC plots due to negligibly small transition enthalpy. Specific features of such transitions are studied by adiabatic calorimetry (e.g., anomaly in heat capacitance) and dilatometry (density changes at transitions).

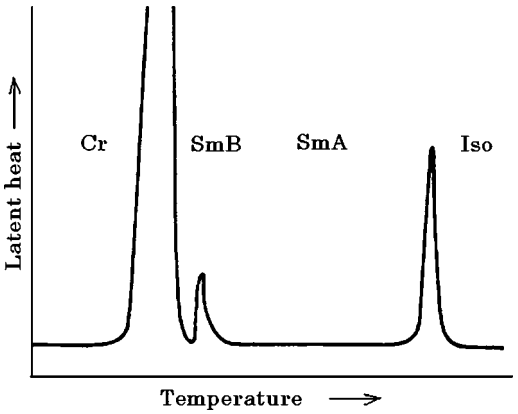

Fig. 4.3 Qualitative example of a DSC spectrum: latent heat of transitions as a function of temperature

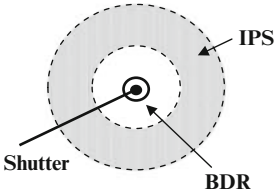

Fig. 4.4 Scheme of an X-ray diffractogram for a smectic A phase. The beam is impinged on the sample perpendicularly to the figure plane and forms a cone of diffraction. The directly transmitted beam is blocked by a shutter. The sharp ring BDR means the small-angle *Bragg diffraction ring* while IPS means diffuse wide-angle *in-plane scattering* halo

4.1.3 X-Ray Analysis

This is a very powerful method [3, 4] and later we shall discuss it in detail in Chapter 5. Here, only a schematic picture is presented, Fig. 4.4. An X-ray beam passes through a liquid crystal preparation and the diffracted beams form a cone with 2ϑ angle at the apex and are registered by a photodetector. In this particular example a smectic A liquid crystal is not oriented and the presented pattern is an analog of a Lauegram observed on crystalline powders. First we see a very sharp ring at small angles. It is a fingerprint of a lamellar structure. Like in solid crystals, the X-ray beam of wavelength λ can be reflected from stacks of parallel molecular layers according to the Bragg law to be discussed in Section 5.2.2: $2d_{hkl} \sin\vartheta = m, \lambda m = 1, 2, 3, \ldots$, where h, k, l are Miller indices (001, 002, etc. in our case), d is interlayer distance and ϑ is the diffraction angle. From this formula d can be found from the ϑ-angle measured: for instance, if $2\vartheta \approx 3^\circ$ for m=1 (first order reflection), then $\sin\vartheta \approx 0.026$ and $\lambda \approx 0.1$ nm, $d \approx 1.9$ nm. Thus, the interlayer distance corresponds to the length of the molecule and the phase is an

orthogonal smectic. A diffuse ring at wide angle shows that the in-plane structure is liquid like therefore the phase is most probably SmA. The average intermolecular distance in the transverse direction may be estimated from the radius of the diffuse ring using the same formula.

4.2 Main Calamitic Phases

4.2.1 Nematic Phase

The isotropic phase formed by achiral molecules has continuous point group symmetry K_h (spherical). According to the group representations [5], upon cooling, the symmetry K_h lowers, at first, retaining its overall translation symmetry T(3) but reduces the orientational symmetry down to either conical or cylindrical. The cone has a polar symmetry $C_{\infty v}$ and the cylinder has a quadrupolar one $D_{\infty h}$. The absence of polarity of the nematic phase has been established experimentally. At least, polar nematic phases have not been found yet. In other words, there is a head-to-tail symmetry taken into account by introduction of the director $\mathbf{n}(\mathbf{r})$, a unit axial vector coinciding with the preferred direction of molecular axes dependent on coordinate ($\mathbf{r}$ is radius-vector).

The nematic phase is characterized by the following properties:

(i) $\mathbf{n}(\mathbf{r}) = -\mathbf{n}(\mathbf{r})$ (absence of polarity) and, in the Cartesian system shown in Fig. 4.5a the director has components $(n_x, n_y, n_z) = (0, 0, 1)$.

(ii) Point group symmetry is $D_{\infty h}$ (according to Schönflies) or ∞/mm (international). There are one ∞-fold rotation axis, i.e., the director axis, the infinite number of vertical symmetry planes containing $\mathbf{n}$ and one mirror plane perpendicular to $\mathbf{n}$. The same symmetry has a discotic nematic phase. The

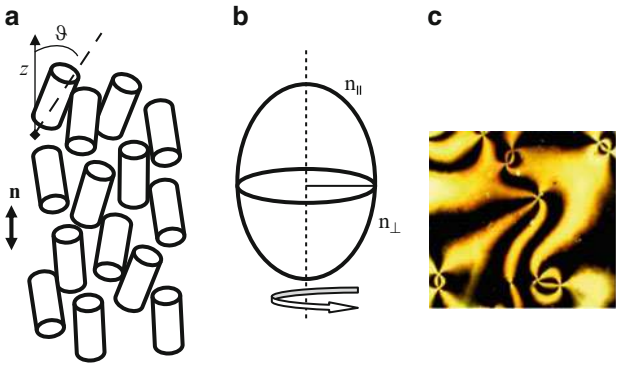

Fig. 4.5 The nematic phase: molecular orientation (**a**), optical indicatrix (**b**) and characteristic microscopic texture (**c**)

orientational order is characterized by a tensor discussed in Chapter 3 whose amplitude (order parameter) is $S = (1/2)<3\cos^2\Theta - 1>$ (here Θ is an angle the individual molecule forms with the direction **n**).

(iii) Translational symmetry is T(3), the translational motion of molecules is possible in any direction, therefore, the density is independent of coordinates, $\rho = \text{const}$, and the nematic phase is the most fluid one. For this reason it is the most interesting for applications to displays.

(iv) It is optically uniaxial phase, as a rule positively uniaxial, $n_z = n_{\parallel} > n_x = n_y = n_{\perp}$. The optical indicatrix presented in Fig. 4.5b has a form of the prolate ellipsoid contrary to oblate optical ellipsoid typical of discotic nematics which, as a rule, are optically negative. The dielectric ellipsoid is discussed in more detail in Section 11.1.1.

(v) The nematic phase has very characteristic microscopic texture observed with crossed polarizers. In Fig. 4.5c we can see typical point disclinations, the nuclei of divergent brushes or threads. The threads (Greek νεμα) have given the name "nematic" to the phase considered. The structure of disclinations is accounted for by modern theory of elasticity, Section 8.4.

4.2.2 Classical Smectic A Phase

The classical SmA phase can form on cooling the nematic phase or directly from the isotropic phase. Now we meet a new feature: the phase becomes periodic in one direction. In Fig. 4.6 the interlayer distance equal in this case to period is marked by letter *d*. Thus, the SmA phase is simultaneously *a one-dimensional solid and a two-dimensional liquid*. There is no correlation between molecular positions in the neighbor layers. Such a phase predominantly forms by more or less symmetric molecules with long alkyl chains.

The SmA phase is characterized by the following properties:

(i) As in the nematic phase, $\mathbf{n}(\mathbf{r}) = -\mathbf{n}(\mathbf{r})$. In the figure the director has components $(n_x, n_y, n_z) = (0, 0, 1)$.

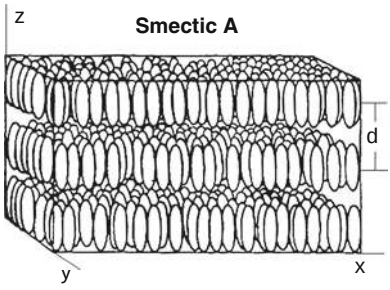

Fig. 4.6 A lamellar structure of the thermotropic smectic A phase

(ii) The point group symmetry is also $D_{\infty h}$. However, the translational invariance retains only in two directions and the symmetry group is different from that of nematics: $D_{\infty h} \times T(2)$.

(iii) The density is independent of x and y, ρ_x, $\rho_y = \text{const}$, however, ρ_z is a periodic function along the normal to smectic layers z. It has to be even function because there is a symmetry plane perpendicular to the director (e.g. it can be the middle plane of the three layer system shown in the Figure): $\rho(z) = \rho_0 + \sum_n^{\infty} \rho_n \cos nqz$. Here $n = 1, 2, 3, \ldots$ and $q = 2\pi/d$ is the wave-vector of the periodic structure. The modulation of density is not very strong, $\rho_n < \rho_0$ and, to the first approximation, the density wave may be represented by a single harmonic ($n = 1$):

$$\rho(z) = \rho_0 + \rho_1 \cos qz \tag{4.1}$$

The value of ρ_1 is usually taken as *translational order parameter*, see Section 6.3.

(iv) The orientational order parameter has the same form as in nematics, but its absolute value is larger $S_A > S_N$. The phase is optically positive.

(v) Typical texture of the SmA is shown in Fig. 4.7a. We see here the so-called "fans" consisted of "focal-conic" domains. Such domains are originated from a layered structure [1, 6]. Although layers are more or less rigid, they can be bent and may form cylinders and tori with central disclination lines (Γ_1) or more complex structures with disclinations of the Γ_2 type. The sketches in Fig. 4.7b represent projections of the tori on the x,z-plane perpendicular to Γ_1 (upper sketches) and on the y,z-plane including Γ_1 (lower sketches).

4.2.3 Special SmA Phases

The structure of the so-called de Vries phase is shown in Fig. 4.8. It is a uniaxial smectic A phase (group $D_{\infty h}$) with very strong molecular tilt (about $\pm 20°$) in any

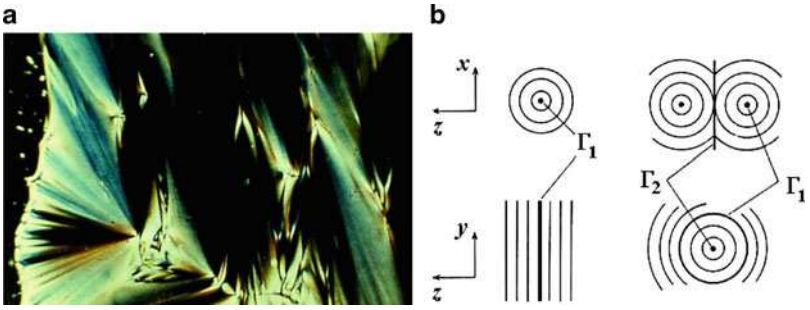

Fig. 4.7 Smectic A: fan-shape texture (**a**) and the structure of typical defects (**b**)

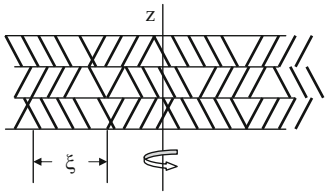

Fig. 4.8 Structure of a uniaxial smectic A phase with very strong molecular tilt (de Vries phase). ξ is tilt correlation length

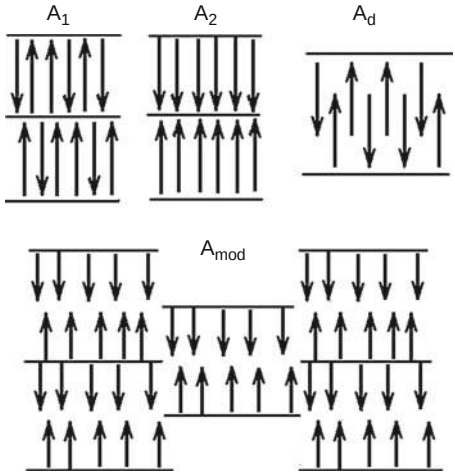

Fig. 4.9 Structure of polar smectic A phases A_1, A_2 and A_d and a frustrated phase A_{mod}

azimuthal direction. The local molecular tilt is correlated along a certain distance ξ within a smectic layer but on average the tilt is zero. Properties of this phase are different from those of the classical SmA, for example, the birefringence is smaller, i.e., n_z is closer to n_x, n_y than in SmA. The dielectric response is also spectacular. De Vries phase formed by chiral molecules manifests very interesting electrooptical effects.

Some compounds consisting of molecules with longitudinal permanent dipoles form locally polar smectic A phases and also so-called frustrated phases. In Fig. 4.9 are shown three structure A_1, A_2 and A_d which have the same point group symmetry but differ by translational symmetry due to specific packing of the molecules. The A_1 phase is the classical SmA discussed above: its interlayer distance, i.e., the structure period, is equal to molecular length. Dipoles are antiparallel within each *nonpolar* layer. A_2 is a smectic with *polar* layers and antiparallel (sometimes-called antiferroelectric) packing of molecular dipoles in the neighbor layers. Phase A_d represents a more general intermediate case. The spectacular orientation of dipoles results in modulation of charge density along the smectic normal and the period of *the charge density wave* may be different from the period of the *mass density* wave. Therefore, there are two waves along the smectic normal, a density one and the electric polarization one. These waves can be *incommensurate* that is the ratio of

their periods is not an integer, e.g., $1 < l'/l < 2$. In some cases, two tendencies, namely, a formation of either monolayer or bilayer structure are in conflict and the resulting phase is "frustrated" or, in other words, is modulated not only along the normal to the layers but also along the smectic plane like the phase A_{mod} shown in the same figure.

4.2.4 *Smectic C Phase*

In the SmC phase the longitudinal molecular axes are tilted from the smectic layer normal by an angle ϑ, Fig. 4.10. The phase has the following properties:

(i) The director **n** coincides with the direction of molecular axes and, as before, $\mathbf{n} = -\mathbf{n}$. Its components are $(n_x, n_y, n_z) = (\sin\vartheta\cos\Phi, \sin\vartheta\sin\Phi, \cos\vartheta)$. The projection of **n** onto the smectic layer plane is called *c-director*, $\mathbf{c} = \sin\vartheta\exp(\pm i\Phi)$. The **c**-director is taken as a two-component order parameter of the C-phase. $\mathrm{Sin}\vartheta$ and Φ may be considered as the amplitude and phase of the tilt angle (sign $\pm$ determines a sign of rotation). In experiment, angle ϑ varies from 0° to 45°.

(ii) The point group symmetry is C_{2h} or 2/m (a twofold axis x and a symmetry plane zy). The symmetry group is $C_{2h} \times T(2)$.

(iii) The density wave has the same form (4.1) as that of the SmA phase.

(iv) The spatial positions of molecules in neighbor layers are uncorrelated but their tilt is correlated.

(v) The phase is optically biaxial, Fig. 4.11a, there is no rotation axis coinciding with the director and $n_1 \neq n_2 \neq n_3$ (z is the smectic normal).

(vi) In SmC the director is free to rotate along the conical surface with an apex angle 2ϑ, therefore, as in a nematic, the Schlieren-texture is observed seen in the central part of Fig. 4.11b. On the other hand, the smectic structure reveals the fan-shape texture seen in the left-bottom corner of the same figure.

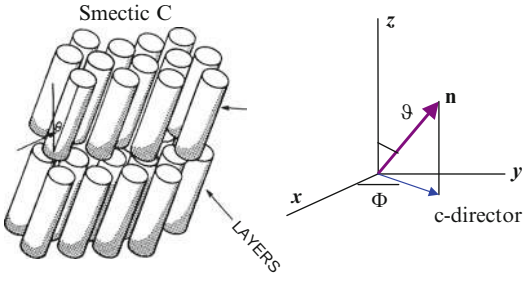

Fig. 4.10 Smectic C. Molecular structure (**a**) and definition of the **c**-director (**b**)

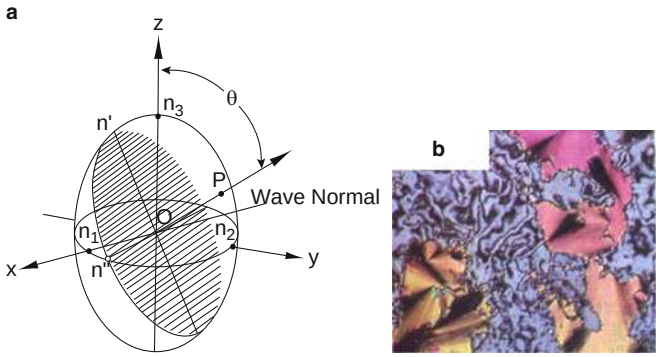

Fig. 4.11 The optical indicatrix (**a**) and the microscopic texture (**b**) of the SmC biaxial phase

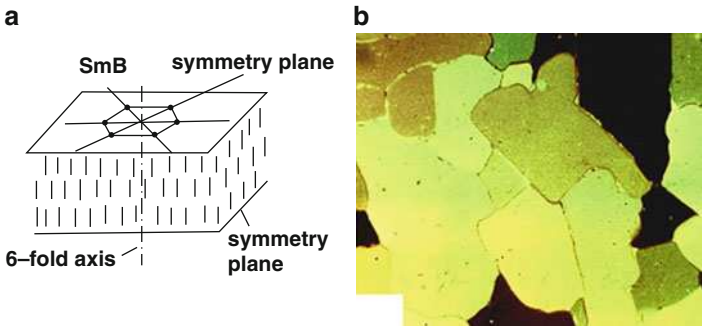

Fig. 4.12 Structure (**a**) and a microscopic texture (**b**) of the smectic B (SmB) phase

4.2.5 Smectic B

In this phase we have:

(i) Head-to-tail symmetry $\mathbf{n} = -\mathbf{n}$.

(ii) One sixfold rotation z-axis, one mirror plane perpendicular to that axis and 12 mirror planes including the sixfold axis. Six of them connect the hexagon angles as shown in Fig. 4.12a and, the other six bisect the angles between those planes. The point group symmetry is D_{6h} (or 6/mmm) and the phase has the following properties:

(a) Optical uniaxiality $n_{\parallel} \neq n_{\perp}$ and, as a rule, $n_z > n_x = n_y$.

(b) Three-dimensional density wave along x, y and z axes:

$$\rho(x, y, z) = \rho_{II} \cos(q_{II} z) \cdot \rho_{\perp} \cos(q_{\perp} x) \cdot \rho_{\perp} \cos(q_{\perp} y) \tag{4.2}$$

with different density modulation depth parallel and perpendicular to the director. In this respect Smectic B should be referred to as a three dimensional

crystal. However, the situation is not as simple and dependent on correlation in molecular positions in neighbor layers. If such correlations do exist, we deal with a normal 3D crystal having a very small shear modulus corresponding to the velocity gradient $\partial v_{x,y}/\partial z$. If there is no interlayer molecular correlations, the phase is called *hexatic* and will be considered in Section 5.7.3 in more detail.

(iii) A typical, so-called mosaic texture of the SmB is shown in Fig. 4.12b.

4.3 Discotic, Bowl-Type and Polyphilic Phases

One should distinguish between the *discotic nematic*, N_D phase shown in Fig. 4.13b and several discotic columnar phases, e.g. that shown in Fig. 4.13a. The discotic nematics form on cooling the isotropic phase consisting of disc-like molecules, e.g. of triphenylen type, see Fig. 4.14. The symmetry reduces from T(3) × O(3) to T(3)× $D_{\infty h}$. The new phase is not miscible with calamitic nematics despite the same symmetry: $\mathbf{n} = -\mathbf{n}$, point group $D_{\infty h}$, ρ = const, optical uniaxiality. However, hydrodynamic properties of discotic nematics are quite different from those of calamitic nematics. A columnar phase is an example of a two-dimensional (2D) crystal and 1D liquid, *a lattice of liquid threads*. The translational motion of molecules is allowed only along their normals, the translation group is T(1) and the point group can be different. For example it is D_{6h} for an orthogonal hexagonal phase or C_{2h} for a tilted phase. We meet even more phases formed by disc-like molecules, namely Isotropic I, nematic N_D, D_0 (columnar orthogonal), D_t (columnar tilted) and K (crystalline) ones.

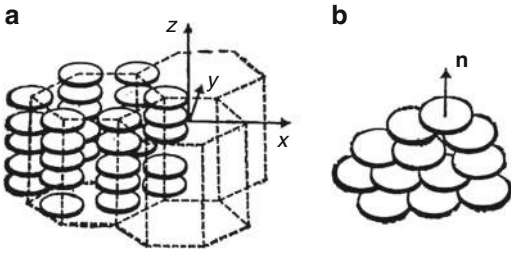

Fig. 4.13 Structure of discotic columnar (**a**) and nematic (**b**) phases

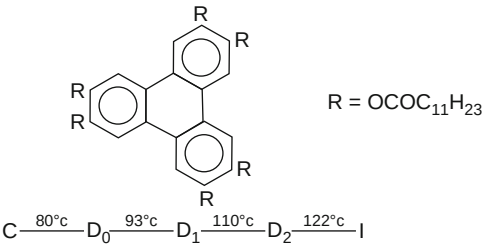

Fig. 4.14 Molecular formula and a phase sequence of a triphenylene compound

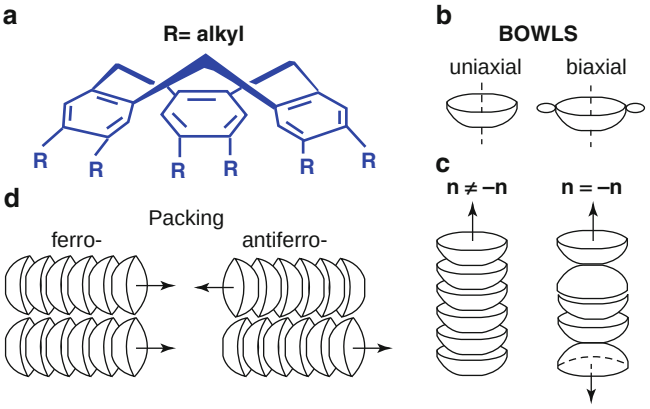

Fig. 4.15 Possible bowl phases: forms of molecules (**a**) and bowls (**b**), polar and non-polar columns consisting of bowl molecules (**c**), and two types of column packing, ferroelectric (*left*) and antiferroelectric (*right*) (**d**)

A molecule that, in principle, may form a bowl phase should itself have the bowl form like that seen in Fig. 4.15a [7]. Molecular bowls may have different symmetry as shown on the top of Fig. 4.15b and the corresponding phases could be either uniaxial or biaxial. The packing of bowls into the columns may have specific features. For example, when all molecules in the column are oriented bottom down then the head-to-to tail symmetry is broken and the column has conical, i.e. polar symmetry $C_{\infty v}$, Fig. 4.15c. Only polar columns may form ferroelectric or antiferroelectric phases shown in Fig. 4.15d.

Actually, such bowl phases are still to be found. However, polar achiral phases have been observed in the so-called polyphilic compounds [8]. The rod-like molecules of these compounds consist of distinctly different chemical parts, a hydrophilic rigid core (a biphenyl moiety) and hydrophobic perfluoroalkyl- and alkyl-chains at opposite edges. Such molecules form polar blocks that, in turn, form a polar phase manifesting pyroelectric and piezoelectric properties with a field-induced hysteresis characteristic of ferroelectric phases.

4.4 Role of Polymerization

There are two types of polymers, which form thermotropic liquid crystals, the side-chain, Fig. 4.16a and the main-chain polymers, Fig. 4.16b. In the side-chain polymers the mesogenic units are attached to a backbone by more or less flexible chains. In the main-chain polymers mesogenic units are incorporated into the polymer backbone and separated from each other by flexible chains [9, 10]. Flexible chains (spacers) are necessary to provide a certain freedom to mesogenic moieties to form an ordered state. For the side-chain polymer to be in the nematic or smectic

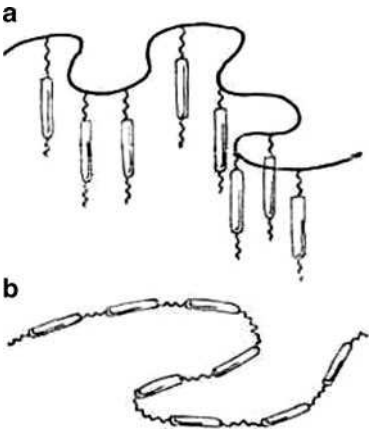

Fig. 4.16 Structure of polymer chains appropriate for side-chain (**a**) and main-chain (**b**) polymer liquid crystals

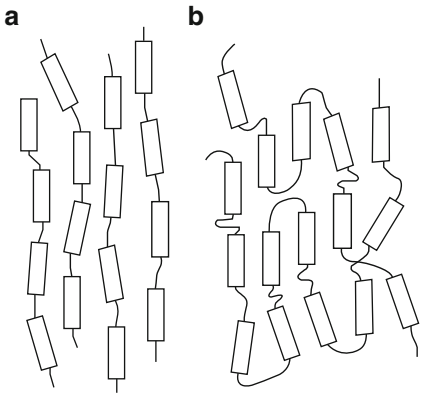

Fig. 4.17 Scheme of packing of main chain polymer mesogenic groups in the nematic (**a**) and smectic A (**b**) phases

phase is quite natural, because mesogenic units can easily be arranged parallel to each other, Fig. 4.17a. However, even in the main chain polymers with long enough flexible spacers between the mesogenic groups, the latter can form nematic and even smectic phases and the flexible backbones are forced to acquire the liquid crystalline structure, Fig. 4.17b.

In the same way one can synthesized liquid crystalline *copolymers* in which mesogenic groups alternate with some functional groups like chiral, polar, photochromic, luminescent, etc., groups useful for various applications especially in nonlinear optics. For example, incorporating chromophores, manifesting a light-induced intramolecular charge transfer, one can develop materials with enhanced nonlinear susceptibility, so-called $\chi^{(2)}$- or $\chi^{(3)}$-materials capable of wave mixing, generation of light harmonics, etc. Polymer liquid crystals with photochromic moieties, showing reversible and multiple photo-induced *cis–trans–cis* isomerization, are very perspective for holographic grating recording, polarimetry, optical

information processing, lasers without mirrors and so on. The nematic phase formed by main-chain polymers can be used in a technological process of manufacturing extra strong polymer fibers, because the material goes through draw plates in the well-oriented nematic state and the fiber contains less defects.

Polymers can form the same thermotropic phases as low-molecular mass compounds (nematic, smectic A, C, B, chiral phases as well). Despite the same symmetry, physical properties of polymer liquid crystals are very specific. They are very viscous due to the entangling of long polymer chains hindering the translational motion (flow). On cooling the polymer liquid crystal acquire a *glassy state* very useful for many applications. For example, one can create some macroscopic structures in the nematic phase very sensitive to external fields (for instance, a grating, or a field induced polar, pyroelectric structure) and then froze it into the glassy state which is not crystalline but mechanically solid and use the latter for applications. You can also make cholesteric polymer doped with a proper luminescent dye for laser devices with distributed feedback (due to natural periodicity of the helical structure). Some polymer liquid crystals can be as elastic as rubber (*elastomers*). They have very good prospects as piezoelectric materials as well as materials having mechanically tunable optical properties.

4.5 Lyotropic Phases

Lyotropic liquid crystalline phases form by water solutions of amphiphilic (particularly biphilic) molecules [11, 12]. The building blocks of those phases are either bilayers, Fig. 4.18, or micelles. The form of the micelles can be spherical or cylindrical, Fig. 4.19a, b. For low concentration of oil in water, the micelles are normal (sketch (a), tails inside, polar heads outside, in water). For high concentration, the structure is inversed ((b) and (c), water and polar heads inside, tails outside). Examples of the structure of some typical lyotropic phases (lamellar, cubic, hexagonal) are shown in Fig. 4.20. Under a microscope they show characteristic features,

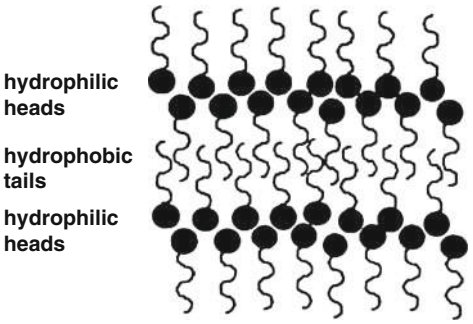

Fig. 4.18 Bilayers formed by biphilic molecules having polar hydrophilic heads and hydrophobic tails

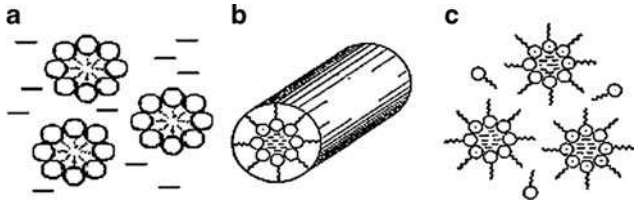

Fig. 4.19 Micelles: spherical normal (**a**), cylindrical inverse (**b**) and spherical inverse (**c**)

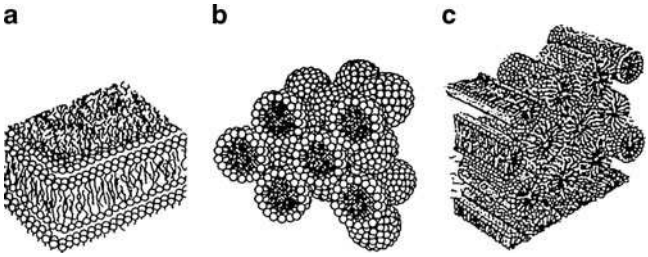

Fig. 4.20 Lamellar, cubic and hexagonal lyotropic phases

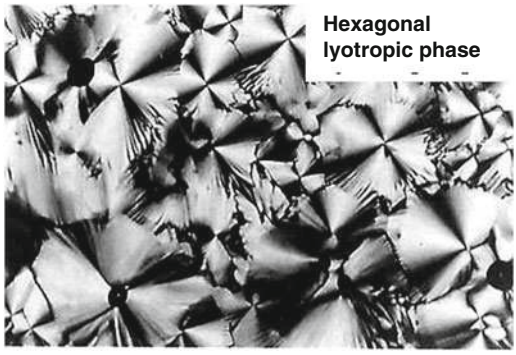

Fig. 4.21 Microphotograph of the hexagonal lyotropic phase texture

e.g., a fan-shape texture is typical of the hexagonal lyotropic phase presented in Fig. 4.21.

There is also a group of the so-called lyotropic nematics. They are intermediate between the isotropic micellar phase and structured (lamellar or hexagonal) phases and can be formed by both discotic and calamitic molecules. The lyotropic nematics can be aligned by an electric or magnetic field and show Schlieren texture as thermotropic nematics. The building blocks of these mesophases are vesicles or similar mesoscopic objects. From the symmetry point of view the nematic phases can be uniaxial or biaxial, as shown in Fig. 4.22. In fact, the biaxial nematics have been found unequivocally only in the lyotropic systems [13].

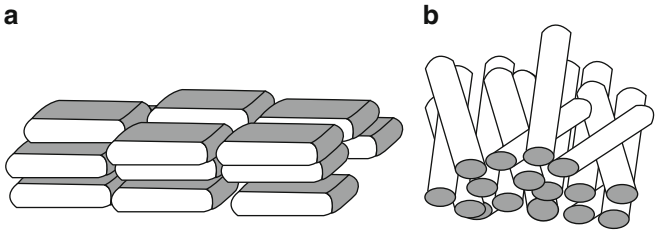

Fig. 4.22 Structure of lyotropic nematics: a phase N_d is formed by disc-like blocks (**a**) and phase N_e by cylindrical rod-like blocks (**b**)

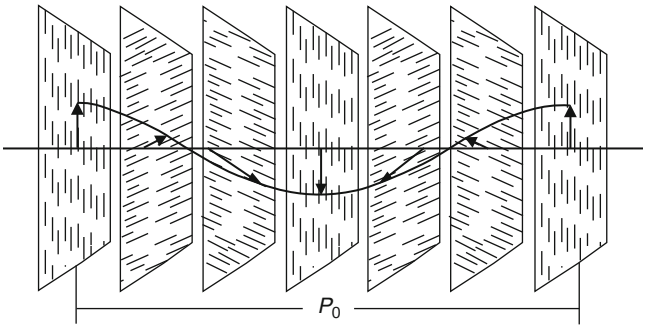

Fig. 4.23 Structure of the cholesteric phase. Each sheet models a cross-section of the helical structure within one period of the helix P_0. The helix axis is directed from the left to the right. The short bars show orientation of chiral molecules within each sheet

Table 4.1 Point group symmetry of main achiral and chiral phases

Phase/ chirality	Achiral	Chiral
Isotropic	K_h	K
Nematic or smectic A	$D_{\infty h}$	D_∞
Smectic C	C_{2h}	C_2

4.6 General Remarks on the Role of Chirality

Chirality is lack of mirror symmetry. The name came from Greek word for "hand". W.H. Thomson (Lord Kelvin) defined it as follows: "any geometrical figure has chirality if its image in a plane mirror cannot be brought into coincidence with itself". Examples of chiral phases are the *cholesteric*, schematically shown in Fig. 4.23, and *smectic C** ones (the asterisk at letter C is used to distinguish this phase from the achiral smectic C). Unfortunately there is no quantitative definition of chirality [14]. The chirality of a molecule results in a spatial modulation of liquid crystalline phases. Table 4.1 shows how the point group symmetry is changed when the achiral liquid crystal material is doped with a chiral compound. The isotropic liquids formed by chiral molecules, e.g. sugar solutions in water, have continuous

group symmetry K (no mirror plane). Experimentally, this can be recognized by a rotation of the polarization plane of transmitted light (optical activity). In case of the racemic solution with equal amount of the right and left isomers of the same molecule, the symmetry is K_h and the optical activity is absent.

The nematic phase has point group symmetry $D_{\infty h}$. If we add some amount of chiral, e.g., right-handed molecules, the symmetry is reduced from $D_{\infty h}$ to D_{∞} (symmetry of a twisted cylinder). Such a phase is called *chiral nematic phase*. Chiral molecules used as a dopant (solute) in nematic solvent considerably modify the nematic surrounding and the overall structure becomes twisted with a helical pitch P_0 incommensurate with a molecular size a, $P_0 \neq na$ (n is an integer) and usually $P_0 \gg a$. Typically, $a < 10$ nm, $P_0 = 0.1$–10 μm.

The pitch of the helix depends on concentration c of a dopant; for small $c\,{P_0}^{-1} \approx \alpha c$ and α is called *helical twisting power* of the dopant [15]. However, with increasing c the dependence becomes nonlinear and the helix handedness can even change sign (the case of cholesteryl chloride dopant in *p*-butoxybenzylidene-*p*′-butylaniline, BBBA, see Fig. 4.24). The same chiral, locally nematic phase with a short pitch in the range of 0.1–1 μm is traditionally called *cholesteric phase* because, at first, it has been found in cholesteryl esters. Such short-pitch phases manifest some properties of layered (smectic) phases.

The smectic C* phase formed by chiral molecules (SmC* phase) has also a helical superstructure having a pitch incommensurate with the smectic layer thickness. Theoretically chiral phases can also be formed by achiral molecules due to very specific packing [16]. For instance, three achiral rod-like molecules *of different length* may form a chiral trimer or a tripod due to Van der Waals interactions between their fragments, see Fig. 4.25a, and such trimers, in their turn, may form a kind of helical structure. Another example is bent-core or banana like-molecules [17]

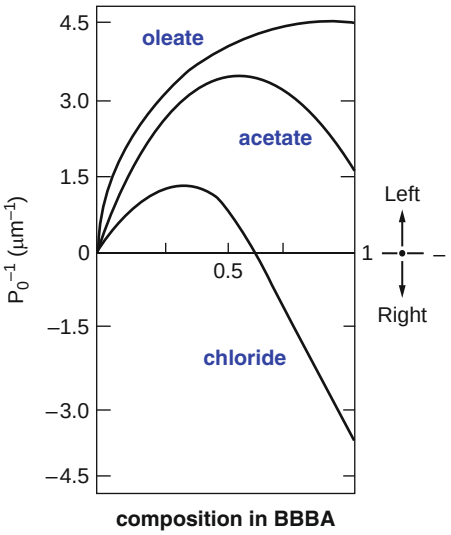

Fig. 4.24 Helical twisting power of different cholesteric dopants in the nematic phase as a function of the content of dopant

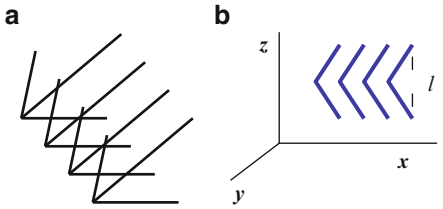

Fig. 4.25 Hypothetical chiral trimers formed by rod like molecules due to specific Van der Waals interaction (**a**) and achiral bent-core molecules capable of formation chiral domains (**b**)

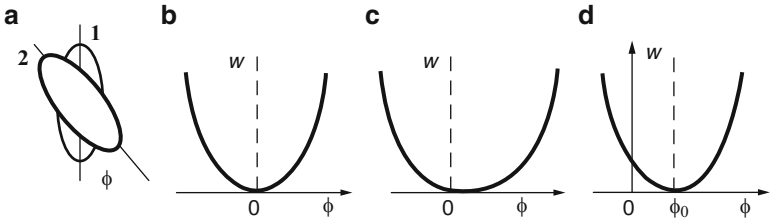

Fig. 4.26 Interaction of two rod-like molecules, one molecule (1) on the top of the other (2) at an angle ϕ (**a**). The forms of the interaction potential in different models: for achiral molecules harmonic (**b**), and anharmonic (**c**) and harmonic potential for chiral molecules (**c**)

that can form a smectic multidomain system with right and left domains depending on the direction of the tilt of long molecular axes l with respect to the x,z-plane Fig. 4.25b. On the other hand, chiral molecules can be packed in such a way that the phase would lose their optical anisotropy, for example in the so-called blue phase (see below) or optically isotropic SmC* phase.

4.7 Cholesterics

4.7.1 Intermolecular Potential

Basically the structure of the molecules forming nematic and cholesteric phases is similar. However, chiral molecules possess a certain chiral asymmetry that results in asymmetry of intermolecular interactions. This asymmetry is weak and, therefore, the helical pitch is much larger than a molecular size. Consider now an interaction potential $V(\phi)$ between two rod-like molecules (1) and (2) as a function of the twist angle ϕ between their long molecular axes, see Fig. 4.26a. Molecule (1) is considered to be fixed. The twist corresponds to rotation of the longitudinal axis of molecule (2) about the axis connecting gravity centers of the two molecules. For achiral molecules, the two-particle potential curve $W(\phi)$ is symmetric, Fig. 4.26b. It may be described in terms of the Legendre polynomial P_2 and order parameter S:

$$W_{12}(\phi) = -vSP_2(\cos\phi) \tag{4.3}$$

For chiral molecules the mirror symmetry is broken and such a curve cannot be symmetric. We can distinguish three cases:

(i) The interaction is still harmonic but centered at a finite angle $\phi_0 \neq 0$ as in Fig. 4.26d:

$$W_{12}(\phi) = -vSP_2 \cos(\phi - \phi_0). \tag{4.4}$$

This is a "classical" cholesteric with local nematic structure. The value of ϕ_0 determines the equilibrium pitch (a is the diameter of a rod-like molecule):

$$P_0 = 2\pi a \Big/ \phi_0 \tag{4.5}$$

(ii) The potential is centered at $\phi_0 = 0$ but the interaction is anharmonic and cannot be described in terms of cylindrically symmetric functions. In this case, the equilibrium pitch is determined by an average ϕ_{av} shown in Fig. 4.26c.

(iii) Both (i) and (ii) factors contribute to chirality together.

Of course, in each case a particular form of the potential curve depends on chemical structure of constituting molecules. For instance, in nemato-cholesteric mixtures, $V(\phi)$ depends on the structure of both a nematic matrix and a chiral dopant.

4.7.2 *Cholesteric Helix and Tensor of Orientational Order*

We can imagine a cholesteric as a stuck of nematic "quasi-layers" of molecular thickness a with the director slightly turned by $\delta\phi$ from one layer to the next one. In fact it is Oseen model [18]. Such a structure is, to some extent, similar to lamellar phase. Indeed, the quasi-nematic layers behave like smectic layers in formation of defects, in flow experiments, etc. Then, according to the Landau–Peierls theorem, the fluctuations of molecular positions in the direction of the helical axis blur the one-dimensional, long-range, positional (smectic A phase like) helical order but in reality the corresponding scale for this effect is astronomic.

In the first approximation, the parameter of the *local orientational order* of a cholesteric liquid crystal is the same uniaxial traceless tensor $Q_{ij} = S(n_i n_j - \delta_{ij}/3)$ as in the nematic phase with the director axis always lying in the x,y-plane, e.g. along the x direction at a selected cross-section of the helix:

$$\tilde{Q} = S \begin{pmatrix} +2/3 & 0 & 0 \\ 0 & -1/3 & 0 \\ 0 & 0 & -1/3 \end{pmatrix}$$

In the helical structure this tensor, as well as the tensor of the dielectric anisotropy (ellipsoid) rotates upon the translation along the z-axis as shown in

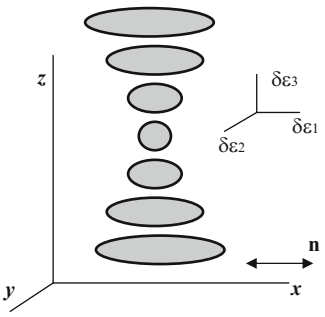

Fig. 4.27 Helical stricture of the ellipsoid of dielectric permittivity for a cholesteric liquid crystal (a very weak biaxiality is determined by component $\delta\varepsilon_3$)

Fig. 4.27. Then, the components of the director are $\mathbf{n} = (\cos qz, \sin qz, 0)$. In the uniaxial approximation, there are only two principal components of the local dielectric tensor, $\varepsilon_{\|}$ and $\varepsilon_{\perp}$ and two refraction indices, $n_{\|}$ and $n_{\perp} = n_z$. As a rule $n_{\|} > n_{\perp}$, and a uniaxial cholesteric is *locally optically positive*. For the overall helical structure, one can introduce average refraction indices, one along the helical axis $n_z = n_{\perp}$, and the other perpendicular to it, ${n_{x,y}}^2 = (1/2)({n_{\|}}^2 + {n_{\perp}}^2)$. Thus the helical axis becomes the optical axis. As a rule, $n_z \approx 1.5$ and $n_{x,y} \approx 1.6$ and the overall helical structure is usually *optically negative*.

4.7.3 Tensor of Dielectric Anisotropy

In general, however, tensor $\tilde{Q}_{ij}$ is biaxial but the biaxiality is small, on the order of ξ/P_0 where ξ is the length corresponding to nematic correlations. This correlation length may be found, for example, from the light scattering in the isotropic phase close to the transition to the nematic phase. Then, at each point, that is *locally*, the anisotropic part of dielectric susceptibility tensor is biaxial and traceless $\delta\varepsilon_1 + \delta\varepsilon_2 + \delta\varepsilon_3 = 0$ with $\delta\varepsilon_2 \approx \delta\varepsilon_3$.

$$\delta\tilde{\varepsilon} = \begin{pmatrix} \delta\varepsilon_1 & 0 & 0 \\ 0 & \delta\varepsilon_2 & 0 \\ 0 & 0 & \delta\varepsilon_3 \end{pmatrix} = \frac{\delta\varepsilon_1}{2} \begin{pmatrix} 2 & 0 & 0 \\ 0 & -1+\eta & 0 \\ 0 & 0 & -1-\eta \end{pmatrix} \tag{4.6}$$

Here η is a measure of biaxiality

$$\begin{aligned} \eta &= (\,\delta\,\varepsilon_2 - \,\delta\,\varepsilon_3)/\,\delta\,\varepsilon_1 = (2\,\delta\,\varepsilon_2 + \,\delta\,\varepsilon_1)/\,\delta\,\varepsilon_1 \\ &= (2\,\delta\,\varepsilon_2 + \,\delta\,\varepsilon_1) + 1. \end{aligned} \tag{4.7}$$

Particularly, for $\eta = 0$ we return to the nematic tensor of dielectric anisotropy with factor 2/3 included in $\delta\varepsilon_1$:

$$\delta\tilde{\hat{\varepsilon}} = \delta\varepsilon_1 \begin{pmatrix} 1 & 0 & 0 \\ 0 & -1/2 & 0 \\ 0 & 0 & -1/2 \end{pmatrix} \tag{4.8}$$

To obtain the tensor of the cholesteric helical structure one should imagine that the local tensor rotates in the laboratory co-ordinate system, or, alternatively, to introduce a rotating co-ordinate system. In the latter case, one should make transformation

$$\delta\tilde{\varepsilon} = \tilde{R}_{\phi}\delta\tilde{\varepsilon}\tilde{R}_{\phi}^{-1} \tag{4.9}$$

where $\tilde{R}_{\phi}$,$\tilde{R}_{\phi}^{-1}$ are the *matrix of rotation* about the z-axis and its *inverse matrix*, respectively. Both matrices are known from the textbooks on the matrix algebra:

$$\tilde{R}_{\phi} = \begin{bmatrix} \cos\phi & -\sin\phi & 0 \\ \sin\phi & \cos\phi & 0 \\ 0 & 0 & 1 \end{bmatrix} \quad \tilde{R}_{\phi}^{-1} = \begin{bmatrix} \cos\phi & \sin\phi & 0 \\ -\sin\phi & \cos\phi & 0 \\ 0 & 0 & 1 \end{bmatrix} \tag{4.10}$$

Note that for our rotation matrix, which is antisymmetric, the inverse matrix is equal to the transposed one. Now using Eqs. (4.9) and (4.10) we write

$$\delta\tilde{\varepsilon} = \tilde{R}_{\phi}\delta\tilde{\varepsilon}\tilde{R}_{\phi}^{-1} = \begin{vmatrix} \cos\phi & -\sin\phi & 0 \\ \sin\phi & \cos\phi & 0 \\ 0 & 0 & 1 \end{vmatrix} \cdot \delta\varepsilon \begin{pmatrix} 1 & 0 & 0 \\ 0 & -1/2 & 0 \\ 0 & 0 & -1/2 \end{pmatrix} \cdot \begin{vmatrix} \cos\phi & \sin\phi & 0 \\ -\sin\phi & \cos\phi & 0 \\ 0 & 0 & 1 \end{vmatrix}$$

and then multiply the dielectric tensor first by the inverse matrix on the right and then multiply the rotation matrix from the left side by the result of the first operation. Next, we obtain the *tensor of dielectric anisotropy of a locally uniaxial cholesteric*.

$$\delta\tilde{\varepsilon} = \frac{\delta\varepsilon}{4} \begin{pmatrix} 1 + 3\cos 2\phi & 3\sin 2\phi & 0 \\ 3\sin 2\phi & 1 - 3\cos 2\phi & 0 \\ 0 & 0 & -2 \end{pmatrix} \tag{4.11}$$

Finally, we can write the *tensors of the orientational order parameter* $\tilde{Q}_{ij}$ in the rotating frame for locally uniaxial and biaxial cholesteric liquid crystal (ChLC):

Uniaxial ChLC:

$$\tilde{Q}_{ij}^{uni} = \frac{3}{8}S \begin{pmatrix} 1 + 3\cos 2\phi & 3\sin 2\phi & 0 \\ 3\sin 2\phi & 1 - 3\cos 2\phi & 0 \\ 0 & 0 & -2 \end{pmatrix} \tag{4.12}$$

Biaxial ChLC

$$\tilde{Q}_{ij}^{bi} = \frac{3}{8}S \begin{pmatrix} 1 + \eta + (3 - \eta)\cos 2\phi & (3 - \eta)\sin 2\phi & 0 \\ (3 - \eta)\sin 2\phi & 1 + \eta - (3 - \eta)\cos 2\phi & 0 \\ 0 & 0 & -2 - 2\eta \end{pmatrix} \tag{4.13}$$

with η defined by Eq. (4.7)

4.7.4 Grandjean Texture

This interesting texture is observed in the so-called Cano wedges formed by two optically polished glasses with a gap filled by a cholesteric liquid crystal (CLC). Let the equilibrium helical pitch of the CLC in a bulky sample is P_0. In the wedge the molecules are oriented along its acute edge. Since the boundary condition are fixed the equilibrium pitch can only be undistorted when the layer thickness is exactly equal to $d' = mP_0/2$ where m is an integer as shown in Fig. 4.28a. In the close proximity of each d' value, the helix can still fit to the boundary conditions at the cost of some pitch compression or dilatation. Therefore rather large areas form with the same number of half-turns within the gap, which are marked by numbers $m = 0$, 1, 2, 3 in Fig. 4.28b. These are *Grandjean zones* separated by the defects called *disclinations* (thin lines seen in the photo, Fig. 4.28c). At each disclination, the number of half-turns changes usually by one. In the zero zone, the cholesteric is unwound but its properties (e.g., elastic moduli) in this quasi-nematic area are different from the corresponding achiral nematic. Grandjean textures are very

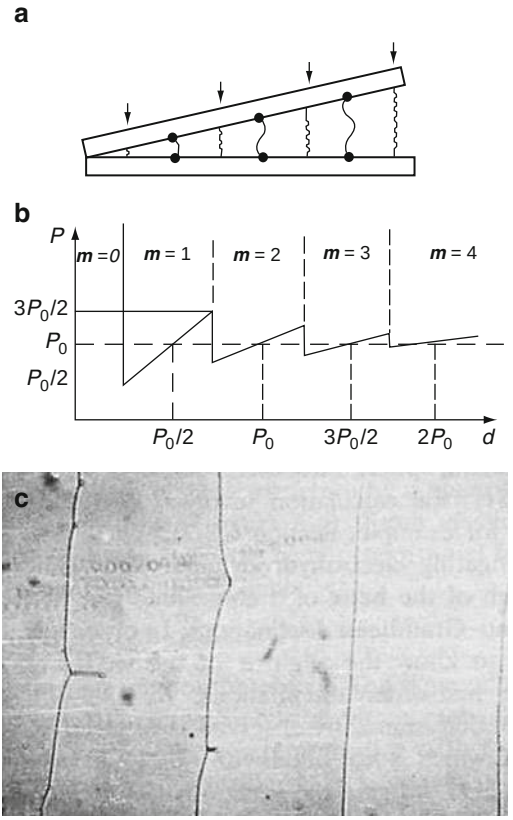

Fig. 4.28 A wedge type cell filled with a cholesteric (**a**) with Grandjean zones marked by numbers 0, 1, 2, 3, 4 . . . and the disclination lines shown by arrows. The distance dependence of the helix pitch in different zones with numbers m is schematically shown in sketch (**b**). Photo of disclinations limiting the Grandjean zones (c)

useful as an experimental tool: one can study and compare different physical, especially electrooptical effects at different thickness under the same conditions (same material, alignment, ambient conditions, fields, etc.) One can also observe the Grandjean zones on preparations without cover slips because a drop of a CLC has an edge with decreasing thickness. Since the free surface can also align liquid crystals the Grandjean zones form in this natural wedge at the border of the preparation. By the way, in smectics such zones exist in a form of microscopic steps, which could be measured by an atomic force microscope (AFM).

4.7.5 Methods of the Pitch Measurements

Due to its periodic structure cholesteric liquid crystals manifest very interesting optical properties. In fact, a cholesteric is one-dimensional photonic crystal having forbidden frequency bands (stop-bands) for a particular circular polarization. This band appears due to the Bragg diffraction of light on the helical structure. In the vicinity of the stop band a giant optical rotation of light is observed. Since the pitch of the helix can easily be changes by external factors such as composition, temperature, UV light, mechanical tension, electric and magnetic field, a variety of tunable optical devices (like filters and lasers) has been suggested. We shall discuss the optical properties of cholesterics in detail in Chapter 12.

The key parameter for the tunability is the helical pitch P_0, which can be found from the measurements of

(i) The wedge thickness in the centers of Grandjean zones, $P_0 = 2d'/m$, as shown in Fig. 4.28.

(ii) The angular position of diffraction spots for the light incident perpendicularly to the helical axis Fig. 4.29a. Such a texture is formed by the so-called homeotropic boundary conditions with liquid crystal molecules oriented perpendicularly to the plane glasses. Due to the head-to-tail symmetry the period of the optical properties is $P_0/2$ and wavevector of the optical structure $q_0 = 4\pi/P_0$. The diffraction spots are located at angles $\pm 2\theta$ symmetric with respect

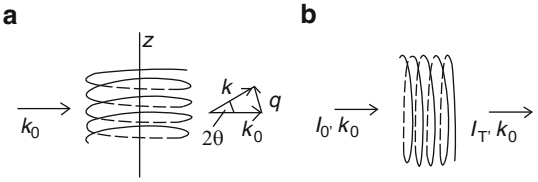

Fig. 4.29 Measurements of the pitch of the helix in a cholesteric. (**a**) Geometry for monochromatic light diffraction on the focal-conic texture. The pitch is found from the angle 2ϑ between the incident and diffracted beams with wavevectors k_0 and k; (**b**) Spectral measurements of the light transmission by a planar cholesteric texture (I_0 and I_T are intensities of the incident and transmitted beam)

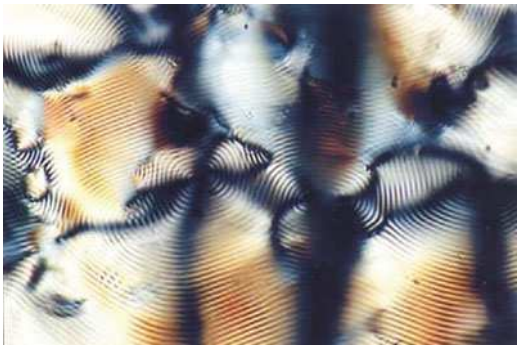

Fig. 4.30 A fingerprint texture of a cholesteric liquid crystal seen in a polarization microscope (the distance between stripes equals a half-pitch)

to the incident beam (zero order diffraction). The modulus of the scattering wavevector is $q = 2k_0 m \sin\theta_m/2$ where incident light vector $k_0 = \omega/c$. The first order diffraction ($m = 1$) is very intense and, using angle $\pi_{m=1}$ and the wavevector conservation law $q = q_0$, the pitch can be found $P_0 = \lambda_0/m \sin\vartheta$.

(iii) The spectral position of the selective reflection or transmission band λ_0 in the planar texture formed by the homogeneous, planar boundary conditions with molecules oriented parallel to the glasses, Fig. 4.29b. In this case, we may use unpolarised light and the Bragg condition for one of the circular polarizations

$$m\lambda = m\lambda_0/\langle n\rangle = 2(P_0/2)\sin\vartheta_0, m = 1, 2, 3... \tag{4.14}$$

with incident angle $\vartheta_0 = \pi/2$ and $m = 1$. Therefore, $P_0 = \lambda_0/<n>$ where $<n>$ is related to the two principal refraction indices $n_{\|}$ and $n_{\perp}$ parallel and perpendicular to the director: $<n> = (n_{\|} + n_{\perp})/2$.

(iv) The distance between stripes observed under a polarization microscope in the *fingerprint texture*, shown in Fig. 4.30. Again due to the head-to-tail symmetry the distance between stripes equals a half-pitch.

4.8 Blue Phases

These phases were an enigma of the centuries. Since the experiments of Reinitzer [19] up to recent times it was not clear whether it was a special texture of the known cholesteric phase or a thermodynamically new phase. The textures of the blue phases are often of blue color, Fig. 4.31. Properties of the blue phases are very interesting from the fundamental point of view.

(i) There are three blue phases BPI, BPII and BPIII (or foggy) phase [20]. All blue phases are usually observed in rather a narrow temperature interval between the isotropic phase and cholesteric (Ch) phase. Recently, however, a wide

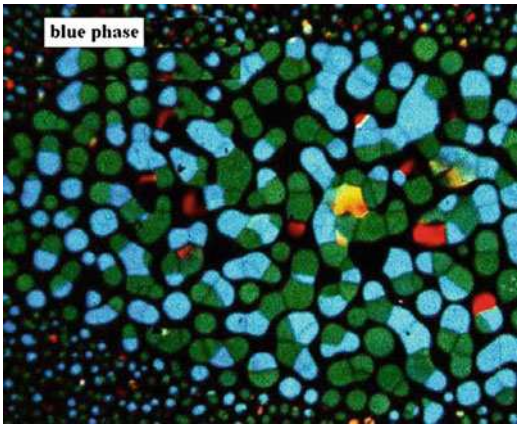

Fig. 4.31 A texture of blue phase BPI

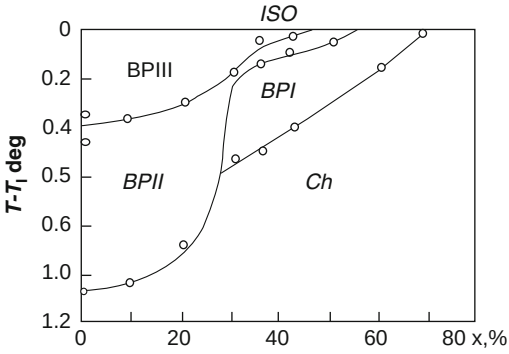

Fig. 4.32 A phase diagram showing phase transition lines between the isotropic, BPIII, BPII, BP1 and cholesteric phase: x is percentage of the racemic component in a racemic-chiral mixture

temperature blue phases have been prepared using stabilization of the helical structure by a polymer network [21]. A typical example of a phase diagram is shown in Fig. 4.32 [20]. In the diagram, the abscissa is a percentage of the racemic component in a mixture with a chiral component of the same compound.

(ii) X-ray diffraction shows that local order is liquid-like.
(iii) Drops of a BP1 show facets typical of solid crystals seen in Fig. 4.31.
(iv) Blue phases strongly rotate the light polarization plane.
(v) Despite properties (iii) and (iv) the blue phases do not show any birefringence. Blue phases are optically isotropic.
(vi) BP1 and BPII show the optical reflections similar to the X-ray reflections from solid crystals. Bragg reflections correspond to the three-dimensional periodicity at the micrometer scale like in three-dimensional photonic band-gap crystals.
(vii) The phase transition between the isotropic and a blue phase III is accompanied by a very blurred anomaly in specific heat (H), and there are also

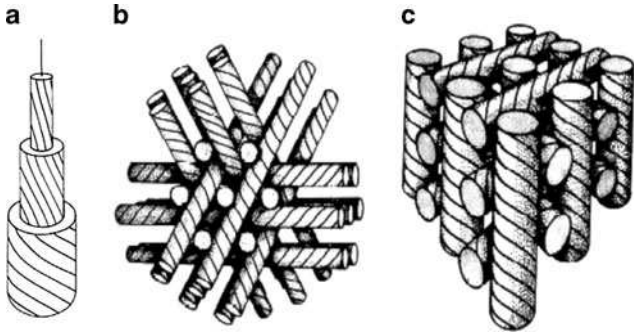

Fig. 4.33 Double-twist cylinder (**a**) and the structure of the body-centered cubic phase BP1 (**b**) and simple cubic phase BPII (**c**), both consisted of double-twist cylinders (adapted from [22])

noticeable *H* anomalies between the BPIII and BPI phases [22] and also at the BP-cholesteric phase transition. This means that we deal not with different textures of the cholesteric phase but with different phases.

(viii) NMR spectra of BP are different from those of the Ch phase.

It has been concluded that blue phases I and II are three-dimensional periodic structures, formed by pieces of the helix, a kind of *regular lattice of defects* having a period comparable with the wavelength of visible light. How such a phase can be modeled? One of the most interesting models is a defect structure made of *double-twist cylinders* as building blocks [23]. The helical structure forms in two directions, Fig. 4.33a. Such cylinders can be packed either in the body-centered lattice forming the BPI phase as shown in Fig. 4.33b or in more symmetric simple cubic lattice, Fig. 4.33c that may correspond to the high temperature BPII blue phase. The foggy phase is, more probably, amorphous. It is important that the concept of a *lattice of defects* is quite general and can be used in other areas of physics of the condensed matter (theory of melting, theory of phase transitions, superfluidity and Abrikosov vortices, structure of amorphous medium, etc).

4.9 Smectic C* Phase

4.9.1 Symmetry, Polarization and Ferroelectricity

The chirality of molecules breaks the mirror symmetry C_{2h} of the achiral smectic C phase. The only symmetry element left is a twofold rotation axis C_2, and the point symmetry group becomes C_2 instead of C_{2h}. The structure of a single smectic C* layer is shown in Fig. 4.34. As in achiral smectic C, the molecules in the layer obey head-to-tail symmetry, the director **n** coincides with average orientation of molecular axes and form angle ϑ with the smectic normal **h**.

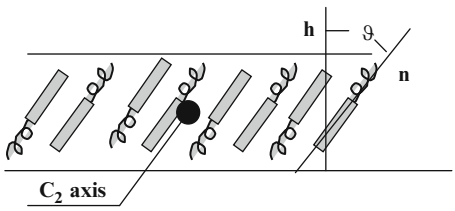

Fig. 4.34 Structure of a single monolayer of chiral smectic C*. Rotation axis C_2 is polar axis. Chiral molecules are tilted through angle ϑ the director **n** forms with layer normal **h**

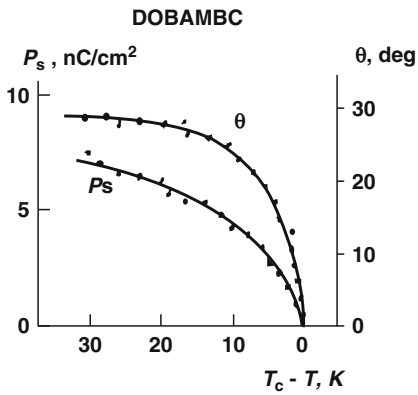

Fig. 4.35 Correlation of temperature dependencies of the molecular tilt ϑ and spontaneous polarization P_s for a ferroelectric compound DOBAMBC (for the formula see Fig. 3.5a)

The smectic C and C* order parameters are the same, the two-component tilt $\vartheta\exp(i\varphi)$. However, the plane of the figure is no longer a mirror plane and the C_2 axis is a *polar axis* directed forward or backward with respect to the tilt plane *h*,*n*. This depends on a sign of handedness. Such symmetry allows for the existence of the *spontaneous polarization* vector $\mathbf{P}_s$ (that is a dipole moment of a unit volume) directed along the polar axis. Thus, each SmC* layer is polar and possess pyroelectric properties. Moreover, the direction of $\mathbf{P}_s$ can be aligned by an electric field in any direction. At a certain boundary conditions provided by e.g. aligning glasses, the layer manifests two memory states, and, under this condition, each smectic layer may be considered *ferroelectric*, for details see Chapter 13. For small tilt angles, the value of the spontaneous polarization is proportional to ϑ as illustrated in Fig. 4.35 by experimental curves for the DOBAMBC (for formula see Fig. 3.5a), the first liquid crystal ferroelectric compound synthesized in Orsay (France) following ideas of Meyer [24]. The value of P_s in DOBAMBC is rather small, about 6 nC/cm^2 at room temperature, however, nowadays there have been synthesized many compounds with P_s of several hundreds nC/cm^2.

4.9.2 Helical Structure

Due to chiral intermolecular interaction the overall multi-layered structure of smectic C* becomes twisted, like in cholesterics. The twist angle of the tilt plane is

$$\varphi = qz = {}^{2\pi z}/_{P_0}$$

that is the tilt plane rotates about z upon translation along z, Fig. 4.36. The period (pitch) of the helical superstructure P_0 is incommensurate to the thickness of a molecular layer. The helicity is a secondary phenomenon. By proper mixing left and right molecular isomers one can compensate for helicity. For racemic mixtures, this is trivial and results in the achiral SmC structure with unpolar layers. However, we can mix right and left isomers of *chemically different* molecules. In this case, the helicity is compensated for, but not the polarity of layers. Alternatively, one can compensate for the spontaneous polarization but keep the helical structure as it is [25].

In the helical structure, the optical ellipsoid of the smectic C* phase rotates together with the tilt plane. Like in cholesterics, we can imagine that helical turns form a stuck of equidistant quasi-layers that results in optical Bragg reflections in the visible range. Therefore, like cholesterics, smectic C* liquid crystals are one-dimensional photonic crystals. However, in the case of SmC*, the distance between the reflecting "layers" is equal to the full pitch P_0 and not to the half-pitch as in cholesterics, because at each half-pitch the molecules in the SmC* are tilted in opposite directions. Hence, we have a situation physically different from that in cholesterics.

In Fig. 4.37 the location of the Bragg reflections on the optical wavelength scale is compared for a cholesteric and smectic C* ($\theta_{SmC^*} = 25^\circ$) liquid crystals. The spectra have been calculated numerically using the Palto's software [26] with the same parameters for both materials: $P_0 = 0.25$ μm, sample thickness $d = 4$ μm and principle refraction indices 1.73 and 1.51. The calculations are made for normal and oblique light incidence angles of $\alpha = 0$ (dash line), and 45° (solid lines). The Bragg formula (3.14) is valid for both materials. However, at the light incidence along the helical axis ($\alpha = 0$) , the left edge of the first order Bragg reflection ($m = 1$) in the cholesteric corresponds to $\lambda_0 = P_0 < n > \approx 380$ nm but, in the smectic C* phase, the first order corresponds to the full pitch $\lambda_0 = 2P_0 < n > \approx 730$ nm. At this wavelength

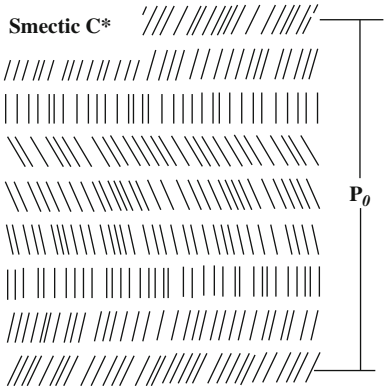

Fig. 4.36 Helical structure of the chiral smectic C* phase; P_0 is a pitch of the helix

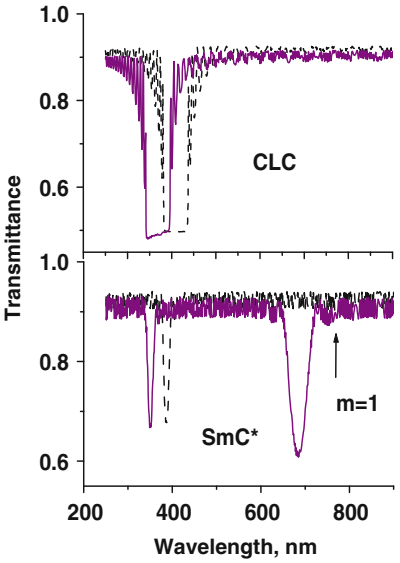

Fig. 4.37 Comparison of the calculated transmission spectra of a cholesteric (*top panel*) and smectic C* (*bottom panel*) for two angles of incoming light incidence: dashed curves for $\alpha = 0$ (along the helical axis), solid curves for $\alpha = 45^\circ$ with respect to the helical axis. Both materials have helical pitch 0.25 μm, refraction indices $n_{\parallel} = 1.73$ and $n_{\perp} = 1.51$, cell thickness 4 μm. Tilt angle for the SmC* is 25°

and $\alpha = 0$, the band is invisible (forbidden) due only to the coincidence of effective refraction indices for the same absolute value of the tilt $|\pm\theta_{smC^*}|$. The band at about 380 nm is the second diffraction order ($m = 2$). In the smectic C* phase, the first order Bragg diffraction band appears only at an oblique light incidence, see the transmission minimum at about 680 nm for $\alpha = 45^\circ$ in the same figure. Such a shift to the shorter waves of both $m = 1$ and $m = 2$ bands in the smectic C* (as well as of $m = 1$ band in the cholesteric) increases with increasing angle of light incidence.

4.10 Chiral Smectic A*

*4.10.1 Uniform Smectic A**

This is a chiral smectic A* with symmetry D_{∞}. Its properties are similar to those of the achiral SmA. However, close to the transition to the smectic C* phase, the chiral smectic A* phase shows interesting pretransitional phenomena in the dielectric and electrooptical effects (the so-called soft dielectric mode and electroclinic effect). They will be discussed in Chapter 13.

4.10.2 TGB Phase

This phase consists of uniform SmA* blocks separated by defect walls [22]. At each wall, the normal to smectic layers in one blocks turns through a small angle with

respect to the layer normal in the preceding block as very schematically shown in Fig. 4.38. From such blocks, a helical structure forms. Thus, the phase is twisted, consists of grains and has defects in a form of grain boundaries. That is why it is called a *twist-grain-boundary* or TGB phase. We should distinguish among the TGBA and TGBC phases based, respectively, on the smectic A* or smectic C* structure of their blocks. The TGB phases having a helical pitch shorter than light wavelength are optically isotropic. Such substances, especially based on side-chain polymers with photochromic moieties are interesting for optical information recording and applications to holography.

4.11 Spontaneous Break of Mirror Symmetry

This phenomenon has been discovered in the liquid crystal phases consisting of so-called banana (or bent-core) shape molecules [17, 27]. A mechanical model in Fig. 4.39a illustrates the idea. Each of the two dumb-bells has symmetry $D_{\infty h}$ with infinite number of mirror planes containing the longitudinal rotation axis and one mirror plane perpendicular to that axis. Imagine now that one of the dumb-bells is lying on the table and we try to put another one on the top of the first one parallel to

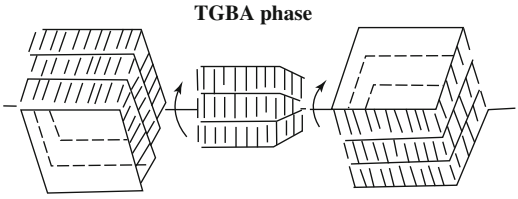

Fig. 4.38 Schematic picture of the block structure of the twist-grain-boundary smectic A* (TGBA) phase

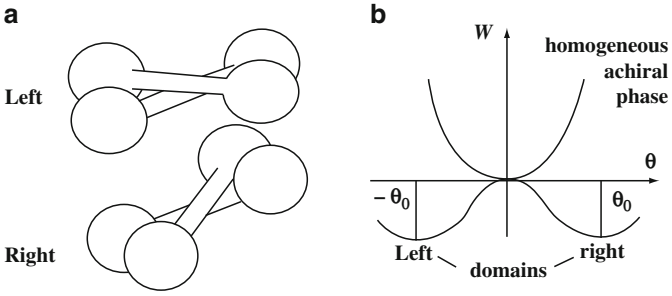

Fig. 4.39 A mechanical model of two interacting dumb-bells illustrating a break of the mirror symmetry (**a**) and the potential curves with two minima corresponding to two possible azimuthal angles between the dumb-bells (**b**). The same curves qualitatively illustrate the energy of the achiral phase and two chiral domains (left- and right-handed) as functions of the tilt angle ϑ of molecules in the smectic layer

the other. Such a construction, although unstable, would have mirror symmetry. In reality, the dumb-bells will form a kind of a chiral *propeller*, left or right, shown in the figure. The reason is that the gravitational potential energy of the upper dumb-bell is lower in a chiral construction. Due to this, the mirror symmetry is broken. Since the formation of right- and left-hand propellers is equally probable, the potential energy roughly has a shape of a two minima curve, see Fig. 4.39b, that will also be discussed below.

Something similar happens with achiral banana or bent-shape molecules. Chemical formula of a typical compound is given in Fig. 4.40. In this particular case, the dipole moment is approximately directed from up to down. The molecules have banana-like shape and located within the plane of the drawing forming a single layers with long molecular axes perpendicular to the smectic plane, Fig. 4.41. Such a monolayer is achiral and can be unpolar (*a*) or polar (*b*). Note that the polar achiral layer possesses spontaneous polarization $\mathbf{P}_s$ located within the figure plane and directed depending on the sign of molecular dipole moment (to the right in the figure). If the direction of $\mathbf{P}_s$ can be switched by an external electric field between two stable positions the monolayer is ferroelectric. A stuck of unpolar or polar layers may form either an unpolar or polar smectic phase. An example (a polar phase) is shown in Fig. 4.41c. Packing of polar layers with opposite in-plane directions of P_s results in the antiferroelectric phase, like in chiral antiferroelectrics (see Chapter 13).

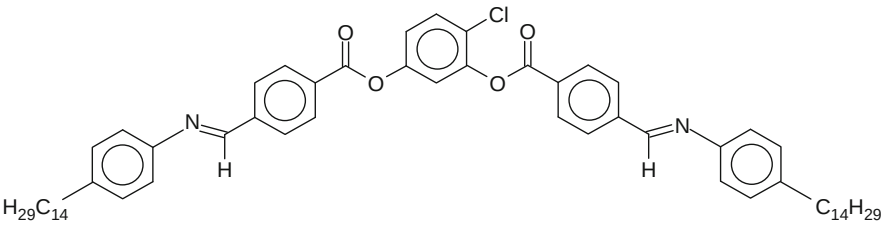

Fig. 4.40 Chemical formula of a typical bent-shape molecule. The electro-negative Cl atom is responsible for the molecular dipole moment directed approximately down close to the vertical axis

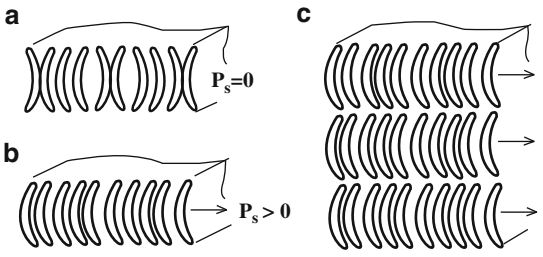

Fig. 4.41 Structure of single non-polar (**a**) and polar (**b**) smectic layers formed by bent-shape molecules: the longitudinal axes are aligned upright and the plane of the figure is mirror plane. Possible polar three-dimensional smectic biaxial phase (**c**)

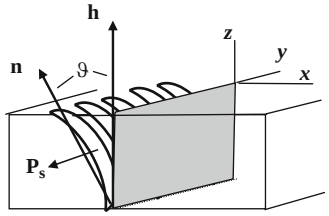

Fig. 4.42 Breaks of the mirror symmetry by the molecular tilt. Due to the collective tilt of molecules the *zy* plane is no longer a mirror plane. Three vectors, namely, molecular dipole moment $\mathbf{P_s}$, the normal to the layers **h** and the director **n** form the right-handed triple of vectors. For the tilt angle equal to $(-\vartheta)$ the triple changes the sense of chirality, i.e. becomes left-handed. As a result, right-handed and left-handed domains are observed

Table 4.2 Symmetry and structural features of the most popular thermotropic liquid crystal phases consisting of rod-like molecules (for the nomenclature we follow [28])

Symbol	Symmetry	Structural features
I or Iso	$K_h \times T(3)$	Ordinary liquid phase with full rotational and translational symmetry
I (chiral)	$K \times T(3)$	Liquid consisted of chiral molecules showing rotation of linearly polarized light
N	$D_{\infty h} \times T(3)$	Uniaxial nematic phase possessing long range orientational order and no translational order
N_b	$D_{2h} \times T(3)$	Biaxial nematic phase possessing long range orientational order and no translational order
N* or Ch	$D_{\infty} \times T(3)$	Chiral nematic or cholesteric phase with twist axis perpendicular to the director and macroscopic periodicity
SmA	$D_{\infty h} \times T(2)$	Uniaxial lamellar smectic A phase possessing one-dimensional periodicity along the director (i.e. layer normal). Quasi-long-range positional order along the layer normal and two-dimensional liquid-like order within the layer plane
SmA*	$D_{\infty} \times T(2)$	Optically active, chiral version of SmA phase
SmC	$C_{2h} \times T(2)$	Optically biaxial, tilted, lamellar phase: the director forms an angle with the normal to layers. Quasi-long-range positional order along the layer normal and two-dimensional liquid-like structure within the layer plane
SmC*	$C_2 \times T(2)$	Optically active chiral analogy of SmC phase showing macroscopic periodicity with twist axis perpendicular to smectic layers. Quasi-long-range positional order along the layer normal and two-dimensional liquid-like structure within the layer plane. Single layers of the same symmetry may form different phases in the bulk: ferroelectric (SmC*), antiferroelectric (SmC_A*) and ferrielectric (SmC_γ*).
TGBA* or TGBC*	$D_{\infty} \times T(2)$ or $C_2 \times T(2)$	Twist-grain-boundary (chiral) phases consisted of twisted grains or blocks of the smectic A* (or C*) phases with defect walls (boundaries) between them
SmB_{hex}	$D_{6h} \times T(1)$	A stack of interacting hexatic layers with three-dimensional, long-range, sixfold, bond orientational order and liquid-like positional correlations within the layers

(*continued*)

Table 4.2 (continued)

Symbol	Symmetry	Structural features
SmF	$C_{2h} \times T(1)$	Tilted analogy of the hexatic phase. A stack of interacting hexatic layers with three-dimensional, long-range, sixfold, bond orientational order and liquid-like positional correlations within the layers
BPI	$O^5 \times T(0)$	Blue phases BPI (body-centered cubic) and BPII (simple cubic) are chiral phases with three-dimensional macroscopic periodicity and liquid-like molecular correlations. Three-dimensional photonic bandgap crystals showing optical activity but no birefringence. BPIII is lower symmetry "foggy" phase strongly scattering light
BPII	$O^2 \times T(0)$	
BPIII	Unknown	
$B_1, B_2, \ldots, B_n$	Unknown	Series of achiral phases formed by banana- or bent-shape molecules. The phase symmetry reduces with suffix *n*. Manifest spontaneous brake of mirror symmetry and interesting ferroelectric and antiferroelectric properties
SmB_{cr}	$D_{6h} \times T(0)$	Crystalline lamellar phase with upright molecules and hexagonal lattice. True three-dimensional positional order. Soft crystal with small shear elastic modulus
SmE	$D_2 \times T(0)$	Biaxial crystal with upright molecules having true three-dimensional positional order. Rectangular in-plane lattice and herringbone packing of molecules (orthorhombic syngony). Soft crystal with small shear elastic modulus

Now we are ready to discuss spontaneous break of mirror symmetry. An achiral phase is spatially uniform and has mirror symmetry, i.e. its potential energy has a minimum located at zero tilt angle ϑ, see Fig. 4.39b. With decreasing temperature, the same molecules can acquire a collective tilt, some of them become tilted to the left with respect to the smectic layer normal (positive ϑ in Fig. 4.42), the others to the right (negative ϑ) in equal amounts. In fact, due to the tilt a triple of non coplanar vectors occurs, the vector of layer normal **h**, the vector of polarization $\mathbf{P}_s$ and the director **n**, that is necessary condition for chirality. This results in a break of the uniform structure and formation of right-handed and left-handed *ferroelectric domains*. Now the potential energy has two minima at the tilt angles $+\vartheta$ and $-\vartheta$ for the two types of domains, like in Fig. 4.39b. The banana phases manifest remarkable electrooptical properties; for example, upon application of a d.c. voltage, the directors rotate in opposite direction in the domains of opposite chirality.

In conclusion of this chapter we demonstrate Table 4.2, in which the most important liquid crystal phases and their structural properties are listed.

References

1. Demus, D., Richter, L.: Textures of Liquid Crystals. Verlag Chemie, Weinheim (1978)
2. Arnold, H., Sackmann, H.: Isomorphiebeziechungen zwischen kristallin-flüssigen Phasen. 4. Mitteilung: Mischbarkeit in binären Systemen mit mehreren Phasen. Z. für Elektrochemie **11**, 1171–1177 (1959)

3. Leadbetter, A.J.: Structural studies of nematic, smectic A and smectic C phases. In: Luckhurst, G.R., Gray, G.W. (eds.) The Molecular Physics of Liquid Crystals, pp. 285–316. Academic, London (1979). Chapter 13
4. Doucet, J.: X-ray studies of ordered smectic phases. In: Luckhurst, G.R., Gray, G.W. (eds.) The Molecular Physics of Liquid Crystals, pp. 317–341. Academic, London (1979). Chapter 14
5. Pikin, S.A.: Structural Transformations in Liquid Crystals. Gordon & Breach, New York (1991)
6. Kleman, M., Lavrentovich, O.D.: Soft Matter Physics. Springer-Verlag, New York (2003)
7. Lam, L.: Bowlics. In: Shibaev, V.P., Lam, L. (eds.) Liquid Crystalline and Mesomorphic Polymers, pp. 324–353. Springer-Verlag, New York (1993)
8. Tournilhac, F., Blinov, L.M., Simon, J., Yablonsky, S.V.: Ferroelectric liquid crystals from achiral molecules. Nature **359**, 621–623 (1992)
9. Vertogen, G., de Jeu, V.H.: Thermotropic Liquid Crystals. Fundamentals. Springer-Verlag, Berlin (1987)
10. Shibaev, V.P., Freidzon, S., Kostromin, S.G.: Molecular architecture and structure of thermotropic liquid crystal polymers with mesogenic side chain groups. In: Shibaev, V.P., Lam, L. (eds.) Liquid Crystalline and Mesomorphic Polymers, pp. 77–120. Springer-Verlag, New York (1993)
11. Pershan, P.S.: Lyotropic liquid crystals. Phys. Today **35**(5), 34–39 (May 1982)
12. Kuzma, M.R., Saupe, A.: Structure and phase transitions of amphiphilic lyotropic liquid crystals. In: Collings, P., Patel, J. (eds.) Handbook of Liquid Crystal Research, pp. 237–258. Oxford University Press, New York (1997)
13. Yu, L.J., Saupe, A.: Observation of a biaxial nematic phase in potassium-laurate -1-decanol-water mixtures. Phys. Rev. Lett. **45**, 1000 (1980)
14. Kuball, H.-G.: From chiral molecules to chiral phases: comment on the chirality of liquid crystal phases. Liq Cryst Today **9**(1), 1–7 (1999)
15. Chilaya, G.S., Lisetskii, L.N.: Helical twisting in cholesteric mesophases. Uspekhi Fis. Nauk **134**, 279–304 (1981). in Russian
16. Kats, E.I.: On the optical activity in liquid crystal mixtures Zh. Eksp. Teor Fiz. *74*, 2320, (1978)
17. Takezoe, H.: Electrooptic and dielectric properties in bent-shape liquid crystals. Jpn. J. Appl. Phys. **Pt.1**(39), 3536–3541 (2000)
18. Oseen, C.W.: The theory of liquid crystals. Trans. Faraday Soc. **29**, 883–900 (1933)
19. Reinitzer, F.: Beiträge zur Kenntniss des Cholesterins. Monathefte für Chemie **9**, 421 (1888)
20. Belyakov, V.A., Dmitrienko, V.E.: Blue phase of liquid crystals. Uspekhi Fis. Nauk **146**, 369–415 (1985)
21. Coles, H.J., Pivnenko, M.N.: "Blue phases" with a wide temperature range. Nature **436**, 997–1000 (2005)
22. Collings, P.: Phase structure and transitions in thermotropic liquid crystals. In: Collings, P., Patel, J. (eds.) Handbook of Liquid Crystal Research, pp. 99–124. Oxford University Press, New York (1997)
23. Grebel, H., Hornreich, R.M., Shtrikmann, S.: Landau theory of cholesteric blue phase: the role of higher harmonics. Phys. Rev. A **30**, 3264–3278 (1984)
24. Meyer, R.B., Liebert, L., Strzelecki, L., Keller, P.J.: Ferroelectric liquid crystals. J. Physique (Paris) Lett. **36**, L69–L71 (1975)
25. Beresnev, L.A., Baikalov, V.A., Blinov, L.M., Pozhidayev, E.P., Purvanetskas, G.V.: First non helicoidal ferroelectric liquid crystal. Pis'ma Zh. Eksp. Teor. Fiz. **33**, 553–57 (1981)
26. Palto, S.P.: Algorithm for solution of optical problem for lamellar anisotropic media. Zh. Eksp. Teor Fiz. **119**, 638–648 (2001) [JETP 103, 469 (2006)]
27. Link, D.R., Natale, G., Shao, R., Maclennan, J.E., Clark, N.A., Korblova, E., Walba, D.M.: Spontaneous formation of macroscopic chiral domains in a fluid smectic phase of achiral molecules. Science **278**, 1924–1927 (1997)
28. Goodby, J.W., Gray, G.W.: Guide to the nomenclature and classification of liquid crystals. In: Demus, D., Goodby, J., Gray, G.W., Spiess, H.-W., Vill, V. (eds.) Physical Properties of Liquid Crystals, pp. 17–23. Wiley-VCH, Weinheim (1999)

Chapter 5
Structure Analysis and X-Ray Diffraction

5.1 Diffraction Studies and X-Ray Experiment

5.1.1 General Consideration

The diffraction of the electromagnetic waves or the de Broglie waves of electrons and neutrons on a liquid, liquid crystalline or crystalline structures results in a characteristic pattern from that one can restore a distribution of density in space or density function $\rho(\mathbf{r})$ [1, 2]. What kind of density we speak about?

The *electron density* is probed by electromagnetic waves, as in optics. In fact, the same theory of light diffraction and dispersion is relevant to the X-ray diffraction for wavelengths comparable to the size of atoms. For X-rays, the wavelength $\lambda_X \approx$ 0.5–1 Å depends on material of the anticathode in an X-ray tube. In a synchrotron, the electromagnetic wave spectrum is very large and determined by the speed of moving electrons. From the experiment we can find the density (or number) of electrons in atomic shells.

An *electric potential* of a substance is probed by charge particles emitted, for example, by an electronic gun or an accelerator. The electron beam is scattered by the electric potential of positive nuclei and negative electrons and the maximum positive potential corresponds to the center of an atom. The electrons in the beam have the de Broglie wavelength λ_e dependent on their velocity v, i. e. on the accelerating voltage V, namely, $eV = m_e v_e^2/2 = W$

$$\lambda_e = h \Big/ m_e v = h \Big/ (2m_e W)^{1/2}. \tag{5.1}$$

Here m_e is electron mass and h is Planck's constant. Hence, for electron energy $W = 1$ eV–10 keV, the wavelength is $\lambda_e \approx$ 10–0.1 Å. From this diffraction experiment we can find the distribution of the electric potential correlated to some extent with the distribution of the mass density. Another technique for mapping the local electric potential is Atomic Force Microscopy [3].

The distribution of the *mass of nuclei* almost equal to the full mass density is probed by neutron beams. To this effect, one can use the so-called thermal or cold

L.M. Blinov, *Structure and Properties of Liquid Crystals*,
DOI 10.1007/978-90-481-8829-1_5,

neutrons with energy $W \approx 0.05$ eV provided by nuclear reactors. The corresponding wavelength is in the proper range for structure analysis, $\lambda_n = 1$–1.5 Å, because the mass of a neutron is large, $m_n = 1840 m_e$.

All these techniques have certain advantages and disadvantages. The electron diffraction experiment requires for vacuum or low pressure gas, and thin films, very often on conductive substrates (otherwise the surface is charged by incoming electrons). On the other hand, the interaction between charges is very strong and one may operate with small samples and short expositions and, due to short wavelengths, the spatial resolution can be very high. In addition, the data processing is sometimes simpler due to a small curvature of the Ewald sphere to be discussed later. Using electrons even light atoms like hydrogen are well seen.

Neutron diffraction requires for larger samples (linear dimension about 1 cm) and the reactors producing short lifetime (minutes) cold neutrons are expensive. On the other hand, in contrast to X-rays, neutrons are sensitive to isotopes and atoms with slightly different atomic mass, such as Co and Ni. In addition, a neutron has an intrinsic magnetic moment about two Bohr magnetons, $p_{\mathrm{m}} = 1.9\ \mu_{\mathrm{B}}$. For this reason, neutrons strongly interact with magnetic moments of electrons and nuclei. Thus, a neutron experiment provides a unique possibility for studying different magnetic structures, spin effects, para- and ferro-magnetism. However, the X-ray technique is the most universal for the structure analysis. In fact, the majority of structures of crystals from the simplest ones to those formed by protein molecules were found by the X-ray diffraction.

5.1.2 X-Ray Experiment

One can use conventional low intensity sources (X-ray tubes) providing very narrow spectral lines, but low intensity. A set-up consists of an X-ray tube (X), beam collimators (C), one or several monochromators (M), a detector (D) and a data acquisition system (PC). A sample is installed in a camera with controllable temperature, Fig. 5.1. In the case of a liquid crystal, a magnetic or electric field is necessary for the sample orientation. Historically, for a long time, fluorescent screens and

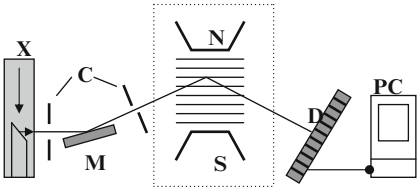

Fig. 5.1 A set-up for a study of X-ray diffraction on liquid crystals: X-ray tube (X), beam collimators (C), mirrors (M), a detector (D) and a data acquisition system (PC). A sample is represented by a stack of parallel layers placed in a camera with controllable temperature installed between the poles of a magnet

photographic films were primary tools for detecting X-rays. The latter are two-dimensional, very cheap and sensitive but their processing requires densitometers for the image digitizing. Since few decades, point detectors have been using everywhere based on the proportional and scintillation counters both one- and two-dimensional. Automatic two-dimensional detectors are very convenient because they grasp the entire diffraction pattern and save a lot of time.

Nowadays, however, synchrotrons are available that provide million times higher intensity and wide spectrum of the polarized emission. One can use different wavelength ranges and short expositions when studying dynamic processes. Of course, there are not so many synchrotron accelerators all over the world but they have many output beams, as shown in Fig. 5.2, and attached are many experimental stations. Such a work is usually organized at the international level.

What does an X-ray diffraction experiment bring about? In fact, a lot:

1. Number of diffraction peaks on a diffractogram, their precise positions and the symmetry of the pattern
2. The peak amplitudes I and areas A under peaks as functions of temperature, pressure, external fields, etc.
3. The peak profile that is the profile of the diffraction intensity $I(q)$ within a particular diffraction spot, which is a function of the diffraction angle or scattering wavevector q. The key problem of X-ray analysis is how to relate $I(q)$ to the electron density function or density correlation function that takes into account thermal fluctuations.

5.2 X-Ray Scattering

5.2.1 Scattering by a Single Electron

Protons and electrons are charge particles interacting with electromagnetic waves and their number and particular location determine the amplitude of scattered waves. As the electrons are very light they contribute much stronger to X-ray scattering than protons (nuclei). In fact intensity of scattering is even measured in electron units. Therefore, scattering by a single electron deserves a brief consideration.

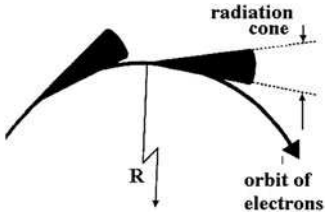

Fig. 5.2 A geometry of electromagnetic wave emission from an accelerator of relativistic particles (synchrotron). R is radius of the synchrotron ring. X-ray emission in the form of the cone is delivered to one of the many experimental stations

Let linearly polarized, plane electromagnetic wave of amplitude E_0 is incident on a free electron, Fig. 5.3. The equation of oscillatory motion of the electron about the centre of coordinate is:

$$m_e(d^2\mathbf{r}/dt^2) = (m_e/e)(d^2\mathbf{d}/dt^2) = e\mathbf{E_0}\cos(\omega t + \alpha) \tag{5.2}$$

where vector $\mathbf{r}$ is displacement of the electron that creates a dipole moment $\mathbf{d} = e\mathbf{r}$. The current produced by moving electron is proportional to its velocity $\mathbf{v}$, i.e. $\mathbf{j} = e\mathbf{v} = d\mathbf{d}/dt$, which, in turn, is a source the electromagnetic field in point P [4].

$$\mathbf{E} = \frac{1}{c^2 R_0}[(\ddot{\mathbf{d}} \times \mathbf{n}) \times \mathbf{n}] = \frac{e^2}{mc^2 R_0}[(\mathbf{E}_0 \times \mathbf{n}) \times \mathbf{n}] \tag{5.3}$$

Vector $(\mathbf{E}_0 \times \mathbf{n})$is perpendicular to vector $\mathbf{n}$ and has modulus $E_0\sin\gamma$ where $\gamma=(\pi/2)-\theta$. Therefore, the modulus of the scattered field amplitude is $E_0\cos2\theta$. Note that the angle between the wavevectors of incident and scattered wave is assumed to be 2θ according to the convention adopted below (see Fig. 5.4) and used throughout the book.

The energy flux is given by the Pointing vector

$$\mathbf{S} = (c/4\pi)E^2\mathbf{n} \tag{5.4}$$

and the dipolar emission energy incident on a small surface element $df = R_0^2 d\Omega$ in a solid angle $d\Omega$ is given by $dW = Sdf = (c/4\pi)E^2R_0^2 d\Omega$. After substituting $E^2 = \mathbf{E}^2$ from Eq. 5.3 we find the intensity of the scattered, polarized wave.

$$dW = \frac{e^4 E_0^2}{4\pi m^2 c^3}\cos^2 2\theta d\Omega \tag{5.5}$$

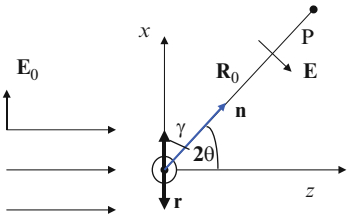

Fig. 5.3 Geometry of scattering linearly polarized electromagnetic wave by a single electron. The incident wave field $\mathbf{E}_0$ causes oscillatory displacement $\mathbf{r}$ of an electron and the scattered wave is detected in point P

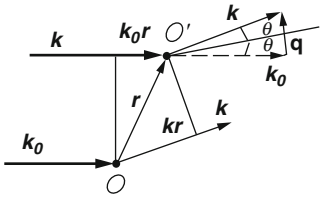

Fig. 5.4 Illustration of an electromagnetic wave scattering by two material points: $\mathbf{k}_0$ and $\mathbf{k}$ are vector of incident and scattered waves, $\mathbf{q}$ is vector of scattering

Now, normalizing Eq. 5.5 by the Pointing vector of the incident wave E_0 we find the *differential cross-section* of one-electron scattering:

$$d\sigma_e = \left(e^2/m_e c^2\right)^2 \cos 2\theta d\Omega \tag{5.6}$$

The emission of the dipole is symmetric with respect to the dipole axis x, Fig. 5.3, and has the ∞-form in the xz plane (no emission exactly along the x-axis). It is spectacular that the cross section is independent of frequency.

In order to obtain the *total cross-section* of scattering we should integrate the diagram over φ from 0 to 2π and over 2ϑ from 0 to π in the polar coordinates with the vertical polar axis x. The angle $\gamma=(\pi/2) - 2\theta$ will be a polar angle and angle φ an azimuthal angle in the zy plane. Then, with a volume element $d\Omega=\sin\gamma d\gamma d\varphi$, the integral $\iint \sin^3\gamma d\gamma d\varphi = 8\pi/3$ and the overall scattering cross-section of an electron irradiated by a linearly polarized light is given by the *Thomson formula*:

$$\sigma_e = \frac{8\pi}{3}\left(\frac{e^2}{m_e c^2}\right)^2 \tag{5.7}$$

Since we are mostly interested in scattering unpolarised X-ray radiation we should average Eq. 5.7 over all directions of vector **E** perpendicular to the direction of the wavevector of the incident wave k_0, i.e. around the z-axis. Then we find the *differential cross-section of one-electron scattering in unpolarized light*:

$$d\sigma_e = \tfrac{1}{2}\left(e^2/m_e c^2\right)^2 (1 + \cos^2 2\theta) d\Omega \tag{5.8}$$

As to the *total cross-section of scattering by free electron irradiated by unpolarized light,* it is described by the same Thomson formula (5.7) that is easy to check by integrating (5.8) over 2θ (from 0 to π) and over φ (from 0 to 2π).

5.2.2 Scattering by Two Material Points

Let the plane wave with wavevector $\mathbf{k}_0$ is incident onto two scattering points fixed at O and O', see Fig. 5.4. The center of the reference polar coordinate system is at point O and point O' is characterized by radius-vector $\boldsymbol{r}$. Both points are sources of secondary spherical waves propagating in all directions (Huygens' principle). The mechanism of scattering is not important because now we consider a very general geometry of wave scattering, not its amplitude. Consider a wave with wavevector $\mathbf{k}$ scattered by two points at angle 2θ with respect to $\mathbf{k}_0$ and introduce the *wavevector of scattering* (or diffraction) as a difference between the two vectors

$$\mathbf{q} = \mathbf{k} - \mathbf{k}_0 \tag{5.9}$$

It is equal to the momentum taken by a fixed material point. In our case, modulus $|\mathbf{k}| = |\mathbf{k}_0|$ (i.e. $\lambda=\lambda_0$). This corresponds to elastic scattering because the points do not take energy from the photons and the light frequency remains unchanged. Hence, as seen from the figure the scattering wavevector amplitude is

$$q = 2k_0 \sin\theta = \frac{4\pi \sin\theta}{\lambda_0} \tag{5.10}$$

and the scattering angle between incident and scattered waves is 2θ.

This is very general equation that will be used further on. From the same figure we can extract another useful relationship between the **q**-vector and the wave path difference Δ accumulated along the distance between the particles. It is just a difference of two scalar products:

$$\Delta = \mathbf{kr} - \mathbf{k}_0\mathbf{r} = (\mathbf{k} - \mathbf{k}_0)\mathbf{r} = \mathbf{qr} \tag{5.11}$$

5.2.3 *Scattering by a Stack of Planes (Bragg Diffraction)*

Let an electromagnetic wave is incident on the system of two parallel planes at an angle θ with respect to the planes. Then, as seen in Fig. 5.5, the scattering vector is again described by Eq. 5.9. Now, let us introduce a new vector, a *wavevector of the structure* with period d: $q_0 = 2\pi/d$. Then, at a certain "resonance" angle θ_0 the wavevectors of scattering and structure coincide:

$$(4\pi/\lambda)\sin\theta_0 = 2\pi/d \text{ or } 2d\sin\theta_0 = \lambda \tag{5.12}$$

The same condition can easily be found by comparison of the wave path difference $2d\sin\vartheta$ with wavelength λ.

For a stack of layers we will have m multiple reflections and equation

$$m\lambda = 2d\sin\theta_0, \quad m = 1, 2, 3... \tag{5.13}$$

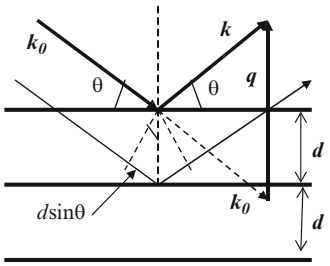

Fig. 5.5 Bragg scattering (or reflection) of an electromagnetic wave by a stack of parallel planes in vacuum (d is period of the stack structure, **q** is vector of scattering)

called Bragg (sometimes Bragg-Wulf) formula for the diffraction (resonance) angles of X-ray scattering from the stack of planes. For example, it could be crystal planes ($h\ k\ l$) or smectic layers with interlayer distance d.

This interlayer distance can be found as $d=\lambda/2\sin\vartheta_0$ from the X-ray experiment measuring the angle of the first-order diffraction spot ($m = 1$) or from higher order reflections. It is convenient to plot the diffracted beam intensity as a function of q; then different diffraction orders are located at equidistant positions, as shown in Fig. 5.6:

$$q = (4\pi/\lambda)\ \sin\vartheta = mq_0 = 2\pi m/d$$

Note that Eqs. 5.9–5.11 tell us nothing about the amplitude of waves and the intensity of scattering because we used only the momentum conservation law.

5.2.4 *Amplitude of Scattering for a System of Material Points*

Generally, the amplitude of a wave scattered by material point O and measured at any distant point P ($\mathbf{R}$) corresponds to the Huygens principle:

$$F_p = \frac{1}{R} f_O \exp i\mathbf{k}R \tag{5.14}$$

and is determined by a scattering efficiency f_O of the point O (depending on its electron mass), a distance R between the scattering center and point P and a wavevector $\mathbf{k}$ of a scattered wave (through multiplier exp$i\mathbf{kR}$). Below we shall disregard term (1/R) (it may be taken into account if necessary) but always operate with vector of scattering $\mathbf{q} = \mathbf{k} - \mathbf{k_0}$ having in mind that k_0 has fixed direction along the selected coordinate axis. It is vector $\mathbf{q}$ that is responsible for all the interfering scattered beams propagating in direction to point P as was shown for two scattering points, see Eq. 5.11.

Consider now N scattering points having different scattering efficiency f_j and located at different distances $\mathbf{r}_j$ from one of the scattering points O selected as

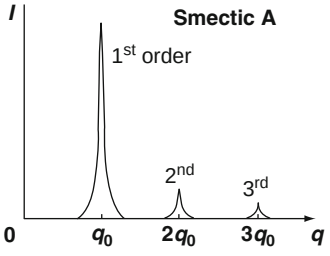

Fig. 5.6 Illustration of the Bragg diffraction with the qualitative angular diffraction spectrum of the smectic A phase

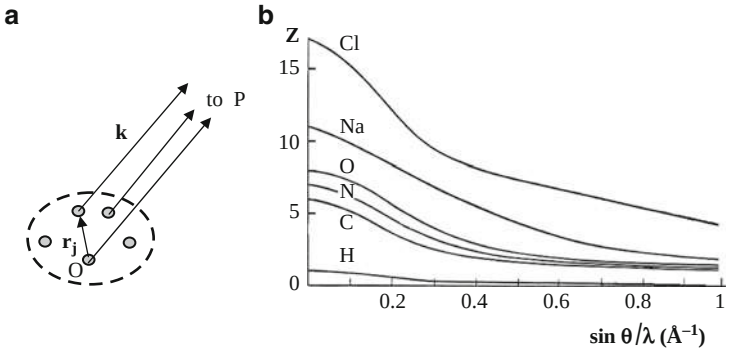

Fig. 5.7 (**a**) Geometry of scattering by several objects with vectors $\mathbf{r}_j$ between them and the beams scattered in direction to point P; (**b**) angular dependencies of scattering intensity by different atoms. The plot shows strong scattering in forward and back directions and the weak scattering in the direction perpendicular to the incident beam

a reference, Fig. 5.7a. All these points contribute to scattering in **q** direction defined by Eq. 5.10. Then the *amplitude of the field of N scattering points* "measured" at point *P* is superposition of all *N*- amplitudes:

$$F_p(\mathbf{q}) = \sum_{j=1}^{N} f_j \exp i(\mathbf{q}\mathbf{r}_j) \tag{5.15}$$

Here **q** is the wavevector of scattering defined by Eq. 5.9 for two material points. Now we make a generalization, i.e. consider a body with *continuous density of scattering points* ρ(**r**) (that is density of electrons, atoms and molecules). Then the scattering amplitude is an integral over the scattering volume in the three-dimensional **r**-space shown by dash line in Fig. 5.7a:

$$F(\mathbf{q}) = \int_V \rho(\mathbf{r}) \exp i(\mathbf{q}\mathbf{r}) dV \tag{5.16}$$

Thus, the amplitude of scattering in point P is just a Fourier integral of the electron density function (generally complex). The variation of the position of point P means variation of scattering vector **q,** therefore suffix P at $F_P(\mathbf{q})$ is skipped. At each **q** we collect total amplitude of scattering from all the body with density ρ(**r**) usually situated far from point P. In the Cartesian system:

$$F(\mathbf{q}) = \iiint_V \rho(x,y,z) \exp i(q_x x + q_y y + q_z z) dx dy dz \tag{5.17}$$

5.2.5 Scattering Amplitude for an Atom

An atom has a spherical symmetry, therefore $\rho_a(\mathbf{r}) = \rho_a(r)$. However, the incident beam propagating along the x-axis breaks the overall spherical symmetry of scattering. In the spherical reference system, with radius r, polar angle ϑ $(0-\pi)$, azimuthal angle ψ $(0 - 2\pi)$, a volume element is $dV = r^2 \sin\vartheta \, d\vartheta d\psi dr$ and $\Delta = \mathbf{qr} \approx qr\cos\vartheta$. The integral (5.16) is triple integral and, at first, we integrate with respect to ϑ:

$$\int_0^{\pi} e^{iqr\cos\vartheta} \sin\vartheta d\vartheta = -\frac{1}{iqr} e^{iqr\cos\vartheta}|_0^{\pi} = \frac{2}{qr}\left(\frac{e^{iqr} - e^{-iqr}}{2i}\right) = \frac{2\sin qr}{qr}$$

Next integrating with respect to φ results in 2π. Now we should integrate (5.16) with respect to r and find the angle (or q-) dependence of the field intensity scattered by an atom

$$F(q) = \int_0^{\infty} 4\pi r^2 \rho_a(r) \frac{\sin qr}{qr} dr \tag{5.18}$$

We see that the scattering amplitude depends only on the modulus of q and is spherically symmetric in the q-space. Since $\rho_a(r)$ is unknown there is no universal formula for each atom but we can analyze two asymptotic cases:

$$\text{for } q \to 0, \ \sin qr/qr \to 1 \text{ and } F(0) = \int_o^{\infty} 4\pi r^2 \rho_a(r) dr = \int_o^{\infty} \rho_a(r) dV = Z$$

and

$$\text{for } q \to \infty, \ \sin qr/qr \to 0, \ F(q) \to 0.$$

Indeed, according to (5.10), for a finite λ_0, the case of $q \to 0$ means $\theta \to 0$ (forward scattering) the scattering amplitude is proportional to the number of electrons Z in the atom. It means strong forward scattering as in case of a single electron. The intensity of scattering will be proportional to Z^2. However, for directions strongly perpendicular to the primary beam the scattering is absent. This is a result of interference of different scattered waves from individual electronic oscillators. The calculated angular dependencies of scattering intensity for different atoms are shown in Fig. 5.7b (in electron charge units) [2]. Since $\sin\theta/\lambda = q/4\pi$, see Eq. 5.10, the abscissa is, in fact, the vector of scattering.

5.3 Diffraction on a Periodic Structure

5.3.1 *Reciprocal Lattice*

Now we consider periodic crystalline structures. The simplest case is one-dimensional structure realized, for instance, in the smectic A phase, see Fig. 5.8a: the density is periodic along x with period a, and wavevector $q = q_x = h(2\pi/a)$, h is an integer. Then the density function can be written as

$$\rho(x) = \sum_{-\infty}^{\infty} \delta(x - ha)$$

and in accordance with (5.16) the scattering amplitude is given by

$$F(q_x) = \sum_{h=-\infty}^{\infty} \frac{1}{a} \int \delta(x - ha) e^{iq_x x} dx = \frac{1}{a} \sum_{-\infty}^{\infty} e^{iq_x ha}.$$

As $\exp(iq_x ha) = 1$ only for $q_x = 2\pi/a$ (otherwise it equals 0) the same equation may be rewritten as

$$F_h(q_x) = F(q_x) = \frac{1}{a} \sum_{-\infty}^{\infty} \delta(q_x - \frac{2\pi}{a} h) \tag{5.19}$$

Therefore, $F(q)$ is a set of the δ-like peaks on the q-scale separated by distances $2\pi/a$! These peaks form a one-dimensional *reciprocal lattice* with basic vector $2\pi/a$, shown in Fig. 5.8b.

In the three-dimensional-lattice, there are three basic vectors **a**, **b,** and **c,** Fig. 5.9a, and we can introduce a concept of the reciprocal three-dimensional lattice. It is a lattice in the wavevector space having the dimension of inverse length for each coordinate in the inverse space. Such a lattice may be built by translations of the elementary cell shown in Fig. 5.9b. The basic vectors of the reciprocal lattice are **a***, **b***, **c*** and the *vector of the reciprocal lattice* is given by

$$\mathbf{H} = \mathbf{H}_{hkl} = h\mathbf{a}^* + k\mathbf{b}^* + l\mathbf{c}^* \tag{5.20}$$

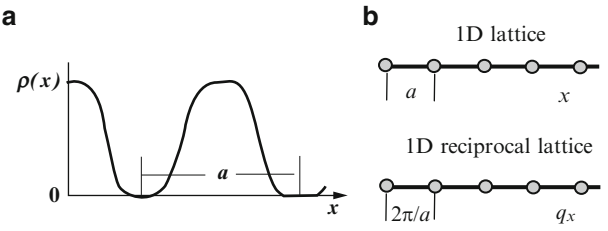

Fig. 5.8 Periodic density distribution (density wave) in one-dimensional crystal (**a**) and one-dimensional direct and reciprocal lattices with periods a and $2\pi/a$ (**b**)

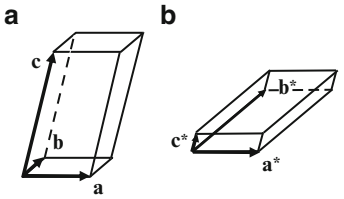

Fig. 5.9 A crystal lattice cell built on the **a, b, c** vector basis (**a**) and a cell of the reciprocal lattice based on vectors **a*, b*, c*** (**b**)

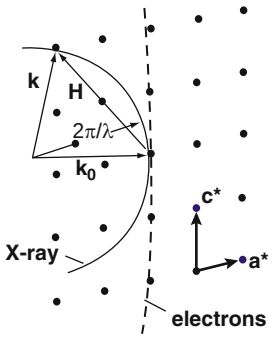

Fig. 5.10 Projection of the Ewald sphere on the a*,c* plane in reciprocal lattice for crystal irradiated by X-rays (*solid semicircle*) and electrons (*dash line*). Radius of the sphere is $2\pi/\lambda$. Lattice vector **H** connects two points of the reciprocal lattice. When vector of scattering ($\mathbf{k} - \mathbf{k}_0$) coincides with **H,** a strong diffraction is observed at a particular angle defined by Eq. 5.10

where *h, k, l* are integers. Vector **H** is a fundamental characteristic of a three-dimensional crystal. In the simplest case of a rectangular cell, the reciprocal lattice has periods $2\pi/a$, $2\pi/b$ and $2\pi/c$. For crystals of other symmetry, $\mathbf{a}^* = 2\pi(\mathbf{b} \times \mathbf{c})/(\mathbf{a}\cdot\mathbf{b} \times \mathbf{c})$, $\mathbf{b}^* = 2\pi(\mathbf{c} \times \mathbf{a})/(\mathbf{a}\cdot\mathbf{b} \times \mathbf{c})$, and $\mathbf{c}^* = 2\pi(\mathbf{a} \times \mathbf{b})/(\mathbf{a}\cdot\mathbf{b} \times \mathbf{c})$ where we see in denominator the mixed product of the three vectors corresponding to the volume of elementary cell.

When the crystal is irradiated by an X-ray beam, its lattice scatters the radiation selectively. A strong diffraction is observed when the wavevector of scattering for a particular angle (i.e. **q**) coincides with the vector of reciprocal lattice, as shown in the Ewald sphere, Fig. 5.10. The condition

$$\mathbf{q} = \mathbf{k} - \mathbf{k_0} = \mathbf{H}$$

means the conservation of linear momentum of electromagnetic wave. Then, according to (5.16) the amplitude of scattering is given by

$$F_{hkl} = \frac{1}{V_c} \int_{V_c} \rho(\mathbf{r}) \exp i\mathbf{r}\mathbf{H}_{hkl} dV \tag{5.21}$$

where integrating is taken over the volume V_c of a single crystallographic cell in the direct space.

Hence, for the elastic scattering, the ends of the scattering vector of the scattered beam **k** must coincide with the points of the reciprocal lattice determined by the three-dimensional Ewald sphere [1] of radius $k = 2\pi/\lambda_0$. The center of the sphere is defined by the direction of $\mathbf{k_0}$ (horizontal in the figure) and one of the points. The X-ray wavelengths are close to the periods of crystal lattices and the sphere curvature is large. For electrons, the wavelength is much shorter, the sphere radius of the corresponding Ewald sphere is longer and the sphere surface in the figure is very flat.

5.3.2 *Intensity of Scattering*

Consider a three-dimensional crystal. For the scattering amplitude of a discrete system of j atoms in an elementary cell we can write a formula similar to (5.15):

$$F_{hkl} = \sum_{j=1}^{N} f_j \exp i(\mathbf{H}_{hkl}\mathbf{r}_j), \tag{5.22}$$

Now the summation is performed over all atoms in one cell and f_j is scattering efficiency of a particular atom. The vector $\mathbf{H}_{\mathrm{hkl}}$ determines the angular positions of the diffraction spots, the coefficient f_{j} determines their form, i.e. the angular distribution of the scattering intensity within the spot. But how to estimate the scattered field intensity related to the energy $dW/d\Omega$ scattered at a certain angle ϑ in a unit solid angle?

The magnitude of the energy flux $Q = dW/d\Omega$ scattered by an object is determined by the number of electrons in the object, their spatial configuration and the differential cross-section of scattering by one electron, given by Eq. 5.8. The latter is normalized to the energy of the primary X-ray beam and is independent of the distance between an object and a detector. From the measurements of the flux we can find the scattering efficiency of an atom f_j, molecule or any object. The spatial configuration of electrons determines the scattering amplitude (*electric field strength*) at the detector and the flux of the energy is proportional to the squared modulus of the complex amplitude that is $|F(\mathbf{q})|^2 = F(\mathbf{q})\ F^*(\mathbf{q})$. Therefore, for incident flux of unpolarized beam $Q_0 = 1$, on account of (5.8), the scattered flux is given by

$$Q(\mathbf{q}) = \left(\frac{e^2}{mc^2}\right)^2 \frac{1 + \cos^2 2\vartheta}{2} |F(\mathbf{q})|^2$$

The differential intensity calculated in that way is related to a point in the diffraction pattern corresponding to wavevector **q**. Usually, all multipliers are excluded, although they can be taken into account when necessary (for example $\cos^2 2\vartheta$), and the scattering intensity $I(\mathbf{q})$ is expressed in relative, "electron units" [electron^2] as follows:

$$I(\mathbf{q}) = |F(\mathbf{q})|^2 = F(\mathbf{q})F^*(\mathbf{q}) \tag{5.23}$$

The intensity can be found from the X-ray diffraction experiment and the result compared with calculated diffraction pattern that is angular spectrum of the scattered X-ray intensity. To this effect, we should make a Fourier transform $F(\mathbf{q})$ of the density function $\rho(\mathbf{r})$ i.e. find the scattering amplitude and then take square of it, $I(\mathbf{q}) = |F^2(\mathbf{q})|$. This works well for solid crystals, but is not always convenient for liquids, liquid crystals and other soft matter materials in which the thermal fluctuations play a very substantial role. In such cases, the so-called *density autocorrelation function* appears to be more convenient. However, before to proceed along that way, we should separate two sources of scattering.

5.3.3 Form Factor and Structure Factor

These are key functions in the X-ray analysis. Let us take Eq. 5.15 for the scattering amplitude of N scattering objects, e.g. by molecules forming a molecular crystal, and write the *scattering intensity*

$$I(\mathbf{q}) = F(\mathbf{q})F^*(\mathbf{q}) = \sum_j^N \sum_k^N f_j(\mathbf{q}) f_k(\mathbf{q}) \exp i\mathbf{q}(\mathbf{r}_j - \mathbf{r}_k)$$

Here $\mathbf{r}_\mathrm{j}$ and $\mathbf{r}_\mathrm{k}$ are the same vectors corresponding to the distances shown in Fig. 7a and sign minus at $\mathbf{r}_\mathrm{k}$ comes from the complex conjugation. Both summations are made from 1 to N. The same equation may be presented in another form:

$$I(\mathbf{q}) = \sum_{j=k}^N f_j(\mathbf{q}) f_k(\mathbf{q}) \exp i\mathbf{q}(\mathbf{r}_j - \mathbf{r}_k) + \sum_{j\neq}^N \sum_k^{N-1} f_j(\mathbf{q}) f_k(\mathbf{q}) \exp i\mathbf{q}(\mathbf{r}_j - \mathbf{r}_k) \quad (5.24)$$

In the first N terms $j = k$, $\mathbf{q}(\mathbf{r}_\mathrm{j} - \mathbf{r}_\mathrm{k}) = 0$ and, this sum corresponds to the intensity coming from the individual atoms or molecules without interference or diffraction. Such scattering and corresponding terms exist even in the gas phase (so-called, "gas component"). Thus $f_j(\mathbf{q})f_k(\mathbf{q}) = F^2_{form}(\mathbf{q})$ is a smooth decaying function of $\mathbf{q}$ like the square of the atom scattering amplitude shown in Fig. 5.7b. The second term includes $N - 1$ times more terms than the first one and has very sharp maxima at $\mathbf{q}(\mathbf{r}_\mathrm{j} - \mathbf{r}_\mathrm{k}) = 2\pi$ due to periodicity of the crystal lattice. For identical objects we may also extract $f_j f_k = F^2{}_{form}(\mathbf{q})$ from the second sum symbols:

$$I(\mathbf{q}) = NF^2_{form}(\mathbf{q}) + NF^2_{form}(\mathbf{q}) \sum_{j\neq}^N \sum_k^{(N-1)} \exp i\mathbf{q}(\mathbf{r}_j - \mathbf{r}_k).$$

The normalized intensity is given by

$$\frac{I(\mathbf{q})}{NF^2_{form}(\mathbf{q})} = 1 + \sum_{j\neq}^N \sum_k^{(N-1)} \exp i\mathbf{q}(\mathbf{r}_j - \mathbf{r}_k) = S(\mathbf{q}) \quad (5.25)$$

where $S(\mathbf{q})$ is a structure factor determined by relative positions of the objects (atoms or molecules) in a medium of given symmetry and the character of their positional correlations. The normalized scattering intensity is given in "electron" units.

From (5.25) we may conclude that the total intensity of scattering of a crystal is a product of a sharp structure factor and a smooth form-factor that is a series of sharp peaks with a smoothly decaying envelope ff_k. The structure factor can be found from the experimental angular dependence of the scattering intensity. But what is the relation between structure factor $S(\mathbf{q})$ and density function?

Theoretically they are related by the Fourier transform

$$S(\mathbf{q}) = \int G(\mathbf{r}) \exp(i\mathbf{qr}) dV \tag{5.26}$$

of a new function, the so-called *density correlation function* $G(\mathbf{r})$. According to (5.26) a diffraction structure factor $S(\mathbf{q})$ related to *intensity pattern* may be calculated form the known $G(\mathbf{r})$ function by direct Fourier transform (this is a *direct problem* of the X-ray analysis). On the contrary, the *density correlation function* $G(\mathbf{r})$ may, in principle, be calculated from the measured function $S(\mathbf{q})$ by the inverse Fourier transform (an *inverse problem*). Below we shall use these procedures, but, at first, let us consider the Fourier transforms and related operations more carefully.

5.4 Fourier Transforms and Diffraction

5.4.1 Principle

We know several important examples of the Foutier transform in physics. For instance, the time evolution of the electric signal $f(t)$ may be related to the frequency specrum $F(\omega)$ of the same signal by a Fourier transform. In the diffraction study we relate spatial periodicity of a density $\rho(\mathbf{r})$ to the spectrum of the wavevectors (or angular spectrum) F (q) of the same structure. The direct Fourier transform of density function is given by operation:

$$F(\mathbf{q}) = \int_V \rho(\mathbf{r}) \exp(i\mathbf{qr}) dV \equiv \Im[\rho] \tag{5.27}$$

The inverse Fourier transform of scattering amplitude is given by:

$$\rho(\mathbf{r}) = \frac{1}{(2\pi)^3} \int_q F(\mathbf{q}) \exp(-i\mathbf{qr}) d\mathbf{q} \equiv \Im^{-1}[\rho] \tag{5.28}$$

Note that factor $(2\pi)^3$ correspond to three-dimensional (3D) case. For 2D and 1D cases we would have $(2\pi)^2$ and (2π), respectively. However, very often the factor $(2\pi)^D$ is skipped at all. The direct and inverse Fourier operators applied consecutively restore the initial density function.

$$\Im^{-1}[\Im[\rho(\mathbf{r})]] = \rho(\mathbf{r})$$

We meet this case in technics. For instance, in an optical microscope, lenses fulfil the direct and inverse Fourier transforms: the light is focused by a condenser onto the object, then diffracted, then collected by an objective, and finally the image is taken by a video camera and seen on a screen. The form of the object is seen as an intensity pattern that is a *flat distribution* of the optical density, because the phases of the waves forming the image are lost. A holographic technique, which always uses an interference of scattered rays with a reference beam having a known phase, allows the restoration of a volume image of the object.

Unfortunately, some important information is also lost in the X-ray diffraction experiment:

1. The phases of scattered rays are not recorded
2. As density ρ is real quantity, $F(\mathbf{q}) = F(-\mathbf{q})$, the scattering pattern is always centrosymmetric (Friedel theorem)
3. A possible range of vectors of scattering $q = (4\pi/\lambda)\sin\vartheta$ is limited by $q_{\max} = 4\pi/\lambda$
4. An absence of lenses for the X-ray range restricts X-ray applications in comparison with optics

Therefore, it is very difficult to solve the *inverse problem* mentioned above, that is to find ρ(**r**) from the data on scattering intensity $I(\mathbf{q})$, and one usually tries different ρ(**r**) or $G(\mathbf{r})$ model functions with subsequent calculations of $S(\mathbf{q})$ and then $I(\mathbf{q})$ for comparison with experiment. Below we consider few examples of such *direct problem* solutions.

5.4.2 Example: Form Factor of a Parallelepiped

Consider diffraction by a single transparent parallelepiped with edge lengths *A, B, C*, Fig. 5.11a.

$$-A/2 \le x \le A/2, -B/2 \le y \le B/2, -C/2 \le z \le C/2$$

Assume density ρ=const within the parallelepiped and ρ=0 outside of its volume. According to Eq. 5.17, the scattering amplitude is

$$F(\mathbf{q}) = \int_{-A/2}^{A/2} \int_{-B/2}^{B/2} \int_{-C/2}^{C/2} \rho \exp i(q_x x + q_y y + q_z z) dx dy dz$$

The integral over $-A/2 < x < A/2$:

$$\rho \int_{-A/2}^{A/2} \exp iq_x x dx = \frac{\rho}{iq_x} \exp(iq_x x)\Big|_{-A/2}^{A/2} = A\rho \frac{\sin(Aq_x/2)}{(Aq_x/2)} = A\rho\Delta_x(A, q_x) \quad (5.29)$$

The plot of scattered field amplitude Δ_x is shown in the upper part of Fig. 5.11b. It is the so-called sine-integral function. The scattering intensity is shown in the lower part of the figure. Integrating over the y and z co-ordinates we obtain the three-dimensional scattering amplitude $F(\mathbf{q}) = \rho V \Delta_x \Delta_y \Delta_z$ and intensity $I(\mathbf{q}) = \rho^2 V^2 (\Delta_x \Delta_y \Delta_z)^2$.

Note that, for infinitely thick parallelepiped ($A \to \infty$), there is no diffraction, only directly transmitted beam is left and the integral becomes δ-function. Generally, the larger parallelepiped dimensions the narrower is the central peak. We shall come back to this point when discussing the diffraction on thin layers of a smectic A liquid crystal.

Consider two interesting particular cases shown in Fig. 5.12:

1. In the top left sketch, the parallelepiped is degenerated into the infinitely thin plane with dimensions $A \to \infty$, $B \to \infty$, $C \to \delta(z)$. All its density is concentrated in

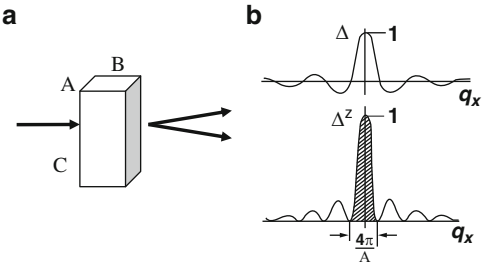

Fig. 5.11 Geometry of the parallelepiped discussed (**a**) and the patterns (**b**) of the diffraction amplitude (*above*) and intensity (*below*)

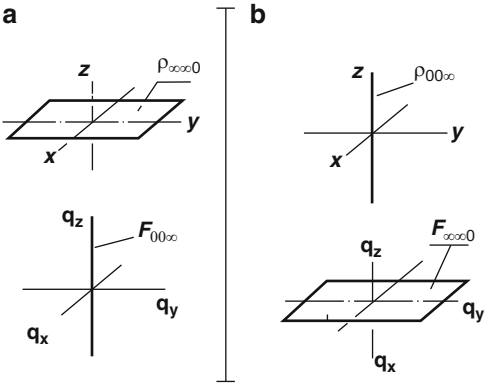

Fig. 5.12 Fourier transforms (lower drawings) of a plane into a line (**a**) and a line into a plane (**b**)

plane x,y that symbolically can be written as $\rho_{\infty\infty 0}$ Then, scattering field amplitude $F(\mathbf{q}) = F_{00\infty}$ is degenerated into a line along the z-axis, as shown in the bottom left sketch. The square of the field amplitude corresponds to the form-factor of an infinite square (or roughly speaking, to a very large square-like molecule).

2. Density $\rho_{00\infty}$ is concentrated along the z line, $C\rightarrow\infty$, $A\rightarrow\delta(x)$, $B\rightarrow\delta(y)$. Then $F(\mathbf{q}) = F_{\infty\infty 0}$, that is the scattering amplitude is degenerated into the q_x, q_y-plane with $\Delta_z \rightarrow\delta(q_z)$, see right sketches. The intensity pattern corresponds to the form-factor of an infinite rod (or, roughly speaking, to a very long rod-like molecule).

5.4.3 Convolution of Two Functions

The structure of a molecular or a liquid crystal is a result of *convolution of two density functions*, the density of a group of atoms in a molecule and periodic density function of a lattice. Let us look at the convolution procedure. By definition, the convolution of two functions $f_1(x)$ and $f_2(x)$ is given by the expression

$$Q(x) = f_1(x)^* f_2(x) = \int_{-\infty}^{\infty} f_1(x')f_2(x-x')dx' \tag{5.30}$$

Here, the asterisk means the convolution operation. Such a convolution gives distribution of one function over a law given by the other. For example, on the top of Fig. 5.13 there are two functions of the same variable x, function $f_1(x)$ and function $f_2(x)=\delta(x-a)$ located at different positions on the x-axis. After their convolution and using $\int_{-\infty}^{\infty}\delta(x)dx = 1$, we shall get

$$\int_{-\infty}^{\infty} f_1(x')\delta(x-a-x')dx' = f_1(x-a)\int_{-\infty}^{\infty}\delta(x-a-x')dx' = f_1(x-a),$$

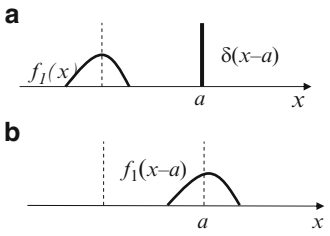

Fig. 5.13 Convolution operation: function $f_1(x)$ convoluted with the other function $\delta(x-a)$ occupies the position of the second function on axis x

and function $f_1(x)$ is translated into function $f_1(x - a)$ keeping the same form, as seen in the lower plot. If the second function consists of two delta functions, $f_2(x)=\delta(x - a)+ \delta(x - b)$, we find our function $f_1(x)$ at both new positions, a and b, i. e. $f_1(x)$ will be doubled. An arbitrary smooth function $f_2(x - x_n)$ can be represented as a sum of n columns of different height or, more strictly, an infinite sum of delta-functions $f_2(x - x_n)=\Sigma a_n\delta(x - x_n)$ $(n=\infty)$. Then $f_1(x)$ will be distributed over the whole sets of the columns, that is over the law given by the $f_2(x - x_n)$ function.

Going back to solid or liquid crystals we can say that the convolution procedure distributes molecular density over the sites of the crystal lattice. On the left side of Fig. 5.14, the two functions, the electron density of a molecule $\rho_{mol}(\mathbf{r})$ and discrete points of the lattice density $\rho_{lattice}(\mathbf{r}) =\Sigma\delta(\mathbf{r}_i - \mathbf{r}_j)$ are shown separately (before convolution). On the right side we see the result of their convolution. Note that the convolution operation $f_1(x)^* f_2(x)$ is dramatically different from the multiplication operation $f_1(x)f_2(x)$. An example is illustrated by Fig. 5.15, in which function $f_2(x)$ is the same $\rho_{lattice}(\mathbf{r})$ function as in the previous picture and $f_1(x)$ is the so called box-function. The latter is equal to 1 within its contour and 0 outside. The multiplication selects only few δ-functions from the whole lattice. On the contrary, the *convolution translates* ρ_{mol} into new functional space, namely the space of $\rho_{lattice}$.

For the future discussion of the liquid crystal structure we need two important theorems. The first of them, the *theorem of convolution* is formulated as follows: a Fourier transform of convolution of two functions $f_1(x)$ and $f_2(x)$ is a product of their Fourier transforms $F_1(q)\cdot F_2(q)$:

$$\Im(f_1{}^* f_2) = \Im(f_1) \cdot \Im(f_2) = F_1(q) \cdot F_2(q) \tag{5.31a}$$

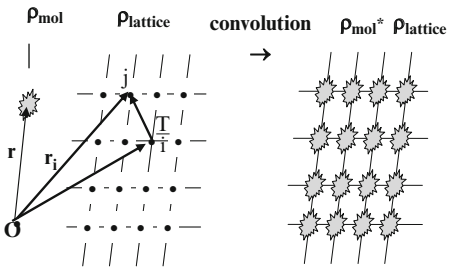

Fig. 5.14 Convolution operation $\rho_{mol}{}^*\rho_{lattice}$ that distribute molecular density ρ_{mol} over the sites of a crystal lattice (filled symbols represent molecules, O is the reference point, $\mathbf{r}$ and $\mathbf{r}_i$ are radius-vectors of a molecule and lattice points, $\mathbf{T}$ is vector of translations)

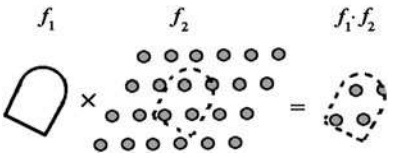

Fig. 5.15 A multiplication operation with a box-function f_1 and function $f_2=\rho_{lattice}(\mathbf{r})$

The second one called the theorem of multiplication is an inverse of the first: the Fourier transform of the product of two functions $f_1(x)$ and $f_2(x)$ is convolution of Fourier transforms of each of them $F_1(q)$*$F_2(q)$:

$$\Im(f_1 \cdot f_2) = \Im(f_1)^* \Im(f_2) = F_1(q)^* F_2(q) \tag{5.31b}$$

5.4.4 Self-Convolution

Let us make the inverse Fourier transform of the scattering intensity (5.23) and use the properties of the Fourier integral:

$$\Im^{-1}\{F(\mathbf{q}) \cdot F^*(\mathbf{q})\} = \rho(\mathbf{r})^* \rho(-\mathbf{r}) = \int \rho(\mathbf{u})\rho(\mathbf{r}+\mathbf{u})d\mathbf{u} = P(\mathbf{r}) \tag{5.32}$$

As a result, we obtain the convolution of the density function ρ(**r**) with the same function inverted with respect of the origin of the reference frame ρ(−**r**). Note that the minus sign appears due to different signs in the exponents for two complex conjugates in (5.28). The P(**r**) function is known as density autocorrelation function or the Paterson function when used in structural analysis. Thus, we may write the inverse and direct Fourier transforms as follows:

$$P(\mathbf{r}) = \int I(\mathbf{q}) e^{-i\mathbf{qr}} d\mathbf{q} \tag{5.33}$$

and

$$I(\mathbf{q}) = \int P(\mathbf{r}) e^{i\mathbf{qr}} dV \tag{5.34}$$

It means that the scattering (or diffraction) intensity and the autocorrelation function are reciprocal Fourier transforms similar to the reciprocal transforms of scattering amplitude $F(\mathbf{q})$ and density ρ(**r**). It should be noted that in statistical physics one widely uses the density *correlation function* $G(\mathbf{r})$ mentioned earlier (5.26) that is related to the structure factor $S(\mathbf{q})$ exactly as the Paterson function is related to intensity of scattering $I(\mathbf{q})$. Below we prefer to use $G(\mathbf{r})$.

Resuming this section, remember that there are two approaches to calculate the scattering intensity $I(\mathbf{q})$:

1. To make a Fourier transform of density $\rho(\mathbf{r})$, in order to find the scattering field amplitude $F(\mathbf{q}) = \int_V \rho(\mathbf{r}) \exp i(\mathbf{qr}) dV$ and then to make a product $I(\mathbf{q}) = F(\mathbf{q})\, F^*(\mathbf{q})$.
2. To make a Fourier transform directly of density correlation function $G(\mathbf{r})$, and obtain intensity structure factor $\mathrm{S}(\mathbf{q})$ that, according to Eq. 5.25 is normalized intensity $I(\mathbf{q})$:.

$$S(\mathbf{q}) = \Im[G(\mathbf{r})] = \frac{I(\mathbf{q})}{NF_{form}^2} \tag{5.35}$$

Further on we shall follow the first approach for discussion of crystals and the second one for discussion of liquids and liquid crystals.

5.5 X-Ray Diffraction by Crystals

We begin this section with an example of the X-ray diffraction on the nematic, smectic A and crystalline smectic B phases. In Fig. 5.16 there is a series of X-ray photos of the same mesogenic compound at different temperatures. In this experiment, the material flow induced by the electric current aligns molecular axes in the nematic phase parallel to the field direction, which is horizontal, but in the SmA phase parallel to the smectic layers. Correspondingly diffraction patterns of the nematic and smectic phase considerably differ from each other. In the crystalline $\mathrm{SmB_{cr}}$ phase the picture shows the six-fold rotation axis perpendicular to the figure plane. Below we shall discuss such pictures in detail, but let us begin with solid crystals.

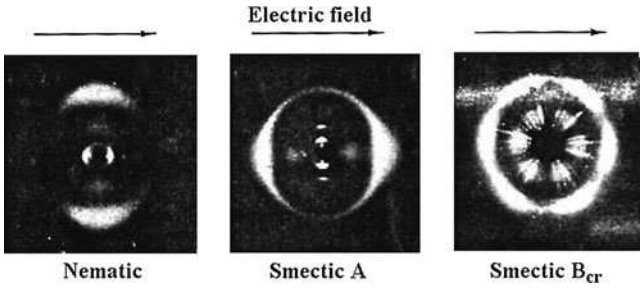

Fig. 5.16 X-ray diffractograms of *p*-anisalamino-cinnamic acid in different phases, nematic, smectic A and crystalline smectic $\mathrm{B_{cr}}$

5.5.1 Density Function and Structure Factor for Crystals

5.5.1.1 Density Function

In crystals this function has three-dimensional periodicity. For simplicity, here we only consider the one-dimensional projection of the three-dimensional crystal. In this case, the density function with period a is very simple

$$\rho(x) = \rho_0 + \sum_m \rho_m \cos mq_0 x, \quad q_0 = 2\pi/a,$$

As shown in Fig. 5.17a it consists of density maxima with a constant amplitude. The width of the peaks is governed by the thermal fluctuations of atoms, $\Delta \approx (kT/\beta)^{1/2}$ (β is a compressibility modulus). At room temperature, such fluctuations may be of the order of 10% of the interatomic distances. At zero temperature the maxima would have the size of atoms or molecules comprising a crystal.

5.5.1.2 The Structure Factor

According to (5.27) the amplitude of scattering $F(\mathbf{q})$ for our one-dimensional crystal is given by Fourier transform of density function $\rho(x)$. Since we have only the sum of cosine functions there are only discrete harmonics at wavevectors $q = mq_0 = 2\pi m/a$. The structure factor (5.25) is proportional to scattered light intensity $F(\mathbf{q})F^*(\mathbf{q})$ and also consists of harmonics represented by δ-functions situated at the same wavevector values $q = 2\pi m/a$ and having amplitude $\rho^2{}_m$:

$$S(q) = \sum_m \rho_m^2 \delta(q - mq_0) \tag{5.36}$$

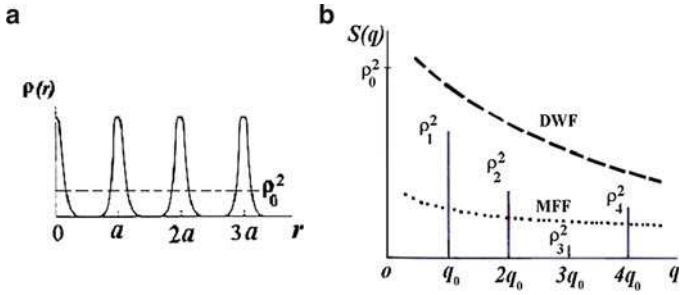

Fig. 5.17 Three-dimensional crystal considered along one direction: density function with equidistant maxima blurred by thermal fluctuations (**a**) and the angular spectrum of the structure factor (**b**). The height of the δ-type maxima is given by squared amplitudes of the density harmonics and is additionally modulated by both the molecular form-factor (MMF) and Debye-Waller factor (DWF)

The correspondent X-ray picture consists of a set of narrow discrete equidistant spots at $q = mq_0$ along the direction of periodicity. The angular spectrum of the structure factor is shown schematically in Fig. 5.17b. The amplitudes of harmonics depend mostly on the shape of the density curve and determine a number and the height of the δ-type maxima. The peak amplitudes are weakly modulated by the molecular form factor (MFF) and additionally by thermal fluctuations through the factor of Debye-Waller (DWF): for the one-dimensional case $I \propto \exp(-<u^2>q^2/3)$ [1]. Here $< u^2 >$ is the mean square amplitude of the thermal oscillations of atoms proportional to temperature. Due to the exponential factor, higher harmonics are much more sensitive to temperature and strongly decrease Bragg diffraction intensity (but not the peak sharpness) with increasing temperature.

5.5.2 A Crystal of a Finite Size

This case is important for thin crystalline films. At first, let us look at the simplest infinite one-dimensional model of the crystal structure, Fig. 5.18, having only zero and first harmonic of density,

$$\rho(x) = \rho_0 + \rho_1 \cos(2\pi x/a).$$

The direct Fourier transform of this function is two delta functions with amplitude ρ_0 and ρ_1 located at $q = 0$ and $q = 2\pi/a$. It is shown in the Inset to Fig. 5.18. Disregarding the zero Fourier harmonic the corresponding intensity of scattering for the infinite one-dimensional crystal is:

$$I(q) = F(q)F^*(q) = \rho_1^2 \delta(q - 2\pi/a).$$

A finite one-dimensional crystal is an analogue of a wave packet confined between $-A/2$ and $A/2$ points, shown in Fig. 5.18. Its scattering amplitude

$$F(\mathbf{q}) = \int_{-A/2}^{A/2} \rho_1 \cdot \cos(2\pi x/a) \cdot \exp(i\mathbf{q}x)dx \tag{5.37}$$

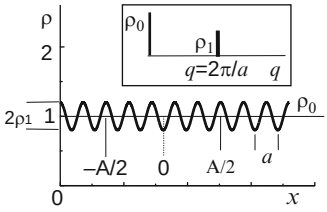

Fig. 5.18 Sine (or cosine) form density function for an infinite sample showing the density wave components ρ_0 and ρ_1 (*main plot*) and its angular spectrum (*inset*)

Within these limits, direct integrating is difficult. However, the scattering amplitude may be found using the convolution theorem (Eq. 5.31a). The integral may be presented as a convolution $f_1(x)$*f_2 (x) where f_1=ρ_1 (like in case of parallelepiped) and $f_2 = \cos(2\pi x/a)$. Applying the convolution theorem we obtain the scattering amplitude from the two amplitudes found earlier, see Eqs. 5.29 and 5.36 for $m = 1$:

$$F(q) = \Im[f_1(x)^* f_2(x)] = F_1(q)F_2(q) = \rho_1 A \frac{\sin(Aq/2)}{(Aq/2)} \cdot \delta(q - q_0)$$

We have again found the scattering field amplitude in the form of sine integral. The correspondent intensity spectrum is similar to that for the parallelepiped, see Fig. 5.11b,

$$I(q) = F(q)F^*(q) = A^2\rho_1^2 \frac{\sin^2[A(q - q_0)/2]}{[A(q - q_o)/2]^2} \tag{5.38}$$

However, there is a shift of the entire parallelepiped diffraction spectrum by q_0 on the wavevector scale; the curve for a parallelepiped without density modulation is centered at $q = 0$ whereas the curve for the modulated structure is centered at $q = q_0$. Such a shifted angular spectrum of diffraction intensity is very similar to that observed on the freely suspended films of smectic A liquid crystals. It allows the determination of both the smectic layer period and the film thickness.

5.6 Structure of the Isotropic and Nematic Phase

5.6.1 Isotropic Liquid

This is the other extreme case with respect to crystals. The density correlation function $G(r)$ is spherically symmetric decaying function. It is very instructive to find, at first, the structure factor (5.26) for any function of the spherical symmetry. We should use spherical frame with volume element $dV = r^2 \sin\vartheta d\varphi d\vartheta dr$:

$$S(q) = \int_0^{2\pi} d\phi \int_0^{\pi} \sin\vartheta d\theta \int_0^{\infty} G(r) e^{i\mathbf{qr}} r^2 dr$$

Since $\mathbf{qr} = qr\cos\vartheta = t$ we substitute $\sin\vartheta d\vartheta$ by $-dt/qr$ and get

$$S(q) = 2\pi \int_0^{\infty} G(r)dr \int_{-qr}^{qr} e^{it} \frac{r^2}{qr} dt = 4\pi \int_0^{\infty} G(r) r^2 \frac{\sin qr}{qr} dr$$

Now, we may use the simplest density correlation function for an isotropic unstructured liquid in the form $G(r) = \rho^2 r^{-1} e^{-\kappa r}$ where $\kappa = \xi^{-1}$ is an inverse value of the correlation length ξ comparable with molecular size [5]. Then, using Euler formula and integrating over r-coordinate we find the structure factor of a liquid without any short-range structure:

$$S(q) = \frac{2\pi\rho^2}{iq}\int_0^\infty e^{-\kappa r}\left(e^{iqr} - e^{-iqr}\right)dr = \frac{2\pi\rho^2}{iq}\left(\frac{1}{\kappa - iq} - \frac{1}{\kappa + iq)}\right)$$
$$= \frac{4\pi\rho^2}{q^2 + \kappa^2} \tag{5.39a}$$

The structure factor and intensity of scattering (5.25) have a spherically symmetric Lorentzian form centered at the zero wavevector $q_c = 0$. The full width on the half a maximum (FWHM) is equal to $2\kappa{=}2/\xi$.

In real liquids there is a short-range positional order because each particular molecule has nearest neighbors forming few so-called coordination spheres. Therefore, each selected molecule "feels" its nearest neighbors and the G-function oscillates. For simplicity, we can take only the first harmonic of density oscillation and write the density correlation function as follows:

$$G(r) \cong \rho_0^2 + \rho_1^2 r^{-1}\exp(-r/\xi)\cos 2\pi r/a \tag{5.39b}$$

This equation shows that *positional correlations* described by the cosine multiplier exponentially decay at a distance ξ, as shown in Fig. 5.19a. The scattering field intensity of a liquid can be found from (5.39b) and (5.35) with the help of the convolution theorem given by Eq. 5.31:

$$I(q) = \Im[G(r)] \cong \rho_0^2\int_0^r \exp(iqr)dr + \rho_1^2\int_0^r r^{-1}\exp(-r/\xi)\cos(2\pi r/a)\exp(iqr)dr$$
$$= \rho_0^2\delta(0) + \rho_1^2[\Im(r^{-1}e^{-r/\xi})^*\Im(\cos 2\pi r/a)]$$

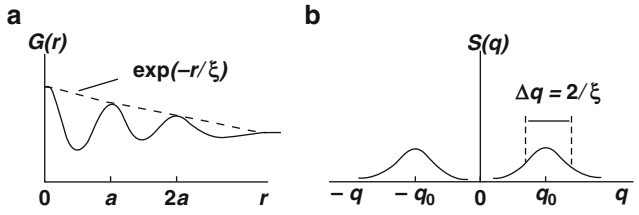

Fig. 5.19 Isotropic phase. Pair density correlation function (**a**) and the corresponding structure factor (**b**)

The first term for $q = 0$ is not interesting (ρ_0 can be found by other techniques, e.g. by dilatometry). The product term with ${\rho_1}^2$ is a result of the convolution theorem and we already have the two Fourier transforms mentioned, namely, the structure factor of unstructured liquid, that is Lorentzian (5.39a) and the structure factor of a crystal that is delta-functions, Eq. 5.36:

$$I(q) \propto S(q) \propto \frac{4\pi\rho_1^2}{q^2 + \xi^{-2}} * \delta(q - 2\pi/a) = \frac{4\pi\rho_1^2}{|q - q_0|^2 + \xi^{-2}} \tag{5.40}$$

Thus, the structure factor of the liquid with a short-range periodicity is the two Lorentzians centered at $q = q_o = 2\pi/a$ and $q = -q_0$, Fig. 5.19b. Their positions are a measure of the molecular size a and their widths are a measure of the characteristic distance ξ for the short range molecular correlations. The total intensity of scattering for positive q is shown in Fig. 5.20a. Note that the curve for the total intensity is slightly asymmetric because this function is a product of the form factor and the structure factor according to Eq. 5.25.

An experimental X-ray pattern for a liquid looks like that shown in Fig. 5.20b. The spot centered at $q = 0$ is very strong and usually screened deliberately off. What is of importance is a diffused ring located at scattering vector q_0 (or scattering angle ϑ_0) given by equation

$$q_0 = \frac{2\pi}{a} = \frac{4\pi \sin\vartheta_0}{\lambda} \text{ i.e., } \quad a = \frac{\lambda}{2\sin\vartheta_0}.$$

Therefore, the average molecular size a can be found from the angle ϑ_0.

5.6.2 *Nematic Phase*

The density correlation function for nematics has the same liquid-like form, but anisotropic, namely, cylindrically symmetric. Along the two principal directions,

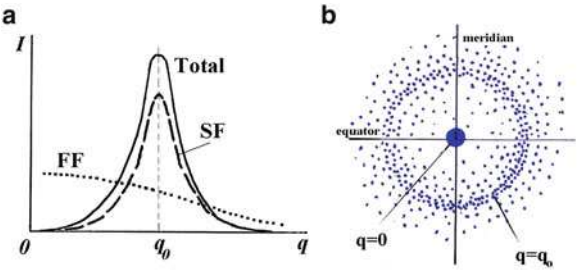

Fig. 5.20 Isotropic phase. Angular dependence of structure factor (SF), molecular form factor (FF) and total intensity of scattering (**a**) and a typical pattern of scattering observed in experiment (**b**)

parallel and perpendicular to the director $n = n_z$, the correlation lengths $\xi_{\|}$ and $\xi_{\perp}$ are different for the x and y directions:

$$G_{\perp}(r_{\perp}) \propto r_{\perp}^{-1} \exp(-r_{\perp}/\xi_{\perp}) \cos q_{\perp} r_{\perp}$$

in the z-direction:

$$G_{||}(z) \propto z^{-1} \exp(-z/\xi_{||}) \cos q_{||} z$$

In the simplest approximation, functions $G_{\perp}(r_{\perp})$ and $G_{\|}(z)$ determine the structure factor. The form-factor contributes to diffraction pattern negligibly for small rod-like molecules comprising typical thermotropic nematics but may be important for biological materials.

An X-ray pattern for a typical nematic with rod-like molecules taken with the help of a photographic film is presented in Fig. 5.21a [6]. The molecules are oriented vertically. Along the vertical, two spots are seen at small angles; they correspond to small wavevector $q_{\|} = 2\pi/a_{\|}$. From this angle of diffraction one can find $a_{\|}$ (length of a rod-like molecule). Along the equator (horizontal line) the spots are separated by larger distance, $q_{\perp}=2\pi/a_{\perp} > q_{\|}$. The $q_{\perp}$ position gives us diameter of a molecule. Usually $a_{\|}/a_{\perp} \approx 4$–5. Thus two molecular dimensions and two correlation lengths can be found [7].

The equatorial spots are extended in the vertical direction and have the form of arcs: the intensity decreases with increasing ϑ-angle as shown in Fig. 5.21b. This is a result of a non-ideal orientational order: the higher the order parameter S, the shorter the arcs. From the diffractogram one can find the distribution of intensity and calculate S [7]. In some cases, even the orientational distribution function for molecules $f(\vartheta)$ can be calculated from experimental data as schematically shown in Fig. 5.22. Generally, the shape of the function is determined by different Legendre polynomials $P_2(\cos\vartheta)$, $P_4(\cos\vartheta)$, etc. (see Section 3.3) and, in principle, different order parameters P_2, P_4 etc. can be found from experiment.

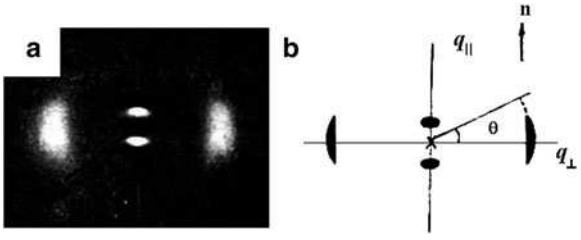

Fig. 5.21 Nematic phase. Typical photo [6] of a diffraction pattern for a nematic liquid crystal with the director aligned vertically (**a**) and the scheme explaining this pattern (**b**)

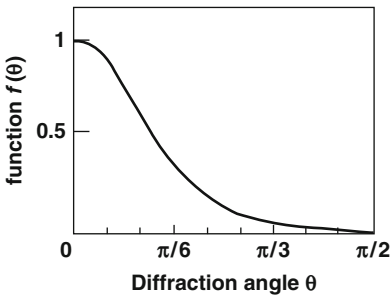

Fig. 5.22 Qualitative picture of the orientational distribution function calculated from the angular dependence of the diffracted intensity along the arc depicted in Fig. 5.22b

5.7 Diffraction by Smectic Phases

5.7.1 Smectic A

Smectic A is a one-dimensional crystal and, at the same time, a two-dimensional liquid. What kind of a diffraction pattern should it have? A naive expectation for a thick (or infinite) sample of the smectic A phase is as follows. If we have a one dimensional density wave in the z-direction $\rho = \rho_1 \cos(2\pi z/a) + ...$ and neglect higher order terms, the intensity along the z-axis ought to be a single Bragg peak in the form of the delta function located at $q = 2\pi/a$ as shown in the Inset to Fig. 5.18. Note that an additional peak related to the ρ_0 term is always situated at $q = 0$. For the directions x and y perpendicular to the director there should be no difference between the density correlation functions for smectic A and nematic phases. Indeed, the naive expectation is correct for the x and y directions; we do have in smectic A liquid like correlations $G(x,y) \propto \exp(-r_\perp/\xi_\perp)$ and the Lorentzian structure factor, as in Fig. 5.19.

However, in experiment [8], instead of the delta-function form of the intensity peaks along the z-direction $\delta(q_{||} - q_0)$, *quasi-Bragg singularities* have been observed with the tails described by a *power-law* as shown in Fig. 5.23a,

$$I(q) \propto (q_{||} - q_0)^{-2+\eta} \tag{5.41a}$$

with small η~0.1, depending on temperature. Such a structure factor may be understood if the density correlation function is not a constant but obeys a power law of the type [8, 9]:

$$G(z) \propto z^{-\eta} \tag{5.41b}$$

Thus, instead of the true long-range order we have a quasi-long-range order with the density correlation function (5.41b) qualitatively shown in Fig. 5.23b.

But what is a physical sense of parameter η? The answer is given by a theorem related to a more general question, whether true one- or two- dimensional crystals

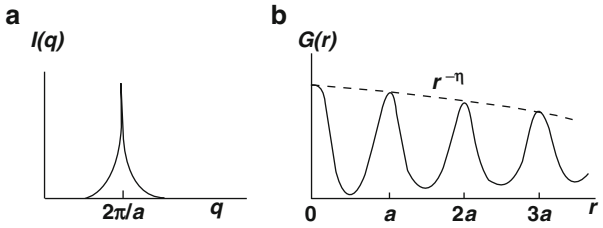

Fig. 5.23 Diffraction intensity (**a**) and density correlation function (**b**) for the smectic A phase with a positional, quasi-long range, molecular order along the symmetry axis

exist in Nature at all, for example, stable one-dimensional smectic A or two-dimensional discotic liquid crystals. Now we encounter a new type of order, known earlier only theoretically.

5.7.2 Landau-Peierls Instability

We know that, at a finite temperature, the position of atoms or molecules in a crystal (or liquid crystal) fluctuate that is density $\rho(\mathbf{r})$ is a fluctuating value. With increasing size of a crystalline sample or a distance with respect to a reference point, the mean square displacement of atoms due to thermal fluctuations is growing. The question to be answered is whether the crystalline structure is stable for the infinite sample. Landau and Peierls [5] have found that the answer depends on dimensionality of crystals.

5.7.2.1 Displacement and Free Energy

Let $\mathbf{u}(x, y, z)$ is a vector of displacement of a small piece of a three-dimensional crystal at its position x, y, z. A characteristic linear size of the piece is L. Our task is to find an expression for the mean square value $< u^2(\mathbf{r}) >$ of the displacement [10]. We begin with the Fourier transform of $\mathbf{u}(x, y, z)$. Now each harmonic of displacement has its amplitude $\mathbf{u}$ [cm] and wavevector $\mathbf{q}$ [cm^{-1}]:

$$\mathbf{u}(\mathbf{r}) = \sum_{\mathbf{q}} \mathbf{u}_{\mathbf{q}} \exp(i\mathbf{q}\mathbf{r}) \tag{5.42}$$

Here, the components of wavevector $\mathbf{q}$ acquire both positive and negative values $\mathbf{u}_{-\mathbf{q}} = \mathbf{u}_{\mathbf{q}}^*$ in the range of $L^{-1} < |q| < a^{-1}$ where a is a lattice constant. We are interested in the additional free energy term δF originated from the displacement:

$$\delta F = \frac{1}{2} C_3 \int_V \left[\frac{\partial u(\mathbf{r})}{\partial \mathbf{r}}\right]^2 d^3 r \tag{5.43}$$

Here, for simplicity, we use a scalar displacement u and a single elasticity coefficient C_3 for a three-dimensional crystal without anisotropy. C_3 has an order of magnitude 10^{10}–10^{11} erg/cm^3 (or 10^9–10^{10} J/m^3). Note that δF cannot depend on displacement explicitly since any vector $\mathbf{u} = \text{const}$ corresponds to a shift of the whole crystal and $\delta F = 0$. Linear terms $\partial \mathbf{u}/\partial x$, etc. do not contribute to δF because δF has minimum at $\mathbf{u} = 0$. Therefore, for small displacements, like in the Hooke law, only terms quadratic with respect to the first derivatives are important. Now, using (5.42) we find the Fourier expansion of derivatives

$$\frac{\partial u}{\partial \mathbf{r}} = \sum_{\mathbf{q}} (iq) e^{i\mathbf{qr}} u_{\mathbf{q}}$$

and insert them into Eq. 5.43 to obtain the expansion of the free energy

$$\delta F = \tfrac{1}{2} \sum_{\mathbf{q}} \sum_{\mathbf{q}'} C_3 u_{\mathbf{q}} u_{\mathbf{q}'} (-1) \mathbf{q}\mathbf{q}' \int_V e^{i(\mathbf{q}+\mathbf{q}')\mathbf{r}} d^3 r.$$

Note that $u_{\mathbf{q}} u_{\mathbf{q}'} = u_{\mathbf{q}} u_{\mathbf{q}}{}^* = |u_{\mathbf{q}}|^2$ and the integral $\int_V e^{i(\mathbf{q}+\mathbf{q}')\mathbf{r}} d^3 r = V \delta_{\mathbf{q}+\mathbf{q}'}$. For $\mathbf{q} = -\mathbf{q}'$ the Kronecker symbol $\delta_{ii} = 1$ and the integral equals the crystal volume V; for $\mathbf{q} \neq \text{-}\mathbf{q}'$ the symbol $\delta_{ij} = 0$ and the integral vanishes. Hence,

$$\delta F = \tfrac{1}{2} V C_3 \sum_{\mathbf{q}} q^2 |u_{\mathbf{q}}|^2 = \sum_{\mathbf{q}} \delta F_{\mathbf{q}}.$$

From this equation and the equipartition theorem $\langle \delta F_{\mathbf{q}} \rangle = k_B T/2$ we find the Fourier component of the mean square displacement (in $\mathbf{q}$-space):

$$\langle |u_{\mathbf{q}}|^2 \rangle = \frac{k_B T}{V C_3 q^2} \tag{5.44}$$

For the mean square displacement in the $\mathbf{r}$-space

$$\langle u^2(\mathbf{r}) \rangle = \sum_{\mathbf{q}} \langle |u_{\mathbf{q}}|^2 \rangle = \frac{V}{(2\pi)^3} \int \langle |u_{\mathbf{q}}|^2 \rangle d^3 q$$

Here the summation is substituted by integration over the volume in the q-space and $(2\pi)^3$ is a factor that relates the volumes in $\mathbf{q}$- and $\mathbf{r}$-spaces in three dimensions. More generally, $(2\pi)^{\mathrm{D}}$ is a factor for any space of D dimension: in the one dimensional space (D = 1), the reciprocal lattice vector length is $q = (2\pi)/a$, for D = 2 the reciprocal lattice area is $q_x q_y = (2\pi)^2/ab$, etc.

Finally, using Eq. 5.44, we can write the value of the mean square displacement in the three dimensional $\mathbf{r}$-space ($d^3 q = 4\pi q^2 \mathrm{d}q$ is a volume of a spherical layer in the q-space):

$$\langle u^2(\mathbf{r})\rangle = \frac{k_B T}{(2\pi)^3 C_3} \int_{q_{\min}}^{q_{\max}} \frac{d^3 q}{q^2} = \frac{k_B T}{2\pi^2 C_3} q\Big|_{2\pi/L}^{2\pi/a} = \frac{k_B T}{\pi C_3}\left(\frac{1}{a} - \frac{1}{L}\right) = const \qquad (5.45)$$

For a space of dimensionality D, we obtain a more general expression:

$$\langle u^2(\mathbf{r})\rangle = \frac{k_B T}{(2\pi)^D C_D} \int_{q_{\min}}^{q_{\max}} \frac{d^d q}{q^2} \qquad (5.46)$$

Now, elastic coefficients C_D have different dimensions, particularly [erg·cm^{-2}] for D = 2 and [erg·cm^{-1}] for D = 1.

5.7.2.2 Stability of Crystallographic Lattices of Different Dimensionality

Let us come back to the *three dimensional crystal* and Eq. 5.45. When crystal size L increases to infinity (i.e. approaches the so-called thermodynamic limit), then

$$\langle u^2(\mathbf{r})\rangle \to \frac{k_B T}{\pi C a} = const$$

and the mean square value of displacement remains independent of the crystal size. From this equation, with $k_B T \approx 4 \times 10^{-14}$ erg and $a \approx 10^{-7}$ cm (molecular crystal) we have small displacements of the other of $u \approx 10^{-9}$ cm (0.1 Å). The crystalline order does not blurred, i.e., remains *true long-range order*.

A *two-dimensional crystal* (D = 2) is nothing more than a single atomic or molecular monolayer. The latter may be prepared from graphene or in the form of a Langmuir film floating on water. For such a monolayer, $d^2 q = 2\pi q dq$ is an area of a ring with circumference $2\pi q$ and width dq and Eq. 5.46 takes the form:

$$\langle u^2(\mathbf{r})\rangle = \frac{k_B T}{2\pi C_2} \int_{q_{\min}}^{q_{\max}} \frac{dq}{q} = \frac{k_B T}{2\pi C_2} \ln\Big|_{2\pi/L}^{2\pi/a} = \frac{k_B T}{2\pi C_2} \ln\frac{L}{a} \qquad (5.47)$$

For $L \to \infty$, this integral diverges with its area logarithmically, that is very slowly. Such a film has quasi-long-range order.

A *one-dimensional crystal* (D = 1) is a single chain of atoms or molecules without any interaction with its surrounding. Eq. 5.46 reads:

$$\langle u^2(\mathbf{r})\rangle = \frac{k_B T}{2\pi C_1} \int_{q_{\min}}^{q_{\max}} \frac{dq}{q^2} = \frac{k_B T}{2\pi C_1} (-q^{-1})\Big|_{2\pi/L}^{2\pi/a} = \frac{k_B T}{4\pi^2 C_1} L \qquad (5.48)$$

For $L \to \infty$ the mean square displacement grows linearly with the chain length and only the short-range order may exist.

Recall that the smectic A phase is a three-dimensional phase which is simultaneously one-dimensional crystal in the direction along the layer normal and two-dimensional liquid in the layer plane. So, the Eq. 5.46 cannot be applied to this strongly anisotropic system. We shall consider this problem in detail after discussion of anisotropic elastic properties of SmA in Chapter 8. Now we only mention that, in comparison to the linearly divergent order of a one-dimensional chain given by Eq. 5.48, the two- dimensional (x,y) liquid structure of smectic layers strongly stabilizes the fluctuations along the smectic layer normal (z). As a result, the divergence of fluctuations with a distance follows the logarithmic law with increasing size of the SmA in the z-direction L, and the order become quasi-long-range. It is the order that results in the power law seen in Fig. 5.23b. Correspondingly, the power index η in Eq. 5.41 can be expressed in terms of SmA interlayer distance l or $q_0 = 2\pi/l$ and elastic moduli for layers compressibility B and director distortion K [11].

$$\eta \approx q_0^2 k_B T / 8\pi (KB)^{1/2} \tag{5.49}$$

The estimates result in the values of η of the order of 0.1–0.5.

5.7.3 *"Bond" Orientational Order in a Single Smectic Layer and Hexatic Phase*

Imagine that we have a film only one molecule thick (a smectic monolayer with or without tilt of molecules). In such a single layer, the nematic orientational order is not discussed although some orientational order (or disorder) of long molecular axes may be important. We are interested in a new type of quasi-long-range order not forbidden by the Landau-Peierls theorem for the two-dimensional systems, Eq. 5.47. A monolayer can be liquid-like i.e. its translational order is absent and molecules may be situated chaotically at any place in the layer plane. Liquid-like order means that not only the distances between molecules are not fixed but also no correlation exists in their angular positions. However, at a reduced temperature the full translational symmetry within the layer plane is broken only partially and the true positional order is not installed. The new order describes the positions of molecular gravity centers along the *connecting lines* or "bonds" (not to be confused with chemical bonds). However, the distances between the molecules are not fixed. For example, in Fig. 5.24 all the molecules in the neighbour areas 1 and 2 sit in the points of hexagonal lattice but, at some distance from the reference area 1, the positions of molecules in area 3 do not coincide with the lattice cross-points. Nevertheless lattice vectors **a** and **b** still look along the grid lines and keep the hexagonal order.

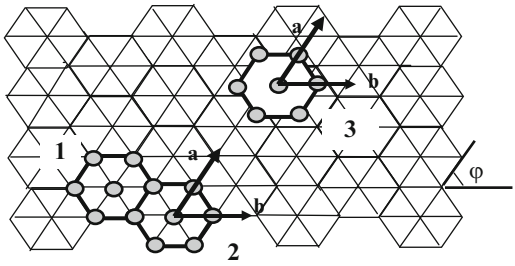

Fig. 5.24 Schematic picture of molecular ordering in a single smectic layer with liquid-like short range positional order and quasi-long range hexatic order

Table 5.1 In-plane order parameters and correlations for two dimensional single layers

Order/layer type	Liquid layer	Hexatic layer	Crystal layer
Positional order	Liquid-like	Liquid like	Quasi-long range
Positional correlations	$\exp(-r/\xi)$	$\exp(-r/\xi)$	$r^{-\eta}$
"Bond" orientation order	Liquid-like	Quasi-long range	Long range
"Bond" correlations $<\psi\psi>$	$\exp(-r/\xi)$	$r^{-\eta}$	Const

A two-dimensional phase with a *bond orientation order* is called *hexatic phase* [12, 13]. It has six-fold symmetry D_{6h} and a new, two-component order parameter

$$\Psi = \Psi_0 \exp i6\varphi(\mathbf{r}) \tag{5.50}$$

where $\varphi(\mathbf{r})$ is the angle a local "bond" vector forms with a reference system. It is a phase with a new order parameter and Ψ_0 is its amplitude. The mean square displacements $< (\delta\varphi)^2 >$ logarithmically decay with a distance from a reference point following Eq. 5.47 although with a special, "bond" elastic modulus K_{bond}. The density correlation function follows the power law decay $G_\Psi(\mathbf{r}) \propto \mathbf{r}^{-\eta_\Psi}$ due to fluctuations in the "bond" angle. The temperature dependent amplitude Ψ_0 of the two-component order parameter Ψ takes the values between 0 and 1. Note the analogy with the two-component order parameter of the smectic C phase, although the symmetry of the two phases is different.

Depending on a material, *single smectic monolayers* can exist in two different modifications, liquid-like and hexatic like. Properties of these monolayers are shown in Table 5.1. Upon melting, a two-dimensional hexatic layer undergoes the transition into the liquid-like layer. It is spectacular that hexatic layers like liquid layers do not support the in-plane shear [14]. The layer can be sheared by as small force (stress) as is wished.

5.7.4 Three-Dimensional Smectic Phases

5.7.4.1 Uniaxial Orthogonal

In three dimensions the situation is different, because there are *interactions between the layers* that may stabilize more ordered phases. Now the in-plane ordering and

the ordering along the layer normal in the three-dimensional, uniaxial, orthogonal (without tilt) smectic phase should be discussed separately. The *in-plane* structural characteristics of the smectic A phase and smectic B_{hex} hexatic phase are presented in Table 5.2. Note that, in the three-dimensional hexatic phase, the quasi-long-range hexatic order inherent to a single monolayer is substituted by the true long-range hexatic order with constant correlation function $G_\Psi(\mathbf{r}_\perp)$. As to the out-of-plane positional order in the hexatic phase, it is quasi-long-range with power law correlations $<\rho_z\rho_z>$ of the $z^{-\eta}$ type [14]. The same table is illustrated by Fig. 5.25. It is seen how a continuous, blurred diffraction ring typical of the smectic A phase is substituted by a six-spot diffraction pattern for the hexatic B_{hex} and then by a six-point pattern for smectic B_{cr} (crystalline) phase. An example of the experimental X-ray diffraction pattern for a thick layers of the smectic A and B_{cr} phases was illustrated by Fig. 5.16.

On the other hand, the experiments with very thin free-suspended films of smectics show that the crystalline order in certain substances with weak interlayer interactions may exist only in the surface layers [11]. In thick films the smectic layers are mostly liquid. However, within the same thin film one may observe the layer-by-layer crystallization. For example, the entire sequence of phase transitions SmA-SmB_{hex}-SmB_{cr} is shifted downward as one advances into the bulk from the

Table 5.2 Order parameters and density correlations for three-dimensional smectic A, hexatic B_{hex} and crystalline B_{cr}

Order/uniaxial phase	SmA	Hexatic-B_{hex}	Crystalline-B_{cr}
In-plane positional order	liquid-like	Liquid like	Long-range
In-plane positional correlations	$\exp(-r/\xi)$	$\exp(-r/\xi)$	const
In-plane "bond" orientation order	$\exp(-r/\xi)$	Long range	Long range
In-plane "bond" order correlations	$\exp(-r/\xi)$	const	const
Interlayer positional order	Quasi-long range	Quasi-long range	Long range
Interlayer positional correlations	$z^{-\eta}$	$z^{-\eta}$	const

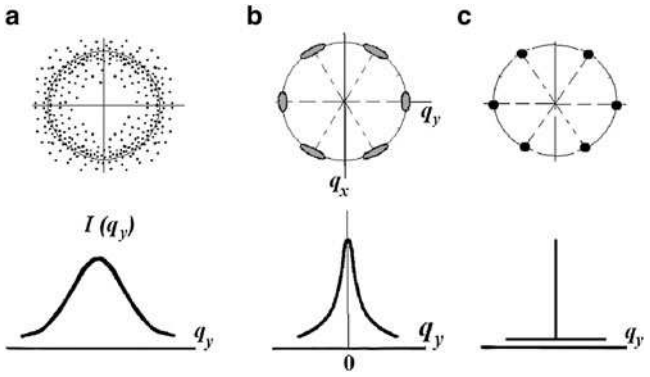

Fig. 5.25 Comparison of in-plane the diffraction patterns for the smectic A (**a**), smectic B_{hex} (**b**) and smectic B_{cr} (**c**) phase. Below are qualitative dependencies of scattering intensity on the diffraction angle for the three phases

first (surface) layer to the second, third, etc. layers *of the same film*. It means that, in the bulk, the liquid-like phase is more stable that the crystalline one and the surface forces are very important.

5.7.4.2 Biaxial Orthogonal

In biaxial orthogonal smectics the symmetry is further reduced. For example, the group theory predicts phase transitions from smectic A (symmetry $D_{\infty h}$) into smectic A_b with symmetry C_{2h}, that is a biaxial SmA phase with a hindered rotation of molecules about their longitudinal axes. It is also possible a transition from SmB into an exotic SmB_q phase with symmetry D_{3h} due to specific distribution of positive and negative electric charges alternating along the perimeter of the hexagonal elementary cell [15]. Such a phase has not been reported yet.

On cooling, the smectic B_{hex} phase (symmetry D_{6h}) can transit into smectic E (SmE) with herringbone packing and point group symmetry C_{2h}. It is shown in Fig. 5.26 together with a sketch of the characteristic X-ray diffractogram. In fact, SmE is true crystalline phase.

5.7.4.3 Biaxial Tilted

When molecular axes (director) are tilted by some angle with respect to the smectic normal we have the remarkable correspondence between the tilted and orthogonal phases: SmC – SmA (both have liquid layer structure); SmF – SmB_{hex} (hexatic layer structure); SmH – SmB_{cryst} (crystalline layer structure).

As an example, consider the X-ray diffraction by the smectic C phase of *p*-diheptyloxyazoxybenzene [16]. Since always there is a possibility to align the director by a magnetic field along a certain, well defined direction (e.g., vertical as in Fig. 5.27) we expect that the diffraction pattern from the layered structure will also be tilted through the same angle with respect to the vertical. However, as a rule,

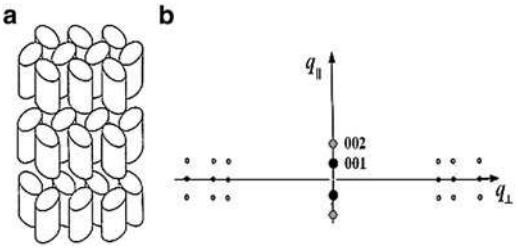

Fig. 5.26 Smectic E phase. The herringbone structure (**a**) and corresponding diffraction pattern (**b**) for two different directions of scattering, parallel ($q_{\parallel}$) and perpendicular ($q_{\perp}$) to the director. As an example, the two Miller indices are shown only for $q_{\parallel}$. They mark Bragg reflections of the first and second orders from the horizontal crystallographic planes

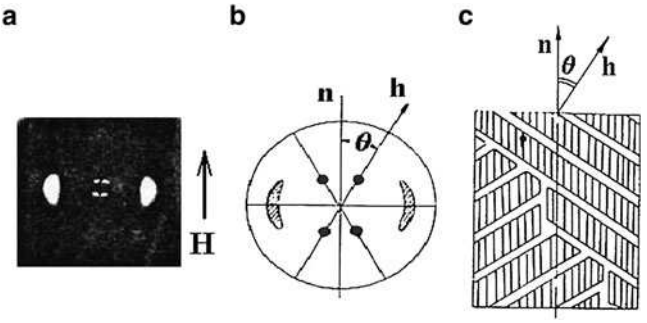

Fig. 5.27 Smectic C phase in the magnetic film along the vertical direction, **H**||**n**. Typical diffractogram (**a**) and its scheme (**b**) showing the four-point picture of reflections from the smectic layers and blurred nematic-like arcs corresponding to sketch (**c**) of the uniform director alignment with broken smectic layers [16]

the layers are broken and acquire a tilt in two opposite directions as shown in sketch Fig. 5.27c. Therefore, the diffraction pattern becomes symmetric (degenerate) with respect to the vertical and, instead a pair of the first order spots, we see four spots on photo (Fig. 5.27a). It is a so-called four-point pattern. The molecular tilt angle ϑ can be found as shown in Fig. 5.27b. The broad arcs at the equatorial (horizontal) line are due to orientational (nematic) order.

References

1. Kittel, C.: Introduction to Solid State Physics, 4th edn. Wiley, New York (1971)
2. Vainstein, B.K.: Diffraction of X-Rays on Chain Molecules. Elsevier, Amsterdam (1966).
3. De Santo, M., Barberi, R., Blinov, L.M.: Electric force microscopic observations of electric surface potentials. In: Rasing, Th, Muševič, I. (eds.) Surface and Interfaces of Liquid Crystals, pp. 194–210. Springer, Berlin (2004)
4. Landau, L.D., Lifshits, E.M.: Theory of Field, 5th edn. Nauka, Moscow (1967), Ch. 9 (in Russian) [see also Landau, L.D., Lifshits, E.M.: Theory of Field, 4th edn. Butterworth-Heinemann, Oxford (1980)]
5. Landau, L.D., Lifshits, E.M.: Statistical Physics, vol. pt.1. Nauka, Moscow (1976). (in Russian) [Statistical Physics, 3 rd edn, Pergamon, Oxford, 1980]
6. Osipov, M.A., Ostrovskii, B.I.: Study of the orientational order in liquid crystals by x-ray scattering. Cryst. Rev. **3**, 113–156 (1992)
7. Vertogen, G., de Jeu, W.H.: Thermotropic Liquid Crystals, Fundamentals. Springer Verlag, Berlin (1988)
8. Als-Nielsen, J., Litster, J.D., Birgenau, R.J., Kaplan, M., Safinia, C.R., Lindegaard-Andersen, A., Mathiesen, S.: Observation of algebraic decay of positional order in a smectic liquid crystal. Phys. Rev. B **22**, 314–320 (1980)
9. Caillé, A.: Remarques sur la diffusion des rayons X dans les smectiques. C. R. Acad. Sci. B **247**, 891 (1972)
10. de Gennes, P.G., Prost, J.: The Physics of Liquid Crystals, 2nd edn. Oxford Science Publications, Oxford (1995)

11. de Jeu, W.H., Ostrovskii, B.I., Shalaginov, A.N.: Structure and fluctuations of smectic membranes. Rev. Mod. Phys. **75**, 181–235 (2003)
12. Halperin, B.I., Nelson, D.R.: Theory of two-dimensional melting. Phys. Rev. Lett. **19**, 2456 (1979)
13. Pershan, P.S.: Structure of Liquid Crystal Phases. World Scientific, Singapore (1988)
14. Pindak, R., Moncton, D.: Two-dimensional systems. Phys. Today (May), 57–66 (1982)
15. Pikin, S.A.: Structural Transformations in Liquid Crystals. Gordon & Breach, New York (1981)
16. Ostrovskii, B.I.: X-ray diffraction study of nematic, smectic A and C liquid crystals. Soviet Sci. Rev. A **12**(pt.2), 85–146 (1989)

Chapter 6
Phase Transitions

Liquid crystals manifest a number of transitions between different phases upon variation of temperature, pressure or a content of various compounds in a mixture. All the transitions are divided into two groups, namely, first and second order transitions both accompanied by interesting pre-transitional phenomena and usually described by the Landau (phenomenological) theory or molecular-statistical approach. In this chapter we are going to consider the most important phase transitions between isotropic, nematic, smectic A and C phases. The phase transitions in ferroelectric liquid crystals are discussed in Chapter 13.

6.1 Landau Approach

In Fig. 6.1 we have an example of the experimental phase diagram for homologues of 4-ethoxybenzene-4′-amino-n-alkyl α-methyl cinnamates [1]. We see that, with increasing length of the alkyl chain, the temperature range of the nematic phase between the isotropic and smectic A phase becomes narrower. This range is limited by solid lines corresponding to the phase transitions between different phases. How to explain this diagram? We may begin with the molecular properties and intermolecular interaction and try to calculate the temperature range of stability of a particular phase, the values of the order parameters and thermodynamic functions such as free energy and others. This approach will be discussed in the end of this chapter. Another approach is based on phenomenological description of the phase transitions and called Landau theory of phase transitions. The key issue is the symmetry of the phases and corresponding order parameters related to a particular transition. Such an approach appeared to be very powerful and relatively simple.

Imagine a series of transitions between phases of different symmetry, as shown in Fig. 6.2, for instance, with decreasing temperature. Our task is to select one of these transitions, find the temperature behaviour of the order parameter and other thermodynamic functions close to the phase transition [2]. To this effect, we should make the following steps.

L.M. Blinov, *Structure and Properties of Liquid Crystals*,
DOI 10.1007/978-90-481-8829-1_6,

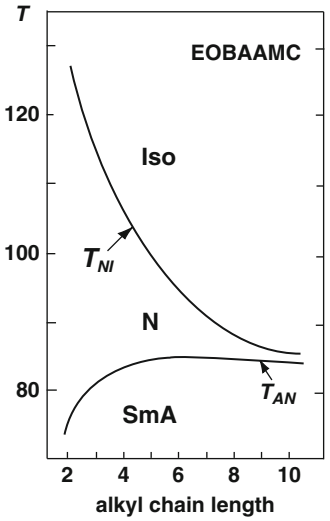

Fig. 6.1 An example of the experimental phase diagram for a homological series of cinnamate derivatives. The scale of the abscissa means a number of alkyl chains in the tail of a particular molecule. The lines show the location of phase transition temperatures

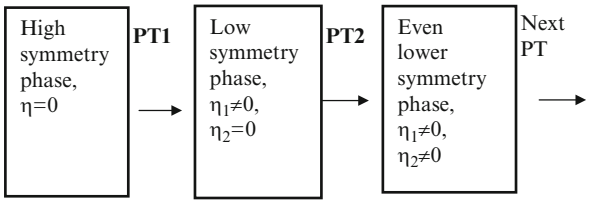

Fig 6.2 Sequence of the phase transitions with decreasing temperature and lowering the phase symmetry. A new order parameter η_1, η_2, etc. is introduced for each new phase with lower symmetry

1. From symmetry consideration we should choose a proper order parameter for the lower symmetry phase (on account of molecular distribution functions).
2. Using smallness of the chosen parameter we expand the free energy density in powers of this parameter, with only the first term temperature dependent.
3. The thermodynamic behaviour of the order parameter in the low symmetry phase is found by a minimization procedure for free energy density.
4. With the order parameter found the free energy may be written explicitly.
5. Other thermodynamic functions are found from the temperature behaviour of the free energy.

As to free energy, below we shall use the Helmholtz free energy $F = U - TS$ (U, S and T are total energy, entropy and temperature, respectively) that is more appropriate for discussion of the systems in terms of temperature and volume V (or density ρ) at constant pressure p. In a more general case, the thermodynamic potential (or Gibbs free energy) $\Phi = F + pV$ appears to be more suitable for an expansion, e.g. when varying pressure p.

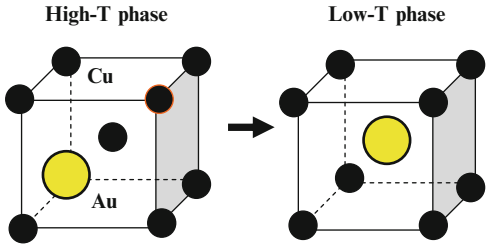

Fig. 6.3 Disorder–order transition in Cu–Au alloy. In the low temperature, low symmetry phase, the atom of gold is more often occupies the central position in the cubic lattice

Consider, as an example, a disorder-order transition in Cu-Au (8:1) alloy. In this case, we can choose the simplest (scalar) order parameter η, which is a normalized difference between probabilities to find either gold or copper atoms in the center of the cubic cell, see Fig. 6.3. In the higher temperature (and higher symmetry) phase an atom of gold has equal probability to be at any lattice site included the central one (but not between the sites), and order parameter $\eta = 0$. In the ideally ordered, zero-temperature phase, an Au atom is always in the central position and $\eta = 1$. Generally, in the low-temperature phase, the central position is more often populated by a gold atom than by a particular copper atom and $0 < \eta < 1$.

Neglecting the mass density change at the transition, the Landau expansion for the free energy density is

$$g(T,\eta) = g(T,0) + \lambda\eta + \frac{1}{2}A(T)\eta^2 + \frac{1}{3}B\eta^3 + \frac{1}{4}C\eta^4 + \cdots \tag{6.1}$$

Here $g(T, 0)$ is free energy of the high-temperature phase and the fractional form of (1/2), (1/3), etc. coefficients is adopted for convenience. In equilibrium, function $g(T, \eta)$ must have a minimum value, therefore at any temperature:

$$\frac{dg}{d\eta} = 0 \quad \text{and} \quad \frac{d^2g}{d\eta^2} > 0$$

Thus, derivative of (6.1) is

$$\lambda + A(T)\eta + B\eta^2 + C\eta^3 + \cdots = 0$$

From here we conclude that coefficient λ in the expansion must be zero; otherwise, the non-zero derivative of free energy $dg(T, \eta = 0)/d\eta = \lambda$ would be present also in the high symmetry phase. However, the presence of such an additional constant term in the high symmetry phase would smooth its own energy minimum what is senseless.

As to the "leading" coefficient $A(T)$ in Eq. 6.1, in the high symmetry phase, it must be positive to provide a minimum of free energy at $\eta = 0$. On the other hand, it must be negative to provide a minimum of the free energy density in the low symmetry phase at a finite value of order parameter $\eta \neq 0$, Fig. 6.4a. Thus, in

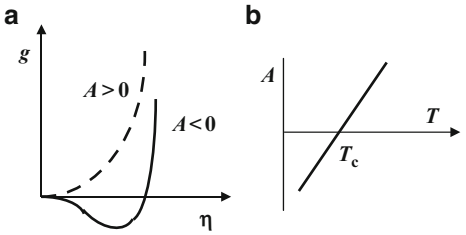

Fig. 6.4 The forms of the free energy density in the high symmetry ($A > 0$) and low symmetry ($A < 0$) phases (*a*) and the temperature dependence of the first term in the Landau expansion (*b*)

general case, when not only temperature is varied but pressure p, composition X, etc., the coefficient $A(T, p, X..)$ should change sign at the phase transition. Therefore, for a transition at temperature $T = T_c$, we can make an expansion of coefficient A in a Taylor series over temperature (for $p, X \cong$ const close to T_c) and write

$$A = a(T - T_c) \quad \text{with} \quad a = \left.\frac{dA}{dT}\right|_{T_c} > 0$$

as sketched in Fig. 6.4b.

Now the excess of the free energy density acquired by the low symmetry phase at the transition is

$$\Delta g = g(T, \eta) - g(T, 0) = \frac{1}{2}a(T - T_c)\eta^2 - \frac{1}{3}B\eta^3 + \frac{1}{4}C\eta^4 + \cdots \tag{6.2}$$

Here the minus sign at the B-term is taken for convenience. The thermodynamic stability condition reads:

$$\frac{d\Delta g}{d\eta} = a(T - T_c)\eta - B\eta^2 + C\eta^3 + \cdots = 0 \tag{6.3}$$

This equation has three roots: $\eta = 0$ for the high-symmetry phase and

$$\eta = \frac{B \pm [B^2 - 4aC(T - T_c)]^{1/2}}{2C} \tag{6.4}$$

for the low symmetry phase. Therefore, the correct temperature dependence of the order parameter is found using only symmetry arguments! Note that coefficients a, B and C are independent of temperature, although their physical sense (molecular nature) is unknown. They may only be found experimentally or using some microscopic molecular models.

Consider a particular case of $B = 0$. Then in the low symmetry phase,

$$\eta = \pm\left[\frac{a(T_c - T)}{C}\right]^{1/2} \tag{6.5}$$

Thus, if the cubic term is absent in the expansion, the system becomes insensitive to the sign of the order parameter. Moreover, the parameter must change continuously at the phase transition from zero to a finite value. Such a $\eta = \pm 1$ symmetry corresponds to *second order transition* (a case of the N-SmA or SmA-SmC transitions). At second order transitions the symmetry changes abruptly but thermodynamic functions change continuously (only their temperature derivatives may change stepwise).

When $B \neq 0$ the two non-zero roots are different, there is no longer $\eta = \pm 1$ symmetry; the order parameter and other thermodynamic functions change discontinuously. This situation corresponds to *first order transition* (a case of the Iso-N transition). There is, however, a possibility to discuss the first order transition even for $B = 0$ when the order parameter is symmetric: to this effect we should put $C < 0$, ignore the fifth order term ($D = 0$) and add a sixth order term. Then we have the Landau expansion of the following type:

$$\Delta g = \frac{1}{2}a(T - T_c)\eta^2 - \frac{1}{4}C\eta^4 + \frac{1}{4}E\eta^6 + \cdots \tag{6.6}$$

This biquadratic equation also describes discontinuity of thermodynamic properties at temperature T_c. We shall discuss such a case later.

6.2 Isotropic Liquid–Nematic Transition

6.2.1 Landau-De Gennes Equation

What is known from experiments on this transition?

1. There is only a small jump of density at transition temperature T_{NI}, about 0.3%. Therefore, the density can approximately be considered constant at both sides of the transition; the pressure is also considered constant.
2. The order parameter is not symmetric, its magnitudes $\mathrm{S}_{\max} = +1$, $\mathrm{S}_{\min} = -1/2$. This asymmetry generates the cubic term, coefficient B must be finite, and the first order transition is expected.
3. The tensor form of the order parameter should be taken into account, in the simplest case, the uniaxial one [3, 4]:

$$Q_{\alpha\beta} = S(n_{\alpha\beta} - {}^1\!/_3\delta_{\alpha\beta}) \tag{6.7}$$

With that order parameter, the Landau-de Gennes expansion of free energy reads:

$$g_N = g_{Iso} + \frac{1}{2}AQ_{\alpha\beta}Q_{\beta\alpha} - \frac{1}{3}BQ_{\alpha\beta}Q_{\beta g}Q_{g\alpha} + \frac{1}{4}C(Q_{\alpha\beta}Q_{\beta\alpha})^2 \quad A = a(T - T_c{}^*) \tag{6.8}$$

Here T_c* is *virtual* second order transition temperature. In real substances it is slightly below T_{NI}. Coefficients B and C are independent of T. Now we choose a proper coordinate system wherein matrices $Q_{\alpha\beta}$ in Eq. 6.8 become diagonal. Then we contract indices (reduce tensor valence) by multiplying the diagonal elements and writing the traces $Q_{\alpha\beta}Q_{\beta\alpha} = (2/3)S^2$ and $Q_{\alpha\beta}Q_{\beta\gamma}Q_{\gamma\alpha} = (2/9)S^3$. Then, we have equations for the excess of the normalized free energy density (in units [erg/cm^3] or [J/m^3] in the SI system) [5, 6]:

$$\Delta g = \frac{g_N - g_{Iso}}{g_{Iso}} = \frac{1}{3}a(T - T_c{}^*)S^2 - \frac{2}{27}BS^3 + \frac{1}{9}CS^4 \tag{6.9}$$

and stability equation:

$$\frac{d\Delta g}{dS} = a(T - T_c{}^*)S - \frac{1}{3}BS^2 + \frac{2}{3}CS^3 = 0 \tag{6.10}$$

6.2.2 Temperature Dependence of the Nematic Order Parameter

Equation 6.10 has three solutions: S = 0 for the isotropic phase and

$$S_{\pm} = \frac{B}{4C}\left\{1 \pm \left[1 - \frac{24aC(T - T_c{}^*)}{B^2}\right]^{1/2}\right\} \tag{6.11}$$

for the nematic phase. First of all, we should establish which sign is correct in solutions (6.11). It is a bit tricky. We define a certain temperature T_c (not necessarily equal to T_c*), at which free energy of the nematic and the isotropic phases are equal, i.e. Δg in Eq. 6.9 is zero. Assuming $T = T_c$, we multiplied Eq. 6.10 by S/3 and subtract it from Eq. 6.9. Then we get

$$\frac{1}{27}BS_c^3 = \frac{1}{9}CS_c^4 \text{ or } S_c^3(CS_c - B/3) = 0 \tag{6.12}$$

As seen from Eq. 6.11, only negative sign in front of brackets can give us $S_c = 0$ at $T_c = T_c$* that is at the same characteristic temperature. Another solution of Eq. 6.12, namely, $S_c = B/3C$, if substituted into Eq. 6.11, results in branch S_+

$$\frac{1}{3} = \left[1 - \frac{24aC(T - T_c{}^*)}{B^2}\right]^{1/2}$$

with a new characteristic temperature $T_c = T_c{}^* + B^2/27aC$. This solution shows a positive jump of $S = B/3C$ at a temperature T_c that is *higher* than the "second order

transition" temperature T_c*. Hence S_+ from (6.11) is a more stable solution than S_-. Therefore, we take sign (+) in solution (6.11) of stability equation:

$$S = \frac{B}{4C}\left\{1 + \left[1 - \frac{24aC(T - T_c^*)}{B^2}\right]^{1/2}\right\} \tag{6.13}$$

Finally, from (6.13) we find one more critical temperature: $T_c^+ = T_c^* + B^2/24aC$ that is even higher than T_c and there is no other real solutions of the stability equation. Totally, we have now three characteristic temperatures:

$$T_c^* \,(\text{virtual second order transition}) < T_c = T_c^* + B^2/27aC \;(\Delta g = 0) < T_c^+ = T_c^* + B^2/24aC \;(\text{jump of S}).$$

Within the range of $T_c^* < T_c^+$ a *hysteresis* in the order parameter should be observed upon the heating and cooling scans. Such hysteresis is often observed under polarization microscope in the form of two-phase textures. If a sample is placed between crossed polarizers, dark spots of the isotropic phase sharply contrasts with bright nematic background (like in Fig. 1.3c) or vice versa. The temperature behaviour of function $S(T)$ is shown in Fig. 6.5a. In the figure:

$$S^+ = B/4C(\text{at}\, T_c^+), \quad S_c = B/3C(\text{at}\, T = T_c), \quad S^* = B/2C\,(\text{at}\, T = T_c^*) \tag{6.14}$$

Hence, the universal ratio $S_c/S^* = 2/3$ is valid for any expansion up to the fourth order term and T_c* can be found by plotting S vs temperature. By the way, in experiment, the phase transition point T_{NI} is associated with temperature T_c.

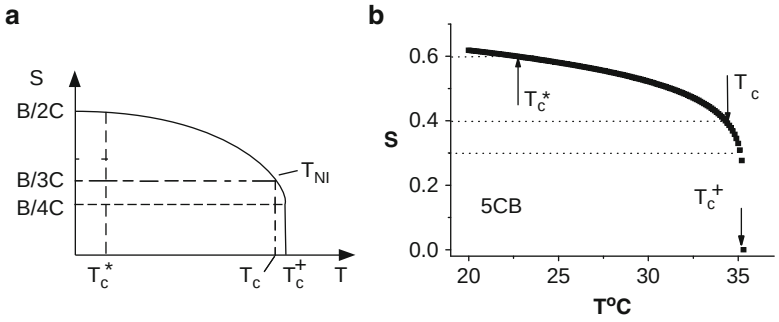

Fig. 6.5 (**a**) Temperature dependence of the order parameter in the Landau-de Gennes model; (**B**) and (**C**) are coefficients of the expansion. $T_{NI} \approx T_c$ is experimental value of the isotropic–nematic phase transition temperature corresponding to equality of free energy densities for the two phases. (**b**) Experimental dependence of the order parameter for 5CB and the characteristic temperature points T_c*, T_c and T_c^+ defined in accordance with the model of panel (a)

6.2.3 Free Energy

It is instructive to look at the free energy density dependence on the nematic order parameter, Eq. 6.9, on both sides of the phase transition. To this effect we need Landau expansion coefficients a, B and C. We may find them, at least, approximately from the experimental dependence of order parameter on temperature $S(T)$. Let us take as an example a nematic compound p-pentyl-cyano-biphenyl (5CB). Function $S(T)$ has been measured earlier by both the optical and nuclear magnetic resonance techniques [7]. The Landau coefficients may be found from this curve as follows. Using the values of the order parameter S^*, S_c and S^+ expressed in terms of coefficients B and C, we can mark the corresponding temperatures T^*, T_c and T^+ on the experimental plot, as shown in Fig. 6.5b. The highest temperature point of the nematic phase is $T^+ = 35.3°C$ where, according to the model, $S^+ = B/4C$. In the experimental plot $S = 0.3$ and, assuming $B = 1$, we find $C = 0.838$. Then, using the difference between the two characteristic temperatures from the experimental plot (b),

$$T_c - T^* = B^2/27aC = 33.7°C - 22.7°C = 11°C,$$

we find $a = 0.004$. Now we have all necessary data to plot the normalized free energy $\Delta g(S)$. If necessary, the absolute values of free energy may be found by multiplying the dimensionless Landau coefficient B by the free energy density of the isotropic phase $g_{iso} = (\rho_{NI}N_{Av}/M)\, k_B\, T_{NI}$. (where k_B is Boltzmann constant, N_{Av} Avogadro number, M molecular weight, ρ_{NI} the density at the transition temperature). In our example, $M = 249$, $\rho_{NI} \approx 1$ g/cm^3, $T_{NI} = T_c \approx 307$ K and $g_{iso} \approx 1 \times 10^8$ erg/cm^3 or 1×10^7 J/m^3 in the SI system.

The result of $\Delta g(S)$ calculation is shown in Fig. 6.6. Considering a cooling process from the stable isotropic phase we shall better understand the physical sense of the three critical temperatures. For $T > T_c^+$ (dot curve 3 in the figure) the absolute minimum is situated at $S = 0$ and this corresponds to the stable isotropic phase. As the temperature approaches T_c from above, in the range of $T_c < T < T_c^+$, a second minimum appears above the abscissa axis, which corresponds to the

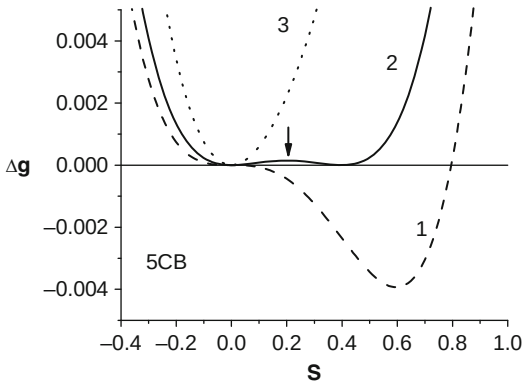

Fig. 6.6 Normalized free energy of 5CB as a function of order parameter S in the vicinity of the N–I transition at different temperatures: T_c^* (curve 1), T_c (curve 2) and T_c^+ (curve 3). The curves are calculated with dimensionless Landau expansion coefficients $a = 0.004$, $B = 1$ and $C = 0.838$ obtained from the experimental curve $S(T)$

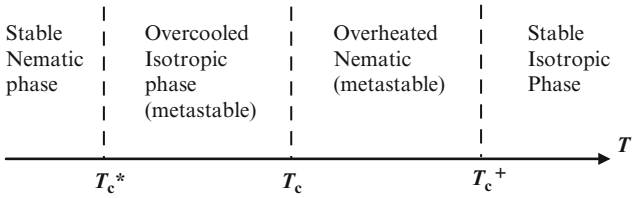

Fig. 6.7 Sequence of phase states observed during the up-and-down temperature scan that manifests a temperature hysteresis near the N–I transition

overheated (metastable) nematic phase with at $S > 0$. At $T = T_c$ the two minima have the same zero free energy density (solid line 2), but between them there is a barrier shown by the arrow. The right minimum for $S \neq 0$ corresponds to the stable nematic state and the left one with $S = 0$ represents the overcooled (metastable) isotropic state. Between T_c and T_c^* the two minima coexist. Finally, for $T < T_c^*$ the left minimum disappears, the metastable isotropic phase becomes unstable and the nematic state becomes absolutely stable (dash curve 1 with a deep minimum). Fig. 6.7 illustrates the sequence of the intermediate phases in the proximity of the NI transition.

6.2.4 *Physical Properties in the Vicinity of the N–Iso Transition*

Physical properties of substance close to N–I phase transition may be related to the parameters of Landau expansion [8]. For example we can calculate an entropy density change at the transition temperature T_c from Eq. 6.9 and $S_c = B/3C$:

$$\Delta\Sigma = -\left.\frac{\partial(g_N - g_{Iso})}{\partial T}\right|_{T_c} = -\frac{1}{3}aS_c^2 = -\frac{aB^2}{27C^2}$$

Correspondingly, the latent heat of the N–Iso transition is

$$\Delta H = \Delta\Sigma T_c = -\frac{aB^2}{27C^2}T_c$$

As we have seen above, Landau expansion coefficients a, B and C can be found from the measurements of order parameter S(T) and ΔH by different techniques, such as microscopy (for T_c), differential scanning calorimetry (for T_c, and ΔH), refractometry or NMR (for S_c).

Two other calculated temperature dependencies are shown in Fig. 6.8 with the characteristic temperatures discussed above. The excess of the specific heat in the nematic phase $C_p = aS\left(\partial^2 S/\partial T^2\right)_P$ is shown in Fig. 6.8a. The temperature dependence obtained from Eq. 6.13 follows a law $C_p \propto (T_c^+ - T)^{-1/2}$ with a step at T_c in agreement with experiment [8]. With decreasing temperature C_p achieves a plateau equal to $a^2/2C$. Another important characteristic is structural susceptibility (not to

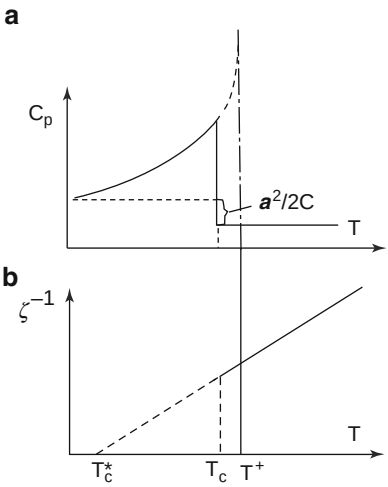

Fig. 6.8 Temperature dependencies of heat capacity (**a**), and inverse value of nematic-like structural susceptibility χ^{-1} (**b**) in the vicinity of N–I phase transition

be confused with the electric χ_E or magnetic susceptibility χ_M) determining the development of order parameter fluctuations in the isotropic phase (short-range order [3]) near the transition to the nematic phase $\zeta^{-1} = \partial^2 \Delta g / \partial S^2$. This is a steepness of the free energy (dot curve 3 in Fig. 6.6) close to its minimum. Above T_c the order parameter is small, S $\rightarrow$ 0, and the terms with S^3 and S^4 in Eq. 6.9 may be disregarded. Then the inverse susceptibility $\zeta^{-1} = {}^2/_3 a(T - T_c)$ follows the Curie law $\zeta \propto 1/T$, see Fig. 6.8b.

This susceptibility can be studied in the isotropic phase by electro-optical or magneto-optical techniques. Indeed, anisotropy of the electric and magnetic susceptibilities is proportional to the order parameter S, see Eq. 3.15. For example, nematic liquid crystal acquires an additional free energy $-(1/2)\chi_a H^2 = -(1/2)\chi^a{}_{\max} S H^2$ in the magnetic field parallel to the director ($\chi_{\max}$ is anisotropy of magnetic susceptibility for the ideal nematic). Then, on account of Eq. 6.9, the energy in the isotropic phase with a short-range nematic order is given by

$$\Delta g(iso) = -\frac{1}{2}\chi_a^{\max} H^2 S + \frac{1}{3} a(T - T_c{}^*) S^2$$

After minimization we obtain the contribution of the magnetic field to the order parameter

$$S_H = \frac{3\chi_a^{\max} H^2}{4a(T - T_c{}^*)}$$

that may be related to a change of the refraction index parallel to the field. The appearance of the birefringence $\delta n(H)$ in the isotropic liquid induced by the magnetic effect is called Cotton-Mouton effect. Its electric field analogue is Kerr effect. In both cases, δn follows the Curie law and the Landau coefficient a may be found from these experiments. Note, however, that the numerical coefficient (3/4)

depends on arbitrariness of numerical coefficients in the original Landau expansion (6.8). We should also underline that here we did not discuss any effects of fluctuations of the order parameter in space $\delta S(\mathbf{r})$; the S-value was considered dependent only on temperature and magnetic field.

In the frame of Landau theory we can also consider the influence of the external magnetic or electric field on the N–I phase transition temperature. Imagine that we apply the electric field E along the director of a nematic and increase temperature. In the case of positive dielectric anisotropy ε_a, even a weak field changes the symmetry of both phases to conical ($C_{\infty v}$), and, strictly speaking, the phase transition vanishes. However, in the continuous temperature dependence of the order parameter, a characteristic inflection point appears that may be considered as an apparent N–I phase transition temperature T_c. The latter may be changed with an applied field.

As the equation for the enthalpy is given by $\partial \Delta g/\partial T = -\Delta H/T_c$ we may write the discontinuity of the free energy density as $\delta \Delta g = -\Delta H \delta T/T_c$. When $\mathbf{E} \parallel \mathbf{n}$ there is a difference between quadratic-in-field energy terms in the nematic and isotropic phases $\Delta g_E = (1/8\pi)(\varepsilon_{\parallel} - \varepsilon_{iso})E^2$. From comparison of the two contributions, the field induced shift δT_E of the transition temperature T_c is given by [9]:

$$\Delta T_E = \frac{(\varepsilon_{\parallel} - \varepsilon_{iso})E^2}{8\pi \cdot \Delta H}$$

For nematics with high positive dielectric anisotropy the difference $\varepsilon_{\parallel} - \varepsilon_{iso} \approx 10$ is substantial and, for a typical value of $\Delta H \approx 2.5 \times 10^7$ erg/cm^3, the shift $\Delta T_E \approx$ 1K is expected for a field strength of 500 statV/cm (or 1.5×10^7 V/m) in agreement with experiment [9].

Concluding this section I would like to underline the significance of coefficient B in the Landau expansion:

1. For $B = 0$, the free energy is symmetric with respect to $\pm\eta$ and we have a second order transition. For small $B \neq 0$ the transition is called weak first order transition because the discontinuity of the order parameter is small and T_c^* becomes close to T_c.
2. The biaxiality of molecules influences the value of B and, in turn, a variation of B may provide, at least, theoretically the biaxiality of the nematic phase.
3. Flexibility of mesogenic molecules also strongly influences B.

6.3 Nematic–Smectic A Transition

6.3.1 Order Parameter

As both the nematic and smectic A phases have quantitatively similar orientational order, we may fix the free energy of the nematic phase and assume the orientational order parameter to be equal in both phases, $S_A = S_N$. Then we introduce a new

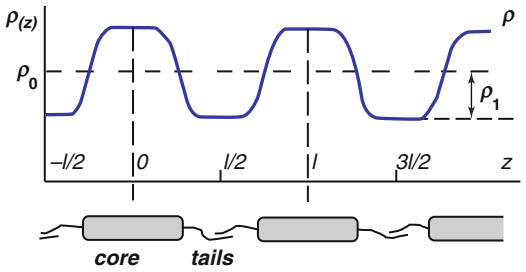

Fig. 6.9 *Below*: A schematic picture of molecular packing in the vertically oriented smectic layers. *Above*: Average density ρ modulated with amplitude ρ_1 and period l of the density wave

order parameter because, in the smectic A phase, a new symmetry element appears, namely, one-dimensional positional order. Recall that, in the SmA phase, local density is modulated, Fig. 6.9,

$$\delta\rho(z) = \rho(z) - \rho_0 = \sum_m \rho_m \cos\left(\frac{2\pi m z}{l} + \varphi_m\right)$$

Here l is interlayer distance and ρ_m is the infinite set of possible complex order parameters (amplitudes and phases of density harmonics with $m = 1,2,3\ldots$) In fact, usually the modulation is not deep and, in the simplest approach, we can leave only the first strongest Fourier harmonic with $m = 1$ and the role of highest harmonics will be discussed later. Then,

$$\delta\rho(z) = \rho_1 \cos\left(\frac{2\pi z}{l} + \varphi_1\right) \tag{6.15}$$

This density wave is usually considered as a complex order parameter $\rho_1 = \exp(i\pi)$ of the smectic A phase in the Landau expansion or free energy at the SmA–N phase transition. Typically, when there is no distortion, one assumes $\varphi_1 = 0$ at $z = 0$ and operates only with the wave amplitude ρ_1 as the real part of the order parameter.

6.3.2 Free Energy Expansion

Due to symmetry $\pm\rho_1$ the free energy density is expanded over even powers of ρ_1 that is without B-term:

$$g_{SmA} = g_N + \frac{1}{2}A\rho_1^2 + \frac{1}{4}C\rho_1^4 + \cdots \text{ with } A = a(T - T_{NA}), a > 0 \tag{6.16}$$

Assuming $g_N = \text{const}$, after minimization of (6.16) with respect to ρ_1 we have

$$\frac{\partial g_{SmA}}{\partial \rho_1} = \rho_1[a(T - T_{NA}) + C\rho_1^2] = 0 \tag{6.17}$$

Solution $\rho_1 = 0$ corresponds to the positionally symmetric (not modulated) nematic phase. The other two solutions correspond to the positionally ordered SmA phase with a continuous growth of the order parameter:

$$\rho_1 = \pm\left[\frac{a(T_{NA} - T)}{C}\right]^{1/2} \tag{6.18}$$

The temperature dependence of ρ_1 may be found from the intensity of the X-ray diffraction at the Bragg angle determined by period l of the smectic layers. The experimental data on $\rho_1(T_{NA} - T)$ for cholesteryl nonanoate [10] (solid bold curve) are compared with the corresponding theoretical dependence (dash line) in Fig. 6.10a. Note that the helical structure of the cholesteric is disregarded because locally, on the scale of the size l, the nematic and cholesteric phases are indistinguishable. From this plot we can find $\rho_1 = 0.31$ at $T_{NA} - T = 10°C$.

Therefore, with $T_{NA} = 348$ K and found ratio $a_1/C_1 = 0.01$ we can plot the free energy in arbitrary units. To this effect, let us write Eq. 6.16 in the dimensionless form:

$$\frac{g_{SmA} - g_N}{{}^1\!/_2 a T_{NA}} = (T_{NA} - T)\rho_1^2 + 0.143\rho_1^4 + \cdots$$

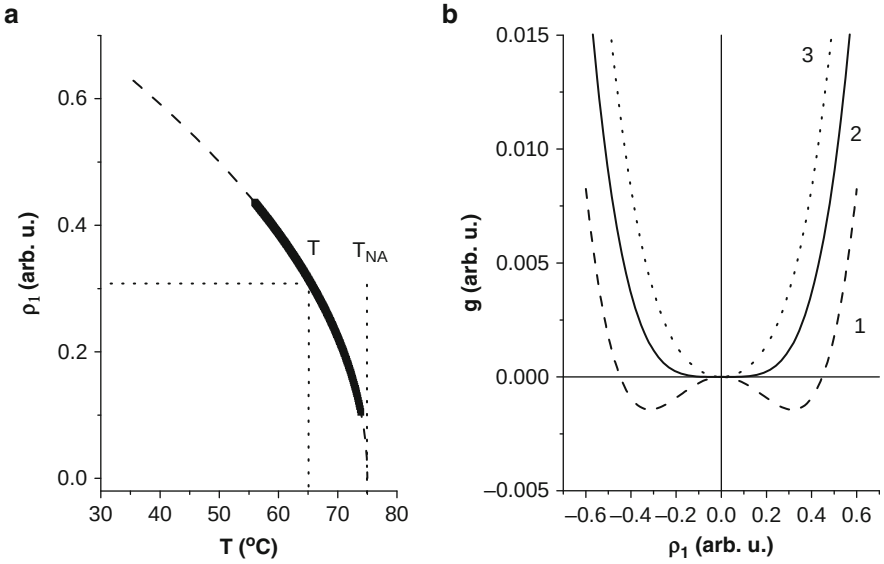

Fig. 6.10 (**a**) Theoretical (*dash curve*) and experimental (*solid curve*) dependence of the smectic A order parameter ρ_1 on temperature; $T_{NA} = 75°C$ for cholesteryl nonanoate [10]. (**b**) Free energy of a smectic A as a function of order parameter ρ_1 for different temperatures: 10°C below the transition (curve 1), $T = T_{NA}$ (curve 2) and 10°C above T_{NA} (curve 3)

The dependencies of the dimensionless free energy on the order parameter at $T < T_{NA}$ (curve 1), $T = T_{NA}$ (curve 2) and $T > T_{NA}$ (curve 3) are presented in Fig. 6.10b. The energy is symmetric about $\rho_1 = 0$. For $T \geq T_c$ the higher symmetry nematic state is stable; curve 3 at finite ρ_1 in the nematic manifests short-range smectic order effect. For $T < T_c$, in the smectic A state, the two minima in curve 1 situated exactly at $\rho_1 = \pm 0.31$ reflect the symmetry of the energy with respect to the phase (0 or π) of the density wave.

We can also discuss the structural susceptibility in the more symmetric (nematic) phase near the SmA-N transition.

$$\chi_{NA}^{-1} = \frac{\partial^2 g_A}{\partial \rho_1^2} = a(T - T_{NA}) \tag{6.19}$$

It is a special *layer formation susceptibility*: close to the phase transition the nematic is very sensitive to the spatially periodic molecular field, which induce the density wave with period l. In order to study this phenomenon one is tempted to use an external *spatially periodic force* with the same period, but, at present, it is technically impossible. Therefore, we cannot find the Landau coefficient a above T_{NA} using some analogy with the Kerr or Cotton-Mouton effects.

However, there is a great deal of studies of pre-transitional effects by the calorimetric and X-ray scattering techniques showing that, in the vicinity of second order N–A transition, a strong fluctuations of the smectic order occur. It means that the order parameter changes in time and space $\rho_1 = \rho_1(\mathbf{r}, t)$. For example, a character of the functional dependence of heat capacity at the nematic–smectic A transition may be very different, varying from a simple step to the divergent cusp-like maximum [11]. The experiment shows that N–A transition may be second or first order. This depends on the width of the temperature range of the intermediate nematic phase between smectic A and isotropic phases: the narrower the range the closer the N–A transition to the first order.

6.3.3 Weak First Order Transition

In reality, the N–A transition is, as a rule, weak first order transition. There are, at least, two ways to understand this in framework of Landau approach. We still use the same smectic order parameter ρ_1 but include additional factors, either (a) higher harmonics of the density wave, or (b) consider the influence of the positional order on the orientational order of SmA, the so-called interaction of order parameters.

6.3.3.1 Role of Higher Order Fourier Components

We keep equality of nematic orientational order parameters in both phases $S_N = S_A$, and take only the amplitude of the second harmonic ρ_2 of the density wave as an additional SmA order parameter

$$\delta\rho(z) = \rho_1 \cos(2\pi z/l) + \rho_2 \cos(4\pi z/l)$$

Therefore we have two order parameters (for the same transition) and the free energy density is:

$$g_{SmA} = g_N + \frac{1}{2}A_1\rho_1^2 + \frac{1}{2}A_2\rho_2^2 - B\rho_1^2\rho_2 + \frac{1}{4}C_1\rho_1^4 + \frac{1}{4}C_2\rho_2^4 + C_{12}\rho_1^2\rho_2^2$$
$$\text{with } A_1 = a_1(T - T_1); \quad A_2 = a_2(T - T_2); \tag{6.20}$$

For a typical situation $\rho_1 > \rho_2$, it is sufficient to take only one cross-term with coefficient B. Coefficients a_1 and a_2 are assumed positive and, in addition, we assume $T_1 > T_2$ because on cooling, the first Fourier harmonic appears at higher temperature, and afterwards, at a lower temperature, the single harmonic law is violated and ρ_2 appears. The minimization of (6.20) with respect to ρ_2 results in

$$\frac{\partial g_{SmA}}{\partial \rho_2} = A_2\rho_2 + C_2\rho_2^3 - B\rho_1^2 + 2C_{12}\rho_1^2\rho_2 = 0 \tag{6.21}$$

Due to smallness of ρ_2, the second and fourth terms are small and we can find ρ_2:

$$\rho_2 \approx \frac{B}{A_2}\rho_1^2 \tag{6.22}$$

Then, substituting ρ_2 into expression (6.20) for free energy and omitting the terms with ${\rho_1}^8$, we obtain a biquadratic equation of the (6.6) type:

$$g_{SmA} = g_N + \frac{1}{2}A_1\rho_1^2 - \frac{1}{4}\left(\frac{2B^2}{A_2} - C_1\right)\rho_1^4 + \frac{1}{6}D_1\rho_1^6 \tag{6.23}$$

where $D_1 = 12C_{12}B^2/{A_2}^2$. Like in the case of Eq. 6.6, the condition for first order transition is

$$2B^2/A_2 - C_1 > 0,$$

otherwise, the transition is second order. Therefore, an appearance of small terms with ρ_2 in the free energy (6.20) results in a weak first order N–SmA transition.

6.3.3.2 Interaction of Two Order Parameters

Experiment shows that:

1. The narrower a range of the nematic phase in a homological series of different compounds (as an example see Fig. 6.11a) the stronger are first order features of the N–SmA transition. In some sense, the SmA phase "feels" the proximity of the isotropic phase. In other words, we may say that, in the isotropic phase, there are traces of both nematic and smectic A *short-range* order.
2. Appearance of the positional order in the SmA phase is accompanied by an increase in the orientational order, $\Delta S = S_A - S_N$. The reason is denser molecular packing within the smectic layers that is more favorable for higher S, Fig. 6.11b.

On account of ΔS, the free energy density of smectic A may be written as follows:

$$g_{SmA} = g_N + \frac{1}{2}A_1\rho_1^2 + \frac{1}{2}A_2(\Delta S)^2 - B\rho_1^2(\Delta S) + \frac{1}{4}C_1\rho_1^4 \tag{6.24}$$

Now we make minimization with respect to ΔS and obtain

$$\frac{\partial g_{SmA}}{\partial \Delta_S} = A_2\Delta S - B\rho_1^2 = 0 \text{ or } \Delta S = \frac{B}{A_2}\rho_1^2 \tag{6.25}$$

Hence, we arrive at exactly the same form the Eq. 6.23 has.

Therefore we again obtain the first order transition for $2B^2/A_2 - C_1 > 0$ and second order for $2B^2/A_2 - C_1 < 0$ and a *tricritical point* for $2B^2/A_2 - C_1 = 0$. The tricritical point (TCP) is located in the continuous phase transition line separating the nematic and smectic A phases [12], see a phase diagram schematically shown in Fig. 6.12. Such a point should not be confused with the *triple point* common for the isotropic, nematic and SmA phases. In Fig. 6.12, for homologues with alkyl chains shorter than l_{cr}, the N–SmA transition is second order and shown by the dashed curve. With increasing chain length the nematic temperature range becomes narrower (like in Fig. 6.1) and, at TCP, the N–SmA transition becomes first order (solid curve).

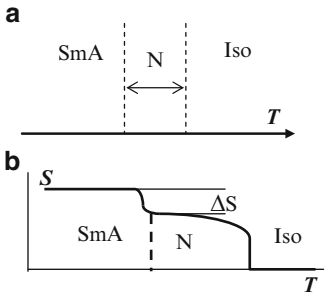

Fig. 6.11 Sequence of phases on the temperature scale (**a**) and qualitative dependence of orientational order parameter S in the nematic and smectic A phases (**b**). With increasing increment ΔS the N–A transition acquires more features of first order transition

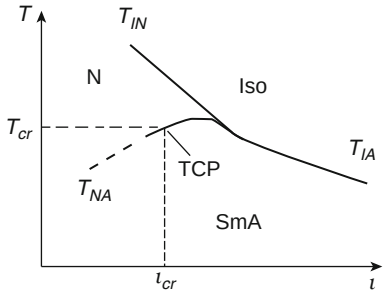

Fig. 6.12 Phase diagram "isotropic liquid–nematic –smectic A" with a tricritical point TCP at temperature T_{cr} and length l_{cr} of alkyl chains

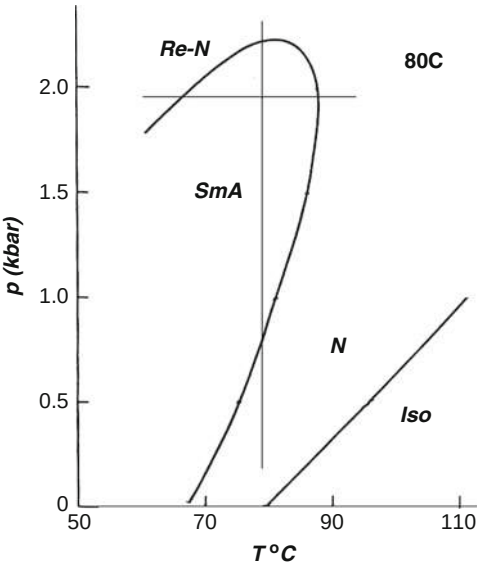

Fig. 6.13 Phase diagram "isotropic phase (Iso)–nematic (N)–smectic A (SmA)–reentrant nematic (Re-N)" of p-octyloxy-cyanobiphenyl in the pressure–temperature coordinates [14]

6.3.4 Re-entrant Phases

As a rule, increasing pressure or decreasing temperature promotes a denser, more ordered phase. There are, however, cases when, upon increasing pressure or decreasing temperature, the smectic A phase is substituted by the nematic phase [13]. Therefore, a more symmetric phase reappears or "re-enters" into consideration. An example [14] is shown in Fig. 6.13. Following the horizontal line at constant pressure of about 2 kbar (1bar $= 10^6$ dyn/cm^2 or 10^5 Pa) from the right to the left we begin from the nematic phase then, with decreasing temperature, cross the SmA phase and enter again the nematic phase. Similar sequence is observed on the down-up way along the vertical line at constant temperature. Such an abnormal behavior can be explained with a molecular model, Fig. 6.14. In fact, reentrant

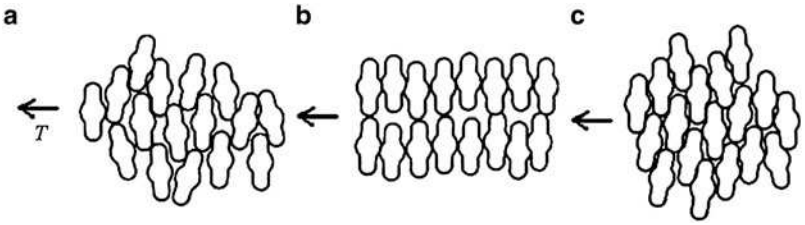

Fig. 6.14 Packing of molecular dimers in the nematic (**a**), smectic A (**b**) and reentrant nematic (**c**) phases. The middle part of dimers formed by rigid biphenyl cores is broader than their end parts formed by molecular tails and the length of the dimers depends on the pressure and temperature

phases are observed in liquid crystals with strongly asymmetric polar molecules such as *p*-octyloxy-*p*′-cyanobiphenyl (8OCB). They form pairs of antiparallel dipoles (or molecular dimers as earlier shown in Fig. 3.9) whose length may depend on temperature and pressure. Such dimers are building elements of mesophases. Then a subtle change in the dimer geometry determines the packing structure shown in Fig. 6.14 that explains the re-entrance phenomena.

6.4 Smectic A–Smectic C Transition

6.4.1 Landau Expansion

In the smectic C phase a new feature appears, a uniform molecular tilt that is characterized by the two-component order parameter $\vartheta \exp(i\varphi)$ [15]. For simplicity, we can fix the azimuth angle φ and operate with a real order parameter ϑ:

$$g_{SmC} = g_{SmA} + \frac{1}{2}A\vartheta^2 + \frac{1}{4}C\vartheta^4 + \frac{1}{6}D\vartheta^6 \tag{6.26}$$

The odd terms are absent due to the $\pm\vartheta$ symmetry. After minimization with respect to ϑ we get

$$\vartheta = \pm\left(\frac{A}{C}\right)^{1/2} = \left[\frac{a(T - T_c)}{C}\right]^{1/2}$$

that is the same temperature dependence of the order parameter ϑ as presented in Fig. 6.10a. The inverse "soft-mode" susceptibility for the uniform tilt

$$\zeta_C^{-1} = \frac{\partial^2 g_C}{\partial \vartheta^2} = a(T - T_{CA}), \tag{6.27}$$

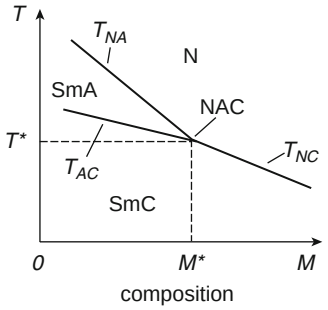

Fig. 6.15 Phase diagram "nematic- smectic A- smectic C" with the triple NAC point at temperature T^* and mixture concentration M^*

as expected, has the same linear temperature dependence as in nematics, see Eq. 6.10 and SmA. This is a typical picture for second order transition.

However, if you take into account the "interaction" of SmA and SmC order parameters, a cross term $\rho_1^2\vartheta^2$ would result in the appearance of the NAC triple point in the phase diagram [8, 16], see Fig. 6.15. In this case, the phase transition lines might correspond to either second or first order transitions; it depends on parameters of the Landau expansion. In experiment, such a phase diagram may be observed when a content of binary mixtures is varied.

6.4.2 *Influence of External Fields*

In the framework of the Landau theory one can analyze the influence of a magnetic or an electric field on the phase symmetry and order parameters [17]. Here we consider the magnetic field influence on the temperature of the smectic A–C transition [11]. Let the magnetic field is applied along the smectic layer normal. Then, it is sufficient to add the field term to the expansion (6.26).

$$g_{SmC} = g_{SmA} + \frac{1}{2}a(T - T_{CA})\vartheta^2 - \frac{1}{2}\chi_a(\mathbf{Hn})^2$$

We assumed small tilt angles and disregard the term with coefficients C and D. For small ϑ the scalar product is $Hn(1-\vartheta^2/2)$ and after minimization we obtain

$$a(T - T_{CA})\vartheta + \chi_a H^2\vartheta = 0$$

Finely, the temperature shift of the A–C phase transition point by the magnetic field is given by:

$$T - (T_{CA} - \frac{1}{a}\chi_a H^2) = 0 \tag{6.28}$$

Therefore, for positive χ_a (or ε_a in case of the electric field) the transition temperature reduced with increasing field.

6.5 Dynamics of Order Parameter

6.5.1 Landau-Khalatnikov Approach

Going back to the beginning of this section, let us recall the conditions of the thermodynamic equilibrium giving the free energy density minimum: $dg/d\eta = 0$ and $d^2\eta/d\eta^2 > 0$.What would happen if these conditions are not fulfilled? For example, due to disturbance by an external field, the order parameter of the system may become different from the equilibrium value. Then, after switching the field off, the order parameter will relax to its equilibrium value. The problem is how to find its relaxation time? Below we shall only consider the second order transition and only a weak deviation from the equilibrium, i.e., small values of derivative $dg/d\eta$.

We neglect fluctuations of the order parameter, and assume that there is a simple linear relationship between a torque $dg/d\eta$ and a relaxation rate $d\eta/dt$. Physically it means that the steeper potential well g(η) (larger $dg/d\eta$), the faster is relaxation (larger $d\eta/dt$) of the induced order parameter. Hence the *Landau–Khalatnikov equation* reads

$$\frac{d\eta}{dt} = -\Gamma \frac{\partial g}{\partial \eta} \tag{6.29}$$

where the rate controlling coefficient Γ is considered to be independent of temperature.

6.5.2 Relaxation Rate

The relaxation rate can be found from the equilibrium Landau expansion (6.1) without B-term:

$$g = g_0 = \frac{1}{2}a(T - T_c)\eta^2 + \frac{1}{4}C\eta^4 + \cdots$$

Its solution for $T < T_c$ has been found above. The equilibrium value of the order parameter is:

$$\bar{\eta} = [a(T_c - T)/C]^{1/2} \tag{6.30}$$

Eq.(6.29) reads:

$$\frac{d\eta}{dt} = -\Gamma[a(T - T_c)\eta + C\eta^3] \tag{6.31}$$

It is convenient to introduce a difference of the order parameters for the distorted and equilibrium medium $\delta\eta = \eta - \bar{\eta}$.

Then, for *the high symmetry (high T) phase*, $\bar{\eta} = 0$ and the linearized Landau–Khalatnikov equation for $\delta\eta$ is given by:

$$\frac{d\eta}{dt} \approx -\Gamma a(T - T_c)\delta\eta = -\frac{\delta\eta}{\tau} \tag{6.32}$$

with a characteristic relaxation time

$$\tau_{hs} = \frac{1}{\Gamma a(T - T_c)} = \frac{\gamma}{a(T - T_c)} \tag{6.33}$$

Coefficient $\gamma = \Gamma^{-1}$ is a kind of friction coefficient (viscosity for liquid crystals) controlling the relaxation process. In the Gauss system $[\gamma] = \text{s.erg/cm}^3 = \text{g.cm/s}$ or Poise. In the SI system $[\gamma] = \text{s·J/m}^3 = \text{s·N/m}^2$ or Pa·s (1 Pa·s = 10 P).

For the low-symmetry phase we make linearization of the right part of Eq. 6.31

$$-\Gamma\eta[(T - T_c)a + C\eta^2] = -\Gamma\eta[(T - T_c)a + C(\bar{\eta}^2 + 2\bar{\eta}\delta\eta + \cdots)]$$

In the brackets, only term $2\bar{\eta}\delta\eta C$ includes increment $\delta\eta$. Thus we keep it and then ignore higher order term with $(\delta\eta)^2$:

$$d\delta\eta/dt = -\Gamma\eta 2C\bar{\eta}\delta\eta = -2\Gamma C(\bar{\eta} + \delta\eta)\bar{\eta}\delta\eta \approx -2\Gamma C\bar{\eta}^2\delta\eta$$

Finally, using Eq. 6.30 for the equilibrium order parameter, we exclude C and obtain for *the low-symmetry phase*:

$$\frac{d\delta\eta}{dt} = 2\Gamma a(T - T_c)\delta\eta = -\frac{\delta\eta}{\tau} \tag{6.34}$$

with a relaxation time

$$\tau_{ls} = \frac{1}{2\Gamma a(T_c - T)} = \frac{\gamma}{2a(T_c - T)} \tag{6.35}$$

The results (6.33) and (6.35) are of principal importance. We already know that at the second order transition the structural susceptibility diverges (Curie law). Now we see that *relaxation times diverge* as well, i.e., on approaching the transition from any side, the relaxation of the order parameter becomes slower and slower and, at

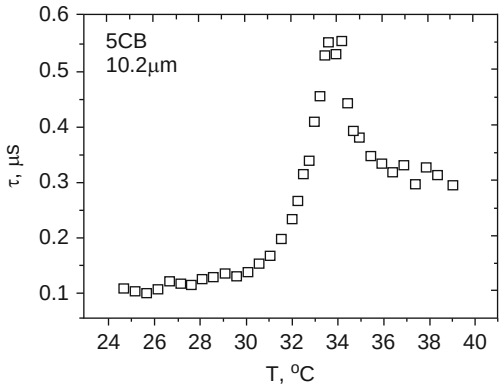

Fig. 6.16 Softening of the N–I phase transition: relaxation time of the orientational order parameter as a function of temperature in *p*-pentyl-cyanobiphenyl (5CB)

the transition, in the linear approximation considered above, the relaxation times are infinite (softening of the transition).

Had we taken higher order terms of $\delta\eta$ into account, the divergence would disappear. The Curie-type order parameter relaxation has been studied on a typical nematic (5CB), see Fig. 6.16. The measurements have been made using a pulse pyroelectric technique [18]. As the nematic–isotropic transition in 5CB is weak first order, it clearly demonstrates some features of the softening: the relaxation time of the orientational order parameter on the nematic side of the NI transition increases five times.

There are also other reasons that truncate the order parameter divergence such as spatial inhomogeneities or external fields. For example, to describe a spatial inhomogeneous system, a term quadratic in the gradient of the order parameter $G(\nabla\eta)^2$ must be added to the density of free energy and all the Landau expansion should be integrated over the system volume:

$$F = \int [g_0 + \frac{1}{2}a(T - T_c)\eta^2 + \frac{1}{4}C\eta^4 + G(\nabla\eta)^2 + \cdots]dV \tag{6.36}$$

Then in the relaxation equation an additional term appears. E.g., in the low-symmetry phase, at $T < T_c$:

$$\frac{\partial\delta\eta}{\partial t} = -\left(\frac{\delta\eta}{\tau} - 2\Gamma G\Delta(\delta\eta)\right)$$

where Δ is Laplace operator. Then, the inhomogeneous distribution of $\delta\eta(\mathbf{r})$ can be expanded in the Fourier series of spatial harmonics and, for each Fourier components with number m, we have different Landau–Khalatnikov equations

$$\frac{d\delta\eta_m}{dt} = -\frac{\delta\eta_m}{\tau_m}$$

with different relaxation times

$$\frac{1}{\tau_m} = \frac{1}{\tau} + \Gamma G m^2 \tag{6.37}$$

Therefore, at $T = T_c$, the relaxation time becomes finite. We meet the same situation in the helical phases as well.

6.6 Molecular Statistic Approach to Phase Transitions

The problem is to derive the equation of state and thermodynamic functions of a particular liquid crystal phase from properties of constituting molecules (a form, a polarizability, chirality, etc.). The problem we are going to discuss is one of the most difficult in physics of liquid crystals and the aim of this chapter is very modest: just to introduce the reader to the basic ideas of the theory with the help of comprehensive works of the others [2, 5, 19]. To consider the problem quantitatively we need special methods of the statistical physics. In this context, the most useful function is free energy F, which is based microscopically on the so-called partition function, see below. For the partition function, we need that energy spectrum of a molecular system, which is relevant to the problem under consideration. The energy spectrum is related to the entropy of the system and we would like to recall the microscopic sense of the entropy.

6.6.1 Entropy, Partition Function and Free Energy

6.6.1.1 Entropy

We consider a small but macroscopic part of a larger molecular system. Even under equilibrium conditions such a subsystem can be found in any of a tremendous number n of statistical configurations or quantum states [2]. Any change in a position, velocity or internal motion of a particular molecule will bring our macroscopic subsystem in the new state with energy E_n. The set of corresponding energy levels is extremely dense as pictured schematically in Fig. 6.17 and we may consider a continuous distribution function $w(E) = w(E_n)$ of the probability for the subsystem *to be in a state with energy* $E = E_n$. A number of the levels below a particular energy E is $\Gamma(E)$. Now we would like to relate the entropy to this energy spectrum.

By definition, the dimensionless entropy is given by

$$s = \ln \Delta\Gamma(\mathrm{E}) \tag{6.38}$$

where $\Delta\Gamma$ is the so-called *statistic weight of a macroscopic state* of our molecular subsystem related to the formidable number of the microscopic quantum states.

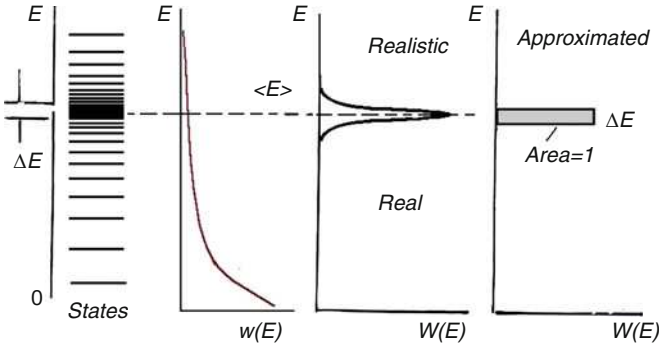

Fig. 6.17 Energy levels of a macroscopic quantum subsystem, probability $w(E)$ for the subsystem to be in a state E_n and probability $W(E)$ for the subsystem to be within the energy interval between E and $E + dE$, more or less realistic and approximated by a rectangular

The probability for a molecular subsystem to have energy in the interval between E and $E + dE$ reads:

$$W(E) = \frac{d\Gamma(E)}{dE} w(E) \tag{6.39}$$

where $d\Gamma/dE$ is density of possible states on the energy scale. Since the energy of our subsystem under fixed experimental conditions fluctuates only negligibly about the average value $<E>$, the density of states and probability $w(E)$ have extremely sharp maxima at $E = <E>$, close to δ-function shown as "realistic" function in Fig. 6.17. Therefore, the normalization condition may be written as

$$\int W(E)dE \approx W(\langle E\rangle)\Delta E = 1 \tag{6.40}$$

On the other hand, the number of the quantum states $\Delta\Gamma$ in the ΔE interval is: $\Delta\Gamma = \frac{d\Gamma(\langle E\rangle)}{dE}\Delta E$, that means $\Delta E = \Delta\Gamma \frac{dE}{d\Gamma(\langle E\rangle)}$. Now the condition (6.40) on account of (6.39) results in:

$$W(\langle E\rangle) \cdot \Delta E = \frac{d\Gamma(\langle E\rangle)}{dE} w(\langle E\rangle) \cdot \Delta\Gamma \frac{dE}{d\Gamma(\langle E\rangle)} = 1$$

Hence $w(\langle E\rangle)\Delta\Gamma = 1$ and the *dimensionless entropy* is found to be related to the distribution function $w(E_n)$

$$s = \ln \Delta\Gamma = -\ln w(\langle E\rangle) = -\langle \ln w(E_n)\rangle \tag{6.41}$$

The transformation of average values in (6.41) follows from the statistical independence of the events described by a distribution function (for $w_{12} = w_1 w_2$, $\ln w_{12} = \ln w_1 + \ln w_2$, etc.).

To have the entropy in the Boltzmann form we write

$$S = k_B s = -k_B \langle \ln w(E_n) \rangle \tag{6.42}$$

Dimension of entropy is [erg/K] or [J/K]. To have an idea of the entropy value, let us take a tremendous number of points in the phase space, e.g. 10^{100}. Then, $s = 230$ and $S = 3{\cdot}10^{-14}$ erg/K are extremely small values with respect to experimentally measured quantities.

Up to now we considered number $\Delta\Gamma$ of the quantum states or "cells" in a multidimensional configuration or phase space, formed by coordinates q_i and momenta p_i ($i = 1,2...l$) where l is the number of degrees of freedom. Each cell had volume of h^l ($h = 2\pi\hbar$ is Planck constant). In general, these states include all possible degrees of freedom, such as translational and rotational motion of all molecules, their internal (atomic) motion, interactions with other molecules, etc. Now, in the classical limit, instead of $\Delta\Gamma$ we introduce a volume in the phase space $\Delta p \Delta q$, in which a subsystem evolves in time. Additionally, to have the absolute value of the entropy, we introduce the volume of the elementary cell in the phase space $(2\pi\hbar)^l$ and write the dimensionless entropy in the form

$$s = \ln \frac{\Delta p \Delta q}{(2\pi\hbar)^l} \tag{6.43}$$

6.6.1.2 Partition Function and Free Energy

In the quantum-mechanical case, a probability $w(E_n)$ for a subsystem to have energy E_n in a quantum state is given by the Gibbs distribution:

$$w_n = Z^{-1} \exp\left(-E_n \Big/ k_B T\right) \tag{6.44}$$

where Z is a constant to be found from normalization procedure

$$\sum_n w_n = Z^{-1} \sum_n \exp(-E_n \Big/ k_B T) = 1,$$

and called a *partition function* that includes all degrees of freedom of the subsystem:

$$Z = \sum_n \exp(-E_n \Big/ k_B T) \tag{6.45}$$

Using Eqs. 6.42 and 6.44 we write entropy in the form

$$S = -k_B \langle \ln w(E_n) \rangle = -k_B \left\langle \ln Z^{-1} \exp\left(-E_n \Big/ k_B T\right) \right\rangle = -k_B \ln Z^{-1} + \frac{\langle E \rangle}{T},$$

equivalent to

$$\langle E\rangle - TS = k_B T \ln Z^{-1}. \tag{6.46}$$

As the macroscopic definition of the free energy is $F = \langle E\rangle - TS,$ we relate the free energy to partition function:

$$F = k_B T \ln Z^{-1} = -k_B T \ln Z \tag{6.47}$$

Finally, on account of (6.45) the free energy acquires a desired *microscopic form*:

$$F = -k_B T \ln \sum_n \exp(-E_n/k_B T) \tag{6.48}$$

This formula is a base for calculation of all thermodynamic functions of any system if the energy spectrum of the latter is known. We shall illustrate this approach considering two simple systems, the ideal gas and a liquid, both consisted of spherical particles.

In the classical case, instead of discrete distribution w_n (E_n) we have a continuous probability function ρ (p,q) that is probability to have a subsystem with given momentum p and co-ordinate q in the configuration space:

$$\rho(p,q) = A \exp(-E(p,q)/k_B T)$$

and, in the expression for the free energy, instead of the partition function we have a configuration integral

$$F = -k_B T \ln \int' \exp\left(-E(p,q)/k_B T\right) d\Gamma$$

where $d\Gamma = dp_i\, dq_i/(2\pi\hbar)^l$ and prime $(')$ means integrating over physically different states. To avoid $(')$ we may integrate over all states of N particles (molecules) but afterward to divide the result by the number of permutations $N!$: $\int' \ldots d\Gamma = (1/N!) \int \ldots d\Gamma$

6.6.2 Equations of State for Gas and Liquid

6.6.2.1 Ideal Gas of Spherical Particles

To illustrate the technique, consider an ideal gas of N spherical, point-like, non-interacting particles or molecules without internal degrees of freedom. The partition

function takes into account only the translational motion with three degrees of freedom (no rotation assumed for spherical particles):

$$Z_{IG} = \sum_n \exp(-E_n/k_BT) = \frac{1}{N!}\left(\sum_k \exp(-\varepsilon_k/k_BT)\right)^N \tag{6.49}$$

Here, k states of energy ε_k belong to an individual particle and the summation should be made over all these states. Since particles do not interact, the statistic sum for N independent particles is a product of N sums calculated for each particle. As explained above, to exclude identical sum corresponding to the same state of the gas, the number of permutation $N!$ is introduced in the denominator.

The translational motion of a particle is classic and the kinetic energy of one molecule is $\varepsilon_k(p_x, p_y, p_z) = (p_x^2 + p_y^2 + p_z^2)/2m$. Therefore, the summation may be substituted by integration over the phase space (V is the physical volume of the gas):

$$\sum_k \exp\left(-\varepsilon_k/k_BT\right) = \sum_k \frac{1}{(2\pi\hbar)^3} \int_V \iiint_p \exp\left(-p_x^2 + p_y^2 + p_z^2/2mk_BT\right) dp_x dp_y dp_z dV$$

$$= V\left(\frac{mk_BT}{2\pi\hbar^2}\right)^{3/2} = V\lambda(T)^3.$$

Note that, in the triple integral, each integral with respect to p_i with limits $(-\infty,\infty)$ has the known Gaussian form: $\int_{-\infty}^{\infty} \exp(-ax^2)dx = \sqrt{\pi/a}$ and $\lambda(T) = (2\pi)^{1/2}\hbar/(mk_BT)^{1/2}$

Now the partition function for N molecules is found:

$$Z_{IG} = \frac{\lambda^{-3N}}{N!}\int d\mathbf{r}_1 d\mathbf{r}_2 ... d\mathbf{r}_N = \frac{\lambda^{-3N}V^N}{N!} \tag{6.50}$$

In (6.50) integrating is made over N-dimensional coordinate space of volume V^N. Then, the free energy (6.47) reads:

$$F = k_BT(3N\ln\lambda(T) - N\ln V + \ln N!) = -k_BTN(\ln V - \ln N - 3\ln\lambda(T) + 1)$$

Here we used the Stirling formula for large N ($\ln N! \cong N\ln(N/e)$, $e = 2.718...$).

Now we can find pressure

$$p = -\partial F/\partial V = \frac{Nk_BT}{V}$$

and obtain the equation of state for the ideal gas with particle concentration or number density $\rho = N/V$:

$$p_{IG}V = Nk_BT \quad \text{or} \quad p_{IG} = \rho k_BT \tag{6.51}$$

6.6.2.2 Equation of State for a Dense Gas or a Liquid

If we would like to discuss a non-ideal dense gas of interacting hard spheres of a finite size, we should introduce a concept of excluded volume to take into account the repulsion of molecules at short intermolecular distances and write the energy of attraction between molecules at large distances. Then the partition function of type (6.48) will include two additional contributions and becomes quite cumbersome. Nevertheless it allows the discussion of the Van der Waals equation of state

$$p = [Nk_BT/(V - b)] - a/V^2 \tag{6.52}$$

on the microscopic level and find the physical sense of parameters a (for attraction) and b (for repulsion) introduced by Van der Waals phenomenologically. For a simple liquid consisting of hard spherical molecules the equation of state may be written in terms of number density ρ:

$$p = p_{hs} - \tfrac{1}{2} J_0 \rho^2 \tag{6.53}$$

Here, the first and second terms describe correspondingly positive pressure due to molecular repulsion and negative pressure due to molecular attractive forces. Our task is to understand the microscopic sense of parameters p_{hs} (index means hard spheres) and J_0. Therefore we need a proper partition function.

Let $u(r_{ij})$ is repulsive and $-W(r_{ij})$ attractive parts of the intermolecular potential for molecules i and j; then the partition function for N spherically symmetric particles of mass m and radius r_0 reads [5]:

$$Z = \frac{\lambda^{-3N}}{N!} \int d\mathbf{r}_1 \ldots d\mathbf{r}_N e_{ij}^N \left\{ \exp\left[{}^1\!/_2 \beta \sum_{k \neq l} W(r_{kl}) \right] \right\}^N \tag{6.54a}$$

Here $\beta = 1/k_BT$, λ is given above when discussing the ideal gas, $e_{ij} = \exp[-\beta u(r_{ij})]$. This function can be written shortly as a product of the part Z_0 including solely repulsive interactions and the thermal average of the term describing attraction between different particles k and l:

$$Z = Z_0 \left\langle \exp\left[{}^1\!/_2 \beta \sum_{k \neq l} W(r_{kl}) \right] \right\rangle \tag{6.54b}$$

First we estimate only the repulsive part Z_0 and then the attractive one.

In Eq. 6.54a, averaging over ensemble (reference system) depends on the type of the ensemble. In the simplest case, we take as a reference the system of hard spheres with repulsive potential of the type of a hard wall, shown in Fig. 6.18a, namely,

$$\text{For } r_{ij} \leq 2r_0: \quad u(r_{ij}) = \infty \text{ and } e_{ij} = 0$$

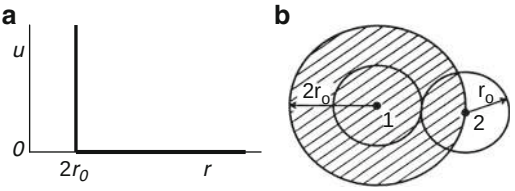

Fig. 6.18 Hard core intermolecular potential (**a**) and illustration of the excluded volume for two spherical particles of radius r_0 (**b**)

and

$$\text{for } r_{ij} \geq 2r_0: \quad u(r_{ij}) = 0 \text{ and } e_{ij} = 1$$

Next, since the hard spheres (or molecules) have their own volume $V_m = (4/3)\pi r^3$ and touch each other, the free volume for their translational motion is reduced. As seen in Fig. 6.18b the presence of sphere 1 reduces the available volume for sphere 2 by $8V_m$. This value is common for two spheres; therefore, the excluded volume per one sphere is $4V_m$. It means that the volume of the whole system is diminished down to the value of $V - 4NV_m$. Then the partition function (6.50) for the ideal gas of point spheres, which corresponds to the same translational degrees of freedom may be corrected for the excluded volume or a packing fraction $\eta = \rho V_m$:

$$Z_0 = \frac{\lambda^{-3N} V^N (1 - 4\eta)^N}{N!} \tag{6.55}$$

Therefore, the part of free energy related to hard sphere repulsion is expressed in terms of density of particles $\rho = N/V$ that on account of Stirling formula is given by

$$F_{hs} = -k_B T \ln Z_0 = N k_B T [3 \ln \lambda + \ln \rho - 1 - \ln(1 - 4\eta)]$$

From here the *repulsive part of pressure* is found

$$p_{hs} = -\frac{\partial F_{hs}}{\partial V} = \frac{N k_B T}{V - 4NV_m} = \frac{N k_B T}{V(1 - 4\eta)}$$
$$\approx \rho k_B T (1 + 4\eta + 16\eta^2 + 64\eta^3 + \cdots) \tag{6.56}$$

The approximation is correct for small density ρ, i.e. small packing fraction η. Note that for $\eta = 0$, we obtain the equation of state (6.51) for the ideal gas $p = \rho k_B T$.

Now we try to estimate the attractive term (a thermal average) in the partition function (6.54a). Due to enormous mathematical difficulties, we get rid of the summation:

$$\left\langle \exp\left[\tfrac{1}{2}\beta \sum_{k \neq l} W(r_{kl}) \right] \right\rangle \approx \exp\left[\tfrac{1}{2}\beta N \rho J_0 \right] \tag{6.57}$$

In fact, instead of summation we have averaged the potential $W(r_{kl})$ with the hard-sphere radial density distribution function ρ_{hs} familiar to us from the discussion of density correlation function of isotropic liquids in Chapter 5. As a result, we obtain a new constant $J_0 = \int W(r)\rho_{hs}(r)dr$. From (6.57) the contribution to free energy due to attraction is found:

$$F_{attr} = -k_B T\left(\frac{1}{2k_B T}N\rho J_0\right) = -\frac{1}{2V}N^2 J_0$$

The pressure due to attractive forces is given by

$$p_{attr} = -\partial F_{attr}/\partial V = {}^1\!/_2 N^2 J_0(-{}^1\!/_{V^2}) = -{}^1\!/_2\rho^2 J_0$$

Finally, we obtain the *equation of state for interacting hard spheres* (attraction and repulsion):

$$p = \frac{\rho k_B T}{1-4\eta} - \frac{1}{2}J_0\rho^2 \tag{6.58}$$

This equation corresponds to both the equation of state for liquids (6.53) and the Van der Waals equation (6.52). However, the phenomenological parameters a and b in (6.52) acquired physical sense. Parameter $b = 4N\rho V_m$ is related to particular molecular volume and density of spheres (molecules), parameter $a = N^2 J_0/2$ points to the properly averaged potential describing molecular attraction.

Thus, we have seen how intermolecular interactions can be taken into account for description of non-ideal gases and even liquids. Now we are much closer to liquid crystals.

6.7 Nematic–Isotropic Transition (Molecular Approach)

6.7.1 Interaction Potential and Partition Function

Consider the simplest case, namely, the nematic phase consisting of uniaxial rod-like molecules. Generally, the intermolecular interaction again consists of the repulsive and attractive parts but both of them become anisotropic. The potential of *pair molecular interaction* can be written in the following general form:

$$W_{12} = W_{12}(\mathbf{r}_{12}, \theta_1, \phi_1, \theta_2, \phi_2) \tag{6.59}$$

Note that Euler angle Ψ is not considered due to the rod-like form of a molecule; the other angles are shown in Fig. 6.19a. Vector $\mathbf{r}_{12}$ connects the gravity centers of rods. If the particular form of W_{12} is known, it can be used for calculation of the

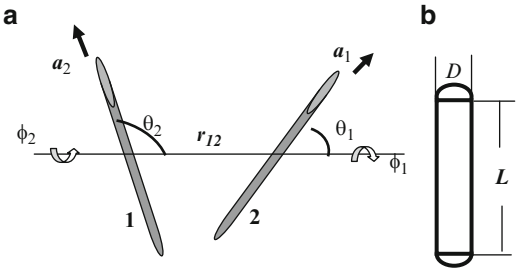

Fig. 6.19 Geometry of interaction between two rod-like molecules (**a**) and geometry of a spherocylinder (**b**)

partition function for N molecules with numbers k and l. The partition function may be written in analogy to expression (6.54a) for simple liquids:

$$Z = Z_{HR}\left\langle \exp\left[{}^{1}\!/_{2}\beta \sum_{k\neq l} W(\mathbf{r}_{kl}\mathbf{a}_k\mathbf{a}_l)\right]\right\rangle \tag{6.60}$$

Again this function includes the repulsive multiplier Z_{HR} and the attractive part. The repulsive part may be considered as a reference for calculation of the thermal average necessary for the attractive part. To find Z_{HR}, we may operate with an excluded volume, although even for hard rods (suffix *HR*) it is very difficult to calculate it. The total procedure is enormously complicated because, even for Z_{HR} known, it requires multiple averaging over (a) all orientations of molecule 1, (b) all orientations of molecule 2, and (c) all distances r_{12}.

Below we shall consider two extreme cases, long hard rods without attraction and rod-like molecules without repulsion. The first approach (by Onsager) may be applied to very long molecules like *tobacco mosaic viruses* and calls for hard mathematics [20]. We shall discuss it very schematically in the next section. The second one (by Maier and Saupe [21]) appeared to be simpler but very powerful and can be applied to many typical nematic liquid crystals. We shall consider it in the subsequent Section 6.7.3.

6.7.2 *Onsager's Results*

Consider a medium consisting of elongated, cylindrically symmetric hard-core molecules in the form of spherocylinders. For spherocylinders shown in Fig. 6.19b we may introduce parameter

$$x = {}^{(L+D)}\!/_{D}, \tag{6.61}$$

that reduces to $x = 2D$ for spherical particles discussed above. A rod has kinetic energy of translations p^2/m and rotation about its short axes ${p_\theta}^2/2I$ and ${p_\phi}^2/2I$

(angles φ and θ are in Fig. 6.19a, I is moment of inertia). Therefore, a rod has five degrees of freedom. In addition rods k and l interact with each other. The interaction potential is $u_{kl} = \infty$ if they overlap each other and $u_{kl} = 0$ without overlapping. The Hamiltonian of the system consisting of N rods is given by

$$H = \sum_{k=1}^{N} T_k + \frac{1}{2} \sum_{k,l=1}^{N} u_{kl} \tag{6.62}$$

and the partition function can be written as

$$Z_{HR} = \frac{1}{N!(2\pi\hbar)^{5N}} \int \left[d\mathbf{r} d\mathbf{p}_i dp_{\theta_i} dp_{\phi_i} d\theta_i d\phi_i \exp(-\beta H) \right]^N \tag{6.63}$$

Onsager used a low-density expansion, that is small packing factor $\eta = \rho V_m$. After a cumbersome calculation procedure he has found the excluded volume $V_{excl}(\mathbf{a}_i \mathbf{a}_j)$ that depends on orientation of the rods. Then, using (6.63) and several approximations concerning averaging, the free energy and the equation of state for hard spherocylinders have been found.

At that stage a uniaxial, orientational order parameter S is introduced in terms of the mean square projections $a_{x,y,z}$ of molecular vector **a**:

$$\langle a_x^2 \rangle = \langle a_y^2 \rangle = (1/3)(1 - S); \langle a_z^2 \rangle = (1/3)(1 + 2S)$$

The order parameter depends on the packing fraction and temperature. With increasing density or decreasing temperature the isotropic phase is substituted by the nematic phase. The equation for S is found in terms of η and γ.

$$S(2S^3 - S - 1 + 3/8\eta\gamma) \tag{6.64}$$

where factor γ includes the molecular anisotropy x:

$$\gamma = \frac{2(x-1)^2}{\pi(3x-1)}$$

Equation 6.64 has three solutions, S = 0 for the isotropic phase and

$$S_{\pm} = \frac{1}{4} \pm \frac{3}{4} \left(1 - \frac{1}{3\eta\gamma} \right)^{1/2} \tag{6.65}$$

for the nematic phase. The solution with sign (+) is stable. A critical condition $3\eta\gamma = 1$ corresponds to the transition from the isotropic to the nematic phase. It is solely determined by molecular parameter γ (or x) and packing density dependent on temperature. The qualitative temperature dependencies are shown

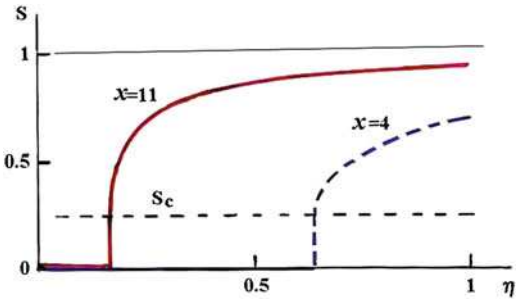

Fig. 6.20 Onsager model: order parameter dependence on molecular packing factor η for two values of spherocylinder anisotropy ratio $x = 4$ (*dash curve*) and $x = 11$ (*solid curve*). $S_c = 0.25$ is the amplitude of the order parameter jump at the phase transition

in Fig. 6.20. For very elongated molecules ($x = 11$) the phase transition appears at much smaller packing density (compare with the curve for $x = 4$). There is no solution for short spherocylinders anisotropy $x < 3.08$. The order parameter changes discontinuously with a jump ($S_c = 0.25$) at the isotropic-nematic transition point (first order transition).

6.7.3 Mean Field Approach for the Nematic Phase

6.7.3.1 Interaction Potential and Partition Function

The potential of pair molecular interaction (6.59) is too difficult to deal with. Much simpler is to use symmetry of the phase of interest (nematic) and construct the form of potential energy of a molecule as if it interacts not with other surrounding molecules but with an average molecular field. This is an essence of the *mean field approximation* [1]. The single molecule potential represents the mean field of all intermolecular forces acting on a given molecule. In this case, we neglect the intermolecular short-range order. Such theories have appeared to be very powerful in the physics of solid state, for instance in magnetism, ferroelectricity and superconductivity.

Consider the nematic phase. It has cylindrical symmetry and the orientational order parameter $<P_2> = {}^1/_2\langle 3\cos^2\vartheta - 1\rangle$ with angle ϑ between a molecular long axis and the symmetry axis (the director **n**). The tasks of the molecular theory is to use the symmetry arguments and properties of molecules and (a) to find the temperature dependence of $<P_2>(T)$, (b) to calculate thermodynamic and other properties in terms of $<P_2>$, (c) to discuss the phase transition from finite $<P_2>$ to zero (N–Iso transition), and (d) to discuss the role of the higher order parameters $<P_4>$, $<P_6>$ etc.

The key problem is a form of the interaction potential. The two-pair potential (6.59) is too complicated and we would like to substitute it by a single molecule potential:

1. At first, the pair potential W_{12} is expanded into two series of spherical harmonics Y_1 and Y_2. Then the dependence of $W_{12}(r_{12})$ on the intermolecular distance

becomes separated from the dependence of W_{12} on molecular orientation. Then only the difference between two angles $\phi_1 - \phi_2$ is considered essential, but not each of the two angles. In addition, due to head-to-tail symmetry, only even terms are left in the expansion. Fortunately, the coefficients of the expansion decrease rapidly with the number of a harmonic.

2. Then, a new, polar coordinate frame was introduced based on the director **n** as a polar axis. To obtain the single molecular potential W_1 as a function of the first molecule orientation with respect to **n**, one has to take three successive averages of W_{12}: (a) over all orientations of intermolecular vector **r**, (b) over all orientations of molecule 2, and (c) over all intermolecular separations |r|.

Finally, the single-molecule potential has been found in the form of expansion over Legendre polynomials:

$$W_1(\cos\vartheta) = v\langle P_2\rangle P_2(\cos\vartheta) + \mu\langle P_4\rangle P_4(\cos\vartheta) + 6^{th} + \cdots \text{terms} \tag{6.66}$$

In the simplest case, we use only the first term:

$$W_1(\cos\vartheta) = -v\langle P_2\rangle P_2(\cos\vartheta). \tag{6.67}$$

Its form is shown in Fig. 6.21. $P_2(\cos\vartheta)$ is a universal *function* varying from $-1/2$ to $+1$ and $v <P_2>$ is a *number* determining the depth of the potential well. Note that parameter v depends on properties of a molecule (shape, electronic structure, etc.).

The even function $f(\cos\vartheta)$ given by the Gibbs distribution describes the probability for a molecule to be at an angle ϑ with respect to the director **n**:

$$f(\cos\vartheta) = Z^{-1}\exp\left(-\frac{W(\cos\vartheta)}{k_B T}\right)$$

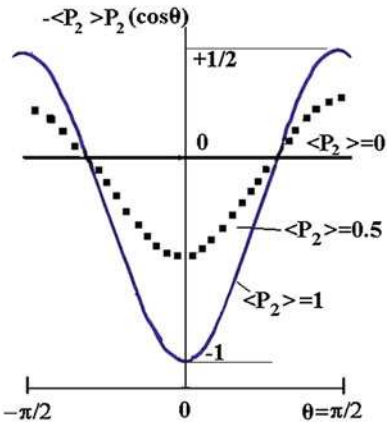

Fig. 6.21 The dimensionless form of the nematic mean field potential as a function of molecular angle ϑ at three different values of $<P_2> = 0$ (*horizontal line*), 0.5 (*dot curve*) and 1 (*solid curve*)

The probability to find the molecule at any angle ϑ within 0 and π equals unity. From here we find the *single-molecule partition function*

$$Z = \int_0^1 \exp\left(-\frac{W(\cos\vartheta)}{k_B T}\right) d\cos\vartheta \tag{6.68}$$

The configuration integral includes only one degree of freedom (ϑ-orientation). Other degrees are ignored because we are only interested in an excess of free energy of the nematic phase with respect to the isotropic phase. At this stage Eq. 6.67 is not yet helpful for the calculation of thermodynamic parameters since it includes unknown value of $<P_2>$ in the mean-field potential W. However, using the *theorem of average*, $<P_2>$ may be written in the form valid for any weight function $f(\cos\vartheta)$:

$$\langle P_2\rangle = \int_0^1 P_2(\cos\vartheta) f(\cos\vartheta) d\cos\vartheta \tag{6.69}$$

Now we combine (6.67), (6.68) and (6.69) and obtain the self-consistent equation for the determination of the orientational order parameter $<P_2>$ as a function of k_BT/v:

$$\langle P_2\rangle = \frac{\int_0^1 P_2(\cos\vartheta) \exp\left[\frac{v\langle P_2\rangle P_2(\cos\vartheta)}{k_B T}\right] d\cos\vartheta}{\int_0^1 \exp\left[\frac{v\langle P_2\rangle P_2(\cos\vartheta)}{k_B T}\right] d\cos\vartheta} \tag{6.70}$$

The equation is complicated but we can vary k_BT/v and, for each given value, calculate numerically $<P_2>$ by integrating over ϑ. The result is universal and shown in Fig. 6.22.

Now we can summarize some preliminary, but important conclusions:

1. The two branches correspond to two ordered phases, one is nematic with positive $<P_2> > 0$, and the other phase (not observed yet) with negative $<P_2>$. The positive branch corresponds to the results of the Landau approach, see Fig. 6.5.
2. At T_c the order parameter $<P_2>$ increases by a jump from 0 to 0.429, therefore, the N–Iso transition is first order transition.
3. The N–Iso transition takes place at $k_BT_c/v = 0.222$. From this value and a typical experimental transition temperature $T_c = 400\text{K}$ we can estimate the height of the potential barrier $v = k_BT_c/0.222 = (1.38 \cdot 10^{-16} \cdot 400)/0.222 = 2.5 \cdot 10^{-13}\text{erg} = 0.15\text{eV}$. However, the molecular nature of parameter v is not clear yet and we cannot calculate the partition function and free energy. It should be discussed using specific molecular models.

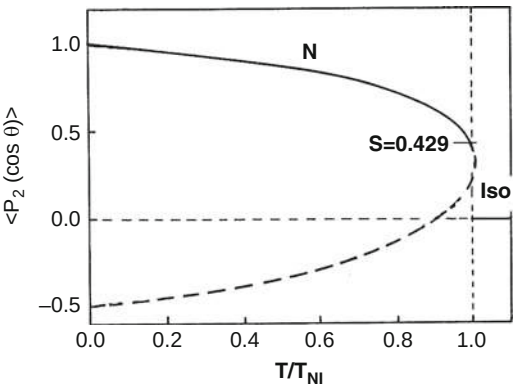

Fig. 6.22 Mean field model of the nematic phase: temperature dependence of the order parameter. The two branches correspond to stable nematic phase with positive order parameter (*solid line*), and unstable phase with negative order parameter (*dash line*). Order parameter discontinuity at $S = 0.429$ indicates the first order N–I transition

6.7.3.2 Maier–Saupe Theory

The results of the simplest mean field approach are very impressing. However, some experimental observations, e.g., different temperature dependencies of the order parameter for different substances, a discontinuity of density at the N–Iso transition have not been explained. The main disadvantages of the simplest theory are (a) lack of the density (or volume) dependence of $<P_2>$ showing a jump at the transition; (b) an oversimplified form of the potential well; and (c) pure phenomenological nature of the depth of the potential well v.

If we come back to Eq. 6.66, then with additional terms (fourth, sixth, etc.) we can find a new partition function and calculate more precisely the thermodynamic parameters (free energy, entropy, etc.). Indeed, the results of such calculations fit much better the experimental data on $<P_2>$ and $<P_4>$ for different materials [22]. But what about the nature of parameters v and μ? For the first and most important of them, the answer is given by the Maier–Saupe theory [21].

All physics of the intermolecular interactions is included in potential W_1. Its general dependence on density (or volume V) is not known. However, a dependence of the form $W_1 \propto -A/V^2$ is consistent with the typical r^{-6}-dependence of intermolecular attractive energy (for instance, in the Lennard-Jones potential r^{12-6}). The V^{-2} form is a result of averaging over three-dimensional volume. This law is valid for London dispersion forces related to "induced dipole – induced dipole" interactions. Since elongated molecules have anisotropic (tensorial) polarizabilities, the idea of Maier and Saupe was to describe their interaction in terms of *anisotropic dispersion forces*. On account of the molecular volume term, $V_m = V/N$, the mean field potential (6.67) takes the form:

$$W_1 = -A/V_m^2 \langle P_2 \rangle P_2(\cos \vartheta) \tag{6.71}$$

This form allows for separation of effects related to packing of molecules (V_m), their ordering ($<P_2>$) and molecular spectral properties (A). The coefficient A was

considered as a constant to be found from experiment. It can also be estimated from the theory of dispersion forces. The classical formula for the interaction energy between the oscillating dipole of one atom with another, neutral atom (or a spherical molecule):

$$w(r) = -\frac{2\hbar\omega\alpha_0^2}{r^6} = -\frac{C}{r^6} \tag{6.72}$$

Here ω is frequency of oscillating electron in the first atom, α_0 is polarizability of the second atom, r is distance between the two. This result is in qualitative agreement with a quantum–mechanical theory developed by London. For calculation of parameter A in (6.71) Maier and Saupe used this basic formula, but in addition they took the anisotropy of molecular polarizability $\Delta\alpha$ into account. It is $\Delta\alpha$ that determines the stability of the nematic phase.

The Maier–Saupe theory is very successful in explanation of density jump at T_{NI}. It can also explain some correlation between the thermal stability of the nematic phase and the anisotropy of molecular polarizability $\Delta\alpha$. Up to now it is very popular among chemists although there are some substances (e.g., cyclohexylcyclohexanes), which have a very stable nematic phase but $\Delta\alpha \approx 0$. Its main drawback is a neglect of short-range (steric) effects taken into account, for instance, by hard-rod Onsager-type models. On the contrary, the hard-rod models do not take long-range interaction into account. The two approaches taken together result in more realistic predictions. However, in general, due to complexity of the problem, all such models present only semi-quantitative picture [23].

References

1. Wojtowicz, P.: Introduction to molecular theory of nematic liquid crystals. In: Priestley, E.B., Wojtowicz, P., Sheng, P. (eds.) Introduction to Liquid Crystals, Chapter 3, pp. 31–43. Plenum Press, New York (1975)
2. Landau, L.D., Lifshitz, E.M.: Statistical Physics, 5th edn. Nauka, Moscow (2001). (in Russian) [see also "Statistical Physics", v. 1, 3rd ed., Pergamon, Oxford, 1980]
3. de Gennes, P.G.: Short-range order effects in the isotropic phase of nematics and cholesterics. Mol. Cryst. Liq. Cryst. **12**, 193–214 (1971)
4. De Gennes, P.G., Prost, J.: The Physics of Liquid Crystals, 2nd edn. Clarendon, Oxford (1993)
5. Vertogen, G., de Jeu, V.H.: Thermotropic Liquid Crystals. Fundamentals. Springer-Verlag, Berlin (1987)
6. Priestley, E.B., Sheng, P.: Landau-de Gennes theory of liquid crystal phase transitions. In: Priestley, E.B., Wojtowicz, P., Sheng, P. (eds.) Introduction to Liquid Crystals, Chapter 10, pp. 143–201. Plenum Press, New York (1975)
7. Khoo, I.C., Wu, S.-T.: Optics and Nonlinear Optics of Liquid Crystals. Word Scientific, Singapore (1993). Chapt. 1
8. Anisimov, M.A.: Critical phenomena in liquid crystals. Mol. Cryst. Liq. Cryst. **(special topics) 162a**, 1–96 (1988)
9. Helfrich, W.: Effect of electric fields on the temperature of phase transitions of liquid crystals. Phys. Rev. Lett. **24**, 201–203 (1970)

10. McMillan, W.L.: X-ray scattering from liquid crystals: 1. Cholesteryl nonanoate and myristate. Phys. Rev. A **6**, 936–947 (1972)
11. Thoen, J.: Thermal methods. In: Demus, D., Goodby, J., Gray, G.W., Spiess, H.-W., Vill, V. (eds.) Physical Properties of Liquid Crystals, pp. 208–232. Wiley-VCH, Weinheim (1999)
12. Pikin, S.A.: Structural Transformations in Liquid Crystals. Gordon & Breach, New York (1981)
13. Cladis, P.E.: Re-entrant phase transitions in liquid crystals. In: Demus, D., Goodby, J., Gray, G.W., Spiess, H.-W., Vill, V. (eds.) Physical Properties of Liquid Crystals, pp. 289–303. Wiley-VCH, Weinheim (1999)
14. Kasting, G.B., Lushington, K.T., Garland, C.W.: Critical heat capacity near the nematic-smectic A transition in octyloxycyanobiphenyl in the range 1-2000 bar. Phys. Rev. B **22**, 321–331 (1980)
15. de Gennes, P.G.: Sur la transition smectique A – smectique C. C. R. Acad. Sci. **274**, 758–760 (1972)
16. Barois, Ph: Phase transition theories. In: Demus, D., Goodby, J., Gray, G.W., Spiess, H.-W., Vill, V. (eds.) Physical Properties of Liquid Crystals, pp. 179–207. Wiley-VCH, Weinheim (1999)
17. Dunmur, D.A., Palffy-Muhoray, P.: Effect of electric and magnetic fields on orientational disorder in liquid crystals. J. Phys. Chem. **92**, 1406–1419 (1988)
18. Blinov, L.M., Ozaki, M., Yoshino, K.: Flexoelectric polarization in nematic liquid crystals measured by a field on-off pyroelectric technique. JETP Lett. **69**, 236–242 (1999)
19. Osipov, M.A.: Molecular theories of liquid crystals. In: Demus, D., Goodby, J., Gray, G.W., Spiess, H.-W., Vill, V. (eds.) Physical Properties of Liquid Crystals, pp. 40–71. Wiley-VCH, Weinheim (1999)
20. Onsager, L.: The effects of shape on the interaction of colloidal particles. Ann. N.Y. Acad. Sci. **51**, 627–659 (1949)
21. Maier, W., Saupe, A.: Eine einfache molekular-statistische Theorie der nematischen kristall-linflüssigen Phase. Teil I, Z. Naturforschg. **14a**, 882–889 (1959). Teil II, Z. Naturforschg. 15a, 287-292 (1960)
22. Wojtowicz, P.: Generalized mean field theory of nematic liquid crystals. In: Priestley, E.B., Wojtowicz, P., Sheng, P. (eds.) Introduction to Liquid Crystals, Chapter 4, pp. 45–81. Plenum Press, New York (1975)
23. Averyanov, E.M.: Steric Effects of Substituents and Mesomorphism. Siberian Department of Russian Academy of Science Publishers, Novosibirsk (2004) (in Russian)

Part II
Physical Properties

Chapter 7
Magnetic, Electric and Transport Properties

Some properties of liquid crystals depend mainly on properties of individual molecules and approximately obey the additivity law. Thus, molecular properties can be translated, of course with some precautions, onto the properties of a mesophase on account of the symmetry of the latter. Quantitatively, the relevant phenomenological characteristics such as magnetic and dielectric susceptibilities, electric and thermal conductivity, diffusion coefficients, etc. can be calculated by averaging molecular parameters with the corresponding *single-particle* distribution function. Other properties of liquid crystals such as elasticity or viscosity dramatically depend on intermolecular interactions and the corresponding *many-particle* distribution functions have to be taken into account. Here we shall start with a discussion of the properties of the first sort. Moreover, we shall limit ourselves mostly to the phases of highest symmetry (uniaxial nematics and smectic A) whose properties are represented by second-rank tensors, discussed in Section 2.5. Throughout this chapter, the director field is considered to be non-distorted, $\mathbf{n}(\mathbf{r}) =$ constant.

7.1 Magnetic Phenomena

7.1.1 Magnetic Anisotropy

In the Gauss system, magnetic induction $\mathbf{B} = \mu\mathbf{H}$ where $\mathbf{H}$ is magnetic field strength. The magnetic permeability $\mu = 1 + 4\pi\chi$ where χ is dimensionless magnetic susceptibility. Except ferromagnetic materials, $4\pi\chi << 1$. e.g., for p-azoxyanisole $<\chi> = -5 \times 10^{-7}$, therefore $\mu \approx 1$.

By definition, a magnetic moment of substance per unit volume is magnetization $\mathbf{M} = \chi\mathbf{H}$. For an anisotropic material, the magnetization vector components are $M_\alpha = \chi_{\alpha\beta}H_\beta$ and the contribution to the free energy density of the mesophase from the magnetic field is given by [1]:

L.M. Blinov, *Structure and Properties of Liquid Crystals*,
DOI 10.1007/978-90-481-8829-1_7,

$$g_{magn} = -\int_0^{H_\alpha} H_\alpha dM_\alpha = -\int_0^{H_\beta} H_\alpha \chi_{\alpha\beta} dH_\beta = -\frac{1}{2}\chi_{\alpha\beta} H_\alpha H_\beta$$

For *uniaxial phases* $\chi_{\alpha\beta} = \chi_\perp \delta_{\alpha\beta} + \chi_a n_\alpha n_\beta$, therefore

$$g_{magn} = -\frac{1}{2}\left[\chi_\perp H^2 + \chi_a (n_\alpha H_\alpha)^2\right] \tag{7.1}$$

or in the vector form

$$g_{magn} = -\frac{1}{2}\left[\chi_\perp H^2 + \chi_a (\mathbf{Hn})^2\right] \tag{7.2}$$

Here $\mathbf{Hn} = H\cos\alpha$ where α is the angle between the director and magnetic field. The second term determines an orientation of the director in the field: for $\chi_a > 0$ the director **n** tends to align parallel to the field; for $\chi_a < 0$ it tends to be perpendicular to **H**. A sign of χ_a is determined by competition of diamagnetic and paramagnetic terms.

7.1.2 Diamagnetism

Diamagnetism is caused by an additional electric current induced by a magnetic field in a molecule. The diamagnetic contribution to $\chi_{\alpha\beta}$ is negative, independent of permanent magnetic moments of molecules and is present in all molecular materials [2].

7.1.2.1 Single Electron

Consider a classical model of a current *i* caused by a rotating electron in the absence of a magnetic field, see Fig. 7.1. When an external magnetic field is applied, an additional, namely, induced current appears due to the Lorentz force acting on a moving electron. The induced current component $\delta\boldsymbol{i}$ tries to screen the external field

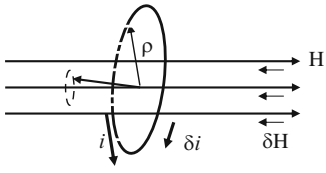

Fig. 7.1 Diamagnetism of a single electron: electron rotation creates current ***i*** in the magnetic field absence and the additional current $\boldsymbol{\delta i}$ is induced by the magnetic field **H**

$\mathbf{H} = H_z$ (the Lenz law). In fact, $\delta \boldsymbol{i}$ comes about due to precession of electronic orbits with angular frequency according to the Larmor theorem:

$$\omega_L = \frac{eH}{2m_e c} \tag{7.3}$$

where $e/2m_e c = \gamma$ [$\mathrm{cm}^{1/2}\mathrm{g}^{-1/2}$] is gyromagnetic ratio, e and m_e are the charge and mass of an electron, c is light velocity. Such a precession of an electron is equivalent to a diamagnetic current:

$$\delta I = -e\frac{\omega_L}{2\pi} = -\frac{e^2 H}{4\pi m_e c^2}$$

Generally, the magnetic moment of a frame with current is $\mathbf{p}_\mathrm{m} = \delta \boldsymbol{I} \times \mathbf{s}$ where $\mathbf{s}$ is vector of the current loop area ($s = \pi <\rho^2>$). Therefore, the induced moment and the susceptibility of single electron moving along the contour perpendicular to $\mathbf{H}$ are given by

$$p_m^e = -\frac{e^2 H}{4m_e c^2}\left\langle \rho^2 \right\rangle, \left\langle \rho^2 \right\rangle = \left\langle x^2 \right\rangle + \left\langle y^2 \right\rangle, \gamma_{magn}^e = \frac{p_m^e}{H} = -\frac{e^2}{4m_e c^2}\left\langle \rho^2 \right\rangle$$

Here, there is no component of the current along z and $<\rho^2>$ is mean square of the distance between the electron and the field axis z. For a circular electron orbit of radius r, we have $<\rho^2> = <r^2>$. In a more general case of electron orbits tilted with respect to **H,** the mean square distance between the electron and the nucleus is $<r^2> = <x^2> + <y^2> + <z^2>$.

7.1.2.2 Molecules

For *spherically symmetric* molecules with electron orbit radius r, $<x^2> = <y^2> = <z^2>$ and $<\rho^2> = (2/3) <r^2>$. Then the magnetic susceptibility of a spherical molecule having Z electrons is

$$\gamma_{magn} = -\frac{Ze^2}{6m_e c^2}\left\langle r^2 \right\rangle \tag{7.4}$$

For *cylindrical molecules* with length L and diameter D, γ_magn is a tensor with principal components

$$\gamma_{magn}^{\parallel} = -\frac{Ze^2}{2m_e c^2}\left\langle D^2 \right\rangle \text{ and } \gamma_{magn}^{\perp} = -\frac{Ze^2}{4m_e c^2}\left\langle L^2 + D^2 \right\rangle \tag{7.5}$$

Hence, the diamagnetic anisotropy of a uniaxial liquid crystal phase with orientational order S and n_v molecules per unit volume can be found:

$$\chi_a^{dia} = -\frac{n_v Z e^2}{2 m_e c^2} S\left[\left\langle D^2 \right\rangle - \tfrac{1}{2}\left\langle L^2 + D^2 \right\rangle\right] \tag{7.6}$$

According to (7.6), anisotropy χ_a^{dia} may be either positive or negative depending on the molecular geometry. A very important structural unit of liquid crystal molecules, a benzene ring has negative diamagnetic susceptibility with the maximum absolute value along its normal due to the maximum $\delta \boldsymbol{i}$ current along the ring perimeter. For this reason, elongated molecules containing two or three benzene rings have *negative susceptibility* with minimum absolute value along their longitudinal axes that is along the director. For such molecules $<L^2 + D^2>/2$ exceeds $<D^2>$ in (7.6) and calamitic uniaxial phases formed by several benzene fragments have *positive diamagnetic anisotropy* χ_a^{dia}. along longitudinal axes. Typically, in nematic and SmA phases shown in Fig. 7.2, the diamagnetic susceptibilities are almost independent of temperature.

In some rare cases, e.g., when a calamitic phase consists of solely aliphatic compounds or cyclohexane derivatives, its anisotropy χ_a^{dia} is very small and can even vanish. As to the discotic mesophases, they have, as a rule, negative diamagnetic anisotropy $\chi_a^{dia} = \chi_{||}^{dia} - \chi_{\perp}^{dia} < 0$ due to a considerably larger value of the susceptibility component perpendicular to the director (for discotics $\chi_{\perp}^{dia}$ would be closer to zero line than $\chi_{||}^{dia}$ in the plot similar to Fig. 7.2).

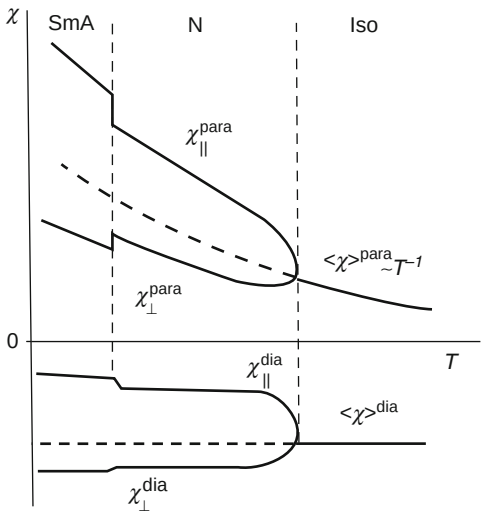

Fig. 7.2 Qualitative temperature dependences of the principal components of diamagnetic (negative) and paramagnetic (positive) susceptibility for calamitic compounds in the isotropic, nematic and SmA phases

7.1.3 Paramagnetism and Ferromagnetism

7.1.3.1 Paramagnetism

The susceptibility of paramagnetic substances is mostly determined by permanent magnetic moments $\mathbf{p}_\mathrm{m}$, which are aligned by the magnetic field. The field induced magnetization is determined by the total projection of n_v molecular magnetic moments in a unit volume onto the field axis

$$M_{para} = n_v p_m \langle \cos\theta \rangle$$

where θ is an angle between individual dipole $\mathbf{p}_\mathrm{m}$ and field $\mathbf{H}$. In the isotropic phase such a distribution is given by the Langevin formula [3]:

$$\langle \cos\theta \rangle = \frac{\int\limits_{\Omega} \exp(-\mathbf{p}_m \mathbf{H}/k_B T)\cos\theta d\Omega}{\int\limits_{\Omega} \exp(-\mathbf{p}_m \mathbf{H}/k_B T) d\Omega} = L(p_m H/k_B T)$$
$$= \mathrm{cth}(p_m H/k_B T) - (k_B T/p_m H) \tag{7.7}$$

Here $x = p_\mathrm{m} H/k_\mathrm{B} T$ and $L(x) = \mathrm{cth}(x) - (1/x)$ is the Langevin function. For $x << 1$, $\mathrm{cth}(x) \approx 1/x + x/3$ -... and $<\cos\theta> \approx x/3$. Therefore, for a weak magnetic field, $p_\mathrm{m} H << k_\mathrm{B} T$, the magnetization is:

$$M_{para} = \frac{n_v p_m^2 H}{3 k_B T} \tag{7.8}$$

What is a nature of p_m in a molecular system? The molecular paramagnetism is mostly originated from the unpaired electron spins. The magnetic moment for a *free electron spin* is

$$p_m^e = -g\ \mu_B \sqrt{s(s+1)}$$

where s is spin quantum number, $\mu_B = {e\hbar}/{2m_e c}$ is Bohr magneton for electron and $g = 2.0023$ is Lande factor. According to (7.8), the spin magnetization and susceptibility follow the Curie law, $\chi \propto T^{-1}$:

$$M_s = n_v \frac{g^2 \mu_B^2 s(s+1)}{3 k_B T} H \text{ and } \chi_s = n_v \frac{g^2 \mu_B^2 s(s+1)}{3 k_B T} \tag{7.9}$$

Typical temperature dependencies of paramagnetic susceptibility χ^{para} are pictured in the same Fig. 7.2 in comparison with χ^{dia}. The order of magnitude of both χ^{dia} and χ^{para} is 10^{-7}. As far as the nature of the *paramagnetic anisotropy* is

concerned, it should be noted that in molecules the unpaired spins are almost free to rotate. Therefore, their alignment, e.g. by an external magnetic field, needs not be accompanied by alignment of molecular skeletons. In reality, however, there is some coupling between spins and molecular axes. The g-factor becomes a tensor due to interaction of the unpaired electron spins with the angular momentum of molecular orbitals (the so-called spin-orbit interaction). This is a reason for the anisotropy of paramagnetic susceptibility of liquid crystals. *For a uniaxial phase*, the paramagnetic anisotropy is given by

$$\chi_a^{para} = \frac{n_v \mu_B^2 s(s+1)}{k_B T} S(g_\perp^2 - g_{||}^2) \tag{7.10}$$

where S is the orientational order parameter and $(g_\perp^2 - g_{||}^2)$ is anisotropy coming from the g^2 value. The latter determines a sign of paramagnetic anisotropy χ_a^{para}. Like diamagnetic anisotropy χ_a^{dia}, χ_a^{para}may be either positive or negative depending on orientation of the g-tensor with respect to the director. For instance, $\chi_a^{para} < 0$ for elongated calamitic complexes of copper II with d^9 electron configuration. Different compounds of this sort can be oriented either perpendicular or parallel to the magnetic field depending on competition with the positive diamagnetic contribution. On the other hand, vanadyl (VO) d^1 complexes manifest both $\chi_a^{para} > 0$ and $\chi_a^{dia} > 0$ and are always oriented along the magnetic field.

7.1.3.2 Ferromagnetism

The ferromagnetism of organic compounds has been observed only recently. These are compounds containing Fe, Ni, Co atoms and the ferromagnetic state is found at very low temperatures (few K), at which a liquid crystal state is not observed yet. However, ferromagnetic materials can be prepared from colloidal suspensions of small solid ferromagnetic particles, even nanoparticles (e.g., magnetite Fe_2O_3 or ferrite Fe_3O_4) in liquids. Such solutions are called *ferrofluids*. Since these particles have permanent magnetic moments $\mathbf{p}_m$, under a magnetic field they can be oriented. In ferrofluids they form chains, which are arranged in ordered patterns.

The same particles can be introduced into liquid crystals, e.g. into nematics [4]. If the guest particles are elongated they may be aligned by a liquid crystal (host) even in the absence of the magnetic field, e.g. by a surface treatment (without macroscopic magnetization). The external magnetic field will orient the magnetic moments of particles, which, in turn, orient the liquid crystal matrix. Such nematic suspensions of particles show very interesting magneto-optical properties (a guest-host effect in ferrofluids).

7.2 Dielectric Properties

7.2.1 Permittivity of Isotropic Liquids

Liquid crystals are anisotropic fluids and the discussion of their dielectric properties is based on the fundamental ideas obtained for isotropic liquids. We recall the relevant results.

7.2.1.1 Dielectric Spectrum

The Maxwell equations for the electromagnetic field in conductive materials such as organic liquids read:

$$\mathrm{curl}\mathbf{E} = -\frac{\mu}{c}\cdot\frac{\partial \mathbf{H}}{\partial t} \quad \text{and} \quad \mathrm{curl}\mathbf{H} = +\frac{\varepsilon}{c}\cdot\frac{\partial \mathbf{E}}{\partial t} + \frac{4\pi}{c}\sigma\mathbf{E} \tag{7.11}$$

Here **E** and **H** are vectors of electric and magnetic field strength, $\varepsilon(\omega)$ and $\mu(\omega)$ are frequency dependent dielectric and magnetic permittivities, σ is permanent conductivity. In the second equation, the two terms describe the displacement and Ohmic current, respectively.

In the limit of $\omega = 2\pi f \to \infty$ no dynamic process in medium can follow the field; the electric polarization $\mathbf{P} = \chi^{\mathrm{E}}\mathbf{E}$ vanishes (i.e. dielectric susceptibility $\chi^{\mathrm{E}} \to 0$) and the displacement vector $\mathbf{D} = (1 + 4\pi\chi^{\mathrm{E}})\mathbf{E}$ coincides with **E**, that is $\varepsilon = 1 + 4\pi\chi^{\mathrm{E}} \to 1$. With decreasing frequency, fast electronic processes have enough time to follow the field and, at optical frequencies, $\varepsilon = n^2$ (n is refraction index) shows peculiarities related to electronic absorption bands (normal and abnormal dispersion). With further decreasing frequency other processes such as molecular rotations and vibrations begin to contribute to the electric polarization and $\varepsilon = n^2$ again increases, see Fig. 7.3.

On the other hand, since for the sine-form field $\partial E/\partial t \propto \omega E$ the role of permanent conductivity σ decreases with increasing frequency, in the high frequency limit $\omega >> 1/\tau_{\mathrm{M}} = 4\pi\sigma/\varepsilon$ a material can be considered as non-conductive. The time $\tau_{\mathrm{M}} = \varepsilon/4\pi\sigma$ is called Maxwell dielectric relaxation time. Later we shall meet it again under another name "space charge relaxation time".

7.2.1.2 Local Field, Clausius-Mossotti and Onsager Equations

The vectors of electric displacement **D** and polarization **P** are also coupled by the additional Maxwell equation:

$$\varepsilon = \frac{\mathbf{D}}{\mathbf{E}} = \frac{\mathbf{E} + 4\pi\mathbf{P}}{\mathbf{E}} = 1 + 4\pi\mathbf{P}/\mathbf{E} \quad \text{and} \quad \chi^{E} = \frac{\mathbf{P}}{\mathbf{E}} = \frac{\varepsilon - 1}{4\pi} \tag{7.12}$$

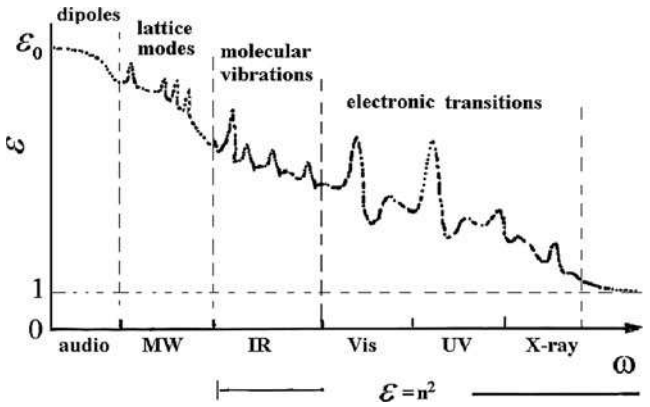

Fig. 7.3 Qualitative frequency spectrum of the dielectric permittivity

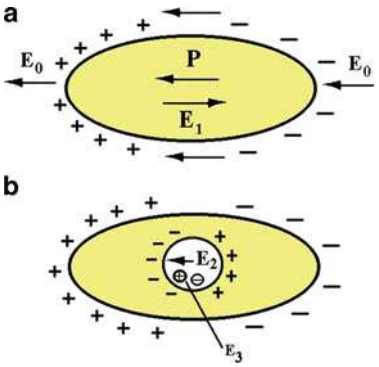

Fig. 7.4 Lorentz model for the local field. Polarization of an ellipsoidal form dielectric sample and appearance of depolarizing field $\mathbf{E}_1$ (**a**), Lorentz cavity field $\mathbf{E}_2$ and the field of individual molecules within the cavity $\mathbf{E}_3$ (**b**)

How can we relate these *macroscopic quantities* to the *microscopic parameters* of molecules such as polarizability or a dipole moment? With some precautions, the polarization of an isotropic liquid may be found as a sum of the field induced molecular dipole moments whose number coincides with the amount of dipolar molecules in the unit volume $n_v = \rho N_A/M$ (ρ is mass density, N_A is Avogadro number, M is molecular mass):

$$\mathbf{P} = \sum_{n_v} \mathbf{p}_e = n_v \gamma \mathbf{E}_{loc} \tag{7.13}$$

Here γ is average molecular polarizability (generally, γ_{ij} is a tensor), $\mathbf{E}_{loc}$ is a local electric field acting on each molecule and $\mathbf{p}_e$ is a field induced electric dipole in a molecule. So, if we find $\mathbf{E}_{loc}$ we could calculate $\mathbf{P}$ and then the value of ε, using Eq. 7.12, and known macroscopic field $\mathbf{E}$ in the sample, see Fig. 7.4a.

The local field can be found, e.g., from some models, particularly the *Lorentz model* [3]. For its discussion we select a single molecule and surround it by a fictitious spherical cavity shown in Fig. 7.4b. Then $\mathbf{E}_{\text{loc}}$ is a sum of four fields:

$$\mathbf{E}_{\text{loc}} = \mathbf{E}_0 + \mathbf{E}_1 + \mathbf{E}_2 + \mathbf{E}_3 \tag{7.14}$$

Here, $\mathbf{E}_0$ is an external field created by charges located outside of the sample;
$\mathbf{E}_1 = -k\mathbf{P}$ is a depolarizing field from the charges formed at the external surfaces (upper sketch);
$\mathbf{E}_2$ is the Lorentz field coming from the charges at the inner surfaces of the cavity; and
$\mathbf{E}_3$ is the field from all molecules inside the cavity except that one we have selected.

The depolarization field is opposite to the external field and factor k is generally a tensor dependent on the shape of the sample. For samples in the form of the ellipsoid, oriented with one of its axes along the field, depolarizing factors become scalars k_i dependent on the ratios of ellipsoid axes. For instance, for a spherical sample $k = 4\pi/3$, for a thin plate with the field perpendicular to its surface, $k = 4\pi$.

From Fig. 7.4a follows that the macroscopic field in the sample $\mathbf{E} = \mathbf{E}_0 + \mathbf{E}_1 = \mathbf{E}_0 - k\mathbf{P}$. When polarization $\mathbf{P}$ is very high, the macroscopic field is considerably reduced. The Lorentz field $\mathbf{E_2}$ is parallel to the external field and, for a spherical cavity, is equal exactly to $+4\pi\mathbf{P}/3$. Therefore, when both the sample and the cavity are spherical,

$$\mathbf{E}_{\text{loc}} = \mathbf{E}_0 - 4\,\pi\mathbf{P}/3 + 4\,\pi\mathbf{P}/3 + \mathbf{E}_3 = \mathbf{E}_0 + \mathbf{E}_3.$$

Due to high symmetry, for all isotropic liquids (and all cubic crystals), field $\mathbf{E}_3$ acting on the selected molecule from its neighbors is exactly compensated. Thus, *for a spherical isotropic sample* the local field is equal to the external field:

$$\mathbf{E}_{\text{loc}} = \mathbf{E}_0$$

For an isotropic sample of an *arbitrary form*, the depolarization field $\mathbf{E}_1$ is form-dependent and $\mathbf{E}_{\text{loc}}$ should be written as

$$\mathbf{E}_{\text{loc}} = \mathbf{E}_0 + \mathbf{E}_1 + 4\,\pi\mathbf{P}/3 = \mathbf{E} + 4\,\pi\mathbf{P}/3 \tag{7.15}$$

It should be noted that, if a sample is connected directly to the electric voltage source (fixed potential difference across electrodes), there is no depolarization charges on the external surfaces of the sample. In this case, $\mathbf{E}_1 = 0$ and the local field acting on a molecule in the cavity is given by

$$\mathbf{E}_{\text{loc}} = \mathbf{E}_0 + 4\,\pi\mathbf{P}/3 = (2\mathbf{E}_0 + \mathbf{D})/3 = \mathbf{E}_0(\,\varepsilon + 2)/3. \tag{7.16}$$

With the local field found, we obtain a relation between the macroscopic field in the sample **E**, polarization **P** and the local field acting on a particular molecule, see Eqs. 7.13 and 7.15:

$$\mathbf{P} = n_v \gamma \mathbf{E}_{loc} = n_v \gamma (\mathbf{E} + \frac{4\pi}{3}\mathbf{P}). \tag{7.17}$$

Solving the latter for **P** we find the microscopic value of electric susceptibility:

$$\chi^E = \frac{\mathbf{P}}{\mathbf{E}} = \frac{n_v \gamma}{1 - \frac{4\pi}{3} n_v \gamma} \tag{7.18}$$

This equation has a singularity at $\gamma \to 3/4\pi n_v$: for large enough molecular polarizability the macroscopic susceptibility and, consequently, polarization become infinite. This phenomenon is called polarization catastrophe. In a more subtle approach, the polarization remains finite and exists even in the absence of the external field (*spontaneous polarization* $\mathbf{P}_s$). The spontaneous polarization is responsible for pyro- and ferroelectricity in solid and liquid crystals, however it is not observed in the isotropic liquid (see Chapters 4 and 13).

Finally, combining (7.18) with definition $\varepsilon = 1 + 4\pi\chi^E$ we arrive at the *Clausius-Mossotti equation* (N_{Av} is Avogadro number):

$$\frac{\varepsilon - 1}{\varepsilon + 2} = \frac{4\pi n_v}{3}\gamma = \frac{4\pi\rho N_{Av}}{3M}\gamma \tag{7.19}$$

This equation relates the macroscopic value of dielectric permittivity ε to microscopic parameters of medium. For instance, from measurements of capacitance of a liquid by a dielectric bridge one finds dielectric constant and then calculates molecular polarizability γ.

Molecular polarizability includes electronic γ_{el} and orientational γ_{or} parts. The first of them is frequency and temperature independent and, at optical frequencies, *the Lorenz-Lorentz formula* is valid:

$$\frac{n^2 - 1}{n^2 + 2} = \frac{4\pi\rho N_A}{3M}\gamma_{el} \tag{7.20}$$

The second, dipolar part of polarizability is related to the orientational susceptibility of permanent dipole moments p_e and can be found from the Langevin equation (7.7) as in the case of paramagnetism (only p_m is substituted by p_e):

$$\mathbf{P}_{dip} = \frac{n_v p_e^2 \mathbf{E}}{3k_B T} \tag{7.21}$$

We see that the dipolar susceptibility obeys the Curie law:

$$\gamma_{or} = \frac{p_e^2}{3k_B T} \tag{7.22}$$

Using the last three equations one can find molecular parameters γ_{el} and p_e from independent measurements of density, refraction index and temperature dependence of dielectric permittivity at a low frequency.

The Clausius-Mossotti equation is based on the simplest (Lorentz) form of the local field. In reality, the induced dipole in the selected molecule also creates an additional, *reaction field* that modifies the cavity field. On account of these factors Onsager has obtained the following equation for dielectric permittivity

$$\varepsilon - 1 = \frac{4\pi\rho N_A}{M} Fh\left(\gamma_{el} + F\frac{p_e^2}{3k_BT}\right) \tag{7.23}$$

where the cavity h and reaction field F factors are:

$$h = 3\varepsilon/2\varepsilon + 1, \quad F = \frac{(2\varepsilon+1)\left(n^2+2\right)}{3(2\varepsilon+n^2)}$$

The Onsager equation agrees quite well with experimental data on liquids and liquid crystals and will be generalized for calculations of the tensor ε_{ij} in nematic liquid crystals.

7.2.2 Static Dielectric Anisotropy of Nematics and Smectics

7.2.2.1 Maier-Meier Theory

In experiment on nematic liquid crystals, both positive and negative anisotropy ε_a is observed, the sign depending on chemical structure. The magnitude of ε_a is often proportional to orientational order parameter S. In the isotropic phase the anisotropy disappears. Typical temperature dependencies of $\varepsilon_{\|}$ and $\varepsilon_{\perp}$ are shown in Fig. 7.5. These observations can be accounted for by the *Maier-Meier theory* [5]. The latter is based on the following seven assumptions:

1. the molecules are spherical with radius a, but their polarizability is tensorial, $\gamma_a = \gamma_{||} - \gamma_{\perp} > 0$
2. the point molecular dipole p_e makes an angle β with the axis of maximum molecular polarizability
3. a nematic liquid crystal has a center of symmetry and characterized by orientational quadrupolar order parameter S
4. the analysis is performed within the framework of Onsager's theory of polar liquids, and the mean dielectric susceptibility $<\varepsilon>$ was taken for the calculation of the Onsager factors h and F, introduced above
5. the dielectric anisotropy is assumed to be small, $\varepsilon_a = |\varepsilon_{||} - \varepsilon_{\perp}| << <\varepsilon>$
6. when calculating the reaction field the tensor nature of electronic polarizability γ_{ij} was neglected and the average value $<\gamma> = (\gamma_{||} + 2\gamma_{\perp})/3$ was used
7. the interaction between molecules is disregarded

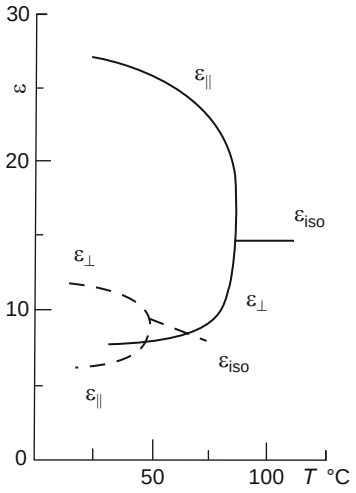

Fig. 7.5 Typical temperature behavior of principal dielectric permittivities for two nematic liquid crystals, one with positive (*solid lines*) and the other with negative (*dash lines*) dielectric anisotropy

With these restrictions, Maier and Meier have calculated two principal components of dielectric permittivity and dielectric anisotropy:

$$\varepsilon_{\|} - 1 = \frac{4\pi\rho N_A}{M} Fh\left\{\langle\gamma\rangle + {}^2\!/_3\gamma_a S + F\frac{p_e^2}{3k_BT}[1 - \frac{1}{2}(1 - 3\cos^2\beta)S]\right\}$$

$$\varepsilon_{\perp} - 1 = \frac{4\pi\rho N_A}{M} Fh\left\{\langle\gamma\rangle - {}^1\!/_3\gamma_a S + F\frac{p_e^2}{3k_BT}[1 + (1 - 3\cos^2\beta)S]\right\}$$

$$\varepsilon_a = \varepsilon_{\|} - \varepsilon_{\perp} = \frac{4\pi\rho N_A}{M} Fh\left[\gamma_a - F\frac{p_e^2}{2k_BT}[(1 - 3\cos^2\beta)\right]S \qquad (7.24)$$

The equations have the Onsager form. In the isotropic phase, $S = 0$, $\varepsilon_{\|} = \varepsilon_{\perp} = \varepsilon_{\text{iso}}$ and equation (7.24) reduces to (7.23). The theory results in the following conclusions:

1. The average molar dielectric susceptibility of the nematic phase $\langle\varepsilon - 1\rangle M/4\pi\rho$ is independent of parameter S and equal to the molar susceptibility of the isotropic phase $<\varepsilon>_N = \varepsilon_{iso}$. Thus, the theory cannot explain a discontinuity of $<\varepsilon>$ at the Iso-N transition shown in Fig. 7.6 by a dashed line.
2. For a specific value of the angle ($\beta \approx 55^{\circ}$) between the dipole moment and the axis of maximum polarizability of the molecule, given by $1 - 3\cos^2\beta = 0$, the contribution from the orientational polarization to ε_a becomes zero [6]. For somewhat larger value of the angle β determined by condition

$$\gamma_a - F\frac{p_2^2}{2k_BT}[(1 - 3\cos^2\beta) = 0,$$

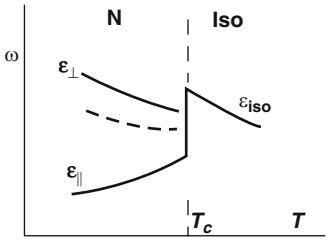

Fig. 7.6 Discontinuity of the average dielectric permittivity at the nematic – isotropic phase transition for a nematic with negative dielectric anisotropy

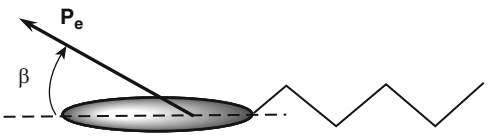

Fig. 7.7 Location of a molecular dipole moment with respect to the longitudinal molecular axis of a molecule. Note that in the Maier-Meier theory the dipole moment forms angle β with the axis of maximum polarizability of a spherical molecule

the dielectric anisotropy completely vanishes. This agrees with experiment: the anisotropy changes sign with a change of the angle β the dipole forms with the long molecular axis, Fig. 7.7, which, indeed, is the axis of maximum polarizability for rod-like molecules. For nematics with molecules having large *longitudinal* dipole moment, the anisotropy is positive, $\varepsilon_a > 0$. For molecules with large *transverse* dipole moment $\varepsilon_a < 0$.

3. The temperature dependence of average dielectric permittivity $<\varepsilon>$ enters the equations both explicitly (term k_BT) and through S (the additional contribution from h and F is weak) while ε_a is directly proportional to S. The latter corresponds to the uniaxial symmetry of the dielectric permittivity with a tensor form of Eq. 3.16.

$$\hat{\varepsilon} = \langle\varepsilon\rangle + \varepsilon_a[n_\alpha n_\beta - (1/3)\delta_{\alpha\beta}] = \varepsilon_\perp\delta_{\alpha\beta} + \varepsilon_a(n_\alpha n_\beta) \tag{7.25a}$$

Note that

$$\langle\varepsilon\rangle = (\varepsilon_{||} + 2\varepsilon_\perp)/3 = \varepsilon_\perp + \varepsilon_{||}/3 - \varepsilon_\perp/3 = \varepsilon_\perp + \varepsilon_a/3$$

Using Eq. 7.25a one can calculate the value of the dielectric permittivity $\varepsilon(\vartheta,\varphi)$ of a uniaxial phase at any angle with respect to the director. Let the director is rigidly fixed by a strong magnetic field along the z-axis, $\mathbf{n} = (0, 0, 1)$. Then the single term $n_z n_z = 1$ is finite and Eq. 7.25a has a familiar form:

$$\hat{\varepsilon} = \begin{pmatrix} \varepsilon_\perp & 0 & 0 \\ 0 & \varepsilon_\perp & 0 \\ 0 & 0 & \varepsilon_\perp \end{pmatrix} + \begin{pmatrix} 0 & 0 & 0 \\ 0 & 0 & 0 \\ 0 & 0 & \varepsilon_a \end{pmatrix} = \begin{pmatrix} \varepsilon_\perp & 0 & 0 \\ 0 & \varepsilon_\perp & 0 \\ 0 & 0 & \varepsilon_{||} \end{pmatrix}$$

Assume that a very weak electric field is applied at angles ϑ and φ, respectively, to the z and x axes: $\mathbf{E} = (E\cos\vartheta\cos\varphi, E\cos\vartheta\sin\varphi, E\cos\vartheta)$. Then we can calculate the components of the displacement vector:

$$\begin{matrix} D_x \\ D_y \\ D_x \end{matrix} = \begin{pmatrix} \varepsilon_\perp & 0 & 0 \\ 0 & \varepsilon_\perp & 0 \\ 0 & 0 & \varepsilon_{||} \end{pmatrix} \cdot \begin{matrix} E\sin\vartheta\cos\varphi \\ E\sin\vartheta\sin\varphi \\ E\cos\vartheta \end{matrix} = \begin{matrix} E\varepsilon_\perp \sin\theta\cos\varphi \\ E\varepsilon_\perp \sin\theta\sin\varphi \\ E\varepsilon_{||}\cos\vartheta \end{matrix}$$

and find $D^2 = D_x^2 + D_y^2 + D_z^2 = \varepsilon^2 E^2 = E^2(\varepsilon_\perp^2 \sin^2\vartheta + \varepsilon_{||}^2 \cos^2\vartheta)$. Hence, the dielectric permittivity $\varepsilon(\vartheta,\varphi)$ is found to be independent of the azymuthal angle φ as expected for a uniaxial material:

$$\varepsilon(\vartheta) = (\varepsilon_\perp^2 \sin^2\vartheta + \varepsilon_{||}^2 \cos^2\vartheta)^{1/2}. \tag{7.25b}$$

It is evident that the same formula (7.25b) is valid for any properties of uniaxial phases described by a tensor of the type (7.25a) such as magnetic susceptibility, thermal and electric conductivity, diffusion and others.

The displacement can be written in the vector form as $\mathbf{D} = \varepsilon_\perp \mathbf{E} + \varepsilon_\mathbf{a}(\mathbf{nE})\mathbf{n}$ and the electric field contribution to the free energy density is given by:

$$g_{el} = -\frac{\mathbf{ED}}{8\pi} = -\frac{\varepsilon_\perp}{8\pi}E^2 - \frac{\varepsilon_a}{8\pi}(\mathbf{nE})^2 \tag{7.26}$$

to be compared with the magnetic counterpart (7.2).

7.2.2.2 SmA Phase and the Role of the Positional Order

Generally speaking, the Maier-Meier theory [5] explains all essential static dielectric properties of the nematic phase [7, 8]. The transition from the nematic to the smectic A phase is accompanied by an increase in the orientational order S. When molecules do not possess very large longitudinal dipoles, the set of Maier-Meier equations is still valid even in the SmA phase. Typically, the dielectric anisotropy increases proportionally to S, as shown in Fig. 7.8. In this case, a periodicity of the smectic A density is not important. However, in many compounds, on approaching the SmA phase, the dielectric anisotropy decreases despite increasing orientational order [9]. It can even change sign either in the nematic or in the smectic phase as shown in Fig. 7.9.

This effect originates from the anisotropic dipole-dipole correlations not accounted for by the Maier-Meier theory operating with a single particle distribution function. When, with decreasing temperature, the smectic density wave $\rho(z)$ develops (even at the short-range scale) the longitudinal dipole moments prefer to form antiparallel pairs and the "apparent" molecular dipole moment becomes smaller. This would reduce positive ε_a. Theoretically, dipole-dipole correlations may be taken into account by introducing the so-called *Kirkwood factors*.

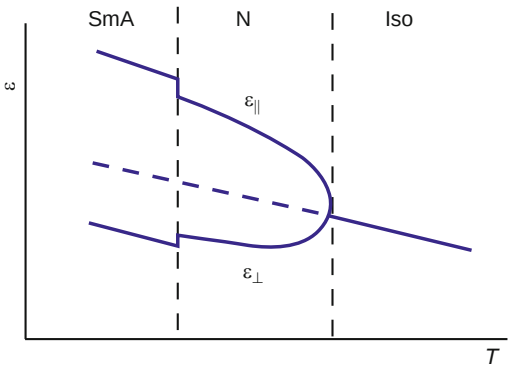

Fig. 7.8 Typical temperature behavior of the principal dielectric permittivities in the nematic and SmA phases

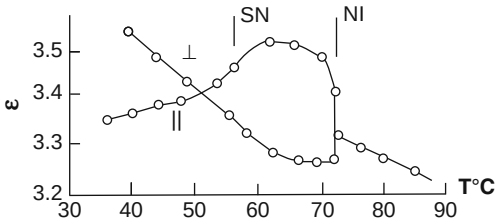

Fig. 7.9 Anomalous temperature behavior of the principal dielectric permittivities within the nematic and SmA phase in di-*n*-heptyl-azoxybenzene (Adapted from [7])

7.2.2.3 Smectic C Case

The point group symmetry of the SmC phase (C_{2h}) is different from that of the N and SmA phases ($D_{\infty h}$). Now the tensor of dielectric permittivity is represented by a biaxial ellipsoid with three different components ε_1, ε_2 and ε_3 as shown in Fig. 7.10. The component ε_3 is parallel to the director ($\varepsilon_3 = \varepsilon_{\parallel}$), ε_2 is parallel to the symmetry axis C_2, and ε_1 is perpendicular to the both ε_3 and ε_2. The biaxiality, however, is weak $\varepsilon_1 \approx \varepsilon_2$.

7.2.3 Dipole Dynamics of an Isotropic Liquid

To set the stage for discussion of frequency dispersion of liquid crystal permittivity we turn back to the isotropic liquids. First we shall find a characteristic relaxation time for molecular dipoles and then discuss real and imaginary components of the permittivity [10].

7.2.3.1 Dipole Relaxation

An applied electric field reduces the symmetry of an isotropic liquid from K_h to $C_{\infty v}$ and creates anisotropy in the angular distribution function of dipoles; the

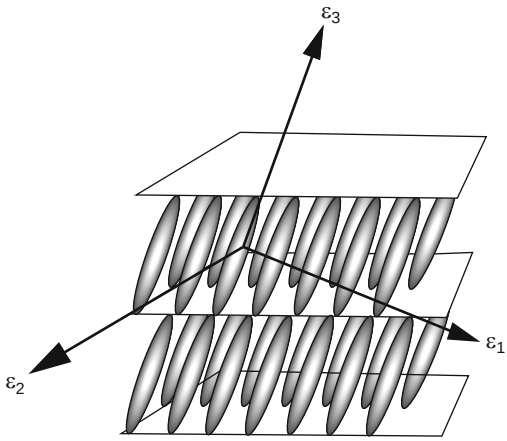

Fig. 7.10 Three principal permittivities of the biaxial SmC phase; ε_3 is parallel to the director, ε_2 is parallel to symmetry axis C_2, and ε_1 is perpendicular to the both ε_3 and ε_2

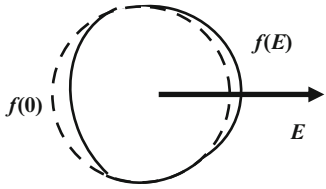

Fig. 7.11 Angular distribution of molecular dipoles in the isotropic phase without external field (*dash curve sphere*) and with the electric field applied (*solid line*)

distribution function becomes elongated in the field direction, Fig. 7.11. If we forget for a while about the role of temperature then the angular motion of the dipoles in the electric field **E** can be described by equation of motion:

$$I\frac{d^2\vartheta}{dt^2}+\xi\frac{d\vartheta}{dt}=-p_eE\sin\vartheta \tag{7.27}$$

Here, ϑ is the decreasing with time angle between the dipole and **E** and ξ is a friction coefficient for a change of ϑ angle [g.cm^{2}s^{-1}]. Usually, due to high viscosity of a liquid, the inertial term may be neglected. Then

$$\frac{d\vartheta}{dt}=-\frac{p_eE\sin\vartheta}{\xi}$$

Since the contribution of the considered dipole to the field-induced polarization is given by its projection on the E-axis, $p_e{}^E=p_e\cos\vartheta$, the rate of the increase of this projection is

$$\frac{dp_e^E}{dt}=-p_e\sin\vartheta\frac{d\vartheta}{dt}=p_e^2\frac{E\sin^2\vartheta}{\xi}$$

From here the kinetic equation may be written for the electric field induced polarization in the system of n_v dipoles in a unit volume with initial arbitrary orientation:

$$\frac{dP_E}{dt} = \frac{n_v p_e^2 E \langle \sin^2 \vartheta \rangle}{\xi} - \frac{P_E}{\tau_D} \tag{7.28}$$

The second term on the right of (7.28) i.e. the dipole disorienting factor describes the relaxation of dipoles due to a finite temperature. The multiplier $<\sin^2\vartheta>$ may be considered as a numerical coefficient $k \approx 2/3$, as if the distribution function is spherical even in the electric field. In fact, a more precise value was found by Debye by averaging the P_E value over ϑ with the field-induced dipole distribution function shown qualitatively in Fig. 7.11. Since the thermal motion of dipolar molecules destroys the field induced polar order, we introduce a thermal relaxation time τ_D, as the first (linear) approximation of the relaxation rate. In order to find this time, we should exclude P_E from the kinetic equation.

In the steady-state regime, $dP_E/dt = 0$, and the value of the dipole polarization is

$$P_E = \tau_D \frac{2 n_v p_e^2 E}{3\xi} \tag{7.29}$$

This value may be compared with that found from the Langevin formula, see Eq. 7.21. From the comparison, the relaxation time for molecular dipoles is found:

$$\tau_D = \frac{\xi}{2 k_B T} \tag{7.30}$$

Now, if we assume that a dipolar molecule has a *spherical form* of volume $(4/3)\pi a^3$ and rotates in continuous medium with viscosity η [units $\mathrm{g.cm^{-1}s^{-1}}$ (Poise)], then the friction force may be written as $\xi = 8\pi\eta a^3$ and $\tau_D = 4\pi\eta a^3/k_B T$. This model is very simple, however, it predicts a correct magnitude and temperature dependence of relaxation times for dipoles in an isotropic liquid.

In the dispersion region $\omega \approx \tau_D^{-1}$, molecular dipoles follow the electric field with some lag, i.e. the orientational component of polarization P has some *phase retardation* with respect to field E. Therefore, the dielectric permittivity becomes complex functions of frequency

$$\varepsilon^* = \varepsilon' + i\varepsilon'' \tag{7.31}$$

The imaginary part describes dissipation of energy due to molecular friction. It is called *dielectric losses* and equivalent to appearance of non-Ohmic electric conductivity. The frequency dependence of ε^* can be written in the form of the *Debye dispersion law* [10]

$$\varepsilon^* - \varepsilon(\infty) = \frac{\varepsilon(0) - \varepsilon(\infty)}{1 - i\omega\tau_D} \tag{7.32}$$

where $\varepsilon(0)$ and $\varepsilon(\infty)$ correspond respectively to zero frequency and to the frequencies essentially exceeding the relaxation frequency region, $\omega >> \tau_D^{-1}$ (in that range, $\varepsilon(\infty) = n^2$, n is refraction index, as shown in Fig. 7.3).

The two components of the permittivity are:

$$\varepsilon' = \varepsilon(\infty) + \frac{\varepsilon(0) - \varepsilon(\infty)}{1 + \omega^2\tau_D^2} \quad \varepsilon'' = \frac{[\varepsilon(0) - \varepsilon(\infty)]\omega\tau_D}{1 + \omega^2\tau_D^2} \tag{7.33}$$

and the corresponding spectra of ε' and ε'' are illustrated by Fig.7.12a. The ratio of the two components determines the phase angle, Fig.7.12b:

$$\tan\phi = \frac{\varepsilon''}{\varepsilon' - \varepsilon(\infty)} = \omega\tau_D \tag{7.34}$$

7.2.3.2 Debye and Cole-Cole Diagrams

Very often a rotation of a complex molecule includes a motion of different molecular dipoles and the dielectric spectrum $\varepsilon''(\omega)$ is not as simple as shown in the picture. It becomes somewhat blurred and the correspondent time τ_D cannot be found with sufficient accuracy. In order to improve the analysis, a simple procedure is used based on the Debye Eq. 7.32.

Note that $\sin\phi = \tan\phi/\sqrt{1 + \tan^2\phi}$ and $\cos\phi = 1/\sqrt{1 + \tan^2\phi}$. Then the equations (**7.33**) can be cast in the new form:

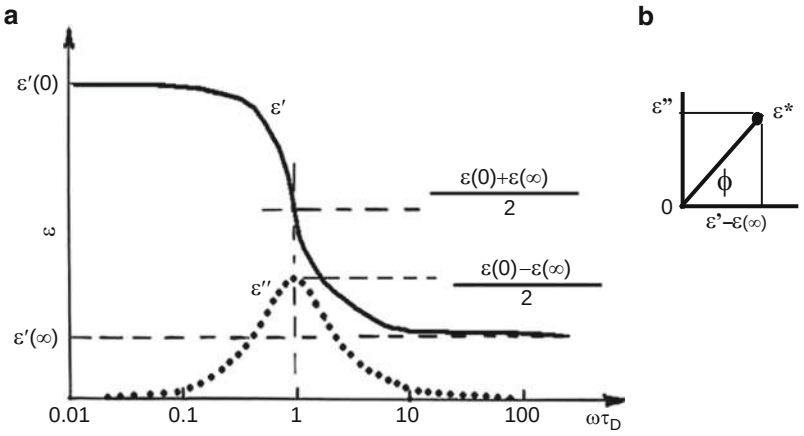

Fig. 7.12 Frequency dependence of the real (*solid line*) and imaginary (*dash curve*) parts of the dielectric permittivity of an isotropic liquid (**a**) and the definition of the phase angle ϕ (**b**)

$$\frac{\varepsilon' - \varepsilon(\infty)}{\varepsilon(0) - \varepsilon(\infty)} = \cos^2\phi = \tfrac{1}{2} + \tfrac{1}{2}\cos 2\phi \quad \frac{\varepsilon''}{\varepsilon(0) - \varepsilon(\infty)} = \sin\phi\cos\phi = \tfrac{1}{2}\sin 2\phi$$

or

$$\varepsilon' = \frac{\varepsilon(\infty) + \varepsilon(0)}{2} + \frac{\varepsilon(0) - \varepsilon(\infty)}{2}\cos 2\phi \quad \varepsilon'' = \frac{\varepsilon(0) - \varepsilon(\infty)}{2}\sin 2\phi \tag{7.35}$$

The new equations may be regarded as the parametric representation of the equation of a circle of radius R with a center at x_0, y_0: $x = x_0 + R\cos 2\phi$ and $y = y_0 + R\sin 2\phi$ with angle ϕ related to frequency by Eq. 7.34. Consequently, plotting the experimental dependence of ε'' against ε' at different frequencies ω should give us a semi-circle ($\varepsilon'' > 0$) with its center at a point $\varepsilon' = \frac{1}{2}[\varepsilon(\infty) + \varepsilon(0)]$, $\varepsilon'' = 0$ and a radius $\frac{1}{2}[\varepsilon(\infty) - \varepsilon(0)]$, as shown by the *Debye diagram*, Fig.7.13a. If, in the experiment, the points do lie on such a circle we can find the single dipole relaxation time from any particular point on the circle using Eq. 7.34.

In a number of cases, the experimental points also form a part of a circle with a center that, however, lies below the ε'' axis, see *Cole-Cole diagram* in Fig. 7.13b. Then the frequency dependence of the dielectric permittivity can be described by the empirical equation

$$\varepsilon^*(\omega) - \varepsilon(\infty) = \frac{\varepsilon(0) - \varepsilon(\infty)}{1 + (i\omega\tau_D)^{1-h}}, \tag{7.36}$$

where the angle $\pi h/2$ defines the position of the center. The relaxation time can be found from the relationship $\omega\tau_D = (v/u)^{1-h}$ after location of the circle center. For $h = 0$, $v/u = \tan\phi$ and the Cole-Cole equation reduces to the Debye equation. The parameter h tends to increase with the number of degrees of freedom in the molecule (for example, through the rotation of the dipole moments of various molecular groups) or with increasing temperature.

In a mixture of different dipolar molecules with strongly different relaxation times, several maxima of ε'' will be observed and several characteristic semi-circles can be drawn. As a rule, the relaxation times do not differ so much and the

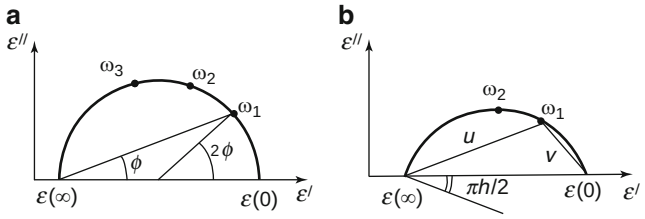

Fig. 7.13 The Debye (**a**) and Cole-Cole (**b**) diagrams for calculations of characteristic dipole relaxation times

corresponding maxima in the dielectric spectra are not resolved. In this case, the Debye and Cole-Cole diagrams are very useful for calculations of different τ_D.

7.2.4 *Frequency Dispersion of $\varepsilon_{||}$ and $\varepsilon_{\perp}$ in Nematics*

7.2.4.1 Relaxation Modes

Basically the experimental observations of dielectric relaxation in nematics are consistent with Fig.7.14. There are three characteristic modes: the rotation of molecules about short molecular axes (the lowest frequency $\omega_1 \approx 10^6$ Hz); the precession of long molecular axes about the director **n** (the middle frequency $\omega_2 \approx 10^8$ Hz); and the fast rotation of molecules about long molecular axes (the highest frequency $\omega_3 \approx 10^9$ Hz) [6]. The corresponding dielectric spectra are shown in Fig.7.15. The most striking feature is strong retardation of the permittivity component parallel to the director, i.e. $\varepsilon_{||}$-relaxation, $\tau_{||} = \omega_1^{-1} = j_{||}\tau_{iso}$ (retardation factor $j_{||} = 10$–100) and some acceleration of $\varepsilon_{\perp}$-relaxation $\tau_{\perp} = \omega_3^{-1} = j_{\perp}\tau_{iso}$ (acceleration factor $j_{\perp} \approx 0.5$) with respect to the ε-relaxation in the isotropic

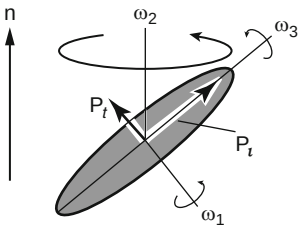

Fig. 7.14 Three characteristic relaxation modes for rotation of molecules in nematic liquid crystals: slow rotation about short molecular axes with frequency ω_1; the precession of long molecular axes about the director **n** with middle frequency ω_2; and fast rotation of molecules about long molecular axes with frequency ω_3

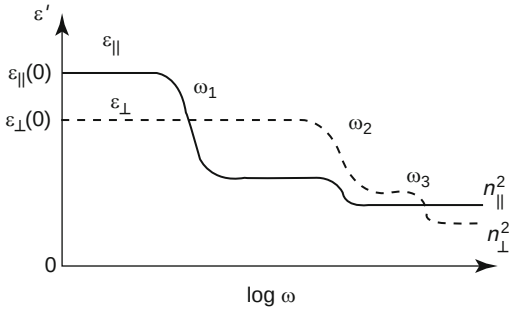

Fig. 7.15 Spectra of principal dielectric permittivities for nematic phase. Characteristic dispersion ranges correspond to relaxation modes with frequencies ω_1, ω_2 and ω_3 illustrated by Fig. 7.14

phase. Moreover, a growth of $\tau_{\|}(T)$ with decreasing temperature (i.e., with increasing S) is much faster than that predicted by the Arrhenius law for viscosity.

Evidently, the nematic order strongly influences the relaxation of $\varepsilon_{\|}$ and $\varepsilon_{\perp}$. An individual rod-like molecule feels the nematic potential curve $W(\cos\vartheta)$, (see Fig. 6.21), whose form is an inverse of the molecular distribution function in Fig. 3.15. In fact, each molecule moves in the potential well of the depth about 0.15 eV with a minimum centered at $\vartheta \approx 0$ or π. This prevents deviation of the molecule through large angles from the director **n**. A primitive, but useful mechanical model for this situation is a rod-like molecule in a rubber tube, Fig. 7.16. For ϑ deviation from 0 to $\pi/2$ the molecule has to overcome a high barrier W_N and its angular velocity and frequency decreases dramatically down to ω_1 (case *a*). The retardation factor depends on the height of the barrier. Theoretically this can approximately be written as

$$j_{\|} = \frac{k_B T}{W_N} \exp \frac{W_N}{k_B T}$$

This expression gives a correct order of magnitude for the retardation factor (for $W_{\mathrm{N}} = 0.16\mathrm{eV}$ and $T = 400\mathrm{K}$, $k_{\mathrm{B}}T/W_{\mathrm{N}} \approx 0.21$ and the retardation factor is about 25). Note that the retardation is controlled not by a molecular dipole moment, but rather by a molecular shape.

For rotation of the same molecule about its long axis (frequency ω_3) there is no barrier (case *b*). To some extent, such rotation in the nematic phase is even easier than in the isotropic phase (friction is less). Therefore, instead of retardation we have acceleration, $j_{\perp} < 1$.

When rigid molecules precess (case *c*) about the director at small ϑ angles within the flat potential minimum they are more or less free. Therefore, frequency ω_2 correspond to a quite fast molecular motion and the precession contributes to both $\varepsilon_{\|}$ and $\varepsilon_{\perp}$(case *c*). All the three dispersion regions are observed by dielectric spectroscopy techniques [11].

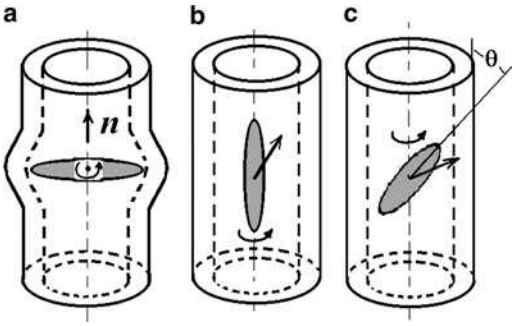

Fig. 7.16 A mechanical model that helps to understand the process of retardation or acceleration of molecular rotation in the nematic potential: slow hindered rotation of molecule at the angles $\vartheta \approx \pi/2$ (**a**), fast accelerated rotation about long molecular axes at the angles $\vartheta \approx 0$ or π (**b**) and quite fast molecular precession within small ϑ-angles (**c**)

7.2.4.2 Dual Frequency Addressing

Experiments show that with increasing molecular length $j_{||}$-factor increases dramatically. For terphenyl derivatives, frequency ω_1 can be shifted down to 1–10 kHz. The simple theory discussed above does not consider a molecular length but intuitively it is understandable in the framework of the same mechanical model. The low frequency dispersion of $\varepsilon_{||}$ is seen in Fig. 7.17 against the background of almost constant $\varepsilon_{\perp}$. Therefore there is an inversion point for the sign of dielectric anisotropy at a certain frequency f_{inv}; $\varepsilon_a > 0$ for $f < f_{\text{inv}}$ and $\varepsilon_a < 0$ for $f > f_{\text{inv}}$. This is very interesting for display applications because an external field of low frequency (say, at 1 kHz) aligns the director (that is the optical axis) along the field, while at an enhanced frequency (say, at 10 kHz) the director is aligned perpendicular to the field. Changing frequency of the field one can switch the director very fast because, in this, so-called dual-frequency addressing regime, the director always suffers a torque $\varepsilon_a E^2$ from a strong field and the switching rate is high $\tau^{-1} \propto \varepsilon_a E^2$. Since the field is never switched off, the slowest process of the director free relaxation is excluded.

7.3 Transport Properties

7.3.1 Thermal Conductivity

According to *Fourier law*, the scalar coefficient of thermal conductivity k relates the thermal flux density Q [in erg/cm^{2}s] to the gradient of temperature $\mathbf{Q} = -k\vec{\nabla}T$ [units of k: erg/cm.s.K]. The corresponding thermal diffusion coefficient [in cm^2/s] includes density of substance ρ and heat capacitance C_{p} (at constant pressure)

$$D_{th} = {}^{k}/_{\rho C_p}$$

and determines the time τ_{T} of the heat transfer over the distance L_{T} called a thermal diffusion length:

$$\tau_{th} = {}^{L_T^2}/_{2D_{th}} \tag{7.37}$$

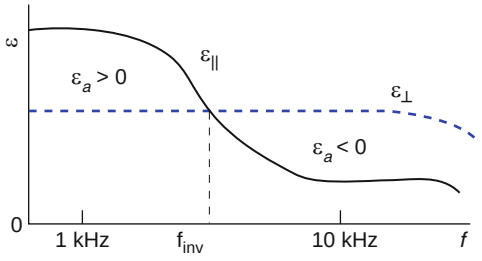

Fig. 7.17 Spectra of principal dielectric permittivity components showing the inversion of the sign of dielectric anisotropy at a particularly low frequency f_{inv}

This formula comes about from the general expression for the diffusion (random) process, like the Brownian motion, and relate average distance passed by a random-walking particle to time τ $\langle x^2 \rangle = 2D\tau$ derived by Einstein and Smoluchowski in the beginning of twentieth century. The temperature dependence of the thermal conductivity in the nematic and smectic A phase resembles that of the magnetic susceptibility [12]. A good example is *p*-octyl-*p*′-cyanobiphenyl (8CB), see Fig. 7.18. No such sharp anomalies in k at the phase transitions are observed as manifested, for instance, by the specific heat discussed in Section 6.2.4. The reason is that the thermal conductivity is mainly determined by a single-particle molecular distribution function whereas the specific heat dramatically depends on the long-range fluctuations of the order parameter.

In anisotropic phases the magnitude of the thermal flux depends on the direction of gradient ∇T:

$$Q_i = -k_{ij} \frac{\partial T}{\partial x_j}.$$

In the case of a uniaxial phase, the thermal conductivity tensor has a familiar form (7.25a): $k_{ij} = k_\perp \delta_{ij} + k_a n_i n_j$, where $k_a = k_{||} - k_\perp > 0$ for calamitic phases and $k_a < 0$ for discotic ones.

At present the coefficients $k_{||}$ and $k_\perp$ are measured by sophisticated techniques such as a.c. adiabatic calorimetry, photoacoustic and photopyroelectric methods. The latter is very sensitive and allows the measurements using small amounts of liquid crystals [13]. The idea is demonstrated by Fig. 7.19. The light beam (shown by arrows) of intensity I is modulated by a chopper according to the law of $I = I_m \cos\omega t$ and absorbed by black paint on the bottom of a quartz block. The heat flux traverses the properly aligned liquid crystal layer (LC) and reaches a crystalline pyroelectric detector. The latter generates an electric signal at frequency ω. A lock-in amplifier (LA) analyzes the amplitude and phase of the signal. The measured amplitude provides the thermal energy reached the detector; the phase

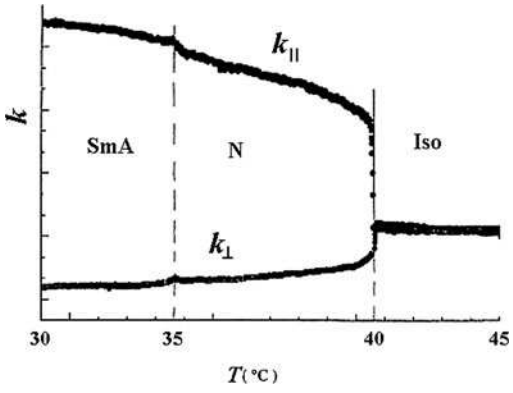

Fig. 7.18 Anisotropy of thermal conductivity of 8CB in the nematic and smectic A phases (Adapted from [12])

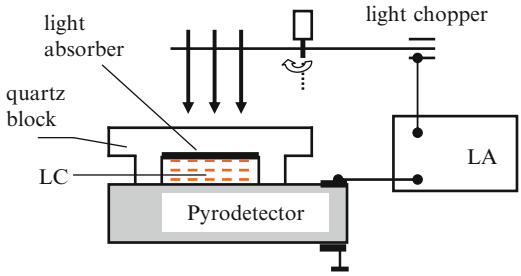

Fig. 7.19 Scheme of the set-up for measuring thermal conductivity and specific heat in liquid crystals

contains information on the time of the heat transfer τ_T related to thermal diffusion coefficient by Eq. 7.37.

7.3.2 *Diffusion*

The diffusion is a kinetic process of molecular transport due to a gradient of molecular concentration c. The coefficient of diffusion D relates the flux of particles to their concentration gradient (first *Fick law*):

$$\mathbf{J} = -D\vec{\nabla}c$$

Note that, in contrast to hydrodynamic processes, there is no mass transport during the diffusion process, the mass velocity $\mathbf{v}(x,y,z) = 0$ and the mass density is constant. For this reason, the diffusion in anisotropic media is described by a simplest second rank tensor D_{ij}:

$$J_i = -D_{ij}\frac{\partial c}{\partial x_j} \quad D_{ij} = D_\perp \delta_{ij} + D_a n_i n_j \quad D_a = D_{||} - D_\perp$$

Microscopically, the diffusion in the isotropic and the nematic phase is thermally activated. However, in this case, the Arrhenius-type process with activation energy ΔE is not related to the orientational potential $W\cos\theta$. In fact, this process is controlled by another potential barrier, namely, the barrier for translational jumps of a molecule from site to site:

$$D_i \propto A_i \exp\left(-\frac{\Delta E}{k_B T}\right)$$

Coefficient A_i, however, depends on molecular orientation function.

Recall the Stokes law, related the force (F) acting on a sphere of radius R to velocity of the sphere in a viscous liquid, $v = F/4\pi\eta R$ (η is viscosity of the liquid). Roughly, by analogy with the sphere in viscous liquid, the diffusion coefficient is

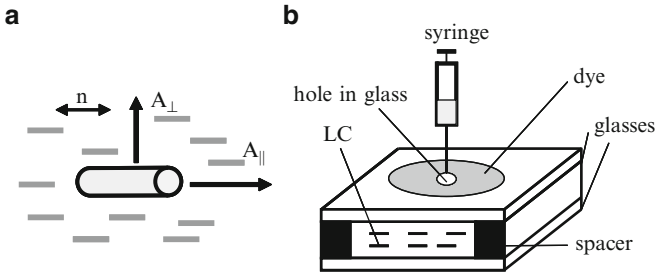

Fig. 7.20 Anisotropy of diffusion amplitudes A_i for a cylindrical molecule (**a**) and a simple technique for measurements of anisotropy of diffusion coefficients $D_{||}/D_{\perp}$ for a dye dissolved in a nematic liquid crystal

proportional to the corresponding molecular dimension. In the nematic phase a cylindrical molecule of length L and diameter D is typically aligns parallel to the director as in Fig. 7.20a. Then the diffusion is also easier (faster) along the director, $A_{||} \propto 1/\pi D > A_{\perp} \propto 1/(LD)^{1/2}$. Consequently, the ratio $D_{||}/D_{\perp} \propto L/D > 1$ and anisotropy $D_a = D_{||}\text{-}D_{\perp} > 0$. Evidently, the order parameter influences the anisotropy of diffusion; roughly $D_a \propto S$ and for $S \to 0$, $D_{||} = D_{\perp} = D_{\text{iso}}$. For nematics at room temperature, typical values of diffusion coefficient are $D_{\text{iso}} \approx 10^{-6}$ cm^2/s, $D_{||}/D_{\perp} \approx 1$–2.

For smectics the situation is different, because an additional potential barrier W_{tr} (for translations) appears for molecules penetrating smectic layers. For instance, in a smectic A, the component parallel to the layers ($D_{\perp}$) follows the same Arrhenius law with approximately same activation energy ΔE as for nematics, however, for the $D_{||}$ component, the activation energy is roughly $\Delta E + W_{tr}$ and the diffusion anisotropy becomes negative:

$$\frac{D_{||}}{D_{\perp}} \propto \frac{L}{D} \exp\left(-\frac{U_{tr}}{k_B T}\right) < 1, D_{||} - D_{\perp} < 0$$

The diffusion coefficient can be measured by several techniques. One of them is very simple, see Fig. 7.20b. A small amount of a dye solution in a liquid crystal is introduced through a hole in a top glass of a sandwich cell filled with the same liquid crystal. The latter is oriented homogeneously, therefore, using a microscope, one can observe the diffusion of dye parallel and perpendicular to the director. After some time τ_D, a dye stain acquires an elliptic form and the ratio of ellipse axes provides the ratio of diffusion coefficients $(l_{||}/l_{\perp})^2 = D_{||}/D_{\perp}$. The absolute value of, e.g., $D_{||}$ can be found from the well known solution of the diffusion equation, $\tau_D^{||} = l_{||}^2/2D_{||}$. In the same way, a small amount of a cholesteric liquid crystal can be introduced into a nematic and a spot is observed, in which the initially homogeneous texture is substituted by an inhomogeneous (e.g., fingerprint) cholesteric texture. The self-diffusion of liquid crystal molecules is studied using quasi-elastic neutron scattering or a spin-echo technique.

7.3.3 Electric Conductivity

7.3.3.1 Mobility of Ions

Now we are dealing with the current term $4\pi\boldsymbol{\sigma}\mathbf{E}/c$ in the Maxwell equation (7.11) for curl$\mathbf{H}$. The overwhelming majority of liquid crystalline phases (nematic, smectic A, C, B, etc.) may be considered as *weak electrolytes*. The charge carriers are ions, which move rather slowly in the electric field. There are some interesting publications concerning columnar discotic phases, in which high mobility of charge carriers has been reported. In principle, in such well-ordered columns of organic molecules, the electron or hole conductivity is possible. Electronic processes are faster than ionic ones and may be studied by a time-of-flight technique. However, below we shall consider only ionic processes as the most important issue for major number of mesophases [14].

The electric conductivity of a liquid is related to the drift velocity v_E of ions with a charge q_i moved by field E. The *current density* depends on concentration of ions n_v in a unit volume of the liquid:

$$j = nq_i v_E \tag{7.38}$$

Units of j: [cm^{-3} × CGSQ × cm/s] = [CGSI/cm^2] or [A/m^2] in the SI system.

In the linear regime, $v_E = \mu E$ where coefficient μ is called ion *mobility*. Hence, the *conductivity* is

$$\sigma = {}^{j}/_{E} = q_i \mu n \tag{7.39}$$

The mobility of ions and their diffusion coefficient are coupled by the *Einstein relationship*:

$$\mu = {}^{q_i}/_{k_B T} D \tag{7.40}$$

and both of them depend on viscosity of a liquid. Note that the energy $k_\mathrm{B}T$ at room temperature is about 0.025 eV and the factor $k_\mathrm{B}T/q$ has dimension of voltage. For ions with charge $q_i = e$ (charge of an electron) and typical diffusion coefficient of organic liquid $D \approx 5 \times 10^{-7}$ cm^2/s, the ion mobility $\mu \approx 6 \times 10^{-3}$ cm^2/statV.s (or 2×10^{-9} m^2/V·s in the SI system).

In a liquid crystal, the anisotropy of diffusion results in an anisotropy of mobility and, consequently, conductivity. The corresponding tensor for a uniaxial phase has a standard form:

$$\sigma_{ij} = \sigma_\perp \delta_{ij} + \sigma_a n_i n_j$$

Like in the case of diffusion, the *anisotropy of conductivity* $\sigma_a = \sigma_{||} - \sigma_\perp$ can be positive (e.g., in conventional nematics) or negative (in smectic A, discotic

mesophases). In typical nematics at room temperature, $\sigma_a \approx 1.2$–1.6 depending on the type of ions and their concentration. Generally, σ_a is proportional to the orientational order parameter, as for other transport phenomena under discussion.

7.3.3.2 Ion Concentration

Where do ions emerge from? Their sources can be different:

1. a residual concentration of ionic impurities can remain after the synthesis of a substance
2. a liquid crystal material can deliberately be doped with some compounds
3. ions can be created by an external electric field either in the bulk (due to the field ionization of neutral molecules) or at the electrodes. The latter is more probable: electrons or holes are injected from an electrode and almost immediately (within 10^{-5} to 10^{-8} s) trapped by neutral molecules of a liquid crystal forming negative or positive ions. Before their recombination the ions participate in the electric current

Consider a doping process. Let an organic salt AB of volume concentration c [cm^{-3}] is introduced into an isotropic solvent. The salt will dissociate to yield anions A^- and cations B^+ with a subsequent recombination, according to the reaction $AB \Leftrightarrow A^- + B^+$. Then the mass action law reads:

$$K_D c(1-\alpha) = K_R(\alpha c)^2$$

Here the rate of the ion dissociation is on the left-hand side (α is the degree of ionization), and the rate of their bimolecular recombination is on the right-hand side ($\alpha c = n_v{}^+ = n_v{}^-$ is a volume concentration of ions), K_D and K_R are corresponding dissociation and recombination constants. The temperature dependent *ionization coefficient* can be written as follows:

$$K = \frac{K_D}{K_R} = \frac{\alpha^2 c}{1-\alpha} \quad \text{or} \quad c = \frac{K(1-\alpha)}{\alpha^2} \tag{7.41}$$

and the degree of ionization is given by

$$\alpha = \frac{-K + K(1 + 4c/K)^{1/2}}{2c} \tag{7.42}$$

Consider three particular cases:

1. For very small concentration of a dopant $c \to 0$ and the first term of the square root expansion $[1 + (2c/K)]$ results in $\alpha \to 1$. The recombination is absent and the concentration of ions is $n_v{}^+ = n_v{}^- = c$
2. For higher concentration of salt, the situation depends on the ionization coefficient. If K is large (strong electrolytes) then again $4c/K << 1$, $\alpha \to 1$ and $n^+ = n^- = c$

3. If, however, K is small (weak electrolyte), $4c/K >> 1$ the numerator of Eq. 7.42 is approximately equal to $-K + (4cK)^{1/2}$, the degree of ionization $\alpha = -K/2 + (K/c)^{1/2}$ and

$$n_v^+ = n_v^- = c\alpha = \sqrt{Kc} - K/2 \tag{7.43}$$

Figure 7.21 illustrates a dependence of the ion concentration on concentration of a salt. It is well seen how the linear dependence becomes sub-linear. A typical value of K is on the order of 10^{19} cm^{-3}.

7.3.3.3 Current-Voltage Curve for Thin Cells

When investigating electro-optical effects, usually we have to deal with the layer thickness of a liquid crystals in the range of 1–50 μm and with the electric field strengths of 10^4 to 10^5 V/cm (≈30–300 statV/cm in the Gauss system). In such instances the field induced drift of charge carriers to electrodes cannot be neglected. However, in many cases, we may still neglect electro-chemical processes at the electrodes.

Assume the simplest ionization-recombination model with field independent K_D and K_R coefficients in a weak or intermediate electric field. The strong field limit will be discussed separately. In the case of $\alpha << 1$, the volume ion concentration $n_v^+ = n_v^- = n_v$ (cm^{-3}) is governed by equation

$$\frac{dn_v}{dt} = K_D c - K_R n_v^2 - \frac{E(\mu_+ + \mu_-)}{d} n_v, \tag{7.44}$$

where d is the gap between the electrodes, μ^+ and μ^- are mobilities of the positive and negative ions, and c is the concentration of a dopant. The third term on the right-hand side describes the process of ion drift to the electrodes. It has a typical form of $-n_v/\tau$ [cm^{-3}s^{-1}].

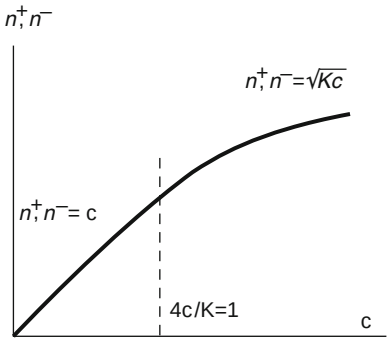

Fig. 7.21 Qualitative dependence of either positive or negative ion concentration on concentration c of a salt

In the steady-state regime, the same equation can be written in the form

$$\frac{dn_v}{dt} = \frac{c}{\tau_D} - \frac{n_v}{\tau_R} - \frac{2n_v}{\tau_T} = 0 \tag{7.45}$$

where $\tau_D = 1/K_D$, $\tau_R = 1/K_R n_v$, $\tau_T = 2d/(\mu^+ + \mu^-)E$ are characteristic times for ionization of molecules, recombination of ions and ion transit to electrodes. Consider again three particular cases.

In the *low field regime* (region 1), τ_T is large, the third term may be neglected. Then from (7.45) we have the previous result $n_v^2 = (K_D/K_R)c = Kc$ and conductivity (7.39) is field independent:

$$\sigma_1 = q(\mu^+ + \mu^-)\sqrt{Kc} \tag{7.46}$$

This corresponds to region 1 of the current-voltage curve in Fig. 7.22.

For *intermediate fields* (region 2), the drift term is important but the recombination rate may be neglected, because the field rapidly removes the generated ions. Now the ion concentration is given by

$$n_v = \frac{\tau_T}{2\tau_D} c = \frac{dK_D c}{(\mu^+ + \mu^-)E}$$

and the apparent conductivity is field dependent

$$\sigma_2 = \frac{qdK_D c}{E} \tag{7.47}$$

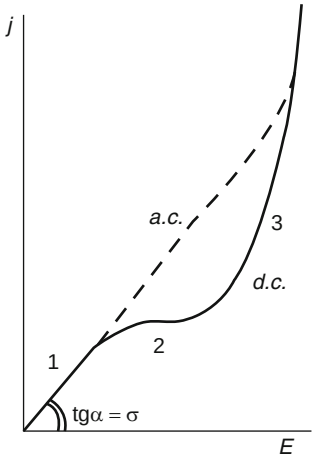

Fig. 7.22 Current-voltage curve for a thin layer of a weak electrolyte between plane electrodes. Solid curve corresponds to a direct current (d.c.) in weak (1), intermediate (2) and strong (3) field regimes. Dash branch is a part of the same curve for an alternating (a.c.) field

Therefore, with increasing field, the current density saturates at the value

$$j = \sigma_2 E = qdK_D c$$

This regime is designated as region 2 in the same figure. The order of magnitude of the ion transit time is $\tau_T = d^2/\mu U \approx 2.5\text{ms}$ ($d = 10\ \mu\text{m}$, $U = 10\ \text{V}$, $\mu = 4.10^{-9}$ m^2/Vs).

For the a.c. current at angular frequency $\omega > 1/\tau_T$, the drift term may be neglected from the beginning. Then, according to Eq. 7.45, the ohmic regime with constant K_D and K_R is valid not only for weak but for intermediate fields as well. In Fig. 7.22, it is pictured by the dash line.

In a strong field, coefficient K_D becomes a function of E due to the field induced ionization of molecules. Then we cross again the recombination term in (7.45) and get

$$K_D(E)c - \frac{E(\mu_+ + \mu_-)}{d} n_v = 0 \quad \text{or} \quad n_v(E) = \frac{dK_D(E)c}{(\mu^+ + \mu^-)E}$$

and the current acquires the form

$$j = qE(\mu^+ + \mu^-)n_v(E) = qcdK_D(E).$$

It depends on the field only implicitly through dissociation constant K_D.

Further, the zero-field dissociation constant is described by the equation

$$K_D(E = 0) = K_D^0 \exp\left(-\frac{W}{k_B T}\right)$$

where W is the electrostatic binding energy of the ion pair. Now, if we assume that the field reduces the energy barrier by $\Delta W \approx \text{const} E^{1/2}$ (exactly as in the Schottky model for the barrier at the metal-insulator contact), then K_D would depend exponentially on the square root of the field strength. Then the current would also exponentially depend on $\sqrt{E}$ and proportional to the cell thickness for a given field strength:

$$j = const \cdot K_D^0 \exp\left(\frac{\beta E^{1/2}}{k_B T}\right) \tag{7.48}$$

This corresponds to violation of the current saturation regime and region 3 in Fig. 7.24.

This simple picture qualitatively agrees with the experimental data. For instance, the linear current growth at low fields with subsequent saturation and further strong increase of the current is often observed in the direct current (d.c.) regime. On the other hand, due to simplicity of the model (as the injection and space charge phenomena are not taken into account) it is not easy to obtain precise quantitative

data and determine relevant material parameters. A technical problem is to avoid uncontrollable impurities. High purity of a liquid crystal material with low conductivity is always desirable, because, if necessary, a well controllable conductive dopants can be introduced on purpose.

7.3.3.4 Frequency Dependence of Ionic Conductivity

In conventional liquids and liquid crystals, the ionic conductivity has no dispersion up to microwave or even optical frequencies. It can be shown by consideration of the equation for the ion oscillation under an external electric field (force $qE\exp(i\omega t)$):

$$m_i \frac{dv}{dt} = qE\exp(-i\omega t) - \xi v \tag{7.49}$$

Here v is velocity of an ion of mass m_i and $-\xi v$ is a friction force; in this case, there is no elastic restoring force familiar from the problem of a pendulum.

Substituting to (7.49) a solution in the form of $v = v_0\exp(-i\omega t)$ we obtain

$$v_0(\xi - i\omega m_i) = qE$$

From here, introducing inverse relaxation time of ions $\tau_i^{-1} = \xi/m_\mathrm{i}$ we find the complex amplitude of ion velocity

$$v_0 = \frac{qE}{m_i(\tau_i^{-1} - i\omega)} = \frac{q\tau_i^{-1}E}{m_i(\omega^2 + \tau_i^{-2})} + i\omega\frac{qE}{m_i(\omega^2 + \tau_i^{-2})} \tag{7.50}$$

and the complex conductivity

$$\sigma* = \sigma' + i\omega\sigma'' = qn_v v = \frac{q^2 n_v \tau_i}{m_i(1 + \omega^2\tau_i^2)} + i\omega\frac{q^2 n_v \tau_i^2}{m_i(1 + \omega^2\tau_i^2)} \tag{7.51}$$

Therefore, for frequencies $\omega << \tau_\mathrm{i}$ the ionic conductivity is constant, $\sigma = q^2 n_v/\xi$.

The friction coefficient can be estimated from the Stokes formula for the friction force

$$F_\xi = \xi v = 6\pi r_0 \eta v \tag{7.52}$$

where r_0 is radius of a spherical ion and η is viscosity of the liquid: $\xi = 6\pi\eta r_0 \approx 2 \times 10^{-7}$ g/s (we take $r_0 = 5\text{Å} = 5 \times 10^{-8}$ cm and viscosity $\eta = 0.1$P). Therefore, in the framework of the Stokes model, the ion conductivity and mobility at $\omega << \tau_\mathrm{i}$ can be written as

$$\sigma = \frac{q^2 n_v}{6\pi r_0 \eta}; \quad \text{and} \quad \mu_i = {}^{\sigma}/_{q n_v} = {}^{q}/_{6\pi r_0 \eta} \tag{7.53}$$

Numerically, for $q = e = 4.8 \times 10^{-10}$ CGSQ and $\xi \approx 2 \times 10^{-7}$ g/s we get the order of magnitude for the mobility $\mu_i \approx 2.4 \times 10^{-3}$ cm^2/statV·s (or 0.8×10^{-9} m^2/V·s) that is close to typical experimental data.

Finally, we estimate the ion translational relaxation time for spherical molecules in a viscous liquid:

$$\tau_i = m_i/\xi = {}^{m_i}/_{6\pi r_0 \eta} \tag{7.54}$$

Typically a mass of an organic molecule (or ion) is $m_i = M m_p \approx 4 \times 10^{-22}$g (here $M \approx 200$ is molecular mass, m_p is proton mass) and, indeed, the estimated relaxation time is very short $\tau_i \approx 2 \times 10^{-15}$s. Thus, the dispersion of the ionic conductivity can only occur in the range of optical frequencies where the physical sense of the friction force is doubtful. By the way, the Stokes approximation seems to be quite good at lower frequencies.

7.3.3.5 Conductivity due to Dielectric Losses

Let us go back to the complex dielectric permittivity $\varepsilon* = \varepsilon' + i\varepsilon''$. Here ε'' describes dielectric losses, i.e. energy dissipation in the range of Debye relaxation of dipoles. We can introduce a parameter $\sigma_D = {}^{\omega\varepsilon''}/_{4\pi}$, which has dimension of electric conductivity ([s^{-1}] in the Gauss system and [F/m·s = C/V·m·s = A/V·m = Ω^{-1}m^{-1}] in the SI system and, in fact, is indistinguishable from the a.c. ohmic conductivity. The values of ε'' and σ_D are essential in the frequency range of dispersion of the ε' component, as we have seen in Section 7.2.4.

What has been said is true for both isotropic liquids and liquid crystals. However, in liquid crystals, due to their specific anisotropy, the ratio $\sigma_D^{\parallel} \big/ \sigma_D^{\perp} = (\varepsilon''_{\parallel}\omega_{\parallel}) \big/ (\varepsilon''_{\perp}\omega_{\perp})$ dramatically depends on frequency and, at least, theoretically can vary from $+\infty$ to $-\infty$. It is seen from a qualitative picture in Fig. 7.23. Due to strongly different dispersion frequency range for real components $\varepsilon'_{\parallel}$ and $\varepsilon'_{\perp}$, the band maxima for imaginary components $\varepsilon''_{\parallel}$ and $\varepsilon''_{\perp}$ are well separated and the ratios $\varepsilon''_{\parallel}/\varepsilon''_{\perp}$ (and $\sigma_D^{\parallel}/\sigma_D^{\perp}$) at the maxima are very large. In addition, at a certain frequency ω_{inv}, the anisotropy of both $\varepsilon''_{\parallel} - \varepsilon''_{\perp}$ and $\sigma_D^{\parallel} - \sigma_D^{\perp}$ changes sign.

The high anisotropy of σ_D can influence the electro-optical behaviour of nematics even at low frequencies, especially for those materials, which have a low frequency inversion of dielectric anisotropy ε_a. An example is shown in Fig. 7.24 related to a material with ε_a inversion at $f = 700$ kHz. The electric conductivity begins to deviate from the ionic, low frequency plateau at 200 Hz and 10 kHz for the longitudinal and transverse components, respectively. At $f = 10$

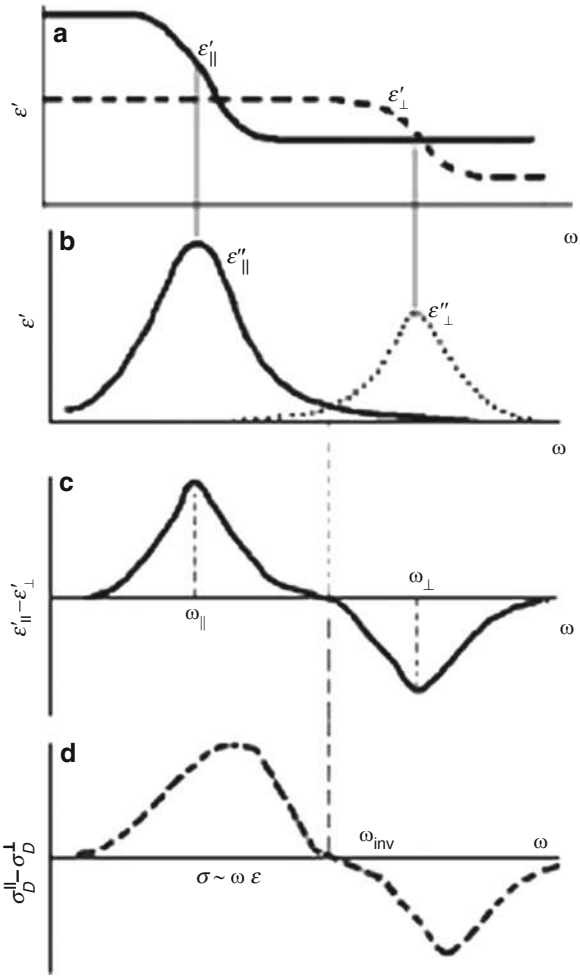

Fig. 7.23 Qualitative frequency spectra of two components of dielectric permittivity ε' (**a**) and ε'' (**b**), and corresponding anisotropy of *imaginary* component of dielectric permittivity $\varepsilon''_{\parallel} - \varepsilon''_{\perp}$ (**c**) and *real a.c. conductivity* $\sigma_D^{\parallel} - \sigma_D^{\perp}$ (**d**) in the Debye relaxation range. ω_{inv} is inversion frequency, at which anisotropy ε_a'' and $\sigma_D^{\parallel} - \sigma_D^{\perp}$ changes sign

kHz the ratio of the two conductivity components reaches 400. The law for the conductivity growth at $\omega\tau_D < 1$ can be derived from the Debye formula (7.32) and allows τ_D to be determined.

$$\sigma_D = \frac{\omega\varepsilon''}{4\pi} = \frac{[\varepsilon(0) - \varepsilon(\infty)]\omega^2\tau_D}{4\pi} \tag{7.55}$$

Such a great growth of conductivity anisotropy dramatically influences the electro-optical behaviour of nematics in this frequency interval.

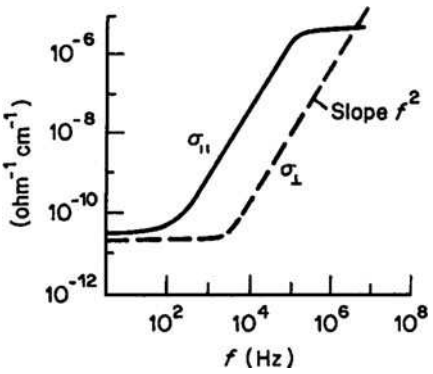

Fig. 7.24 Low frequency spectrum of the principal components of real a.c. conductivity $\sigma_{\parallel}$ and $\sigma_{\perp}$ for a typical nematic liquid crystal having frequency dispersion of $\varepsilon_{\parallel}$ in the 1 MHz range

It is instructive to compare the ratio $\sigma_{\parallel}/\sigma_{\perp} \approx 1.5$ for ionic processes with a much higher ratio $\sigma_D^{\parallel}/\sigma_D^{\perp} \approx 10^2 - 10^3$ for the conductivity due to dielectric losses. In the first case, the orientational nematic potential W_N does not influence the translational motion of ions and $\sigma_{\parallel}/\sigma_{\perp}$. In the second case, the losses $\varepsilon''_{\parallel}$ come in from the field induced alignment of the longitudinal molecular axes against the potential barrier and dramatically depend on W_N whereas losses $\varepsilon''_{\perp}$ caused by molecular rotation about the longitudinal molecular axes are independent of W_N. Therefore, ratios $\varepsilon''_{\parallel}/\varepsilon''_{\perp}$ (and $\sigma_D^{\parallel}/\sigma_D^{\perp}$) are very large.

7.3.3.6 Space Charge Relaxation

Many phenomena in liquid crystals such as formation of double electric layers at interfaces, screening any electric polarization by ions, triggering electro-hydrodynamic processes, etc. are related to the so-called space charge. The latter can be imagined as a cloud of a non-compensated charge, say, positive $+\delta q(\mathbf{r})$ at some place in medium with a coordinate $\mathbf{r}$. The charge of the opposite sign, $-\delta q(\mathbf{r})$ is situated in another place, see Fig. 7.25a. The total charge is zero but the electrical neutrality is disturbed locally.

In strongly conductive materials, like metals, the local electric current in the medium will immediately restore the charge neutrality everywhere. If the local neutrality is disturbed in weakly conductive materials, it takes some time to restore it. It is very easy to find this time. Consider a capacitor with a gap d, capacitance C and charge $\pm q_0$ on the limiting plates of area A, Fig.7.25b. At first, the dielectric is assumed to be ideal, $\sigma = 0$. Upon connecting the external resistor R the charge will relax producing current I given by equation

$$I = \frac{dq}{dt} = C\frac{dU}{dt} = \frac{U}{R}.$$

Hence, $q = CU = q_0 \exp(-t/RC)$, that is the charge relaxes with time constant RC.

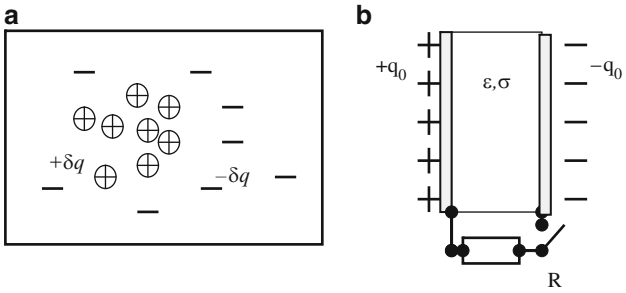

Fig. 7.25 Formation of space charge in a weakly conductive material (**a**) and the capacitor-resistance circuit for the calculation of charge relaxation time (**b**)

The same charge would relax with time constant *RC* even without the external resistance if the material inside is conductive with the same resistance *R*. In that case the relaxation time can be expressed as follows (*A* and *d* are area and thickness of the sample):

$$\tau_M = RC = \left(\frac{d}{\sigma A}\right) \cdot \left(\frac{\varepsilon A}{4\pi d}\right) = \frac{\varepsilon}{4\pi\sigma} \tag{7.56}$$

We can see that relaxation time τ_M is independent of the sample dimensions and includes only material parameters, namely, specific conductivity σ and dielectric constant (real part $\varepsilon = \varepsilon'$). This time is called *space charge relaxation time*. It is the same Maxwell dielectric relaxation time we met in Section 7.2.1. Note that time τ_M has no relation to the dispersion frequency of ionic conductivity $(\tau_i)^{-1}$, neither to Debye dipole relaxation time.

As the space charge relaxation in medium is caused by the counter motion of positive and negative charge carriers in a diffusion process, there should be a characteristic diffusion length related to this motion:

$$L_D = (2D\tau)^{1/2} = \sqrt{\frac{D\varepsilon}{2\pi\sigma}} \tag{7.57}$$

Recalling the Einstein relationship $D = \mu k_B T/q_i$ and $\sigma = q_i n_v \mu$ where q_i is charge of a particle (e.g. ion) we obtain

$$L_D = \sqrt{\frac{k_B T\varepsilon}{2\pi q_i{}^2 n_v}} \tag{7.58}$$

This is a so-called *Debye screening length* playing a crucial role in any phenomena related to the local disturbance of the electric neutrality. For instance, of great technical importance are metal-dielectric contacts or *p-n* semiconductor junctions or contacts between liquid crystal and colloidal particles or metal electrodes. For

liquid crystals, due to anisotropy of ε, the length L_D is also different for two principal directions (∥ and ⊥ to the director).

7.3.3.7 Measurements of Anisotropy $\varepsilon_a(\omega)$ and $\sigma_a(\omega)$

A widely spread technique includes a dielectric bridge (DB) measuring the capacitance and conductance of a liquid crystal cell at various frequencies (typically $1–10^6$ Hz) and temperatures. A small thermostat with a liquid crystal cell is placed in the gap between two poles of a magnet. The thickness of the liquid crystal layer should be fairly large (~100 μm) to avoid effects of boundaries. The electrodes must have high conductivity (e.g., made of gold) and must not be covered by any aligning layers. The amplitude of the a.c. voltage across the electrodes must be small enough (usually about 0.1 V) to avoid any influence of the electric field on the liquid crystal alignment. The orientation of the liquid crystal director is fixed by the external magnetic field of high enough strength ($\mathbf{H} \geq 2$ kOe), therefore, one always has $\mathbf{n} \| \mathbf{H}$. In Fig. 7.26 the magnetic field is directed vertically but the cell is rotated about the horizontal axis. In that way, the cell normal (i.e., the direction of **E**) is installed either parallel to **H** for measurements of $\varepsilon_{\|}$ and $\sigma_{\|}$ (as shown in the figure) or perpendicular to it for measurements of $\varepsilon_{\perp}$ and $\sigma_{\perp}$.

7.3.3.8 Characteristic Times Related to the Discussed Phenomena (Resume)

In the present chapter we have met many characteristic times related to different physical processes. It will be useful to collect them altogether:

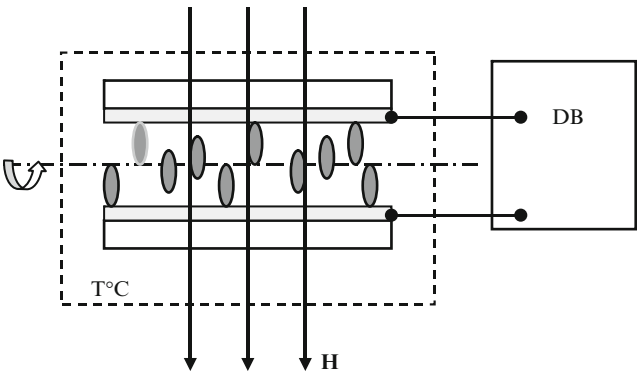

Fig. 7.26 Scheme of the setup for measurements of the principal components of dielectric permittivity and electric conductivity using a dielectric bridge (DB)

$\tau = L^2/2D$	General expression for a time of diffusion of a particle along distance L (D is diffusion coefficient).
$\tau_{th} = L^2/2D_{th} = \rho C_p L^2/2k$	Thermal diffusion time (ρ, C_p and k are density, specific heat and thermal conductivity).
$\tau_L = \frac{1}{2}(K_R K_D c)^{-1/2}$	Langevin time for chemical relaxation (K_D, K_R are dissociation and recombination rates for ions, c is solute concentration).
$\tau_T = L^2/\mu U$	Voltage induced transit time for charge carriers with mobility μ.
$\tau_M = \varepsilon/4\pi\sigma$	Maxwell space charge relaxation time, ε and σ are dielectric permittivity (real part) and conductivity.
$\tau_i = m_i/\xi$	Relaxation (collision) time for motion of ions of mass m_i and friction coefficient ξ.
$\tau_D = 4\pi\eta a^3/k_B T$	Debye relaxation time of dipoles in a liquid (a is molecular radius, η is viscosity of medium).
$\tau_D^{\parallel} = j_{\parallel}\tau_D;\ \tau_D^{\perp} = j_{\perp}\tau_D$	Debye relaxation times in a liquid crystal ($j_{\parallel}$, $j_{\perp}$ are amplification factors).

References

1. De Gennes, Prost, J.: The Physics of Liquid Crystals, 2nd edn. Clarendon, Oxford (1995)
2. Dunmur, D., Toriyama, K.: Magnetic properties of liquid crystals. In: Demus, D., Goodby, J., Gray, G.W., Spiess, H.-W., Vill, V. (eds.) Physical Properties of Liquid Crystals, pp. 102–112. Wiley-VCH, Weinheim (1999)
3. Kittel, Ch: Introduction to Solid State Physics, 4th edn. Wiley, New-York (1971)
4. Brochard, F., de Gennes, P.G.: Theory of magnetic suspensions in liquid crystals. J. Phys. (Paris) **31**, 691–708 (1970)
5. Maier, W., Meier, G.: Eine einfache Theorie der dielektrischen Eigenschaften homogen orientierter kristallinflüssiger Phasen des nematischen Typs, Z. Naturforschg. 16a, 262–267 (1961); Hauptdielektrizitätskonstanten der homogen geordneten kristallinflüssigen Phase des *p*-Azoxyanizols, *ibid*, 16a, 470–477 (1961)
6. Dunmur, D., Toriyama, K.: Dielectric properties. In: Demus, D., Goodby, J., Gray, G.W., Spiess, H.-W., Vill, V. (eds.) Physical Properties of Liquid Crystals, pp. 129–150. Wiley-VCH, Weinheim (1999)
7. de Jeu, W.H.: The dielectric permittivity of liquid crystals. In: Liebert, L. (ed.) Liquid Crystals, pp.109–174 (series Solid State Physics, eds.: Ehrenreich, H., Seitz, F., Turnbull, D.), Academic, New York (1978)
8. de Jeu, W.H.: Physical Properties of Liquid Crystalline Materials. Gordon & Breach, New York (1980)
9. de Jeu, W.H., Lathouwers, Th W., Bordewijk, P.: Dielectric properties of di-*n*-heptyl azoxybenzene in the nematic and in the smectic A phases. Phys. Rev. Lett. **32**, 40–43 (1974)
10. Frölich, H.: Theory of dielectrics, 2nd ed., Chapt. 3, Clarendon Press, London (1978)
11. Wrobel, S.: Dielectric relaxation spectroscopy. In: Haase, W., Wrobel, S. (eds.) Relaxation Phenomena, pp. 13–35. Springer-Verlag, Berlin (2003)
12. Thoen, J.: Thermal methods. In: Demus, D., Goodby, J., Gray, G.W., Spiess, H.-W., Vill, V. (eds.) Physical Properties of Liquid Crystals, pp. 208–232. Wiley-VCH, Weinheim (1999)
13. Zammit, U., Martinelli, M., Pizzoferrato, R., Scudieri, F., Martelucci, M.: Thermal conductivity, diffusivity, and heat capacity studies at the smdctic-A – nematic transition in alkylcyanobiphenyl liquid crystals. Phys. Rev. A **41**, 1153–1155 (1990)
14. Blinov, L.M.: Electro-Optical and Magneto-Optical Properties of Liquid Crystals. Wiley, Chichester (1983)

Chapter 8
Elasticity and Defects

8.1 Tensor of Elasticity

8.1.1 Hooke's Law

Liquids have a finite and very high (as compared to gases) compressibility modulus and zero static shear modulus. For example, a boat floating on water can easily be shifted just by a finger. Even very viscous liquids, for instance, polymers, rubber, and, surprisingly, stain-glass windows have no static shear modulus although they have a dynamic shear modulus at a short time scale or at high frequencies. In fact, to shear a liquid, we should not overcome any potential barrier. In contrast to liquids, the isotropic solids, e.g., ceramics or fine polycrystalline materials have not only compressibility modulus but also one shear modulus finite. As to single crystals, they have many elastic moduli; the lower symmetry the larger a number of their moduli.

What about liquid crystals?

1. In nematic liquid crystals we see a novel feature. There is no shear modulus as in isotropic liquids, but the orientational, for example, torsional elasticity appears. Such elasticity is also characteristic of crystals but, in that case, the corresponding moduli are much smaller than the other moduli. The orientational elasticity determines almost all fascinating properties and applications of nematics.
2. Other liquid crystal phases combine many types of elasticity of solid crystals with orientational elasticity and we encounter enormous variations of the magnitude of elasticity moduli from almost zero to that typical of three-dimensional crystals.

Everything that is discussed below is based on the *Hooke law*. Consider a very simple example, a one-dimensional reversible extension of a long rod with cross-section A along the x-axis, see Fig. 8.1. The force per unit area

$$\sigma_x = \frac{F}{A} = K\frac{l}{L} = K\frac{u_x}{x} = Ku \tag{8.1}$$

L.M. Blinov, *Structure and Properties of Liquid Crystals*,
DOI 10.1007/978-90-481-8829-1_8,

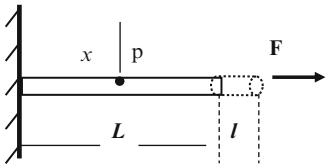

Fig. 8.1 Illustration of the linear one-dimensional displacement of a solid material under an external force (Hooke's law)

causes a *relative displacement* l/L or u_x/x at any point $p(x)$ with corresponding proportionality coefficient that is elastic modulus K. Therefore, in the simplest one-dimensional case, the Hooke law relates the two vector projections, the *stress* σ_x and the relative deformation (*strain*) u_x by scalar Young modulus K (dyn/cm^2 or N/m^2):

$$\sigma_x = Ku_x \tag{8.2}$$

The elastic energy accumulated in the volume L due to the deformation is given by

$$W = \int_0^l Fdl = \int_0^l \frac{AK}{L} ldl = \frac{Kl^2}{2L} A = \frac{Ku_x^2}{2} LA = \frac{1}{2} Ku_x^2 V$$

and the *density of elastic energy* in the one-dimensional case is given by

$$g = \frac{W}{V} = \frac{1}{2} Ku_x^2. \tag{8.3}$$

The stress always causes strain and fundamental Eqs. (8.2) and (8.3) have to be generalized to describe anisotropic media.

8.1.2 Stress, Strain and Elasticity Tensors

8.1.2.1 Stress Tensor

Generally, any vector of a surface force acting on a body can be decomposed into tangential (f_x, f_y, shear) and normal (f_z, pressure) components (index $j = x, y, z$) as shown in Fig. 8.2a. In its turn, the element of surface $\boldsymbol{A}$ is a vector characterized by its area A and outward-directed unit vector $\mathbf{s}$ that has also three projections in the Cartesian laboratory frame (index i). Therefore, the second rank stress tensor [1] is defined as

$$\sigma_{ij} = \frac{s_i f_j}{A} \tag{8.4}$$

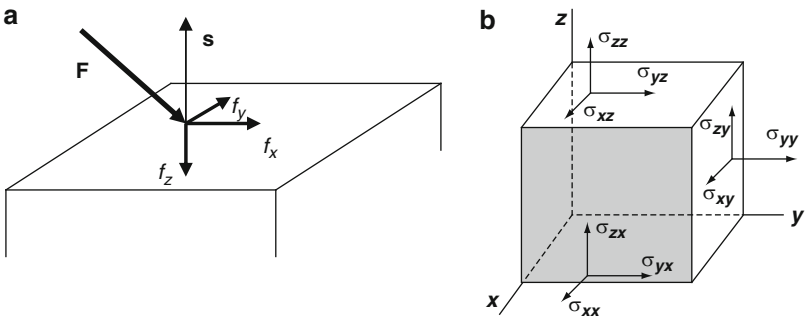

Fig. 8.2 Vector of force **F** acting on a body and its tangential (f_x, f_y, shear) and normal (f_z, pressure) components (**a**) and the nine components of the stress tensor (**b**). Note that the surface element vector is directed outward from the bulk

(dimension of pressure, dyn/cm^2 or N/m^2 in the SI system)

Generally σ_{ij} has $3 \times 3 = 9$ components, illustrated by Fig. 8.2b. The diagonal components (σ_{11}, σ_{22}, σ_{33}) corresponds to pressure, off-diagonal ones correspond to shear. Since σ_{ij} is symmetric tensor ($\sigma_{ij} = \sigma_{ji}$), only six components are different. Usually, in addition to the surface forces, the volume forces like gravitation or electric force are included into the stress tensor.

8.1.2.2 Strain Tensor

We consider a piece of soft matter in which the distortion is not uniform in space but rather local [2]. Any displacement of point p to point p' caused by the stress tensor and shown in Fig. 8.3a–c can be considered as a combintion of four basic displacements. They are (1) translations, (2) rotation of the entire body as a solid piece without deformation, (3) shear distortion, (4) expansion or compression.

Now we are going to discuss the components of the correspondent tensors (translation is excluded). We go back to Eq. (8.2) and instead of $u_x/x = l/L$ write: $u_x = e_{xx}x$ or $\partial u_x = e_{xx}\partial x$

For small distortions, the coefficient $e_{xx} = \partial u_x/\partial x$ will be a function of x, y, z, describing an extension along the x-axis. Along y- and z-axes the extensions wil be described by coefficients

$$e_{yy} = \frac{\partial u_y}{\partial y}, e_{zz} = \frac{\partial u_z}{\partial z} \tag{8.5}$$

The diagonal tensor coefficients with equal suffixes describe compression-dilatation.

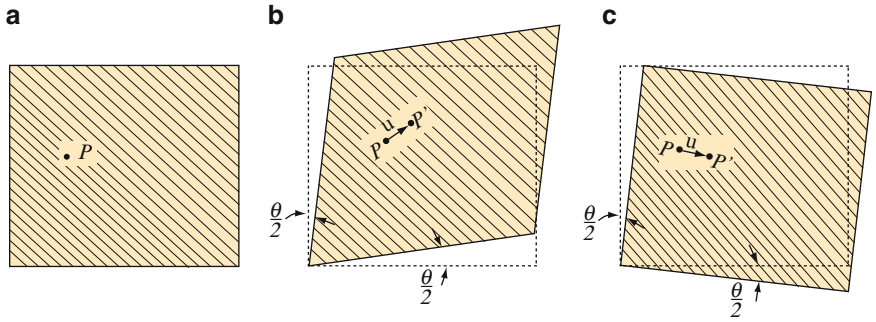

Fig. 8.3 A non-deformed body (**a**) and illustration of difference between a shear distortion (**b**) and pure body rotation (**c**)

There is also shear distortion, which can be described by angles θ/2 as shown in Fig. 8.3b. In this case, the displacement along the *y*-direction is proportional to *x* and *vice versa*:

$$u_x = \frac{\theta}{2} y; u_y = \frac{\theta}{2} x \text{ and } u_x = e_{xy} y; u_y = e_{yx} x$$

with the same angle for $e_{xy} = e_{yx} = \theta/2$. However, we cannot yet define e_{xy} and e_{yx} as simple derivatives of type $(\partial u_x/\partial y)$ or $(\partial u_y/\partial x)$ because similar displacements describe the pure rotation of the body without any deformation as shown in Fig. 8.3c.

$$u_x = \frac{\theta}{2} y; u_y = -\frac{\theta}{2} x$$

Note the opposite sign for the θ angle in the u_y component. To obtain the pure shear we may construct a combination

$$e_{xy} = e_{yx} = \frac{1}{2}\left(\frac{\partial u_y}{\partial x} + \frac{\partial u_x}{\partial y}\right)$$

Then the negative displacements (rotation) will be excluded and positive (shear) remains unchanged. Even more generally, we construct two combinations, one for *pure shear*

$$e_{ij} = \frac{1}{2}\left(\frac{\partial u_j}{\partial x_i} + \frac{\partial u_i}{\partial x_j}\right) \tag{8.6}$$

and the other for pure rotation

$$\omega_{ij} = \frac{1}{2}\left(\frac{\partial u_j}{\partial x_i} - \frac{\partial u_i}{\partial x_j}\right) \tag{8.7}$$

which are, in fact, symmetric (shear) and antisymmetric (rotation) parts of the common tensor describing "shear + rotation".

Finally, the total strain is described by a symmetric second rank (3 × 3) *strain tensor* e_{kl} with diagonal elements $\partial u_i/\partial x_i$ (8.5) related to expansion/compression and off-diagonal elements $\partial u_i/\partial x_j$ (8.6) related to shear.

8.1.2.3 Tensor of Elasticity

For small strain, the relationship between the strain and stress is linear as in the Hooke law [3]:

$$\sigma_{ij} = \sum_{k,l} K_{ijkl} e_{kl} = K_{ijkl} e_{kl} \tag{8.8}$$

Here, the right part of the equation is abbreviation of the middle part suggested by Einstein: since symbols k and l appear twice as suffixes at K_{ijkl} and e_{kl}., we may remember this and remove a bulky symbol of the sum. By this convention, we always must make a summation over the repeated suffixes. The elasticity tensor K_{ijkl} is a fourth rank tensor with 9 × 9 = 81 components (81 mathematically possible elastic moduli!). However, even in crystals of the lowest symmetry (the triclinic system) due to physical equivalence of $K_{ijkl} = K_{jikl} = K_{ijlk} = K_{klij}$, a number of moduli reduces to 21.

With enhanced phase symmetry a number of moduli further reduces and we have:

- Six moduli for the tetragonal system (e.g., of symmetry D_{4h})
- Five moduli for hexagonal system (D_{6h})
- Three moduli for cubic system (O): one for compression and two for shear, namely, perpendicularly to cube edge and to cube diagonals, respectively)
- Two for isotropic solid (compressibility and shear)
- One for an isotropic liquid (compressibility)

The density of elastic distortion energy (a scalar quantity) is quadratic in strain:

$$g_{dist} = \frac{1}{2} K_{ijkl} u_{ij} u_{kl} \tag{8.9}$$

After summation over all suffixes we have maximum 21 scalar terms in the lowest symmetry case. For the isothermal processes, g_{dist} gives a direct contribution to the free energy of the system.

8.2 Elasticity of Nematics and Cholesterics

8.2.1 Elementary Distortions

The static continuum theory of elasticity for nematic liquid crystals has been developed by Oseen, Ericksen, Frank and others [4]. It was Oseen who introduced the concept of *the vector field of the director* into the physics of liquid crystals and found that a nematic is completely described by four moduli of elasticity K_{11}, K_{22}, K_{33}, and K_{24} [4,5] that will be discussed below. Ericksen was the first who understood the importance of asymmetry of the stress tensor for the hydrostatics of nematic liquid crystals [6] and developed the theoretical basis for the general continuum theory of liquid crystals based on conservation equations for mass, linear and angular momentum. Later the dynamic approach was further developed by Leslie (Chapter 9) and nowadays the continuum theory of liquid crystal is called Ericksen-Leslie theory. As to Frank, he presented a very clear description of the hydrostatic part of the problem and made a great contribution to the theory of defects. In this Chapter we shall discuss elastic properties of nematics based on the most popular version of Frank [7].

8.2.1.1 Specific Features of Elasticity of Nematics

As already mentioned, for the fixed direction of the nematic director **n** the shear modulus is absent because the shear distortion is not coupled to stress due to the material "slippage" upon a translation. The compressibility modulus B is the same as for the isotropic liquid. New feature in the elastic properties originates from the spatial dependence of the orientational part of the order parameter tensor, i.e. director $\mathbf{n}(\mathbf{r})$. It is assumed that the modulus S of the order parameter $Q_{ij}(\mathbf{r})$ is unchanged. In Fig. 8.4 we can see the difference between the translation and rotation distortion of a nematic.

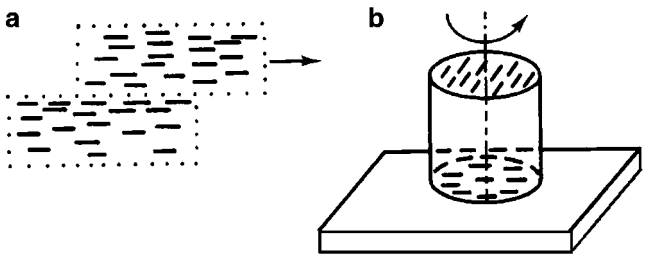

Fig. 8.4 A difference between the translation (**a**) and rotation (**b**) distortion of a nematic: there is no elastic modulus for translation of a moving layer with respect of the immobile layer but the twist of the upper layer with respect to the bottom one is described by the twist elastic modulus

Let us assume that a liquid is incompressible, $B \to \infty$, and discuss orientational (or torsional) elasticity of a nematic. In a solid, the stress is caused by a change in the distance between neighbor points; in a nematic the stress is caused by the curvature of the director field. Now a *curvature tensor* dn_i/dx_j plays the role of the strain tensor u_{ij}. Here, indices $i, j = 1, 2, 3$ and x_i correspond to the Cartesian frame axes. The linear relationship between the curvature and the torsional stress (i.e., Hooke's law) is assumed to be valid. The stress can be caused by boundary conditions, electric or magnetic field, shear, mechanical shot, etc. We are going to write the key expression for the distortion free energy density g_{dist} related to the "director field curvature". To discuss a more general case, we assume that g_{dist} depends not only on quadratic combinations of derivatives $\partial n_i/\partial x_j$, but also on their linear combinations:

$$g_{dist} = K_{ij}\frac{\partial n_i}{\partial x_j} + \frac{1}{2}K_{ijlm}\frac{\partial n_i}{\partial x_j}\cdot\frac{\partial n_l}{\partial n_m} \tag{8.10}$$

As we shall see further on, the terms linear in $\partial n_i/\partial x_j$, allow us to discuss not only conventional nematics with $D_{\infty h}$ symmetry but also some "biased" nematic phases. For example, we can discuss the phases with a spontaneous twist (cholesterics with broken mirror symmetry) or a spontaneous "splay" (uniaxial polar nematics with broken head-to-tail symmetry, $\mathbf{n} \neq -\mathbf{n}$). For a standard nematic only quadratic terms will remain.

8.2.1.2 Elementary Distortions

Consider elementary distortions of a nematic. The undistorted director $\mathbf{n} = (0, 0, 1)$ is aligned along the z-axis, Fig. 8.5a. For instance, at a distance δx from the origin of the Cartesian frame O the director has been turned through some angle in the zOx plane like in Fig. 8.5b. The relative distortion is then described by the ratio of δn_x, an absolute change of the x-component of the director, to distance δx, over which the distortion occurs. In the same sketch, but in the zOy plane we see similar fan-shape or splay distortion δn_y. Thus for the two *elementary splay distortions* we write:

$$\frac{\partial n_x}{\partial x} = a_1;\ \frac{\partial n_y}{\partial y} = a_5;$$

When discussing the deviations of the director δn_x and δn_y at a distance δz from O illustrated by Fig. 8.5c. we define two elementary *bend* distortions:

$$\frac{\partial n_x}{\partial z} = a_3;\ \frac{\partial n_y}{\partial z} = a_6;$$

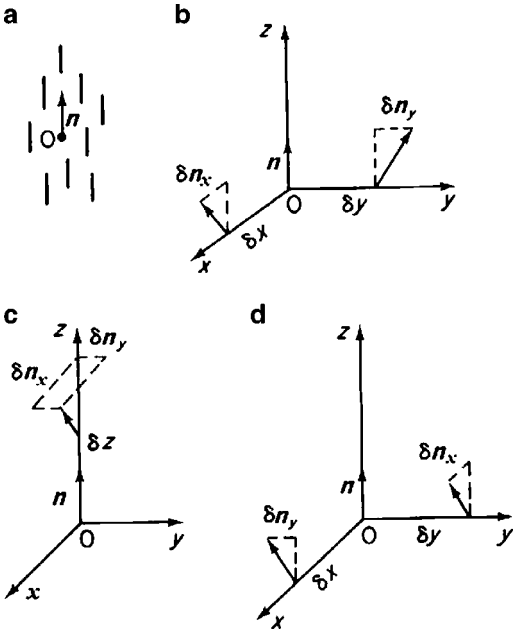

Fig. 8.5 Elementary distortions of the director field for particular geometry (**a**) with $n \parallel z$: splay (**b**), bend (**c**) and twist (**d**)

In the same way, in Fig. 8.5d we see two elementary *twist* distortions (minus appears due to different signs of δn_y and δn_x for the same handedness of rotation about x and y axes).

$$\frac{\partial n_x}{\partial y} = a_2; -\frac{\partial n_y}{\partial x} = a_4;$$

Now the components of the director field $n_x(x,y,z)$ and $n_y(x,y,z)$ can be expressed in terms of the six relative distortions mentioned (only six but not nine because of our assumption $n_z = \text{const} = 1$). For small deviations, we get:

$$\begin{aligned} n_x &= a_1 x + a_2 y + a_3 z + O(r^2); \\ n_y &= a_4 x + a_5 y + a_6 z + O(r^2); \\ n_z &= 1 + O(r^2); \end{aligned}$$

where $O(r^2)$ describes higher order terms depending on $r^2 = x^2 + y^2 + z^2$.

8.2.1.3 Curvature Distortion Tensor

From consideration of the simple case with a particular choice of the z-axis parallel to the director and $n_z \approx 1 + \ldots$, $\partial n_z/\partial x_j \approx 0$, we construct a "reduced" curvature distortion tensor $n_{i,j} = \frac{\partial n_i}{\partial x_j} = \begin{pmatrix} \partial n_x/\partial x & \partial n_x/\partial y & \partial n_x/\partial z \\ \partial n_y/\partial x & \partial n_y/\partial y & \partial n_y/\partial z \end{pmatrix} = \begin{pmatrix} a_1 & a_2 & a_3 \\ a_4 & a_5 & a_6 \end{pmatrix}$.

Here, symbol "comma" between suffixes in $n_{i,j}$ means spatial derivatives. In the general case, with three missing elementary distortions a_7, a_8, and a_9 the *curvature distortion tensor* is given by:

$$n_{i,j} = \begin{pmatrix} a_1 & a_2 & a_3 \\ a_4 & a_5 & a_6 \\ a_7 & a_8 & a_9 \end{pmatrix} \tag{8.11}$$

With this tensor we may turn back to Eq. (8.10) for energy density and discuss two strain tensors, K_{ij} and K_{ijlm}.

8.2.2 Frank Energy

8.2.2.1 Elasticity Tensors

(i) K_{ij} *tensor*. Since g_{dist} ia a scalar, the tensor of elasticity coefficients K_{ij} is also of the second rank with nine components. This tensor has no quadrupolar symmetry like the familiar order parameter tensor Q. However due to the uniaxial symmetry, particularly, polar conical symmetry, the energy g_{dist} is invariant with respect to the rotation of our frame about the z-axis ($x' = y$, $y' = x$, $z' = z$). Thus, this tensor reduces to the form

$$K_{ij} = \begin{pmatrix} K_1 & K_2 \\ -K_2 & K_1 \end{pmatrix} \tag{8.12}$$

At this stage, two moduli K_1 and K_2 remain finite, for a spontaneous splay and twist, respectively (*virtual polar cholesteric*).

However, when molecules have mirror symmetry (achiral molecules), the inversion center appears and g_{dist} becomes invariant with respect to the following frame transformation: $x' = -x$, $y' = -y$, $z' = -z$. As a result, modulus K_2 vanishes and we have a tensor corresponding to a *polar nematic:*

$$K_{ij} = \begin{pmatrix} K_1 & 0 \\ 0 & K_1 \end{pmatrix} \tag{8.13}$$

(modulus K_2 remains, however, in the cholesteric phase).

(ii) K_{ijlm} *tensor*. Generally it has 81 components, however, for $\mathbf{n} \| z$ in Eq. (8.11) coefficients $a_{7,8,9} = 0$ and due to this only 36 components remain. Now we can again apply the symmetry arguments. A conventional nematic has a uniaxial symmetry. This further reduces the quantity of moduli down to 18. Among them only five coefficients are independent, namely K_{11}, K_{22}, K_{33}, K_{24} and K_{12} ($K_{15} = K_{11} - K_{22} - K_{24}$):

$$K_{ijlm} = \begin{pmatrix} K_{11} & K_{12} & 0 & -K_{12} & K_{15} & 0 \\ K_{12} & K_{22} & 0 & K_{24} & K_{12} & 0 \\ 0 & 0 & K_{33} & 0 & 0 & 0 \\ -K_{12} & K_{24} & 0 & K_{22} & -K_{12} & 0 \\ K_{15} & K_{12} & 0 & -K_{12} & K_{11} & 0 \\ 0 & 0 & 0 & 0 & 0 & K_{33} \end{pmatrix} \tag{8.14}$$

Next, taking the head-to-tail symmetry into account we make the following transformation of the frame: $x' = x$, $y' = y$, $z' = -z$. Now coefficients K_{12} disappear. At this atage, only four different moduli are left, K_{11}, K_{22}, K_{33}, K_{24}.

8.2.2.2 Elastic Energy of the Conventional Nematic for n||z

First let us go back to the same particular case with a constraint $\boldsymbol{n}$||z, and discuss the free energy of a conventional (uniaxial, nonpolar) nematic liquid crystal. We combine elementary distortions corresponding to splay (a_1 + a_5), bend (a_3 + a_6) and twist (a_2 + a_4) and present the free energy as a sum of these combinations squared.

$$g_{dist} = \frac{1}{2}\left[K_{11}(a_1 + a_5)^2 + K_{22}(a_2 + a_4)^2 + K_{33}(a_3 + a_6)^2\right] \tag{8.15a}$$

Now, we would like to write the same in a more compact vector form. To do this, consider vector forms for each of the three contributions.

Let us write the divergence of vector $\mathbf{n} = (0, 0, 1)$ with $dn_z = 0$:

$$div\mathbf{n} = \frac{\partial n_x}{\partial x} + \frac{\partial n_y}{\partial y}$$

Evidently, this corresponds to the splay term ($a_1 + a_5$). Now we write curl$\mathbf{n}$ under condition $dn_z = 0$

$$curl\mathbf{n} = -\frac{\partial n_y}{\partial z}\mathbf{i} + \frac{\partial n_x}{\partial z}\mathbf{j} + \left(\frac{\partial n_y}{\partial x} - \frac{\partial n_x}{\partial y}\right)\mathbf{k}$$

and see that it does not fit to any of terms in Eq. (8.15a). However, the scalar product

$$\mathbf{n} \cdot curl\mathbf{n} = -n_x\frac{\partial n_y}{\partial z} + n_y\frac{\partial n_x}{\partial z} + n_z\left(\frac{\partial n_y}{\partial x} - \frac{\partial n_x}{\partial y}\right) \approx \left(\frac{\partial n_y}{\partial x} - \frac{\partial n_x}{\partial y}\right)$$

with neglected the first two products of the second order of magnitude fits to the twist term (a_2 + a_4)! Finally the vector product

$$\mathbf{n} \times curl\mathbf{n} = -\left(\frac{\partial n_x}{\partial z}\mathbf{i} + \frac{\partial n_y}{\partial z}\mathbf{j}\right)$$

under condition n_x, $n_y << n_z \approx 1$) fits to the bend term. Indeed, despite sign "minus" and the vector form it contributes to the quadratic bend term of the "reduced" free energy:

$$g_{dist} = \frac{1}{2}\left[K_{11}\left(\frac{\partial n_x}{\partial x} + \frac{\partial n_y}{\partial y}\right)^2 + K_{22}\left(\frac{\partial n_x}{\partial y} - \frac{\partial n_y}{\partial x}\right)^2 + K_{33}\left[\left(\frac{\partial n_x}{\partial z}\right)^2 + \left(\frac{\partial n_y}{\partial z}\right)^2\right]\right] \tag{8.15b}$$

8.2.2.3 Frank Formula

To have the free energy density in a more general form including all the nine elementary distortions $a_1, a_2 \ldots a_9$ we should add the terms $\partial n_z/\partial z$, $\partial n_z/\partial x$ and $\partial n_z/\partial$y and rewrite the Eq. (8.15b) in the vector notations for arbitrary distortion of **n** with respect to the Cartesian frame. Then we obtain *Frank formula* for the density of elastic energy in the general vector form:

$$g_{dist} = \frac{1}{2}[K_{11}(\mathrm{div}\mathbf{n})^2 + K_{22}(\mathbf{n} \cdot \mathrm{curl}\mathbf{n})^2 + K_{33}(\mathbf{n} \times \mathrm{curl}\mathbf{n})^2] \tag{8.16}$$

Here, we have splay, twist and bend terms corresponding to a particular bulk distortion. In experiment, they can be realized in different way using variable cell geometry and boundary conditions. For example, such distortions may be created mechanically as shown in Fig. 8.6. The important condition is to anchor the director firmly at the boundaries.

But what about the K_{24} term? The so-called *saddle-splay* modulus K_{24} is important only for particular situations, in which a distortion has a two- or three-dimensional structures such as nematic droplets in the isotropic solutions [8] or blue phases [9]. The free energy term including modulus K_{24} is a so-called "divergence" term because it has a form of div**n** to the first degree. Hence, if one performs the

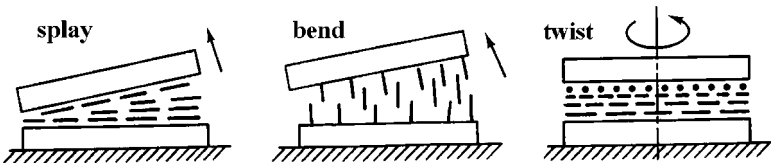

Fig. 8.6 Splay, bend and twist distortions in nematics confined between two glasses that align liquid crystal at the surfaces either homogeneously (for splay and twist) or homeotropically (for bend)

minimization of the free energy using the Euler-Lagrange variation procedure (Section 8.3), the divergence term $\partial n/\partial z$ would contribute only to the boundary conditions and, in the one-dimensional geometry, the contribution of the saddle-splay elasticity vanishes. However, in a more complex geometry the coefficient K_{24} becomes important. For example, in very thin films with tangential (planar along x) boundary conditions on one side and homeotropic (along z) on the other side, a uniform hybrid structure in the xz-plane is not stable. Instead, the absolute minimum of the free energy is realized for a periodic structure of linear defects (stripe domains) with distortion in the film plane xy [10].

The nematic elastic moduli have dimension of force. The three moduli in Frank energy (8.16) are always positive, modulus K_{24} may be positive or negative. Roughly, all of them are of the same order of magnitude that may be estimated from the molecular interaction energy W divided by intermolecular distance $l \approx 5$ Å. If for W we take the temperature of nematic-isotropic transition ($k_BT \approx 0.033$ eV at $T = 400$ K), the elastic modulus would be $K \approx W/l \approx 1 \cdot 10^{-6}$ dyn (Gauss system) or $1 \cdot 10^{-11}$ N (SI system). If we take the nematic potential $W_N \approx 0.15$ eV the estimated modulus would be five time larger. The experimental values are in the range of 10^{-7} – 10^{-6} dyn. The data on elastic moduli for most popular liquid crystals (*p*-azoxyanisol (PAA), *p*-methoxy-benzylidene-*p'*-butylaniline (MBBA) and pentyl-cyanobiphenyl (5CB) are collected in the Introduction to book [11].

8.2.3 Cholesterics and Polar Nematics

8.2.3.1 Cholesterics

If molecules are chiral, the coefficient K_2 from tensor (8.12) becomes finite. Formally it is possible to add it to the Frank energy introducing a scalar quantity $q_0 = K_2/K_{22}$ and obtain the following expression:

$$g_{dist} = \frac{1}{2}[K_{11}(\mathrm{div}\mathbf{n})^2 + K_{22}(\mathbf{n} \cdot \mathrm{curl}\mathbf{n} + q_0)^2 + K_{33}(\mathbf{n} \times \mathrm{curl}\mathbf{n})^2] \tag{8.17}$$

Then, expanding the second term $K_{22}(\mathbf{n} \cdot \mathrm{curl}\mathbf{n})^2 + 2K_{22}q_0(\mathbf{n} \cdot \mathrm{curl}\mathbf{n}) + K_{22}q_0^2$ we note that the last item is not interesting because independent of distortion and the gradient term $K_{22}q_0(\mathbf{n} \cdot \mathrm{curl}\mathbf{n})$ is the only one that distinguishes the free energy of a cholesteric from that of the nematic. For a cholesteric with a pure twist along the z-axis, the components of the director are $\mathbf{n} = (\cos\varphi z, \sin\varphi z, 0)$. This results in $\mathbf{n}\mathrm{curl}\mathbf{n} = -d\varphi/dz$. Then, for any form of $\varphi(z)$, the twist contribution to elastic energy density (8.17) is given by

$$g_{dist}(z) = \frac{1}{2}K_{22}\left(\frac{d\varphi(z)}{dz} - q_0\right)^2 \tag{8.18}$$

The minimum of (8.18) corresponds to the equilibrium helical (harmonic) structure with wavevector $q_0 = d\varphi/dz$ and pitch $P_0 = 2\pi/q_0$. Equation (8.18) is correct as long as $P_0 >> a$ where a is molecular size. In the opposite case, local biaxiality becomes important (practically, $P_0 \approx 1$ μm, $a \approx 1$ nm).

8.2.3.2 Polar Nematics

In precisely the same way, a spontaneously splay-deformed structure must correspond to the equilibrium condition with finite coefficient $K_1 \neq 0$ in tensor (8.13). The corresponding term should be added to the splay term with $(\mathrm{div}\mathbf{n})^2$. If the molecules have, e.g., pear shape they can pack as shown in Fig. 8.7b. In this case, the local symmetry is $C_{\infty v}$ (conical) with a polar rotation axis, which is compatible with existence of the spontaneous polarization. However, such packing is unstable, as seen in sketch (b), and the conventional nematic packing (a) is more probable. The splayed structure similar to that pictured in Fig. 8.7b can occur close to the interface with a solid substrate or when an external electric field reduces the overall symmetry (*a flexoelectric effect*).

8.3 Variational Problem and Elastic Torques

8.3.1 Euler Equation

Consider a nematic liquid crystal layer confined between two glass plates. This structure is of great technical importance. The most of liquid crystalline displays are based on it. The directors at opposite walls ($z = 0$ and $z = d$) are rigidly fixed at

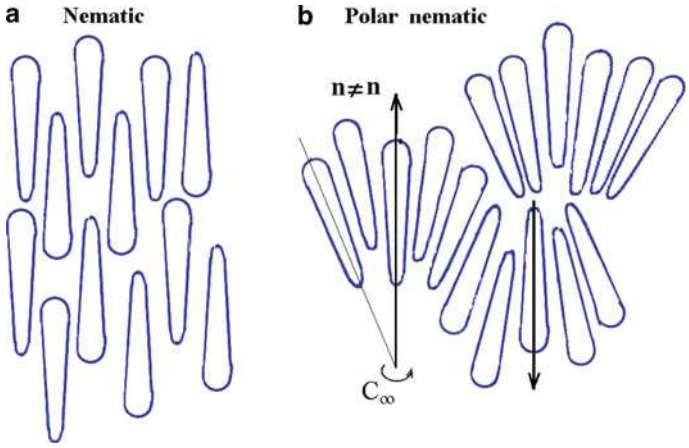

Fig. 8.7 Packing of conical (*pear-shape*) molecules in the conventional nematic phase (**a**) and in a hypothetical polar nematic phase (**b**)

right angle to each other, therefore such a cell is called π/2-twist nematic cell. Along x and y the layer is infinite, the director $\mathbf{n}(z)$ depends only on one coordinate. How to find a director distribution along the z-axis?

For simplicity we ignore the influence of external fields. The problem is to find that distribution of the director angle $\varphi(z)$ over cell thickness, which satisfies the minimum of the elastic free energy F for fixed boundary conditions. This is a typical variational problem although very simple in our particular case. The idea of a variational calculation is not to find a value of the integral of a function $g(z, \varphi, \varphi')$ over the interval $0 \leq z \leq d$ for known $\varphi(z)$, but to find such an *unknown function* $\varphi(z)$ that provides the minimum of the integral. Due to the great importance of this mathematical problem for liquid crystals consider it in more detail.

Consider a functional F (scalar number, e.g. it might be free energy of the liquid crystal sample):

$$F = \int_a^b g(z, \phi(z), \phi'(z))dz \tag{8.19}$$

Here g is a function of all the three arguments z, $\varphi(z)$ and $d\varphi/dz$. The equation is valid for any continuous function $g(z)$ with continuous derivatives g', g'' defined within interval $[a, b]$. For instance, g might be density of free energy of a liquid crystal per unit volume, $\varphi(z)$ be an angle the director forms with a selected reference axis and d the thickness of the sample. The values of function g are fixed at both ends of the interval $\varphi(a) = \varphi_a$ and $\varphi(b) = \varphi_b$. In our simplest example, infinitely strong anchoring of the director is assumed at the boundaries.

Our task is to find the necessary condition for the extremum of the functional F. Let us assume that function $\varphi(z)$ in Fig. 8.8 corresponds to an extremum of F, i.e. $F = F_{\text{extr}}$ for $\varphi(z)$ (actually, for physical reasons an extremum to be found corresponds to a minimum). Then we introduce a new, probe function $\phi(z) + \alpha\eta(z)$ where α is a small numerical parameter and $\eta(z)$ is an arbitrary function equal to zero at both ends of the $[a, b]$ interval. The additional item $\alpha\eta(z)$ is called *variation of* $\varphi(z)$ *function* that will result in variation δF of functional F. Now if we vary α, the functional F changes. Therefore, after substituting the new functions with variable α into $g(z)$, we obtain F as a function of parameter α:

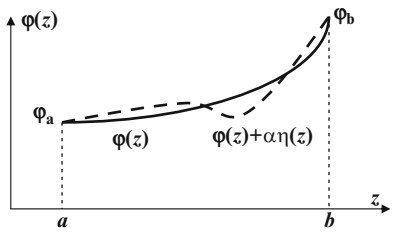

Fig. 8.8 Illustration of variation procedure: one searches for such a function $\varphi(z)$ that satisfies to an extremum of functional (8.19). $\varphi(z) + \alpha\eta(z)$ is arbitrary probe function

$$F(\alpha) = \int_a^b g[z, \phi(z) + \alpha\eta(z), \phi'(z) + \alpha\eta'(z)]dz \tag{8.20}$$

Next we shall explore a new idea: as we vary $\phi(z) + \alpha\eta(z)$ and the functional F reaches an extremum then the varied function $F(\alpha)$ must have an extremum at $\alpha = 0$ (due to the assumption that $\varphi(z)$ corresponds to F_{extr}). Therefore, the derivative $dF/d\alpha = 0$ at $\alpha = 0$. Hence, after differentiation (8.20) with respect to α under the integral, we obtain the expression valid at $\alpha = 0$:

$$F'(0) = \frac{dF}{d\alpha} = \int_a^b \left[\frac{\partial g}{\partial \phi}(z, \phi, \phi')\eta(z) + \frac{\partial g}{\partial \phi'}(z, \phi, \phi')\eta'(z)\right]dz = 0, \tag{8.21}$$

where we used $\frac{\partial g}{\partial \alpha} = \frac{\partial g}{\partial(\phi+\alpha\eta)} \cdot \frac{\partial(\phi+\alpha\eta)}{\partial \alpha} = \frac{\partial g}{\partial \phi} \cdot \eta$ (for $\alpha = 0$) and the same for the term with φ'.
Integrating by parts the second term in (8.21) we get:

$$F'(0) = \int_a^b \frac{\partial g}{\partial \phi} \cdot \eta(z)dz + \left[\frac{\partial g}{\partial \phi'}\eta(z)\right]_a^b - \int_a^b \eta(z)\frac{d}{dz}\left(\frac{\partial g}{\partial \phi'}\right)dz$$

$$= \left[\frac{\partial g}{\partial \phi'}\eta(z)\right]_a^b + \int_a^b \eta(z)\left[\frac{\partial g}{\partial \phi} - \frac{d}{dz}\left(\frac{\partial g}{\partial \phi'}\right)\right]dz = 0$$

The first term is zero because $\eta(z) = 0$ at the ends of the interval $[a, b]$. And since $\eta(z)$ is arbitrary, the expression in the brackets under the integral must be zero. Hence, we arrive at the differential *Euler equation*:

$$\frac{\partial g}{\partial \phi} - \frac{d}{dz}\frac{\partial g}{\partial \phi'} = 0 \tag{8.22}$$

What have we gained? Very much! Now, in order to find the function $\varphi(z)$ corresponding to g_{min} we have to solve a second order differential equation (8.22), instead of solving an integral-differential equation (8.19). Two arbitrary constants are to be found from the boundary conditions given for $\varphi(z)$.

8.3.2 Application to a Twist Cell

To illustrate the variation technique that is very useful for subsequent discussions of electro-optical effects, consider a simplest example. For a twist cell shown in

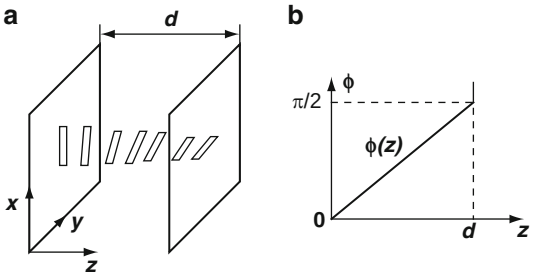

Fig. 8.9 Twist cell in the zero field: geometry of the problem (**a**) and the calculated distribution of angle φ(*z*) (i.e. the director angle) over the cell thickness (**b**)

Fig. 8.9a, we are interested in the coordinate dependence of the azimuthal director angle φ(*z*), which is rigidly fixed at the two boundaries, φ(0) = 0, φ(*d*) = π/2. The equilibrium director distribution to be found corresponds to the minimum of the elastic free energy for the cell as a whole. First, we should write an expression for the density of Frank elastic energy. The director at any point *z* is given by $\mathbf{n} = \cos\phi(z)\mathbf{i} + \sin\phi(z)\mathbf{j}$. There is no *z*-component, $n_z = 0$, even no pretilt at the boundaries.

The free energy per unit area in the *x, y* plane is very simple because we have no derivatives over *x* and *y*, therefore

$$\mathrm{curl}\mathbf{n} = -\frac{\partial n_y}{\partial z}\mathbf{i} + \frac{\partial n_x}{\partial z}\mathbf{j} = -\cos\phi\frac{d\phi}{dz}\mathbf{i} - \sin\phi\frac{d\phi}{dz}\mathbf{j};$$

$$\mathbf{n}\mathrm{curl}\mathbf{n} = -\frac{d\phi}{dz} \text{ and } (\mathbf{n}\mathrm{curl}\mathbf{n})^2 = \left(\frac{d\phi}{dz}\right)^2.$$

From here and Eq. (8.17), the density g_{dist} and the total Frank energy are given by

$$g_{dist} = \frac{1}{2}K_{22}\left(\frac{d\phi}{dz}\right)^2; \quad F = \frac{1}{2}\int_0^d K_{22}\left(\frac{d\phi}{dz}\right)^2 dz \tag{8.23}$$

To find φ(*z*) we should write the Euler equation for functional (8.23). In that equation we have neither *z* nor φ(*z*) given explicitly and should only use differentiation with respect to φ'(*z*). Now Euler's equation reads:

$$-\frac{d}{dz}\frac{\partial g}{\partial \phi'} = -K_{22}\frac{d^2\phi}{dz^2} = 0 \tag{8.24}$$

This equation may be considered as a balance of torques in the bulk, although in this particular case, the elastic forces are balanced by the fixed boundary conditions

and the rotation of the director is possible only together with the cell substrates. After the first integration we obtain:

$$q = d\phi/dz = \text{const} = C \tag{8.25}$$

This is an important result showing a linear distribution of azimuthal angle over the layer thickness. The second integration gives us the value of the constant. It depends on the difference between the azimuthal angles fixed at the opposite boundaries. In our cell, $\varphi_1 = 0$ at z = 0 and $\varphi_2 = \pi/2$ at z = d. Therefore $\phi = Cz = \pi z/2d$; this linear dependence is illustrated by Fig. 8.9b. Equation (8.25) is valid for any uniform twist distortion; for instance, for nematics twisted through angles $\pi/4$ or π the functions $\varphi = (\pi z/4d)$ and $\varphi = (\pi z/d)$, respectively. The linear dependence remains even in the case of non-rigid boundary conditions, however, external magnetic or electric fields can easily distort such a uniform distribution.

It is instructive to calculate the value of the elastic energy (per unit area) of a typical twisted cell, discussed above. Using (8.23), the free energy is given by

$$F = \frac{1}{2}\int_0^d K_{22}\left(\pi/2d\right)^2 dz = \frac{\pi^2 K_{22}}{8d}$$

Taking cell thickness $d = 10$ μm (10^{-3}cm), $K_{22} = 3{\cdot}10^{-7}$ dyn (or $3{\cdot}10^{-12}$ N) we find $F \approx 3.7{\cdot}10^{-4}$ erg/cm^2 or 0.37 μJ/m^2 in SI units.

The example of the variational procedure considered in this section was very simple, because we operated only with one independent variable (angle φ). Sometime one needs to minimize the energy with respect to two variables; in fact, we met this case in Section 6.3.3 for an infinite medium. For two variables, the system of two Euler equations can be constructed using the same procedure as earlier. However, very often one deals with some constraints as, for example, in the case of the director that has three projections satisfying the constraint $n_x^2 + n_y^2 + n_z^2 = 1$. In such cases the Lagrange multipliers are introduced to solve the variational problem, however this, more general Euler – Lagrange approach will not be used in this book.

8.3.3 "Molecular Field" and Torques

The director **n** of a nematic can be re-aligned from its equilibrium position by an external magnetic (or electric) field because these fields exert torques onto **n**. If the field is strong enough and magnetic χ_a or dielectric ε_a anisotropy is positive, the director will be aligned along the field. On the other hand, being deflected from the equilibrium state by $\delta\mathbf{n}$, the director relaxes back due to elasticity. It looks

like the director feels a sort of "molecular field" that causes it to rotate back to the equilibrium position. The "molecular field" should not be confused with the mean field used in the molecular theory and characterized by the nematic potential curve discussed in Chapters 3 and 6.

Mathematically the "molecular" field vector **h** can be found using the Euler-Lagrange approach by a variation of the elastic and magnetic (or electric) parts of the free energy with respect to the director variable **n**(**r**) (with a constraint of $\mathbf{n}^2 = 1$). For the elastic torque, in the absence of the external field, the splay, twist and bend terms of **h** are obtained [9] from the Frank energy (8.16):

$$\begin{aligned}
\mathbf{h}_{splay} &= K_{11}\nabla(div\mathbf{n}) \\
\mathbf{h}_{bend} &= K_{33}\{[(\mathbf{n}\times cirl\mathbf{n})\times curl\mathbf{n}] + curl[\mathbf{n}\times(\mathbf{n}\times cirl\mathbf{n})\} \\
\mathbf{h}_{twist} &= -K_{22}\{[(\mathbf{n}\cdot cirl\mathbf{n}\cdot\mathbf{n})\cdot curl\mathbf{n}] + curl[(\mathbf{n}\cdot cirl\mathbf{n}\cdot\mathbf{n})]\cdot\mathbf{n}\}
\end{aligned}$$

In the one-constant approximation $K_{11} = K_{22} = K_{33} = K$ and the expression for the molecular field becomes very simple, similar to (8.24):

$$\mathbf{h}_{dist} = K\nabla^2\mathbf{n} \tag{8.26}$$

This approximation is useful when solving problems related to the field behavior of liquid crystals. In the thermodynamic equilibrium, the director is always aligned along the molecular field vector, **n**||**h**. When there is an external electric or magnetic field (see for details Section 11.2.1), the corresponding terms given by

$$\mathbf{h}_E = -\frac{\varepsilon_a}{4\pi}(\mathbf{En})\mathbf{E} \quad \mathbf{h}_H = -\chi_a(\mathbf{Hn})\mathbf{H} \tag{8.27}$$

should be added to the molecular field. Such a non-zero sum of all these vectors creates a torque exerted on the director

$$\Gamma = \mathbf{n}\times\sum\mathbf{h}_i \tag{8.28}$$

which causes the director rotation. Actually the torque due to the molecular field can be balanced by other (e.g. viscous) torques. In this way, we can write a torque balance equation.

$$\mathbf{n}\times\sum\mathbf{h}_i + \text{viscous torque} + \text{others} = 0 \tag{8.29}$$

8.3.4 Director Fluctuations

This is another important example of a successful application of the theory of elasticity. In Section 11.1.3 we shall discuss the nature of strong light scattering by

nematics. In fact, such scattering is caused by small values of the Frank elastic moduli. The latter results in strong thermal fluctuations of the director. Here, we consider a simple approach to calculation of the amplitude of the director fluctuations suggested by de Gennes [12].

We again consider the director $\mathbf{n}_0$ oriented along the z-axis. Its fluctuating part has components $(n_x, n_y, 0)$. The total Frank elastic energy, related to the fluctuations in volume V, is given by the integral of free energy density (8.15b):

$$F = \frac{1}{2}\int_V \left\{ K_{11}\left(\frac{\partial n_x}{\partial x} + \frac{\partial n_y}{\partial y}\right)^2 + K_{22}\left(\frac{\partial n_x}{\partial y} - \frac{\partial n_y}{\partial x}\right)^2 + K_{33}\left[\left(\frac{\partial n_x}{\partial z}\right)^2 + \left(\frac{\partial n_y}{\partial z}\right)^2\right]\right\} d\mathbf{r} \tag{8.30}$$

The Fourier harmonics n_x and n_y of the director fluctuating field are represented by volume integrals ($\mathbf{q}$ is wavevector**):**

$$n_x(\mathbf{q}) = \int_V n_x(\mathbf{r})\exp(i\mathbf{qr})d\mathbf{r} \text{ and } n_y(\mathbf{q}) = \int_V n_y(\mathbf{r})\exp(i\mathbf{qr})d\mathbf{r} \tag{8.31}$$

Now the corresponding free energy is represented by a sum of the q harmonics:

$$F = \frac{1}{2V}\sum_q \left\{ K_{11}|n_x(\mathbf{q})q_x + n_y(\mathbf{q})q_y|^2 + K_{22}|n_x(\mathbf{q})q_y - n_y(\mathbf{q})q_x|^2 \right.$$
$$\left. + K_{33}q_z^2\left[|n_x(\mathbf{q})|^2 + |n_y(\mathbf{q})|^2\right]\right\}$$

The $\mathbf{q}$-vector consists of three components (q_x, q_y, q_z) and the obtained quadratic form for $n_x(\mathbf{q})$ and $n_y(\mathbf{q})$ is complicated because it is not diagonal. However, it can be made diagonal if one takes a simplified geometry corresponding to the symmetry of a scattering experiment. To this effect, de Gennes selected new coordinate axes: the axis $\mathbf{e}_2$ was chosen to be perpendicular to the $\mathbf{n}_0$ (i.e. to z-axis) and simultaneously perpendicular to the scattering vector $\mathbf{q}$, as shown in Fig. 8.10a. The other axis $\mathbf{e}_1$ was chosen to be perpendicular to the z-axis and $\mathbf{e}_2$. Now the $\mathbf{q}$-vector is resolved not into three components but only into two: $q_z = q_\parallel$ and $q_\perp$ ($\parallel$ and $\perp$ to the director). Correspondingly we have two normal modes of fluctuations.

In Fig. 8.10b, we see that the fluctuation mode $n_1(\mathbf{q})$ is a mixture of the splay and bend distortions, and the component $n_2(\mathbf{q})$ is a mixture of twist and bend distortions. This may be clarified as follows: the splay-bend (SB) mode on the left side of Fig. 8.10b corresponds to realignment of the molecules within the q,z-plane as q evolves and there is no twist here. In contrast, on the right side of the same figure the molecules are deflected from the qz-plane of the figure; therefore, the twist and bend are present but the splay is absent (TB mode).

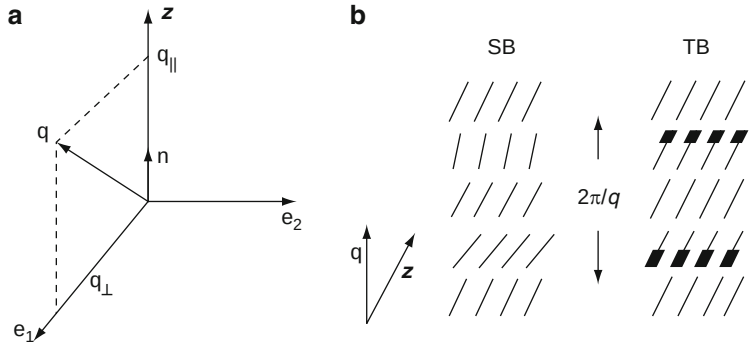

Fig. 8.10 New coordinate axes, $\mathbf{e}_1$ and $\mathbf{e}_2$ appropriate to the normal modes of director fluctuations in a nematic liquid crystal (**a**) and the structure of the normal modes, namely splay-bend (SB) and twist-bend modes (TB)

After the transform to the new variables $n_\alpha(\mathbf{q})$ ($\alpha = 1, 2$) the equation for the free energy reads:

$$F = \frac{1}{2V} \sum_q \sum_{\alpha=1,2} |n_\alpha(q)|^2 \left(K_{33} q_{||}^2 + K_\alpha q_\perp^2 \right) \tag{8.32}$$

Here K_α is the combination of Frank elastic moduli K_{11} and K_{22}.

The last equation has a remarkable feature: the different Fourier components of fluctuations are decoupled because they are normal modes for the system. This allows us to apply the *principle of equipartition*, according to which the energy of each mode is equal to $k_B T/2$. Therefore, for each mode with $\alpha = 1, 2$, the final equation for the mean-square magnitude of the director fluctuations reads:

$$\left\langle |n_\alpha(q)|^2 \right\rangle = V \frac{k_B T}{K_{33} q_{||}^2 + K_\alpha q_\perp^2} \tag{8.33}$$

The latter transformation is based on the Gibbs distribution that gives us the probability of the mean square value $|n_\alpha(\mathbf{q})|^2$for a particular director fluctuation with wavevector $\mathbf{q}$ when the average value $\langle |n_\alpha(\mathbf{q})|^2 \rangle$for all fluctuations is known:

$$w \propto \exp\left[-\frac{V(K_{33} q_{||}^2 + K_\alpha q_\perp^2) |n_\alpha(\mathbf{q})|^2}{k_B T} \right] = \exp\left[-\frac{|n_\alpha(\mathbf{q})|^2}{<|n_\alpha(\mathbf{q})|^2>} \right]$$

From Eq. (8.33) for the mean square amplitude of the director fluctuations, we can derive the amplitude of the fluctuations of the dielectric tensor and then find the *cross-section* for the light scattering, see Section 11.1.3. The de Gennes description of the director fluctuations in the continuous medium [12] was a strong argument against the so-called swarm models of liquid crystals. That model was based on the

concept of rather large blocks (or swarms) with the molecules uniformly aligned within a swarm and variable orientation of swarms as a whole [13]. Such discontinuity was considered to be responsible for the strong light scattering by nematics. Nowadays the continuous theory is the corner-stone of the physics of liquid crystal.

8.4 Defects in Nematics and Cholesterics

8.4.1 Nematic Texture and Volterra Process

8.4.1.1 Textures

The concept of defects came about from crystallography. Defects are disruptions of ideal crystal lattice such as vacancies (point defects) or dislocations (linear defects). In numerous liquid crystalline phases, there is variety of defects and many of them are not observed in the solid crystals. A study of defects in liquid crystals is very important from both the academic and practical points of view [7,8]. Defects in liquid crystals are very useful for (i) identification of different phases by microscopic observation of the characteristic defects; (ii) study of the elastic properties by observation of defect interactions; (iii) understanding of the three-dimensional periodic structures (e.g., the blue phase in cholesterics) using a new concept of "lattices of defects"; (iv) modelling of fundamental physical phenomena such as magnetic monopoles, interaction of quarks, etc. In the optical technology, defects usually play the detrimental role: examples are defect walls in the twist nematic cells, shock instability in ferroelectric smectics, Grandjean disclinations in cholesteric cells used in dye microlasers, etc. However, more recently, defect structures find their applications in three-dimensional photonic crystals (e.g. blue phases), the bistable displays and smart memory cards.

Generally, microscopic observations reveal different types of defects, which may be 0-dimensional (points), one-dimensional (lines) and two-dimensional (walls). Typical nematic textures are

1. The thread texture usually observed in thick layers
2. Schlieren texture observed in thin cells

In Fig. 8.11 an example is given of a Schlieren texture in the nematic phase observed under a polarisation microscope. The polariser and analyser are always crossed and their positions with respect to photos (a) and (b) differ by 45° as shown by small crosses. On both photos characteristic brushes (threads) are seen originated and terminated at some points. The points are linear singularities (disinclinations or just disclinations) to be discussed below. Note the difference between a number of brushes originated or terminated in different points: only two brushes in points 1 and 5 and four brushes in points 2, 3 and 4. It is evident that the pictures discussed are related to the local orientation of the director, i.e. to the structure of

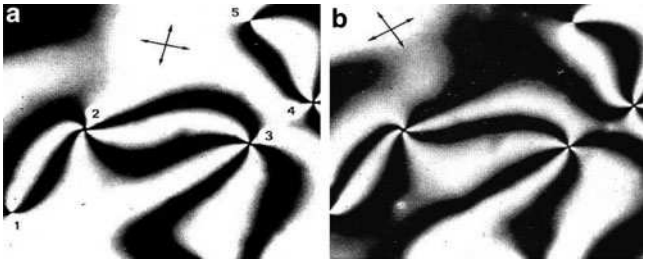

Fig. 8.11 Schlieren texture observed between crossed polarizer and analyzer. Orientation of polarizers differs in photos (**a**) and (**b**) by 45°

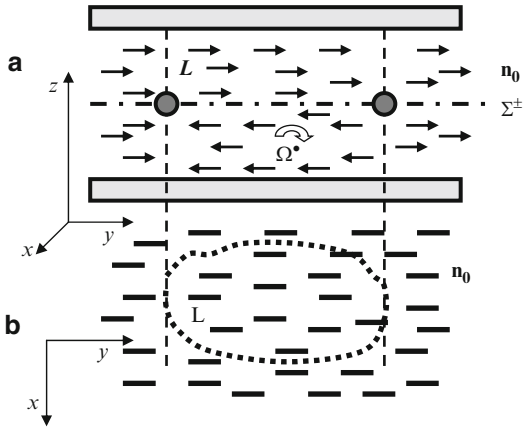

Fig. 8.12 Volterra process in nematic liquid crystal placed between two glasses with side view (**a**) and top view (**b**). The part of the nematic shown by arrows directed from the right to the left was initially removed (virtually), turned by angle π about the Ω-axis and put back into the empty cavity. A plane wall $\boldsymbol{\Sigma}^{\pm}$ and a linear disclination loop *L* are formed

the director field $\mathbf{n}(\mathbf{r})$. To understand the nature of the brushes, let us form some defects artificially.

8.4.1.2 Volterra Process

The major part of the arrows directed to the right in Fig. 8.12a correspond to the initial orientation of the director $\mathbf{n}_0$ in the planar nematic slab. However, the part of the slab shown by arrows directed to the left is virtually taken from the sample by some "mysterious force", turned about axis Ω through angle π and put back into the slab. After this operation called Volterra process, the director is everywhere again parallel to $\mathbf{n}_0$ due to the $\mathbf{n}_0 = -\mathbf{n}_0$ symmetry and such a structure in each of the two parts (initial and turned) is topologically stable. However, in the close proximity of the plane $\boldsymbol{\Sigma}^{\pm}$, on the scale of molecular size, the director changes its orientation by

π. The plane $\Sigma^{\pm}$ parallel to the substrate and horizontal in sketch (a) is called a wall defect or just a *wall*.

There is also a vertical wall around the block shown by a dot-line loop in the *xy*-projection in sketch (b) below. The wall $\Sigma^{\pm}$ is not seen under microscope, but the loop L surrounding the reoriented area and called a *disclination* is well seen as a thin line. Very often the reoriented area surrounded by the vertical wall takes all the thickness between the glasses without formation of wall $\Sigma^{\pm}$ within the bulk.

The rotation angle Ω is not necessarily equals π, it may be 2π, 3π or, more generally $\Omega = 2\pi \cdot s$ where s is *strength of a disclination*. The disclinations of strength $s = \pm 1/2$ or ± 1 are observed very often, however, those of strength $s = \pm 3/2$ or even ± 2 are very rare.

8.4.2 Linear Singularities in Nematics

8.4.2.1 Disclination Strength

Consider a disclination with its ends fixed at the opposite plates of a planar nematic cell. Such a disclination "connects" the two glass plates as in Fig. 8.13a. If we are looking at it from the top along the *z*-direction we can see the director distribution **n** (*x, y*) in the *xy*-plane around the disclination. In a polarization microscope, in the same cell, we can see different **n**(*x, y*) patterns corresponding to disclinations shown in Fig. 8.14. A point in the middle of each sketch shows the disclination under discussion that has its own strength *s*.

The strength of a disclination is defined as follows. We traverse the disclination line along the closed contour counterclockwise as shown in sketch (b) and count the angle Δϕ the director acquires as a result of the traverse. It is evident that after the full turn $\Delta\phi = m\pi$ where $m = 0, 1, 2\ldots$ and, by convention, the strength $s = m/2$. In fact, we deal with a solution of the Laplace equation, see the next paragraph. Let us count Δϕ from the horizontal axis in Fig. 8.14. Then, upon the traverse in the counter-clockwise direction, for disclinations of strength $s = \pm 1/2$ and $s = \pm 1$, the

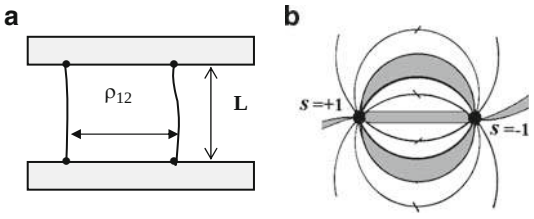

Fig. 8.13 Two disclinations fixed by their end at the two glasses limiting a layer of a nematic liquid crystal. They interact with each other by the elastic force proportional to $1/\rho_{12}$ (**a**). The structure of the director field **n**(**r**) near the two disclinations of positive and negative strength and four dark brushes corresponding to the $s = \pm 1$ disclinations (**b**)

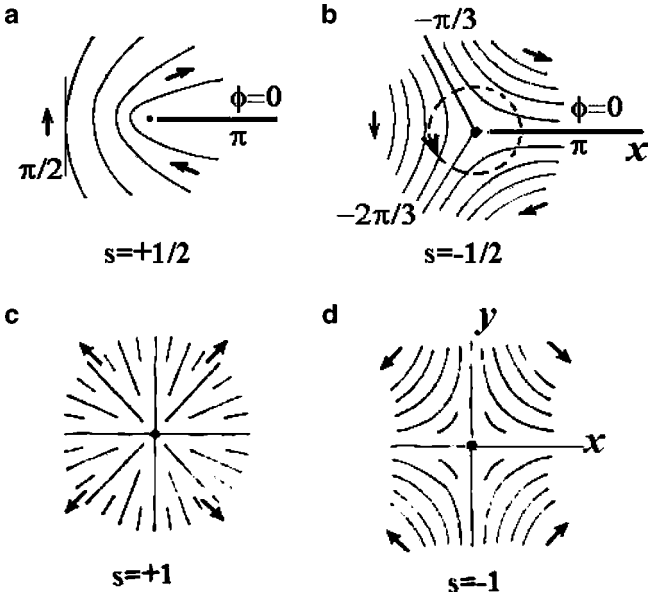

Fig. 8.14 Structure of the director field $\mathbf{n}(\mathbf{r})$ around a disclination of different strength s. The values of s $= \pm 1/2$ and ± 1 are shown under each sketch

director angle changes through $\pm\pi$ and $\pm 2\pi$, respectively. The presence of disclinations of strength $s = \pm 1/2$ is a characteristic feature of any liquid crystalline phases with head-to-tail symmetry, $\mathbf{n} = -\mathbf{n}$.

Note that the dark brushes in Fig. 8.11 mark the areas where the director is either parallel or perpendicular to a polariser crossed with analyser. Therefore, a number of brushes attached to a disclination (either 2 or 4 in the photo) is $N = 4s$. In Fig. 8.13b the scheme is shown of the four brushes attached to two disclinations of opposite sign ($s = \pm 1$) corresponding to Fig. 8.14a, b. As to the sign of s, it can be established by a rotating of a pair of crossed polarisers: for their clockwise rotation the brushes rotate either clockwise (sign +) or anticlockwise (sign −). Note the analogy with the electric charges: $s = +1$ corresponds to a source and $s = -1$ to a drain. Correspondingly the director lines are divergent or convergent. The lines of $\mathbf{n}(\mathbf{r})$ are similar to the electric field lines, see Fig. 8.13b. Defects of the same strength but opposite sign may annihilate with each other as the electric charges of opposite sign do. It happens, e.g., at temperatures close to the nematic-isotropic transition.

8.4.2.2 The Director Field Around Disclination

The problem is to find the distribution of the director around a disclination [14]. To solve it we can use the elasticity theory discussed in Section 8.3. Let a liquid crystal layer is situated in the x, y plane of drawing, and singularity L is parallel to the

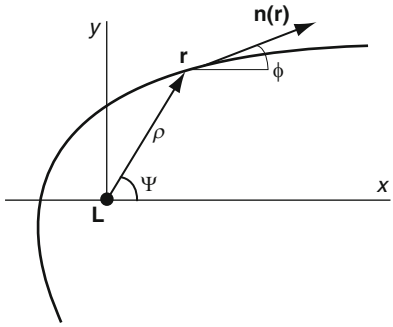

Fig. 8.15 Geometry for calculation of the director distribution around a disclination L. Ψ is the azimuthal angle for an arbitrary point **r** in the x, y plane of the nematic layer; φ is the director angle in point **r**

normal z to the layer, see Fig. 8.15. Point L is chosen as the reference system center and **r** is radius-vector of an arbitrary point r characterized by length ρ and angle Ψ. We are going to relate the director angle $\phi(\mathbf{r})$ to the radius-vector angle $\Psi(\mathbf{r})$. The components of the director field $\mathbf{n}(\mathbf{r})$ in the x,y-plane are independent of z:

$$\mathbf{n}(\mathbf{r}) = [\cos\varphi(x,y),\ \sin\varphi(x,y),\quad 0].$$

In the one-constant approximation, the distortion free energy per unit volume is given by

$$g_{dist}(\mathbf{r}) = \frac{1}{2}K\left[\left(\frac{\partial\varphi}{\partial x}\right)^2 + \left(\frac{\partial\varphi}{\partial y}\right)^2\right] \tag{8.34}$$

Now we introduce a cylindrical coordinate frame: $x = \rho\cos\Psi, y = \rho\sin\Psi$ and z, write down the gradient of ϕ in that frame

$$\nabla\varphi = \frac{\partial\varphi}{\partial\rho}\cdot\vec{\rho} + \frac{1}{\rho}\cdot\frac{\partial\varphi}{\partial\Psi}\cdot\vec{\psi} + \frac{\partial\varphi}{\partial z}\vec{k}$$

and substitute it in 8.34. Then, neglecting the z-dependence, we get the free energy density

$$g_{dist}(\rho,\Psi,z) = \frac{1}{2}K\left[\left(\frac{\partial\varphi}{\partial\rho}\right)^2 + \frac{1}{\rho^2}\left(\frac{\partial\varphi}{\partial\Psi}\right)^2\right].$$

Further, if we consider the most important practical cases (see Figs. 8.11 and 8.14), we find that the director angle ϕ does not change too much with distance ρ from the disclination, but changes very strongly with angle Ψ. Therefore we can leave only the second term, that is the angular part, especially important for small ρ:

$$g_{dist}(\Psi) = \frac{1}{2} K \frac{1}{\rho^2} \left(\frac{\partial \varphi}{\partial \Psi} \right)^2 \tag{8.35}$$

The corresponding Euler equation (8.24)

$$K \frac{\partial^2 \varphi}{\partial \psi^2} = 0 \tag{8.36}$$

has the general solution $\varphi = A\Psi + \varphi_0$. As follows from Fig. 8.14, the change of angle ϕ by 2π corresponds to the same director field, and the first arbitrary constant A must satisfy condition $A = \pm 1, \pm 2, \ldots$ for any nematic liquid crystals (a polar nematic included). For unpolar ones (e.g., conventional nematics) $A = \pm 1/2, \pm 1, \pm 3/2 \ldots$ Therefore, $A = s$ (the disclination strength) and the director angle at any azimuth Ψ is found:

$$\varphi = s\Psi + \varphi_0 \tag{8.39}$$

For instance, $s = 0$ corresponds to a uniform state with the director oriented at angle ϕ_0 with respect to the x-axis. In the case of $s = +1/2$ shown in Fig. 8.14a, counting Ψ counterclockwise from the horizontal line x where $\phi_0 = 0$ and $\Psi_0 = 0$, we find from (8.39) that the director changes its direction from 0 to π as shown in the figure by two arrows.

8.4.2.3 Energy of a Disclination

We are interested in the elastic energy stored around the disclination per its unit length, $l = 1$, see Fig. 8.16. The free energy is given by the same Eq. (8.35) and the limits for integration correspond to the sample radius $\rho_{\max}$ and a *core* of the disclination a that is excluded from consideration:

$$F_{discl} = \frac{1}{2} K \int_0^{2\pi} d\psi \int_a^{\rho_{\max}} \frac{1}{\rho^2} \left(\frac{d\varphi}{d\psi} \right)^2 \rho d\rho \tag{8.40}$$

As $d\varphi/d\Psi = s$, the energy of a disclination per unit length

$$F_{discl} = \pi K s^2 \ln\left(\rho_{\max}/a\right) \tag{8.41}$$

diverges logarithmically when $\rho \to \infty$. However, this condition is not realistic because all preparations have finite limits and there are also additional confinements due, for instance, to other defects, etc. In practice, $\rho_{\max} \approx 10 - 100$ μm, $a \approx 10$ nm, $\ln(\rho_{\max}/a) \approx 10$ and $F_{discl} \approx 30\ K \approx 3.10^{-5}$ erg/cm (or 3.10^{-10} J/m).

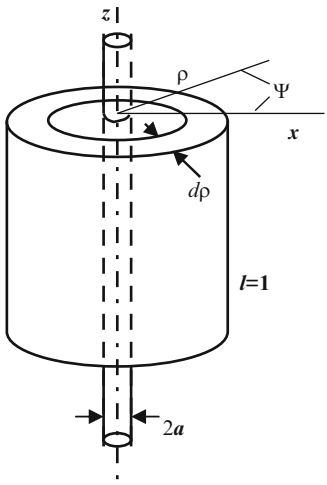

Fig. 8.16 Geometry for calculation of the energy of a linear disclination with radius a ($l = 1$ is unit length)

If there are two disclinations separated by distance ρ_{12}, then the energy of their interaction per unit thickness of the sample $L = 1$ (see Fig. 8.13a) follows from (8.41):

$$W_{12} \approx -2\pi K s_1 s_2 \ln \rho_{12}/a \tag{8.42}$$

The force of interaction between them $dW/d\rho$ is proportional to $1/\rho_{12}$. Here we see an analogy with the force of interaction between two infinite parallel wires carrying electric currents. For disclinations of opposite sign $s_1 s_2 < 0$ the interaction energy is positive and decreases with decreasing distance. Therefore such disclinations attract each other.

8.4.3 Point Singularities and Walls

8.4.3.1 Point Singularities in the Bulk (Hedgehogs)

There are some military applications of hedgehogs like a barbed wire or hedgehogs against tanks, Fig. 8.17a. In the peaceful field of liquid crystals, at a certain temperature, hedgehogs are observed in spherical drops of nematics floating in an isotropic liquid. A conoscopic image of such a drop is shown in the same figure (b). The liquid provides an alignment of the director perpendicular to the boundary. Then, in the centre of the drop, appears a point defect (c) called *hedgehog* that has radial distribution of the director around it. Two such hedgehogs interact with each other very specifically: their interaction energy is proportional to the distance

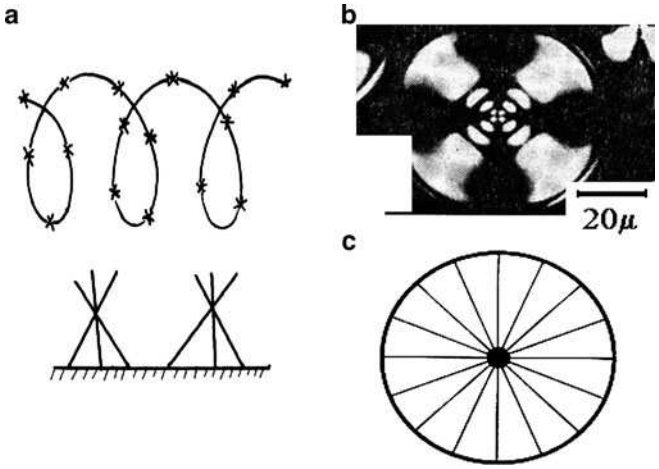

Fig. 8.17 *Hedgehogs*. Some military applications (**a**), a conoscopic image of a spherical nematic drop floating in an isotropic liquid (**b**), and the structure of the director inside the drop with a point defect in the center called a hedgehog (**c**)

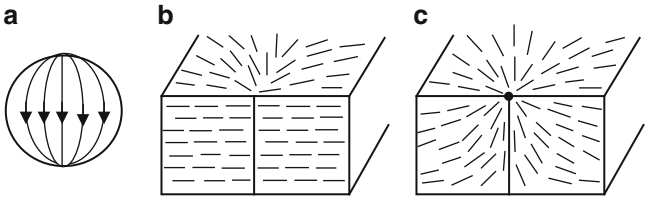

Fig. 8.18 *Boodjooms*. Structure of the director with two boodjooms in a nematic drop with tangential alignment of molecules at the surfaces (**a**), linear disclination with a point defect at the boundary of a nematic layer (**b**), and the same point defect (boodjoom) after annihilation of the linear disclination (**c**)

between them, as between two quarks. Such an interesting analogy has been discussed in the literature [15].

8.4.3.2 Point Singularities at the Surfaces (Boodjooms)

A variation of temperature or the chemical content of the isotropic solvent for the nematic drops results in a change of the alignment of the liquid crystal at the drop boundary from perpendicular (homeotropic) to parallel (homogeneous). Then the director pattern within the drop changes from that containing one singular point in the centre (hedgehog, Fig. 8.17c) to the new pattern with two singular points at the "north" and "south" poles. These are defects with a funny name boodjooms, coming from L. Carrol's story "Alice in the Wonderful Land", are seen in Fig. 8.18a.

Another example is formation of boodjooms at the cell surfaces. Now we are interested not in the linear disclinations responsible for the Schlieren texture but in their nuclei at the solid substrates limiting a liquid crystal cell. The linear disclinations of strength $s = \pm 1$ may annihilate within the bulk due to some reconstruction of the director field induced, for instance, by temperature or a flow of the material. For example, a bulk disclination of strength $s = +1$ shown by the solid vertical line in Fig. 8.18b disappears but its nuclei localized at the surfaces transform into new, surface defects. Fig. 8.18c illustrates the situation at one of the two surfaces. The escaped line leaves behind it a boodjoom. We meet such a situation in thick planar cells where the Schlieren textures with four brushes are observed.

8.4.3.3 Walls

Walls are two-dimensional defects or planes separated area of the liquid crystals with different director alignment. We met them once when having discussed the Volterra process. Another well known example is the so-called hybrid cell, in which the initial alignment of the director is parallel to one boundary surface $\vartheta(0) = \pi/2$ and perpendicular to the other $\vartheta(d) = 0$. In such a cell, the structure of the director field in the bulk is degenerate in the sense that the elastic energy is the same for the two director patterns shown in Fig. 8.19. Between the two orientations with $+\vartheta(z)$ or $-\vartheta(z)$, there is a defect plane (a wall) where the director changes its orientation within a very narrow layer. When we look at the texture in a polarization microscope (top view in the same figure) we can see thin lines separating the area with $\pm\vartheta(z)$ tilt. The total areas occupied by the $+\vartheta$ and $-\vartheta$ domains are approximately equal. At the normal incidence of light, the areas of different tilt look similarly but the walls between them are well seen. Such degeneracy in hybrid cells can be removed by special treatment of a planar surface providing a small pretilt angle $\vartheta(0) < \pi/2$.

Another example is a twist nematic cell with a planar orientation of the director at both boundaries $\vartheta = \pi/2$ differing by their azimuth, $\varphi = 0$ and $\pi/2$. In such cells, the areas with the director twist in the bulk by angle $+\pi/2$ and $-\pi/2$ have the same

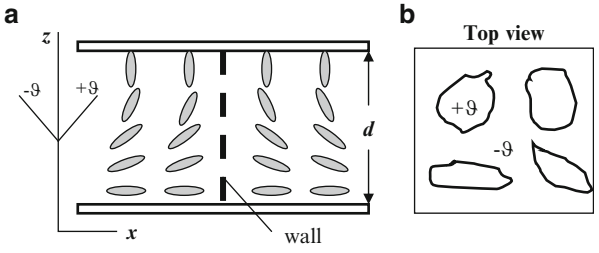

Fig. 8.19 Walls. Hybrid nematic cell with planar and homeotropic director alignment at opposite boundaries with a wall between the two degenerate patterns differing by a tilt angle sign (**a**), and the top view on the different tilt areas surrounded by walls (**b**)

energy. They are separated by walls, which scatter light. In the display technology, a small amount of a chiral impurity is added to a nematic material in order to remove the degeneracy.

8.4.4 Defects in Cholesterics

8.4.4.1 Singular τ- and λ-Lines in the Planar Texture

We have briefly discussed the cholesteric Grandjean texture in Section 4.7.4. In that case the defects appear in the wedge-type cells having continuously changing thickness. But even in the planar cholesteric texture observed along the helical z-axis, we may see some defects, namely, singular lines which are more complex than the corresponding disclinations in the nematic phase. A cholesteric may be represented by a stuck of quasi-layers with interlayer distance $P_0/2$. Therefore, we can use some concepts of dislocation theory from the solid state physics. To understand the appearance of such defects consider again the Volterra process [16].

In Fig. 8.20a we see a stack of the quasi-layers with vertical helical axis. The dash and dot lines show the orientation of the director parallel and perpendicular to the plane of drawing, respectively. We make a virtual cut S along a dash line terminated by point L and then separate two lips as shown by two arrows in the figure. The borders of the gap S_1 and S_2 are turned correspondingly up and down through angles $\pm\pi/2$. Then we add some cholesteric material to the right of the S_1–S_2 line with layers orientated parallel to the initial helical axis. Note that the director is not discontinuous at S_1–S_2 line, Fig. 8.20b. Finally, the structure relaxes and we arrive at a new situation with linear defect τ^- shown in sketch (c). The director is discontinuous at the core of line L where $\mathbf{n}\perp$L. This singular line (disclination) is called τ^- -line. If, from the beginning, we had made a cut S along the neighbour quasi-layer with the director perpendicular to the cut (shown

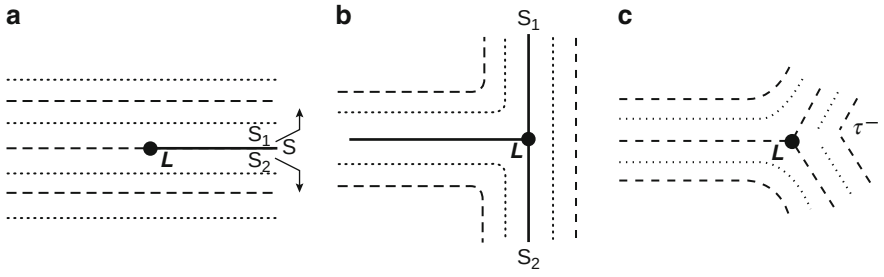

Fig. 8.20 Volterra process. A stack of the cholesteric quasi-layers with vertical helical axis and a cut S shown by the solid line terminated in point L (**a**). The cut is open up-down and the cholesteric material is added on the right of the cut (**b**). The final structure of the quasi-layers after relaxation leaving a line defect τ^- (**c**)

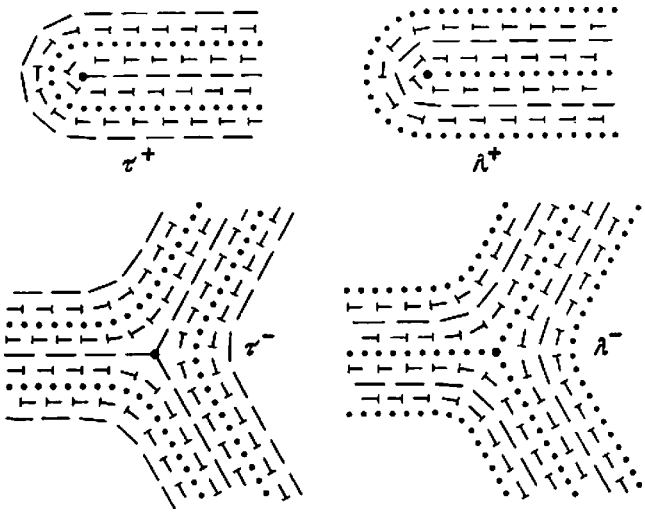

Fig. 8.21 Structure of the director field around different singular lines (disclinations) in a cholesteric liquid crystal: τ^-, λ^- and τ^+, λ^+. Signs (−) and (+) correspond to different Volterra processes

by dots) and repeated exactly the same procedure, we would arrive at another structure with a new distribution of the director and a singular line called λ^- -line. The latter has no core because the director $\mathbf{n} \| \mathbf{L}$ is continuous at this disclination. The structures of the director around the τ^-- and λ^--lines are compared in Fig. 8.21 (lower plot). There are also τ^+- and λ^+ singular lines shown in Fig. 8.21 (upper plot) which can be obtained using another type of the Volterra process, see [16] for details.

8.4.4.2 Defects in the Polygonal or Fingerprint Textures

When the limiting glasses are treated by a surfactant, the director aligns perpendicular to boundaries. Such an alignment (homeotropic) is, in principle, hardly compatible with the helical structure shown in the Inset to Fig. 8.22 and a number of defects form. A typical polygonal texture (another name is *finger-print texture*) is shown in the photo (same figure). By measuring the distance l between neighbour stripes we can determine the pitch of the helix from the microscopic observations ($P_0 = 2\,l$). Another type of defects in this geometry is focal-conic domains related to the quasi-lamellar structure of a cholesteric. They are not so well pronounced as similar domains in the genuine lamellar phases, such as the smectic A phase, and we shall see their features in the next Section.

Earlier in Section 4.8 we discussed the blue phases observed in cholesterics close to the transition to the isotropic phase. The whole appearance of the blue phase is owed to the defects, which form a three dimensional lattice.

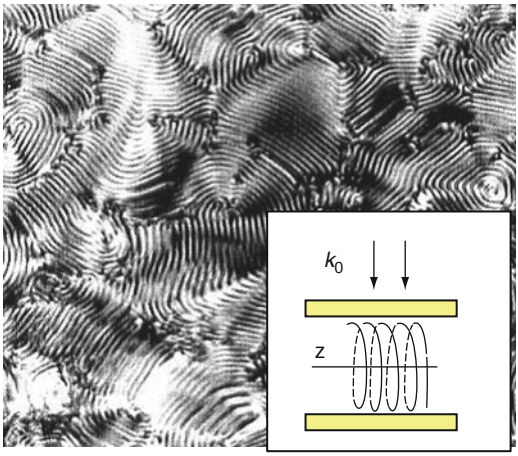

Fig. 8.22 Microscopic finger-print texture of the cholesteric phase observed in geometry shown in the *Inset*; *arrows* indicate the direction of the incident light on the texture

8.5 Smectic Phases

8.5.1 Elasticity of Smectic A

8.5.1.1 Free Energy

SmA is a one-dimensional lamellar crystal with the interlayer distance almost rigidly fixed. In order to discuss elasticity we need an additional variable that would describe the lamellar structure. Consider a small distortion of smectic layers [17]. In Fig. 8.23 dash and solid lines indicate undisturbed and distorted layers, respectively. Short rods perpendicular to the lowest solid line indicate local directors, which are always perpendicular to the layers. Now, we introduce a layer displacement along the z-axis, $u = u_z$. In fact, it is a scalar field $u_z(x, y, z)$, depending generally on all the three co-ordinates. Its derivatives describe two types of elasticity:

1. Elasticity $\partial u/\partial z$ corresponding to a change in the interlayer distance due to compressibility along z
2. Elasticity due to layer curvature $\partial u/\partial x$ and $\partial u/\partial y$. As seen from the figure, the director angle ϑ in the x, z plane for small distortions is given by $\vartheta \approx \partial u/\partial x = -\delta n \approx -n_x$.

   Due to uniaxiality, the same is true for n_y and all the three components are

$$n_x = -\frac{\partial u}{\partial x} << 1; n_y = -\frac{\partial u}{\partial y} << 1; n_z \approx 1 \tag{8.43}$$

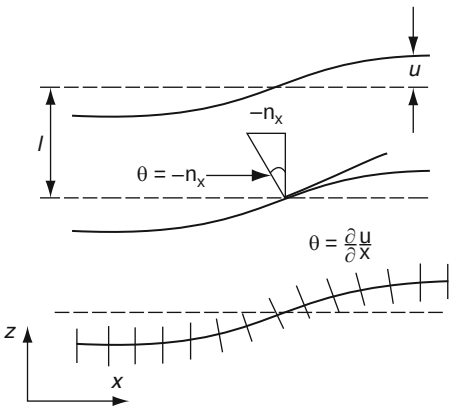

Fig. 8.23 Distortion of smectic layers (*solid lines*) from their equilibrium position (*dash lines*). In the SmA phase, the director shown by short rods crossing the lower layer is always parallel to the layer normal

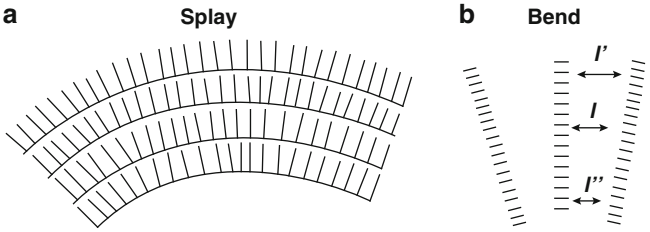

Fig. 8.24 A splay (**a**) and bend (**b**) distortion of smectic A

The distortion free energy density can be expanded around its equilibrium value g_0, but, in the simplest case, only quadratic components are held:

$$g_{dist} = g_0 + \frac{1}{2}B\left(\frac{\partial u}{\partial z}\right)^2 + \frac{1}{2}K_{11}\left(\frac{\partial^2 u}{\partial x^2} + \frac{\partial^2 u}{\partial y^2}\right)^2 \tag{8.44}$$

Here B and K_{11} are moduli of layer compressibility and layer curvature, respectively.

Why does the free energy density acquire this particular form? First, in the curvature term with modulus K_{11}, we must use the second derivatives because the first derivatives correspond to a pure rotation of all the layers that does not cost energy. The higher derivatives are ignored for small distortions. For the compressibility term, the first derivative ($\partial u/\partial z$) is sufficient. Second, both the compressibility and the curvature terms must be squared due to head-to-tail symmetry and parabolic form of the density increment g_{dist}-g_0 as a function of distortion (Hooke's law). However, the question arises why is only splay modulus K_{11} taken into account in (8.44) and not the other two Frank moduli K_{22} and K_{33}. Considering the splay and bend distortions of the SmA phase in Fig. 8.24 we can see that only the splay distortion is allowed because it leaves the interlayer distance and the

layer thickness unchanged. The bend would evidently change an interlayer distance, $l \neq l'$ or l'', that would require too much energy. The absence of twist corresponds to scalar product n·curln = 0 in the Frank energy (8.16). This condition is fulfilled for the director components $n_x = -\partial u/\partial x$ and $n_y = -\partial u/\partial y$, $n_z = 1$ because curl$\mathbf{n} = (\partial^2 u/\partial z \partial y)\mathbf{i} - (\partial^2 u/\partial z \partial x)\mathbf{j}$ and $\mathbf{n} = \mathbf{k}$. Thus, in (8.44) we may hold the single curvature modulus K_{11}.

The order of magnitude of the splay modulus is the same as that in nematics $K_{11} \approx 10^{-7} - 10^{-6}$ dyn (or $10^{-12} - 10^{-11}$ N in SI system). Modulus B found for a liquid crystal 8OCB at temperature 60°C is $B = 8 \cdot 10^6$ erg/cm^3 (or $8 \cdot 10^5$ J/m^3 in the SI system) [18]. In that experiment, the compression-dilatation distortion of smectic layers was induced by an external force from a piezoelectric driver.

8.5.1.2 Wave-Like Distortion

It is very instructive to consider a behaviour of the smectic layers attached to a corrugated surface. This would explain why the uniform smectic phase is much more transparent than the nematic phase. The geometry is shown in Fig. 8.25a. A solid substrate is assumed to have a one-dimensional cosine-form relief:

$$z(x) = \alpha \cos qx$$

with a period $\Lambda = 2\pi/q$. We are interested in a distance L *(penetration length)* along z, at which the distortion is smoothed out. In other words, how far do smectic layers "feel" the influence of the surface? The distortion of the layers is given by:

$$u(x, z) = u_0(z) \cos qx \quad \text{with} \quad u_0(z = 0) = \alpha.$$

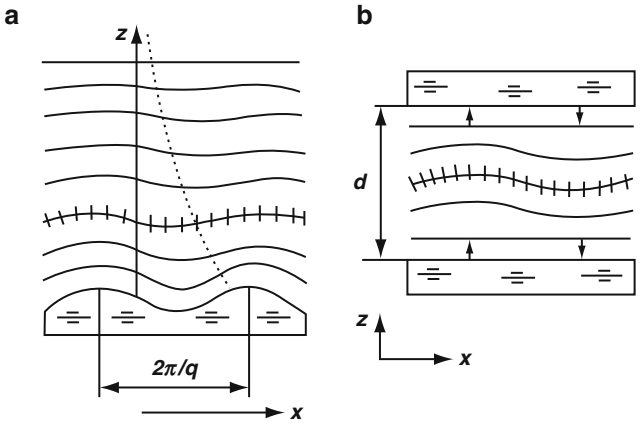

Fig. 8.25 Distortion of a homeotropically aligned SmA liquid crystal by a corrugated surface of solid boundary plate with the dotted line pictured an exponential decay of the distortion (**a**) and the wave-like splay distortions in a thin layer with the arrows indicating the direction of the induced local pressure (**b**)

The elastic energy density averaged over the *x,y*-plane reads:

$$g_{dist} = \frac{1}{2}B\left(\frac{du_0}{dz}\right)^2\langle\cos^2 qx\rangle + \frac{1}{2}K_{11}q^4u_0^2\langle\cos^2 qx\rangle$$
$$= \frac{1}{4}B\left[\left(\frac{du_0}{dz}\right)^2 + \lambda_s^2 q^4 u_0^2\right] \tag{8.45}$$

Here $<\cos^2 qx> = 1/2$ and

$$\lambda_s = \left(K_{11}/B\right)^{1/2} \tag{8.46}$$

is *a smectic characteristic length* ($\lambda \approx 1$ nm).

Now we make minimisation of (8.45) writing the Euler equation $\frac{\partial g}{\partial u_0} - \frac{d}{dz}\left(\frac{\partial g}{\partial u_0'}\right) = 2\lambda_s^2 q^4 u_0 - \frac{d}{dz}2u_0' = 0$ and get

$$\frac{d^2u_0}{dz^2} - \lambda_s^2 q^4 u_0 = 0 \tag{8.47}$$

This equation has a solution: $u_0(z) = \alpha\exp(-z/L_p)$. Thus, the distortion "propagates" into the bulk over a penetration distance

$$L_p = \frac{1}{q^2\lambda_s} = \frac{\Lambda^2}{4\pi^2\lambda_s} \tag{8.48a}$$

This distance is quite large. For instance, for period of the surface relief $\Lambda = 1$ μm and smectic length $\lambda = 1$ nm, the penetration length is 2.5 mm and the larger the period of a distortion the longer the penetration length.

The result obtained has very interesting consequences: (i) to have well aligned SmA samples, very flat glasses without corrugation are needed; (ii) even small dust particles or other inhomogeneities create characteristic defects in the form of semi-spheres (see Fig. 8.29b below) and well seen under an optical microscope; (iii) layers are often broken (not bent) by external factors: in particular, strong molecular chirality may result in the formation of defect phases like twist-grain-boundary phase; (iv) the thermal fluctuations of director in smectic A phase are weak and the smectic samples are not as opaque as nematic samples. In fact there is a critical cell thickness for short-wave fluctuations.

Consider a SmA layer of thickness d between two glasses, Fig. 8.25b. Flat surfaces stabilise the parallel arrangement of the layers while thermal fluctuations excite wave-like splay distortions. In thin cells these fluctuations are markedly suppressed: for $d>>L_p$ they are very strong, for $d<<L_p$ they are quenched for any wavevector. For a fixed cell thickness, we can find a critical wavevector q_c for

surviving fluctuations. Assume that the critical penetration length $L_{pc} = d/\pi$. Then, from (8.46), the critical wave vector is

$$q_c = \left(1/L_{cp}\lambda_s\right)^{1/2} = \left(\pi/d\lambda_s\right)^{1/2} \tag{8.48b}$$

For typical values of $d \approx 10$ μm and $\lambda \approx 1$ nm, $q_c \approx 1.8{\cdot}10^7$ m^{-1} and only those fluctuations survive whose period is less than $\Lambda < \Lambda_c = 2\pi/q_c \approx 0.35$ μm.

8.5.2 Peierls Instability of the SmA Structure

In Section 5.7.2 we discussed a general problem of stability of one, two- and three-dimensional phases. Here, we shall analyze stability of the smectic A liquid crystal, which is three-dimensional structure with one-dimensional periodicity. The question of stability is tightly related to the elastic properties of the smectic A phase. Consider a stack of smectic layers (each of thickness l) with their normal along the z-direction. The size of the sample along z is L, along x and y it is $L_\perp$, the volume is $V = L_\perp{}^2\mathrm{L}$. Fluctuations of layer displacement $u(\mathbf{r}) = u(z, r_\perp)$ along z and in both directions perpendicular to z can be expanded in the Fourier series with wavevectors q_z and $q_\perp$ (normal modes):

$$u_q = \int u(\mathbf{r}) \exp(i\mathbf{qr}) d\mathbf{r}$$

Then, on account of (8.44), the free energy of distortion in the volume $\Omega = (2\pi)^3/V$ in the wavevector space (q_x, q_y, q_z), which is a sum (or an integral in the q-space) of the energy of all normal modes, reads:

$$F = \frac{1}{2(2\pi)^3} \int_\Omega d^3q \left(Bq_z^2 + K_{11}q_\perp^4\right) |u(\mathbf{q})|^2 \tag{8.49}$$

The Gibbs distribution gives us probability of the mean square value $|u(\mathbf{q})|^2$ for a particular fluctuation of the layer distortion when the average value $\langle |u(\mathbf{q})|^2 \rangle$ for all fluctuations is known:

$$w \propto \exp\left[-\frac{V(Bq_z^2 + K_{11}q_\perp^4)|u(\mathbf{q})|^2}{k_BT}\right] = \exp\left[-\frac{|u(\mathbf{q})|^2}{<|u(\mathbf{q})|^2>}\right]$$

From this equality and using Eq. (8.49), the mean-square average of the fluctuation amplitude is found

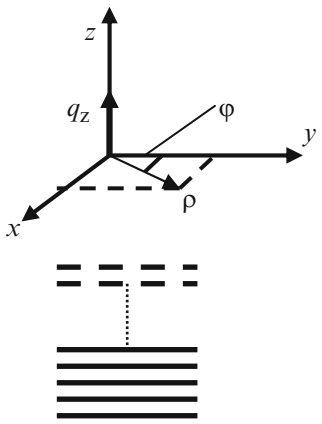

Fig. 8.26 Cylindrical coordinates selected for a stack of smectic layers that becomes unstable in the infinitely thick sample

$$\left\langle u^2(\mathbf{q})\right\rangle = \frac{k_B T}{(2\pi)^3}\int\limits_{\Omega}\frac{d^3q}{Bq_z^2 + K_{11}q_\perp^4} \tag{8.50}$$

In fact, we used the equipartition theorem showing that each normal mode has the same energy $k_BT/2$. Factor 1/2 disappeared from (8.50) because each $u(q)$ corresponds to two fluctuation modes with wavevectors $\pm q$. The integration should be made in cylindrical co-ordinates according to the symmetry of SmA, for geometry see Fig. 8.26:

$$\rho = \sqrt{q_x^2 + q_y^2} = q_\perp\sqrt{2};\quad d\rho = \sqrt{2}dq_\perp \text{ and } \rho d\rho = 2q_\perp dq_\perp,$$

Now the limits of integration are changed:

$$\frac{2\pi}{L} \le q_z \le \frac{2\pi}{l};\ \frac{2\pi}{L_\perp} \le q_\perp \le \frac{2\pi}{a_0} \text{ and } 0 \le \varphi \le 2\pi$$

Here a_0 is radius of a rod-like molecule. However, we can assume infinitely large sample in the x, y direction, $L_\perp \to \infty$ and, in addition, $a_0 \to 0$. Then, after introducing $\lambda_s = (K_{11}/B)^{1/2}$ and integrating over φ we obtain the double integral:

$$\left\langle u^2(\mathbf{q})\right\rangle = \frac{k_BT}{4\pi^2}\iint\frac{2q_\perp dq_z dq_\perp}{Bq_z^2 + K_{11}q_\perp^4} = \frac{k_BT}{4\pi^2K_{11}}\int\limits_{2\pi/L}^{2\pi/l} dq_z \int\limits_0^\infty \frac{2q_\perp dq_\perp}{\lambda_s^{-2}q_z^2 + q_\perp^4} \tag{8.51}$$

The integral over $q_\perp$ has a form $\int\limits_0^\infty \frac{dm}{k^2+m^2} = \frac{1}{k}\arctan\frac{m}{k}\Big|_0^\infty = \frac{\pi}{2k}$ where we put $k = q_z/\lambda_s$ and $m = q_\perp^2, dm = 2q_\perp dq_\perp$. Now, integrating over q_z using $dq_z = \lambda_s dk$, we arrive at the final result:

$$\left\langle u^2(\mathbf{q})\right\rangle = \frac{k_B T}{4\pi^2 K_{11}} \int_{2\pi\lambda/L}^{2\pi\lambda/l} \frac{\pi\lambda_s}{2k} dk = \frac{k_B T \lambda_s}{8\pi K_{11}} \ln\frac{L}{l} = \frac{k_B T}{8\pi (BK_{11})^{1/2}} \ln\frac{L}{l} \tag{8.52}$$

This formula shows that, when the size of the sample along the layer normal increases to infinity ($L \to \infty$) the average mean square magnitude of the fluctuation in the interlayer distance diverges, $<u^2(\mathbf{q})> \to \infty$. Formally, the ideal smectic A structure becomes unstable. However, the divergence is logarithmic that is very smooth. Such fluctuations destroy the true long-range positional order along z. Instead, the quasi-long range positional order forms that was discussed in Section 5.7.2. In experiments, the quasi-long range order manifests itself by deviation of the X-ray Bragg reflections from the δ-function form.

8.5.3 Defects in Smectic A

There are many types of defects originated from the layered structure of the smectic A phase. Here, we shall only present a brief survey of the most important cases.

8.5.3.1 Steps and Dislocations

Steps are observed at the edge of the drop of a smectic preparation on a surfactant covered glass, as shown in Fig. 8.27. In the blown part of the same figure, the structure of each step containing a single π-disclination is seen. In the three dimensional picture of Fig. 8.28, we can see a difference between the π-disclination and another defect, called an *edge dislocation* which is typical of solid crystals. In the smectic A, and additional smectic layer is incorporated between two other molecular layers, and the edge of the irregular layer forms such a dislocation.

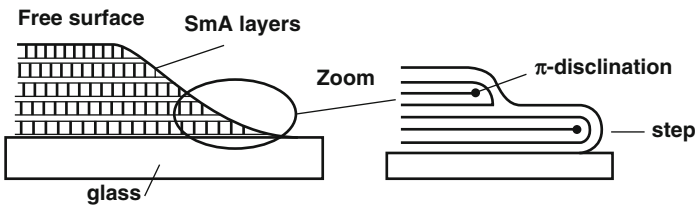

Fig. 8.27 Steps at the edge of a drop of the smectic A phase (*left*); the structure of each step containing a single π-disclination is seen in the blown part (*right*)

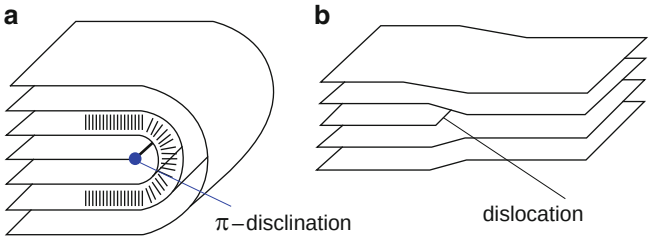

Fig. 8.28 Illustration of the difference between a π-disclination and an *edge dislocation* in the smectic A

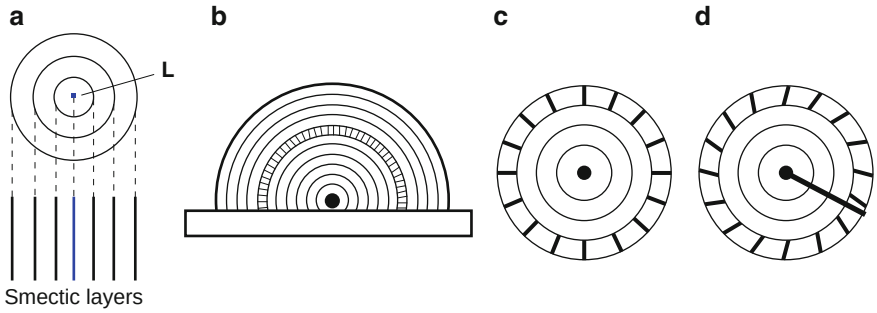

Fig. 8.29 Structure of some defects in the SmA phase, namely, cylinder (**a**), semi-sphere (**b**), and radial hedgehog (**c**) and a monopole in SmC (**d**)

8.5.3.2 Cylinders, Tores, Hedgehogs

Many structural defects compatible with the incompressible smectic layers can be observed under a microscope. Among them are cylinders, tores and hemispheres observed at the surfaces, radial hedgehogs observed in smectic drops, etc. Three of them are presented in Fig. 8.29a–c. Note that in all defect structures of this type, the splay distortion plays the fundamental role but bend and twist are absent. Other, more special defects, namely, the walls composed of screw dislocations, are observed in the TGBA phase.

8.5.3.3 Focal-Conics

These are the most striking features of smectic textures [19]. Smectic layers of constant thickness (incompressible, modulus $B \rightarrow \infty$) form surfaces called *Dupin cyclides*. We have seen some of them, which have the form of tori including disclinations, see Fig. 4.7b. Such cyclides can fill any volume of a liquid crystal by cones of different size. An example is a *focal-conic pair*, namely, two cones with a common base. The common base is an ellipse with apices at A and C and foci at O and O', see Fig. 8.30a. The hyperbola B–B' passes through focus O. The focus of

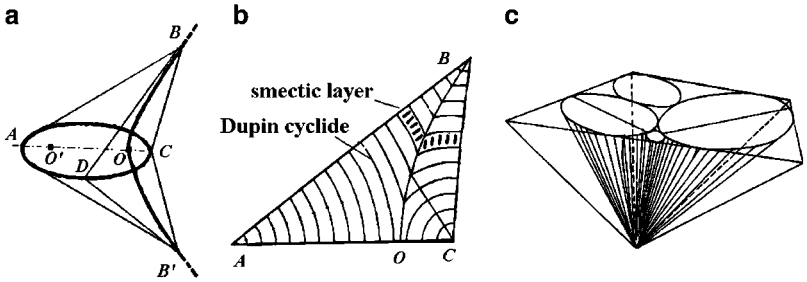

Fig. 8.30 Focal-conic defect structure in SmA: A pair of cones with a common elliptical base and a hyperbola connecting cone apices (**a**); cross-section of the upper cone by plane ABC with gaps between lines (Dupin cyclides) indicating the smectic layers (**b**); filling the space of the sample by cones of different size (**c**)

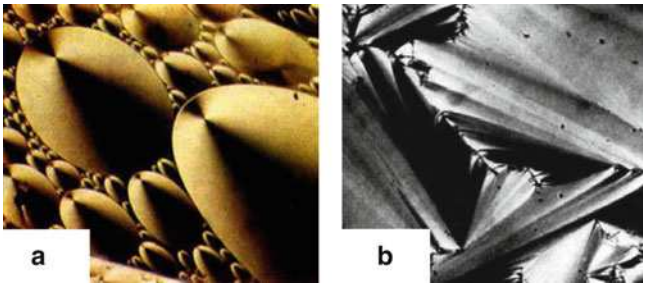

Fig. 8.31 Photos of some focal conic textures: polygonal (**a**); and fan-shape (**b**) textures

the hyperbola C coincides with the apex of the ellipse C. Using multiple lines such as BD and B'D one can build two conical surfaces with apices at B and B'.

The bulk of the cones is filled by smectic layers. Fig. 8.30b represents the cross-section of the upper cone by plane ABC. Note that along the line OB smectic layers are continuous although their slope is changed. Using such cones all the space occupied by a liquid crystal can be filled, Fig. 8.30c. It is very fascinating that such "mathematical structures" are indeed observed in experiment! A variety of observed focal conic textures is very large. The microscopic photos in Fig. 8.31, illustrate two of them. Photo (a) shows rather large but short polygons (*polygonal texture*) and photo (b) demonstrates the so-called *fan-shape texture* with very narrow, elongated polygons.

8.5.4 Smectic C Elasticity and Defects

8.5.4.1 Elastic Energy

In the smectic C phase the director is free to rotate about the normal z to the smectic layers. In the general case, the smectic layers are considered *compressible*. The elastic

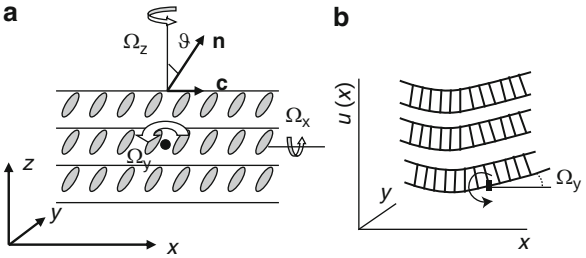

Fig. 8.32 Smectic C. Definition of rotation axes Ω_x, Ω_y and Ω_z (**a**) and layer distortion $u = u(x)$

energy of the smectic C phase may be analysed in terms of four variables, the compressibility $\gamma = \partial u/\partial z$ ($u = u_z$) as in smectics A, and three axial vectors $\mathbf{\Omega}_i(\mathbf{r})$ shown in Fig. 8.32a; the x-axis coincides with the **c**-director. Then, according to Fig. 8.32b, the derivatives of layer distortion $u = u(x)$ are given by:

$$-\frac{\partial u}{\partial x} = \mathbf{\Omega}_y \text{ and } -\frac{\partial \mathbf{\Omega}_y}{\partial x} = \frac{\partial^2 u}{\partial x^2}$$

The sign minus takes into account the sense of rotation about the y-axis. By analogy

$$\frac{\partial u}{\partial y} = \mathbf{\Omega}_x \text{ and } \frac{\partial \mathbf{\Omega}_x}{\partial y} = \frac{\partial^2 u}{\partial y^2}$$

and the rotation through angle $\mathbf{\Omega}_z$ about the z-axis does not create distortion u.

The free energy density of distortion must be a quadratic function of $\nabla\mathbf{\Omega}$. It consists of three groups of terms describing (1) the nematic-like distortion of the **c**-director (g_c), (2) distortion of the smectic layers (g_l) and (3) the cross terms (g_{cl}):

$$g = g_c + g_l + g_{cl}$$

Totally we obtain $4 + 4 + 2 = 10$ elastic moduli [9]. When the interlayer distance is fixed, only four nematic-like moduli are left (with dimension [energy/length]).

8.5.4.2 Defects in Smectics C

Like in the nematic phase, the textures of SmC reveal blurred Schlieren patterns with linear singularities of strength $s = \pm 1$. The singularities of $s = \pm 1/2$ are not observed due to the reduced symmetry (C_{2h}) of the SmC phase. Chiral smectics C* are periodic structures and the helical pitch can be measured under a microscope either from the Grandjean lines or as a distance between the lines indicating periodicity, like in Fig. 8.22 for the cholesteric phase. On the other hand, like in

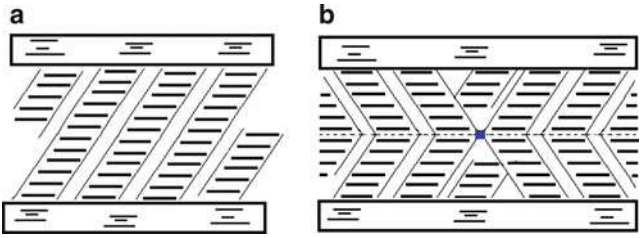

Fig. 8.33 Smectic C phase: the uniform structure (**a**) and the structure with chevrons and a disclination between them (**b**)

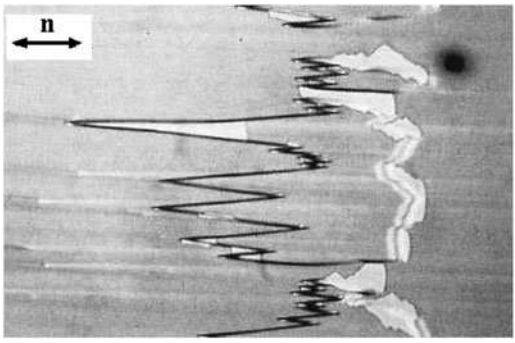

Fig. 8.34 A typical appearance of the zigzag defect in the chiral SmC* phase

SmA phase, the stepped drops as well as polygonal and fan-shape textures are also observed.

Normally, the smectic C phase should form the lowest energy uniform texture shown in Fig. 8.33a. However, more often we see so-called chevrons, see Fig. 8.33b, which usually form on cooling from the smectic A phase. In both cases, at the boundaries, molecules are aligned parallel to the surface without any tilt. The apex of a particular chevron can be oriented either to the left or to the right. The areas of the left and right chevrons are separated by a disclination line having a form of a zigzag. In the same figure, the core of such a line is pictured by the point. When observed from the top the zigzag defects are seen. One of such a zigzag is demonstrated by photo, Fig. 8.34. Such zigzag defects play the detrimental role in the displays based on SmC* ferroelectric liquid crystals.

Upon transition from the SmA to the SmC phase, due to appearance of the molecular tilt, radial hedgehogs discussed in Section 8.5.3 transform into other defects, called monopoles. Their characteristic feature is a disclination line going from the centre along a radius, Fig. 8.29d. The name "monopole" was inherited from the Dirac magnetic monopole, an isolated magnetic charge in the form of the hedgehog with an adjacent singularity in the field of the magnetic vector-potential $\mathbf{A}(\mathbf{r})$. The mathematical treatment of the magnetic monopole (not discovered yet) and SmC monopole observed in smectic drops is very similar [15].

References

1. Dunmur, D., Toriyama, K.: Elastic Properties. In: Demus, D., Goodby, J., Gray, G.W., Spiess, H.-W., Vill, V. (eds.) Physical Properties of Liquid Crystals, pp. 151–178. Wiley-VCH, Weinheim (1999)
2. Feynman, R.P., Leighton, R.B., Sands, M.: The Feynman Lectures on Physics, vol. 2. Addison-Westley, Reading, MA (1964)
3. Landau, L.D., Lefshitz, E.M.: Theory of Elasticity, 3rd edn. Nauka, Moscow (1969) (in Russian) (see also Theory of Elasticity. Pergamon, London (1959))
4. Sluckin, T.J., Dunmur, D.A., Stegemeyer, H.: Crystals that flow: Classic Papers in the History of Liquid Crystals. Taylor & Francis, London (2004) (Sect. C, pp. 139–161; 335–363)
5. Oseen, C.W.: The theory of liquid crystals. Trans. Faraday Soc. **29**, 883–899 (1933)
6. Ericksen, J.L.: Hydrostatic theory of liquid crystals. Arch. Rat. Mech. Anal. **9**, 371–378 (1961)
7. Frank, F.C.: On the theory of liquid crystals. Disc. Faraday Soc. **25**, 19–28 (1958)
8. Kleman, M., Lavrentovich, O.: Soft Matter Physics. Springer, New York (2003)
9. De Gennes, P.G., Prost, J.: The Physics of Liquid Crystals, 2nd edn. Clarendon Press, Oxford (1995)
10. Lavrentovich, O.D., Pergamenshchik, V.M.: Patterns in thin liquid crystal films and the divergence ("surfacelike") elasticity. In: Kumar, S. (ed.) Liquid Crystals in the Nineties and Beyond" S, pp. 251–298. World Scientific, Singapore (1995)
11. Blinov, L.M., Chigrinov, V.G.: Electrooptic Effects in Liquid Crystalline Materials. Springer, New York (1993)
12. De Gennes, P.G.: Fluctuations d'orientation et diffusion Rayleigh dans un cristal nématique. C.R. Acad. Sci. Paris **266**, 15–17 (1968)
13. Ornstein, L.S., Kast, W.: New arguments for the swarm theory of liquid crystals. Trans. Farad. Soc. **29**, 930–944 (1933)
14. Vertogen, G., de Jeu, W.H.: Thermotropic Liquid Crystals. Fundamentals. Springer, Berlin (1987)
15. Kurik, M.V., Lavrentovich, O.D.: Defects in liquid crystals: homotopic theory and experimental investigations. Usp. Fiz. Nauk. **154**, 381–431 (1988) [Sov. Phys. Uspekhi 31, 196 (1988)]
16. Kléman, M.: Points, Lines and Walls. Wiley, Chichester (1983)
17. De Gennes, P.G.: Conjectures sur l'etat smectique. J. Physique (Paris) 30, Colloq. C.4, C4-62–C4-68 (1969)
18. Bartolino, R., Durand, G.: Plasticity in a smectic A liquid crystal. Phys. Rev. Lett. **39**, 1346–1349 (1977)
19. Bouligand, Y.: Defects and textures. In: Demus, D., Goodby, J., Gray, G.W., Spiess, H.-W., Vill, V. (eds.) Physical Properties of Liquid Crystals, pp. 304–374. Wiley-VCH, Weinheim (1999)

Chapter 9
Elements of Hydrodynamics

9.1 Hydrodynamic Variables

We shall discuss here the macroscopic dynamics of liquid crystals that is an area of hydrodynamics or macroscopic properties related to elasticity and viscosity. With respect to the molecular dynamics, which deals, for example, with NMR, molecular diffusion or dipolar relaxation of molecules, the area of hydrodynamics is a long scale, both in space and time. The molecular dynamics deals with distances of about molecular size, $a \approx 10$ Å, i.e., with wavevectors about 10^7 cm^{-1}, however, in the vicinity of phase transitions, due to critical behaviour, characteristic lengths of short-range correlations can be one or two orders of magnitude larger. Therefore, as a limit of the hydrodynamic approach we may safely take the range of wavevectors $q \ll 10^6$ cm^{-1} and corresponding frequencies $\omega \ll c_s q \approx 10^5 \cdot 10^6 = 10^{11}$s^{-1} ($c_s$ is sound velocity).

In the hydrodynamic limit one considers only those variables whose relaxation times decrease with increasing wavevector of the corresponding visco-elastic modes. For instance, a small vortex made by a spoon in a glass of tea relaxes faster than a whirl in a river, or, after a tempest, short waves at the sea surface disappear faster then waves with a large period. The relaxation of cyclones in atmosphere takes days or weeks. As a rule, the hydrodynamic relaxation times follow the law $\tau \sim Aq^{-2}$. The strings of a guitar also obey the same law.

For the isotropic liquid, one introduces five variables related to the corresponding conservation laws. The variables are density of mass ρ, three components of the vector of linear momentum density $m\mathbf{v}$, and density of energy E. When electric charges enter the problem, the conservation of charge must be taken into account. Then we are in the realm of *electrohydrodynamics*.

For nematic liquid crystals, the symmetry is reduced and we need additional variables. The nematic is degenerate in the sense that all equilibrium orientations of the director are equivalent. According to the Goldstone theorem the parameter of degeneracy is also a hydrodynamic variable; for a long distance process $q \to 0$ and the relaxation time should diverge, $\tau \to \infty$. In nematics, this parameter is the director $\mathbf{n}(\mathbf{r})$, the orientational part of the order parameter tensor. For a finite distortion of the director over a large distance ($L \to \infty$), the distortion wavevector $q \to 0$ and the

L.M. Blinov, *Structure and Properties of Liquid Crystals*,
DOI 10.1007/978-90-481-8829-1_9,

orientational relaxation requires infinite time. By the way, the magnitude S of the order parameter tensor is not a hydrodynamic variable. The director field **n**(**r**) is indeed an independent variable, because it may rotate even in the immobile nematic phase, for example, in the case of the pure twist distortion induced by a magnetic field. On the other hand a flow of the nematic can influence the vector field **n**(**r**) and vice versa. Thus, two variables **v**(**r**) and **n**(**r**) are coupled. Together with two components of the director (due to the constraint $\mathbf{n}^2 = 1$) the number of hydrodynamic variables for a nematic becomes seven [1,2].

For discussion of dynamics of lamellar *smectic phases* it is important to include another variable, the layer displacement u (**r**) [3] or, more generally, the phase of the density wave [4]. This variable is also hydrodynamic: for a weak compression or dilatation of a very thick stack of smectic layers ($L \to \infty$) the relaxation would require infinite time. On the other hand, the director in the smectic A phase is no longer independent variable because it must always be perpendicular to the smectic layers. Therefore, total number of hydrodynamic variables for a SmA is six. For the smectic C phase, the director acquires a degree of freedom for rotation about the normal to the layers and the number of variables again becomes seven.

Why we are interested in hydrodynamics? Because we are interested in variety of flow phenomena in different geometry, the variety of viscosities of liquid crystals in different regimes, enormous viscosity of helical and layered structures, understanding of thermal convection, flow instabilities, etc. Moreover, in an external electric field, the electrohydrodynamic instabilities arise which need a background for their interpretation. At first, however, we recall hydrodynamics of an isotropic liquid.

9.2 Hydrodynamics of an Isotropic Liquid

Our task is to derive the equation for motion of the isotropic liquid in order to prepare a soil for discussion the dynamic properties of nematics. In this Section, we follow the approach [5] using two conservation laws.

9.2.1 Conservation of Mass Density

Consider conservation of mass density, $\rho(x, y, z, t)$. The mass continuity equation comes from consideration of the balance of the mass density in the volume V and its flux through the surface surrounding the volume with subsequent application of the Gauss theorem:

$$\frac{\partial \rho}{\partial t} = -\nabla \rho \mathbf{v} + \text{sources} \tag{9.1}$$

Here the velocity $\mathbf{v}(x, y, z, t)$ of a liquid is "measured" in a particular fixed point in space x, y, z. It is not the velocity of a small unit volume of moving liquid. "Sources" mean the presence of sources and sinks in the volume discussed. If we are not interested in propagation of sound i.e. ignore a local compression and dilatation we may put $\delta\rho = 0$ and $\rho = \text{const}$. Then, it is the case of *incompressible liquid*:

$$\partial\rho/\partial t = -\rho\nabla\mathbf{v} + \text{sources}$$

and, in the stationary regime, $\text{div}\mathbf{v} = \text{sources}$.

For the subsequent discussion let us write down the continuity equation in the tensor form:

$$\frac{\partial\rho}{\partial t} = -\frac{\partial(\rho v_j)}{\partial x_j} + \text{sources} \tag{9.2}$$

9.2.2 Conservation of Momentum Density

9.2.2.1 Ideal Liquid

Consider now the conservation of momentum density (or linear momentum vector $\rho\mathbf{v}$). First we write this law for the ideal (without viscosity) liquid in two different presentations. The *Lagrange form* of the equation of motion of the element of liquid coincide with the Newton form ($md\mathbf{v}/dt = \mathbf{F}$):

$$\rho\frac{d\mathbf{v}}{dt} = -\text{grad}\ p + \mathbf{f} \tag{9.3}$$

Here, p is scalar pressure, vector $\mathbf{f}$ is the volume force in (dyn/cm^3) coming, e.g., from the gravity, electric or magnetic field (e.g., for gravity force $\mathbf{f} = \rho\mathbf{g}$) and vector $\mathbf{v}$ is *velocity of moving liquid particle* as if the measuring device is placed on the particle. However, in hydrodynamics, the velocity is usually considered as a *vector field* defined in each point of the space. The change of velocity $d\mathbf{v}$ within time interval dt consists of two terms: one of them, namely, $(\partial\mathbf{v}/\partial t)dt$ is taken at fixed coordinates x, y, z of the reference point and the other part is delivered by different particles arriving from the neighbor points located at a distance $d\mathbf{r} = dx\mathbf{i} + dy\mathbf{j} + dz\mathbf{k}$ from the reference point (the so-called convective term):

$$dx(\partial\mathbf{v}/\partial x) + dy(\partial\mathbf{v}/\partial y) + dz(\partial\mathbf{v}/\partial z) = (d\mathbf{r}\nabla)\mathbf{v}.$$

Therefore, the total velocity *in the reference point* satisfies the equation

$$\frac{d\mathbf{v}}{dt} = \frac{\partial \mathbf{v}}{\partial t} + (\mathbf{v}\nabla)\mathbf{v}, \tag{9.4}$$

where $(\mathbf{v}\nabla\mathbf{v})$ is called convection term. Correspondingly the equation of the motion of an ideal liquid in the *Euler form* is given by:

$$\rho \frac{\partial \mathbf{v}}{\partial t} + \rho(\mathbf{v}\nabla)\mathbf{v} = -\text{grad}\ p + \mathbf{f} \tag{9.5}$$

The same equation can be written in the tensor form:

$$\rho \frac{\partial v_i}{\partial t} = -\rho v_j \frac{\partial v_i}{\partial x_j} - \frac{\partial p}{\partial x_i} + f_i \tag{9.6}$$

Now we define the rate of the momentum change:

$$\frac{\partial \rho \mathbf{v}}{\partial t} = \rho \frac{\partial \mathbf{v}}{\partial t} + \frac{\partial \rho}{\partial t}\mathbf{v}$$

or in tensor notations

$$\frac{\partial}{\partial t}\rho v_i = \rho \frac{\partial v_i}{\partial t} + \frac{\partial \rho}{\partial t} v_i$$

and rewrite this rate on account of Eqs. (9.6) and (9.2):

$$\frac{\partial \rho v_i}{\partial t} = -\rho v_j \frac{\partial v_i}{\partial x_j} - v_i \frac{\partial (\rho v_j)}{\partial x_j} - \frac{\partial p}{\partial x_i} + f_i \tag{9.7}$$

Using identity $\partial p/\partial x_i \equiv \delta_{ij}\partial p/\partial x_j$ with Kronecker symbol δ_{ij} we may present the result in the compact form of the *law of momentum conservation* for the ideal liquid:

$$\frac{\partial}{\partial t}\rho v_i = -\frac{\partial \Pi_{ij}}{\partial x_j} + f_i \tag{9.8}$$

where a symmetric second rank tensor

$$\Pi_{ij} = p\delta_{ij} + \rho v_i v_j, \tag{9.9}$$

is called *tensor of momentum density flux* (in units dyn/cm^2). It includes only the reversible part of the momentum transfer, because there is no energy dissipation by the flow of the ideal liquid. Note that the form of Eq. (9.8) is very similar to the form of density conservation law (9.2).

9.2.2.2 Viscous Liquid

For viscous liquids the law for the mass conservation remains unchanged. As to the momentum density conservation, it keeps the same form (9.8) but tensor Π_{ij} should be changed to take the dissipation into account. Now we write

$$\Pi_{ij} = p\delta_{ij} + \rho v_i v_j - \sigma'_{ij} = -\sigma_{ij} + \rho v_i v_j \tag{9.10}$$

The new tensor

$$\sigma_{ij} = -p\delta_{ij} + \sigma'_{ij} \tag{9.11}$$

called stress tensor, includes the pressure term -$p\delta_{ij}$ and the term σ'_{ij} called *viscous stress tensor*. The latter describes the irreversible transfer of momentum in a moving liquid.

Now let us try to imagine the form of tensor σ'_{ij}. In Fig. 9.1, the upper part of the liquid is moving, the lower part is immobile. The components of σ'_{ij} are the tangential shear forces acting on a unit area having its normal along the x_j-axis while the liquid moves along the x_i-axis. This force is caused by the gradients of momentum $\partial\rho v_i/\partial x_j$ (or just velocity gradients $\partial v_i/\partial x_j$ in case of incompressible liquid with constant ρ) otherwise there is no friction force. The momentum is transferred from upper to lower layers (momentum flux). The correct form of this tensor should exclude the rotation of a liquid as a whole because such a rotation does not result in friction at all. Therefore we write a *symmetric* shear rate tensor for the incompressible liquid as we did earlier Eq. (8.6) when we discussed the shear distortion of the solid (soft) matter [6]:

$$A_{ij} = \frac{1}{2}\left(\frac{\partial v_i}{\partial x_j} + \frac{\partial v_j}{\partial x_i}\right) \tag{9.12}$$

Then, for not very strong gradients, there should be linear relationship between σ'_{ij} and A_{ij} and we may write

$$\sigma'_{ij} = \eta\left(\frac{\partial v_i}{\partial x_j} + \frac{\partial v_j}{\partial x_i}\right) \quad \text{where} \quad i,j = x,y,z \tag{9.13}$$

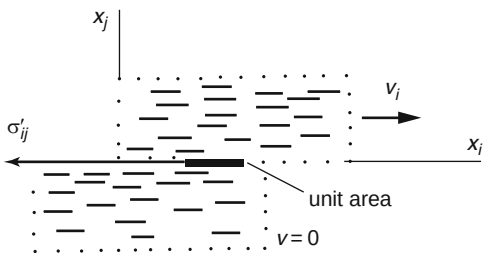

Fig. 9.1 Geometry of shear of isotropic liquid and illustration of the component σ'_{ij} of the viscous stress tensor

Here η is *shear viscosity coefficient*. For the case shown in the Fig. 9.1, $x_i = x$, $x_j = z$, the velocity has only component v_x and the gradient of velocity has a simple form $\partial v_x/\partial z$. Then $\sigma'_{xz} = \eta \partial v_x/\partial z$. The dynamic viscosity coefficient η is measured in Poise ($g{\cdot}s^{-1}cm^{-1}$). Sometimes one uses the so-called kinematic viscosity η/ρ measured in Stokes (cm^2s^{-1}). The SI unit for dynamic viscosity is Pa·s ($N{\cdot}m^{-2}s$). Numerically 1 Pa·s =10 P.

A more general form of the viscous stress tensor (for compressible liquid) has two different terms, one is the same corresponding to shear (9.13) with viscosity η and the other is compressibility with viscosity coefficient called *second viscosity* ζ. Both the coefficients are positive scalars.

By defining the shape of a selected small volume in the moving liquid, e.g., a cube, we clearly see that the viscous force acting on the cube arises from the differences in stress tensors on opposite faces of the cube. Consequently, the force is determined by the spatial derivatives of tensor Π_{ij} including σ'_{ij} as seen from Eqs. 9.8 and 9.10. The viscous tensor in turn, according to Eq. (9.13), is proportional to spatial derivatives of the velocity **v.** Hence, in many simple cases, the viscous force is given by vector $\eta\nabla^2\mathbf{v}$.

9.2.3 Navier-Stokes Equation

In the next step, the equation of motion for an isotropic, incompressible, and viscous liquid may be cast in different forms depending on the dimensionless Reynolds number

$$Re = \rho v l/\eta \tag{9.14}$$

where l is a characteristic dimension of the flow structure, for instance a tube diameter. In the case of relatively low velocity of a viscous liquid in narrow capillaries ($Re \ll 1$), the convection term in (9.5) is disregarded, and Eq. (9.8) on account of (9.10) becomes the well known *Navier-Stokes equation*:

$$\rho\frac{\partial \mathbf{v}}{\partial t} = -\vec{\nabla}p + \mathbf{f} + \eta\nabla^2\mathbf{v} \tag{9.15}$$

where $\vec{\nabla}p$ is vector of pressure gradient and **f** is an external volume force.

As a simple example, consider a spherical particle of radius R_p moving by an external force **f** with given velocity in a viscous liquid with $Re \ll 1$. Then $dv/dt = 0$, gradient of pressure is absent and the external force is equal to the friction force:

$$\mathbf{f} = -\eta\nabla^2\mathbf{v}. \tag{9.16}$$

If the particle is moving in the z-direction with velocity v_0, the velocity of the liquid $v_z(r)$ decreases from v_0 to 0 as a function of the polar transverse coordinate r.

By integrating the right part of the last equation over r, Stokes has found the relationship between the acting force and the velocity of the particle:

$$f = 6\pi R_p \eta v_z \tag{9.17}$$

By measuring velocity of a spherical particle sinking in a liquid under gravity force the viscosity of the liquid can be found (the buoyancy effect should be taken into account). Note that in Section 7.3.3, using an electric field as an action force, the same Stokes' law has been applied (with some precautions) to evaluation of velocity and mobility of spherical ions in isotropic liquids or nematic liquid crystals

For large Reynolds numbers, $Re = \rho v l/\eta > 1$ the flow in no longer laminar and even becomes turbulent. Then, the convective term $(\mathbf{v}\nabla)\mathbf{v}$ should be added to the left part of the Navier-Stokes equation

$$\rho \frac{\partial \mathbf{v}}{\partial t} + \rho(\mathbf{v}\nabla)\mathbf{v} = -\vec{\nabla} p + \mathbf{f} + \eta \nabla^2 \mathbf{v} \tag{9.18}$$

This situation is encountered in the physics of electrohydrodynamic instabilities.

Resuming the discussion of isotropic liquids note that the four basic equations for conservation of mass and momentum include only four material parameters: mass density ρ, compressibility β, viscosity η and second viscosity ζ. Other two parameters, namely, thermal conductivity κ and specific heat capacity C_p (or C_V) would come about as soon as the energy conservation law is applied to thermal processes. So, the isotropic liquid is completely described by six parameters.

9.3 Viscosity of Nematics

9.3.1 Basic Equations

Here the discussion of viscous properties of nematic liquid crystals is based on the approach developed by F. Leslie [7]. For the nematic phase we have the equation for conservation of mass, the modified equations for conservation of momentum and energy E and one additional equation for conservation of the angular momentum of the director [8,9]. Totally there are seven equations: two for scalar quantities (ρ and E), three for momentum ($m\mathbf{v}$) and two for director (due to condition $\mathbf{n}^2 = 1$), which completely describe the hydrodynamics of nematics. In this case

1. The equation for mass conservation for an incompressible nematic can still be used in the form of $\mathrm{div}\mathbf{v} = 0$.
2. The dissipation related to the pure director rotation has to be taken into account when writing the conservation energy equation. In addition, the heat transfer becomes anisotropic and the thermal conductivity is described by two coefficients $\kappa_{\parallel}$ and $\kappa_{\perp}$.

3. Instead of the equation for conservation of the linear momentum for the director, the conservation of the angular momentum is used. Leslie had taken into account not only the velocity gradients, but also the orientation of the director **n** and its relative rotation rate **N**. In fact, vector **N** is linear director velocity with respect to the liquid that may rotate itself:

$$\mathbf{N} = \frac{d\mathbf{n}}{dt} - [\omega \times \mathbf{n}] \tag{9.19}$$

Figure 9.2 shows the case in that the director $\mathbf{n}(t)$ rotates faster than liquid particles. In the figure, $\mathbf{r}(t)$ and $\mathbf{v}$ are radius-vector and linear velocity of a liquid particle, $\boldsymbol{\omega} = (1/2)\text{curl}\mathbf{v}$ is angular velocity of liquid, $(\boldsymbol{\omega} \times \mathbf{n})$ is that component of director linear velocity, which is solely caused by rotating liquid and $d\mathbf{n}/dt = (\boldsymbol{\Omega} \times \mathbf{n})$ is total linear velocity of the director with respect to immobile laboratory frame (in the figure $\boldsymbol{\Omega} > \boldsymbol{\omega}$ is angular velocity of the director in the laboratory frame).

The second rank viscous stress tensor found by Leslie for the incompressible nematic phase consists of nine matrix elements, each of them having the form:

$$\begin{aligned}\sigma'_{ij} &= \alpha_1 n_i n_j n_k n_l A_{kl} + \alpha_2 n_j N_i + \alpha_3 n_i N_j \\ &+ \alpha_4 A_{ij} + \alpha_5 n_j n_p A_{pi} + \alpha_6 n_i n_p A_{pj}\end{aligned} \tag{9.20}$$

with $i,j = x, y, z$. The corresponding six viscosity coefficients α_i are called *Leslie coefficients*. In fact, only five of them are independent, because due to *Parodi's relationship* $\alpha_6 - \alpha_5 = \alpha_2 + \alpha_3$ [10].

Let us look more carefully at each term in a particular tensor component σ'_{ij}. The three terms including the velocity gradient tensor A_{ij} are related to shear due to the mass flow in different director configurations. Among them the term with α_4 is the only one that is independent of **n** and **N**. Therefore, it exists even in the isotropic phase and $\alpha_4 = 2\eta$. The terms with α_2 and α_3 depend only on the director components and director rate (velocity) components **N** but do not contain velocity gradients; they describe a physical situation involving pure director rotation without

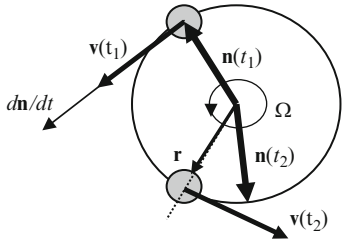

Fig. 9.2 Mutual rotation of a small spherical volume of a nematic liquid crystal and the director **n** rotating within this volume (**v** and **ω** are linear and angular velocity of small liquid volume; $d\mathbf{n}/dt$ and **Ω** are linear and angular velocities of the director with respect to immobile laboratory frame (here $\boldsymbol{\Omega} > \boldsymbol{\omega}$)

flow. For example, it could be a famous Frederiks transition used in display technology, if the director reorientation is so slow that a relatively weak effect of the mass transfer (i.e. backflow effect) is neglected.

According to the form of tensor σ'_{ij} (9.20), α_4 is independent of the nematic order parameter Q, coefficients α_2, α_3, α_5, α_6 are proportional to Q, and $\alpha_1 \propto Q^2$ (the latter is usually smaller than the others). The values of the Leslie coefficients for a popular liquid crystal E7 at 25°C are (in Poise, 1 P = 0.1 Pa·s): $\alpha_1 = -0.18$, $\alpha_2 = -1.746$, $\alpha_3 = -0.214$, $\alpha_4 = 1.736$, $\alpha_5 = 1.716$, $\alpha_6 = \alpha_2 + \alpha_3 + \alpha_5 = 0.244$.

- 4. Finally, the equation of motion for the director of a nematic has no analogy in a system of equations for isotropic liquid and is given by
-

$$I\frac{\partial \Omega}{\partial t} = [\mathbf{n} \times \mathbf{h}] - \Gamma \tag{9.21}$$

Here I is "moment of inertia for the director" and $\mathbf{\Omega}$ is vector of total angular velocity of the director, $d\mathbf{n}/dt = (\mathbf{\Omega} \times \mathbf{n})$ as shown in Fig. 9.2**.** Equation (9.21) is formally analogous to the Newton equation

$$Id\omega/dt = \mathbf{M}-\mathbf{G}$$

for rotational motion of a solid body in viscous medium with angular frequency **ω,** a torque of external force **M** and a frictional torque **G**.

In our case, the first term $(\mathbf{n} \times \mathbf{h})$ on the right side of (9.21) describes the torque exerted on the director due to both an external field and the elastic forces of the nematic, that is due to the molecular field **h** discussed in Sections 8.3.3 and 11.2.1. This torque has the same form as the external torque $\mathbf{M} \times \mathbf{H}$ exerted by the magnetic field **H** on the magnetization **M** of substance. Vector $\mathbf{\Gamma}$ in (9.21) describes a frictional torque consisting of two parts related to the director velocity **N** relatively liquid and to the liquid velocity gradient or shear rate tensor A_{ij} given by Eq. (9.12):

$$\Gamma = \mathbf{n} \times [\gamma_1 \mathbf{N} + \gamma_2 A_{ij}\mathbf{n}] \tag{9.22}$$

The coefficients of friction for the director have the dimensions of viscosity and are particular combinations of Leslie coefficients, $\gamma_1 = \alpha_3 - \alpha_2$, $\gamma_2 = \alpha_3 + \alpha_2$.

It is significant that only two coefficients of viscosity enter the equation for motion of the director. One (γ_2) describes the director coupling to fluid motion. For example, if the director turnes rapidly under the influence of the magnetic field, then, due to friction, this rotation drags the liquid and creates flow. It is the backflow effect that will be described in more details in Section 11.2.5. The other coefficient (γ_1) describes rather a slow director motion in an immobile liquid. Therefore, the kinetics of all optical effects caused by pure realignment of the director is determined by the same coefficient γ_1. However a description of flow demands for all the five viscosity coefficients.

9.3.2 Measurements of Leslie coefficients

9.3.2.1 Laminar Shear Flow

When the nematic flows through a capillary its apparent viscosity depends on the velocity of flow, more precisely, on shear rate. M. Miesowicz made first experiments on properly aligned nematics by a strong magnetic field and found different viscosity coefficients for differently aligned preparations [11]. The idea is illustrated in Fig. 9.3. The liquid crystal layer of thickness d is placed between two plates. The upper plate is moving along x with velocity $\boldsymbol{v}_0$, but the lower plate is immobile. This creates a gradient of velocity or shear rate $dv_x/dy = (v_0/d)$, hence $v_x(y) = (v_0/d)y$. The correspondent component of the viscous tensor is given by

$$\sigma'_{xy} = \eta^{dv_x}/_{dy} \tag{9.23}$$

where η is an apparent viscosity coefficient independent of shear rate. In fact, Miesowicz used slowly oscillating upper plate in the x-direction and measured damping of the oscillations. The director was fixed by a strong magnetic field either along z (geometry a) or along y (geometry c). Without field, the shear itself orients the director along x (geometry b). Using this technique the three flow viscosities coefficients $\eta_a = 3.4$, $\eta_b = 2.4$ and $\eta_c = 9.2$ cP have been measured for p-azoxyanisole at 122°C and, nowadays they are called Miesowicz coefficients.

It would be very instructive to relate the experimental (Miesowicz) and theoretical (Leslie) coefficients of viscosity. Our task now is to use the viscous tensor (9.20) and find the relationships between the coefficients for each of the three basic orientations of the director, namely $n_x = 1$, $n_y = 1$, or $n_z = 1$. At first, we shall prepare some combinations of parameters useful in all the geometries mentioned:

1. As we have only one component of shear dv_x/dy the tensor of shear (9.12) for our geometry becomes very simple:

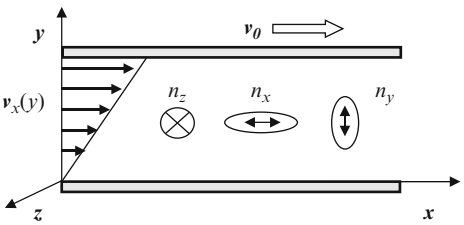

Fig. 9.3 Miesowicz's experiment. Upper plate oscillates in the x-direction and one measures damping of the oscillations. The director is fixed by a strong magnetic field either along z (n_z, geometry a) or along y (n_y, geometry c). Without field, the shear itself aligns the director along x (geometry b)

$$2A_{ij} = 2A_{xy}$$
$$= \begin{bmatrix} \partial v_x/\partial x & \partial v_x/\partial y & \partial v_x/\partial z \\ \partial v_y/\partial x & \partial v_y/\partial y & \partial v_y/\partial z \\ \partial v_z/\partial x & \partial v_z/\partial y & \partial v_z/\partial z \end{bmatrix} + \begin{bmatrix} \partial v_x/\partial x & \partial v_y/\partial x & \partial v_z/\partial x \\ \partial v_x/\partial y & \partial v_y/\partial y & \partial v_z/\partial y \\ \partial v_x/\partial z & \partial v_y/\partial z & \partial v_z/\partial z \end{bmatrix}$$
$$= \begin{bmatrix} 0 & v_0/d & 0 \\ v_0/d & 0 & 0 \\ 0 & 0 & 0 \end{bmatrix} \tag{9.24a}$$

2. Vectors n_pA_{pi} and n_pA_{pj}:

$$n_pA_{pi} = n_pA_{px} = [0, n_y(v_0/2d), 0]; \quad n_pA_{pj} = n_pA_{py} = [n_x(v_0/2d), 0, 0]; \tag{9.24b}$$

(here, multiplying the corresponding matrices we used a column n_p=(n_x, n_y, n_z) and the first and second rows of (9.24a).

3. Scalar products:

$$n_jn_pA_{pi} = {n_y}^2(v_0/2d) \text{ and } n_in_pA_{pj} = {n^2}_x(v_0/2d) \tag{9.24c}$$

4. Vector $\boldsymbol{\omega} = (1/2)\text{curl}\mathbf{v}$ for $\mathbf{v} = (v_0y/d, 0, 0)$: $\boldsymbol{\omega} = (0, 0, -v_0/2d)$.
5. Director velocity $\boldsymbol{N}$ (9.19) in the steady state conditions ($d\mathbf{n}/dt$=0):

$$N = -[\omega \times \mathbf{n}] = (-n_yv_0/2d, n_xv_0/2d, 0) = (v_0/2d)(-n_y\mathbf{i} + n_x\mathbf{j}) \tag{9.24d}$$

Now we are ready to consider the three geometries with different director alignment marked by symbols with letters n_x, n_y, n_z in Fig. 9.3.

Geometry (a), $n_z = 1$ (Director Perpendicular to the Shear Plane)

In this case $n_x = n_y$ =0. Hence, $\boldsymbol{N} = 0$ and terms with coefficients α_2 and α_3 in viscous tensor (9.20) vanish. Terms with α_5, α_6 also disappear because vector n_pA_{xy} has only x- and y-components and forms zero scalar product with $n_z = (0, 0, 1)$. The term with α_1 also vanish because $n_kn_pA_{kl}$ is a scalar, in front of which there is a product $n_in_j = n_xn_y = 0$. It is only finite when the director has both x and y projections finite.

Therefore, in (9.20) we have only one finite term for the viscous stress tensor component:

$$\sigma'_{xy} = \eta\frac{dv_x}{dy} = \alpha_4A_{xy} = \frac{\alpha_4}{2}\cdot\frac{v_0}{d} \tag{9.25}$$

and

$$\eta_a = \alpha_4/2.$$

We see that a nematic liquid crystal behaves as an isotropic liquid when the plane of the shear (y,z) is perpendicular to the director.

Geometry (b), $n_x = 1$ (Director in the Shear Plane Parallel to the Velocity of Upper Plate)

In this case, $n_y = n_z = 0$ and $N = N_y = (v_0/2d)n_x$. The term with $\alpha_1$vanishes due to $n_x n_y = 0$. The term $\alpha_2 n_j N_i = \alpha_2 n_y N_x$ also vanishes due to $n_y = 0$. Then, according to (9.24c), the term

$$\alpha_5 n_j n_p A_{pi} = \alpha_5 n^2{}_y (v_0/2d) = 0.$$

What is left? The "isotropic" term $\alpha_4 v_0/2d$ is always finite. The term $\alpha_3 n_i N_j = \alpha_3 n_x N_y = \alpha_3 v_0/2d$, and, according to (9.24c), the term $\alpha_6\, n_i n_p A_{pj} = \alpha_6\, n^2{}_x (v_0/2d) = \alpha_6 v_0/2d$. Therefore, three terms contribute to σ'_{xy}:

$$\sigma'_{xy} = \alpha_3 N_y + (\alpha_4 + \alpha_6) A_{xy} = (\alpha_3 + \alpha_4 + \alpha_6)^{v_0}/_{2d} \tag{9.26}$$

and

$$\eta_{\mathrm{b}} = \tfrac{1}{2}(\alpha_3 + \alpha_4 + \alpha_6)$$

Geometry (c), $n_y = 1$ (Director in the Shear Plane Perpendicular to the Upper Plate Velocity)

In this case, $n_x = n_z = 0$ and $N = N_x = (-n_y v_0/2d, 0, 0)$. The term with α_1 is again absent, and α_6, α_3 vanish because $\alpha_3 n_i N_j = \alpha_3 n_x N_y = 0$ and $\alpha_6 n_i n_p A_{pj} = \alpha_6\, n^2{}_x (v_0/2d) = 0$.

Now, the terms $\alpha_2 n_j N_i = \alpha_2 n_y N_x = -\alpha_2 v_0/2d$, and $\alpha_5 n_j n_p A_{pj} = \alpha_5\, n_y{}^2 (v_0/2d) = \alpha_5 (v_0/2d)$ contribute to σ'_{xy}, as well as the "isotropic" term $\alpha_4 v_0/2d$. Hence,

$$\sigma'_{xy} = \alpha_2 N_x + (\alpha_4 + \alpha_5) A_{xy} = (-\alpha_2 + \alpha_4 + \alpha_5)^{v_0}/_{2d} \tag{9.27}$$

and

$$\eta_{\mathrm{c}} = \tfrac{1}{2}(-\alpha_2 + \alpha_4 + \alpha_5)$$

Therefore, the viscous tensor component σ'_{xy} corresponding to shear dv_x/dy has been found for all the three geometries.

With the Miesowicz technique one can measure three combinations of the Leslie viscosity coefficients from Eqs. (9.25) to (9.27). On account of the Parodi relationship, to find all five coefficients, one needs, at least, two additional measurements. In particular, the ratio of coefficients α_3/α_2 can be measured by observation of the director field distortion due to capillary flow of a nematic. The last combination $\gamma_1 = \alpha_3 - \alpha_2$ can be found from the dynamics of director relaxation.

9.3.2.2 Poiseuille Flow in Magnetic Field

The mass of an isotropic liquid with density ρ and viscosity η flowing out from the cylindrical capillary of radius R and length L in a time unit is governed by the Poiseuille-Stokes law,

$$Q = \pi R^2 \rho v = \frac{\pi \rho p' R^4}{8L\eta} \tag{9.28a}$$

where v is the flow velocity and p' is the fixed difference in pressure between the open ends of the capillary. From this law the velocity of liquid is given by

$$v = p'R^2/8L\eta = \nabla p R^2/8\eta \tag{9.28b}$$

where $\nabla p = p'/L$ is the pressure gradient.

In a strong magnetic field, the director of overwhelming majority of liquid crystals aligns parallel to the field. This is widely used in viscosimetry of liquid crystals. The Poiseuille flow in nematic liquid crystals has carefully been studied by Gähwiller [12]. In the experimental scheme of Fig. 9.4, a flat capillary is placed between poles of a magnet. The flow velocity is directed along z. The cross-section of the capillary is not a square; in the ideal case, $a \ll b$ and one deals with the well-defined shear rate $\partial v_z/\partial x$ (in the discussed experiment, $a = 0.4$ mm, $b = 40$ mm). In the absence of the field, the director is solely oriented by shear flow $\mathbf{n} = n_z$. This corresponds to case b with Miesowicz viscosity coefficient $\eta_2 = \eta_b = (1/2)(\alpha_3 + \alpha_4 + \alpha_6)$. When the director is oriented by field $\mathbf{H}$ in the y-direction perpendicularly to side a, i.e., to the shear plane, as shown in the figure, it does not interact with the shear (case a, $\eta_3 = \eta_a = \alpha_4/2$.). When the capillary is turned by 90 degrees so that its short side $a \| H_y$, the director is oriented along the shear rate (case c) and the Miesowicz coefficient $\eta_1 = \eta_c = (1/2)(-\alpha_2 + \alpha_4 + \alpha_5)$ is measured. Therefore, for properly selected parameters of a capillary, both experiments discussed give the same results.

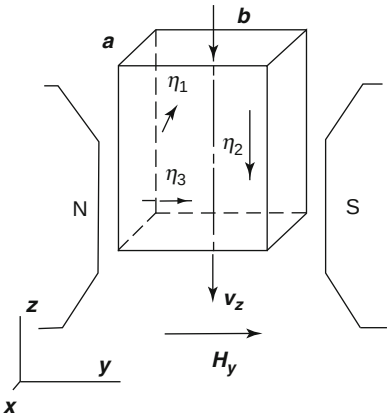

Fig. 9.4 Geometry of the Gähwiller experiment. A flat capillary is placed between S and N poles of a magnet. The flow velocity is directed along $-z$ and due to condition a≪b the shear rate has only $\partial v_z/\partial x$ component. The magnetic field is fixed along y and the cell with a liquid crystal may be rotated about the z-axis by 90°

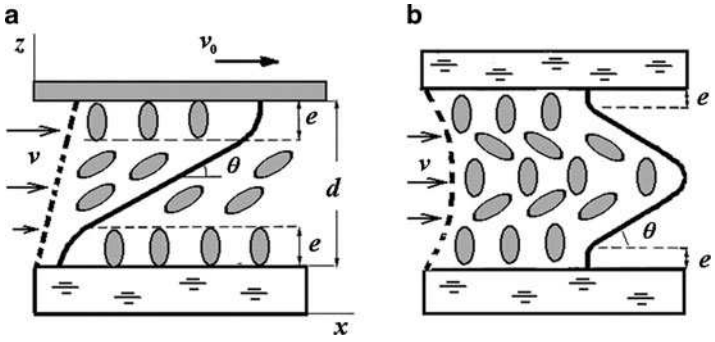

Fig. 9.5 Shear (**a**) and Poiseuille (**b**) flow in thin planar capillary filled with nematic liquid crystal. Dash lines show distribution of the v_x velocity component while the solid lines represent the director profile at high shear rate. Non-distorted close-to-surface layers are marked by e

9.3.2.3 Capillary Flow and Determination of α_2 and α_3

For a study of liquid crystals, flat plane capillaries with transparent plates are very convenient, because in this case we can create and observe a proper orientation of the director. There can be distinguished a simple shear flow and the Poiseuille flow, both shown in Fig. 9.5. As discussed above, the shear flow occurs when the upper plate is moving with constant velocity v_0 and the lower plate is fixed. Then, for small v_0, the profile of velocity of isotropic liquid is linear (the dash line in Fig. 9.5a). The Poiseuille flow occurs when the liquid is moved between two immobile plates under an external pressure, as discussed in the previous paragraph. In this case the profile has a form of parabola (the dash line in Fig. 9.5b). In both

cases, for an isotropic liquid, the viscosity is independent of the shear rate $\partial v_x/\partial z$ that is the flow is Newtonian.

The latter is not true for liquid crystals. Imagine that initially we have a uniform alignment of the director. In the case, shown in Fig. 9.5, such alignment is homeotropic that is perpendicular to the plates, although it is not important, as we shall see below. In the absence of external fields, the shear and Poiseuille flows distort the initial uniform alignment (solid lines in the figure). This is a result of coupling between the flow and the director. The flow causes realignment of the director everywhere except thin boundary layer. With increasing shear rate the director in the bulk becomes more and more parallel to the limiting plates. For a simple shear flow, in the limit of infinite shear rate the direction of the director saturates at angle ϑ_s depending on three Leslie coefficients [8]:

$$\cos 2\theta_s = -\frac{\gamma_1}{\gamma_2} = -\frac{\alpha_2 - \alpha_3}{\alpha_5 - \alpha_6} \tag{9.29a}$$

Using the Parodi relationship we get

$$\cos 2\theta_s = \frac{1 - \alpha_3/\alpha_2}{1 + \alpha_3/\alpha_2} = \frac{1 - \tan^2\theta_s}{1 + \tan^2\theta_s},$$

from which we arrive at the saturation angle θ_s:

$$\tan \vartheta_s = {}^{\alpha_3}/_{\alpha_2} \tag{9.29b}$$

As a rule, α_2 is large and negative but α_3 is one or two orders of magnitude smaller and usually also negative. Therefore angle θ_s is small (in 5CB $\theta_s \approx 1.5°$). However, the measurements of ϑ_s by optical methods allows the determination of the ratio α_3/α_2.

It is interesting that, in some materials, in a certain temperature range, α_3 can change sign and become positive. Then the flow is no longer laminar and a flow instability in the form of director tumbling is observed. How can we explain the sign inversion of nematic viscosity? We should remember that α_3 is a special coefficient that describes coupling a flow with the director. For the flow rate fixed, this coefficient defines the direction of director rotation and depends on both a molecular form and, short-range smectic-like fluctuations [13]. Figure 9.6

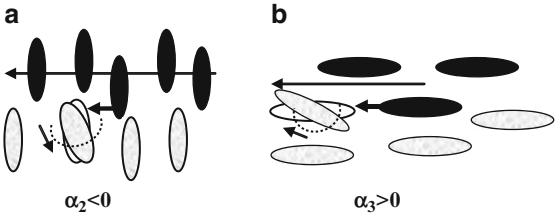

Fig. 9.6 A picture of collisions of ellipsoidal molecules that may qualitative explain different signs of the director rotation for negative α_2 and positive α_3 coefficients

may help to understand this. Imagine that dark molecules move to the left along x and the bright ones are immobile. Then a shear appears. When the director is perpendicular to flow (case α_2) then, after collisions with dark molecules, the bright ones rotate anti-clockwise (this corresponds to negative α_2). When the director is parallel to the flow (case α_3), collisions with dark molecules may result in the clockwise rotation of the bright molecules (then α_3 is positive). Note, that flow independent coefficient for the director rotation $\gamma_1 = \alpha_3 - \alpha_2$ is always positive.

9.3.2.4 Determination of γ_1

In the simplest case, one follows the relaxation of the director without flow of a liquid. It is sufficient to consider only the equation for the director motion (9.21). In the simplest geometry of Fig. 9.7, a planar nematic layer of thickness d is confined between two glasses. The boundary conditions on both glasses correspond to the fixed alignment of the director **n** parallel to the y-axis. We create a distortion of the liquid crystal by a magnetic field applied along the x-axis. The distortion occurs only within the xy-plane and is described by the azimuthal angle φ between the director and the y-axis. The director components are ($\sin\varphi$, $\cos\varphi$, 0). In the field slightly exceeding the threshold for distortion, the distortion angle follows a harmonic law $\varphi = \varphi_0\cos(\pi z/d)$ shown by the dash line in the figure. When the field is switched off, the distortion relaxes and we can follow the dynamics of the director relaxation by, e.g., an optical technique.

To describe this effect we should write Eq. (9.21) for the director motion, i.e., the balance of torques. However, up to now, nobody has observed any effect related to the inertia of the director. Such effects would result in oscillatory character of the director relaxation. The inertial term for the director in a unit volume can be estimated as a sum of the inertia moments of the molecules in this volume. Let consider a spherical ball of 1 cm^3 volume (diameter $D \approx 1.2$ cm). The typical molecular volume is $V_m = M/\rho N_{av} \approx 10^{-21}$ cm^3, the molecular diameter a is about

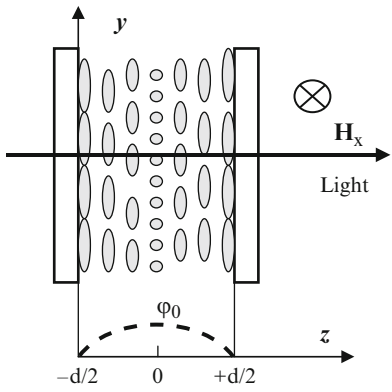

Fig. 9.7 Geometry of the twist effect that may be used for observation of director relaxation and determination of viscosity coefficient γ_1. Dash line shows the distortion profile in the magnetic field H_x

10^{-7} cm and the moment of inertia of a molecule is $\rho V_m a^2$. We have a sum of $n = 1/V_m$ cm^{-3} molecular moments of inertia in the ball, i.e. $\Sigma = n\rho V_m a^2 = \rho a^2 = 10^{-14}$ g/cm. At the same time, the moment of inertia of the ball as a whole is of the order of $\rho D^2 \approx 1$ g/cm. The difference between the two estimations is 14 orders of magnitude! For a particle of 1 μm^3 volume, the ratio would still be as high as 10^6. Indeed the director has almost no inertia and its motion in rather viscous liquid crystals is strongly overdamped. Therefore, one can always assume $I \approx 0$. Then Eq. (9.21) becomes simpler:

$$[\mathbf{n} \times \mathbf{h}] - \Gamma = 0 \tag{9.30}$$

As during relaxation the external field is switched off, the molecular field includes only the elastic torque. For the pure twist distortion and our geometry, the molecular field vector **h** is opposite to the magnetic field, i.e. directed opposite to x- axis. Its absolute value is $K_{22}\partial^2\varphi/\partial z^2$ (Section 8.3.3). The torque $(\mathbf{n} \times \mathbf{h})$ is directed along z and has the same absolute value.

The viscous torque is given by Eq. (9.22). Due to the absence of flow it contains only one term, namely,

$$\Gamma = \gamma_1[\mathbf{n} \times \mathbf{N}] \tag{9.31}$$

where the angular velocity of the director is $(\mathbf{n} \times \mathbf{N}) = (\mathbf{n} \times d\mathbf{n}/dt) = (\mathbf{n} \times [\mathbf{\Omega} \times \mathbf{n}]) = \mathbf{\Omega} = d\boldsymbol{\varphi}/dt$ directed along z (here the formula for the double vector product $\mathbf{a} \times \mathbf{b} \times \mathbf{c} = \mathbf{b(ac)} - \mathbf{c(ab)}$ was used).

Then the equation of motion reads [14]:

$$K_{22}\frac{\partial^2\varphi}{\partial z^2} = \gamma_1\frac{\partial\phi}{\partial t} \tag{9.32}$$

The solution has the following form

$$\varphi = \varphi_0 \cos {}^{\pi z}/_{d} \exp(-{}^{t}/_{\tau}) \tag{9.33}$$

Substituting this form into (9.32) we find the characteristic relaxation time:

$$\tau = \frac{\gamma_1 d^2}{\pi^2 K_{22}} = \frac{\gamma_1}{K_{22}q^2} \tag{9.34}$$

In conclusion, from the measurements of τ the coefficient $\gamma_1 = \alpha_3 - \alpha_2$ could be found if the cell thickness and elastic modulus are known. Note that γ_1 coefficient is the most important for applications. Then, using data on the ratio α_3/α_2 we can find α_3 and α_2 separately. Further, using the known coefficient for the isotropic phase viscosity $\alpha_4 = 2\eta_a$, the coefficients $\alpha_5 = 2\eta_c - 2\eta_a + \alpha_2$ and $\alpha_6 = 2\eta_b - 2\eta_a - \alpha_3$ can be calculated and, for the particular nematic liquid crystal, the applicability of the Parodi relationship $\alpha_6 - \alpha_5 = \alpha_2 + \alpha_3$ verified. As to α_1 it can be found from

the Poiseuille flow in the magnetic field oriented at some angle φ with respect to the y-axis in the xy plane (Fig. 9.4) in order to have finite both $n_i = n_x$ and $n_j = n_y$ director components in tensor (9.20). However α_1 is usually smaller than the other coefficients and often can be ignored.

9.4 Flow in Cholesterics and Smectics

9.4.1 Cholesterics

The equations for hydrodynamics of cholesterics are basically the same as for nematics, but there are some specific features related to the helical structure.

9.4.1.1 Shear

Consider shear in three basic geometries shown in Fig. 9.8. In each sketch the helix axis **h** is aligned differently with respect to plane xy of the shear rate [15].

Geometry I, $\mathbf{h}\|x$, $s_{yx} = \partial v_y/\partial x\|\mathbf{h}$ and $\mathbf{v}\perp\mathbf{h}$

In the left part of the figure, the helical axis is parallel to the velocity gradient (shear) shown by two arrows. When cell thickness is less than the cholesteric pitch, $d \ll P_0$, and the rate of shear is small, then an effective viscosity is given by averaging two Miesowicz coefficients:

$$\eta_I = \eta_a\eta_b/\eta_a + \eta_b.$$

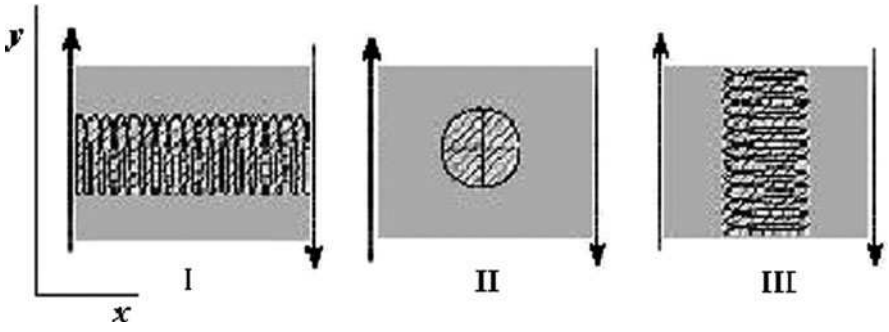

Fig. 9.8 Three different geometries of a shear of a cholesteric liquid crystal: helical axis $\mathbf{h}\|x$ (I), $\mathbf{h}\|z$ (II) and $\mathbf{h}\|y$ (III)

For higher shear rates the helix is unwound, the director becomes almost parallel to the flow lines ($\mathbf{n}\|\mathbf{v}$) and $\eta_I \approx \eta_b$ as in nematics.

Geometry II, $\mathbf{h}\|\mathbf{z}$, $s_{yx} = \partial v_y/\partial x \perp \mathbf{h}$ and $\mathbf{v}\perp\mathbf{h}$

In the middle part of the figure, the helical axis is perpendicular to the flow direction and the effective viscosity at low shear rate equals

$$\eta_{II} = \tfrac{1}{2}(\eta_b + \eta_c).$$

At high shear rate, due to helix unwinding, we again have $\eta_{II} \approx \eta_I \approx \eta_b$. For small distortions, in both cases, the disturbed helical structure relaxes with a rate of the general hydrodynamic form

$$\tau = \gamma_1/K_{22}q_0^2 = \gamma_1 P_0^2/K_{22}\pi^2 \tag{9.35}$$

Geometry III, $\mathbf{h}\|\mathrm{y}$, $s_{yx} = \partial v_y/\partial x \| \mathbf{h}$, and $\mathbf{v}\|\mathbf{h}$

In the right part of the figure, the direction of the flow coincides with the helical axis. This case is especially interesting because it results in the so-called permeation effect.

9.4.1.2 Permeation Effect

In experiments with cholesteric liquid crystals (geometry III), extraordinary high viscosity η_{III} is observed, few orders of magnitude higher than the viscosity of the isotropic phase or a non-twisted nematic. It seems surprising because the local structure of nematics and cholesterics is the same. In addition such a flow is strongly non-Newtonian: with increasing shear rate (s) η_{III} decreases, as schematically shown in Fig. 9.9. In the case of the Poiseuille flow, the viscosity depends also on the radius of a capillary.

The explanation of these observations has been given in terms of the so-called permeation effect [16]. Helfrich assumed that the helical structure with wavevector $\mathbf{q_0}$ is fixed by the boundary conditions at the walls of a cylindrical capillary of radius R. Schematically it is shown by "fixation points" at each period of the helix in Fig. 9.10a. The liquid crystal flows out of the capillary with a constant velocity $\mathbf{v}\|\mathbf{q_0}$. Therefore, the mass of the liquid of density ρ escaping the capillary in a time unit is given by $Q = \pi R^2 \rho v$. The flow velocity is considered to be uniform along the capillary radius (except the boundary layer $l \ll R$). At the same time molecules

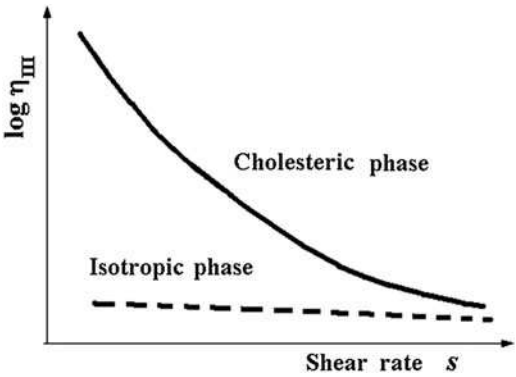

Fig. 9.9 Comparison of the dependencies of the viscosity coefficient on shear rate for the cholesteric and isotropic phases

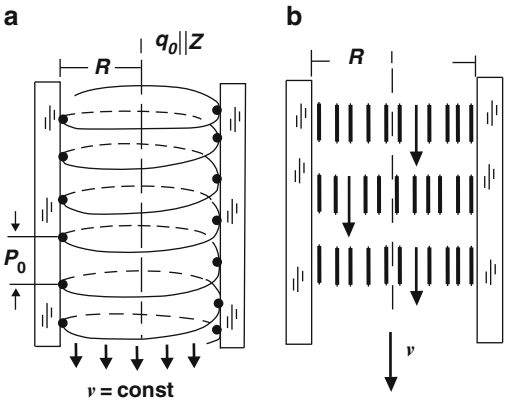

Fig. 9.10 Poiseuille flow in a cylindrical capillary with permeation effect in the cholesteric (**a**) and smectic A (**b**) phases

are free in the bulk and may rotate about the z-axis. In such a situation the director $\varphi(z) = q_0 z$ must rotate like a screw with angular velocity Ω:

$$\Omega = \frac{d\varphi}{dt} = \frac{d\varphi}{dz} \cdot \frac{dz}{dt} = q_0 v, \tag{9.36}$$

and this rotation exerts a friction torque from the capillary walls on the director: $\Gamma = \gamma_1 \Omega$.

The work $\nabla p v$ made by the external pressure gradient ∇p must be equal to the energy dissipated in unit volume and unit time due to the friction $\gamma_1 (d\varphi/\mathrm{d}t)^2 = \gamma_1 \Omega^2$. Therefore, $\nabla p v = \gamma_1 \Omega^2 = \gamma_1 v^2 q_0^2$.

From here, we obtain the relationship between the pressure gradient and flow velocity of a cholesteric:

$$\nabla p = \gamma_1 q_0^2 v \tag{9.37a}$$

Note that the Poiseuille-Stokes equation for an isotropic liquid (9.28b) or for a nematic would give us

$$\nabla p = \frac{8v\eta}{R^2} \tag{9.37b}$$

From comparison of the last two formulas we can find the apparent viscosity for a cholesteric:

$$\eta_{app} = \gamma_1 (q_0 R)^2 / 8 = \gamma_1 k_p \tag{9.38}$$

According to this simplest theory, the amplification factor due to chirality can be as high as $k_\mathrm{p} \approx 10^7$ ($R = 0.1$ cm, $q_0 = 2\pi/P_0 \approx 10^5$ cm^{-1}). The coefficient k_p is called *permeation coefficient* because the molecules permeate through the fixed cholesteric quasi-layers. In reality k_p is smaller than 10^7 due to a non-ideal helical structure, surface defects, non-uniform velocity profile etc., but, nevertheless, the effect is very remarkable.

9.4.2 Smectic A Phase

9.4.2.1 Flow and Viscosity

For the smectic A phase the permeation effect is even more important [16]. In fact, with the layers fixed at the walls of a capillary, a smectic may flow only as a whole, like a plug, without velocity gradients, Fig. 9.10b. The velocity is again given by equation $\nabla p = k_p v$, where k_p is the permeation coefficient depending on the smectic characteristic length λ_s given by Eq. (8.46), conventional nematic viscosity η and temperature:

$$k_p = \frac{\eta}{\lambda_s^2} \cdot \frac{T_{NA} - T}{T_{NA}} \tag{9.39}$$

The smaller the temperature difference $T_{NA} - T$, the smaller is the smectic order parameter, that is the amplitude of the density wave. Consequently, the permeation coefficient in SmA should decrease upon approaching the SmA-N transition. Indeed, in experiment, very close to T_{NA} the Poiseuille flow is observed, as in the nematic phase, but already at $T_\mathrm{NA} - T > 0.3$ K the plug flow occurs with apparent viscosity two orders of magnitude larger than η.

If both the compressibility and the permeation effect are disregarded, the structure of the viscous stress tensor σ_ij is identical for the SmA and nematic phases

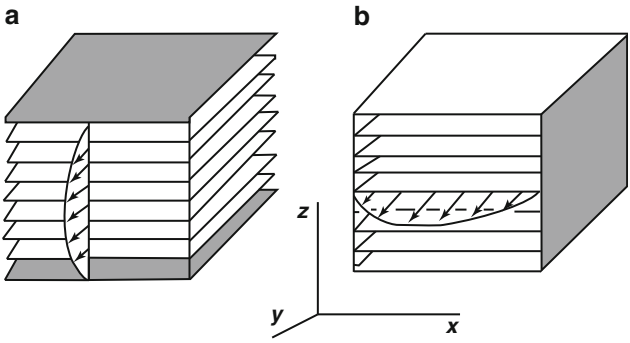

Fig. 9.11 Two geometries for easy flow in Smectic A: flow velocity in both cases is in the layer plane but shear is either perpendicular to layers (**a**) or parallel to them (**b**). For the flow velocity along the layer normal the permeation effect is observed, see Fig. 9.10b

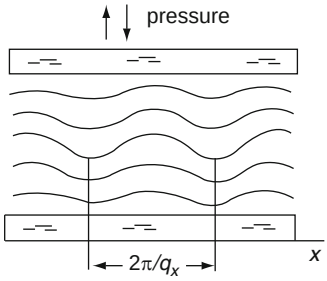

Fig. 9.12 Undulation or wave-like instability in the smectic A layer subjected to a dilatation-compression distortion

due to the same point group symmetry, $D\infty_h$. There are five independent viscosity coefficients for SmA as for a nematic [17]. However, tensor (9.20) can only be used when the velocity has no component along the layer normal z as shown by examples in Fig. 9.11 for velocity v_y and gradient $\partial v_y/\partial z$ in case (a) and velocity v_y and gradient $\partial v_y/\partial x$ in case (b). In these two examples of the Poiseuille flow the viscosities are given by

$$\eta_a = {}^1\!/_2(\mu_0 + \mu_2 - 2\lambda_1 + \lambda_4) \quad \text{and} \quad \eta_b = {}^1\!/_2\mu_0$$

New viscosity coefficients μ_i and λ_i are related to Leslie coefficients. In particular, $\mu_0 = \alpha_4$ (viscosity of an isotropic liquid). Viscosimetry of SmA liquid crystals is difficult. For instance, in geometry (a), the upper and lower plates should be parallel with a great accuracy (few nanometers); otherwise defects appear. However, for several compounds the correspondent viscosities have been measured. In geometry (b) there was found a shear rate threshold: above the threshold the isotropic behaviour (α_4) was observed. At lower rates, defects control a flow.

9.4.2.2 Undulation Instability

In the experiment, it is possible to create a dilatation of the smectic layers with piezoelectric drivers. Evidently, an increase of the interlayer distance would cost a lot of energy. Instead, at a certain critical dilatation $\chi_c = 2\pi\lambda_s/d$, where $\lambda_s = (K_{11}/B)^{1/2}$, a wave-like or undulation distortion is observed as illustrated by Fig. 9.12. The wavevector of the distortion is proportional to inverse geometrical average of cell thickness and smectic characteristic length, $q_x = \pi/\sqrt{\lambda_s d}$. Therefore, a typical undulation period is about 0.3 μm ($d \approx 10$ μm, $\lambda_s \approx 0.01$ μm) and may be observed optically. A similar instability arises in cholesterics under the influence of the magnetic or electric field, see Section 12.2.3.

References

1. De Gennes, P.G.: The Physics of Liquid Crystals. Clarendon Press, Oxford (1975)
2. Chandrasekhar, S.: Liquid Crystals, 2nd edn. Cambridge University Press, Cambridge (1992)
3. De Gennes, P.G., Prost, J.: The Physics of Liquid Crystals, 2nd edn. Clarendon Press, Oxford (1995)
4. Kats, E.I., Lebedev, V.V.: Dynamics of Liquid Crystals. Nauka, Moscow (1988) (in Russian) (Fluctuation Effects in the Dynamics of Liquid Crystals. Springer, New York (1993)).
5. Landau, L., Lifshitz, E.: Hydrodynamics, 3rd edn. Nauka, Moscow (1986) (in Russian) (see also Fluid Mechanics, 2nd edn. Pergamon, Oxford (1987)).
6. Feynman, R.P., Leighton, R.B., Sands, M.: The Feynman Lectures on Physics, vol. 2. Addison-Westley, Reading, MA (1964).
7. Atkin, R.J., Sluckin, T.J., Stewart, I.W.: Reflection on the life and work of Frank Matthews Leslie. J. Non-Newtonian Fluid Mech. **119**, 7–23 (2004)
8. Leslie, F.: Some constitutive equations for liquid crystals. Arch. Ration. Mech. Anal. (Germany) **28**, 265–283 (1968)
9. Leslie, F.M.: Introduction to nematodynamics. In: Dunmur, D., Fukuda, A., Luckhurst, G., INSPEC (eds.) Physical Properties of Liquid crystals: Nematics, pp. 377–386, London (2001).
10. Parodi, O.: Stress tensor for nematic liquid crystals. J. Phys. (Paris) **31**, 581–584 (1970)
11. Miesowicz, M.: The three coefficients of viscosity of anisotropic liquids. Nature **158**, 27 (1946); Influence of the magnetic field on the viscosity of para-azoxyanisole. Nature **136**, 261 (1936).
12. Gähwiller, C.: The viscosity coefficients of a room-temperature liquid crystal (MBBA). Phys. Lett. **36A**, 311–312 (1971); Direct determination of the five independent viscosity coefficients of nematic liquid crystals. Mol. Cryst. Liq. Cryst. **20**, 301–318 (1973).
13. Helfrich, W.: Molecular theory of flow alignment of nematic liquid crystals. J. Chem. Phys. **50**, 100–106 (1969)
14. Brochard, F., Pieranski, P., Guyon, E.: Dynamics of the orientation of a nematic-liquid-crystal film in a variable magnetic field. Phys. Rev. Lett. **28**, 1681–1683 (1972)
15. Leslie, F.M.: Continuum theory of cholesteric liquid crystals. Mol. Cryst. Liq. Cryst. **7**, 407–420 (1969)
16. Helfrich, W.: Capillary flow of cholesteric and smectic liquid crystals. Phys. Rev. Lett. **23**, 372–374 (1969)
17. Schneider, F., Kneppe, H.: Flow phenomena and viscosity. In: Demus, D., Goodby, J., Gray, G.W., Spiess, H.-W., Vill, V. (eds.) Physical Properties of Liquid Crystals, pp. 352–374. Wiley-VCH, Weinheim (1999).

Chapter 10
Liquid Crystal – Solid Interface

10.1 General Properties

10.1.1 Symmetry

Now we are interested in phenomena at an interface between a liquid crystal and another phase (gas, liquid or solid) [1, 2]. Why is it important? First, the structure of a liquid crystal in a thin interfacial layer is different from that in the bulk and manifests many novel features. Second, the interface plays a decisive role in applications, because liquid crystals are always used in a confined geometry. There are two approaches to the surface problems, microscopic and macroscopic. In the first approach, we are interested in a structure and properties of interfacial liquid crystal layers at the molecular level; in the second one, we ignore the microscopic details and use only symmetry properties and the concept of the director.

What does occur at the interface? Consider, for example, a contact of a liquid crystal with a solid substrate shown in Fig. 10.1. We notice that

(i) There is a change in symmetry; the interface is not a mirror plane, there is a new, polar vector, namely the normal **h** to the interface. Therefore, an interfacial layer has properties of a polar phase.
(ii) The properties change continuously along the surface normal for the phase of the same symmetry. Macroscopically we can consider a change of order parameters with distance. In a particular case of the nematic phase, both the absolute value of the orientational order $|Q| = S$ and the direction of the director **n** can depend on distance from the interface. The positional order can also change.
(iii) The molecules at the surface are in different surrounding in comparison with those in the bulk. Therefore, the molecular interactions and, hence, the thermodynamic properties are also different. Even new liquid crystal phases can form at the surface. For instance, if in the bulk a uniaxial nematic is stable, at the surface it could be transformed in either a uniaxial smectic A or biaxial nematic.

L.M. Blinov, *Structure and Properties of Liquid Crystals*,
DOI 10.1007/978-90-481-8829-1_10,

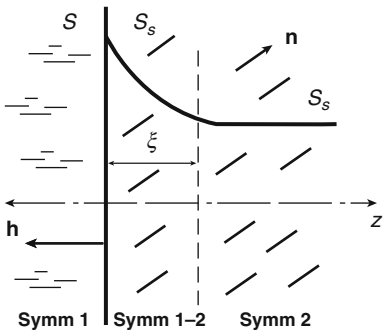

Fig. 10.1 A liquid crystal phase at the interface with an isotropic phase (gas, liquid, amorphous solid) with a surface layer of thickness ξ and a qualitative dependence of an order parameter (e.g. orientational) on the distance z from the surface (S_s) to the bulk (S_B) values (**n** is director)

(iv) The elastic moduli such as K_{24} and K_{13} often neglected in the description of bulk properties becomes important at the interface.

10.1.2 Surface Properties of a Liquid

As throughout the book, at first we review properties of isotropic liquids at an interface and then switch to liquid crystals.

10.1.2.1 Surface Tension

Due to a difference in molecular forces in the bulk and at the interface, there is an excess of energy in a surface layer. For instance, one should make a work to increase an interface A between a gas and a liquid. When a chemical composition of the contacting phases is fixed, the surface tension is

$$\sigma = \frac{dF}{dA} \tag{10.1}$$

where the free energy of the surface $F = E - TS$ takes into account not only a change in the internal energy E but also entropy S.

The surface tension determines capillary effects, wetting phenomena and a shape of liquid drops, in particular, the spherical shape of small radius drops when the gravity is not essential. The corresponding excess pressure in a drop of radius ρ is $\Delta p = 2\sigma/\rho$ (Laplace-Young formula). Small drops of the nematic phase are, strictly speaking, not spherical due to anisotropy of the surface tension but practically they may be considered spherical. The surface tension of both a liquid crystal and a solid substrate determines orientation of the liquid crystal director on the substrate.

10.1.2.2 Adsorption

The adsorption is a non-uniform spatial distribution of different chemical species at an interface between different media [3]. The situation at the liquid–gas interface is illustrated by Fig. 10.2. If there is some concentration of surface-active (surfactant) molecules in water, they "prefer" to leave the bulk and go to the surface. The reason is that water does not like such guests, because surfactant molecules destroy a network of hydrogen bonds formed by water molecules. The break of the network would cost considerable decrease in entropy. Therefore, water pushes its guests out to the surface. Then, at the water surface, we see a peak of concentration of surfactant molecules. In this way the total surface energy is reduced and the surface tension decreases. For instance, the excess of foreign molecules on the water surface creates a certain pressure on a floating barrier in a Langmuir trough and the barrier shifts in the direction of the pure water surface. The so-called surface pressure exerted onto the barrier is $\pi = \sigma_0 - \sigma$ where σ_0 is surface tension of pure water. Measuring the temperature dependence $\pi(T)$ one can study single monolayers of liquid crystalline compounds forming on water different two-dimensional phases as discussed in Section 5.7.3.

In liquid crystal cells the adsorption of impurities from the bulk to a liquid crystal – glass (or other solid substrates) interfaces can change conditions for alignment of the liquid crystal and often results in a misalignment of liquid crystals undesirable for displays. On the other hand, using adsorption phenomena and Langmuir-Blodgett technology one can prepare ultra-thin polymer films on the solid substrates. Such films can be rubbed by soft brushing or scribed by Atomic Force Microscopes or modified by polarised light for desirable alignment of liquid crystals. In some cases, a "negative" adsorption is observed when foreign molecules are expelled from the surface into the bulk. Such desorption increases surface tension. Adsorption of ions at the electrodes of a liquid crystal cell may create a space charge at the interface that dramatically influences conditions for the current flow through a liquid crystal especially at low frequencies.

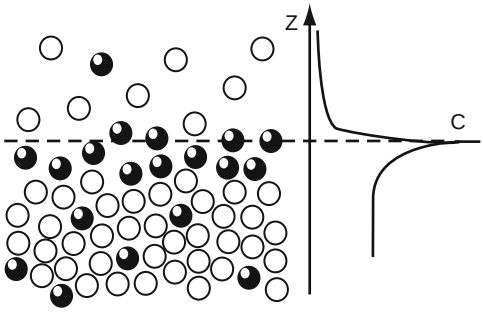

Fig. 10.2 Adsorption of surfactant molecules (*black spheres*) at the interface between water (*white spheres*) and air. The *curve C* qualitatively pictures the surfactant concentration as a function of the distance *z* from the interface shown by the *dash line*

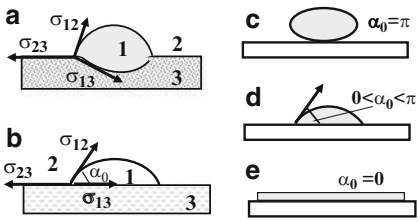

Fig. 10.3 Surface tension in a three-phase system. Illustration of the Neumann triangle (**a**) and Young law (**b**) and the three cases of wetting phenomena: non-wetting (**c**), partial wetting (**d**) and complete wetting (**e**)

10.1.2.3 Wetting

Consider a drop of a liquid on a soft substrate, Fig. 10.3a [3]. There are three phases in contact: liquid (1), gas (2) and soft substrate (3). The soft substrate could be an elastomer or a liquid different from the liquid (1). At any point of the contact line the equilibrium condition is the vector sum of the corresponding tensions for each pair of contacting phases:

$$\vec{\sigma}_{12} + \vec{\sigma}_{23} + \vec{\sigma}_{13} = 0$$

This is a so-called *Neumann triangle* valid for any three phases.

When a substrate is solid, see Fig. 10.3b, the vertical component of its deformation is negligible and we may only consider the equilibrium of horizontal projections of the surface tension vectors (*Young's law*):

$$\sigma_{12} \cos \alpha_0 = \sigma_{23} - \sigma_{13} \tag{10.2}$$

and the ratio $(\sigma_{23} - \sigma_{13})/\sigma_{12}$ determines the equilibrium contact angle α_0.

The surface tension at a liquid-solid interface σ_{13} may be controlled by temperature, composition of the liquid or adsorption. We can distinguish three different cases, shown in Fig. 10.3c–e: non-wetting (c), partial wetting (d) and complete wetting (e). The three cases are characterized by their equilibrium contact angles: $\alpha_0 = \pi$; $\pi > \alpha_0 > 0$; $\alpha_0 = 0$, respectively.

The spreading parameter $S = \sigma_{23} - (\sigma_{13} - \sigma_{12})$ determines a *wetting transition:* for $S > 0$ one observed complete wetting, for $S < 0$ the wetting is partial. The wetting transition is often observed with volatile liquids on solid substrates. The dynamics of the complete wetting is very interesting: at first, a microscopically thin precursor forms that advances rather fast over the substrate followed by a macroscopic edge of the liquid film. Afterwards all amount of liquid forms a uniform layer. This has been observed in both isotropic and nematic liquids [4].

10.1.3 Structure of Surface Layers

The most interesting case is a contact of a nematic liquid crystal with a solid substrate because in most devices a nematic is sandwiched between transparent

glasses, conductive or non-conductive. The interaction with a substrate causes many effects such as a change in the orientational order parameter, appearance of a short range positional order, appearance of a surface dipolar layer, etc. [5].

10.1.3.1 Surface Induced Change in the Orientational Order Parameter

A qualitative picture, Fig. 10.4, shows the distance dependencies of the orientational order parameter for homeotropically aligned nematic liquid crystal at the solid substrate. The problem is to explain such dependencies [6]. The influence of the surface on the orientational order parameter may be discussed in terms of the modified Landau–de Gennes phase transition theory. Consider a semi-infinite nematic of area A being in contact with a substrate at $z = 0$ and uniform in the x and y directions. When writing the free energy density a surface term $-W\delta(z)S$ must be added to the standard expansion of the bulk free energy density:

$$g = g_0(S) + K^* \left(\frac{dS}{dz}\right)^2 - \frac{W\delta(z)S}{A} \tag{10.3}$$

where

$$g_0(S) = a(T - T^*)S^2 + bS^3 + cS^4$$

is a uniform part of the free energy density, which describes the first order N-I phase transition, T^* is "virtual second order" transition temperature for the bulk, a, b, c are Landau expansion coefficients and K^* is a new "gradient" elastic modulus, other than Frank moduli K_{ii}. The surface term is chosen in the spirit of the mean field theory with a cylindrically symmetric potential of a substrate

$$W(\vartheta, z) = W\delta(z)\langle P_2(\cos\vartheta)\rangle.$$

Here $\delta(z)$ is Dirac delta function, showing that the surface potential $W = W(z = 0)$ is short-range, ϑ is an angle between the longitudinal axis of a rod-like molecule and the director at the surface $\mathbf{n_s}$. The surface potential W may be positive as in Fig. 10.4a or negative, Fig. 10.4b. In this consideration, a change of the

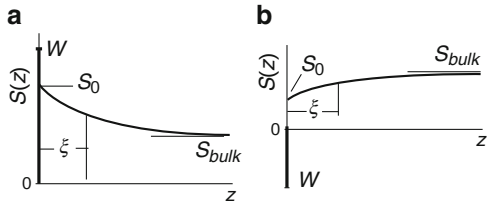

Fig. 10.4 Qualitative dependencies of the orientational order parameter of the nematic phase on the distance z from the surface. The positive (**a**) and negative (**b**) surface potential W has the form of the δ-function. The temperature is fixed

mesophase symmetry, in particular, an appearance of the polar axis in the nematic phase is disregarded.

The free energy per unit area is given by

$$F/A = \int_0^\infty \left[g_0(S) + K^* \left(\frac{dS}{dz} \right)^2 \right] dz - \frac{WS_0}{A} \tag{10.4}$$

Now we need two minimizations: (i) over function $S(z)$ with fixed S_0 ($z = 0$) and (ii) over the boundary value S_0. In our case, the standard Euler equation $\partial F/\partial S - d/dz(\partial F/\partial S') = 0$ reads:

$$g_0{}'(S) - 2K^* \frac{d^2S}{dz^2} = 0. \tag{10.5}$$

Its first integral: $K^* \left(\frac{dS}{dz}\right)^2 = g_0(S) + C$

The constant C is found from $dS/dz|_{z\to\infty} = 0$, i.e. $C = -g_0(S_{bulk})$.

Then we get:

$$\xi_0^2 \left(\frac{dS}{dz} \right)^2 = \frac{g_0(S) - g_0(S_{bulk})}{aT_{NI}} \tag{10.10}$$

Here, we have introduced a surface correlation length, marked off in Fig. 10.4:

$$\xi_0 \equiv \left(\frac{K^*}{aT_{NI}} \right)^{1/2}, \tag{10.11}$$

with the first order transition temperature T_{NI} in the bulk. Now Eq. (10.10) for the free energy density becomes dimensionless.

Next, we substitute (10.10) into (10.4) and after minimization $dF/dS_0 = 0$ find the condition $2[g_0(S_0) - g_0(S_{bulk})]^{1/2} = W/A$. Using this condition the equation (10.10) may be integrated with the proper limits:

$$(aT_{NI}^0)^{1/2} \int_{S(z)}^{S_0} \frac{dS}{[g_0(S) - g_0(S_{bulk})]^{1/2}} = \frac{z}{\xi_0} \tag{10.12}$$

This equation has been solved numerically [6] for the order parameter $S(z,T,S_0)$ depending on the distance z from the boundary, the surface potential (included in S_0) and temperature (included in $g_0(S_{bulk})$). The found distance dependence is similar to that shown in Fig. 10.4a for the positive surface potential. The calculated thickness of the surface layer is about $10\xi_0$.

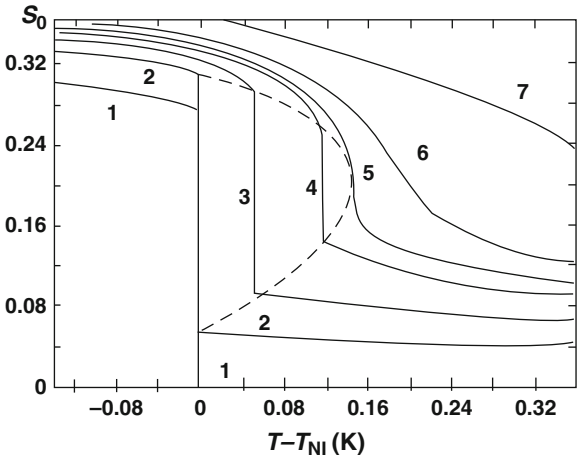

Fig. 10.5 Calculated order parameter at the surface S_0 as a function of temperature. The numbers at the curves corresponds to different surface potential in dimensionless units: $W = 0$ (1), 0.0056 (2), 0.008 (3), 0.01 (4), $W_c = 0.01078$ (5), 0.012 (6), 0.017 (7). Note that at W_c the discontinuity of the first order N-Iso phase transition disappears (adapted from [7])

The surface order parameter S_0 shows very interesting features. Fig. 10.5 illustrates the calculated dependence of S_0 on temperature with parameters of a liquid crystal 5CB. The different curves correspond to the different values of the surface potential. According to the positive sign of the surface potential W, we see an expected increase in the orientational order in the surface nematic phase (negative values of T-T_{NI}). Further, the increasing potential W shifts the N-I transition point to higher temperatures. At $W = W_c$, the phase transition at the surface disappears and the surface order parameter becomes a continuous function of temperature. For high values of the surface potential, the orientational order at the interface remains finite even at temperatures well above the N-I transition point in the bulk.

The picture predicted by this figure has been confirmed by birefringence measurements on the isotropic phase [7]. Such measurements are much more precise than attempts to measure the influence of an interface on the order parameter in the nematic phase, because the isotropic phase has no background birefringence coming from the bulk. For nematic preparations with the director homogeneously aligned along the surface of a solid substrate, the birefringence is observed at temperatures markedly exceeding the N-I transition point, Fig. 10.6. Moreover, it depends on the surface potential as predicted by theory.

The thickness of the "quasi-nematic" layers adjacent to the substrate and shown in the Inset to Fig. 10.6 can be estimated from the observed birefringence. For two boundaries the phase retardation δ between the ordinary and extraordinary rays is given by

$$2\delta \approx \frac{4\pi\langle\Delta n\rangle\xi_0}{\lambda}$$

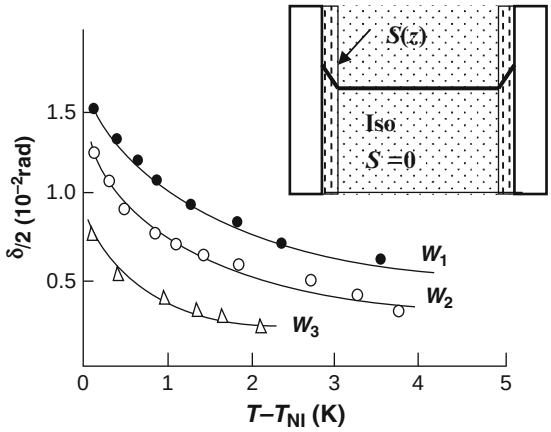

Fig. 10.6 Temperature dependence of birefringence of thin surface layers in the isotropic phase. Surface potential $W_1 > W_2 > W_3$. Inset: geometry of birefringence measurements with molecules aligned parallel to the surfaces and the gradient of the order parameter $S(z)$ within the surface layers

where λ is light wavelength and $<\Delta n>$ is average optical anisotropy of the surface layers. For typical values of $\Delta n \approx 0.1$–0.2, $\xi \approx 4$–10 nm.

Some solid surfaces induce disorder in nematic liquid crystals. It means that the order parameter at the interface is lower than the bulk value. For instance, evaporated SiO layers of a certain thickness due to their roughness decrease the order parameter of MBBA from the bulk value $S_b \approx 0.6$ down to $S_0 \approx 0.1$–0.2. In some cases, the surface order parameter may be equal to zero (surface melting).

10.1.3.2 Surface-Induced Smectic Ordering

Let the director of the nematic phase is perpendicular to a flat interface. Then we can anticipate two effects. First, a polar surface layer should appear due to the break of the cylindrical symmetry, $\mathbf{n} \neq -\mathbf{n}$. Second, due to some positional correlation of the centers of molecules in several layers adjacent to the surface, the nematic translational invariance can be broken. It means that the surface induces the short-range smectic A order. In the framework of the Landau theory, the smectic order decays with distance from the interface according to the exponential law

$$\rho_1(z) = \rho_1(0)\exp(-z/\lambda_s)$$

where both the smectic wave amplitude ρ_1 and smectic correlation length λ_s induced by the surface increase with decreasing temperature T. More precisely, both the parameters depend on the proximity $(T - T_{NA})$ to the nematic $\rightarrow$ smectic A transition because at $T = T_{NA}$, $\lambda_s \rightarrow \infty$ and the smectic phase becomes stable everywhere.

In the X-ray experiments on nematic 8CB, the smectic ordering was observed at the free surface (air-nematic interface). The same phenomenon has also been observed at the solid-nematic interface by the X-ray, an electrooptical technique and molecular force measurements. The principle of the latter is shown in Fig. 10.7. For two mica cylinders submerged in nematic liquid crystal, their interaction force measured with a balance oscillates with a distance between the cylinders and the period of oscillations was found to be equal to molecular length l. This clearly shows the periodicity in density characteristic of a smectic phase [8].

A powerful technique for the study of molecular orientation at the surface is scanning tunnel microscopy (STM): a weak tunnel electric current (of the order of 0.1 nA) is measured between an extremely sharp (atomic size) tip and the conductive substrate. The motion of the tip over the surface is controlled by piezoelectric drivers and a computer. As a result, we can see a current pattern correlating with the surface relief. For example, on cooling the 11th and 12th homologues of cyanobiphenyl from the isotropic phase to a room temperature smectic phase, different types of surface layers are formed on conductive MoS_2 substrates [9]: a compound 11CB having intermediate nematic phase forms single-row monolayers whereas compound 12CB forms double-row ones, see Fig. 10.8. The structure of monolayers depends on substrate properties and temperature and the latter can control the realignment of a liquid crystal in the bulk, i.e. cause *anchoring transitions* [10].

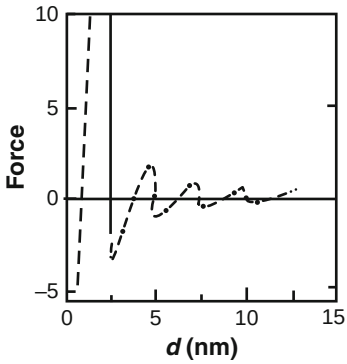

Fig. 10.7 Periodic force between two mica cylinders separated by nematic liquid crystal with molecules aligned perpendicular to cylinder surfaces as a function of the gap between the latter

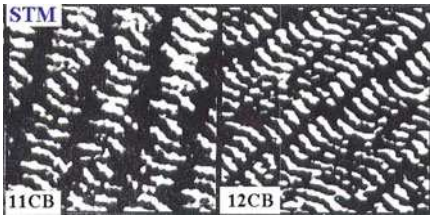

Fig. 10.8 Scanning Tunnel Microscope images of smectic compounds on MoS_2 substrates taken at room temperature and showing the one-row (for 11CB) or two-rows (for 12CB) molecular organization

10.1.3.3 Polar Surface Order and Surface Polarization

The interfaces in general, and particularly with solid substrates break the head-to-tail symmetry of a liquid crystal phase and induce polar orientational order. The symmetry is reduced to the conical group $C_{\infty v}$. The latter allows a finite value of the second-order nonlinear susceptibility χ_2 responsible for the second optical harmonic generation [11]. This phenomenon has been observed in experiments on generation of the second harmonic in a ultrathin nematic layers on a solid substrate as shown in Fig. 10.9.

The polar order parameter is the first Legendre polynomial $P_1 = (\mathbf{Lh}) = \cos\theta$ where **L** is a new polar vector parallel to **n** and called polar director. The polar order contributes to the elastic surface energy linearly while the quadrupolar (nematic) order contributes quadratically with a sign dependent on surface treatment:

$$\begin{aligned} F(P_1) &= -\sigma_p(\mathbf{Lh}) = -\sigma_p \cos\theta \\ F(P_2) &= \pm\tfrac{1}{2}W(\mathbf{Lh})^2 = \pm\tfrac{1}{2}W(\mathbf{nh})^2 = \pm\tfrac{1}{2}W\cos^2\theta \end{aligned} \tag{10.13}$$

where angle θ is counted from the external normal to the nematic layer **h** [7]. Therefore, both contributions to the free energy vanish when both **L** and **n** perpendicular to **h.** However, when **L**,**n** || **h** the two contributions can compete with each other. For instance, for $\theta = 0$ the linear term is negative and favors this alignment (homeotropic) but, the quadratic term with positive sign at W is unfavorable. It could be a reason for an oblique alignment of the director often observed at the free surface of a nematic.

Note that the polar vector reflects only polar symmetry of the interfacial layer and may be associated with the conical (not rod-like) form of the molecules. However, when the electric charges are involved in the game, the same polar order may results in appearance of the macroscopic surface electric polarization $\mathbf{P}_{\text{surf}}$ that is the dipole moment of a unit volume [units: CGS(charge)·cm/cm^3 = CGSQ/cm^2 = StatV/cm, or C/m^2 in SI system]. When an electric field is applied to a liquid crystal the surface polarization contributes to the free energy of a surface layer

$$F(P_{surf}) = -\mathbf{P}_{surf}\mathbf{E} \tag{10.14}$$

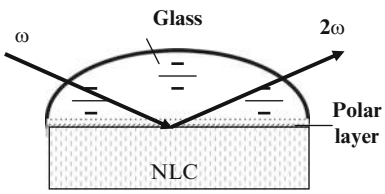

Fig. 10.9 Optical second harmonic generation by a polar layer at the interface between nematic liquid crystal and glass: due to non-linear interaction with surface layer the incident beam of frequency ω is partially converted into the beam of frequency 2ω

The problem of the surface polarization have been raised [12] macroscopically in connection with the bulk flexoelectric distortion [13] discussed in the next chapter. On the microscopic level, we can distinguish between three different mechanisms of $\mathbf{P}_{\text{surf}}$, explained with the help of Fig. 10.10.

Ionic Polarization

A monolayer of ionic species can be adsorbed at the interface with a solid substrate (a Helmholtz monolayer), Fig. 10.10a. A diffuse layer of ions of the opposite sign with density $\rho(z)$ provides the overall electrical neutrality. This mechanism is not specific for liquid crystals, it takes place in the isotropic liquids as well. However, in liquid crystals the surface field $\mathbf{E} = 4\pi\mathbf{P}_{\text{surf}}$ can interact with the director and change orientation of the latter. Qualitatively, the ionic polarization can be estimated as $P_{\text{surf}} = qn\xi_{\text{D}}$ where n is the number of charges q and ξ_{D} is a characteristic (Debye) length for the charge distribution.

Dipolar Polarization

It comes in due to a polar interaction of dipoles with a substrate. A head or a tail of a molecule may have different chemical affinity to the substrate material, Fig. 10.10b. The molecules with electric dipole moment $\mathbf{p}_{\text{e}}$ form a dipolar monolayer whose polarization $P_{\text{surf}} = p_{\text{e}}n$ depends on the surface density of dipoles n. The polar layer thickness is determined by the characteristic diffusion length $\xi_d = (2D\tau)^{1/2}$ where D is a molecular diffusion coefficient and τ is a characteristic time for molecular rotation. We can encounter the same mechanism in isotropic liquids, however, in

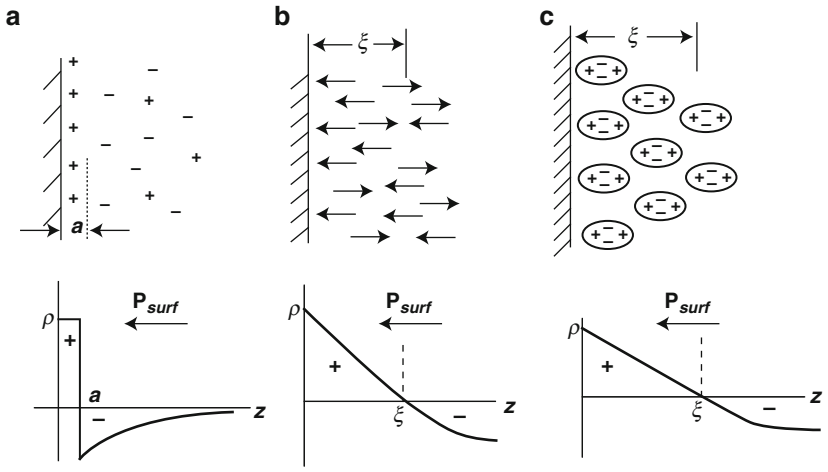

Fig. 10.10 A schematic picture of the charge distribution as a function of the distance from the liquid crystal–solid interface for ionic (**a**), dipolar (**b**) and quadrupolar (**c**) mechanisms of surface polarization P_{surf}

liquid crystals the diffusion coefficients and relaxation times are different for different director orientation and different dipolar structure of the constituent molecules. For longitudinal and transverse molecular dipoles, the same characteristic times $\tau_{\parallel}$ and $\tau_{\perp}$ are involved, which we met before when having discussed dielectric properties in Section 7.2.4.

Ordoelectric (Quadrupolar) Polarization

This polarization is related to the quadrupolar nature of any uniaxial phase, Fig. 10.10c. In the conventional nematic phase of symmetry $D_{\infty h}$ and order parameter tensor $\widehat{Q}$, each molecule or a building block may, on average, be represented by a quadrupole, and the phase may be characterized by a *tensor of density of the quadrupolar moment*

$$\widehat{Q}_{qu} = -q_{qu}\widehat{Q} = -q_{qu}S(n_i n_j - \delta_{ij}/3) \tag{10.15}$$

Here S is nematic order parameter amplitude and $q_{qu}S$ is the modulus of tensor $\widehat{Q}_{qu}$ (see Eq. 3.16), q_{qu} being a scalar coefficient with dimension [charge/cm]. Recall now that polarization is a gradient of charge density for any charge distribution (dipolar, quadrupolar, etc.). Therefore, the gradient of the orientational order parameter creates the polarization:

$$\mathbf{P} = -q_{qu}\nabla\widehat{Q} \tag{10.16}$$

This may be illustrated by appearance of the electric polarization in a hybrid cell, in which the quadrupolar molecules are oriented differently at the opposite interfaces, namely, homogeneously on the right plate and homeotropically on the left one Fig. 10.11. The molecular quadrupoles have an elongated form with positive charges at the apices. Therefore negative and positive charges are accumulated at the left and right plates, respectively, and the bulk polarization vector $\mathbf{P}(z)$ has its z-projection oriented from right to left. Note that in a hybrid cell the polarization occurs due to a change of the orientational part of tensor $\widehat{Q}$ i.e. the director $\mathbf{n}(\mathbf{r})$ without a change of its amplitude S. In this case we deal with a *flexoelectric polarization* [13], see for details Section 11.3.1. The flexoelectric mechanism may also be responsible for the surface polarization.

A change of the order parameter modulus $S(\mathbf{r})$ can also create polarization, for example due to transformation of the ellipsoidal shape of $\widehat{Q}$ tensor in space. In this case we deal with the so-called *ordoelectric polarization* [14]. Indeed, decreasing S value results in less extended (less prolate) ellipsoid form without reorientation of its principal axes. Such a transformation may be caused by a scatter of the rigid molecular quadrupoles with respect to the director axis: the stronger the scatter, the lower is the quadrupole order S and the less prolate ellipsoid $\widehat{Q}$. This is illustrated by Fig. 10.12: in sketch (a) the order parameter is stronger at the surface and

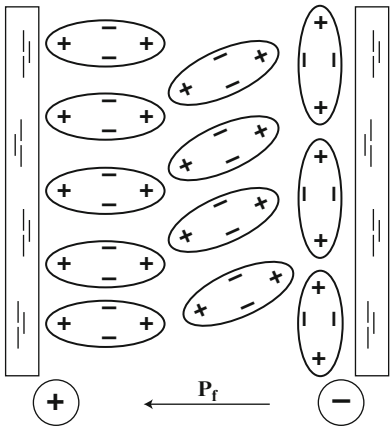

Fig. 10.11 A hybrid cell illustrating the appearance of polarization due to the gradient of quadrupolar density of charge (the molecular quadrupoles touch the *left* and *right* surfaces by their (+) and (−) sides, respectively)

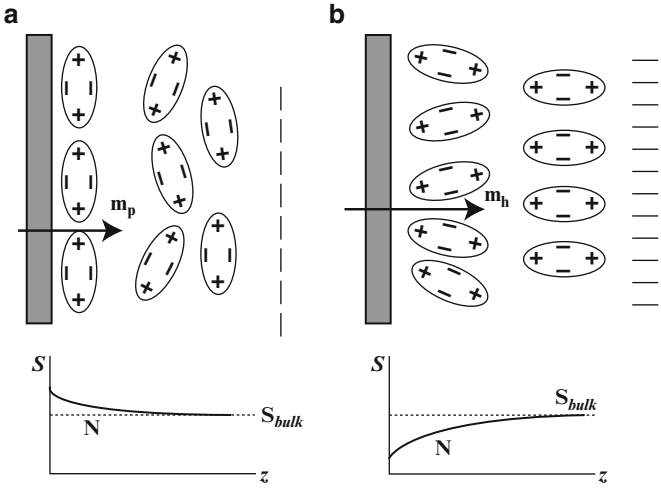

Fig. 10.12 Ordoelectric surface polarization. In sketch (**a**) the order parameter is larger at the surface and smaller in the bulk; in sketch (**b**) the order parameter is smaller at the surface than in the bulk. Corresponding gradient curves $S(z)$ for a nematic liquid crystal are qualitatively pictured in the bottom sketches. Vectors $\mathbf{m}_p$ and $\mathbf{m}_h$ show the directions of the surface polarization

decreases in the bulk due to statistical misalignment of quadrupolar molecules. On the contrary, in sketch (b) the order parameter is lower at the surface than in the bulk.

According to Eq. (10.16) the gradient of the order parameter amplitude $\nabla S(z)$ will inevitably result in the surface ordoelectric polarization:

$$\mathbf{P}_{surf} = q_{qu}(\nabla S)\left(n_i n_j - \frac{1}{3}\delta_{ij}\right) \tag{10.17}$$

For a fixed orientation of **n**, the surface polarization is a function of $\nabla S(z)$ and has dimension [CGSQ/cm^2 or C/m^2 in the SI system]. The sign of $\mathbf{P}_{surf}$ depends on the sign of the gradient ∇S that is on a technique of liquid crystal alignment and, evidently, on the sign of molecular quadrupoles. In Fig. 10.12 the direction of the ordoelectric polarization in the two cases is given by vectors m_p (planar alignment) and m_h (homeotropic alignment).

The surface polarization can be measured by different means. The most straightforward one is based on the pyroelectric technique [15]. To measure $\mathbf{P}_{surf}$ one has to deal only with one surface of a cell with uniform director alignment, either planar or homeotropic at both interfaces. The main idea is to use a spatially dependent temperature increment in order to separate the contributions to the pyroelectric response coming only from the surface under study and not from the opposite one. By definition, the pyroelectric coefficient is $\gamma = dP/dT$ where P is macroscopic polarization of a liquid crystal and T is temperature. If we are interested only in the polarization originated from the orientational order we can subtract the "isotropic" contribution to γ and calculate P in the nematic or SmA phases by integrating the pyroelectric coefficient, starting from a certain temperature T_i in the isotropic phase:

$$P(T) = \int_{T_i}^{T} \gamma(T) dT \tag{10.18}$$

In order to measure $\gamma(T)$ we have to change temperature by a small amount ΔT and record a pyroelectric response in the form of voltage U_p across the load resistor R shunted by input capacitance and cell capacitance. The most convenient, dynamic regime of γ measurements is based on heating the sample surface of area A by absorbed light of a pulse laser, Fig.10.13. The light is absorbed by a semitransparent electrode or by a dye dissolved in the liquid crystal. For a very fast (in comparison with RC) jump of temperature, to the end of a laser pulse t_p, the pyroelectric voltage reaches the magnitude $A\gamma\Delta T/C$ and pyroelectric coefficient can be found at a given temperature. Then, on cooling the cell from the isotropic phase the temperature dependence $\gamma(T)$ is found and, after integrating according to (10.18), we obtain $P = P_{surf}$. An example of temperature dependence of P_{surf} integrated over the cell

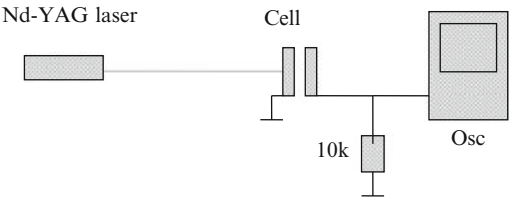

Fig. 10.13 Setup for the measurements of the surface polarization by a pyroelectric technique: short pulse of a Nd-YAG laser heats the polar surface layer of a liquid crystal and the pyroelectric current is detected by an oscilloscope

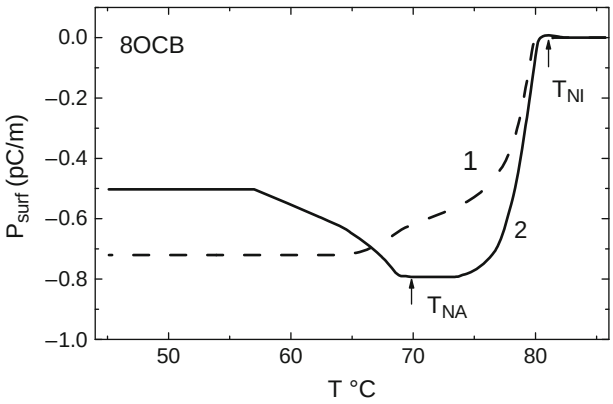

Fig. 10.14 Experimental temperature dependence of surface polarization in 8OCB liquid crystal having the nematic and smectic A phase; planar (*curve 1*) and homeotropic (*curve 2*) alignment

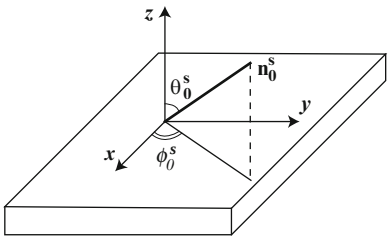

Fig. 10.15 Easy direction for the equilibrium alignment of the director ($\mathbf{n}_0^s$) at the surface and definition of the zenithal (ϑ_0^s) and azymuthal (ϕ_0^s) director angles

thickness is shown in Fig. 10.14 for two types of alignment, planar (curve 1) and homeotropic (curve 2). Note that the temperature behaviour of the two polarizations is quite different close to the N-SmA transition. We may guess that few dipolar smectic layers formed at the interface contribute stronger to P_{surf} than a not stratified nematic surface layer.

10.2 Surface Energy and Anchoring of Nematics

10.2.1 Easy Axis

Let the interface be in the *xy*-plane, as shown in Fig.10.15. The equilibrium position of the director **n** (the so-called easy direction or *easy axis*) is defined by the zenithal (ϑ_0^s) and azymuthal (ϕ_0^s) angles counted from the *z* and *x* axes, respectively. At the free surface of the nematic the easy direction appears spontaneously but at the nematic-solid interface it is predetermined by a specific treatment of the solid surface. We can distinguish the homeotropic ($\vartheta_0^s = 0$), planar ($\vartheta_0^s = \pi/2$) and tilted

($0 < \vartheta_0^s < \pi/2$) alignment. In turn, the planar orientation can be homogeneous with a unique angle ϕ_0^s, multistable when several easy directions are possible at a crystalline or specially prepared substrate, or degenerate if all ϕ_0^s-angles are equally probable and the cylindrical symmetry exists with respect to the surface normal. The same is true for the projections of the director on the *xy* plane in the case of the tilted orientation. Further on the angle of the director at the surface will be counted from the easy axis although other conventions may be used as, for instance, above in connection with Eq. (10.13).

Surface free energy of the nematic phase $F^s(\vartheta^s, \phi^s)$is minimal for the easy direction ($\vartheta^s = \vartheta_0^s, \phi^s = \phi_0^s$). The anisotropy of the surface energy is a characteristic feature of liquid crystals, $F^s = F_{iso}^s + F_a^s$. Here, two terms represent the isotropic and anisotropic parts. They differ from each other by several orders of magnitude. The isotropic part, which is, in fact, the surface tension introduced earlier is of the order of 100 erg·cm^{-2} (or 0.1 J·m^{-2}). The values for F_a^s-energy are scattered over five orders of magnitude from 10^{-5} to 1 erg·cm^{-2} (or $10^{-8} - 10^{-3}$ J·m^{-2}). F_a^s shows how much energy one has to spend in order to deflect the director from the easy direction, to which it is anchored in the ground state. That is why the anisotropic part of the surface energy is usually referred to as *anchoring energy*.

In order to consider any mechanical or electro-optical effects for a liquid crystal layer placed between two solid substrates one must solve a problem of the distribution of the director over the layer with allowance for the boundary conditions. The standard variational procedure allows such calculations when the surface energy depends only on orientation of the director (angles ϑ^s and ϕ^s) at both boundaries but not on their spatial derivatives.

10.2.2 Variational Problem

For consistency we go back to the problem of the twisted cell discussed in Section 8.3.2, however, the director angles φ at the boundaries will be not constant but can be changed due to elastic and external torques. Let a nematic layer be confined by two plane surfaces with coordinates $z_1 = -d/2$ and $z_2 = +d/2$ and the director is allowed to be deviated only in the *xy*-plane through angle φ (there is no tilt, the angle $\vartheta = \pi/2$ everywhere, and the azimuthal anchoring energy is finite).

$$F(\varphi) = \int_{-d/2}^{+d/2} g\left(\varphi, \frac{\partial \varphi}{\partial z}\right) dz + F_1^s(\varphi^s) + F_2^s(\varphi^s) \tag{10.19}$$

Here, g is Frank energy density, $F_{1,2}^s$ are surface energies at opposite boundaries.

Our task is to find the equilibrium alignment of the director everywhere between and at the solid surfaces. It is determined by minimization of the integral equation (10.19), i.e. by solution of the correspondent differential Euler equation for the bulk

$$\frac{\partial g}{\partial \varphi} - \frac{d}{dz}\left[\frac{\partial g}{\partial(\partial\varphi/\partial z)}\right] = 0 \tag{10.20}$$

with boundary conditions

$$-\left[\frac{\partial g}{\partial(\partial\varphi/\partial z)}\right]_1 + \frac{\partial F_1}{\partial \varphi_1} = 0 \text{ and } \left[\frac{\partial g}{\partial(\partial\varphi/\partial z)}\right]_2 + \frac{\partial F_2}{\partial \varphi_2} = 0 \tag{10.21}$$

The first terms in both Eqs. (10.21) correspond to the contribution from the bulk to the surface energy. How to understand the influence of the bulk on the surface? In fact, the two equations (10.21) represent the balance of elastic and surface torques at each boundary (indices 1 and 2). One of them comes from the bulk elasticity and deflects the director from the easy axis. The other is a torque from the surface forces that tries to hold the director at its equilibrium (easy) direction. The two equations themselves are brought about from the minimization procedure.

Let show it using mathematics. As was said, the boundary conditions are not fixed and the free energy depends on them. Let $\varphi(z)$ be a solution of the Euler equation for $F(\varphi)$ with fixed boundary conditions i.e. Eq. (10.20). Now we shall make variation of the boundary conditions in order to find the minimum of free energy with the surface terms included.

For example, we can calculate a derivative $\partial F/\partial \varphi_1$. If we fix z_1, z_2 and φ_2 and change only φ_1, the new solution for $\varphi(z)$ will get an increment $\delta\varphi(z)$. Correspondingly the free energy will get an increment ΔF. Ignoring highest order terms and using $\delta\varphi' \approx (\delta\varphi)'$ we obtain:

$$\Delta F = \int_{z_1}^{z_2} \left(\frac{\partial g}{\partial \varphi}\delta\varphi + \frac{\partial g}{\partial \varphi'}\delta\varphi'\right) dz \tag{10.22}$$

The second term of (10.22) can be integrated by parts:

$$\Delta F = \frac{\partial g}{\partial \varphi'}\delta\varphi\Big|_{z_1}^{z_2} + \int_{z_1}^{z_2} \left(\frac{\partial g}{\partial \varphi} - \frac{\partial}{\partial z}\frac{\partial g}{\partial \varphi'}\right)\delta\varphi dz \tag{10.23}$$

Note that the expression under the integral vanishes because $g(\varphi)$ satisfies the Euler equation (10.20). In addition, $\delta\varphi\ (z_2) = 0$, because φ_2 is fixed. Finally, the change in the bulk free energy due to variation of φ_1 is given by

$$\Delta F = -\frac{\partial g}{\partial \varphi'}\delta\varphi\Big|_{z_1}$$

and the elastic torque exerted by the bulk on the φ-director at the surface is given by

$$\frac{\partial F}{\partial \varphi_1} = -\frac{\partial g}{\partial \varphi'}\bigg|_{z_1}. \tag{10.24}$$

This is a contribution to be equalized by the surface torque $\partial F^s/\partial\varphi|_{z_1}$. The same is valid for the opposite boundary at z_2, see Eqs. (10.21). Thus, two expressions (10.21) are indeed torque balance equations for the director angle φ at the two boundaries.

10.2.3 Surface Energy Forms

In order to solve equations (10.20) and (10.21) we must know the explicit angular dependence of functions F_1^s and F_2^s. Their simplest form is the so-called *Rapini energy* [16]:

$$F^s = F^s_{iso} + \tfrac{1}{2}W\sin^2\delta\varphi^s \tag{10.25}$$

Here, $\delta\varphi^s = \varphi^s - \varphi_0^s$ is an angle of director deflection from the equilibrium angle φ_0^s and W is usually referred to as anchoring energy.

When both angles ϑ^s and $\varphi^s$are changed, two *Rapini energies* should be introduced: Azimuthal (for fixed ϑ^s):

$$F_a^{\varphi}(\vartheta^s) = \tfrac{1}{2}W^{\varphi}(\vartheta)\sin^2(\varphi^s - \varphi_0^s) \tag{10.26a}$$

Zenithal (for fixed φ^s):

$$F_z^{\vartheta}(\varphi^s) = \tfrac{1}{2}W^{\vartheta}(\varphi)\sin^2(\vartheta^s - \vartheta_0^s) \tag{10.26b}$$

The zenithal anchoring is often called polar, but this word is misleading because polar anchoring is related to polar director **L** as given by Eq. (10.13). Thus, the Rapini form corresponds to the sine-squared shape potential well for any director deviation β ($\delta\vartheta^s$ or $\delta\varphi^s$) from the easy direction (ϑ_0^s,φ_0^s):

$$F_a^{\beta} = \tfrac{1}{2}W\sin^2\beta \tag{10.27}$$

This function is shown by curve 1 in Fig. 10.16.

The Rapini term is the first one ($j = 1$) in an expansion of F^s in the Legendre polynomial series in terms of $\sin^{2j}\beta$:

$$F^s = F^s_{iso} + \sum_j W_j\sin^{2j}\beta,\ j = 1, 2.3... \tag{10.28}$$

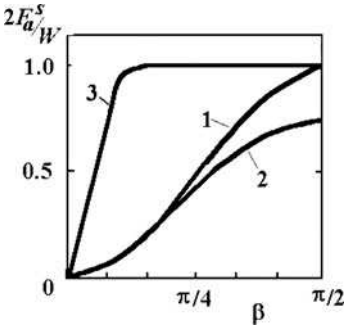

Fig. 10.16 Shapes of the surface potential curves: Rapini potential (1), Legendre expansion with two terms (2) and elliptic-sine profile (3)

To improve agreement with experiment, higher order terms of expansion (10.28) are used and this change the angle dependence of the energy as shown by curve 2 in Fig. 10.16 (for both $j = 1$ and 2 terms with ratio $W_2/W_1 = 0.5$). Some experimental data could be fitted better with other shapes of the surface potential, for example, with the elliptic sine-squared shape, $0 \le k \le 1$ [1]: $F_a^s = \frac{1}{2}Wsn^2(\beta, k)$.

Surely, this form is more general because it reduces to Rapini's one for $k = 0$, however, it requires numerical calculations. The corresponding angle dependence (for k close to 1) is shown by curve 3 in Fig. 10.16.

When the surface energy depends not only on the director itself but also on its spatial derivatives, $F^s = F^s(\varphi^s, {}^{\partial\varphi}/_{\partial z}\big|_s)$, then the so-called divergent elastic moduli K_{13} and K_{24} should be taken into account. In such cases, boundary conditions may become non-local in the sense that, for a finite cell thickness d and potential W, a situation at a boundary z_1 influences the conditions at the opposite boundary z_2.

10.2.4 Extrapolation Length

Consider again an important and fairly simple example: a twisted structure with a rigid boundary condition at $z = 0$ (easy axis y, $\varphi_1 = 0$, $W_1 \to \infty$) and soft boundary condition at $z = d$ (easy axis x, $\varphi_2 = \pi/2$, anchoring energy $W_2 = W_0$). Fig. 10.17a clarifies the corresponding geometry. Due to the bulk elastic torque acting on the director at $z = d$, the director deflects from the easy axis through angle φ_d, and forms the angle $\pi/2 - \varphi_d$ with the y-axis. Our task is to find the profile of $\varphi(z)$ for different W_0. The free energy is

$$F = \tfrac{1}{2}K_{22}\int_0^d \left(\frac{d\varphi}{dz}\right)^2 dz + \tfrac{1}{2}W_0({}^{\pi}/_2 - \varphi_d)^2 \qquad (10.29)$$

Here we use Rapini surface energy (10.25) and approximation $\sin(\pi/2 - \varphi_d) \approx (\pi/2 - \varphi_d)$.

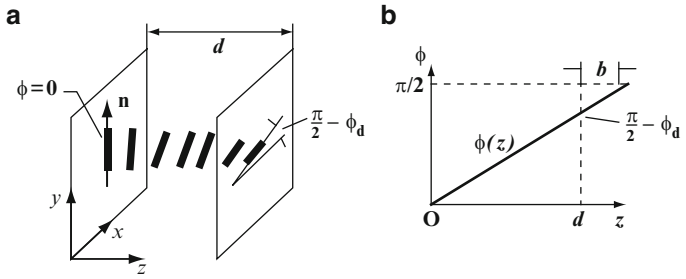

Fig. 10.17 Twisted structure with a rigid boundary condition at $z = 0$ and soft boundary condition at $z = d$. The geometry of the director distortion (**a**) and illustration of the extrapolation length b and linear dependence of the director angle $\phi(z)$ (**b**)

The Euler equation for the bulk is the same as earlier, see Eq. (8.24):

$$-K_{22}\frac{\partial^2\varphi}{\partial z^2} = 0 \tag{10.30}$$

The first boundary condition is $\varphi = 0$ at $z = 0$; the second one represents the torque balance at $z = d$ according to Eq. (10.21) and (10.29):

$$K_{22}\left.\frac{\partial\varphi}{\partial z}\right|_d + W_0(\pi/2 - \varphi_d) = 0 \tag{10.31}$$

The general solution of the bulk equation (10.30) is a straight line $\phi(z) = Az + B$ with $B = 0$ due to $\varphi = 0$ at $z = 0$ and $\varphi(d) = \varphi_d = Ad$. Now the second boundary condition reads:

$$K_{22}A - W_0(\pi/2 - Ad) = 0 \text{ that is } A = \frac{\pi W_0}{2(K_{22} + W_0 d)}.$$

Finally, we find the dependence of the twist angle on the z-coordinate in a twist cell with soft director anchoring at one boundary:

$$\varphi(z) = Az = \frac{\pi W_0 z}{2(K_{22} + W_0 d)} = \frac{\pi z}{2(d + \frac{K_{22}}{W_0})} = \frac{\pi}{2(d+b)}z. \tag{10.32}$$

Recall that for rigid director anchoring on both boundaries we had $\phi(z) = \pi z/2d$, see Section 8.3.2. Now, however, the situation is different and the solid line $\varphi(z)$ in Fig. 10.17b shows the new profile. If we extrapolate φ to $\pi/2$, the profile would correspond to a virtual cell with rigid anchoring on both interfaces and enlarged apparent thickness $d' = d + b$. The additional thickness $b = K_{22}/W_0$ is called *extrapolation length* and it is a measure of the anchoring strength, very useful for discussion of different field effects. For typical values of $K_{22} \approx 10^{-6}$ dyne (or 10^{-11} N

in SI system) and W_0 varied in the range of 10^{-3} – 1 erg/cm^2 (or 10^{-3} – 1 mJ/m^2) the values of extrapolation length $b = 10^{-3} - 10^{-6}$ cm (10–0.01 μm).

10.3 Liquid Crystal Alignment

10.3.1 Cells

In most practical applications and when examining liquid crystals, the sandwich type cells pictured in Fig. 10.18a are used. A flat capillary with a thickness of 1–100 μm is made from two glass plates with transparent electrodes. The separation between the plates is fixed by means of an insulating spacer (Mylar, mica, Teflon, polyethylene, etc.). To fix a very narrow gap (about 1–3 μm) glass bids or pieces of thin glass threads of proper diameter are placed between glasses. In sandwich cells light is incident along the direction of the electric field or, if required, at a specified angle to it. Sometimes, e.g., when investigating the flexoelectric effect, cells with a planar arrangement of electrodes are more suitable, see Fig. 10.18b. In that case, to reduce an applied voltage, the separation between the electrodes, which are made of metallic foil or metal evaporated in vacuum, is in the range from tens of microns to few millimeters, however, even for a millimeter gap, the amount of light passing through the cell is often insufficient. A more convenient cell has interdigitated electrodes, which can be either transparent or opaque, see Fig. 10.18c. The electrodes are deposited by photolithography methods. In such structures, a large light aperture is achieved with relatively small distances (about 10 μm) between the electrodes and one can operate with low voltages to have quite strong field strength.

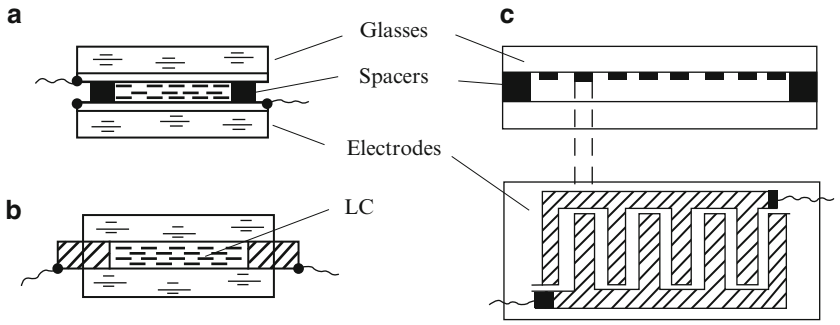

Fig. 10.18 Electrooptical cells of sandwich (**a**) and planar type (**b**) and the structures with in-plane interdigitated electrodes (**c**)

10.3.2 Alignment

10.3.2.1 Planar Homogeneous and Tilted Alignment

Most commonly, a planar alignment is produced by mechanical rubbing of the surface of the glass with paper or cloth (Chatelain's method [17]) or using special machines with rotating brushes. The pressure under the brushes and their angular velocity is well controlled. The rubbing creates a mechanical nano-relief on the polymer coating of a glass or an electrode material in the form of ridges and troughs, Fig. 10.19, which promotes the orientation of molecules along these formations. In other words, rubbing creates an easy axis for the director **n**. The technique is very simple, provides sufficiently strong anchoring of the director to the surface but, in the display technology, requires additional washing and drying the substrates. Another contact method is pattering the aligning layers with molecular size resolution by scribing a polymer coated surface by a cantilever of an atomic force microscope. The quality of alignment is very good, but the process is rather slow. Good results are obtained by evaporation of metals or oxides (e.g., SiO) onto the surface at oblique incidence, Fig. 10.20a. This method can also be applied to the orientation of various smectic mesophases.

A very important technique for optical device technology is photo-alignment of photosensitive polymers illuminated by polarized light [18]. Such a technique is non-contact and allows the design of multi-pixel structures using photo-masks. In some substances (polymers included) the absorbed light causes directional destroying molecules. In other materials, the light induces a molecular realignment resulting in an optical anisotropy of the film promoting the alignment of the liquid crystal

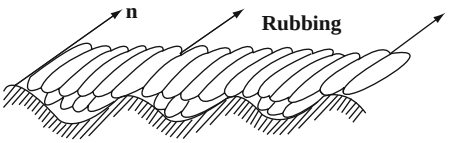

Fig. 10.19 A mechanical nano-relief obtained as a result of unidirectional rubbing the polymer surface; long polymer molecules are schematically represented by *ellipsoids*

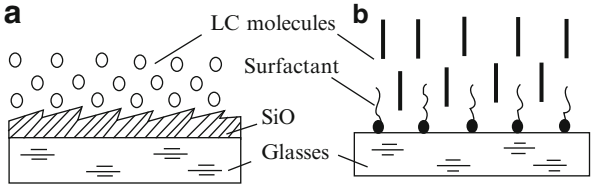

Fig. 10.20 Schemes of the planar homogeneous alignment of a nematic by an obliquely evaporated thin film of SiO (**a**) and homeotropic alignment by a monolayer of surfactant molecules (**b**)

contacting the film. Laser ablation and ion beam irradiation of polymers seem to be competing alignment techniques for displays [19].

A tilted orientation of molecules at a given angle to the surface is achieved using layers of SiO produced by oblique evaporation at a very large angle (80–90 deg) between the normal to the surface and the direction to the SiO source. Tilted orientation of the nematic liquid crystal molecules can also be achieved by using photosensitive films irradiated by obliquely incident light.

10.3.2.2 Homeotropic Alignment

Carefully cleaned or etched glass surfaces are conducive to a homeotropic orientation. Some crystalline cleavages (Al_2O_3, $LiNbO_3$) also align nematics homeotropically. However, the most popular technique for the homeotropic alignment is utilization of surfactants. The mechanism of homeotropic alignment by an ultrathin (even monomolecular) layer of a surfactant is demonstrated in Fig. 10.20b. An alignment layer can be obtained by withdrawing the substrate from the solution of surfactant, by polymerization of the organosilicon films directly on the substrate, and, in particular, by using a plasma discharge. Moreover, surfactant molecules can be introduced directly into the liquid crystal (e.g. lecithin or alkoxybenzoic acids) where they form the aligning layers by adsorption at the interface with a substrate.

10.3.2.3 Multistable Alignment

When a nematic is put in contact with a crystalline substrate, the surface of which possesses the N-fold rotational symmetry (e.g., $N = 6$ for mica, $N = 4$ for NaCl), the director is free to choose any of those N easy axes. In experiments, the orientation depends on the pre-history of the sample. A director field $\mathbf{n}(\mathbf{r})$ in a nematic drop put on the surface of a crystal acquires the same N-fold symmetry. In a sandwich cell, when crystalline axes of the opposite interfaces coincide, different domains are observed, with uniform structure or twisted through an angle $2\pi/N$ [20]. Using a properly oriented external in-plane field one can switch domains from one of the possible N orientations to another. Thus we have multistable alignment. When the crystalline axes of the opposite interfaces do not coincide, many domains with different twist angles are possible.

Vacuum evaporation of SiO films onto glass substrates at a grazing angle can also result in multistable alignment. Usually, the evaporation provides either the planar ($\perp$ to the evaporation plane) or tilted (in the evaporation plane) orientations. However, in a certain range of the incidence angle of the SiO beam and thickness of a film the *bistable alignment* is achieved. The director is aligned at a certain polar angle to a substrate and takes one of the two azimuthal angles located symmetrically with respect to the evaporation plane. The electric field can switch the director from one stable position to the other; thus the electrically controlled surface bistability has been demonstrated [21]. Multistable alignment can also be achieved

by combination of several factors, e.g., using a microrelief in the form of a diffraction grating and treatment of the aligning film by polarized UV light.

The change in the director alignment at the surface can occur spontaneously when temperature is varied (anchoring transition) due to the adsorption or desorption phenomena discussed earlier. However, close to the phase transition to the isotropic phase, the order parameter and other related properties (surface tension, elasticity) are markedly changed. Due to this, close to the transition, a nematic liquid crystal aligned by a fluoropolymer with very low anchoring energy continuously changes the angle of the alignment at the interface from zero to π/2 demonstrating a continuous anchoring transition [22].

10.3.3 Berreman Model

The macroscopic theory of elasticity can explain why longitudinal ridges and troughs on the surface of a glass are conducive to the planar homogeneous alignment of nematic liquid crystals [23]. For simplicity, a sinusoidal shape is chosen for the cross-section of a surface relief with the wavevector q directed along x, see Fig. 10.21a:

$$a(x) = A \sin qx \tag{10.33}$$

The amplitude A is assumed to be small and the components of the director **n** at any distance from the surface remain in the figure plane at an angle $\theta(x,z)$ with respect to the x-axis: $n_x = \cos\vartheta \approx 1$, $n_y = 0$, $n_z = \sin\vartheta \approx \vartheta$. With a distance z from the surface the amplitude of the relief decreases and deeply in the bulk the director is parallel to the x-axis. From Fig. 10.21a, we can see that such a director field requires some energy due to elastic bend distortion. If the director were parallel to the grooves $\mathbf{n} = n_y$ everywhere as in Fig. 10.21b the director field would be uniform with zero elastic energy. Therefore Berreman has calculated the extra energy for the geometry (a) with respect to the case (b).

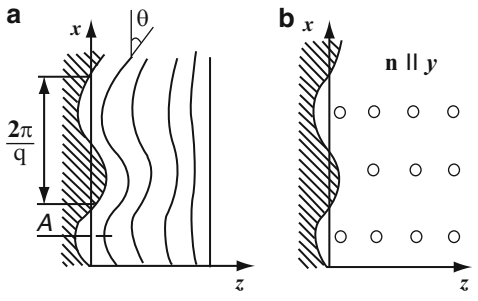

Fig. 10.21 Berreman model [23] illustrating an elastic free energy difference between the two configurations of the director, perpendicular (**a**) and parallel (**b**) to grooves of the surface relief

At the surface ($z = 0$) the z-component of the director is assumed to be tangential to the relief (strong anchoring boundary condition):

$$\vartheta(z=0) = n_z(x) = {}^{\partial a}/_{\partial x} = Aq\cos qx \tag{10.34}$$

In the one constant approximation ($K_{ii} = K$), the Frank distortion energy (8.15) can be written in terms of the angle ϑ:

$$g_d = \frac{K}{2}\left[\left(\frac{\partial\vartheta}{\partial z}\right)^2 + \left(\frac{\partial\vartheta}{\partial x}\right)^2\right] \tag{10.35}$$

The minimization gives us the Laplace equation:

$$\frac{\partial^2\vartheta}{\partial x^2} + \frac{\partial^2\vartheta}{\partial z^2} = \nabla^2\vartheta = 0 \tag{10.36}$$

with a solution

$$\vartheta(x,z) = Aq\cos(qx)\exp(-qz) \tag{10.37}$$

that satisfies the boundary condition (10.34) and the second boundary condition of $\vartheta = 0$ at $z \to \infty$.

Then, we find derivatives

$$\frac{\partial\vartheta}{\partial x} = -Aq^2\sin qx\cdot\exp(-qz);\ \frac{\partial\vartheta}{\partial z} = -Aq^2\cos qx\cdot\exp(-qz),$$

and substitute them into (10.35) to obtain the energy density

$$g_d = \frac{K}{2}(Aq^2)^2\exp(-2qz). \tag{10.38}$$

Hence, the major part of the elastic energy is concentrated within a layer of π/q thickness. Integrating over z we find for the total elastic energy per unit area

$$F_d = \int_0^\infty g_d(z)dz = \frac{1}{4}KA^2q^3 \tag{10.39}$$

Thus, the orientation of the director perpendicular to the grooves costs an excess elastic energy quadratically dependent on the relief depth A and inversely proportional to the cube of its period $\Lambda = 2\pi/q$. For typical values of $A = 1$ nm, $\Lambda = 20$ nm and modulus $K = 10^{-6}$ dyn, $F_d = 8.10^{-2}$ erg/cm^2 (or 8.10^{-2} mJ/m^2), which is close to experimental data. If a relief is two-dimensional in the x- and y-direction (e.g. at an etched surface) the director acquires the most profitable, homeotropic alignment along the z-axis.

References

1. Blinov, L.M., Chigrinov, V.G.: Electrooptic Effects in Liquid Crystal Materials. Springer-Verlag, New York (1993). Chapter 3
2. Sonin, A.A.: The Surface Physics of Liquid Crystals. Gordon & Breach, Amsterdam (1995)
3. Kleman, M., Lavrentovich, O.: Soft Matter Physics. Springer-Verlag, New York (2003). Chapter 13
4. Yokoyama, H.: Interfaces and thin films. In: Collings, P., Patel, J. (eds.) Handbook of Liquid Crystal Research, pp. 179–235. Oxford University Press, New York (1997)
5. Muševič, I.: Interfacial and surface forces in nematics and smectics. In: Rasing, Th, Muševič, I. (eds.) Surface and Interfaces of Liquid Crystals, pp. 41–56. Springer, Berlin (2004)
6. Sheng, P.: Boundary-layer phase transitions in nematic liquid crystals. Phys. Rev. A **26**, 1610–1617 (1982)
7. Blinov, L.M., Kats, E.I., Sonin A.A.: Surface physics of thermotropic liquid crystals. Usp. Fiz. Nauk. **152**, 449–477 (1987) (Sov. Phys. Uspekhi **30**, 604 (1987)
8. Horn, R.G., Israelashvili, J.N., Perez, E.: Forces due to structure in a thin liquid crystal film. J. Phys. (Paris) **42**, 39–52 (1981)
9. Hara, M.: STM studies of anchoring phase transitions at nematic interfaces. In: Dunmur, D., Fukuda, A., Luckhurst, G. (eds.) Physical Properties of Liquid crystals: Nematics, pp.503–514. INSPEC, London (2001)
10. Ryschenkov, Yu, Kleman, M.: Surface defects and structural transitions in very low anchoring energy nematic thin films. J. Chem. Phys. **64**, 404–409 (1976)
11. Guyot-Sionnest, P., Hsiung, H., Shen, Y.R.: Surface polar ordering in a liquid crystal observed by optical second harmonic generation. Phys. Rev. Lett. **57**, 2963–2966 (1986)
12. Prost, J., Pershan, P.S.: Flexoelectricity in nematic and smectic-A liquid crystals. J. Appl. Phys. **47**, 2298–2313 (1976)
13. Meyer, R.B.: Piezoelectric effect in liquid crystals. Phys. Rev. Lett. **22**, 917–921 (1969)
14. Barbero, G., Dozov, I., Palierne, J.F., Durand, G.: Order electricity and surface orientation in nematic liquid crystals. Phys. Rev. Lett. **56**, 2056–2059 (1986)
15. Blinov, L.M., Barnik, M.I., Ohoka, H., Ozaki, M., Yoshino, K.: Separate Measurements of the Flexoelectric and Surface Polarization in a Model Nematic Liquid Crystal MBBA: on Validity of the Quadrupolar Approach. Phys. Rev. E **64**, 031707–031713 (2001)
16. Rapini, A., Papoular, M.: Distorsion d'une lamelle nematique sous champ magnetique conditions d'ancrage aux parois. J. Phys. (Paris) **30**, Colloq. C4, 54–56 (1969)
17. Chatelain, P.: Sur l'orinetation des cristaux liquides par les surfaces frottées. CR. Acad. Sci. **213**, 875–876 (1941)
18. Chigrinov, V., Kozenkov, V., Kwok, H.-S.: Photoalignment of Liquid Crystalline Materials: Physics and Application. Wiley, Chichester (2008)
19. Muševič, I., Nieuwkerk, C., Rasing, T.H.: Introduction. In: Rasing, T.H., Muševič, I. (eds.) Surface and Interfaces of Liquid Crystals, pp. 3–15. Springer, Berlin (2004)
20. Blinov, L.M., Sonin, A.A.: The interaction of nematic liquid crystals with anisotropic substrates. Mol. Cryst. Liq. Cryst. **179**, 13–25 (1990)
21. Barberi, R., Durand, G.: Controlled textural bistability in nematic liquid crystals. In: Collings, P., Patel, J. (eds.) Handbook of Liquid Crystal Research, pp. 567–589. Oxford University Press, New York (1997)
22. Patel, J.S., Yokoyama, H.: Continuous anchoring transition in liquid crystals. Nature **362**, 525–527 (1993)
23. Berreman, D.: Solid surface shape and the alignment of the adjacent liquid crystal. Phys. Rev. Lett. **28**, 1683–1686 (1972)

Part III
Electro-Optics

Chapter 11
Optics and Electric Field Effects in Nematic and Smectic A Liquid Crystals

11.1 Optical Properties of Uniaxial Phases

11.1.1 Dielectric Ellipsoid, Birefringence and Light Transmission

11.1.1.1 Dielectric Ellipsoid

We begin with the electric displacement vector $D_j = \varepsilon_{ij}E_i$ where $i, j = x', y', z'$ are Cartesian coordinates and the summation over repeated indices is inferred. The tensor of dielectric permittivity is symmetric $\varepsilon_{ij} = \varepsilon_{ji}$and generally (even for biaxial medium) has six independent components. If an insulator is placed in the electric field, the stored electric energy density is given by

$$g_{electr} = \frac{1}{8\pi}\mathbf{E}\cdot\mathbf{D} = \frac{1}{8\pi}E_i\varepsilon_{ij}E_j \tag{11.1}$$

or

$$8\pi g_{elect} = \varepsilon_{x'x'}E_{x'}^2 + \varepsilon_{y'y'}E_{y'}^2 + \varepsilon_{z'z'}E_{z'}^2 + 2\varepsilon_{y'z'}E_{y'}E_{z'} + 2\varepsilon_{x'z'}E_{x'}E_{z'} + 2\varepsilon_{x'y'}E_{x'}E_{y'}$$

This is an equation of an ellipsoid arbitrary oriented with respect to any Cartesian frame [1]. The frame may be chosen in such a way that the ellipsoid will be oriented with its principal axes along the co-ordinate axes. In the new frame x, y, z, the tensor is diagonal that is all the off-diagonal terms vanish:

$$8\pi g_{elect} = \varepsilon_{xx}E_x^2 + \varepsilon_{yy}E_y^2 + \varepsilon_{zz}E_z^2 \tag{11.2}$$

The same energy may be expressed in terms of the electric displacement vector components:

$$8\pi g_{elect} = \frac{D_x^2}{\varepsilon_{xx}} + \frac{D_y^2}{\varepsilon_{yy}} + \frac{D_z^2}{\varepsilon_{zz}} \tag{11.3}$$

L.M. Blinov, *Structure and Properties of Liquid Crystals*,
DOI 10.1007/978-90-481-8829-1_11, © Springer Science+Business Media B.V. 2011

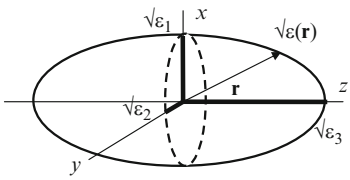

Fig. 11.1 Dielectric ellipsoid for a biaxial medium

and now the constant energy curves ($8\pi g_{elect}$) form ellipsoids in the space D_x, D_y, D_z,.

Finally we go back to the x ,y, z space replacing vector $\mathbf{D}/\sqrt{8\pi g_{elect}}$ by vector $\mathbf{r}$. Then we obtain the dielectric ellipsoid shown in Fig. 11.1 with three semi-axes equal to $\sqrt{\varepsilon_3}$, $\sqrt{\varepsilon_3}$, $\sqrt{\varepsilon_3}$ and satisfying to equation

$$\frac{x^2}{\varepsilon_1}+\frac{y^2}{\varepsilon_2}+\frac{z^2}{\varepsilon_3}=1 \tag{11.4}$$

From this ellipsoid we can find $\sqrt{\varepsilon}$ for any direction specified by radius-vector $\mathbf{r}$, see the figure. For example such an ellipsoid corresponds to the biaxial phase of the SmC liquid crystal. In this case all the three semi-axes are different $\varepsilon_1 = \varepsilon_{xx} \neq \varepsilon_2 = \varepsilon_{yy} \neq \varepsilon_3 = \varepsilon_{zz}$. For a *uniaxial phase* (nematic, smectic A) the ellipsoid degenerates into an ellipsoid of revolution that is invariant for rotation about, e.g., the z-axis. For an isotropic liquid or a cubic crystal the ellipsoid degenerates into a sphere of radius $\sqrt{\varepsilon}$.

At optical frequencies $\varepsilon = n^2$ and the same ellipsoid becomes the so-called "optical indicatrix" with its semi-axes exactly equal to refraction indices n_1, n_2 and n_3.

$$\frac{x^2}{n_1^2}+\frac{y^2}{n_2^2}+\frac{z^2}{n_3^2}=1 \tag{11.5}$$

Therefore, electromagnetic waves with polarization vectors along x, y or z axes propagate with three different velocities c/n_1, c/n_2 and c/n_3. In addition, two waves with the same wave normal $\mathbf{h}$ but orthogonal polarizations $\mathbf{s}$ propagate in different directions; the wavevector of the ordinary ray is parallel to the normal, $\mathbf{k}_o \| \mathbf{h}$, but wavevector $\mathbf{k}_e$ for the extraordinary ray forms an angle with $\mathbf{h}$. It means that the *Snell law* is not fulfilled for the extraordinary index of biaxial crystals. This results in a double refraction phenomenon. For biaxial crystals the double refraction occurs even at normal light incidence onto their surface; for uniaxial ones only at oblique incidence.

11.1.1.2 Extraordinary Index of a Birefringent Layer

The most interesting for applications are *uniaxial phases* in which $n_1 = n_2 = n_\perp$ and $n_3 = n_\parallel$. For $\mathbf{k} \parallel \mathbf{n}$, z ($\mathbf{n}$ is the director) light of any polarization propagates along the

optical axis with the same velocity $c/n_\perp$ (no extraordinary ray). For example, this corresponds to the normal incidence of light onto homeotropically aligned nematic layer (case *a* in Fig. 11.2). For an arbitrary angle between **k** and **n**, the beam of unpolarised light can always be decomposed into two beams. The ordinary ray with electric polarization vector **e** $\perp$ **n** propagates with velocity c/n_o independent of the incidence angle. The extraordinary ray propagates with velocity c/n_e; Index n_e depends on the incident angle and can be found from the optical indicatrix. For example, in Fig. 11.2b, a nematic liquid crystal has a tilted orientation with an angle α between the light vector **e** and the director **n**. Then the refraction index for the extraordinary ray as a function of the tilt angle $\vartheta = \pi/2 - \alpha$ between **n** and z is given by:

$$n_e(\vartheta) = \frac{n_{||} n_\perp}{\sqrt{n_{||}^2 \cos^2\vartheta + n_\perp^2 \sin^2\vartheta}} \tag{11.6}$$

Here $n_{||}$ and $n_\perp$ are principal refractive indices of the nematic (semi-axes of the ellipsoid).

This result came about from the consideration of the ellipsoid cross-section in plane (n, k) and the position of point P on the indicatrix, see Fig. 11.3. The projections of the segment $n_e(\vartheta)$ on the semi-axes of the ellipse are

$X = n_e(\vartheta)\cos\vartheta$, $Z = n_e(\vartheta)\sin\vartheta$ and $Y = 0$

The point P is situated on the indicatrix, therefore, from (11.5) we obtain the expression

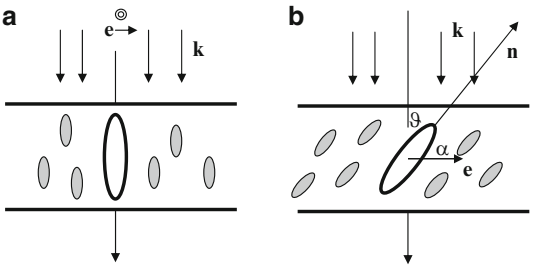

Fig. 11.2 Normal light incidence on a planar layer of a nematic liquid crystal with homeotropic (**a**) and tilted (**b**) alignment (**k** is light propagation vector, **e** is light polarization vector, **n** is the director)

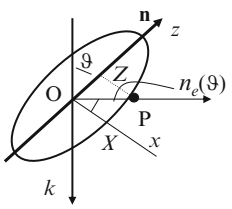

Fig. 11.3 The geometry for calculation of the extraordinary refraction index $n_e(\vartheta)$ for the tilted nematic shown in Fig. 11.2b. Z and X are projections of segment OP on the long and short ellipsoid axes

$$\frac{n_e^2(\vartheta)\cos^2\vartheta}{n_\perp^2}+\frac{n_e^2(\vartheta)\sin^2\vartheta}{n_\parallel^2}=1$$

and then arrive at Eq. (11.6):

$$n_e(\vartheta)=\left(\frac{\cos^2\vartheta}{n_\perp^2}+\frac{\sin^2\vartheta}{n_\parallel^2}\right)^{-1/2}=\frac{n_\parallel n_\perp}{\sqrt{n_\parallel^2\cos^2\vartheta+n_\perp^2\sin^2\vartheta}}$$

For example, for the homeotropic orientation, $\vartheta = 0$ and $n_e(\vartheta) = n_\perp$; for homogeneous planar alignment $\vartheta = \pi/2$ and $n_e(\vartheta) = n_\parallel$.

11.1.1.3 Light Ellipticity

Consider the normal incidence of unpolarised monochromatic light of wavelength λ onto a homogeneously aligned ($\mathbf{n} \parallel x$) nematic or SmA layer of thickness d. The layer is between the polariser (P) and an analyser (A) with an arbitrary angle χ between them, Fig. 11.4. We are interested in the light polarization and intensity of the transmitted beam [2]. The reflected light intensity is negligible (few percents of the incident intensity), the absorption in a liquid crystal, is absent and both polarizers and analyser considered to be ideal.

The amplitude E of the linearly polarised light beam after a polarizer can be projected onto the two principal directions of the nematic, parallel and perpendicular to the optical axis x:

$$E_\parallel = a = E\cos\varphi; E_\perp = b = E\sin\varphi; \tag{11.7}$$

The ordinary and extraordinary rays passing the layer acquire an additional phase shifts equal, respectively, to $2\pi n_o d/\lambda$ and $2\pi n_e d/\lambda$, therefore their phase difference is $\delta = \left(2\pi/\lambda\right)(n_e - n_o)d$.

Generally, the interference of two fields results in an *elliptic polarization*. It can be shown if we consider time dependencies of the fields. After the liquid crystal layer, the output fields are:

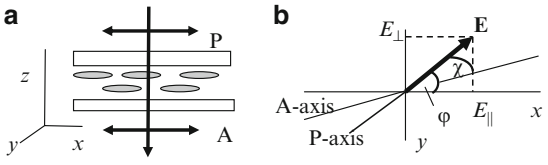

Fig. 11.4 Transmission of unpolarised light through a homogeneously aligned nematic (or smectic A) layer; geometry of experiment with polarizer P and analyser A (**a**) and definition of characteristic angles φ and χ (**b**)

$$x = a\cos\omega t, y = b\cos(\omega t - \delta) = b(\cos\omega t\cos\delta + \sin\omega t\sin\delta) \tag{11.8}$$

From these two equations for we obtain $y/b - \cos\omega t\cos\delta = \sin\omega t\sin\delta$ and

$$\sin\omega t \cdot \sin\delta = \frac{y}{b} - \frac{x}{a}\cos\delta$$

or

$$\sin^2\omega t \cdot \sin^2\delta = \frac{y^2}{b^2} - \frac{2xy}{ba}\cos\delta + \frac{x^2}{a^2}\cos^2\delta.$$

In addition, using $\cos\omega t = x/a$ we may write $\cos^2\omega t \cdot \sin^2\delta = \frac{x^2}{a^2}\sin^2\delta$.

Now we make a sum of the last two equations and exclude the time dependence. Then we arrive at the equation for the output field (but before an analyser) in the form of the equation for an ellipse:

$$\frac{x^2}{a^2} + \frac{y^2}{b^2} - \frac{2xy}{ab}\cos\delta = \sin^2\delta \tag{11.9}$$

The orientation of the ellipse axes depends on polarizer angle φ (through a and b) and phase retardation δ. Consider few interesting consequences of (11.9).

Case 1 Corresponds to the So-Called λ/4 Plate

The layer thickness satisfies the condition $(n_e - n_o)d = \lambda/4$, i.e., $\delta = \pi/2$, and the ellipse becomes oriented along the principal axes of the nematic layer and the ratio of its semi-axes depends only on polarizer angle φ:

$$\frac{x^2}{a^2} + \frac{y^2}{b^2} = 1 \tag{11.10}$$

Particularly, for $\varphi = \pm\pi/4$ i.e. $a = \pm b$ the equation for an ellipse degenerates into the equation for a circumference:

$$x^2 + y^2 = a^2 \tag{11.11}$$

The light beam transmitted through the layer becomes left or right circularly polarised. Thus a λ/4 plate converts the linear polarization to one of the possible circular polarizations, left or right dependent on a sign of parameter b as illustrated by Fig. 11.5. Note that, in the figure, the right polarization corresponds to the electric vector of light **e** rotating clockwise for an observer looking at the incoming beam (according to the convention used in many classical books, for instance in [2,3]). However, more recently, another convention is often used according to

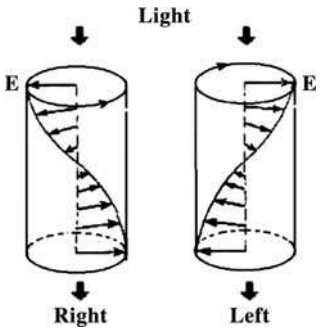

Fig. 11.5 Right and left circular polarization of light according to the classical convention (according to the modern connection the handedness is reversed)

which the right polarization of light follows the right screw law [4]. Personally, I like more the second one, however, throughout the book we follow the traditional convention.

Case 2 Corresponds to the λ Plate

The layer thickness satisfies the condition $(n_e - n_o)d = \lambda$, i.e., $\delta = 2\pi$. Then, according to (11.9), the ellipse degenerates into the straight line $^{x}/_{a} - {}^{y}/_{b} = 0$ or $y = xb/a = x{\cdot}\tan\varphi$. This means that after the cell the light is linearly polarised. The same equation is valid for $\delta = 2k\pi$ where k is any integer. The angle φ is determined by the angular position of polarizer; for $\varphi = \pi/4$ the cell transmit light without change of polarization, $y = x$.

11.1.1.4 Light Transmission (Cell Between Polarizers)

The transmitted light intensity is calculated as follows. The analyser can only transmit the field components parallel to its axis, that is projections of $E_{\|}$ and $E_{\perp}$ on the analyser direction A, see again Fig. 11.4:

$$E_{\|}^{A} = E\cos\varphi\cos(\varphi - \chi); \quad E_{\perp}^{A} = E\sin\varphi\sin(\varphi - \chi); \tag{11.12}$$

The total light intensity I after an analyser is a result of interference of the two rays

$$I = I_{\|}^{A} + I_{\perp}^{A} + 2(I_{\|}^{A} I_{\perp}^{A})^{1/2}\cos\delta. \tag{11.13}$$

Then

$$I = E^2\{[\cos\varphi\cos(\varphi - \chi)]^2 + [\sin\varphi\sin(\varphi - \chi)]^2 + \tfrac{1}{2}\sin 2\varphi\sin 2(\varphi - \chi)\cos\delta\}$$

and using $\cos^2(2\varphi - \chi) = \frac{1}{2}[1 + \cos 2(2\varphi - \chi)]$ and $\cos\delta = (1 - 2\sin^2\frac{\delta}{2})$ we find the transmitted intensity:

$$I = E^2[\cos^2\chi - \sin 2\varphi \sin 2(\varphi - \chi)\sin^2\delta/2] \tag{11.14}$$

Consider again two important particular cases:

Case a, parallel polarizers, A ∥ P. In this case $\chi = 0$ and

$$I_{||} = E^2(1 - \sin^2 2\varphi \cdot \sin^2\delta/2) \tag{11.15}$$

There are maxima of transmission for $\varphi = 0, \pi/2, \pi\ldots$etc, and $I_{||}$ (max) $= E^2$, when the incoming polarization coincides with the principal axes x or y. Between them there are minima of transmission corresponding to $\varphi = \pi/4, 3\pi/4, 5\pi/4\ldots$. Their intensities $I_{||}$ (min) $= E^2 \cos^2(\delta/2)$ do not show full darkness (except a special value for phase retardation when $\cos^2(\delta/2) = 0$).

Case b, crossed polarizers, A ⊥ P. Now $\chi = \pi/2$ and

$$I_{\perp} = E^2\sin^2 2\varphi \cdot \sin^2\delta/2 \tag{11.16}$$

Now minima for $\varphi = 0, \pi/2, \pi\ldots$ correspond to complete darkness and the maximum intensity is observed at $\varphi = \pi/4, 3\pi/4, 5\pi/4\ldots$ This case is the most interesting because provides a high contrast for a cell under a microscope. Let us select the angle $\varphi = \pi/4$ between the director and polarizer. Then we have maximum light intensity after analyser

$$I_{\perp}(\max) = E^2\sin^2\frac{\delta}{2} = E^2\sin^2\frac{\pi(n_e - n_o)d}{\lambda} \tag{11.17}$$

The light intensity has an oscillatory character as a function of cell thickness d, optical anisotropy $\Delta n = n_e$-n_o and wavelength λ. This can be used for measurements of Δn.

11.1.1.5 Measurements of Birefringence of Nematics

For example, we can use a wedge form cell, in which thickness $d(x)$ changes along the optical axis of a nematic, see Fig. 11.6. The nematic director is parallel to x, the polarizer P is installed at an angle of 45° to the x-axis and analyser A is crossed with polarizer. If such a cell is illuminated by a filtered light of wavelength λ, then, a series of contrast interference stripes is seen which are parallel to the y-direction. The dark stripes correspond to $d\Delta n/\lambda = 0, 1, 2\ldots k$ and the distance between them is constant, $l = \lambda\sin\alpha/\Delta n$ where α is the angle of the wedge. The latter can be found from the "stripes of equal thickness" in a part of the wedge not filled with the

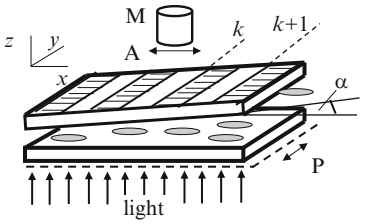

Fig. 11.6 Scheme of simple measurements of optical anisotropy $\Delta n = n_{\parallel} - n_{\perp}$ by observation of interference lines in a wedge-form nematic cell placed between cross polarisers (α: wedge angle; P: polarizer; A: analyzer; M; microscope; k: order of interference). The same scheme can easily be modified to measure refraction indices $n_{\parallel}$ and $n_{\perp}$ separately as explained in the text

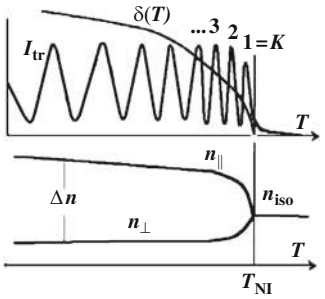

Fig. 11.7 Temperature dependencies of the transmitted light intensity I_{tr} and phase retardation δ (*above*) and principal refraction indices (*below*)

nematic. With known wedge angle one can also use the "stripes of equal thickness" for measurements of $n_{\parallel}$ and $n_{\perp}$ separately: to this effect the electric vector of a linearly polarised light should be installed parallel or perpendicular to the director and analyser is not used.

The temperature dependence of $\Delta n = n_{\parallel} - n_{\perp}$ where $n_{\parallel}$ and $n_{\perp}$ are principal indices of a nematic (lower plot in Fig. 11.7) can simply be measured using geometry of Fig. 11.4. A cell with fixed thickness d about 30 μm and well-aligned nematic (or a smectic with intermediate nematic phase) is heated up to the isotropic phase. Due to a decrease in Δn with increasing temperature, the transmitted intensity oscillates and these oscillations can be numbered as 1,2,3..k counted from the isotropic phase. This way the phase retardation $\delta(T) = 2\pi d\Delta n(T)/\lambda = 2\pi, 4\pi, 6\pi \ldots 2k\pi$ can be plotted as a function of temperature and $\Delta n(T)$ found from Eq. (11.17), see upper plot in Fig. 11.7. The absolute values of n_{iso} and $n_{\perp}$ can easily be found with a refractometer although one can meet some problems with refractometry of $n_{\parallel}$. We can also change the direction of the director by external factors (electric and magnetic fields, acoustic vibrations, flow of a liquid crystal) and follow these changes by birefringence measurements with high accuracy. For a comprehensive review of experimental data on optical properties of liquid crystal see [5].

11.1.1.6 Twist Structure

Consider one more particular case related to elliptic polarization of light that passes a birefringent layer. Let the layer be very thin, $d \to 0$ and the principal axis of the layer forms an angle φ with the input linear polarization. Then we go back to the general form of the ellipse (11.9) and using smallness of phase shift δ ($\cos\delta \approx 1 - \delta \approx 1$ and $\sin^2\delta \approx \delta^2$) get

$$\frac{x^2}{a^2} + \frac{y^2}{b^2} - \frac{2xy}{ab}(1 - \delta) = \delta^2. \tag{11.18}$$

Neglecting $\delta << 1$ in parentheses we obtain

$$\frac{x}{a} - \frac{y}{b} = \delta. \tag{11.19}$$

This equation describes a straight line

$$y \approx \frac{b}{a}x - b\delta = \frac{E\sin\phi}{E\cos\phi}x - b\delta = x\tan\phi - b\delta$$

showing that the outgoing beam is linearly polarised and its electric vector forms a small angle $b\delta$ with respect to the vector of the *linearly polarised* incident beam. So, there is no ellipticity!

Now imagine a stack of very thin plates or layers, in which the director turns by a small angle upon proceeding from one layer to the next one. Then, after each passage of a successive plate, the electric vector of the beam rotates through a small angle and such a stack of plates "guides" the light polarisation. We can prepare such a "stack" using different boundary conditions for alignment of the nematic. For instance, if the directors at the top and bottom glasses are strictly perpendicular to each other, the nematic is twisted through angle $\pi/2$, as discussed in Section 8.3.2. It is of great importance that the light polarization follows the $\pi/2$-twisted structure at any wavelength. This is so-called "waveguide" or Mauguin regime [6]. When light leaves the entire nematic cell its electric vector is turned through $\pi/2$ with respect to the electric vector of the incident beam. It is evident that, a planar cell is non-transparent when installed between crossed polarizers with polarizer P parallel (or perpendicular) to the director, because an analyser absorbs light almost completely, Fig. 11.8a. A homeotropic cell is also non-transparent when observed through crossed polarizers. On the contrary, a twist cell completely transmits light under the same conditions, Fig. 11.8b.

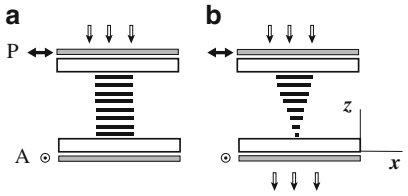

Fig. 11.8 A planar cell installed between crossed polarizers is non-transparent (**a**) whereas a twist cell rotates the linear polarization through π/2 and transmits light (**b**). Polarizer P is parallel to the director at the input plate

11.1.2 Light Absorption and Linear Dichroism

11.1.2.1 Extinction Index, Absorption Coefficient, Optical Density

An electromagnetic wave propagating with velocity v in a medium is described by the wave equation:

$$\Delta \mathbf{E} - \frac{1}{v^2}\frac{\partial^2 \mathbf{E}}{\partial t^2} = 0.$$

Assuming $\mathbf{E}(\mathbf{r}, t) = \mathbf{E}(\mathbf{r})\exp(-i\omega t)$ we exclude the time dependence and get the Helmholtz equation:

$$\Delta \mathbf{E} + \varepsilon\mu\frac{\omega^2}{c^2}\mathbf{E} = 0$$

where ε and μ are dielectric and magnetic permeability and c light velocity in vacuum.

For the plane wave $\mathbf{E(r)} \propto \exp i\mathbf{kr}$ and we obtain the dispersion relation: $k^2 = \varepsilon\mu\omega^2/c^2$. For the absorbing medium the wavevector amplitude k becomes complex:

$$k* = (\varepsilon\mu)^{1/2}\frac{\omega}{c} \approx (n + i\kappa)\frac{\omega}{c} \tag{11.20}$$

The absorbing medium can be described in terms of a complex refraction index $n^* = n + i\kappa$ where n is real refraction index and κ is real *extinction index*. For non-magnetic medium $\mu \approx 1$ and $(n + i\kappa)^2 = n^2 - \kappa^2 + 2in\kappa = \varepsilon* = \varepsilon' + \varepsilon''$ we find the relations between the components of ε* and n*:

$$n^2 - \kappa^2 = \varepsilon' \text{ and } 2n\kappa = \varepsilon'' \tag{11.21}$$

From (11.21) it is seen how any kind of energy dissipation contributes to real part of the dielectric permittivity ε′ at optical frequencies.

The dimensionless extinction index κ can be related to the absorption coefficient α_{abs} (cm^{-1}) by the well-known *Buger law* for the light intensity I transmitted through an absorbing layer of thickness z (the reflection is ignored):

$$I = I_0 \exp(-\alpha_{abs} z) \tag{11.22}$$

Indeed, comparing (11.22) with a general form for imaginary part of $Imk^* = i\kappa\omega/c$, we find

$$I \propto (E \exp ikz)^2 = E^2 \exp(-\frac{2\kappa\omega}{c} z) = E^2 \exp(-\frac{4\pi}{\lambda} \kappa z)$$

and then obtain

$$\alpha_{abs} = \frac{2\kappa\omega}{c} = \frac{4\pi\kappa}{\lambda} \tag{11.23}$$

In experiment, a spectrometer usually measures the so-called *absorbance or optical density* D of a sample with thickness d:

$$D = \log_{10} {}^{I_0}/_{I} = \log_{10} {}^{1}/_{T} = \alpha_{abs} d \log_{10} e = 0.434 \alpha_{abs} d \tag{11.24}$$

Note that here, the losses due to reflection from and scattering in the sample are disregarded.

This relationship may be used for calculation of the absorption coefficient α_{abs} and extinction coefficient κ from measured values of D. A typical absorption spectrum of a liquid crystalline substance in the isotropic phase is shown in Fig. 11.9a. In the UV part of the spectrum, the absorption originates from molecular electronic transitions (with vibronic structure). Except for dyes, the long-wave edge of organic compounds is situated at about 250–350 nm depending on particular molecular structure. As a rule, liquid crystalline materials are transparent in the

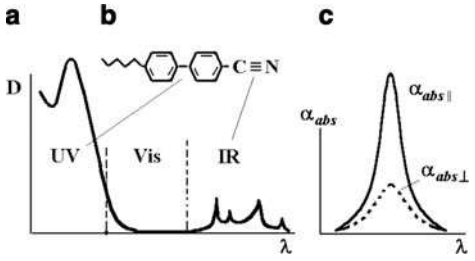

Fig. 11.9 Typical absorbance spectrum of a mesogenic compound (in the isotropic phase) with absorption bands in the visible and infrared spectra (**a**), typical molecular moieties responsible for the UV and IR absorption (**b**) and characteristic polarization absorption spectra (dichroism) in the nematic phase (**c**)

visible and near IR range (400–2,500 nm) although thick layers can strongly scatter light. Some IR absorption bands are very characteristic; they are caused by vibrations related to particular molecular bonds, e.g., -C = O, -C-F, -C ≡ N, -C-H, stretch vibration of benzene ring, etc. Such bands can be used for identification of substances by IR spectroscopy.

Each particular electronic or vibrational band originates from a quantum transition between two energy states i and j characterised by a transition dipole moment $\mathbf{p}_{tr}$ that is a vector. The molecule only absorbs light when $(\mathbf{e}\mathbf{p}_{\mathrm{tr}}) \neq 0$, i.e., when there is a non-zero projection of the light electric vector $\mathbf{e}$ onto $\mathbf{p}_{tr}$. The absorption cross-section of a molecule σ_{abs} in (cm^2) units is proportional to $|\mathbf{p}_{tr}|^2$ and can be related to the absorption coefficient and a number of molecules in a unit volume n_v [cm^{-3}] as $\sigma_{abs} = \alpha_{abs}/n_v$.

11.1.2.2 Linear Dichroism

Generally, the transition moment can be oriented at an arbitrary angle to the molecular frame but the symmetry imposes some constraints. Consider a cyanobiphenyl compound as an example, see Inset to Fig. 11.9b. This molecule, has two transitions especially interesting for us.

1. The electronic transition between the π and π* states of a π-electron delocalized over the biphenyl moiety due to a chain of conjugated single and double bonds.
2. The vibration transition of the triple bond C≡N in the cyano-group.

For both transitions the dipole moment $\mathbf{p}_{\mathrm{tr}}$ is directed exactly along the longitudinal molecular axis. Thus, if such molecules form the nematic phase, the absorption coefficient would depend on the average angle between the light polarization vector $\mathbf{e}$ and the longitudinal molecular axes, i.e., between $\mathbf{e}$ and the director $\mathbf{n}$.

As a result, the absorption acquires properties of a second rank tensor with two principal components $\alpha_{abs\parallel}$ and $\alpha_{abs\perp}$ ($\parallel$ and $\perp$ to $\mathbf{n}$). The qualitative absorption spectra for two polarizations are shown in Fig. 11.9c. For the isotropic phase, due to complete averaging over oscillator directions the tensor degenerates into a scalar $\alpha_{abs} = (\alpha_{abs\parallel}+2\alpha_{abs\perp})/3$.

We can introduce a *dichroic ratio* $K = \alpha_{abs\parallel}/\alpha_{abs\perp}$ or, in terms of the optical density, $K = D_{\parallel}/D_{\perp}$. In the isotropic phase $K = 1$. In the nematic phase, if the alignment were ideal ($S = 1$) the dichroic ratio would be infinite, $K \to \infty$. Thus we can use a factor similar to ratio $S = \varepsilon_a/\varepsilon_a^{max}$ (see Section 3.5.2)

$$S_{abs} = \frac{\alpha_{abs||} - \alpha_{abs\perp}}{\alpha_{abs||} + 2\alpha_{abs\perp}} = \frac{K-1}{K+2} \tag{11.25}$$

as a measure of the orientational order parameter of the nematic or SmA phase.

Experiments [7] show that, for a properly selected absorption bands with $\mathbf{p}_{\mathrm{tr}} \parallel \mathbf{n}$ or $\mathbf{p}_{\mathrm{tr}} \perp \mathbf{n}$ one can obtain S_{abs} values very close to S measured by other techniques such

as NMR, magnetic anisotropy or birefringence. Moreover, if the angle β between the longitudinal molecular axis l and selected moment $\mathbf{p}_{tr}$ is known the parameter S_{abs} can still be found using a correction factor dependent on β:

$$S_{abs} \cdot \left(1 - \frac{3}{2}\sin^2\beta\right) = \frac{K-1}{K+2}. \tag{11.26}$$

When $\mathbf{p}_{ij}$ forms with l a "magic" angle $\beta_m \approx 54.7^\circ$ the dichroism is not observed at all ($K = 1$), for $\beta < \beta_m$ the dichroic ratio $K > 1$; for $\beta > \beta_m$ $K < 1$. For small angles β formula (11.26) works quite well. Note that the order parameter S is the fundamental characteristic of a liquid crystal microscopically related to a more or less rigid molecular skeletons. Therefore, $S_{abs} \equiv S$ should be considered as a value independent of the electronic oscillator angle β.

Sometimes it is difficult to perform measurements in the UV or IR range on a pure liquid crystal. Then, genuine orientational order parameter of the mesophase S can be estimated using dichroism of guest dye molecules dissolved in a liquid crystal. Then the dichroism measurements can be made in the visible range where good quality polarisers and fast spectrometers are available. However, the dye molecules should have molecular structure similar to that of the liquid crystal molecules; only in this case $S_{abs}(\text{dye}) \approx S$.

11.1.2.3 Kramers – Kronig Relations

The real and imaginary parts of the complex refraction index $n^*(\omega) = n(\omega) + i\kappa(\omega)$ are related to each other through the *Kramers-Kronig* relation:

$$n(\omega) - 1 = \frac{2}{\pi}\int_0^\infty \frac{u\kappa(u)}{u^2 - \omega^2}du \tag{11.27}$$

Here ω and u are the same angular frequencies lettered differently in order to perform a proper integration [8,9].

Mathematically, integral Kramers-Kronig relations have very general character. They represent the Hilbert transform of any complex function $\varepsilon(\omega) = \varepsilon'(\omega) + i\varepsilon''(\omega)$ satisfying the condition $\varepsilon * (\omega) = \varepsilon(-\omega)$(here the star means complex conjugate). In our particular example, this condition is applied to function n(ω) related to dielectric permittivity ε(ω). The latter is Fourier transform of the time dependent dielectric function ε(t), which takes into account a time lag (and never advance) in the response of a substance to the external, e.g. optical, electric field. Therefore the Kramers-Kronig relations follow directly from the causality principle.

For practical purpose, the Eq. (11.27) is very useful because, using a spectroscopic technique, it is much easier to measure the frequency dependence of the extinction index κ(ω) than the frequency dependence of the real value of refraction

index $n(\omega)$. In the ideal case, having $\kappa(\omega)$ at *any* wavelength ($\lambda = 2\pi c/\omega$) from 0 to ∞, we would obtain exact $n(\omega)$ values over the whole spectrum from the UV to microwave range. In practice, however, the accuracy is limited by an experimentally available range of $\kappa(\omega)$. On the other hand, very often the frequency range of the desirable values of $n(\omega)$ is also limited and the calculation technique may still be applied.

Consider a typical absorption spectrum $\alpha_{abs}(\lambda)$ measured in the range from λ_s to λ_l shown in Fig. 11.10a. It corresponds to a liquid crystal (in the isotropic phase) with some amount of a dye dissolved in it. The liquid crystal has a strong absorption in the UV whereas the dye has UV absorption similar to that of the liquid crystal, but additionally absorbs in the visible range. We meet such a situation in the display technology (guest-host effect) or in the technology of non-linear optical materials. The spectrum of $n(\lambda)$ qualitatively corresponding to $\alpha_{abs}(\lambda)$ is shown below. Such a picture follows from the light dispersion theory and from Eq. (11.27). The background value n_b is provided by all short-wave absorption bands not included in the spectrum ($\lambda < \lambda_s$). That part of the whole spectrum is unknown.

Going from the left to the right along the wavelength axis (i.e. $\omega \rightarrow 0$) we subsequently meet regions of anomalous and normal dispersion located on the left and right slopes of each absorption band. It is very important, that the structure of the $n(\lambda)$ curve in the vicinity of each absorption band $\alpha_{abs}(\lambda)$ is determined exclusively

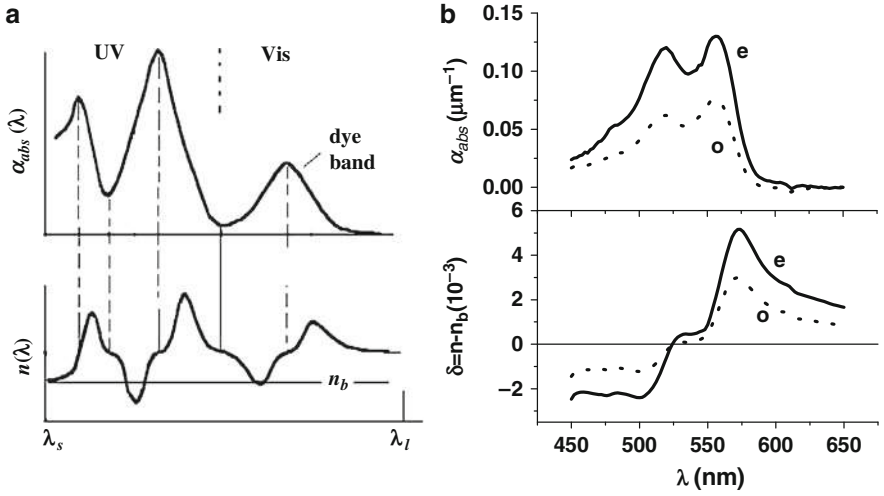

Fig. 11.10 Kramers-Kronig relations: (**a**) Qualitative spectra of absorbance of an isotropic liquid with admixture of a dye in the UV and visible range (*above*) and corresponding spectrum of the refraction index (*below*); (**b**) Experimental polarization spectra of absorption coefficient α_{abs} for a nematic liquid crystal E7 doped with a small amount of dye Chromene (*upper plot*) and corresponding spectra of the increment of refraction indices δ for two polarizations calculated with Eq. (11.29) (*lower plot*). For both plots symbols (*e*) and (*o*) mean linear polarizations parallel and perpendicular to the director

by the spectral features of that particular band and, with increasing λ, the value of $n(\lambda)$ is systematically growing upon crossing each new band encountered.

Therefore, *for the practical purpose*, using $\alpha_{abs} = 2\ \kappa\omega/c$, we can rewrite Eq. (11.27) for a limited spectral range u_1–u_2 related to our experiment as follows [10]:

$$n(\omega) = n_b + \frac{c}{\pi}\int_{u_1}^{u_2} \frac{\alpha(u)}{u^2 - \omega^2}\,du \tag{11.28}$$

or in terms of the wavelength:

$$n(\lambda) = n_b + \frac{1}{2\pi^2}\int_{\lambda_l}^{\lambda_s} \frac{\alpha(\lambda')}{1 - \left(\lambda'/\lambda\right)^2}\,d\lambda' \tag{11.29}$$

It is easy to calculate numerically a spectral dependence of $n(\lambda)$–n_b. The only problem is to find n_b. A practical way is to measure n_b at a convenient wavelength, using, say, a laser and after this, to pin the whole spectrum to this particular point.

The technique described can also be applied to measuring the dispersion of each principal components $n_{\|}$ and $n_{\perp}$ of the refraction index for nematic or SmA liquid crystals using spectral data on principal absorption coefficients. An example of our measurements and calculations is shown in Fig. 11.10b. On the upper plot are presented the experimental polarization absorption spectra $\alpha_{abs}(\lambda)$ ($\|$ and $\perp$ to the director) of a homogeneously oriented, 10 μm thick cell filled with nematic liquid crystal mixture E7 doped with 0.5% of lasing dye Chromene. On the lower plot, the spectra of the refraction index increment $\delta = n - n_b$ calculated for each polarization are given. We see that a small amount of dye substantially changes the refraction index of the mixture in the vicinity of its absorption bands (by $5{\cdot}10^{-3}$ in the maximum). Such an effect can influence the performance of the liquid crystal dye lasers. Note that, for solid anisotropic films of dyes, $\alpha_{abs\|}(\lambda)$ may reach values as high as 10 μm^{-1} and the corresponding increment δ (at absorption maxima) approaches 0.4 – 0.5 (compare with $n_b \approx 2$).

11.1.3 Light Scattering in Nematics and Smectic A

Light scattering in nematics is very strong. A thick (hundreds of micrometer) homeotropically oriented preparation between crossed polarisers does not look black under a microscope but rather sparking at random. In the beginning of the liquid crystal history it was taken as a strong argument in favour of the so-called "swarm" model. Later Chatelain [11] made a series of careful experiments using polarised light. He observed strong anisotropy of light scattering in nematics. When the electric vector of the scattered light **s** was perpendicular to the electric vector of

incident light **f**, light scattering was 10^6 times stronger than in the isotropic liquid. For **s** ∥ ***f***, the scattering was much weaker but still considerably stronger than in the isotropic phase.

Where does such a strong scattering anisotropy originate from? It is evident that the optical anisotropy of nematic liquid crystals plays the crucial role. In fact, the scattering is caused by fluctuations of the director **n**, i.e. the local orientation of the order parameter tensor. The local changes in orientation of **n** imply local changes in orientation of the optical indicatrix.

11.1.3.1 Isotropic Phase

Let us recall the reason for the light scattering in gas or in isotropic liquid. In that case, we deal with fluctuations of the mass density. They can be represented by a sum of normal elastic vibration modes (Fourier harmonics) with wavevector **q** and frequency Ω. When such a particular mode interacts with light of frequency ω and wavevector **k** the conservation laws for energy and momentum read:

$$\Omega = \omega' - \omega \text{ and } \pm \mathbf{q} = \mathbf{k}' - \mathbf{k} \tag{11.30}$$

where ω′ and **k**′ are frequency and wavevector of the scattered light. When $\Omega << \omega$ we have a case of quasi-elastic scattering with $\mathbf{k}' \approx \mathbf{k}$. Then, we have the same Eq. (5.10) for the wavevector of scattering,

$$q = 2k \sin 2\theta = 2\left(\omega n/c\right) \sin 2\theta, \tag{11.31}$$

where n is refraction index, c velocity of light and 2θ is the angle between **k**′ and **k**, Fig. 11.11a. Note that, in this case, normal vibrations are nothing more than sound waves with velocity v_s and simple dispersion law $\Omega = v_s q$. The frequency shift

$$\Delta\omega = \Omega = \pm q v_s = \pm 2\omega n\left(v_s/c\right) \sin 2\theta \tag{11.32}$$

due to interaction of the incident light wave with the sound wave results in the appearance of two satellites on both sides of the main frequency (*Rayleigh line*), namely, ω + Ω and ω − Ω called *Mandelshtam-Brillouin doublet*.

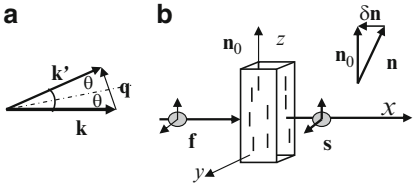

Fig. 11.11 Geometry of quasi-elastic scattering in general (**a**) and scattering on the director fluctuations with director **n**∥*z*, and vectors of incident (**f**) and scattered (**s**) light polarizations

It follows from the theory of elastic scattering ($\omega = \omega'$) that, for small modulation or fluctuation of dielectric permittivity ($\delta\varepsilon << \varepsilon_\perp$), the *differential cross section* for the scattered light per unit solid angle around k' is given by

$$\sigma = \left(\frac{\omega^2}{4\pi c^2}\right)^2 \left[\mathbf{f}\hat{\varepsilon}(\mathbf{q})\mathbf{s}\right]^2 \tag{11.33}$$

where **f** and **s** are polarisation vectors of the incident and scattered light and $\hat{\varepsilon}(\mathbf{q})$is the spatial Fourier component of the dielectric permittivity, which scatters light with wavevector **q**. This expression is independent of the physical mechanism of scattering and can be found in textbooks on optics. For scalar ε (mass density fluctuations) and $\mathbf{f} \perp \mathbf{s}$, $\sigma = 0$ because the incident field E_i has no projection on the induction vector $D_s = \varepsilon E_s = 0$. In this type of scattering, maximum scattering intensity is observed when polarizations of the incident and scattered light coincide with each other, **f**‖**s.**

11.1.3.2 Nematic Phase

The strong light scattering by nematics is due to specific properties of their dielectric tensor (n_i and n_j are components of the director, see Section 7.2.2):

$$\hat{\varepsilon} = \varepsilon_\perp \delta_{ij} + \varepsilon_a (n_i n_j) \tag{11.34}$$

Consider a slab of a nematic with the director $\mathbf{n} = \mathbf{n}_0 + \delta\mathbf{n}$ having small fluctuating components n_x, $n_y << n_z \approx 1$, see Fig. 11.15b. The slab is illuminated by a light beam along the x-direction with linear polarization in the y,z plane, $\mathbf{f} = f_y\mathbf{j} + f_z\mathbf{k}$. The scattered beam propagates in the same direction and has polarization $\mathbf{s} = s_y\mathbf{j} + s_z\mathbf{k}$. We would like to find the "polarization structure" of the scattering cross-section σ_{fs}. To this effect, we only take the anisotropic part of the dielectric tensor responsible for fluctuations and $s \leftarrow f$ scattering. Using Eq. (11.33) we have

$$\sigma_{fs} \propto \mathbf{s} \cdot \varepsilon_a (n_\alpha n_\beta) \cdot \mathbf{f} = \varepsilon_a \mathbf{s} \cdot \begin{pmatrix} n_x^2 & n_x n_y & n_x n_z \\ n_y n_x & n_y^2 & n_y n_z \\ n_z n_x & n_z n_y & n_z^2 \end{pmatrix} \cdot \begin{pmatrix} 0 \\ f_y \\ f_z \end{pmatrix}$$
$$= \varepsilon_a \mathbf{s} \cdot \begin{pmatrix} n_x n_y f_y + n_x n_z f_z \\ n_y^2 f_y + n_y n_z f_z \\ n_z n_y f_y + n_z^2 f_z \end{pmatrix}$$

Then, neglecting second order terms $n_x n_y$ and ${n_y}^2$ and non-fluctuating term with ${n_z}^2 \approx 1$ we obtain:

$$\sigma_{fs} \propto \varepsilon_a (s_y\mathbf{j} + s_z\mathbf{k}) \cdot (n_x f_z \mathbf{i} + n_y f_z \mathbf{j} + n_y f_y \mathbf{k}) = \varepsilon_a n_y (s_y f_z + s_z f_y) \tag{11.35}$$

Now we see that only fluctuations of the director in the y-direction are essential, $\delta n = n_y$, because n_z – fluctuations are not related to the director realignment and n_x – fluctuations are not seen by the transverse light wave incident from the x-direction.

Considering the term $s_y f_z + s_z f_y$ we can distinguish two important particular cases:

Case A: $\boldsymbol{f} \parallel \mathbf{n}_0 \| z$ and $\boldsymbol{f} \perp \delta\mathbf{n}$

Then only the first term remains in Eq. 11.35. It means that there is no scattering with polarization $\mathbf{s} \parallel \boldsymbol{f}$ and the maximum scattering corresponds to s_y that is $\mathbf{s} \perp \boldsymbol{f}$

Case B: $\boldsymbol{f} \perp \mathbf{n}_0$

Then we have only the second term with f_y and again there is no scattering with polarization $\mathbf{s} \parallel \boldsymbol{f}$. The maximum scattering corresponds to s_z that is $\mathbf{s} \perp \boldsymbol{f}$. Indeed, maximum scattering by the director fluctuation is always takes place when $\mathbf{s} \perp \boldsymbol{f}$ in agreement with experiments on liquid crystals and in contrast to the case of scattering by the density fluctuations in liquids and gases.

As to the large amplitude of light scattering in nematics it is explained by very low elasticity of the nematic phase with respect to the director distortion that is small Frank moduli K_{ii} discussed below in Section 8.2. The strict theory of light scattering in the static and dynamic regime has been developed by de Gennes [12]. His expression for the mean square amplitude of the director fluctuations has been discussed earlier, see Eq. (8.33). Using that equation and the tensor of dielectric anisotropy (11.34), de Gennes found the amplitude of the dielectric tensor fluctuations. After substitution of the dielectric tensor (11.34) into Eq. (11.33) the differential cross-section for the light scattering by a nematic was given by

$$\sigma_\alpha = V\left(\frac{\varepsilon_a \omega^2}{4\pi c^2}\right)^2 \frac{k_B T}{K_{33} q_{||}^2 + K_\alpha q_\perp^2}(s_y f_z + s_z f_y) \tag{11.36}$$

We can see that large optical anisotropy (factor ε_a^2 in the first multiplier) and small energy terms (Kq^2 in denominator of the second multiplier) are responsible for the high intensity of scattering. In addition, due to the factor of q^2, especially strong scattering is observed in small solid angles around the incident beam. Finally, the polarization factor (the third multiplier) makes the scattering extremely anisotropic. Eq. (11.36) is useful for the determination of elastic moduli from the intensity of scattering in different geometries and the viscosity coefficients from the optical frequency spectra of scattering [13].

11.1.3.3 Smectic A Phase

The SmA phase has the same symmetry and the same dielectric ellipsoid as in nematics, therefore, everything said above about the birefringence and dichroism is valid for the SmA phase. However, due to specific elastic properties of the layered structure, the director fluctuations are strongly quenched, and the SmA preparations are much more transparent than the nematic ones. This is related to specific elastic properties of the lamellar SmA phase [14].

According to Fig. 8.23 in Section 8.5.1, a fluctuation component of the layer displacement $u_z = u$ along the x-direction (within the smectic layer) is described by $u(x) = u \cos q_\perp x$. Since the director angle $\vartheta_f \approx \partial u/\partial x = q_\perp u$, the free energy density in Eq. (8.49) can be rewritten in terms of the ϑ_f-angle fluctuations:

$$g_{dist}(q) = \frac{1}{2}\left(B\frac{q_z^2}{q_\perp^2} + K_{11}q_\perp^2\right)\cdot\vartheta_f^2 \tag{11.37}$$

For a cell of thickness d the z-component of the fluctuation wavevector is $q_z = m\pi/d$, see Fig. 11.12a where the corresponding harmonics are marked off by the numbers 1, 2, 3, etc. For fluctuations along the x-axis, there is a critical vector equals $q_c = (\pi/d\lambda_s)^{1/2}$ (Eq. 8.48b), and, according to Eqs. (8.50) and (11.37), the intensity of the scattered light is given by

$$I \propto \langle\vartheta^2\rangle = \frac{k_BT}{K_{11}\left(q_\perp^2 + \lambda_s^{-2}q_z^2/q_\perp^2\right)} = \frac{k_BT}{K_{11}\left(q_\perp^2 + m^2q_c^4/q_\perp^2\right)} \tag{11.38}$$

This formula predicts that, in the SmA phase, in a typical geometry of Fig. 11.12b, scattering vanishes in two limits:

1. For large scattering angles 2θ and wavevectors $q_\perp$

$$q_\perp >> q_c,\ I \propto 1/q_\perp^2 \to 0$$

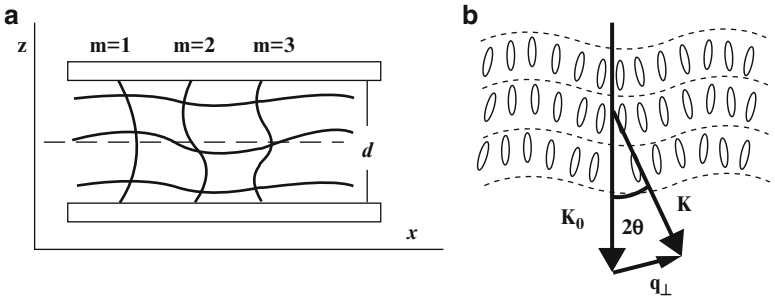

Fig. 11.12 Light scattering by the smectic A phase. Fluctuating elastic modes in the z and x directions in a planar cell with director $\mathbf{n}_0 \parallel z$ (**a**) and typical geometry of scattering on fluctuating smectic layers (**b**)

2. For small scattering angles $2\theta \to 0$:

$$q_\perp \to 0 \text{ and } I \propto \frac{q_\perp^2}{m^2 q_c^4} \to 0$$

The maximum scattering occurs at some resonance values of the wavevector $q_\perp = m^{1/2} q_c$. In fact, light propagating along z probes different q_z modes with the number m. However, in comparison with nematics, well aligned, defect-free SmA liquid crystals are weakly scattering.

11.2 Frederiks Transition and Related Phenomena

11.2.1 Field Free Energy and Torques

Consider a nematic liquid crystal with director $\mathbf{n} = (1, 0, 0)$ aligned along the x-axis, Fig. 11.13. The liquid crystal is placed in the magnetic field oriented at an angle α with respect to the director, $\mathbf{H} = (H\cos\alpha, 0, H\sin\alpha)$, the diamagnetic anisotropy $\chi_a = \chi_{\parallel} - \chi_\perp$ being positive. We are interested in the excess free energy of the nematic due to the magnetic field. First we find the magnetization vector:

$$\begin{aligned}\mathbf{M} = \breve{\chi}\mathbf{H} &= (\chi_{||} H\cos\alpha)\mathbf{i} + (\chi_\perp H\sin\alpha)\mathbf{k} \\ &= \chi_\perp[(H\sin\alpha)\mathbf{k} + (H\cos\alpha)\mathbf{i}] + \chi_a(H\cos\alpha)\mathbf{i}\end{aligned}$$

or, on account of $(\mathbf{Hn}) = \cos\alpha$ and $\mathbf{n} = \mathbf{i}$, we obtain the magnetisation vector in the form

$$\mathbf{M} = \chi_\perp \mathbf{H} + \chi_a(\mathbf{Hn})\mathbf{n} \tag{11.39}$$

When, instead of the magnetic field, an electric field is applied at some angle to the director of a nematic liquid crystal, in analogy to (11.39), the electric polarization $\mathbf{P}$ is given by

$$\mathbf{P} = \chi_\perp^E \mathbf{E} + \chi_a^E(\mathbf{En})\mathbf{n} \tag{11.40}$$

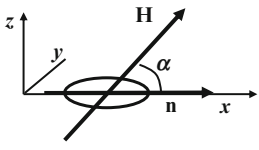

Fig. 11.13 Vector diagram for calculations of magnetisation and free energy of a nematic liquid crystal in a magnetic field

The magnetic field exerts a *torque on the magnetisation*:

$$\Gamma_H = \mathbf{M} \times \mathbf{H} = \chi_a(\mathbf{Hn})\mathbf{n} \times \mathbf{H} \tag{11.41}$$

that directed along the y-axis in Fig. 11.13. Correspondingly, the electric field $\mathbf{E}$ exerts the torque on the polarization $\mathbf{P}$:

$$\Gamma_E = \mathbf{P} \times \mathbf{E} = \chi_a^E(\mathbf{En})\mathbf{n} \times \mathbf{E} = \frac{\varepsilon_a}{4\pi}(\mathbf{En})\mathbf{n} \times \mathbf{E} \tag{11.42}$$

Note that, from the tensor form $\hat{\varepsilon} = 1 + 4\pi\hat{\chi}^E$, follows $\varepsilon_a = 4\pi\chi_a^E$ because the unity is included in the isotropic part of tensor $\hat{\varepsilon}$.

In each particular situation, these torques may be balanced by the elastic, surface or viscous torques. The magnetic and electric field torques may be obtained differently. Using minimisation of the free energy with respect to the director one obtains the "molecular field" introduced earlier, see Eq. (8.27) and then finds the torques as vector products with the director. Let us show it. The magnetic free energy density is given by

$$g_H = -\int_0^H \mathbf{M}d\mathbf{H} = -\int_0^H [\chi_\perp \mathbf{H} + \chi_a(\mathbf{Hn})\mathbf{n}]d\mathbf{H} = -\frac{1}{2}[\chi_\perp H^2 + \chi_a(\mathbf{Hn})^2] \tag{11.43}$$

The first term in (11.43) is independent of the director; the absolute value of the second one is maximal for $\mathbf{H} \parallel \mathbf{n}$ that correspond to the minimum of magnetic free energy. Minimisation of (11.43) results in a vector of the "molecular field"

$$\mathbf{h}_H = \frac{\partial g_H}{\partial n} = -\chi_a(\mathbf{nH})\mathbf{H}$$

directed along $\mathbf{H}$ and coinciding with (8.27). The torque exerted by the "molecular field" on the director will be

$$\Gamma_H = \mathbf{h}_H \times \mathbf{n} = \chi_a(\mathbf{Hn})\mathbf{n} \times \mathbf{H} \tag{11.44}$$

that coincides with (11.41).

For the fixed electric field applied to the sample from the electrodes, instead of Helmholtz free energy one should minimise the thermodynamic potential density:

$$g_E = -\frac{1}{4\pi}\int_0^H \mathbf{D}d\mathbf{E} = -\frac{1}{8\pi}[\varepsilon_\perp E^2 + \varepsilon_a(\mathbf{En})^2] \tag{11.45}$$

By analogy, the "molecular field" coming from minimisation of (11.45) is given by (8.27) and the corresponding torque exerted by $\mathbf{h}_E$ on the director is equal to (11.42):

$$\Gamma_E = \mathbf{h}_E \times \mathbf{n} = \frac{\varepsilon_a}{4\pi}(\mathbf{En})\mathbf{n} \times \mathbf{E} \tag{11.46}$$

Example: Let the electric field 1 V/μm is applied at an angle of $\alpha = \pi/3$ to the director of liquid crystal 5CB ($\varepsilon_\perp = 6.7$, $\varepsilon_\parallel = +19.7$). What are the values of the free energy density and the electric torque? We use the Gauss system: $E = 1/(300 \cdot 10^{-4}) = 33.3$ statV/cm, $(\mathbf{En}) = E\cos(\pi/3)$; the energy(11.45) and torque (11.46) are $g = (6.7 + 13 \cdot 0.25)E^2/8\pi = 439$ erg/cm^3 (or 43.9 J/m^3 in the SI system) and $\Gamma_E = (13/4\pi) \cdot E^2\cos(\pi/3) \cdot \sin(\pi/3) = 493$ erg/cm^3 (49.3 J/m^3 in the SI system).

11.2.2 Experiments on Field Alignment of a Nematic

We shall discuss a very important macroscopic effect used in almost all the types of modern displays. In his original experiment Frederiks [15] used a liquid crystal *p*,*p*′-azoxyanisol (PAA), the grandfather of all other nematics, Fig. 11.14c. It was oriented homeotropically in a wedge-form gap between a flat and convex glasses as shown in Fig. 11.14a, b. The cell with PAA was placed between crossed polarizers, heated up to about 120°C and observed with an optical system. All this construction was installed between the poles of a magnet. In the figure, a magnetic field **H** was oriented horizontally. In the absence of the field the cell looked black. With increasing field **H** the PAA realignment began very sharply at a certain critical field strength H_c depending on the gap thickness d. Therefore, the birefringence appeared and the optical pattern resembled the Newton rings, but the contrast was much higher. It was shown that product $H_c d = \text{const}$.

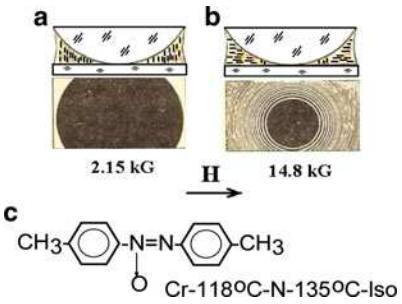

Fig. 11.14 Experiment by Frederiks. Homeotropically aligned nematic PAA in a weak (**a**) and a strong (**b**) magnetic field and the correspondent optical pictures seen between crossed polarizers; above a certain field a distortion occurs that causes the interference pattern. (**c**) The chemical formula of PAA (*p*,*p*′-azoxyanisol)

What is the physics of the observed phenomenon? In the absence of an external field, the elastic free energy is minimal for the vertical alignment of the director. We know that PAA has positive anisotropy of magnetic susceptibility and the magnetic field should align the director horizontally. However, such a rotation of the director seems impossible as the magnetic torque $\mathbf{\Gamma}_H$ is zero because, according to (11.44), the molecular field equals $\mathbf{h}_H = -\chi_a(\mathbf{Hn})\mathbf{H}$ and, in the experiment, $\mathbf{H} \perp \mathbf{n}$ results in $(\mathbf{Hn}) = 0$. Therefore, the system must accumulate some threshold amount of the magnetic field energy and then, accompanied by a small thermal fluctuation of the director, abruptly change its state so that the elastic and magnetic field forces will be in balance satisfying the minimum of free energy. This abrupt field-induced change of the director alignment is called *Frederiks transition*. The threshold field is proportional to the inverse thickness of the nematic layer and this will be discussed below.

In practice we meet numerous situations, but there are three basic geometries shown in Fig. 11.15. All upper sketches correspond to $H < H_c$, lower ones to $H > H_c$. In case (a), initially $n_x = 1$, $n_y = 0$, $n_z = 0$ and just above the threshold the z-component of the director appears. The distortion $\partial n_z/\partial z = \cos\vartheta$ corresponds to the splay term in the Frank energy (modulus K_{11}). In case (b), initially $n_z = 1$, $n_y = 0$, $n_x = 0$ and above the threshold, the component n_x appears. The term $\partial n_x/\partial z = \sin\vartheta$ corresponds to the bend term (modulus K_{33}). In both the cases, with further increase of $H > H_c$ the distortion becomes of the mixed type. In case (c), initially $n_x = 1$, $n_z = 0$, $n_y = 0$ but above the threshold, n_y appears. The term $\partial n_y/\partial z$ corresponds to the twist term (angle φ, modulus K_{22}). In this simple geometry, the twist distortion is "pure"; it does not mixed with bend or splay.

11.2.3 Theory of Frederiks Transition

Our task now is to find the threshold field strength for the distortion and the distribution of the director $\mathbf{n}(z)$ over the cell thickness above the threshold. This time we shall take an initial homeotropic alignment, case (b) in Fig. 11.15. In its modern form, the theory was developed by Saupe [16].

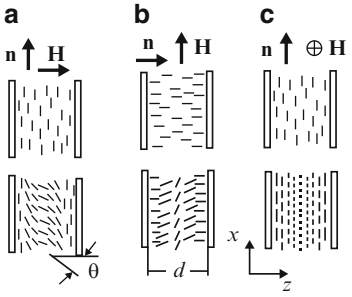

Fig. 11.15 Three basic configurations of the director and the magnetic field for the Frederiks transition onset, namely, splay (**a**), bend (**b**) and twist (**c**)

11.2.3.1 Simplest Model

The geometry of the problem is illustrated in more details by Fig. 11.16. A plane nematic layer with normal z and thickness d is confined between two infinitely wide plates. The magnetic field is applied along x. The molecules are rigidly fixed (anchoring energy $W \to \infty$) at the opposite boundaries ($\vartheta_{0,d} = 0$). When the field exceeds the critical one (H_c), the director turns through an angle $\vartheta(z)$ in the direction of H. Due to the up-and-down symmetry of our cell, the deflection angle must be symmetric with respect to the middle of the cell and the maximum deflection $\vartheta_m = \vartheta(d/2)$ occurs at $z = d/2$ as shown schematically by the dot curve.

Our task is to find an analytical expression for $\vartheta(z)$ at different fields. The scheme is as follows. First we shall write a proper integral equation for the free energy. Then, following the variational procedure discussed in Section 8.3, we compose the Euler equation corresponding to the free energy minimum and solve this differential equation for $\vartheta(z)$. To simplify the problem we use the one-constant approximation $K_{11} = K_{22} = K_{33} = K$. In our geometry, $\vartheta \approx n_x$ and only one derivative, namely the bend term with $\partial n_x/\partial z$, is essential in the Frank free energy form (8.15):

$$F = \frac{1}{2}\int_0^d \left[K\left(\frac{d\vartheta}{dz}\right)^2 - \chi_a H^2 \sin^2\vartheta(z)\right] dz \tag{11.47}$$

The magnetic part of the energy is given by Eq. (11.43).

Thus we have an integral equation for $F = F(z, \vartheta, \vartheta')$. The Euler equation of the general form

$$\frac{\partial F}{\partial \vartheta} - \frac{\partial}{\partial z}\frac{\partial F}{\partial \vartheta'} = 0$$

gives us the expression

$$-2\chi_a H^2 \sin\vartheta\cos\vartheta - K\frac{\partial}{\partial z}2\frac{\partial\vartheta}{\partial z} = 0$$

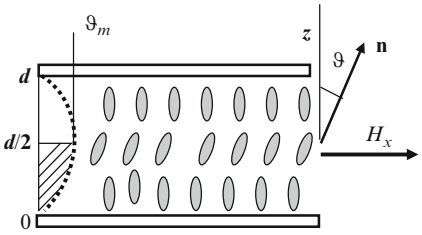

Fig. 11.16 Magnetic field induced Frederiks transition in a homeotropically aligned nematic liquid crystal. Below the threshold the director is parallel to z; magnetic field is in the x-direction. Dot line shows the distortion above the threshold with maximum angle ϑ_m in the middle of the cell

Therefore we obtain the differential equation, which express the balance of the elastic and magnetic torques:

$$\xi^2 \frac{\partial^2 \vartheta}{\partial z^2} + \sin\vartheta\cos\vartheta = 0 \tag{11.48}$$

where ξ is the so-called *magnetic field coherence length*.

$$\xi = \frac{1}{H}\sqrt{\frac{K}{\chi_a}} \tag{11.49}$$

We can easily check by differentiation that the first integral of (11.48) is

$$\left(\frac{\partial\vartheta}{\partial z}\right)^2 = -\frac{1}{\xi^2}(\sin^2\vartheta(z) - C).$$

As in the middle of the cell $\partial\vartheta/\partial z|_{d/2} = 0$, the arbitrary constant C is easily found:

$$C = \sin^2\vartheta_m.$$

Hence,

$$\frac{d\vartheta}{dz} = \frac{1}{\xi}(\sin^2\vartheta_m - \sin^2\vartheta)^{1/2} \tag{11.50}$$

The next step is to integrate (11.50). We can do it for the lower half of the cell 0- $d/2$ (dashed area in Fig. 11.16):

$$\frac{d}{2\xi} = \int_0^{\vartheta_m} \frac{d\vartheta}{\sqrt{\sin^2\vartheta_m - \sin^2\vartheta}} = F(\sin\vartheta_m) \tag{11.51}$$

First order elliptic integrals $F(k)$ are tabulated and our problem is solved. In Fig. 11.17a the distribution of the director is qualitatively shown for increasing field from $H = 0$ to H_4.

11.2.3.2 Threshold Condition

However, to make the result more transparent we shall look more carefully at a simpler case of small distortions. From Fig. 11.17a one can see that, for a small distortion, the director profile has a sine form. Consider, at first, a very severe

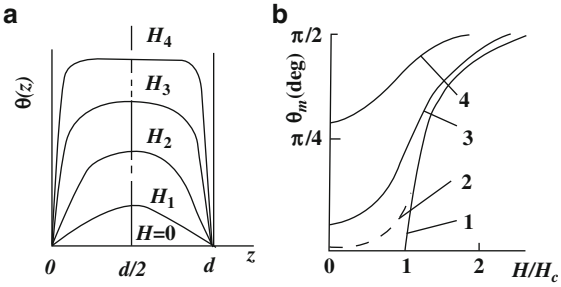

Fig. 11.17 (**a**) Qualitative picture of the director distribution over the cell thickness with increasing magnetic field from $H = 0$ to H_4 in the form of elliptic-sine functions (homeotropic alignment, $\vartheta_0 = 0$). (**b**) Absence of the threshold field for the initial tilted director alignment; calculation of the maximum distortion angle ϑ_m changing with variation of the initial uniform director tilt ϑ_0: no tilt (curve 1 showing threshold at $H/H_c = 1$), tilt angle $\vartheta_0 = 1.7°$ (curve 2), 10° (curve 3), 50° (curve 4)

approximation $\sin\vartheta \approx \vartheta$, and $\sin\vartheta_m \approx \vartheta_m$. Then the torque balance equation (11.48) reads:

$$\xi^2 \frac{\partial^2 \vartheta}{\partial z^2} + \vartheta = 0. \tag{11.52}$$

Evidently the general solution is a harmonic function, e.g. $\vartheta = \vartheta_m \sin qz + B$ with wavevector $q = \pi/d$. From the boundary condition at $z = 0$ or $z = d$ we immediately find $B = 0$. Substituting $\vartheta = \vartheta_m \sin qz$ into the approximate equation we get

$$-\xi^2 q^2 + 1 = 0.$$

As we are interested in the extremely small ϑ-angles, this result gives us the threshold condition,

$$\xi_c = \frac{d}{\pi} \tag{11.53a}$$

or, according to (11.49), the threshold magnetic field is given by

$$H_c = \frac{\pi}{d}\sqrt{\frac{K}{\chi_a}} \tag{11.53b}$$

Thus we have obtained a nice result in complete agreement with the Frederiks measurements, $H_c d = \text{const}$, but we have not found yet the amplitude ϑ_m of the sine-form solution.

We can find ϑ_m going back to the strict equation (11.51), and using the second approximation, take $\sin\vartheta \approx \vartheta - \vartheta^3/3!+\ldots$, (and same for $\sin\vartheta_m$). Then, neglecting terms of the order of ϑ^6 and higher,

$$\sqrt{\sin^2\vartheta_m - \sin^2\vartheta} \approx \sqrt{\vartheta_m^2 - \vartheta^2} \cdot \sqrt{1 - \tfrac{1}{3}(\vartheta_m^2 + \vartheta^2)}$$

and using expansion $(1-x)^{-1/2} \approx 1 + x/2+\ldots$we obtain

$$\frac{1}{\sqrt{\sin^2\vartheta_m - \sin^2\vartheta}} \approx \frac{1 + \frac{1}{6}(\vartheta_m^2 + \vartheta^2)}{\sqrt{\vartheta_m^2 - \vartheta^2}} \cdot$$

Now the equation (11.51) takes the approximate form:

$$\frac{d}{2\xi} = \int_0^{\vartheta_m} \frac{d\vartheta}{\sqrt{\sin^2\vartheta_m - \sin^2\vartheta}} \approx \int_0^{\vartheta_m} \frac{d\vartheta}{\sqrt{\vartheta_m^2 - \vartheta^2}} + \frac{1}{6}\vartheta_m^2 \int_0^{\vartheta_m} \frac{d\vartheta}{\sqrt{\vartheta_m^2 - \vartheta^2}} + \frac{1}{6}\int_0^{\vartheta_m} \frac{\vartheta^2 d\vartheta}{\sqrt{\vartheta_m^2 - \vartheta^2}}$$

Finally, using standard integrals

$$\int_0^{\vartheta_m} \frac{d\vartheta}{\sqrt{\vartheta_m^2 - \vartheta^2}} = \arcsin\frac{\vartheta}{\vartheta_m}\Big|_0^{\vartheta_m} = \frac{\pi}{2}$$

and

$$\int_0^{\vartheta_m} \frac{\vartheta^2 d\vartheta}{\sqrt{\vartheta_m^2 - \vartheta^2}} = -\frac{\vartheta}{2}\sqrt{\vartheta_m^2 - \vartheta^2}\Big|_0^{\vartheta_m} + \frac{\vartheta_m^2}{2}\arcsin\frac{\vartheta}{\vartheta_m}\Big|_0^{\vartheta_m} = 0 + \frac{\vartheta_m^2}{2}\cdot\frac{\pi}{2}$$

we arrive at the expression

$$\frac{d}{2\xi} \approx \frac{\pi}{2}\left(1 + \frac{\vartheta_m^2}{6} + \frac{\vartheta_m^2}{12} + \ldots\right) = \frac{\pi}{2}\left(1 + \frac{\vartheta_m^2}{4} + ..\right)$$

and finally to the form:

$$\frac{d}{\pi\xi} = \frac{\xi_c}{\xi} = \frac{H}{H_c} \approx \left(1 + \frac{\vartheta_m^2}{4} + ..\right) \tag{11.54}$$

The result contains two terms, the first one presents the same threshold condition $d = \xi_c\pi$, already found above and the sum of the first and the second term allows us to find the amplitude of the low-field sine-form distortion:

$$\vartheta_m \approx \sqrt{\frac{4d}{\xi\pi}} = 2\sqrt{\frac{\xi_c}{\xi} - 1} = 2\sqrt{\frac{H}{H_c} - 1} \tag{11.55}$$

This form shows that the distortion develops at $H > H_c$ smoothly, without a jump as in the case of second order thermodynamic transitions.

11.2.4 Generalizations of the Simplest Model

Equations (11.53a) and (11.55) have been derived using several assumptions:

1. The electric field case has not been considered and that situation is more difficult for two reasons. First the dielectric anisotropy ε_a can be comparable with average $<\varepsilon>$ and therefore the field in a distorted nematic is no longer uniform in the z-direction. In addition, a liquid crystal can be conductive, and this can result in some specific features, for example, there could be a flow of mass even in the steady-state regime.
2. A difference in Frank elastic constants was ignored.
3. The field direction was selected along one of the principal axis of the liquid crystal.
4. The infinitely strong anchoring was assumed.
5. A steady-state situation was only considered. For example, a transient flow of a nematic (backflow) that occurs even in the case of the magnetic field was disregarded.

Below we shall consider qualitatively other situations (all of them are easily modeled numerically).

11.2.4.1 Electric Field Case

Now the free energy density has a form (11.45) wherein, due to a large ε_a the field **E** becomes dependent on coordinates. In this case, one should operate with electric displacement **D**. For example, in the case of the Frederiks transition and the splay geometry of Fig. 11.15a the field strength is:

$$E(z) = \frac{4\pi D_z}{\varepsilon_z} = \frac{4\pi D_z}{\varepsilon_\perp \sin^2\vartheta(z) + \varepsilon_{||}\cos\vartheta(z)}$$

Evidently, that the correction does not influence the threshold condition:

$$E_c = \frac{\pi}{d}\sqrt{\frac{4\pi K}{\varepsilon_a}} \tag{11.56}$$

Thus, in full analogy with (11.53b), the threshold voltage $U_c = E_c d$ is independent of thickness! However, already at relatively small amplitude of the director deflection from its initial orientation, ϑ_m depends on ε_z and one should correct Eq. (11.54) for dielectric anisotropy $\varepsilon_a/\varepsilon_\perp$:

$$\frac{E}{E_c} = \frac{U}{U_c} \approx 1 + \frac{1}{4}\left(1 + \frac{\varepsilon_a}{\varepsilon_\perp}\right)\vartheta_m^2 \tag{11.57}$$

11.2.4.2 Anisotropy of Elastic Properties

The Saupe solution (11.51) is not valid for different K_{11} and K_{33}. To take into account a ratio of $\kappa = K_{33} - K_{11}/K_{11}$ one more term should be added to the approximate form (11.57). Then we arrive at an even more correct form [17]:

$$\frac{E}{E_c} \approx 1 + \frac{1}{4}\left(1 + \frac{\varepsilon_a}{\varepsilon_\perp} + \kappa\right)\vartheta_m^2 \tag{11.58}$$

For positive κ the initial slope of the $\vartheta(z)$ curves in Fig. 11.17a would be steeper, for $\kappa < 0$ smoother.

11.2.4.3 Oblique Field or Tilted Alignment

If the electric (or magnetic) field is applied at a certain angle to the director in the initial state, it creates a finite torque on the director and the Frederiks transition becomes "thresholdless". The same situation occurs if the field is applied along the cell normal z but the initial alignment of a nematic is tilted at an angle $0 < \vartheta_0 < \pi/2$. With increasing magnetic field the director deflection angle ϑ_m in the middle of the cell is growing without threshold as shown in Fig. 11.17b (results of calculations, MBBA, $d = 24$ μm [18]).

11.2.4.4 Weak Anchoring

When the anchoring energy W^s is finite and the field is applied, the director *at the surface* has a certain freedom to turn under the action of the elastic torque from the bulk. Then, the profile of $\vartheta(z)$ changes. The sine-form is still can be taken as an approximation but its half-period is no longer equal to cell thickness d. Instead we have $d + 2b$ where $b = K_{ii}/W^s$ is the surface extrapolation length already discussed in Section 10.2.4. Figure 11.18 clarifies the situation. Therefore, the threshold field for the weak anchoring conditions is reduced according to formula:

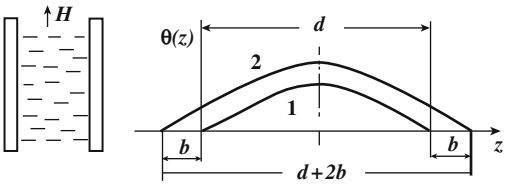

Fig. 11.18 Profiles of the director angle $\vartheta(z)$ in the same magnetic field for rigid (curve 1) and weak (curve 2) anchoring in the cell geometry shown on the left side

$$H_c = \frac{\pi}{d+2b}\sqrt{\frac{K}{\chi_a}} \tag{11.59}$$

In principle, the measurements of this threshold allow us to find the value of b and then W^s. However, very thin cells have to be used to have d comparable with b (less than 1 μm). Note that, at the ordinate axes, curve 2 cuts angles ϑ_0 and ϑ_d off. They depend on the anchoring strength that can be different at either interfaces. The general solution of the same problem for arbitrary fields (up to saturation of distortion, i.e. break of anchoring) is also known [19] and we discuss it below.

11.2.4.5 Break of Anchoring

Equation (11.53a) states that, for the infinitely strong anchoring, the threshold for the director field distortion is determined by equality of the field coherence length ξ (magnetic or electric) to the characteristic length of the cell d or, more precisely, to the reciprocal wavevector of the weak distortion d/π. Equation (11.59) points out that, for a weak anchoring, one reaches the threshold with increased characteristic length $(d + 2b)$ and, consequently, field coherence length $\xi_c = (d + 2b)/\pi$. For infinitely weak anchoring, $\xi_c \to \infty$ and the distortion is thresholdless.

Now the question arises, how strong should be the field in order to force the director to be parallel to the field everywhere in the cell, including near-surface regions. Surely, for infinitely strong anchoring ($b = 0$), such a field is infinite and, for $b \to \infty$, the threshold tends to zero. Therefore, for $b >> d$ the value of π/b can be taken as a wavevector of the uniform distortion throughout the cell and, by analogy with Eq. (11.53a), we may write the threshold condition for the director saturation

$$\xi_b = \frac{b}{\pi} = \frac{K}{\pi W_s} \tag{11.60}$$

or the *break-of-anchoring field*. The formulas for the magnetic and electric fields sufficient to overcome surface energy W_s and to break anchoring are given by:

$$H_b = W_s\sqrt{\frac{1}{\chi_a K}} \text{ and } E_b = W_s\sqrt{\frac{4\pi}{\varepsilon_a K}} \tag{11.61}$$

Here, for the threshold estimation, we used an isotropic approximation with elastic modulus K. A precise value of the saturation field can be obtained without such an approximation. For a homogeneous planar cell it can be found from the equation [20]:

$$\text{cth}\left[\frac{\pi}{2}\frac{E_{sat}}{E_F}\left(\frac{K_{11}}{K_{33}}\right)^{1/2}\right] = \frac{\pi K_{33}}{W_s d}\cdot\frac{E_{sat}}{E_F}\left(\frac{K_{11}}{K_{33}}\right)^{1/2} \tag{11.62}$$

Here E_{sat}/E_F represents the ratio of the saturation field $E_{sat} = E_b$ to the Frederiks transition field (electric or magnetic). As $E_{sat}/E_F \approx d/b \gg 1$, the left part of Eq. (11.62) is close to 1. Therefore, assuming $K_{11} = K_{33} = K$, we turn back to Eqs. (11.60) and (11.61). In the next chapter we shall meet the break of anchoring effect when discussing bistable devices.

11.2.5 Dynamics of Frederiks Transition

It is simpler to examine the dynamics of the Frederiks effect for the experimental geometry of Fig. 11.15c, since a pure twist distortion is not accompanied by the backflow effect (see the next Section). For a twist distortion we operate with the azimuthal director angle $\varphi(z)$ ($\sin\varphi \approx n_y$) and the equation for rotation of the director that expresses the balance of elastic, magnetic field and viscous torques is given by

$$K_{22}\frac{\partial^2\varphi}{\partial z^2} + \chi_a H^2 \sin\varphi\cos\varphi = \gamma_1\frac{\partial\varphi}{\partial t}. \tag{11.63}$$

Here, the first two terms came from minimisation procedure of the free energy, see Eqs. (8.15) and (11.43) and the viscous term was discussed earlier, see Eqs. (9.31) and (9.32) [21]. In terms of the phase transition theory, Eq. (11.63) may be regarded as the Landau-Khalatnikov equation discussed in Section 6.5.1. It describes the director rotation in magnetic field H with rotational viscosity $\gamma_1 = \alpha_2 - \alpha_3$ and without the director inertia term. In the limit of small φ-angles, it reduces to the linear form:

$$K_{22}\frac{\partial^2\varphi}{\partial z^2} + \chi_a H^2\varphi = \gamma_1\frac{\partial\varphi}{\partial t} \tag{11.64}$$

with general solution $\varphi = \varphi_m \exp(t/\tau_R)\sin(\pi z/d)$. By substitution this into (11.64) we find the characteristic time for the director reaction to the field:

$$\tau_R = \frac{\gamma_1}{\chi_a H^2 - K_{22}\pi^2/d^2} = \frac{\gamma_1}{K_{22}(\xi^{-2} - \xi_c^{-2})} \tag{11.65}$$

where the field coherence length (11.49) includes the twist modulus K_{22}. At the threshold ($\xi = \xi_c$) there is a singularity, $\tau_R \to \infty$. Above the Frederiks transition threshold $H > H_c$ and τ_R is positive and distortion rises. When the applied field is switched off, the field induced distortion relaxes with the decay time

$$\tau_D = \frac{\gamma_1}{K_{22}q^2} \tag{11.66}$$

as for a typical hydrodynamic mode.

When the distortion is weak it is described only by the single Fourier harmonic with wavevector $q = 2\pi/\Lambda$ where $\Lambda = 2d$. With increasing field, the distortion is characterised by elliptic-sine functions, Fig. 11.17a, with higher harmonics. Therefore we have multiple odd sine harmonics with wavevectors $q_m = m\pi/d$ ($m = 1, 2, 3 \ldots$). Then, according to (11.66), each harmonic decays with its own time, the higher the number m the faster is the decay (in analogy with string of a guitar):

$$\tau_D^m = \frac{\gamma_1}{K_{22}m^2q^2}, m = 1, 2, 3... \tag{11.67}$$

11.2.6 Backflow Effect

We know that the shear-induced flow of a nematic liquid strongly influences the alignment of the director (Section 9.3.2), i.e. there is a coupling of the two vector fields, the director $\mathbf{n}(\mathbf{r})$ and velocity of the liquid $\mathbf{v}(\mathbf{r})$. It is quite natural to think that the opposite effect should also exist. Indeed, one observes a strange, not monotonic director rotation during its relaxation from the field-induced quasi-homeotropic alignment to the initial, field-off planar one. Normally, the elastic force should smoothly rotate the director from $\theta = 0$ (parallel to the cell normal) to 90°, but, in experiment, the director angle may exceed 90° during the relaxation. As a result, in the optical transmission one observes a characteristic bump.

The reason for this is a flow of the nematic, which is lunched by the director rotation. The flow arises in the beginning of the director relaxation process when the elastic torque exerted on the director is very high near both interfaces due to a strong curvature of the director field. However, the curvature at the two interfaces has different sign, see Fig. 11.19a, where $\delta\vartheta(z) = (\pi/2) - \vartheta$. Therefore, the flow of nematic fluid coupled to the director rotation (backflow) at the two interfaces is

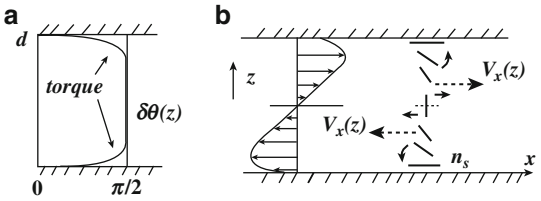

Fig. 11.19 Backflow effect. The profile of the director in the field-on regime with steep parts close to interfaces at $z = 0$ and $z = d$ (**a**). The direction of the torques is shown by small arrows in the right part of sketch (**b**) and a profile of the velocity is shown by thin arrows in the left part of the sketch. The strongest gradient of velocity is in the middle of the cell (*dash arrows*)

opposite. It is shown in Fig. 11.19b by velocity arrows. In the middle of the cell the gradient of velocity (shear) is very strong (shown by dash arrows). No wander that, in the middle of the cell, where the elastic torque is weak, the flow-induced torque prevails and rotates the director to the angles θ exceeding 90°.

It is interesting that, although the same effect is also observed during the director relaxation from the field-on planar texture to the field-off homeotropic one, it is much weaker. Note that, in the first case, we deal with the bend distortion near surfaces (torque M_B), but, in the second case, with the splay one (torque M_S). In both cases, a strong elastic torque rotates the director, let say, with the same angular rate **N**. However, due to friction a viscous torque appears, which is exerted by rotating molecules onto adjacent parts of the liquid crystal. The absolute value of the viscous torque related to the bend distortion $M_b = \frac{1}{2}(\gamma_1 - \gamma_2)N = -\alpha_2 N$ considerably exceeds the torque related to the splay $M_s = \frac{1}{2}(\gamma_1 + \gamma_2)N = \alpha_3 N$ because $|\alpha_2| >> |\alpha_3|$. Therefore, the backflow is especially important for the initial homeotropic orientation. Note that there is no backflow for the twist distortion that does not change the position of the centers of gravity of the molecules.

If we are going to discuss the problem of the director relaxation with allowance for the backflow, we should write two equations of motion, one for the director and the other for the mass of liquid [22]. Each of the equations should include coupling terms describing influence of the director motion on the flow and *vice versa*. According to Fig. 11.19, the splay and bend distortions take place in the *xz* plane and the vector of flow velocity is assumed to have only one component, $\mathbf{v} = v_x(z)$ parallel to the substrates because the *y* -component is forbidden by symmetry and the *z*-component should vanish according to the mass continuity equation ($\mathrm{div}\mathbf{v} = 0$). Therefore, in the absence of an external force and neglecting the convective term and pressure in the tensor of momentum density flux (9.10), the equation for momentum conservation (9.8) is given by:

$$\rho \frac{\partial v_x}{\partial t} = \frac{\partial \sigma'_{xz}}{\partial z} = \frac{\partial}{\partial z}\left(A\frac{\partial \vartheta}{\partial t} + B\frac{\partial v_x}{\partial z}\right) \tag{11.68}$$

Here, director $\mathbf{n} = (\sin\vartheta \approx \vartheta, 0, \cos\vartheta \approx 1)$, the term with friction coefficient *B* is the standard Navier-Stokes terms (9.15) of the type $\rho\partial v/\partial t = \eta\partial^2 v/\partial z^2$ (*B* is

combination of Leslie coefficients coming from the viscous stress tensor for nematics σ'_{xz} (9.20)). The coupling term with friction coefficient A takes into account the influence of the director rotation with angular velocity $N = \partial\vartheta/\partial t$ on the flow acceleration controlled by Leslie coefficients α_2 and α_3 (backflow effect).

The second equation describes the relaxation of the director

$$\gamma_1 \frac{\partial \vartheta}{\partial t} = K \frac{\partial^2 \vartheta}{\partial z^2} - A \frac{\partial v_x}{\partial z} \tag{11.69}$$

It is the same general equation (9.22) for director motion adapted to our simple situation: we have the familiar form (9.32) for the elastic and viscous torques and, in addition, the coupling term with the same coefficient A describing the torque exerted on the director by shear $\partial v_x/\partial z$.

Numerical solution of the two equations results in the time variation of the velocity $v_x(z)$ and director $\vartheta(z)$ along the cell thickness as shown in the same Fig. 11.19 for a particular time t. At a certain moment, the angle ϑ in the middle of the cell may cross zero (vertical line) and change sign. In the figure the profile of velocity is antisymmetric. The question arises how this symmetry is consistent with initial symmetry of the cell. The symmetry is indeed broken locally on the scale of one vortex. But in the neighbor area the direction of the director rotation is different and the flow velocity has an opposite sign. Therefore the total dynamic symmetry of the whole cell is consistent with boundary conditions. The backflow effect considerably influences the dynamic of the director relaxation and this phenomenon is used in bistable displays (Chapter 12). By controlling the velocity of flow using a special form of the applied voltage one can select one of the two final stable field-off states.

11.2.7 Electrooptical Response

If a nematic liquid crystal has negligible conductivity the results of Sections 11.2.1–11.2.5 for the Frederiks transition induced by a magnetic field may be directly applied to the electric field case. To this effect, it suffices to substitute **H** by **E** and all components of magnetic susceptibility tensor χ_{ij} by correspondent components of dielectric permittivity tensor ε_{ij}. From the practical point of view the electrooptical effects are much more important and further on we discuss the optical response of nematics to the electric field.

11.2.7.1 Splay-Bend Distortions

We discuss the splay-bend distortion induced by an electric voltage applied to a cell similar to that shown in Fig. 11.16 using two transparent electrodes at $z = 0$ and $z = d$. The distortion is easy to observe optically for the cell birefringence. The splay-bend cell behaves like a birefringent plate discussed in Section 11.1.1 but now the plate birefringence is controlled by the field. The optical anisotropy

$\Delta n(z) = n_e - n_o$ depends on the angle of the director $\vartheta(z)$, which has a certain distribution over the cell thickness. In the absence of the twist, the splay-bend distortion is limited by the x,z-plane, the ordinary refraction index is independent of ϑ, $n_o = n_\perp$, but the extraordinary index $n_e(\vartheta)$ given by Eq. (11.6) becomes a function of position z of the dielectric ellipsoid within the cell thickness.

$$n_e(z) = \frac{n_{||} n_\perp}{\left[n_{||}^2 \cos^2\vartheta(z) + n_\perp^2 \sin^2\vartheta(z)\right]^{1/2}} \tag{11.70}$$

The corresponding phase retardation is obtained by integrating (11.70) over the cell thickness:

$$\delta = \frac{2\pi}{\lambda} \int_0^d [n_e(z) - n_o) dz = \frac{2\pi d \langle \Delta n \rangle}{\lambda} \tag{11.71}$$

The averaged value of $<\Delta n>$ and, consequently, δ are voltage dependent. Usually a liquid crystal cell equipped with thin tin dioxide (SnO_2) or indium-tin-oxide (ITO) electrodes is placed between two crossed polarizers and illuminated by filtered white light or laser light (for example, of a He-Ne laser, $\lambda = 632.8$ nm) and the transmitted intensity is recorded using a photodetector, Fig. 11.20. The output light intensity depends on the angle ϕ between the axis of the polarizer and the projection of the director on the cell plane and on the phase retardation $\delta(U)$ controlled by voltage:

$$I = I_0 \sin^2 2\varphi \cdot \sin^2 \frac{\delta(U)}{2}$$

The oscillations of I (U) are well seen in the experimental plot, Fig. 11.21. The measurements were made at 27°C on 55 μm thick cell filled with a mixture having $\varepsilon_a = 22$. From the I (U) curve, the field dependence of the phase retardation $\delta(U)$ and the Frederiks transition threshold U_c were obtained. In turn, from $E_c = U_c/d$ and Eq. (11.56) the splay elastic constant K_{11} was found. The bend modulus K_{33} was calculated from the derivative $d\delta/dU$. The same material parameters may be found for the whole temperature range of the nematic phase.

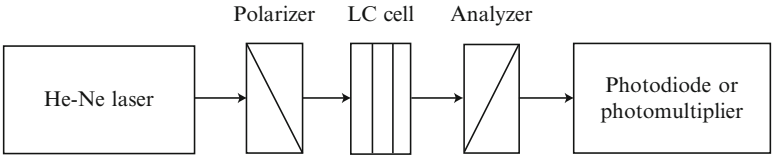

Fig. 11.20 A typical set-up for electrooptic measurements of liquid crystal physical parameters

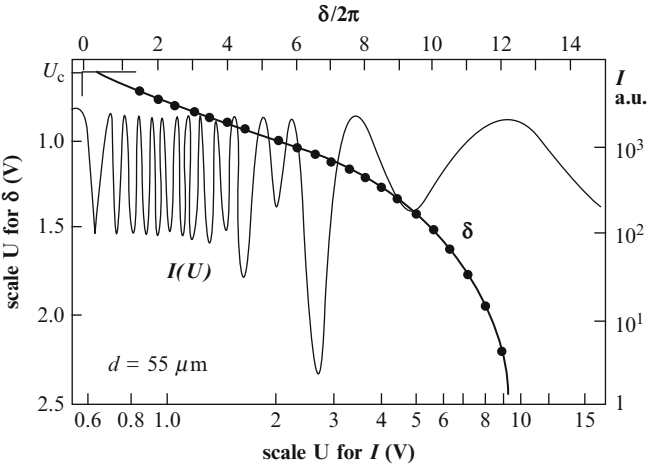

Fig. 11.21 The oscillating experimental curve *I(U)* (*right axis*) is voltage dependent intensity of the light transmitted by the 50 μm thick planar nematic cell placed between crossed polarizers (the logarithmic voltage scale for *I(U)* is the bottom axis). The pointed curve is the voltage dependence of phase retardation δ calculated from curve *I(U)* with a Frederiks transition threshold at U_c (the scale for δ(*U*) is on the top axis and its argument i.e. voltage is on the left axis)

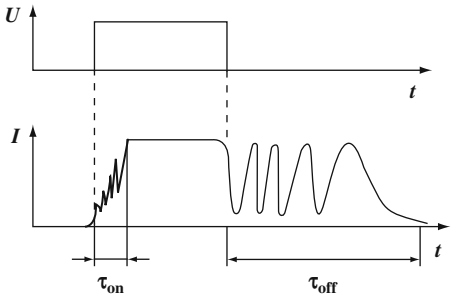

Fig. 11.22 Dynamic of the electrooptical response of a planar nematic cell: the voltage pulse *U* (*upper plot*) and the transient intensity of transmitted monochromatic light *I* (*lower plot*)

Note that the voltage necessary to modulate monochromatic light by 2π (between two spikes) is less than 0.1 V. The modulation by π or 2π can also be obtained in dynamics, during switching the field on and off. The oscillograms are shown in Fig. 11.22. By proper selection of the voltage shape and using the dual frequency mode of addressing (for materials with frequency inversion of sign of dielectric anisotropy), one can modulate the optical transmission as fast as 1 μs. Of course, solid state modulators are much faster, but we should not forget that a liquid crystal cell may consist of thousands pixels and be controlled by low voltages. Such regimes are used for image processing in adaptive optics and other applications.

11.2.7.2 Twist and Supertwist Effects

Let the director at the two opposite electrodes be aligned along x and y, respectively. As discussed in Sections 8.3.2, for strong anchoring at the boundaries, the azimuthal angle φ in the bulk changes linearly with z. Then, under condition $\Delta nd/\lambda > 1$ such a twisted layer rotates the polarization vector of light of any wavelength λ through the angle $\pi/2$. This is the waveguide regime already discussed in Section 11.1.1. With typical values of $\Delta n \approx 0.15$, $\lambda \approx 0.5$ μm, this regime takes place for cell thickness $d > 3$ μm. Therefore, a typical twist cell of thickness about 5 μm placed between crossed polarizer and analyser oriented, respectively along x and y, is completely transparent (with some attenuation due to non-ideal polarizers). However, upon application of a voltage, the director is realigned along the field, the twist cell no longer rotates the light polarization, and the outgoing light is completely absorbed by the analyser. For parallel polarizers, on the contrary, the OFF-state is dark and the ON-state bright. It is important that the so-called twist effect is almost insensitive to light wavelength [23].

Twist cells are widely used in modern technology of simple, low-informative displays (watches, calculators, telephones, dashboards, etc). Their advantages are high contrast, simplicity and stability. But for high information displays their contrast characteristics are not steep enough. This hampers the application of twist cells to multiplexing schemes. Multiplexed displays use electrodes in the form of the x,y matrix and each pixel is situated on an intersection of the x and y bars. When a selected pixel is activated by voltage U, other pixels along the same x and y bars inevitably activated by voltage $U/2$ (the so-called cross-talk effect). Therefore, to activate solely one selected pixel, the contrast curve must be steep and the larger the number of bars in a matrix the steeper should be the contrast curve. For this reason, the cells with an initial director twist angle larger than $\pi/2$, the so-called *supertwist cells* are more preferable for high information content displays. In addition they show better angular characteristics but, unfortunately, they are more sensitive to the cell gap and have longer response times.

11.2.7.3 Guest-Host Effect

This effect is a version of the splay-bend Frederiks transition, but it is observed in liquid crystals doped with dyes. The liquid crystalline matrix (the host) is subjected to the influence of a field; the function of the dye (the guest) is to enable the effect to be seen with only one polarizer or even without any.

In the Fig. 11.23a a typical electro-optical cell is shown with a homogeneous alignment of a nematic and $\varepsilon_a > 0$. A small amount (few percents) of a proper dye is dissolved in the liquid crystal. The dye molecules are elongated in shape, and the dipole moment of their long-wave optical transition is parallel to the long molecular axis. In the absence of a field, the optical density of the cell varies with the linear polarization of the light $\mathbf{e}$ from $D_{\parallel}$ ($\mathbf{e} \parallel \mathbf{n}$) to $D_{\perp}$ ($\mathbf{e} \perp \mathbf{n}$). When a voltage exceeding the threshold for the Frederiks transition is applied to the cell, the liquid crystal is

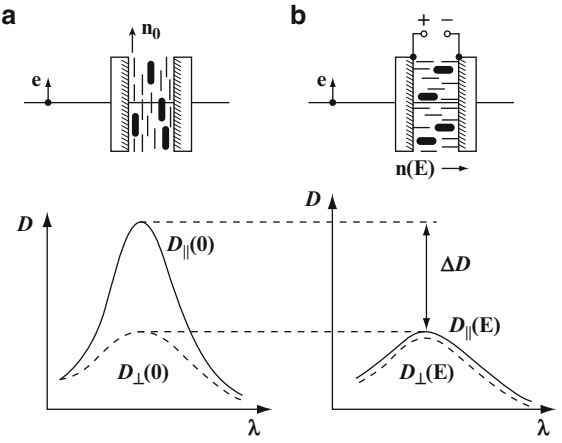

Fig. 11.23 Guest-host effect. Field-off (**a**) and field-on (**b**) cell configurations and absorbance spectra for a nematic liquid crystal doped with a dye having elongated molecules shown by small black spherocylinders

realigned along the field and so the dye molecules are reoriented. If the field is strong enough, the optical densities for light of both polarizations become the same, Fig. 11.23b. Therefore, for the light polarised along the initial alignment of the director, the field induced decrement of density $\Delta D(E) = D_{\parallel}(0) - D_{\perp}(0)$ is very large. The ratio of the corresponding transmitted light intensities for the field-on and field-off states can be as high as 100. This effect is interesting for colour displays. For more detailed information about various electrooptical effects and liquid crystal displays and other devices see [24].

11.3 Flexoelectricity

We know that the quadratic-in-field coupling of an electric field to the dielectric tensor contributes to the free energy density with the term $g_E = -\varepsilon_a E^2/8\pi$. When liquid crystals possess macroscopic electric polarization **P** (spontaneous or induced by some external, other than electric field factors), then an additional, linear-in-field term $g_E = -\mathbf{PE}$ is added to the free energy density. One of such a source of the macroscopic electric polarization is orientational distortion of a liquid crystal.

11.3.1 Flexoelectric Polarization

11.3.1.1 Dipolar and Quadrupolar Flexoelectricity

Let us look at Fig. 11.24. In the upper two sketches, we can see undistorted nematic liquid crystals with pear- and banana-shape molecules. Such nematics in the bulk

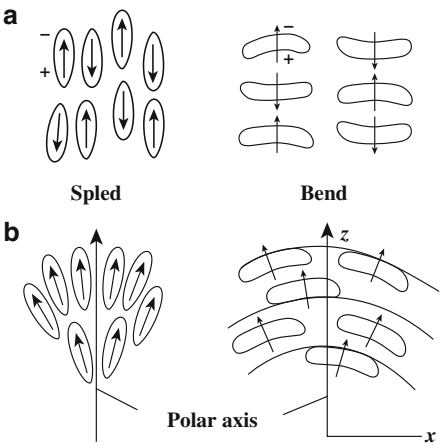

Fig. 11.24 Dipolar flexoelectric polarization. Pear-shape and banana-shape molecules in undistorted nematic liquid crystals without any polar axes (**a**) and appearance of polar axes and flexoelectric polarization along the z-direction in the same nematics due, correspondingly, splay and bend distortion (**b**)

are non-polar due to free or partially hindered rotation of molecules (even polar) about all their axes. Imagine now that, in the absence of the electric field, the same nematics are subjected to the splay (left) or bend (right) distortions, respectively. For example, such distortion arises spontaneously in wedge form cells with rigid boundary conditions for the director. For a moment we may forget that molecules have dipoles. Nevertheless, due to the change in symmetry from cylindrical $D_{\infty h}$ to conical $C_{\infty v}$ (for splay) or to C_{2v} (for bend), in both cases the corresponding polar axes appear. Their directions are shown by long vertical arrows. It is not surprising because the splay (**n**div**n**) and bend (**n** $\times$ curl**n**) distortions are vectors.

The new polar symmetry allows for the existence of macroscopic polarization, large or small, depending on the magnitude of the strain and molecular dipole moments shown by small arrows. Due to the distortions, the densest packing of our pears and bananas results in some preferable alignment of molecular skeletons in such a way that molecular dipoles look more up than down. By definition, the dipole moment of the unit volume is electric polarization. These simple arguments brought R. Meyer to the brilliant idea of *piezoelectric* polarization [25]:

$$\mathbf{P}_f = e_1 \mathbf{n}\, div\mathbf{n} - e_3(\mathbf{n} \times curl\mathbf{n}) \tag{11.72}$$

The term piezoelectric was borrowed from the physics of solids by analogy to the piezoelectric effect in crystals without center of symmetry. As a rule, the piezoelectric polarization manifests itself as a charge on the surfaces of a crystal due to a translational deformation, e.g. compression or extension. Piezo-effects are also characteristic of polar liquid crystalline phases, e.g., of the chiral smectic C* phase. The polarization, we are interested now, is caused by the mechanical curvature (or flexion) of the director field, and, following De Gennes, we call it *flexoelectric*.

In Eq. (11.72) there are two terms related, respectively to the splay and bend distortions with corresponding flexoelectric coefficients e_1 and e_3. Indeed, the div**n**

is scalar and vector $\mathbf{P}_f$ (splay) coincides with the director **n**. In the case of bend, with director components (n_x=1, 0, 0), the curvature vector curl**n** = $(\partial n_x/\partial z)$**j** (along y) and **n** × curl**n** = $n_x(\partial n_x/\partial z)$**k,** therefore vector $\mathbf{P}_f$ (bend) is also directed along z, as shown in the same figure. Note, that the twist distortion corresponding to scalar product **n**·curl**n** cannot create polarization.

Now, what would happen if molecules have no dipole moments? Would flexoelectricity be observed? Generally yes, because in addition to the dipolar mechanism, there is, at least, one more, namely, the quadrupolar one. An example is shown in Fig. 11.25: a splay distortion creates additional positive charges at the bottom of the ensemble of quadrupoles due to an enhanced packing density. The upper part is less positively charged, therefore polarization $\mathbf{P}_f$ is directed down [26]. A similar difference in the negative charge density will be seen for the bend distortion. Now, if we introduce the density of the quadrupole moment, as a sum of molecular quadrupole moments in a unit volume that is a tensor of quadrupole density, see Eq. (10.17), then its gradient is the vector of flexoelectric polarization. Since this tensor is proportional to the orientational order parameter Q, the quadrupolar contribution to the flexoelectric polarization (for $e = e_1 + e_3$ in the first approximation) is given by:

$$P_f^Q = e\nabla\widehat{Q} \tag{11.73}$$

We already discussed this case in relation to the surface polarization (Section 10.1.3). Generally both dipolar and quadrupolar mechanisms contribute to $\mathbf{P}_f$ but the temperature dependence of the corresponding coefficients is different, $e_q \propto S(T)$ for the quadrupolar mechanism, but $e_d \propto S^2(T)$ for the dipolar one. The flexoelectric coefficients have the dimension of (CGSQ/cm or C/m) and the order of magnitude, $e \sim 10^{-4}$ CGS units (or ~3 pC/m). The flexoelectricity is also observed in the SmA phase [27].

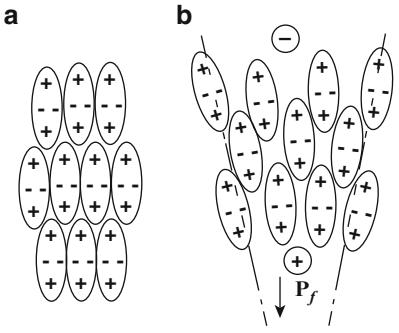

Fig. 11.25 Quadrupolar flexoelectric polarization. Undistorted nematic phase consisted solely of molecular quadrupoles (**a**) and appearance of a polar axis and flexoelectric polarization due to splay distortion (**b**). Note that in the lower part of (**b**) the density of positive charges is larger than in the upper part whereas in sketch (**a**) these densities are equal

11.3.1.2 A Hybrid Cell

The director at one of the boundaries of a hybrid cell is aligned homeotropically, at the opposite boundary homogeneously as was shown earlier in Fig. 10.11. Therefore, a hybrid cell has intrinsic bend-splay distortion and must have a projection of the macroscopic polarization along the cell normal. We can clearly see in Figs. 10.11 and 11.25 how the quadrupolar polarization emerges. The molecules may have positive ($e_0 > 0$) quadrupoles shown in Fig. 11.25 or negative ones ($e_0 < 0$) seen in Inset to Fig. 11.26b.

For a hybrid cell the flexoelectric polarization can easily be calculated. In Fig. 11.26a, the profile of the director is $\mathbf{n}(z)$ with boundary conditions $\vartheta(0) = \pi/2$ and $\vartheta(d) = 0$. These angles are rigidly fixed. The components of the director are $n_x = \sin\vartheta$, $n_y = 0$, $n_z = \cos\vartheta$. To calculate the polarization we have to find distribution $\mathbf{P}_f(z)$ using Meyer's equation (11.72), and after integrating over z, to obtain total polarization of the cell. In the considered geometry:

$$\mathbf{n} = \mathbf{i}\sin\vartheta(z) + \mathbf{k}\cos\vartheta(z);\ \mathrm{div}\mathbf{n} = -\sin\vartheta\frac{d\vartheta}{dz};\ \mathrm{curl}\mathbf{n} = \cos\vartheta\frac{d\vartheta}{dz}\mathbf{j};$$

$$\mathbf{n}\times\mathrm{curl}\mathbf{n} = (-\mathbf{i}\cos\vartheta + \mathbf{k}\sin\vartheta)\cos\vartheta\frac{d\vartheta}{dz}$$

Then splay and bend polarization contributions are:

$$P_f^{splay} = -e_1\sin\vartheta\frac{d\vartheta}{dz}\cdot(\mathbf{i}\sin\vartheta + \mathbf{k}\cos\vartheta)$$

$$P_f^{bend} = -e_3\cos\vartheta\frac{d\vartheta}{dz}(-\mathbf{i}\cos\vartheta + \mathbf{k}\sin\vartheta)$$

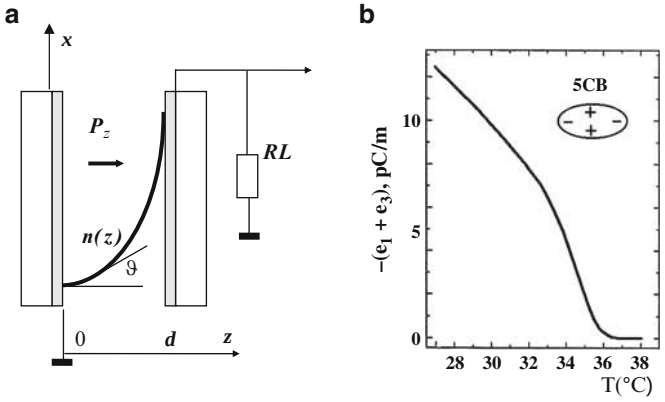

Fig. 11.26 A scheme of a hybrid cell that supports the splay-bend distortion and manifests the flexoelectric polarization (**a**) and an experimental temperature dependence of the sum of flexoelectric coefficients in the nematic phase of liquid crystal 5CB (**b**)

Combining the x and z components we obtain projections of the total flexoelectric polarization on the x- and z- axes with $P_{fy} = 0$:

$$P_{fx} = \left(-e_1 \sin^2\vartheta + e_3 \cos^2\vartheta\right) \frac{d\vartheta}{dz} \tag{11.74a}$$

$$P_{fz} = -\tfrac{1}{2}(e_1 + e_3) \sin 2\vartheta \frac{d\vartheta}{dz} \tag{11.74b}$$

From (11.74) we see, that the z-component depends on the sum $e = e_1 + e_3$ and, for negative e, P_{fz} should be directed from the homeotropic to planar interface. After integrating over cell thickness the average cell polarization along z is given by

$$\langle P_{fz} \rangle = \frac{1}{d} \int_0^d P_{fz} dz = \frac{e_1 + e_3}{4d} (\cos 2\vartheta_d - \cos 2\vartheta_0) = -\frac{e_1 + e_3}{2d}. \tag{11.75}$$

Therefore, if we could measure the z-component of the polarization of a hybrid cell we find $e = e_1 + e_3$. The main problem is screening the polarization by free charges. What we do measure is a change in polarization, induced by some external factors, but not polarization itself.

11.3.1.3 Measurements of P_f

It is not difficult to measure the temperature derivative dP_f/dT that is pyroelectric coefficient within the temperature range of the nematic phase. Then, integrating it over temperature from the temperature point where $P_f = 0$ we can find $P_f(T)$. As a zero point, any temperature T_i within the isotropic phase may be taken.

We measure pyroelectric coefficient $\gamma = dP_f/dT$, using heating the hybrid cell by short (~10 ns) laser pulses, as shown in Fig. 10.13. The only difference from the surface polarization measurements is using a hybrid cell instead of uniform (planar or homeotropic) cells [28]. The laser pulse produces a temperature increment about $\Delta T \approx 0.05$ K and the flexoelectric polarization changes. To compensate this change, a charge passes through the external circuit and the current $i = dq/dt$ is measured by an oscilloscope. From the identity (A is cell area)

$$i = \frac{\partial q}{\partial t} = A \frac{\partial P}{\partial t} = A \frac{\partial P}{\partial T} \frac{\partial T}{\partial t} = A\gamma \frac{\partial T}{\partial t}$$

the polarization is given by

$$P_f(T) = \int_{T_i}^{T} \gamma(T) dT. \tag{11.76}$$

With a short laser pulse, the derivative $\partial T/\partial t$ is just a jump, therefore, pyroelectric coefficient $\gamma(T)$ can be easily calculated at any temperature of the nematic phase. An example of the $P_f(T)$ dependence is shown in Fig. 11.26b. The maximum value of e for 5CB is $-3.6{\cdot}10^{-4}$ CGS (or –12 pC/m). It means that the molecular quadrupole has the form shown in the Inset to the same figure. There are some other methods to find the sum of the flexoelectric coefficients based, e.g., on the electro-optical techniques but they are not as straightforward as the pyroelectric technique.

For conventional nematics the order of magnitude $\approx 10^{-4}$ CGS of the flexoelectric coefficient is quite reasonable. There are, however, nematics composed of bent-shape (banana-like) molecules with transverse dipole moments for which three orders of magnitude larger flexoelectric coefficient has been reported [29]. If such a material is placed between two flexible polymer sheets covered with electrodes and subjected to periodic bending, the current in the range of few nA is observed. The reason for such a giant effect is probably related to the formation of big polar clusters in the nematic phase, that is to a short-range order effect related to the break of quadrupolar symmetry similar to the break of mirror symmetry that discussed in Section 4.11. Whatever mechanism is, the effect may be useful for micro-devices converting mechanical energy in the electric one.

11.3.2 Converse Flexoelectric Effect

11.3.2.1 Uniform Distortion

As has been shown, the splay and bend distortions of a nematic create electric polarization. There is also a converse effect; the external electric field causes a distortion due to the flexoelectric mechanism. For example, if the banana-shape molecules with transverse dipoles are placed in the electric field, the dipoles are partially aligned along the field and their banana shape induces some bend. This effect takes place even in nematics with zero dielectric anisotropy.

Let the director of a nematic liquid crystal be aligned homeotropically ($\mathbf{n} \parallel z$) and the uniform field $\mathbf{E} \parallel x$ as shown in Fig. 11.27a. For negative ε_a, in the absence of the flexoelectric effect, such a situation is stable at any field strength. However, in experiment [30] the bend distortion is observed and its magnitude calculated. For zero anchoring energy and small distortions, the components of the director are: $n_z = \cos\theta(z) \approx 1; n_x = \sin\theta(z) \approx \theta(z)$ and $n_y = 0$, hence,

$$div\mathbf{n} = {}^{\partial n_z}/_{\partial z} = -\sin\vartheta\,{}^{\partial\vartheta}/_{\partial z};\ \text{and}\ \mathbf{n}\,div\mathbf{n} \approx -\sin\vartheta\,{}^{\partial\vartheta}/_{\partial z}\mathbf{k};$$
$$\text{curl}\mathbf{n} = {}^{\partial n_x}/_{\partial z}\mathbf{j} = {}^{\partial\vartheta}/_{\partial z}\mathbf{j};\ \text{and}\ \mathbf{n}\times\text{curl}\mathbf{n} = \mathbf{k}\times{}^{\partial\vartheta}/_{\partial z}\mathbf{j} = -{}^{\partial\vartheta}/_{\partial z}\mathbf{i}.$$

Therefore, for a small distortion, we can leave only the x-component of the total flexoelectric polarization (11.72):

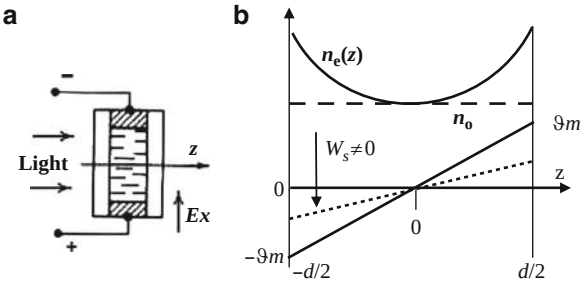

Fig. 11.27 Converse flexoelectric effect: (**a**) Structure of the electrooptical cell. (**b**) Distribution of the director angle over the cell thickness pictured by lower straight lines for zero (*solid line*) and finite (*dot line*) anchoring energies, respectively. The upper curves show spatial dependence of two principal refraction indices n_o (*dash line*) and n_e (z) (*solid line*)

$$P_{fx} \approx e_3 \frac{\partial \theta}{\partial z}$$

For $\varepsilon_a = 0$, the free energy density in the bulk includes only the flexoelectric and the elastic (bend) terms:

$$g = -P_{fx}E + \frac{K_{33}}{2} \cdot \left(\frac{\partial \theta}{\partial z}\right)^2 = \frac{K_{33}}{2} \cdot \left(\frac{\partial \theta}{\partial z}\right)^2 - e_3 E \frac{\partial \vartheta}{\partial z} \tag{11.77}$$

Here we ignore the surface energy ($W_s = 0$) and the director is free to deflect at both boundaries perpendicular to z. According to Euler equation (8.22), the minimisation over $\partial\vartheta/\partial z$ results in the torque balance:

$$0 - \frac{d}{dz}\left(K_{33}\frac{\partial \vartheta}{\partial z} - e_3 E\right) = \quad 0 \quad \text{or} \quad \left(K_{33}\frac{\partial \vartheta}{\partial z} - e_3 E\right) = const \tag{11.78}$$

Hence

$$\frac{\partial \theta}{\partial z} = \frac{e_3 E}{K_{33}} + \mathrm{C}_1;$$

In zero field $\partial\vartheta/\partial z = 0$ everywhere, therefore $\mathrm{C}_1 = 0$,

$$\theta = \frac{e_3 E}{K_{33}} z \quad \text{and} \quad P_f = \frac{e_3^2 E}{K_{33}} = const \tag{11.79}$$

Here $z = 0$ is taken in the middle of the layer. The resulting distortion angle is shown in Fig. 11.27b. In the middle of the cell the director keeps its equilibrium

orientation and the maximal deflection angles of the director occur at the restricting surfaces,

$$\theta_m = \pm \frac{e_3 E d}{2K_{33}}.$$

Such an antisymmetric distortion differs from the symmetric distortion characteristic of the Frederiks transition. It is instructive to compare these two cases. In Fig. 11.28 the space distributions of the director **n** and its x-projection $n_x = \sin\vartheta \approx \vartheta$ are pictured for the Fredericks transition (*a*) and flexoelectric effect (*b*); the anchoring energy at both surfaces is infinitely strong in case (*a*) and finite in case (*b*).

Note that, in the free energy density expansion (11.77), the flexoelectric term is proportional to the first derivative $\partial\vartheta/\partial z$. Therefore, upon integration over the cell thickness, it gives only surface energy terms $W(\vartheta_{\pm d/2})$. Correspondingly, the torque balance (11.78) shows the absence of the flexoelectric torque in the bulk of a cell for the uniform field E_x:

$$\frac{d}{dz}\left(K_{33}\frac{\partial\vartheta}{\partial z} - e_3 E_x\right) = K_{33}\frac{d^2\vartheta}{dz^2} \tag{11.80}$$

Evidently, the distortion comes in from the boundaries. It means that weak anchoring of a nematic liquid crystal at the surfaces is a necessary condition for the one-dimensional distortion considered. It is interesting that, for a finite, but weak anchoring, the linear profile of $\vartheta(z)$ remains, although the maximum values ϑ_m at the glass surfaces ($z = -d/2$ and $+d/2$) reduces. The higher the anchoring energy the smaller is ϑ_m. In experiment this may look like a decrease in an effective flexoelectric coefficient. The profiles of the director angles and refraction indices are shown in Fig. 11.27b, the solid and dotted lines for ϑ correspond to $W_s = 0$ and $W_s > 0$, respectively.

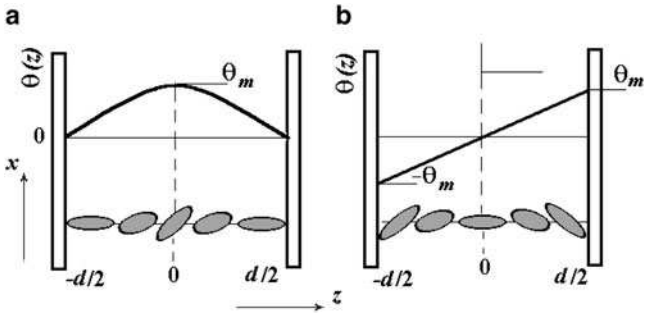

Fig. 11.28 Comparison of the distortion profile (molecular picture below and angle $\vartheta(z)$ *above*) for the Frederiks transition with infinite anchoring energies (**a**) and flexoelectric effect with finite anchoring energies (**b**) (homeotropic initial director alignment in both cases)

11.3.2.2 Electrooptical Properties

Due to the linear profile of $\vartheta(z)$ it is very easy to calculate the phase retardation of the initially homeotropic cell for the normal light incidence, $\mathbf{k}\|z$. Without electric field, the longest axis of the dielectric ellipsoid coincides with the director axis z. Therefore, refraction index for any polarization is $n_o = n_\perp$. With increasing field E_x, due to deflection of the director within plane xz, the y- and x-components of the refraction index will correspond to the ordinary and extraordinary rays, $n_y = n_o = n_\perp$, $n_x(z) = n_e(z)$. Integration provides us with the average extraordinary index:

$$<n_e> = \frac{1}{d}\int_{-d/2}^{d/2} \frac{n_\perp n_{||}}{\left(n_\perp^2 \sin^2\vartheta + n_{||}^2 \cos^2\vartheta\right)^{1/2}} dz$$

For small distortions, expanding $\sin\vartheta \approx \vartheta$, $\cos\vartheta \approx 1-\vartheta^2/2!$, $\cos^2\vartheta \approx 1-\vartheta^2+..$ we obtain

$$<n_e> = \frac{1}{d}\int_{-d/2}^{d/2} \frac{n_\perp}{\left[1-\left(1-n_\perp^2/n_{||}^2\right)\vartheta^2\right]^{1/2}} dz$$

$$\approx \frac{1}{d}\int_{-d/2}^{d/2} \left[n_\perp + \frac{n_\perp}{2}\left(1-n_\perp^2/n_{||}^2\right)\vartheta^2\right] dz$$

Substituting $\theta = e_3 E z/K_{33}$ from (11.79) (case of zero anchoring energy) and integrating we obtain

$$<n_e> \approx n_\perp + \frac{n_\perp}{2d}\left(1-n_\perp^2/n_{||}^2\right)\left(\frac{e_3 E}{K_{33}}\right)^2 \int_{-d/2}^{d/2} z^2 dz \quad \text{with} \quad \int_{-d/2}^{d/2} z^2 dz = \frac{d^3}{12}$$

Finally the phase retardation $\delta = 2\pi d(n_e - n_o)/\lambda$:

$$\delta = \frac{2\pi}{\lambda}\left(\frac{e_3}{K_{33}}\right)^2 \left(1-\frac{n_\perp^2}{n_{||}^2}\right)\frac{n_\perp d^3}{24} E^2 \tag{11.81}$$

The dependencies $\delta \propto d^3$ and $\delta \propto E^2$ agree well with experiment [30]. Therefore, in principle, we can find e_3 from the measured value of the cell retardation because usually K_{33} is known from the Frederiks transition threshold. However, in a real experiment it is almost impossible to have zero anchoring energy. For the finite anchoring energy, we can only find ratio e_3/W_s and the accuracy of determination

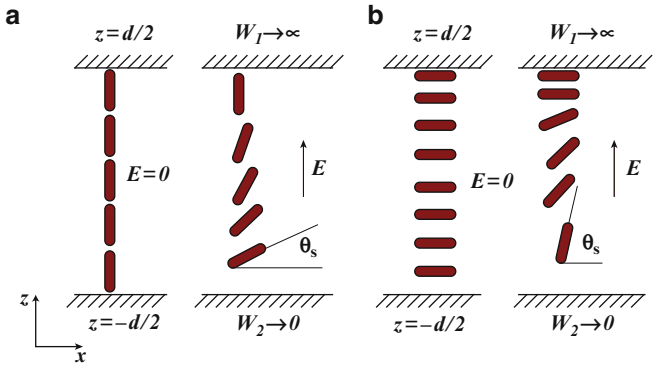

Fig. 11.29 Conversed flexoelectric effect in cells with homeotropic (**a**) and homogeneous (**b**) director alignment and electric field applied along the cell normal. Weak anchoring energy at the bottom plate allows the flexoelectric deflection of the director ϑ_s at the surface propagating up in the vertical direction ($\varepsilon_a = 0$)

of e_3 depends on the value of W_s, which varies within several orders of magnitude and is difficult to measure with sufficient accuracy. Another factor that may influence the estimation of flexoelectric coefficients is the surface polarization discussed above. When the dielectric anisotropy is finite the distortion has a more complicated character due to a competition of the dielectric (as for Frederiks transition) and flexoelectric torques [31].

The flexoelectric effect can also be observed in other geometries. For example, the field can be applied along the normal of an electrooptical cell. For a homeotropic cell, the splay flexoelectric distortion shown in Fig. 11.29a is observed for $\varepsilon_a \geq 0$ and weak anchoring energy, at least, at one interface. Another interesting geometry where the splay flexoelectric distortion is also possible is a planar homogeneous alignment of the director with asymmetric anchoring: it is strong on the top and weak at the bottom, see Fig. 11.29b. In both cases, the surface flexoelectric torque is equal to $(e_1 + e_3)E\vartheta_s$ [31].

11.3.2.3 Dynamics of the Flexoelectric Effect

Consider the same bend distortions caused by field E_x and shown in Fig. 11.28 and assume that distortions are small. What happens if we switched the field off? In the torque balance equation for "Frederiks" distortion (*a*), we shall have two contributions, elastic and viscous:

$$K_{33}\frac{\partial^2\vartheta}{\partial z^2} = \gamma_1\frac{\partial\vartheta}{\partial t} \tag{11.82}$$

with general solution $\vartheta = \vartheta_m \exp {}^{t}/_{\tau} \sin qz$ where $q = \pi/d$. In this case, we have a relaxation process with a single spatial Fourier harmonic and the characteristic bulk

relaxation time is basically controlled by the cell thickness: $\tau_{bulk} = \gamma_1/K_{33}q^2 = \gamma_1 d^2/\pi^2 K_{33}$. For the finite anchoring the situation is similar; we should just substitute thickness d by $d + 2b$ where b is surface extrapolation length given by $b = K_{33}/W^s$. For the anchoring energies $W^s \approx 10^{-3} - 10^{-2}$ erg/cm^2 (homeotropic alignment), $b \approx 10^{-3} - 10^{-4}$cm, $d + 2b \approx 30$ μm ($3 \cdot 10^{-3}$ cm), $\gamma_1 \approx 1$ P, and $K_{33} \approx 10^{-6}$ dyn, the relaxation time is $\tau_{bulk} = \gamma_1/K_{33}q^2 \approx 1$ s.

Equation (11.82) is valid for the flexoelectric distortion (b) as well, but it does not have a sine-form profile and we cannot expect a simple relaxation process. Moreover, this distortion is controlled by boundary conditions that generally include the Rapini-type surface torque, elastic and flexoelectric torques:

$$K_{33}\left.\frac{\partial\theta}{\partial z}\right|_{z=\pm d/2} \pm W_i^s\theta\big|_{z=\pm d/2} - e_3 E = 0 \tag{11.83}$$

For free relaxation, the term $e_3E = 0$ but the Rapini terms W^s at each surface dramatically influence the relaxation process. The relaxation time of the director at the surface τ_s is controlled by the wavevector $q_s \approx \pi/b$. For the same parameters as above $\tau_s = \gamma_1/K_{33}q_s^2 \approx 1 - 100$ ms that is $\tau_s << \tau_{bulk}$ and relaxation process starting from the surface propagates into the bulk. When an oscillating field is applied to a cell the waves of the director realignment spread from the boundaries into the bulk [32]. It is very convenient to observe the near-surface director oscillations using total internal reflection technique [33]. With such a technique the flexoelectric effect is observed at frequencies as high as 10 kHz.

11.3.3 Flexoelectric Domains

There is a very interesting example of the flexoelectric torque acting on the director in the bulk. In a typical planar nematic cell the director is strongly anchored at both interfaces, $\mathbf{n_s} = (1, 0, 0)$ and the electric field is directed along z. The conductivity is low and the dielectric anisotropy is either zero or small negative, such that the dielectric torque may only weakly stabilize the initial planar structure. Upon the dc field application, a pattern in the form of stripes parallel to the initial director orientation in the bulk $\mathbf{n}_0 \| x$ is observed in the polarization microscope. The most interesting feature of these domains is substantial field dependence of their spatial period as shown in Fig. 11.30 [34].

The period of the stripes and the threshold voltage for their appearance have been found [35] by minimising the free energy of the nematic in an electric field, taking into account the flexoelectric ($\mathbf{P}_f\mathbf{E}$) and dielectric $\varepsilon_a(\mathbf{En})^2/4\pi$ terms. The solution of the torque balance equations for angles φ (counted from x within the xy plane) and ϑ (counted from x within the xy plane) has been found in the form of equations

$$\varphi = \varphi_0 \sin(qy)\cos(\pi z/d), \vartheta = \vartheta_0 \cos(qy)\cos(\pi z/d)$$

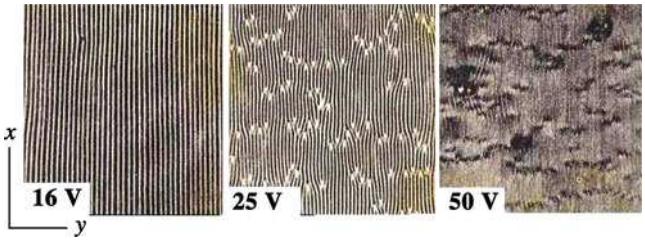

Fig. 11.30 Flexoelectric instability. Photos of flexoelectric domains with a period variable by electric field (nematic cell thickness 12 μm)

The emergence of the pattern has a threshold character. The critical voltage and the stripe width at the threshold are given by:

$$U_c = \frac{2\pi K}{|e|(1-\mu)}$$

and

$$w_c = \frac{d}{\pi}\left(\frac{1+\mu}{1-\mu}\right)^{1/2} \tag{11.84}$$

where

$$\mu = \frac{\varepsilon_a K}{4\pi e^2}$$

and

$$e = e_1 + e_3$$

Therefore, in a nematic with compensated anisotropy, $\varepsilon_a \approx 0$, the threshold voltage is controlled exclusively by ratio K/e, therefore the flexoelectric coefficient is easily found from the bulk effect, $e \approx 2 \cdot 10^{-4}$ CGSE at room temperature [34].

It is very peculiar that the spatial distribution of the director field of the modulated structure forms a chiral structure. This became evident much later [36] when the numerical calculations had been made in the same geometry with director components $n_x \approx 1, n^0{}_y = \cos qy, n^0{}_z = \sin qy$. Thus the projections of the director on the zy plane, i.e. $n_\perp = (n_y, n_z)$ rotate about the x-axis upon translation along the y-axis. The corresponding picture is demonstrated in Fig. 11.31. The calculations show that the chirality changes its handedness when the sign of the electric field applied in the z-direction inverses. Therefore, we again see the field induced break of the mirror symmetry.

As shown both in experiments and calculations, the domain period w decreases with increasing voltage approximately as $w \sim U^{-1}$. This is a very rare or even

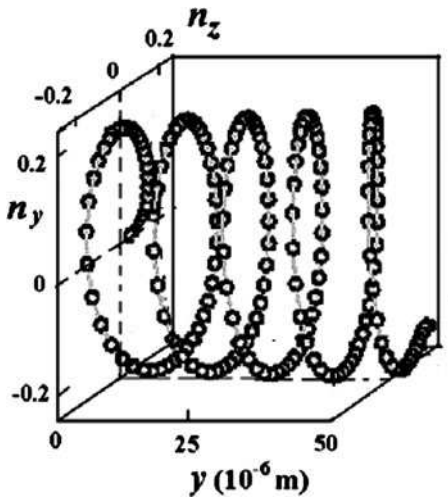

Fig. 11.31 Flexoelectric instability. Periodic structure of the field induced director distribution along the y-axis represented by projections n_z and n_y

unique case: in fact, the "flexoelectric cells" discussed represent diffraction gratings with period controlled by the electric field. Such gratings have been used for processing of optical information.

11.4 Electrohydrodynamic Instability

In this Section, we shall briefly discuss the electrohydrodynamic (EHD) instabilities of nematics, which are caused by an electric field induced flow of the substance. There are many interesting critical phenomena of this sort discussed in detail elsewhere [7,37,38], but here we shall consider in more detail only one but very representative example of the EHD instability owed to the anisotropy of electric conductivity.

11.4.1 The Reasons for Instabilities

Let us take a small volume of a liquid and consider two forces, the gravity force that push that volume down and the buoyancy force that push it up. Such a situation happens when a liquid is heated from below in a shallow pan: then, with increasing temperature, warm bottom layers of the liquid tend to rise but the upper cool layers tend to sink, Fig. 11.32a. Evidently, the two vertical forces (both along the z-axis) counteract and we are tempted to conclude that warm liquid would penetrate through the cold one. In reality, however, a nice steady-state periodic pattern of flow is observed in the horizontal plane xy due to up and down vertical streams.

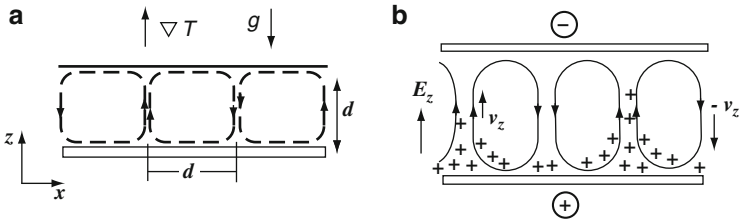

Fig. 11.32 A convective instability caused by a temperature gradient (**a**) and electrohydrodynamic instability caused by unipolar charge injection (**b**) in an isotropic liquid

Such a pattern occurs at a critical value of the vertical temperature gradient ∇T_c and has a form of a two-dimensional hexagonal lattice. This is another example of a break of the symmetry of the system caused by convective hydrodynamic instability, the so-called *Benard instability*.

Imagine now that there is a capacitor filled with an insulating liquid and the electric field E is applied along the normal to the capacitor plates. Assume that the lower electrode injects positive charges Q into the liquid, Fig. 11.32b, and there appears the space charge discussed in Section 7.3.3. Then, under the action of the electric field, the charged liquid layers will be pushed up against the counteracting gravity force like in the previous example. To reduce the energy, the charge layer will not move as an entire block but will be broken into vortices almost cylindrically symmetric about the z-axis. That results in a periodic distribution of the space charge within the xy plane. Therefore, one again observes an appearance of the convective instability, this time electrohydrodynamic one.

In both the cases considered, an optical contrast of the patterns observed in isotropic liquids is very small. Certainly, the anisotropy of liquid crystals brings new features in. For instance, the anisotropy of dielectric or diamagnetic susceptibility causes the Fredericks transition in nematics and wave like instabilities in cholesterics (see next Section), and the flexoelectric polarization results in the field-controllable domain patterns. In turn, the anisotropy of electric conductivity is responsible for instability in the form of rolls to be discussed below. All these instabilities are not observed in the isotropic liquids and have an electric field threshold controlled by the corresponding parameters of anisotropy. In addition, due to the optical anisotropy, the contrast of the patterns that are driven by "isotropic mechanisms", i.e. only indirectly dependent on anisotropy parameters, increases dramatically. Thanks to this, one can easily study specific features and mechanisms of different instability modes, both isotropic and anisotropic. The characteristic pattern formation is a special branch of physics dealing with a nonlinear response of dissipative media to external fields, and liquid crystals are suitable model objects for investigation of the relevant phenomena [39].

Assume that our capacitor is filled by a nematic mixture with $\varepsilon_a \approx 0$ well aligned along the x-axis and let the same charge injection mechanism works. Then, in a dc regime, the periodic flow will inevitably interact with the director. The maximum realignment, i.e. the deflection of the director angle ϑ in the z-direction, will be

observed where the shear rate has maximum, namely, in the middle of the vortices as shown by thick lines in Fig. 11.33a. On the contrary, the velocity is maximal where the space charge is accumulated. Such a mechanism of the director alignment is especially strong when the anisotropy of electric conductivity $\sigma_a = \sigma_{||} - \sigma_{\perp}$ is high. The conductivity induced torque M_y may even exceed the dielectric torque if dielectric anisotropy ε_a is not very strong. It is the torque, which is responsible, for example, for alignment of the director in the nematic phase and smectic layers in the SmA phase (in both cases along the flow lines) shown earlier in Fig. 5.16. The same torque described by Carr et al [40] is responsible for the Carr-Helfrich instability. The latter is also driven by the space charge, however, accumulated due to anisotropy of conductivity in the bulk of the nematic *without any injection*.

11.4.2 Carr-Helfrich Mode

This mode is observed at the ac current at frequencies not exceeding the inverse of the space charge relaxation time $\omega_q = 1/\tau_q = 4\pi\sigma/\varepsilon$. When a sine-form electric field is applied to homogeneously oriented fairly conductive nematics with negative dielectric anisotropy, a very regular vortex motion is often observed. In fact, such vortices have a form of long rolls perpendicular to the initial alignment of the director. They are usually called Williams domains [41], see photo in Fig. 11.33b. The instability appears in thin cells (d = 10 – 100 μm) and has a well-defined voltage threshold independent of thickness. Upon illumination, the rolls behave like lenses: they form a diffraction grating and focus light onto the screen, Fig. 11.34.

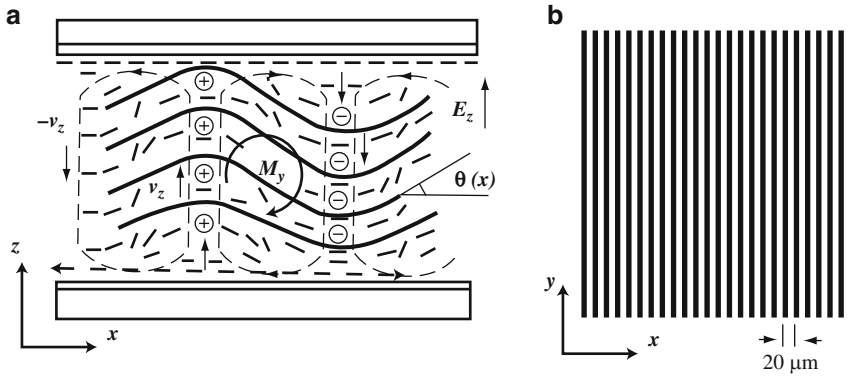

Fig. 11.33 Carr-Helfrich EHD instability in nematic liquid crystals: (**a**) onset of the instability showing a competition of the elastic and hydrodynamic torques; (**b**) photo of Williams domains observed at a voltage 7.5 V in a 20 μm thick cell filled with liquid crystal MBBA

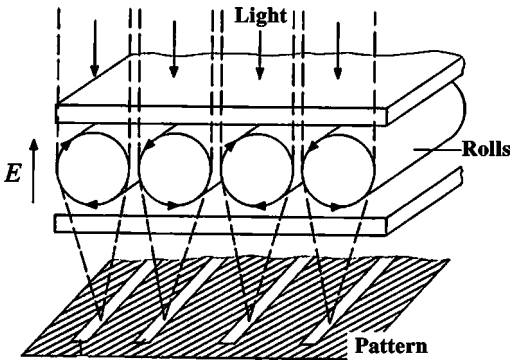

Fig. 11.34 Roll-type vortex motion of a liquid crystal and the pattern of black and white stripes in the screen plane due to diffraction on the roll structure

11.4.2.1 The Instability Threshold in the Simplest Model

The physical mechanism of the instability is related to several coupled phenomena discussed by Helfrich [42]. His elegant calculation of the instability threshold is reproduced here for the simplest steady state one-dimensional model shown in Fig. 11.33a. A homogeneously aligned nematic liquid crystal layer of thickness d is stabilised by the rubbed surfaces of the limiting glasses. The dielectric torque is considered negligible ($\varepsilon_a = 0$). At first, a small director fluctuation $\vartheta(x)$ with a period $w_x \approx d$ is postulated:

$$\vartheta(x) = \vartheta_m \cos\frac{\pi x}{w_x} \tag{11.85}$$

With the field applied, this fluctuation causes a slight periodic deflection of the electric current lines along the director proportional to the anisotropy of conductivity $\sigma_a = \sigma_{||} - \sigma_\perp > 0$. This creates the x-component of the current that, in turn, results in the accumulation of a space charge $Q(x)$ close to the points where angle $\vartheta = 0$. Therefore, the x-component of the field (E_x) emerges. The electric current density is $J_i = \sigma_{ij}E_j$ where the tensor of the electric conductivity has a standard form:

$$\sigma_{ij} = \sigma_\perp \delta_{ij} + \sigma_a n_i n_j$$

According to our geometry, $\mathbf{E} = (E_x, 0, E_z)$, $\mathbf{n} = (\cos\vartheta, 0, \sin\vartheta)$ and the conductivity is given by

$$\hat{\sigma}_{xz} = \sigma_\perp \begin{pmatrix} 1 & 0 \\ 0 & 1 \end{pmatrix} + \sigma_a \begin{pmatrix} \cos^2\vartheta & \cos\vartheta \sin\vartheta \\ \cos\vartheta \sin\vartheta & \sin^2\vartheta \end{pmatrix}$$

Then the x-component of the current for small ϑ is given by

$$J_x = \sigma_\perp E_x + \sigma_a E_x \cos^2\vartheta + \sigma_a E_z \sin\vartheta \cos\vartheta \approx \sigma_{||} E_x + \sigma_a E_z \vartheta$$

where the new component of electric field E_x is related to the space charge distribution $Q(x)$ by the Poisson equation:

$$\mathrm{div}\mathbf{E} = \frac{\partial E_x}{\partial x} = \frac{1}{\varepsilon_{||}} 4\pi Q(x) \tag{11.86}$$

and **J** obeys the current conservation law:

$$\mathrm{div}\mathbf{J} = \frac{\partial J_x}{\partial x} = \sigma_{||} \frac{\partial E_x}{\partial x} + \sigma_a E_z \frac{\partial \vartheta}{\partial x} = 0 \tag{11.87}$$

Combining (11.85–11.87), we get the periodic space charge distribution over x:

$$Q(x) = \frac{\sigma_a \varepsilon_{||} E_z \vartheta_m}{4\pi\sigma_{||} w_x} \sin\frac{\pi x}{w_x} \tag{11..88}$$

Due to the space charge and corresponding force $-Q(x)E$ the nematic liquid begins to move with a velocity v_z determined by reduced form of the Navier-Stokes equation (7.16):

$$\eta \frac{\partial^2 v_z}{\partial x^2} = -Q(x)E_z \tag{11.89}$$

where $\eta = (1/2)\ (\alpha_4 + \alpha_5 \_ \alpha_2)$ is a combination of Leslie's viscosity coefficients α_i.

At a certain critical voltage the destabilising shear-induced torque $M_y = \alpha_2(\partial v_z/\partial x)$, which comes from the interaction of a field driven charged volume of a liquid with the director, becomes large enough to equalise the stabilising elastic torque. This balance of the elastic and hydrodynamic torques is the condition for the onset of instability:

$$K_{33} \frac{\partial^2 \vartheta}{\partial x^2} = \alpha_2 \frac{\partial v_z}{\partial x} \tag{11.90}$$

Integrating once Eq. (11.89) on account of (11.88) we obtain the shear rate

$$\frac{\partial v_z}{\partial x} = \frac{E_z^2 \sigma_a \varepsilon_{||} \vartheta_m}{4\pi\eta\sigma_{||}} \cos\frac{\pi x}{w_x} \tag{11.91}$$

and finally, combining (11.90) and (11.91) and using Eq. (11.85), we have an equation for ϑ equivalent to (11.52). It solution results in the threshold voltage for the instability:

$$U_{crit} = E_{crit} d = \left[\frac{4\pi^3 K_{33}\sigma_{||}\eta}{(-\alpha_2)\varepsilon_{||}\sigma_a}\right]^{1/2} \cdot \frac{d}{w_x} \tag{11.91}$$

Above the threshold a periodic pattern of vortices forms with a period of $w_x \approx d$ along the x-axis. The entire process is governed by the anisotropy σ_a in the

denominator. The threshold is diverged when anisotropy σ_a vanishes, e.g., in nematics with a short-range smectic order close to the N-SmA phase transition. The threshold is proportional to the ratio η/α_2 of the two viscosities. Roughly speaking, they are proportional to each other, thus the threshold weakly depends on viscosity and the instability may easily be observed in very viscous, e.g., polymer liquid crystals. The reason is a compensation for the two effects: on the one hand, in very viscous media the velocity of vortex motion is low (low η) but, on the other hand, the coupling between the flow and the director is strong (high α_2). A more precise expression for the threshold voltage derived by Helfrich [42] includes also a finite value of dielectric anisotropy. The dependencies predicted by the simplest theory have been confirmed qualitatively by many experiments [7].

Going back to Fig. 11.33a we may see that, for the same structure of the director fluctuation $\vartheta(z)$, when the field direction changes sign, the space charge sign is also reversed. However, their product (the electric force $Q(x)E$) keeps its direction. It means that the Carr-Helfrich instability may be observed at the ac voltage. Indeed, in experiment the instability is observed up to the frequency $\omega_q = 4\pi\sigma_{\parallel}/\varepsilon_{\parallel}$ correspondent to the space charge oscillation along the x-axis. The theory of the ac regime of the same instability requires the consideration of a set of two coupled linear equations for the space charge $Q(x)$ and curvature $\psi(x) = \partial\vartheta/\partial x$ dependent on time and the problem of the threshold has been solved for frequencies below and above ω_q [43].

11.4.2.2 Behaviour Above the Threshold

At voltages higher than the threshold, the one-dimensional roll structure subsequently transforms in more complex hydrodynamic patterns. One can distinguish the zigzag, fluctuating and other domain structures, which, in turn, are substituted by a turbulent motion of a liquid crystal. To calculate the wavevectors and amplitudes of the distortions a set of nonlinear equations must be solved. More generally, the problem for describing a transition from a regular electrohydrodynamic vortex motion to turbulence is a part of the classical problem concerning the transition from the laminar to turbulent flow of a liquid. Some progress has been achieved in understanding the nonlinear behaviour of nematics in terms of bifurcation mechanisms, phase transitions and dynamic chaos theory [44].

As known from general theory of dissipative dynamic systems, after a finite number of bifurcations the system undergoes to the dynamic chaos. This scenario is also observed in the electrohydrodynamic convective motion. With increasing voltage the velocity of vortices increases rapidly and the periodic flow of a liquid transforms to turbulence. Turbulent motion in nematic liquid crystals results in a highly non-uniform distribution of the director accompanied by very strong, *dynamic scattering of light*, briefly called DSL. The DSL effect have been initially proposed for manufacturing field-controllable shutters and displays, and the seminal paper [45] was the starting point for development of the modern technology of liquid crystal materials and displays.

Reference

1. Yariv, A.: Quantum Electronics, 3rd edn. J. Wiley & Sons, NY (1989)
2. Born, M., Wolf, E.: Principles of Optics. Pergamon Press, Oxford (1980)
3. de Gennes, P.G., Prost, J.: The Physics of Liquid Crystals, 2nd edn. Clarendon Press, Oxford (1995)
4. Yeh, P., Gu, C.: Optics of liquid crystal Displays. J. Wiley & Sons, NY (1999)
5. Khoo, I.-C., Wu, S.-T.: Optics and Nonlinear Optics of Liquid Crystals. World Scientific, Singapore (1993)
6. Mauguin, C.: Sur les cristaux liquides de Lehman. Bull. Soc. Fr. Miner. **34**, 71–117 (1911)
7. Blinov, L.M.: Electro-Optical and Magneto-Optical Properties of Liquid Crystals. J. Wiley & Sons, Chichester (1983)
8. Yech, P.: Optical Waves in Layered Media. Appl. Opt. Wiley, New York (1988).
9. Landau, L.D., Lifshits, E.M.: Electrodynamics of Continuous Media. Nauka, Moscow (1982) (in Russian). (see also Electrodynamics of Continuous Media. Pergamon, London (1960))
10. Aver'yanov, E.M.: Effects of Local Field in Optics of Liquid Crystals. Nauka, Novosibirsk (1999) (in Russian)
11. Chatelain, P.: Sur la diffusion, par les cristaux liquides du type nematique, de la lumier polarisee. Act. Cryst. **1**, 315–323 (1948)
12. De Gennes, P.G.: Fluctuations d'orientation et diffusion Rayleigh dans un cristal nématique. C. R. Acad. Sci. Paris **266**, 15–17 (1968)
13. Groupe d'Etude des Cristaux Liquides: Dynamics of fluctuations in nematic liquid crystals. J. Chem. Phys. **51**, 816–822 (1969)
14. de Gennes, P.G.: Theory of the smectic state of liquid crystals. J. Physique (Paris) 30, Colloq. C4, 65–71 (1969).
15. Freedericksz, V., Repiewa, A.: Theoretisches und Experimentelles zur Frage nach der Natur der anisotropen Flüssigkaiten. Zs. Physik **42**, 532–546 (1927)
16. Saupe, A.: Die Biegungselastizität der nematischen Phase von Azoxyanisol. Z. Naturforschg. **15a**, 815–822 (1960)
17. Deuling, H.J.: Elasticity of nematic liquid crystals. In: Liebert, L. (ed.) Liquid Crystals, pp. 77–107. (Ehrenreich, H., Seitz, F., Turnbull, D. (eds.) series Solid State Physics). Acad Press, New York (1978).
18. Rapini, A., Papoular, M.: Distorsion d'une lamelle nematique sous champ magnetique conditions d'ancrage aux parois. J. de physique, 30, Colloq C4, 54–56 (1969).
19. Nehring, J., Kmetz, A.R., Scheffer, T.J.: Analysis of weak-boundary-coupling effects in liquid crystal displays. J. Appl. Phys. **47**, 850–857 (1976)
20. Ong, H.L., Meyer, R.B., Hurd, A.J.: Multistable orientation in a nematic liquid crystal cell induced by external field and interfacial interaction. J. Appl. Phys. **55**, 2809–2815 (1984)
21. Brochard, F., Pieranski, P., Guyon, E.: Dynamics of the orientation of a nematic-liquid-crystal film in a variable magnetic field. Phys. Rev. Lett. **28**, 1681–1683 (1972)
22. Van Doorn, C.Z.: Transient behaviour of a twisted nematic liquid-crystal layer in an electric field. J. Physics (Paris), 36, Colloq. C1, 261–263 (1975).
23. Schadt, M., Helfrich, W.: Voltage dependent optical activity of a twisted nematic liquid crystals. Appl. Phys. Lett. **18**, 127–128 (1971)
24. Chigrinov, V.G.: Liquid Crystal Devices: Physics and Applications. Artech House, Boston (1999)
25. Meyer, R.B.: Piezoelectric effect in liquid crystals. Phys. Rev. Lett. **22**, 917–921 (1969)
26. Prost, J., Marcerou, J.P.: On the macroscopic interpretation of flexoelectricity. J. de physique **38**, 315–324 (1977)
27. Prost, J., Pershan, P.S.: Flexoelectricity in nematic and smectic-A liquid crystals. J. Appl. Phys. **47**, 2298–2313 (1976)
28. Blinov, L.M., Barnik, M.I., Ohoka, H., Ozaki, M., Shtykov, N.M., Yoshino, K.: Surface and Flexoelectric Polarization in a Nematic Liquid Crystal 5CB. Eur. J. Phys. E **4**, 183–192 (2001)

29. Harden, J., Mbanga, B., Éber, N., Fodor-Csorba, K., Sprunt, S., Gleeson, J.T., Jákly, A.: Giant flexoelectricity of bent-core nematic liquid crystals. Phys. Rev. Lett. 97, 157802(1–4) (2006).
30. Schmidt, D., Schadt, M., Helfrich, W.: Liquid crystalline curvature electricity: the bending mode of MBBA. Z. Naturforsch. **27a**, 277–280 (1972)
31. Derzhanski, A., Petrov, A.G., Mitov, M.D.: One-dimensional dielectric-flexoelectric deformations in nematic layers. J. physique (Paris) **39**, 273–285 (1978)
32. Derzhanski, A., Petrov, A.G.: Flexoelectricity in nematic liquid crystals. Acta Phys. Polonica **A55**, 747–767 (1979)
33. Blinov, L.M., Durand, G., Yablonsky, S.V.: Curvature oscillations and linear electro-optical effect in a surface layer of a nematic liquid crystal. J. Phys. II France **2**, 1287–1297 (1992)
34. Barnik, M.I., Blinov, L.M., Trufanov, A.N., Umansky, B.A.: Flexoelectric domains in liquid crystals. J. Physique (Paris) **39**, 417–422 (1978)
35. Bobylev, YuP, Pikin, S.A.: Threshold piezoelectric instability in liquid crystals. Zh. Exp. Teor. Fiz. **72**, 369–374 (1977)
36. Palto, S.P., Mottram, N.J., Osipov, M.A.: Flexoelectric instability and spontaneous chiral-symmetry breaking in a nematic liquid crystal cell with asymmetric boundary conditions. Phys. Rev. E, 75, 061707(1–8) (2007).
37. Blinov, L.M.: Behavior of liquid crystal in electric and magnetic fields. In: Demus, D., Goodby, J., Gray, G.W., Spiess, H.-W., Vill, V. (eds.) Physical Properties of Liquid Crystals, pp. 375–432. Wiley-VCH, Weinheim (1999).
38. Dubois-Violette, E., Durand, G., Guyon, E., Manneville, P., Pieranski, P.: Instabilities in nematic liquid crystals. In: Liebert, L. (ed.) Liquid Crystals, pp. 147–208. (Ehrenreich, H., Seitz, F., Turnbull, D. (eds.) series Solid State Physics), Academic Press, New-York, (1978).
39. Kramer, L., Pesch, W.: Electrodynamic convection in nematics. In: Dunmur, D., Fukuda, A., Luckhurst, G. (eds.) Physical Properties of Liquid crystals: Nematics, pp. 441–454. INSPEC, London (2001).
40. Carr, E.F., Flint, W.T., Parker, J.H.: Effect of dielectric and conductivity anisotropies on molecular alignment in a liquid crystal. Phys. Rev. **A11**, 1732–1736 (1975)
41. Williams, R.: Domains in liquid crystals. J. Chem. Phys. **39**, 384–388 (1963)
42. Helfrich, W.: Conduction induced alignment in nematic liquid crystals. Basic models and stability consideration. J. Chem. Phys. **51**, 4092–4105 (1969)
43. Dubois-Violette, E., de Gennes, P.G., Parodi, O.: Hydrodynamic instabilities of nematic liquid crystals under a.c. electric field. J. Physique (Paris) **32**, 305–317 (1971)
44. Buka, A., Kramer, L. (eds.): Pattern Formation in Liquid Crystals. Springer, New York (1995)
45. Heilmeier, G., Zanoni, L.A., Barton, L.A.: Dynamic scattering: a new electrooptic effecting certain classes of nematic liquid crystals. Proc. I.E.E.E **56**, 1162–1171 (1968)

Chapter 12
Electro-Optical Effects in Cholesteric Phase

12.1 Cholesteric as One-Dimensional Photonic Crystal

A cholesteric forms a helical structure and its optical properties are characterised by the tensor of dielectric permittivity rotating in space. We are already familiar with the form of the cholesteric tensor (see Section 4.7). It was Oseen [1] who suggested the first quantitative model of the helical cholesteric phase as a periodic medium with local anisotropy and very specific optical properties. First we shall discuss more carefully the *Bragg reflection* from the so-called "cholesteric planes".

12.1.1 Bragg Reflection

12.1.1.1 Experimental Data

The most characteristic features of cholesteric liquid crystals are as follows:

1. There is a strong *rotation of the plane of polarisation* of linearly polarised light ($\Psi \approx$ 10–100 full revolutions per mm to be compared, e.g., with 24°/mm in quartz). The sign of the optical rotation changes at a certain wavelength λ_0 of the incident light as shown by curve OR in Fig. 12.1.
2. The regions of rotation with different handedness are not separated by an absorption band as in typical gyrotropic materials. Instead, there is a band of a *selective reflection* of the beam with a particular circular polarization, curve R in Fig. 12.1. The beam with the opposite circular polarization is transmitted without any change, therefore the reflection is negligible and not shown in the plot. Only one band is observed in the wavelength spectrum without higher diffraction orders.
3. The electric vectors of the circularly polarised incident and reflected light are rotated in the same direction when viewed against the wavevectors of each beam. In contrast, upon reflection from a conventional mirror the beam changes the sign of rotation. An example is shown in Fig. 12.2. Note that, in this figure, the circular light handedness is defined not conventionally: for the right circular

L.M. Blinov, *Structure and Properties of Liquid Crystals*,
DOI 10.1007/978-90-481-8829-1_12,

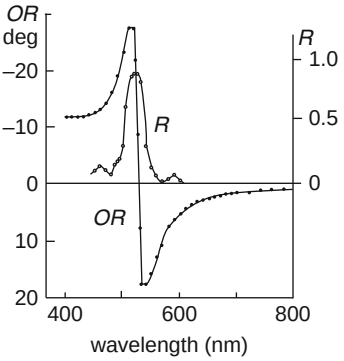

Fig. 12.1 Spectra of optical rotatory power (OR) and selective reflection (R) of a planar cholesteric texture for light propagation parallel to the helical axis.

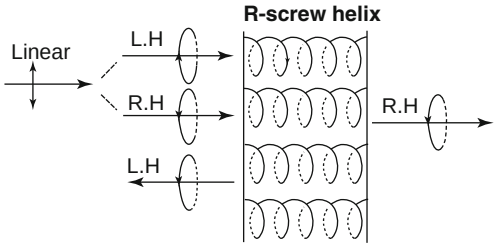

Fig. 12.2 Transmission and reflection of linearly polarized light through the planar cholesteric structure. The linear light is decomposed into two circularly polarized components, left-handed (L. H.) and right handed (R.H). In this particular case, the handedness is defined according to the modern convention, see the text

polarization, the observer looking *at the light source* sees the counterclockwise rotation of the light electric vector. This "new definition" (as discussed in Section 11.1.1) is used here deliberately because I may suggest a *mnemonic rule:* a right-hand circular beam goes as easily (i.e. transmitted) through the right-hand helix as a right-hand screw goes into a right-hand female screw. And this may be explained as follows: the right-hand circularly polarized light going along the right helix does not see periodicity of the helix and, therefore, does not diffract. In the figure we see the right-screw helical cholesteric structure that transmit the right-hand (R.H.) circularly polarised light and completely reflects the left circular polarized light (L.H.) without change of its handedness. By the way, direct modelling of the light transmission or reflection results in exactly that situation, which corresponds to the non-conventional case. Nevertheless, further on we follow the old convention.

4. The wavelength of selected reflection λ_0 (in vacuum) depends on the angle of light incidence i measured from the layer normal, namely, $\lambda_0 = 2(P_0/2) <n> \cos i$. It is the same *Bragg condition* discussed in Section 5.2.2, $\lambda_0 = 2d\sin\Theta$. However, in the case of the X-ray diffraction on a stack of the layers in vacuum, we used refraction index $n = 1$, sliding angle $\Theta = (\pi/2) - i$, and interlayer

distance d instead of *half-pitch* $P_0/2$. The factor ½ appeared in a cholesteric because, due to the head-to-tail symmetry $\mathbf{n} = -\mathbf{n}$, the period of its optical properties is doubled.

We see that the optical properties of cholesterics are quite peculiar. How to explain them on the quantitative basis?

12.1.1.2 The Simplest Model

Consider the optical properties of a cholesteric helix shown in Fig. 12.3a under the following assumptions:

1. The light propagates along the helical axis z, and the helix is regarded as ideal, corresponding to the sinusoidal form for the variation of the director.
2. The semi-infinite structure is assumed, bordered at the front plane by a dielectric of the same refractive index as the average refractive index of the cholesteric $<n>$. In such a case, we neglect the reflection from the front boundary.
3. The optical anisotropy is small, i.e. $n_{\parallel} \approx n_{\perp} \approx <n>$ and $\Delta n = n_{\parallel}\text{-}n_{\perp} \ll <n>$.
4. The wavevectors of the incident light and the cholesteric helix have the same amplitude, $k_i = q_0$.

Now we would like to understand why only one diffraction maximum is observed in the normal reflection from the cholesteric helix and why the reflected light is circularly polarized. Therefore, at first, we write the Bragg condition on account of possible higher diffraction orders:

$$m\lambda_0 = P_0 <n> \cos i \tag{12.1}$$

where m is the order of diffraction (i.e. reflection). By analogy with crystals, the values of $m = 2, 3\ldots$ seem to allow the presence of higher order reflections. However, the latter are not observed in experiment on the cholesteric structure for the normal incidence of light ($i = 0$). This is a result of some selection rules: the reflections with $m = 2, 3,..$ are forbidden due to a specific form of the dielectric permittivity tensor of a cholesteric.

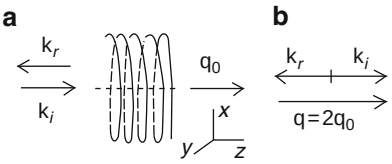

Fig. 12.3 The geometry for discussion of the Bragg diffraction in a cholesteric (**a**) and illustration of the wavevector conservation law (**b**). $\mathbf{k}_i$ and $\mathbf{k}_r$ are wavevectors of the incident and reflected beams, $\mathbf{q}_0$ is the helix wavevector

To show this, it is necessary to insert the Fourier components $\varepsilon(\mathbf{q})$ of the dielectric permittivity tensor $\hat{\varepsilon}(q)$ of the cholesteric into the general formula for the scattering cross section $\sigma \propto (\mathbf{r} \cdot \hat{\varepsilon}(\mathbf{q}) \cdot \mathbf{f})^2$ as already discussed for nematics in Section 11.1.3. Here $\mathbf{f}$ and $\mathbf{r}$ are polarization vectors for the incident and reflected light, $\mathbf{q}$ is the wavevector of scattering coinciding in this simple geometry with the wavevector of the reflected wave [2].

Tensor $\hat{\varepsilon}(\mathbf{q})$ is Fourier transform of cholesteric tensor $\hat{\varepsilon}(\mathbf{r})$. The latter is obtained from the nematic tensor $\hat{\varepsilon}_N(\mathbf{r})$ using the rotation matix $\hat{R}$ as explained in Section 4.7.3: $\hat{\varepsilon} = \hat{R}\hat{\varepsilon}_N\hat{R}^{-1}$. The rotation matrix and local nematic tensor can be taken in their simplest, "plane" form because now the director has only two non-zero components ($n_x = \sin\phi(z)$, $n_y = \cos\phi(z)$, $n_z = 0$), and in our geometry only components of the optical field E_x and E_y are of interest. Therefore

$$\begin{aligned}\hat{\varepsilon}(z) &= \begin{bmatrix}\cos q_0 z & -\sin q_0 z\\ \sin q_0 z & \cos q_0 z\end{bmatrix}\cdot\begin{bmatrix}\varepsilon_{||} & 0\\ 0 & \varepsilon_{\perp}\end{bmatrix}\cdot\begin{bmatrix}\cos q_0 z & \sin q_0 z\\ -\sin q_0 z & \cos q_0 z\end{bmatrix}\\ &= \begin{bmatrix}<\varepsilon_{2D}> + \frac{\varepsilon_a}{2}\cos 2q_0 z & \frac{\varepsilon_a}{2}\sin 2q_0 z\\ \frac{\varepsilon_a}{2}\sin 2q_0 z & <\varepsilon_{2D}> - \frac{\varepsilon_a}{2}\cos 2q_0 z\end{bmatrix}\\ &= \langle\varepsilon_{2D}\rangle\begin{bmatrix}1 & 0\\ 0 & 1\end{bmatrix} + \frac{\varepsilon_a}{2}\begin{bmatrix}\cos 2q_0 z & \sin 2q_0 z\\ \sin 2q_0 z & -\cos 2q_0 z\end{bmatrix}\end{aligned} \tag{12.2}$$

Here we introduced $\varepsilon_a = \varepsilon_{||} - \varepsilon_{\perp}$, a two-dimensional average $\langle\varepsilon_{2D}\rangle = \frac{1}{2}(\varepsilon_{||} + \varepsilon_{\perp})$ and also used the expression $\cos^2\alpha = (1/2)(1 + \cos 2\alpha)$. Note that the wavevector of a cholesteric $q_0 = 2\pi/P_0 > 0$ (right-handed helix). Left-handed helix is described by $q_0 < 0$.

As an example, we can apply the Fourier transform to a single component $\varepsilon_{xx}(z)$ from tensor (12.2):

$$\varepsilon_{xx}(\mathbf{q}) = (\varepsilon_a/2)\int_V \cos(2q_0 z)\exp(iqz)dz \tag{12.3}$$

Here, scattering vector $\mathbf{q} = \mathbf{k}_i - \mathbf{k}_r$ and the integral can only be non-zero (equal to ½) if $q \pm 2q_0 = 0$. Since $\mathbf{k}_i = \mathbf{q}_0$ we have two possibilities: either $|\mathbf{k}_r| = q_0 + 2q_0 = 3q_0$ or $|\mathbf{k}_r| = q_0 - 2q_0 = -q_0$. Only the second case satisfies the *conservation of energy* i.e. frequency $\omega = c|\mathbf{k}_r|/n = cq_0/n$. Therefore, our scattering vector is $\mathbf{q} = 2\mathbf{q}_0$ as shown in Fig.12.3b.

For $q = 4q_0$ $(m = 2)$ the integral is zero and the second order reflection is absent (the same is true for all integers $m \geq 2$). Thus, only the first order reflection with $q = +2q_0$ is possible and $\varepsilon_{xx}(2q_0) = \varepsilon_a V/4$.

From the structure of tensor $\hat{\varepsilon}$ (12.2) it is seen that $\varepsilon_{yy} = -\varepsilon_{xx}$ and $\varepsilon_{xy} = \varepsilon_{yx}$. The latter two are imaginary due to the Euler expansion of $\sin(2q_0 z)$. Therefore, for the anisotropic part of the $\hat{\varepsilon}(\mathbf{q})$tensor in the wavevector space, we may write an expression

$$\hat{\varepsilon}(\mathbf{q}) = \hat{\varepsilon}(2q_0) = \tfrac{1}{4}\varepsilon_a V\hat{M}$$

where

$$\widehat{M} = \begin{pmatrix} 1 & i \\ i & -1 \end{pmatrix}$$

and V is the sample volume. This form allows us to find the polarisation of the reflected beam $\mathbf{r}$. Indeed, the polarization vector of the reflected beam is given by

$$\mathbf{r} = \begin{pmatrix} r_x \\ r_y \end{pmatrix} = \widehat{M} \cdot \begin{pmatrix} f_x \\ f_y \end{pmatrix} = \begin{pmatrix} f_x + if_y \\ if_x - f_y \end{pmatrix} = (f_x + if_y)\mathbf{i} + (if_x - f_y)\mathbf{j} = r_x\mathbf{i} + r_y\mathbf{j} \tag{12.4}$$

From Eq. (12.4) we see that $r_y = ir_x$. It means that the reflected light is circularly polarised in agreement with experiment.

Therefore, the simplest model predicts the existence of one maximum of selective reflection centered at the wavelength $\lambda_0 = \langle n \rangle P_0$ and the circular polarisation of the reflected beam. However, the spectral dependence of the selective reflection and the magnitude of the angle of the light polarisation rotation by the cholesteric structure can only be discussed by analysing the Maxwell equations for the optical waves propagating in the periodic medium.

12.1.2 Waves in Layered Medium and Photonic Crystals

There are several examples of waves in periodic media:

1. Electron or neutron waves (Ψ-functions) in crystals
2. X-ray (electromagnetic) waves in crystals
3. Light waves in the natural media such as opal, mother-of-pearl, beetle shells, etc.
4. Light waves interacting with artificial diffraction gratings, one or two dimensional and three dimensional *photonic bandgap crystals*, in particular, artificial opals
5. Acoustic waves between periodically arranged columns in a theatre

A common feature of all these media is a spatial periodicity with a period comparable to that of the external wave of any sort. In the three dimensional case, the diffraction may result in light localisation and trapping like electrons may be completely localised in a disordered metal (metal–insulator transition).

12.1.2.1 Hill and Mathieu Equations

Theoretically one should solve a wave equation with dielectric permittivity periodic in one, two or three dimensions but, for simplicity, consider a medium with periodic

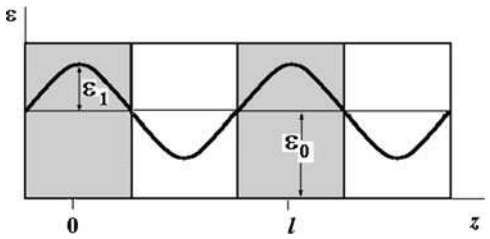

Fig. 12.4 Periodic medium with modulation of scalar dielectric permittivity

modulation of dielectric permittivity in one direction, Fig. 12.4. A wave equation for the electric field in the one-dimensional case is called Hill equation [3]:

$$\frac{d^2E}{dz^2} + \varepsilon(z)\mu\frac{\omega^2}{c^2}E = 0 \tag{12.5}$$

where $\mu \approx 1$ is magnetic susceptibility. The analysis of the Hill equation is a large area of mathematics. In the simplest case of the cosine (or sine) form of the spatial modulation of the scalar parameter $\varepsilon(z) = \varepsilon_0 + \varepsilon_1 \cos(2\pi z/l)$ shown in the figure, we obtain a standard form of the Mathieu wave equation

$$\frac{d^2E}{dz^2} + (\eta + \gamma\cos^2\xi)E = 0 \tag{12.6}$$

where l is period of the structure, $\xi = \pi z/l$ is the normalised coordinate along the z-axis and dimensionless parameters γ and η are related to the amplitude of the dielectric permittivity modulation ε_1 and the average value of permittivity ε_0 as shown in Fig. 12.4,

$$\gamma = \left(\frac{\omega l}{\pi c}\right)^2 \varepsilon_1$$

and

$$\eta = \left(\frac{\omega l}{\pi c}\right)^2 (\varepsilon_0 - \varepsilon_1).$$

The general solution of Eq. (12.6) is given by the *Floquet-Bloch theorem* as a sum of products of a spatially periodic amplitudes $A(\xi)$ and $B(\xi)$ with oscillating exponential functions

$$E(\xi) = D_1 A(\xi)\exp i\beta\xi + D_2 B(\xi)\exp(-i\beta\xi) \tag{12.7}$$

where D_1 and D_2 are arbitrary constants. The solution describes two waves with dimensionless wavevectors $\pm\beta = \pm(l/\pi)k = \pm(l/\pi)(\omega\langle n\rangle/c)$ propagating in

opposite directions. Due to periodicity of A and B, the electromagnetic waves can be presented as a discrete sum of infinite numbers of spatial Fourier harmonics

$$E = \sum_{m=-\infty}^{m=+\infty} A_s \exp[i(k + mq_0)z], \tag{12.8}$$

where q_0 is the vector of one-dimensional reciprocal lattice, $q_0 = 2\pi/l$, as discussed in Section 5.3.1. Usually the periodicity of E on the wavevector axis allows one to consider only the waves with wavevectors in the range $-\pi/l \leq k \leq \pi/l$, i.e. in the first *Brillouin zone*.

The Mathieu equation has no analytical solution despite ε is scalar and its solutions can only be found numerically. The crucial parameter is the depth of the ε-modulation.

1. When ε_1 (i.e. γ) is zero we have ordinary Maxwell equation for uniform medium.
2. For very shallow ε-relief, $\varepsilon_1 \ll \varepsilon_0$, γ is small, $\eta > 0$ and the waves are propagating although with velocities depending on the z-coordinate.
3. In the intermediate case $\varepsilon_1 < \varepsilon_0$ and $\gamma \approx \eta$, we observe a photon energy (or frequency) bands either allowed or forbidden for the wave propagation. Therefore, there are some selection rules for the Bragg diffraction of electromagnetic waves on the periodical structure. Here, we see a deep analogy with the Bloch - de Broglie waves in crystals. For this reason we speak of photonic crystals.
4. For a very deep relief, $\varepsilon_1 > \varepsilon_0/2$, $\eta < 0$ and $\gamma > \eta$, the waves cannot propagate at all. In such a structure one may observe only evanescent waves.

From the analysis of the Mathieu equation, we can make the following general conclusions which are useful for further discussion of cholesteric liquid crystals:

1. For a scalar ε there is no general analytical solution even for the one-dimensional problem.
2. The wave characteristics are independent of the wave polarisation.
3. A monochromatic wave is superposition of infinite number of plane waves: one- or two-waves approximations can only be used for waves with $k \ll \pi/l$ (far from the gaps).
4. There exists an infinite number of forbidden zones with the frequency gap $\Delta\omega$ decreasing with increasing the zone number.

12.1.2.2 One Dimensional Photonic Band-Gap Structure (Modelling)

An example of the numerical solution of the Maxwell equations for a one-dimensional photonic crystal is shown in Fig. 12.5a and b. I have modelled a stack of five alternating layers, each with optical thickness of $\lambda/4$: dielectric layers with thickness $d_d = 0.075$ μm and refraction index $n_d = 2$ and air gaps between them with

thickness $d_{\text{air}} = 0.15$ μm and refraction index $n_{air} = 1$. In fact, I have verified the analytical result of a seminal paper [4] using the Palto's software [5] based on the direct numerical solution of the Maxwell equations. In Fig. 12.5a the several band-gap (or stop-bands) for the unpolarised light transmission are seen in the curve marked off by the "stack", which are separated by equal frequency intervals. The width of the stop-bands is determined by the difference of the refraction indices $n_d - n_{air} = 1$: the larger the difference the wider the stop-band. Note that, within the stop band, the transmission of the unpolarized beam completely vanishes.

For the stack considered here $d_d n_d = d_{air} n_{air} = 0.15$ μm $= \lambda/4$ and the position of the first Bragg transmittance minimum ($m = 1$) is expected at $\lambda_B(m = 1) = 2 <n> (d_d + d_{air}) = 2(d_d n_d + d_{air} n_{air}) = 0.6$ μm. It is instructive to compare the results obtained for such a stack with the transmission of a slab of a cholesteric liquid crystal whose Bragg diffraction wavelength is approximately located at the same wavelength λ_B as for the stack stop-band at $m = 1$. The cholesteric slab has the following parameters: the pitch is $P = 0.4$ μm, slab thickness $d = 20$ μm (50 full helical turns), $n_o = 1.5$, $n_e = 1.7$, $<n> = 1.6$, therefore, $\lambda_B = P<n> = 0.64$ μm. The slab is bordered by infinitely thick glasses with refraction index $n_g = 1.5$. We see in Fig. 12.5a that in the cholesteric spectrum marked off by "CLC" there is a stop-band corresponding to $m = 1$ and period $P/2$, as discussed above. Therefore a cholesteric liquid crystal may be regarded as a one-dimensional photonic crystal.

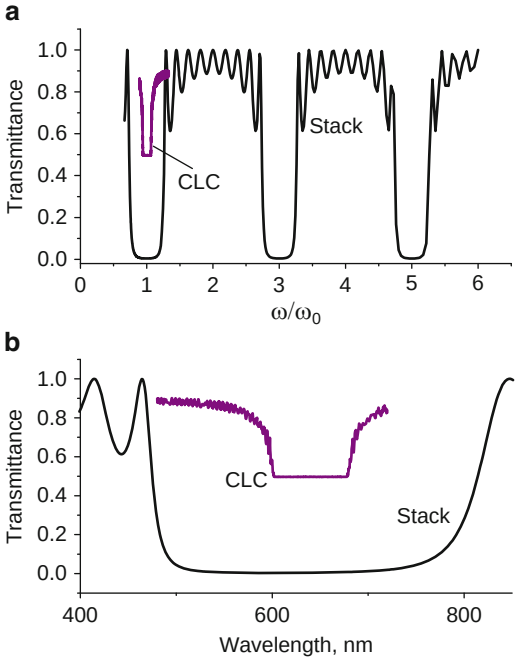

Fig. 12.5 Comparison of the non-polarized light transmission by a stack of dielectric layers and a cholesteric liquid crystal (CLC). The two materials have the same Bragg reflection frequency (numerical calculations, for parameters see the text). (**a**) Transmission spectra on the frequency scale showing the absence of high harmonics in the case of CLC; (**b**) blown transmission spectra at the wavelength scale showing the flat form of the CLC Bragg band and oscillations of transmission at the edges of the band

As discussed in the previous section, indeed, there is only one stop-band in the cholesteric transmission spectrum. This is only valid for the light propagating along the helical axis. The minimum transmission of an unpolarized light is 0.5, because one circular polarization is totally reflected. As in the case of a stack, the width of the band is determined by the difference $\Delta n = n_e - n_o$. In the case of our cholesteric, $\Delta n = 0.2$, that is much less than for the virtual stack modeled and, for this reason, in Fig. 12.5 the cholesteric spectrum is much narrower than the stack spectrum. However, anisotropy $\Delta n = 0.2$ is quite large for both liquid crystals and real stacks made of alternating dielectric films. The structure of the cholesteric stop-band on the wavelength scale is well seen in Fig. 12.5b: there is a wide plateau between the two wavelengths corresponding to $\lambda_o = Pn_o$ and $\lambda_e = Pn_e$. A number of fringes on both sides of the stop-band increases with increasing slab thickness and their amplitude is determined by the reflection coefficient between the cholesteric and surrounding media. In our case, the fringes are not well seen because the surrounding glasses have refraction index close to the average index of the cholesteric.

12.1.3 Simple Analytical Solution for Light Incident Parallel to the Helical Axis

Our task is to find the spectrum of eigenmodes propagating along the helical axis of a cholesteric liquid crystal and discuss some consequences of that. It is very rare and even unique case when, despite chirality and anisotropy of a medium, there is an analytical solution found many years ago by *De Vries* [6]. Here, we follow a rather simple and very elegant analytic solution of this problem given by *Kats* [7].

12.1.3.1 Wave Equations

We again consider an electromagnetic wave propagating parallel to the helical axis of an infinite cholesteric medium ($\mathbf{k} \parallel \mathbf{q}_0 \parallel z$) in the geometry corresponding to Fig. 12.3. Therefore non-zero components of the electric field E_x and E_y depend only on z. The Helmholtz wave equation

$$\frac{\partial^2 \mathbf{E}}{\partial z^2} = \frac{1}{c^2}\hat{\varepsilon}\frac{\partial^2 \mathbf{E}}{\partial t^2} \tag{12.9}$$

is written using the dielectric permittivity tensor (12.2) with dimensionless dielectric anisotropy $\delta = (\varepsilon_{\parallel} - \varepsilon_{\perp})/(\varepsilon_{\parallel} + \varepsilon_{\perp}) = \varepsilon_a/2 <\varepsilon_{2D}>$ where $<\varepsilon_{2D}> = (\varepsilon_{\parallel} + \varepsilon_{\perp})/2$

$$\hat{\varepsilon}(z) = \begin{bmatrix} \varepsilon_{xx} & \varepsilon_{xy} \\ \varepsilon_{yx} & \varepsilon_{yy} \end{bmatrix} = \langle \varepsilon_{2D} \rangle \begin{bmatrix} (1 + \delta \cos 2q_0 z) & \delta \sin 2q_0 z \\ \delta \sin 2q_0 z & (1 - \delta \cos 2q_0 z) \end{bmatrix}$$

For the field components we write

$$\frac{\partial^2 E_x}{\partial z^2} = \frac{1}{c^2}\left(\varepsilon_{xx}\frac{\partial^2 E_x}{\partial t^2} + \varepsilon_{xy}\frac{\partial^2 E_y}{\partial t^2}\right) \quad \text{and} \quad \frac{\partial^2 E_y}{\partial z^2} = \frac{1}{c^2}\left(\varepsilon_{yx}\frac{\partial^2 E_x}{\partial t^2} + \varepsilon_{yy}\frac{\partial^2 E_y}{\partial t^2}\right)$$

Using $E_x(z,t) = F_x(z)\exp i\omega t, E_y(z,t) = F_y(z)\exp i\omega t$ we exclude the time dependence and, on account of $k^2 = \omega^2 <\varepsilon_{2D}>/c^2$, obtain the set of equations for the field amplitudes, which contains all optical properties of the cholesteric:

$$\begin{aligned} \frac{\partial^2 F_x}{dz^2} + k^2[F_x + F_x\delta\cos 2q_0 z + F_y\delta\sin 2q_0 z] = 0 \\ \frac{\partial^2 F_y}{dz^2} + k^2[F_y - F_y\delta\cos 2q_0 z + F_x\delta\sin 2q_0 z] = 0 \end{aligned} \tag{12.10}$$

These equations become simpler if one introduces circular field components:

$$E_+ = F_x + iF_y \quad \text{and} \quad E_- = F_x - iF_y \tag{12.11}$$

Then, $F_x = \frac{1}{2}(E_+ + E_-)$ and $F_y = \frac{1}{2i}(E_+ - E_-)$

For the circular components on account of $\exp(\pm i\alpha) = \cos\alpha \pm i\sin\alpha$, Eqs. (12.10) read:

$$\begin{aligned} \frac{\partial^2 F_+}{\partial z^2} + k^2[F_+ + F_-\delta\exp(2iq_0 z)] = 0 \\ \frac{\partial^2 F_-}{\partial z^2} + k^2[F_- + F_+\delta\exp(-2iq_0 z)] = 0 \end{aligned} \tag{12.12}$$

12.1.3.2 Dispersion Relation

Now we shall look for a solution of Eq. (12.12) in a form compatible with the *Floquet-Bloch* theorem:

$$\begin{aligned} F_+ = A_+\exp i(\beta + q_0)z \\ F_- = A_-\exp i(\beta - q_0)z \end{aligned} \tag{12.13}$$

Here β is a wavevector of an electromagnetic wave, which can propagates in our periodic structure (an eigenmode). Equations (12.13) state that, due to periodicity of the medium, the difference in wavevectors of possible modes should be equal to the "lattice vector" of the structure $(\beta + q_0) - (\beta - q_0) = 2q_0$ (remember, that, in a cholesteric, the period of the ε-modulation is $P_0/2$). Substituting F_+ and F_- into Eq. (12.12) we find

$$\begin{aligned}[k^2 - (\beta + q_0)^2]A_+ + \delta k^2 A_- &= 0\\ \delta k^2 A_+ + [k^2 - (\beta - q_0)^2]A_- &= 0.\end{aligned} \tag{12.14}$$

The two equations have a non-trivial solution only if the corresponding determinant $(a_{11}a_{22}–a_{12}a_{21}) = 0$. From this condition we have a biquadratic equation for determination of the wave vector β as a function of k or frequency ω. This is a *dispersion relation*

$$\beta^4 - 2(k^2 + q_0^2)\beta^2 + [(k^2 - q_0^2)^2 - k^4\delta^2] = 0 \tag{12.15}$$

Its solution for the wave vectors of the two propagating modes is given by

$$\beta^2 = k^2 + q_0^2 \pm k\sqrt{4q_0^2 + k^2\delta^2} \tag{12.16}$$

Note that the dispersion relation of the type β(ω) is the key equation for discussion of the spectrum of the photonic band-gap. Indeed the derivative $v_g = d\omega/d\beta$ is nothing else as the group velocity of light in the considered sample. When this derivative tends to zero the velocity decreases and eventually the light does not propagate. We say the light stops. The inverse ratio $d\beta/d\omega$ defines the density of the possible wavevectors $d\beta$ for the unit frequency interval $d\omega$. It is so-called density of optical β-modes (DOM) or density of photonic states (DOS), the concept playing the principal role in calculation of properties of photonic crystals, see, for instance [4,8]. Due to great importance of the dispersion relation, it is useful to present it in a more familiar form of the frequency (i.e., photon energy) depending on wavevector. Since the wavevector of the incident light wave $k = \omega <\varepsilon_{2D}>^{1/2}/c$ is proportional to light frequency, Eq. (12.15) may be rewritten as

$$k^4(1 - \delta^2) - 2k^2(\beta^2 + q_0^2) + (\beta^2 - q_0^2)^2 = 0 \tag{12.17}$$

After substituting the values of β into the field equations (12.13) we find the analytical solution of the original wave equation (12.9). Usually δ is small, about 0.01–01 but it is important for our consideration and cannot be ignored. However, for a moment, consider a limit of infinitely small anisotropy, $\delta \to 0$. Then from Eq. (12.15) we have

$$\beta^2 = k^2 + q_0^2 \pm 2kq_0$$

that is four solutions for β: $\beta_1 = \pm(k + q_0)$ and $\beta_2 = \pm(k - q_0)$. Equivalently, from Eq. (12.17) we get four solutions for k: $k_1 = \pm(\beta + q_0)$ and $k_2 = \pm(\beta - q_0)$. Four solutions mean that, at any frequency ω, we have four circularly polarised eigenwaves shown in Fig. 12.6a. The four waves differ by their polarisation and direction of propagation. The curve numbers in the figure corresponds to the following wavevectors: $-(\beta - q_0)$ (curve 1), $-(\beta + q_0)$ (curve 2), $(\beta - q_0)$ (curve 3) and

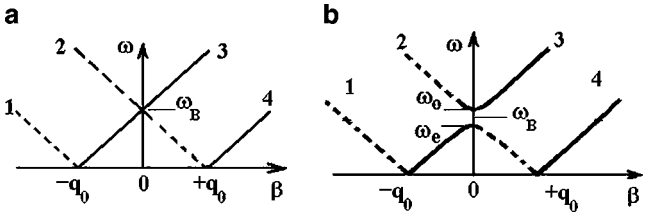

Fig. 12.6 Dispersion relation for a cholesteric that has helical structure with wavevector q_0. The abscissa corresponds to the wavevectors of the eigenmodes propagating in the medium and the ordinate is the frequency of the incident light proportional to its wavevector, $k = \omega\varepsilon^{1/2}/c$. (**a**) Very small optical anisotropy $\delta \to 0$: two pairs of circularly polarized eigenmodes propagate in opposite direction without diffraction and each pair consists of a right- and left polarized beams. Note the absence of a stop-band on the ω-scale at frequency ω_B. (**b**) Finite optical anisotropy δ: modes 2 and 3 propagating in opposite directions suffer diffraction on the periodic structure and a stop-band appears with a frequency gap $\Delta\omega = \omega_o - \omega_e$ centered at Bragg frequency ω_B

$(\beta + q_0)$ (curve 4). The dashed (1, 2) and solid (3, 4) lines correspond to back and forward propagating waves, respectively, because their slopes corresponding to group velocities $d\omega/d\beta$ have different signs. The crossover of lines 2 and 3 at $\beta = 0$ and $k = q_0$ determines the Bragg frequency $\omega_B <\varepsilon_{2D}>^{1/2}/c = q_0 = 2\pi/P_0$.

The situation changes when the optical anisotropy is finite. Consider a particular case of small wavevectors $\beta \approx 0$. Then from Eq. (12.17) we have

$$(k^2 - q_0^2)^2 - k^4\delta^2 = 0 \quad \text{or} \quad k^2 = \frac{q_0^2}{(1 \pm \delta)} \approx q_0^2(1 \mp \delta) \tag{12.18}$$

Since both q_0 and $\delta = \varepsilon_a/2 <\varepsilon_{2D}>$ are fixed material parameters and $k^2 = \omega^2 <\varepsilon_{2D}>/c^2$, the allowed frequency at $\beta = 0$ takes two values

$$\omega_e = cq_0\sqrt{\frac{\varepsilon_{||}}{\langle\varepsilon_{2D}\rangle}} \quad \text{and} \quad \omega_o = cq_0\sqrt{\frac{\varepsilon_{\perp}}{\langle\varepsilon_{2D}\rangle}} \quad \text{with} \quad \sqrt{\varepsilon_{||}} = n_{||}, \sqrt{\varepsilon_{\perp}} = n_{\perp}$$

Between the two frequencies there is *a gap*. Above we have qualitatively discussed an appearance of the forbidden frequency bands. Now, in Fig. 12.6b we see the frequency gap formed by the corresponding dispersion curves. The width of the gap

$$\Delta\omega = cq_0\Delta n/\langle n\rangle \tag{12.19}$$

determines the spectral interval of the Bragg diffraction where only two waves (no. 1 and 4 in the figure) can propagate at any ω. The gap in Fig. 12.6b corresponds to the minimum in the optical transmission at $\lambda_0 = 600$–670nm in Fig. 12.5. The other two waves (nos. 2 and 3) cannot propagate within the gap: due to the diffraction they are completely reflected.

12.1.3.3 Rotation of Linearly Polarised Light

Giant optical rotatory power is observed at wavelengths corresponding to the slopes of the selective reflection curve. In some cases, its magnitude reaches 3°/μm. A sign of rotation changes at some wavelength within the reflection band, see Fig. 12.1. In that figure, the reflection band (stop band for transmission) has no flat top, the band is narrow because the particular cholesteric material has low optical anisotropy $\Delta n \approx 0.01$.

The magnitude of the rotation angle per unit length can be found from the same theory. To this effect, we consider the incident wave whose wavevector is far from the Bragg resonance on both sides of the latter $|k - q_0| \gg q_0\delta$. Then, the dispersion relation (12.16) for propagating waves becomes simpler if we use an expansion $(1 + x)^{1/2} \approx 1 + x/2$:

$$\beta^2 = k^2 + q_0^2 \pm 2q_0 k\sqrt{1 + \frac{k^2\delta^2}{4q_0^2}} \approx (k \pm q_0)^2 + \frac{k^3\delta^2}{4q_0} + \ldots$$

Applying the same expansion for the second time, we find moduli of wavevectors $|\beta_1|$ and $|\beta_2|$:

$$\begin{aligned} |\beta_1| &= (k + q_0) + \frac{k^3\delta^2}{8q_0(k + q_0)} \\ |\beta_2| &= (k - q_0) - \frac{k^3\delta^2}{8q_0(k - q_0)} \end{aligned} \tag{12.20}$$

We can see that there are two modes with wavevectors $\beta_1 - q_0$ and $\beta_2 + q_0$ compatible with dispersion relation (12.16). Further, according to Eqs. (12.14), the field amplitude ratios for the two modes are dramatically different:

$$\frac{A_+}{A_-} = \frac{\delta k^2}{(\beta + q_0)^2 - k^2} \quad \text{and} \quad \frac{(\beta - q_0)^2 - k^2}{\delta k^2} \tag{12.21}$$

Indeed $A_+/A_- \gg 1$ for the first wave and $A_+/A_- \ll 1$ for the second wave.

We see that the two waves are nearly circular and polarised in opposite directions. The optical rotation Ψ of linearly polarised light per unit length is defined as a half of the wavevector difference between the two circular waves with refraction indices $n_1$and n_2

$$\Psi = \psi/d = \Delta k/2$$

Therefore, from Eq. (12.20) we get

$$\Delta k = (|\beta_1| - q_0) - (|\beta_2| + q_0) = \frac{k^3\delta^2}{8q_0(k + q_0)} + \frac{k^3\delta^2}{8q_0(k - q_0)} = \frac{k^4\delta^2}{4q_0(k^2 - q_0^2)} \tag{12.22}$$

Remembering that $k^2 = <\varepsilon_{2D}> (2\pi/\lambda_0)^2$ and $\delta = \varepsilon_a/2\langle\varepsilon_{2D}\rangle = (n_{||}^2 - n_{\perp}^2)/(n_{||}^2 + n_{\perp}^2)$, for the optical rotatory power we finally find

$$\Psi = \frac{k^2\delta^2}{8q_0\left(1 - \lambda_0^2/\lambda_B^2\right)} = \frac{\pi P_0(n_{||}^2 - n_{\perp}^2)}{8\lambda_0^2(n_{||}^2 + n_{\perp}^2)\left(1 - \lambda_0^2/\lambda_B^2\right)} \tag{12.23}$$

Here λ_0 is the wavelength of the linearly polarised incident light (in vacuum) and $\lambda_B = = P_0 <\varepsilon_{2D}>^{1/2}$ is the wavelength of the Bragg reflection maximum. In this approximation, the value of ψ diverges at $\lambda_0 \to \lambda_B$, however, the formula describes both the spectral shape and the magnitude of the optical rotation on both sides of the Bragg reflection maximum (except the top of the reflection band) in agreement with experimental data shown in Fig. 12.1.

12.1.3.4 Waveguide Regime

This case corresponds to a large pitch of a cholesteric with respect to the wavelength $P_0 \gg \lambda_0$ that is a small wavevector of the helical structure and rather high frequency of the incident light satisfying a condition of $k\delta \gg q_0$. Then, from Eq. (12.16)

$$\beta^2 = k^2 + q_0^2 \pm k^2\delta \approx k^2 \pm k^2\delta$$

and, according to Eqs. (12.14) for $q_0 \to 0$ the ratio $A_+/A_- = k^2\delta/\pm k^2\delta = \pm 1$. This corresponds to the linearly polarised waves with polarisation vector rotating in space following the helical structure. We meet such a *waveguide (or Mauguin) regime* [9] in cholesterics with very long pitch, $\lambda_0 \ll P_0(n_{||} - n_{\perp})$ and also in the case of the twisted nematic cell, already discussed in Section 11.1.1.

12.1.4 Other Important Cases

12.1.4.1 Cholesteric Slab of Finite Thickness

In thin cells there is an additional effect of the interference from the parallel boundaries resulting in the spectral oscillations observed on both sides of the Bragg maximum. Such fringes are well seen in Fig. 12.7, the corresponding numerical calculations being made for the cholesteric slab of thickness 4 μm. Of course, in this case, the theory is more difficult [3].

12.1.4.2 Oblique Incidence of Light

When light impinges on a cholesteric at some angle *i* with respect to the helical axis, the following new features should be mentioned:

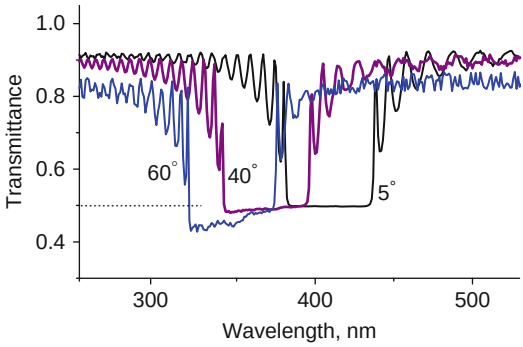

Fig. 12.7 Calculated transmission spectra of a cholesteric for non-polarized light and different angles of incoming light incidence: 5°, 45° and 60° with respect to the helical axis. Both materials have helical pitch 0.25 μm, refraction indices $n_{\parallel} = 1.73$ and $n_{\perp} = 1.51$, cell thickness 4 μm

1. The spectral maximum of the Bragg reflection λ_{B1} is displaced to the short-wave side with the increase of i, see Fig. 12.7.
2. An infinite number of reflections of higher orders emerge. The correspondent minima of the transmission λ_{B2}, λ_{B3} etc. are not seen in Fig. 12.7 because they are deeply in the UV region. The frequency range of the reflection (energy gap) is reduced with the order of reflection m and the peaks of reflections (or pits of transmission) becomes sharper.
3. Higher orders of reflection have a complicated spectral and angular dependence. There is a fine structure in the form of spectral satellites separated from the main harmonic by a distance dependent on the incidence angle [3].
4. In the applied electric field the high order reflections may appear even for the incident light propagating parallel to the helical axis as discussed in Section 12.2.2.

12.1.4.3 Diffraction and Scattering

Diffraction on the one-dimensional helical structure. Such a structure can be obtained from the initial quasi-planar texture with a small tilt (e.g. in the x-direction) of the helical axis with respect to the cell normal z. A cholesteric should have positive dielectric anisotropy. Then upon application of the strong electric field E_z the helix unwinds. After switching the field off, a one-dimensional helical structure appears with the axis parallel to the cell boundaries. When white light is incident onto that structure as shown in Fig. 4.29a the helix behaves as a diffraction grating and iridescent colours are observed [10]. The spectral positions of the diffraction maxima depend on the light incidence angle as expected from the theory. For a monochromatic light the diffraction spots are located at angles $\pm 2\theta$, which are symmetric with respect to the incident beam direction and satisfy the conditions $q = 2mk_0 \sin \vartheta = q_0 = 4\pi/P_0$. Therefore $P_0 = \lambda_0/m \sin \vartheta$, where λ_0 is light wavelength in air. Note that the refraction index of the medium is not included in the formula. In fact, it appears twice, once in the wavevector conservation law

within the medium and then in the Snell law for the diffracted beam leaving the medium for air. Therefore, n is compensated, at least, for small diffraction angles 2θ. The period of the optical properties in this geometry is close to $P_0/2$ although may depend on cell thickness. The first order diffraction ($m = 1$) is very intense, the highest orders are much weaker (even should absent in the ideal case). By measuring scattering angle 2θ one can find the pitch of the helix.

Scattering by inhomogeneous focal-conic structure. When a white light beam is incident at an angle α on a non-aligned layer of a short-pitch cholesteric liquid crystal the scattered light shows iridescent colours. The reason lies in a light diffraction from randomly oriented cholesteric planes. By averaging variable Bragg conditions a formula has been derived [11] that relates the scattered wavelength to the observation angle β:

$$\lambda = \frac{P_0\langle n\rangle}{m}\cos\left(\tfrac{1}{2}\arccos\frac{\sin\alpha}{\langle n\rangle} + \tfrac{1}{2}\arccos\frac{\sin\beta}{\langle n\rangle}\right) \tag{12.24}$$

With this equation and knowing the angles of incidence α, and of reflection β of monochromatic light, one can also determine the helical pitch of the cholesteric liquid crystal.

When the pitch changes with variation of temperature the colours also change. This phenomenon is used in thermography, a sensitive technique for measurements of the distribution of temperature over various objects, for example, in medicine for making temperature maps of human skin. In technics, cholesterics are used for the estimation of the temperature distribution over plane electronic circuits and other objects with a relatively flat surface.

12.2 Dielectric Instability of Cholesterics

In this chapter we consider the most characteristic phenomena related to the electric field interaction with chiral, quasi-layered structure of cholesteric liquid crystals.

12.2.1 Untwisting of the Cholesteric Helix

12.2.1.1 De Gennes–Meyer Model for Field Induced Cholesteric–Nematic Transition

In the simplest case, this transition is observed in a cholesteric with positive dielectric or diamagnetic anisotropy in the electric or magnetic field applied perpendicular to the helical axis. Let a helix has a pitch P_0 in the absence of a field and the thickness of a sample is much larger than P_0. Therefore, the boundary

conditions can be neglected. Such a model was investigated by Meyer and de Gennes [12,13] for a cholesteric having anisotropy of magnetic susceptibility χ_a and placed in magnetic field **H** perpendicular to the helical axis **h.** Inevitably, in the initial state, in certain parts (A) of the helix, the molecules are arranged favourably relative to the field, but in other parts (B) they are arranged unfavourably, Fig. 12.8a. Due to $\chi_a > 0$, the latter would tend to realign themselves along the field.

With the field applied, regions A will increase in size and regions B decreased. A decrease in the dimensions of the B regions would cost very large elastic energy $K_{22}(\partial\varphi/\partial z)^2$. In a strong field, regions B transforms into thin two-dimensional defects (walls) perpendicular to z with the director turned by angle π across the wall. If a number of regions B were reduced by increasing period (pitch) of the structure, the total elastic energy would be lower. Therefore, our structure becomes unstable: a strong field tries to expel all the walls from the helical structure. As a result of such instability, at a certain critical field H_u, the helical structure transforms into a uniform (nematic) structure. We can say, that there occurs a cholesteric to nematic phase transition with a threshold field H_u.

The threshold field can be calculated thermodynamically by comparison of the free energy of the helical and uniform structures in the presence of the field. In our geometry, the free energy density of a cholesteric in a magnetic field is

$$g_{Ch} = \frac{1}{2}\left[K_{22}\left(\frac{d\varphi}{dz} - q_0\right)^2 - \chi_a H^2 \cos^2\varphi\right] \tag{12.25}$$

where φ is an angle between the field and the director. For the unwound, nematic-like cholesteric, $\partial\varphi/\partial z = 0$, $\varphi = 0$ or π, and the free energy density is given by

$$g_N = \frac{1}{2}\left[K_{22}(-q_0)^2 - \chi_a H^2\right] \tag{12.26}$$

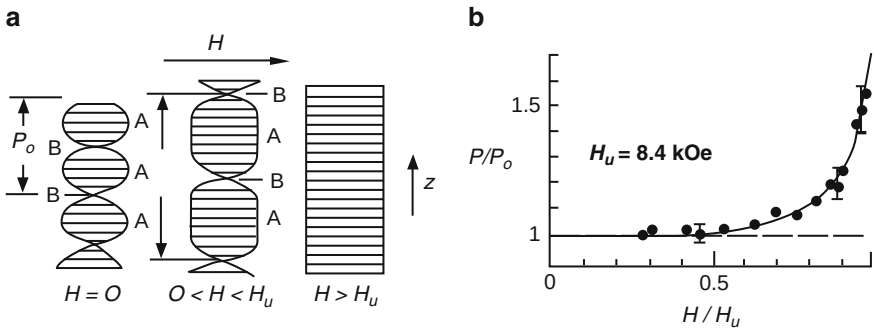

Fig. 12.8 Influence of a magnetic field **H** on the planar cholesteric texture having $\chi_a > 0$. The helical axis is parallel to z. *Horizontal lines* show the projections of the director parallel to **H.** Helix unwinding according to de Gennes (**a**) and Meyer experiment (**b**)

The difference between the two densities (12.25) and (12.26) reads

$$\Delta g = g_{ch} - g_N = \frac{1}{2}\left[K_{22}\left(\frac{d\varphi}{dz} - q_0\right)^2 - K_{22}q_0^2 - \chi_a H^2(\cos^2\varphi - 1)\right]$$
$$= \frac{1}{2}K_{22}\left[\left(\frac{d\varphi}{dz}\right)^2 - 2q_0\frac{d\varphi}{dz}\right] + \frac{1}{2}\chi_a H^2 \sin^2\varphi$$

Introducing the field coherence length $\xi^2 = K_{22}/\chi_a H^2$ and integrating over one period of the helix P_0 along the z-axis we find the free energy

$$\frac{\Delta F}{\chi_a H^2} = \frac{1}{\chi_a H^2}\int_0^{P_0} \Delta g dz = \int_0^{P_0}\left[\frac{1}{2}\xi^2\left(\frac{d\varphi}{dz}\right)^2 - q_0\xi^2\frac{d\varphi}{dz} + \frac{1}{2}\sin^2\varphi\right]dz \qquad (12.27)$$

The Euler equation (8.22) corresponding to the minimal free energy density (12.27) within a period of the structure reads:

$$\xi^2\frac{d^2\varphi}{dz^2} = \sin\varphi\cos\varphi \text{ or } \frac{1}{2}\xi^2\frac{d}{dz}\left(\frac{d\varphi}{dz}\right)^2 = \sin\varphi\cos\varphi\frac{d\varphi}{dz}$$

This equation is easily integrated:

$$\xi^2\left(\frac{d\varphi}{dz}\right)^2 = 2\int_z \sin\varphi\cos\varphi\frac{d\varphi}{dz}dz = 2\int_\varphi \sin\varphi\cos\varphi d\varphi = \sin^2\varphi + C \qquad (12.28)$$

For the particular periodic structure shown in Fig. 12.8a with angle φ counted from the field H direction, the derivative $d\varphi/dz = 0$ at any values of z where $\varphi = 0$ or π (middle points of regions A). Therefore, $C = 0$ and $\xi(d\varphi/dz) = \pm\sin\varphi$, where for the right-handed helix the sign at the right side is either positive (if φ belongs to an interval from 0 to π) or negative (if $\pi < \varphi < 2\pi$). Then, substituting Eq. (12.28) into Eq. (12.27) we find

$$\frac{\Delta F}{\chi_a H^2} = \int_0^{P_0}\xi^2\left[\left(\frac{d\varphi}{dz}\right)^2 - q_0\frac{d\varphi}{dz}\right]dz = \xi^2\int_0^{2\pi}\left(\frac{d\varphi}{dz} - q_0\right)d\varphi$$
$$= 2\xi\int_0^{\pi}\sin\varphi d\varphi - q_0\xi^2\int_0^{2\pi}d\varphi = 2\xi(2 - \pi q_0\xi)$$

Therefore $\Delta F = \dfrac{2K_{22}}{\xi}(2 - \pi q_0\xi)$ and the threshold condition ($\Delta F = 0$) for the helix unwinding reads

$$\xi_u = \frac{2}{\pi q_0} \quad \text{or} \quad H_u = \frac{\pi^2}{P_0}\sqrt{\frac{K_{22}}{\chi_a}}. \tag{12.29}$$

This result is in good agreement with experiment. It tells us that, at $H > H_u$ cholesteric should become uniform. Moreover, for each value of $H < H_u$, de Gennes has estimated a stationary value of the pitch [12]:

$$P(H) = P_0\left[1 + \frac{\chi_a^2 P_0^4}{32(2\pi^4)K_{22}^2}H^4 + \ldots\right] \tag{12.30}$$

The results (12.29) and (12.30) are in very good agreement with experiments made under thermodynamic equilibrium. Figure 12.8b shows the results obtained by R. Meyer [14] on rather a thick cell ($d = 130$ μm) filled with a cholesteric mixture based on *p*-azoxyanisol (PAA). The mixture was not oriented by boundaries and contained a number of defects. Meyer mentioned that, in order to reach the equilibrium state for each value of magnetic field, "the tendency to hysteresis was overcome by cycling the field while observing the cell". This comment is very important, because the hysteresis is a fingerprint of the topological constraints discussed below.

For the electric field, in Eqs. (12.29) and (12.30) we should substitute $\varepsilon_a/4\pi$ for χ_a. Therefore, if we apply magnetic field (or electric field more convenient for practical purposes) to a cholesteric sample for a long enough time, we should change the helical pitch of the sample according to Eq. (12.30). Such a field-induced pitch tuning would be very promising for applicable to fast displays, tunable photonic filters, diffraction gratings and lasers. Unfortunately, pitch tuning may be realized only via an intermediate, very slow stage of the defect formation.

12.2.1.2 Topological Limitation

What is a reason for such a disappointing situation with tuning the helical pitch by electric or magnetic field? It is very simple: despite the fact that field unwinding of the cholesteric helix is thermodynamically profitable there is a strong topological limitation on the unwinding process. It can be understood as follows. In Fig. 12.9 there is a helical structure of the director field **n** (shown by arrows) with vertical helical axis **h**. We assume that the helix is either infinite or limited by two boundaries with infinitely weak azimuthal anchoring at least at one of the boundaries. It means that there is no confinement, which would prevent a free rotation of the non-anchored director at that boundary. Therefore unwinding the helix due, for instance, to a heating process is possible.

Now, imagine that dielectric anisotropy is positive and we apply a certain electric field $\mathbf{E} \perp \mathbf{h}$ to structure (a) with equilibrium pitch P_0 trying to increase the pitch twice, $P_E \rightarrow 2P_0$, as shown in sketch (b). To do this we must turn the director

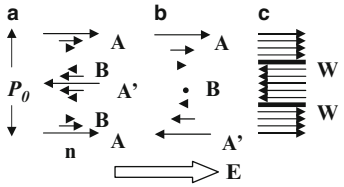

Fig. 12.9 Field behaviour of a cholesteric helix ($\varepsilon_a > 0$). (**a**) Zero-field structure, (**b**) unfavorable structure with a larger field induced pitch, (**c**) favorable wall structure with unchanged pitch

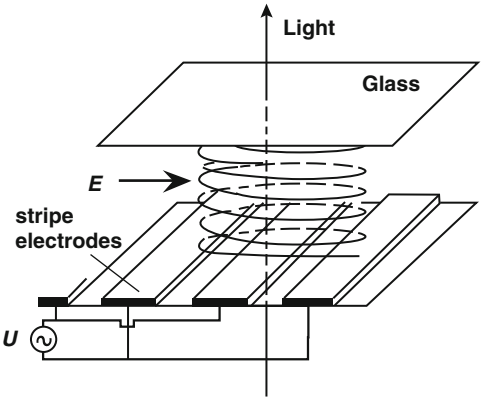

Fig. 12.10 Helical structure of a cholesteric liquid crystal between two glass plates. On the bottom plate, an array of metal interdigitated electrodes is deposited. The array is covered by a polyimide layers and rubbed to align the molecules in the plane of the substrate. The upper glass is also covered by polyimide but not rubbed

from the central favourable position A'($\mathbf{n}\|\mathbf{E}$, $\varepsilon_a > 0$) to the unfavourable position B, where $\mathbf{n}\perp\mathbf{E}$, and this situation takes place within each period. Moreover, the director must make a $\pi/2$-turn against the field to change its initial A position (at the bottom) to new position A'. In other words, the director should overcome a high potential barrier. Therefore, a very serious topological problem exists for the ideal cholesteric helix. In reality, the structure (c) very often forms with favourable orientation of the director everywhere. The positions of the walls W separating areas where $\mathbf{n}$ differs by π are fixed and the energy of the structure (c) with the same initial pitch P_0 is, of course, larger than the more profitable stationary structure with an enhanced pitch.

The numerical modelling with software [5] and experiment [15] confirm this picture. In the experiment, a cell was used pictured in Fig. 12.10. The dielectric anisotropy of the material is $\varepsilon_a = +7.8$ and the electric voltage is applied between the in-plane interdigitated electrodes with a gap 20 μm. In calculations, both the zenithal and azimuthal anchoring strengths at the bottom substrate is strong, $W_{z1} = W_{a1} = 0.1$ erg/cm^2. At the upper substrate the zenithal anchoring energy W_{z2} is also that strong, therefore the director is always confined within the plane of substrates perpendicular to the helical axis. However, the azimuthal anchoring energy at the second substrate is negligibly small $W_{a2} = 0.001$ erg/cm^2 and provides easy rotation (sliding) of the director in the substrate plane.

Figure 12.11 shows the calculated distribution of the azimuthal angle φ for the planar cholesteric structure of thickness $d = 25P_0$, however, only two periods are

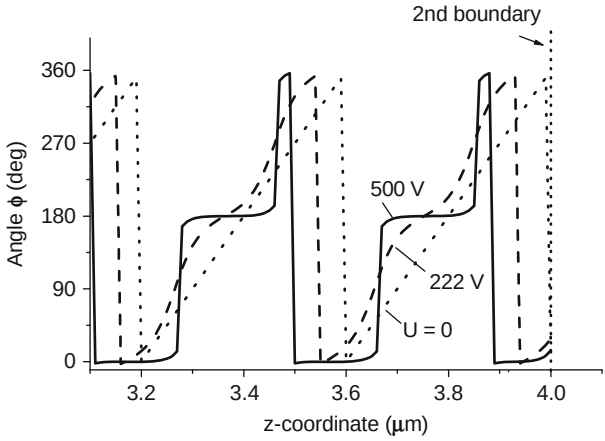

Fig. 12.11 Calculated director azimuth φ for the last two periods of the helix adjacent to the top boundary of the cell (see Fig. 12.10). It repeatedly increases from 0° to 360° within each period P_0. Without field the dependence φ (z) is linear. With increasing voltage the director is progressively reoriented but the period remains unchanged. Cell parameters: thickness $d = 4$ μm, pitch $P_0 = 2.5$ μm, $\varepsilon_a = 7.8$, twist elastic modulus $K_{22} = 9 \times 10^{-7}$ dyn

shown for clarity. It is seen that, with increasing voltage, the director is progressively realigned along the field direction but the period of the distorted helix remains unchanged (some total shift of the curves along the z-coordinate is due to boundary effects). Note that within each period there are horizontal parts of the curves that correspond to very narrow ranges of angle φ. These are field induced defects (walls) having half-pitch periodicity which called π-solitons observed also in SmC* materials (see Section 13.4.2).

The calculated field induced transmission of the same planar cholesteric texture in the non-polarized light is shown in Fig. 12.12. It is clearly seen that, with increasing field, the Bragg minimum is only slightly shifted to *shorter* wavelengths due to a distortion of the helix seen in the previous figure and then disappeared at a field of about 25V/μm. Therefore, in the absence of defects the field cannot increase the period of the helix. An essential increase of the cell thickness does not influence the result. The measurements of the field dependence of the transmission spectra of a cholesteric with the same parameters have confirmed the absence of the red shift of the Bragg minimum [15].

The characteristic field, at which the Bragg band disappears, is considerably higher than the critical field ($E_u = 7$ V/μm) calculated from the thermodynamic approach, see Eq. (12.29). However, the periodic structure with very thin defect walls separating area of opposite director orientation (φ = 0 or π) may still exist but not seen optically. Metastable, non-unwound helical structures are also observed at field strengths $E > E_u$ in experiments with short voltage pulses when the defects have not enough time to form.

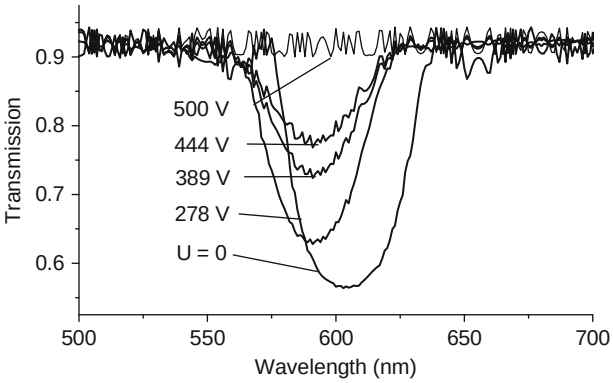

Fig. 12.12 Calculated optical transmission spectra of the planar cholesteric texture as functions of the electric voltage applied (unpolarized light). Principal refraction indices used are $n_{\|} = 1.550$, $n_{\perp} = 1.474$, for other parameters see Fig. 12.11

12.2.2 Field Induced Anharmonicity and Dynamics of the Helix

Let us come back to Fig. 12.11. It is evident that a sufficiently strong electric field perpendicular to the helical axis causes a snake-like picture of the director field with the pitch of the helical structure remaining unchanged. It means that the distribution of the x- and y- components of the director is no longer described by a simple sine law but contains a contribution of higher harmonics. The amplitudes of the field induced harmonics characterize a degree of the field-induced anharmonicity of the helical structure. The higher harmonics of the helix had been observed long ago [16], but only recently understood as very promising issue for applications. Indeed, with an experimental cell of the type shown in Fig. 12.10 one can detect several spectacular effects.

Let us simulate an appearance of the higher harmonics and optical properties of the cholesteric structure with the following parameters typical of chiral materials based on the well-known nematic mixture E7: helical pitch 0.4 μm, elastic modulus $K_{22} = 5 \times 10^{-7}$ dyn (or 5 pN); principal dielectric permittivity values $\varepsilon_{\|} = 20$, $\varepsilon_{\perp} = 8$; refraction indices $n_{\|} = 1.7$, $n_{\perp} = 1.5$. Cell thickness is $d = 10$ μm, zenithal and azimuthal anchoring energies is strong ($W_{z,a} = 0.1$ erg/cm^2) at both boundaries. The electric voltage is applied across the in-plane electrodes separated by a distance of l =20 μm, see Fig. 12.10. The helix is confined by two glasses with refractive index $n_g = 1.5$.

The inset to Fig. 12.13 shows the calculated space dependence of the x-component of the director $n_x(z)$ within one period of the cholesteric structure. The voltage applied to the in-plane electrodes is either 0 or 200 V ($E = 10$ V/μm). As expected, at the field applied, the apices of the curve $n_x(z)$ for $U = 200$ V become very flat. The main plot of Fig. 12.13 represents the Fourier transform of the director component $n_x(q/2\pi)$. In zero field, on the wavevector axis, the helix is represented

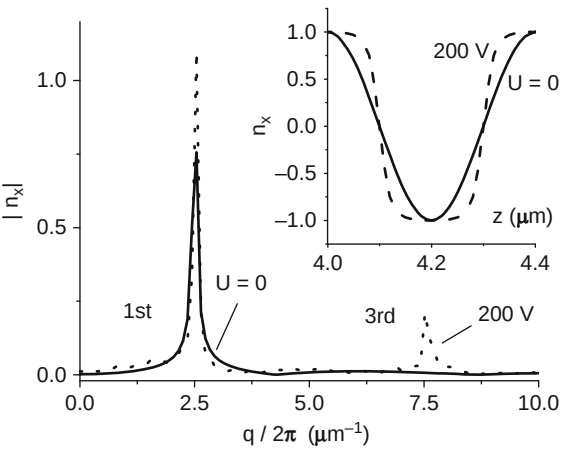

Fig. 12.13 *Inset*: calculated space dependence of the x-component of the director $n_x(z)$ within one period of the cholesteric structure. Main plot: Fourier transform $n_x(q)$ showing appearance of the third harmonic of the helix in a strong field. In both plots *solid lines* correspond to zero voltage, *dot* (or *dash*) *curves* to $U = 200$ V. For parameters see the text

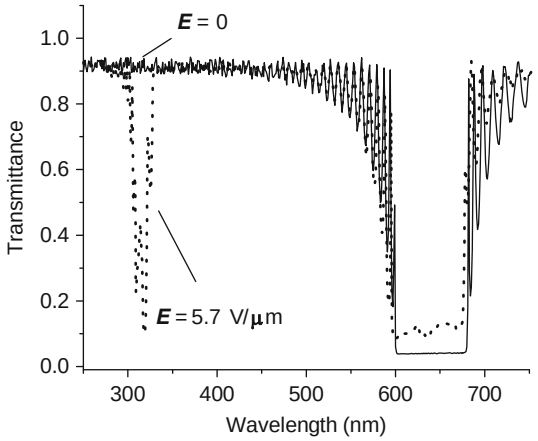

Fig. 12.14 Calculated transmission spectra of a planar cholesteric texture in zero field and in field $E = 5.7$ V/μm applied perpendicular to the helical axis. Note appearance of the strong second order photonic stop-band even for non-polarized light

by a single harmonic at $q/2\pi = q_0/2\pi = 1/P_0 = 2.5\ \mu m^{-1}$. At $U = 200$ V, a strong third harmonic of the distorted helix appears at $q/2\pi = 3q_0/2\pi = 3P_0 = 7.5\ \mu m^{-1}$. The amplitude of the field induced third harmonic reaches the value as high as 27% of the first harmonic amplitude at zero field. Note that characteristic relaxation time of any elastic distortion mode is described by universal (hydrodynamic) formula $\tau = \gamma/Kq^2$, where γ is a rotational viscosity. Therefore, the higher the harmonic of distortion the shorter is its relaxation time. This fact is of *principal importance* for the fast devices based on the helix anharmonicity [15].

Figure 12.14 shows the calculated transmission spectra of a cholesteric mixture in zero field and at $E = 5.7$ V/μm. In this case, the pitch is 0.4 μm and the cell thickness $d = 10$ μm. The incident light is circularly polarised. Upon application of the field, a strong second Bragg reflection band emerges. The transmission is almost

completely suppressed within a narrow spectral band. Within this range, using electric field one can directly modulate light without polarizers.

The appearance of the high harmonics in the director distribution results in considerably faster electro-optical switching. The dynamics of the cholesteric helix in the electric field is described by the balance of viscous, elastic and electric torques in the infinitely thick sample is given by

$$\gamma_1 \frac{\partial \varphi}{\partial t} = K_{22} \frac{\partial^2 \varphi}{\partial z^2} + \frac{\varepsilon_a}{4\pi} E^2 \sin\varphi \cos\varphi \tag{12.31}$$

A low field only slightly changes the angle φ keeping only the first harmonic of the structure with wavevector $2\pi/P_0$. Then, as soon as the field is switched off, the helical structure $\varphi_E(z)$ would relax to the field-off structure according to the same equation (12.31) without the field term. With $\partial\varphi/\partial z \cong q_0$ we find solution

$$\varphi = \varphi_E \sin q_0 z \exp\left(-\frac{K_{22} q_0^2}{\gamma_1} t\right)$$

and the field-free relaxation time

$$\tau_1 = \frac{\gamma_1}{K_{22} q_0^2} \tag{12.32}$$

Note that in contrast to nematics τ_1 is controlled by the helical pitch $P_0 = 2\pi/q_0$ and not by cell thickness d. At a strong field, the distortion involves several harmonics with number m and wavevectors $q_m = 2\pi m/P_0$ and each harmonic relaxes with its own time

$$\tau_m = \frac{\gamma_1}{K_{22} m^2 q_0^2}. \tag{12.33}$$

For instance, the third harmonic of the distorted helix relaxes nine-times faster than the first one and this agrees with experimental data showing submillisecond response times of the cholesteric helix in the external electric field.

It is very spectacular that the electrooptical cell shown in Fig. 12.10 can provide very high and spectrally tunable optical contrast between the field -off and -on states. To this effect, we install the cell between two polarizers and each of them should precisely be oriented at particular angles. Using variable optical anisotropy the spectral band of high contrast may be done either very narrow and tunable (for large Δn) or very wide for white light applications (small Δn).

12.2.3 Instability of the Planar Cholesteric Texture

For unwinding the helical structure, Eq. (12.29) relates the threshold coherence length to a characteristic size of the system, namely, the pitch of the helix $\xi_u = P_0/\pi^2$.

In Chapter 11 we have found that, for the Frederiks transition in nematics, the threshold field coherence length is determined by the cell thickness, $\xi_F = d/\pi$, see Eq.(11.53). Now we shall briefly discuss another type of instability with a threshold determined by the geometrical average of the two parameters mentioned $(P_0 d)^{1/2}$ [17].

Let both the helical axis and the electric field are parallel to the normal z of a cholesteric liquid crystal layer of thickness d and $\varepsilon_a > 0$. In the case of a very weak field the elastic forces tend to preserve the original stack-like arrangement of the cholesteric quasi-layers as shown in Fig. 12.15a. On the contrary, in a very strong field, the dielectric torque causes the local directors to be parallel to the cell normal, as shown in Fig. 12.15c. At intermediate fields, due to competition of the elastic and electric forces an undulation pattern appears pictured in Fig. 12.15b. Such a structure has two wavevectors, one along the z-axis (π/d) and the other along the arbitrary direction x within the xy-plane. The periodicity of the director pattern results in periodicity in the distribution of the refractive index. Hence, a diffraction grating forms. Let us find a threshold field for this instability.

In the absence of the field, the director components are $\mathbf{n} = (\cos q_0 z, \sin q_0 z, 0)$ and $q_0 = \partial\varphi/\partial z$. For a small field perturbation, both the conical distortion appears (angle ϑ) and the azimuthal angle φ slightly changes. The new components of the director are:

$$\begin{aligned} n_x &= \cos(q_0 z + \varphi) \approx \cos q_0 z - \varphi \sin q_0 z \\ n_y &= \sin(q_0 z + \varphi) \approx \sin q_0 z + \varphi \cos q_0 z \\ n_z &= \vartheta \cos q_0 z \end{aligned} \tag{12.34}$$

If we intend to calculate precisely the threshold field for the two-dimensional distortion we should write the Frank free energy with the director components (12.34) and the field term $(\varepsilon_a/4\pi)(\mathbf{En})^2$ and then make minimization of the free energy with respect to the two variables φ and ϑ [18]. For a qualitative estimation of the threshold we prefer to follow the simple arguments by Helfrich [17]. We consider a one-dimensional (in layer plane xy) periodic distortion of a cholesteric

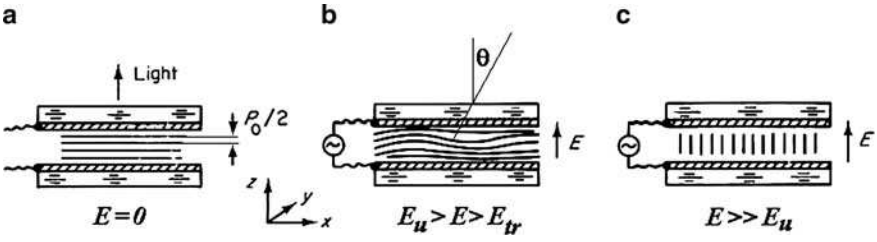

Fig. 12.15 A planar cholesteric structure in the electric field parallel to the helical axis ($\varepsilon_a > 0$). The local director orientation is shown by *solid lines*: field-off planar alignment (**a**), undulated structure in a weak field $E_u > E > E_{th}$ (**b**), and the homeotropic structure in the field exceeding the threshold for helix unwinding $E > E_u$ (*c*)

with helical axis and electric field E parallel to axis z and layer thickness $d \gg P_0$. Further, the deformation is assumed to be sinusoidal along both the x- axis (period equals w) and the z-axis (half-period equals d). Hence, we have two variables: one of them is the x- and z-dependent tilt angle ϑ of the helical axis with respect to the cell normal, see Fig. 12.15b,

$$\theta = -\theta_m \sin(\pi z/d) \sin(2\pi x/w) \tag{12.35a}$$

and the other is x- and z-dependent difference between the wavevectors of the distorted and the equilibrium helix, $\Delta q = q - q_0$ ($q_0 = 2\pi/P_0$):

$$\Delta q = \Delta q_m \cos(\pi z/d) \cos(2\pi x/w) \tag{12.35b}$$

The splay and bend distortions are described by angle ϑ while the twist distortion is related to a slight change of the period of the helical structure. The maximum values of two variables ϑ_m and Δq_m are coupled to each other by equation

$$\theta_m = \frac{2d}{w} \cdot \frac{\Delta q_m}{q_0} \tag{12.36}$$

that can be understood with the help of Fig. 12.15b. Indeed, due to strong anchoring the number of helical turns in the cell is fixed, but for the helical axis tilted through angle ϑ the helical pitch becomes larger ($\approx P_0/\cos\vartheta$) and the wavevector q smaller by Δq_m. In addition, for fixed cell thickness d and q_0, with decreasing period of distortion w, the tilt angle ϑ_m will be larger because the $\sin(2\pi/w)$ function in Eq. (12.35a) becomes sharper. Using Eq. (12.36) we have only one independent variable.

Now we are looking for a difference between the elastic energies of structures (a) and (b) in Fig. 12.15 irrespective of a source of the distortion. For a small distortion and director compounds $n_x = \cos\vartheta \approx 1$, n_y and $n_z = \sin\vartheta \approx \vartheta$ the highest order terms for splay, bend and twist are $\mathrm{div}\mathbf{n} = \partial\vartheta/\partial z$, $\mathbf{n} \times \mathrm{curl}\mathbf{n} = -\partial\vartheta/\partial x$ and $\mathbf{n}\mathrm{curl}\mathbf{n} = -\partial n_y/\partial z = \Delta q_m$. Then, using Eqs. (12.35) we can write the Frank energy density:

$$g_{elast} = \frac{1}{8}\left[K_{11}\left(\frac{\pi}{d}\right)^2 + K_{33}\left(\frac{2\pi}{w}\right)^2\right]\vartheta_m^2 + \frac{1}{4}K_{22}(\Delta q_m)^2$$

Here, the average values of $<\cos^2\vartheta> = <\sin^2\vartheta> = 1/2$ are used. As the cell thickness is assumed to be large, $d \gg w$ Helfrich discarded the splay term and the elastic free energy density is reduced to the form

$$g_{elast} = \frac{1}{8}\left[K_{33}\left(\frac{2\pi}{w}\right)^2\right]\vartheta_m^2 + \frac{1}{4}K_{22}(\Delta q_m)^2. \tag{12.37a}$$

When the electric field applied parallel to the helical axis is used to create the distortion, the electric free energy density is given by:

$$g_E = \frac{(\varepsilon_a/2)E^2}{4\pi}\vartheta_m^2. \tag{12.37b}$$

It includes term $(\varepsilon_\parallel - \varepsilon_\perp)/2$ because in the problem discussed, the torque is controlled by anisotropy $\varepsilon_{\parallel h} - \varepsilon_{\perp h}$ defined with respect to the helical axis as $\varepsilon_{\parallel h} = \varepsilon_\perp$ and $\varepsilon_{\perp h} = (\varepsilon_\parallel + \varepsilon_\perp)/2$ (in addition, small anisotropy $\varepsilon_a \ll <\varepsilon>$ is assumed).

On account of Eqs. (12.36) and (12.37) the total free energy density reads

$$g = \frac{1}{8}\left[K_{33}\left(\frac{2\pi}{w}\right)^2 + 2K_{22}\left(\frac{q_0 w}{2d}\right)^2 - \frac{\varepsilon_a E^2}{4\pi}\right]\vartheta_m^2 \tag{12.38}$$

Now we can find the period of the distortion using minimisation (12.38) with respect to w ($\partial g/\partial w = 0$):

$$w^2 = \left(\frac{2K_{33}}{K_{22}}\right)^{1/2}(P_0 d) \tag{12.39}$$

This period is determined solely by the elastic forces. In fact, the instability with the same period can be caused by other external factors, for example, by a magnetic field or by an electrohydrodynamic process caused by conductivity of the material [19].

Now the threshold field E_{th} for the instability can be found from Eqs. (12.38) and (12.39):

$$E_{th} = 2\pi(K_{22}K_{33})^{1/4}\left(\frac{2\pi}{\varepsilon_a P_0 d}\right)^{1/2} \tag{12.40}$$

We can see that, for our one-dimensional distortion in the xy plane the threshold coherence length $\xi_{th} \propto E_{th}^{-1} \propto \sqrt{P_0 d}$ is determined by the geometrical average of the two characteristic lengths. The numerical coefficients in Eq. (12.40) should not be taken too seriously due to the qualitative nature of our consideration. Nevertheless, in experiment the distortion emerges at the fields higher than the Fredericks transition threshold but lower than the helix unwinding one. As a rule, due to rotational symmetry of the planar cholesteric texture having helical axis along z we observe not a one-dimensional stripe pattern but a two-dimensional grid in the xy plane, see Ref. [19].

12.3 Bistability and Memory

12.3.1 Naive Idea

Let an electro-optical cell based on a liquid crystal, possesses two *optically different* stable configurations having the same equilibrium elastic energy. Then imagine that we can switch the cell between the two states by relatively short low-voltage pulses and keep the structure in either state for an infinitely long time. Such a cell would represent a bistable optical memory device. For instance, it may be a display consuming very little energy from the voltage source because the source is used only during switching. Such displays can also be useful for many applications from small smart cards and electronic books to gigantic advertising tableaux.

The simplest but not the best idea of a bistable structure is shown in Fig. 12.16a. A nematic liquid crystal layer of thickness d is placed between two plates and the directors at the plates are aligned perpendicular to each other with $\varphi_0 = 0$ and $\varphi_d = \pi/2$. Assume the infinitely strong anchoring. Then the nematic is twisted left or right by $+\pi/2$ or $-\pi/2$ and both the twisted structures have the same total energy including the elastic and surface terms. The elastic distortion energy F_d of a structure twisted through angle φ has been calculated in Section 8.3.2:

$$F_d = \frac{K_{22}\varphi^2}{2d} \tag{12.41}$$

This energy is shown by the dashed parabola in Fig. 12.16b. If we release the anchoring condition at the top interface, the nematic would relax to the uniform structure with zero elastic energy. However, due to strong anchoring energy $W_s \gg F_d$, the total free energy of the twisted structure $F = F_d + W_s$ shows two minima almost exactly at the $\pm\pi/2$ twist angles at the horizontal level of $F_d(\pi/2)$. If we realign the director at the top interface by an external force through an angle $\pm\delta\varphi_s$ the surface energy will dramatically increase. Therefore we have two minima on the angular dependence of the total free energy with a barrier between these stable states. We say that the cell is bistable.

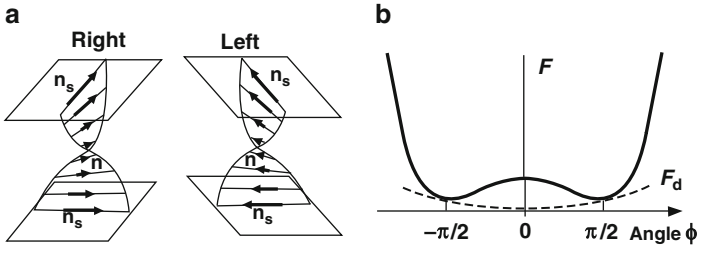

Fig. 12.16 Bistable twist cell. Right- and left-handed twist-structures of a nematic liquid crystal with the same elastic energy (**a**) and the angular dependence of total free energy (**b**)

The two stable twist states have different optical properties. For example, the electric vector of a linearly polarised light is rotated by the two structures in opposite directions. If the Mauguin regime ($d\Delta n > \lambda$) is not strictly fulfilled the two structures can be distinguished using crossed polarizers.

The problem, however, arises with the mechanism of selection of the right and left structures. For example, if a nematic has positive dielectric anisotropy, the applied electric field will align the director into the third, ON- state along the cell normal, from which afterwards, in the absence of the field, it will relax to both twisted stable states with equal probability. Actually a multi-domain structure forms with many defects (walls) between domains. Of course, it is possible to apply an in-plane electric field directed along the angle $\pi/4$. Then, in the middle of the cell, it will be parallel to the director in right-handed domains but perpendicular to the director in the left-handed domains (or *vice versa* for the field angle of $-\pi/4$). Due to this, the right domain will grow at the cost of the left one and finally the overall right-handed twist structure will be restored. However, this process requires a motion of the domain walls and, therefore, is very slow.

12.3.2 Berreman–Heffner Model

12.3.2.1 A Cell and Free Energy

We would like to consider this particular model in more detail because it demonstrates interesting physical aspects of the bistability problem. Generally, chiral nematics better suited to bistable devices as they have an additional degree of freedom. By doping nematics with chiral compounds a variety of materials with variable pitch can be prepared. The principal idea of Berreman and Heffner [20] was to design a cell having two stable textures (states) with low enough energy barrier between them. Then one can switch them by reasonable voltage. It has been found that, using fine tuning the helical pitch to the cell thickness, the barrier becomes especially low when, instead of cholesteric textures with directors parallel or perpendicular to the cell normal z, the other textures were used with the director strongly tilted with respect to z. For this purpose, the director at the transparent electrodes was tilted using evaporation of silicon monoxide from a grazing direction. The zenithal angles of the director about 55° with respect to z were found to be optimal.

In the test cells to be discussed below, the values of the helical pitch and the tunable cell thickness are close to each other (about 28 μm). Therefore, as shown in Fig. 12.17 the full pitch structure ($n = 2$) is the most stable (n means a number of half-pitches). The elastic energy of the two states ($n = 0$ and $n = 2$) is calculated with allowance for the twist, bend and splay distortions. Solid lines in Fig. 12.18 demonstrate dependencies of the elastic energy of the two states on thickness-to-pitch ratio in the absence of an external field. In the figure, the free energy is normalized to the unit cell area and factor d/K_{22}. It is seen that the free energy for

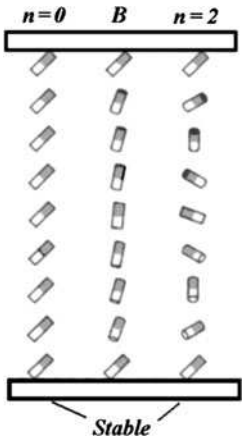

Fig. 12.17 Berreman–Heffner bistable cell. Director configuration of the cell with two stable states (unwound with $n = 0$ and twisted with $n = 2$ half-turns) in the absence of field and the barrier state B in a weak electric field

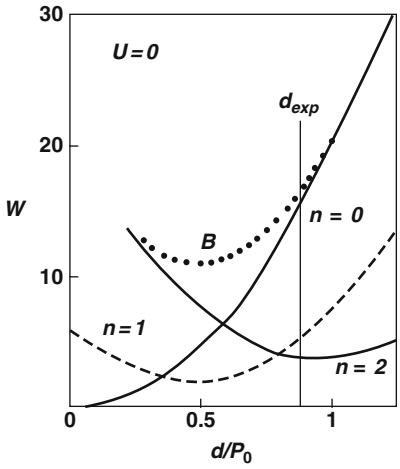

Fig. 12.18 Zero field free energy of the states with different number of half turns n as a function of cell thickness d normalized to pitch P_0. *Solid lines* show the energy of the two stable states to be switched. Low energy ($n = 1$) state is excluded from consideration for topological reasons. B marks the high energy barrier state playing the dominant role in the field-on state

the states ($n = 0$) and ($n = 2$) is equal at the ratio of $d/P_o \approx 0.6$. However, the optimum cell thickness for the bistable operation found from experiment is larger, $d_{exp}/P_o = 0.89$. It is that thickness, at which the energy of both states would reach the barrier state (B) at relatively low voltage. The voltage dependence of the energy for the cell of that particular thickness is shown in Fig. 12.19. Here voltage U is normalized to the Frederiks transition threshold U_0. With increasing U/U_0, the two stable states, indeed, merge at $U/U_0 \approx 1.8$ (cross point). The energy of the barrier state B is also changing and that curve also merges with the other two in point R at $U/U_0 \approx 2$. Point R may be called the *turn point*, from which the system can relax to one of the two states in the absence of voltage.

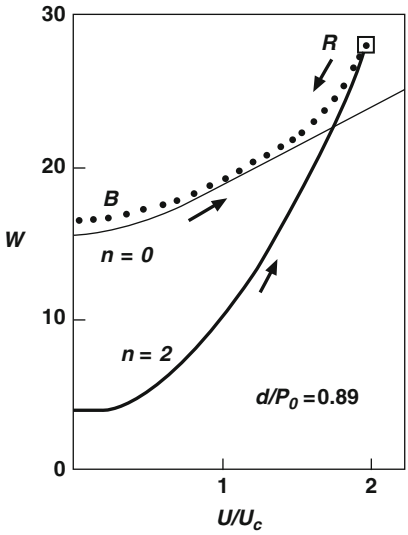

Fig. 12.19 Voltage dependence of the free energy for the uniform ($n = 0$) and twisted ($n = 2$) states. R is the turn point from the barrier state to one of the two stable initial states

12.3.2.2 Backflow and Director Relaxation

But how to force the system relax to a particular state selected by an experimentalist? Berreman and Heffner [20] suggested to exploit the *backflow effect* discussed in Section. 11.2.6. We know that, upon relaxation of the director from the field-ON quasi-homeotropic state (barrier state B) to a field-OFF state, a flow appears within the cell. The direction of the flow depends on the curvature of the director field, which is more pronounced near the electrodes. Moreover it has the opposite sign at the top and bottom electrodes, see the molecules distribution in state B in Fig. 12.17. Due to this, the close-to-electrode flows create a strong torque exerted on the director mostly in the middle of the cell that holds the director to be more or less parallel to the boundaries in favour of the ($n = 2$) initial state in Fig. 12.17.

Therefore, if we switch the field off abruptly, the backflow will bring the system into the twisted ($n = 2$) state. However, if we smoothly reduce the field to zero, the backflow will be negligible and, according to Fig. 12.19, the system will follow curve B (state B) downward and smoothly transform into state ($n = 0$). This selection of the final state has been confirmed experimentally using different forms of the voltage pulse either with the abrupt rear edge or the rear edge consisted of several steps down.

12.3.2.3 Topological Problem and Trap States

Now let us go back to Fig. 12.18 and have a look at the dashed curve ($n = 1$) with the lowest free energy in the field-OFF regime. An interesting question arises why

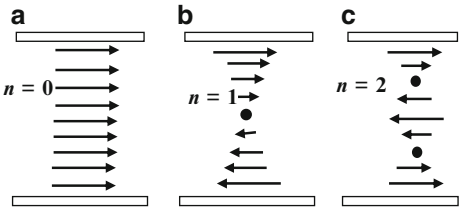

Fig. 12.20 Three planar cholesteric structures with different number of helix half-turns. Structures (**a**) and (**c**) can be transformed into each other by continuous distortion. The central structure (**b**) is topologically incompatible with the other two structures

this state is not used as one of the two stable states. Here we again meet a *topological problem* related to helix untwisting. Consider for clarity a non-tilted that is planar cholesteric texture with infinitely strong anchoring at two boundaries. In Fig. 12.20 we see three possible structures, uniform one ($n = 0$) and two twisted, the π-state ($n = 1$) and the 2π-state ($n = 2$). Note that the direction of arrows at the opposite interfaces are the same in the (a) and (c) sketches but different in the central (b) sketch. Therefore, we can continuously transform structure (a) into (c) and *vice versa*. On the contrary, transformation of the central π-structure ($n = 1$) into either left of right structure is impossible without break of anchoring, for instance, at the bottom boundary. Such a transformation would take much higher energy than the continuous transition.

We meet the same problem in the Berreman–Heffner non-planar cell: the π-structure ($n = 1$) is topologically different from the two stable states. However, despite a high barrier, both the uniform and the 2π states may little by little relax to the "forbidden" lowest energy π-state. This is possible via slow formation of intermediate defect states of the cholesteric structure. This will reduce the lifetimes of both stable states; they become quasi-stable. The topologically forbidden π-state behaves as a trap, and one needs strong voltage pulses to destroy the trap in order to continue the bistable switching. It is a disadvantage of the Berreman–Heffner model.

It would be better not to deal with such a trap state at all. To avoid it, there has been suggested another configuration with the same quasi-stable states, uniform 0-state and twisted 2π-state, but now the ratio $d/P_0 \approx 1$ corresponds to the lowest energy 2π-structure [21]. The system may stay for a long time in either state without trapping and be switched at a low voltage from the beginning. However, now another problem appears: the difference in energy of the 0- and 2π-states is larger than in the previous case. Thus, the reliable selection of a desired memory state using backflow becomes more difficult unless the liquid crystal has high ratio of elastic constants $K_{33}/K_{22} > 3$. Such a material has been designed and the low-voltage bistability demonstrated. In principle, in the bistable devices a dual-frequency addressing regime discussed in Section 7.2.4 should be very efficient. Indeed, using positive ε_a at low frequency, one can easily force the director to reach the uniform homeotropic state. Operating with high frequency and negative ε_a it is

easy to reach the planar 2π-state. However, at present, this technique is not used due to complexity of the corresponding addressing circuits.

12.3.3 Bistability and Field-Induced Break of Anchoring

Using field-induced break of anchoring discussed in Section 11.2.4 one can overcome topological problems [22]. The advantage is that we can design a cell with two long living ground states having very high energy barrier between them. The long-life states are very important in the display technology, because the ratio of the switch-OFF and switch-ON times determines a number of addressed lines of the screen or the so-called multiplexing of the display. Note that in a standard display, switching of each pixel is controlled by a separate thin-film transistor that complicates technology and increases price of the display.

Figure 12.21a and b shows schematically two ground states, the uniform one ($n = 0$) and π-twisted ($n = 1$). As mentioned before the transitions between them are topologically blocked. There is a small but principal difference between this pair of states and the pair of the corresponding states in Fig. 12.20: at the top plate the director is slightly tilted and the anchoring energy is made weak to facilitate the break of anchoring. The optimum thickness-to-pitch ratio is $d/P_o \approx 1/4$. This means that the π/2-twist is the equilibrium state and costs no elastic energy and the elastic energies of the two non-equilibrium stable states (0 and π) are higher and nearly equal. With increasing voltage, at a certain critical value, the two non-equilibrium states merge into one. In the new state, the director is uniformly aligned along the field almost everywhere except at the bottom interface, Fig. 12.21c. When the voltage is reduced the system reaches a bifurcation point, at which two scenarios are possible depending on the rate of the voltage decay: fast decay causes a backflow that drives the system into the π-twisted state ($n = 1$); smooth decay results in the uniform state ($n = 0$).

In principle, topologically blocked states may exist for unlimited time. The main problem is to break anchoring without breakdown of the sample. Anchoring is broken when an electric field coherence length become comparable to a surface extrapolation length. Therefore, a critical voltage U_b necessary for the break of anchoring is proportional to the anchoring energy. The latter should be as low as

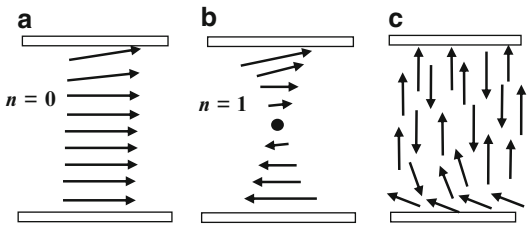

Fig. 12.21 Two long-living topologically stable field-off states (**a**, **b**) and the field induced state (**c**) in a bistable device using the break of anchoring effect

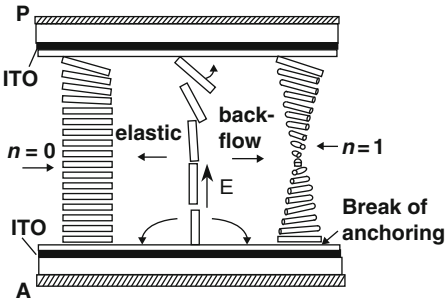

Fig. 12.22 Operation of BiNem® bistable device. Two stable states are the uniform ($n = 0$) and π-twisted ($n = 1$). Anchoring is strong at the top plate and weak at the bottom one. A strong field pulse E breaks anchoring and creates a transient quasi-homeotropic texture. If the rear edge of the pulse is short, the backflow develops and the pulse writes a signal in the form of the π-twisted texture. To erase the signal, a strong pulse with a step-like rear edge creates the same transient state, which relaxes to the uniform stable texture due solely to the elastic force

possible. For instance, to have $U_b \approx 15$ V the zenithal anchoring energy should be as low as 0.2 erg/cm^2. The shape of the voltage pulses is also important because the system behaviour at the bifurcation point depends on the steepness of the rear edge. Figure 12.22 shows the operation principle of the recently described bistable display [23]. In this case the break of anchoring occurs at the bottom electrode where the zenithal anchoring of the director is weak. Beautiful colour images, stable in time and easily switchable have been demonstrated.

12.4 Flexoelectricity in Cholesterics

As has been mentioned in Section 11.3.1, the twist itself does not produce flexoelectric polarization. However, an interesting flexoelectric effect is observed when the twist distortion is combined with the splay-bend distortion [24,25]. In that case, the cholesteric axis $\mathbf{h}_0$ is homogeneously oriented in the plane of the cell along z, see Fig. 12.23a, and an electric field is applied to transparent electrodes of a sandwich cell along the x-axis, $\mathbf{E} \perp \mathbf{h}_0$. The dielectric anisotropy is negative, $\varepsilon_a \leq 0$. In the field-OFF state, the director components are parallel to the xy-plane, $n_x = \cos\varphi$, $n_y = \sin\varphi$ and the conical distortions is absent, see Fig. 12.23 (b) for $E = 0$. If the cell is filled with a short pitch cholesteric $P_0 = 2\pi/q_0$ it behaves like a uniaxial optical plate with the optical axis directed along $\mathbf{h}_0$. When the field is applied, a periodic splay-bend distortion appears due to the flexoelectric torque $M_f = P_f E$ in the surface regions. This distortion has been considered in Section 11.3.2 for nematics. Interacting with the natural twist of the cholesteric, the director leaves the xy-plane as shown in the picture. For the conical distortion the new components of the director are given by

$$n_x = \cos\varphi; n_y = \sin\varphi\cos\Psi; n_z = -\cos\varphi\sin\Psi$$

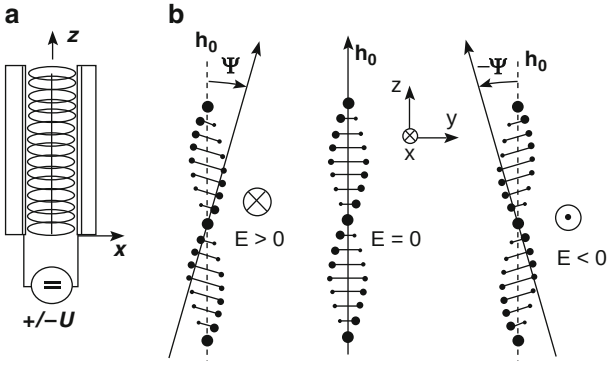

Fig. 12.23 Flexoelectric distortion in a cholesteric liquid crystal. (**a**) The d.c. field from the source U is applied to the cell along the x-axis. (**b**) The field induced director distortion for positive and negative field directed perpendicular to the plane of the figure along the x-axis; it is seen how the cholesteric quasi-layers are tilted though angle Ψ from their field-OFF configuration within the x, y-plane shown in the central sketch

The turn of the director everywhere through angle Ψ is equivalent to the turn of the optical axis about the x-axis through the same angle. The sign and the magnitude of the deviation angle Ψ depend on polarity and strength of the applied field, respectively. It can be estimated as follows.

For weak anchoring and $\varepsilon_a \cong 0$ by analogy with a nematic (see Eq. 10.77), the free energy of the distortion includes the elastic term due to the bend-distortion (we assume $K = K_{11} = K_{33}$) and the flexoelectric term with an average coefficient e. The second elastic term is due to the cholesteric helical structure (modulus K_{22}):

$$g = \frac{1}{2}K\left(\frac{\partial\varphi}{\partial y}\right)^2 \pm \frac{1}{2}K_{22}\left(q_0 - \frac{\partial\varphi}{\partial z}\right)^2 - eE\frac{\partial\varphi}{\partial y} \tag{12.42}$$

Minimisation with respect to $\partial\varphi/\partial z$ results in $\partial\varphi/\partial z = q_0$. Minimization with respect to $\partial\varphi/\partial$y results in $\partial\varphi/\partial y = eE/K$, see analogy with Eq. (11.79) for nematics. These two derivatives can be imagined as two projections of wavevector **k,** which will show the direction of the field-induced helical axis**.** In zero field $\mathbf{k} = \mathbf{q}_0 \| \mathbf{h}_0$. In the field-ON state the components of vector **k** are $|\mathrm{k}|\cos\Psi = q_0$ and $|\mathrm{k}|\sin\Psi = eE/K$, and these components define the position of the new optical axis. Therefore, the angle of the optical axis rotation is given by

$$\tan\Psi = \frac{eE}{q_0 K,} \tag{12.43}$$

which is linear in the electric field E for small distortions.

The rise and decay of the flexoelectric distortion is controlled by periodicity of the helix,

$$\tau = \frac{\gamma_1}{K_{22}q_0^2} \tag{12.44}$$

Therefore, for short pitch cholesterics with pitch about 0.3 μm, the characteristic time of the director switching is short, $\tau < 100$ μs ($\gamma_1 \approx 1$ P or 0.1 Pa·s in SI, $q_0 = 2\pi/P_0 \approx 2 \times 10^5$ cm^{-1} or 2×10^7 m^{-1}, $K_{22} \approx 3 \times 10^{-7}$dyn or 3×10^{-12} N). Indeed, experiments show that the effect of the realignment of the helical axis is less than 100 μs, and the speed of the response is independent of the field strength.

References

1. Oseen, C.W.: The theory of liquid crystals. Trans. Faraday Soc. **29**, 883–899 (1933)
2. de Gennes, P.G., Prost, J.: The Physics of Liquid Crystals, 2nd edn. Oxford Science Publications, Oxford (1995)
3. Belyakov, V.A.: Diffraction Optics of Complex-Structured Periodic media. Springer-Verlag, New York (1992)
4. Bendikson, J.M., Dowling, J.P., Scalora, M.: Analytic expressions for the electromagnetic mode density in finite, one-dimensional, photonic band-gap structure. Phys. Rev. E **53**, 4107–4121 (1996)
5. Palto, S.P.: Algorithm for solution of optical problem for lamellar anisotropic media. Zh. Eksp. Teor Fiz. **119**, 638–648 (2001) [JETP 103, 469 (2006)]
6. De Vries, Hl: Rotatory power and optical properties of certain liquid crystal. Acta Cryst. **4**, 219–226 (1951)
7. Kats, E.I.: Optical properties of cholesteric liquid crystals. Zh. Eksp. Teor Fiz. **59**, 1854–1856 (1970) [JETP 32, 1004 (1971]
8. Joannopoulos, J.D., Meade, R.D., Winn, J.N.: Photonic Crystals: Molding the Flow of Light. Princeton University Press, Princeton (1995)
9. Mauguin, C.: Sur les cristaux liquides de Lehman. Bull. Soc. Fr. Miner. **34**, 71–117 (1911)
10. Chilaya, G., Hauk, G., Koswig, H.D., Sikharulidze, D.: Electric-field controlled color effect in cholesteric liquid crystals and polymer-dispersed cholesteric liquid crystals. J. Appl. Phys. **80**, 1907–1909 (1996)
11. Fergason, J.L.: Liquid crystals in nondestructive testing. Appl. Optics **7**, 1729–1737 (1968)
12. De Gennes, P.-G.: Calcul de la distorsion d'une structure cholesteric par un champ magnetic. Sol. State Comms. **6**, 163–165 (1968)
13. Meyer, R.B.: Effect of electric and magnetic field on the structure of cholesteric liquid crystals. Appl. Phys. Lett. **12**, 281–282 (1968)
14. Meyer, R.B.: Distortion of a cholesteric structure by a magnetic field. Appl. Phys. Lett. **14**, 208–209 (1969)
15. Blinov, L.M., Palto, S.P.: Cholesteric helix: topological problem, photonics and electro-optics. Liq. Cryst. **36**, 1037–1045 (2009)
16. Blinov, L.M., Belyayev, S.V., Kizel', V.A.: High-order reflections from a cholesteric helix induced by an electric field. Phys. Lett. **65A**, 33–35 (1978)
17. Helfrich, W.: Deformation of cholesteric liquid crystals with low threshold voltage. Appl. Phys. Lett. **17**, 531–532 (1970)
18. Chandrasekhar, S.: Liquid Crystals. Cambridge University Press, Cambridge (1977)
19. Blinov, L.M.: Electro-Optical and Magneto-Optical Properties of Liquid Crystals. Wiley, Chichester (1983). Chapter 6
20. Berreman, D.W., Heffner, W.R.: New bistable liquid-crystal twist cell. J. Appl. Phys. **52**, 3032–3039 (1981)
21. Palto, S.P., Barnik, M.I.: Bistable switching of nematic liquid crystal layers with ground 2π-state. Zh. Eksp. Teor. Fiz. **127**, 220–229 (2005)

22. Barberi, R., Durand, G.: Controlled textural bistability in nematic liquid crystals. In: Collings, P.J., Patel, J.S. (eds.) Handbook of Liquid Crystal Research, pp. 567–589. Oxford University Press, New York (1997). Chapter XV
23. Joubert, C., Angele, J., Boissier, A., Pecout, B., Forget, S.L., Dozov, I., Stoenescu, D., Lallemand, S., Lagarde, P.M.: Reflective bistable nematic displays (BiNem®) fabricated by standard manufacturing equipment. J. SID **11**, 17–24 (2003)
24. Patel, J.S., Meyer, R.B.: Flexoelectric Electro-optics of a Cholesteric Liquid Crystal. Phys. Rev. Lett. **58**, 1538–1540 (1987)
25. Patel, J.S., Lee, S.-D.: Fast linear effect based on cholesteric liquid crystals. J. Appl. Phys. **66**, 1879–1881 (1989)

Chapter 13
Ferroelectricity and Antiferroelectricity in Smectics

13.1 Ferroelectrics

13.1.1 Crystalline Pyro-, Piezo- and Ferroelectrics

The discussion of ferroelectricity in liquid crystalline phase is based on the concepts developed for the solid crystals. Therefore, we have to start from a brief survey of the elementary physics of ferroelectricity in crystals [1, 2].

13.1.1.1 Polarization Catastrophe in Liquids and Solids

In Section 7.2.1 we discussed polarization of molecular isotropic liquids. We introduced the equations for dielectric permittivity ε and dielectric susceptibility χ^E and wrote the microscopic definition of the polarization vector **P** as a sum of dipole moments in the unit volume $n_v = \rho N_A/M$ (ρ is density, N_A is Avogadro number, M is molecular mass):

$$\varepsilon = \frac{\mathbf{D}}{\mathbf{E}} = \frac{\mathbf{E} + 4\pi\mathbf{P}}{\mathbf{E}}, \quad \chi^E = \frac{\mathbf{P}}{\mathbf{E}} = \frac{\varepsilon - 1}{4\pi}, \quad \mathbf{P} = \sum_n \mathbf{p}_e = n\gamma\mathbf{E}_{loc}. \tag{13.1}$$

Here $\mathbf{p}_e$ is the electric dipole induced by the electric field in a molecule having mean molecular polarizability γ. Then we used the Lorentz approximation for the local field acting on a molecule and found corresponding field induced polarization. From that we have obtained the electric susceptibility of the dielectric (Eq. 7.18):

$$\chi^E = \mathbf{P}/\mathbf{E} = n_v\gamma/[1 - (4\pi/3)n_v\gamma] \tag{13.2}$$

This formula is very important for the further discussion because it predicts the "polarization catastrophe". For small molecular polarizability γ, susceptibility χ^E depends linearly on γ. However, when $\gamma \to 3/4\pi n_v$, the denominator of (13.2) tends to zero and χ^E diverges.

L.M. Blinov, *Structure and Properties of Liquid Crystals*,
DOI 10.1007/978-90-481-8829-1_13, © Springer Science+Business Media B.V. 2011

Its physical sense is well seen from the equations (7.17) for $\mathbf{P}$ and $\mathbf{E}_{\text{loc}}$. For a fixed concentration of molecules and given local field, the polarization should be linear function of γ. However, with increasing $\mathbf{P}$, $\mathbf{E}_{\text{loc}}$ itself begins to grow and this results in the non-linear, avalanche-like increase of susceptibility. Finally, for small, densely packed molecules (n_v is large) with high polarizability γ, χ^{E} would tend to infinity. It means that an infinitesimally low field, even a small fluctuation of a local field, may create a finite polarization. In other words, polarization may appear spontaneously, without any applied field. The appearance of the spontaneous polarization is a necessary (but not sufficient) condition for phenomenon called ferroelectricity.

What's about liquid ferroelectric? Let us examine the qualitative criterion

$$k = (4/3)\pi n_v \gamma = (4/3)\pi \rho \gamma N_{\text{A}}/M \tag{13.3}$$

for the polarization catastrophe in liquids having non-polar molecules. In this case, the Lorentz formula for the local field is approximately valid. We can take, e.g., liquid benzene ($\rho \approx 0.9\text{g/cm}^3$, $M = 78$, electronic polarizability $\gamma_{\text{e}} \approx 1.25 \times 10^{-23}\ \text{cm}^{-3}$). Then $k \approx 0.09 << 1$ and liquid benzene cannot be polarised spontaneously. Even for hypothetical liquids consisted of smaller molecules with higher electronic polarizability it would be difficult to reach criterion (13.3). More perspective are liquids whose molecules carry permanent dipole moments p_{e} which additionally contribute to γ due to orientational polarizability γ_{or}. Let us take liquid nitrobenzene ($\rho \approx 1.2\text{g/cm}^3$, $M = 123$) with quite a large dipole moment, $p_{\text{e}} \approx 4$ Debye $= 4 \cdot \times 10^{-18}$ CGS). The application of the Lorenz formula for $\mathbf{E}_{\text{loc}}$ would result in equation (7.22) for orientational polarizability $\gamma_{or} = p_e^2/3k_BT \approx 1.3 \times 10^{-22}\text{cm}^{-3}$ at room temperature. Then, coefficient $k \approx 3.2$ would exceed the criterion for the polarization catastrophe, however, this is incorrect result, because the Onsager reaction field discussed in Section 7.2.1 has not been taken into account. In reality, the dipole–dipole interaction in nitrobenzene and other known dipolar liquids is not sufficient to form a spontaneously polarised state.

In solid crystals, the situation is different because (i) their packing is denser; (ii) ionic crystals consist of small ions of high polarizability; (iii) different ions interact with each other forming large dipoles and (iv) there is a possibility to overcome the limitation posed by the Lorenz formula for the local field. Indeed due to crystal anisotropy, at least, for some directions the criterion for the polarisation catastrophe is weaker. On the other hand, in solids there are strong elastic forces counteracting the electric force and hindering displacement of ions. Nevertheless, a spontaneously polarised state is quite typical of many crystals, the molecular organic crystals included.

13.1.1.2 Pyro-, Piezo- and Ferroelectrics

Totally there are 32 crystallographic classes. Among them we can distinguish 11 unpolar classes, 11 neutral-polar classes and ten polar classes. Unpolar classes have

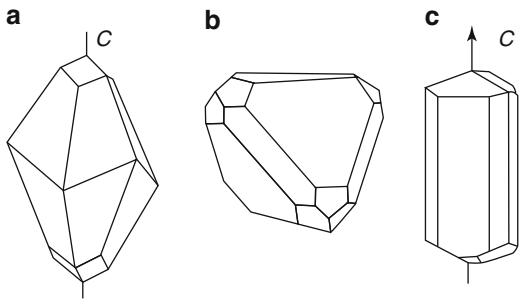

Fig. 13.1 Examples of non-polar, piezoelectric and pyroelectric crystals: calcite (**a**), ZnS (**b**) and tourmaline (**c**). An *arrow* shows the direction of the polar axis in tourmaline

no polar directions at all. They have a centre of symmetry and show no polar properties. The polarisation can be induced only by external electric field. An example is calcite having inversion centre and symmetry D_{3d} shown in Fig. 13.1a.

Piezoelectrics. In the neutral-polar classes there are polar directions (not axes), which can be described by several vectors with their vector sum equal to zero. Such crystals do not possess spontaneous polarization and do not manifest polar properties (such as pyroelectric, photogalvanic or linear electrooptical effects); however, the polarization can be induced not only by an electric field but also by a pure mechanical stress. These crystals are called piezoelectrics. Examples are crystals of quartz or ZnS having cubic symmetry with four polar direction but no polar axis, Fig. 13.1b. Such crystals are used in technics as microphones, mechanical micro-motors and sensors, etc.

Pyroelectrics. In a crystal belonging to polar classes there is only one polar axis with a symmetry of the polar vector. These crystals are also piezoelectric, but, in addition, manifest spontaneous polarization P_s and all other polar properties. Such crystals are called pyroelectrics. An example is tourmaline having symmetry C_{3v} and shown in Fig. 13.1c. Pyroelectric crystals are also used in techniques as piezoelectrics and also as detectors of infrared light or a heat flow. There are many organic pyroelectric crystals, e.g., *p*-nitroaniline, one of the best generators of the optical second harmonic.

Ferroelectrics. Speaking in terms of the polarisation catastrophe we can say that, in the most of pyroelectrics $k > 1$, and the catastrophe occurs upon crystallisation of the substance. In this case the polarisation is forever fixed along the direction of the polar axis even upon variation of temperature or an external field. However, there are some crystals belonging to the same point groups as pyroelectrics but having not so stable spontaneous polarisation. The direction of P_s, that is the direction of the vector of polar axis, can be inverted by an external electric field. In fact, this direction is degenerate and there are two equivalent energy states. One of the two minima of the free energy may be selected by an external field and this is another type of bistability in addition to discussed in Section 12.3.3. The switching between the two states is characterised by a certain threshold and hysteresis. This possibility of the polarisation switching between two stable states is usually taken as a criterion to distinguish such (soft) ferroelectrics from the normal (rigid) pyroelectrics. The bistability is the sufficient condition for ferroelectricity [3].

In ferroelectrics criterion k only slightly exceeds unity. For this reason, with increasing temperature, the ferroelectric state or phase can be destroyed by the phase transition into the non-ferroelectric (paraelectric) phase with zero spontaneous polarization. Sometimes this *ferroelectric transition* at temperature T_c is taken as an additional criterion for ferroelectricity, although there are crystals, in which a ferroelectric phase survives up to the crystal melting. Experimentally, close to T_c the dielectric constant very often obeys the Curie law, $\varepsilon = C/(T_c - T)$, where C is Curie constant. A good example of a ferroelectric crystal is $BaTiO_3$, in which two stable states are characterised by two different sites the Ti^{4+} ion occupies in the crystallographic lattice. Among crystalline ferroelectrics there are some organic crystals and even polymers, e.g., poly-vinylidene-fluoride (PVDF), in which the spontaneous polarisation is owed to collective alignment of the C–F dipoles perpendicular to the backbone of the polymer.

13.1.1.3 Simplest Description of a Proper Ferroelectric

In the proper ferroelectrics, the spontaneous polarisation appears as a result of the polarisation catastrophe or, in other words, due to electric dipole–dipole interactions. There are also improper ferroelectrics, in particular, liquid crystalline ones, in which a structural transition into a polar phase occurs due to other interactions and, consequently, P_s appears as a secondary phenomenon. We shall discuss this case later. For simplicity, the square of spontaneous polarisation vector can be taken as a scalar order parameter for the transition from the higher symmetry paraelectric phase to the lower symmetry ferroelectric phase. Therefore, in the absence of an external field, we can expand the free energy density in a series over $P_s^2(T)$ and this expansion for ferroelectrics is called Landau–Ginzburg expansion:

$$g = g_0 + \tfrac{1}{2} AP_s^2 + \tfrac{1}{4} BP_s^4 + \tfrac{1}{6} CP_s^6 + \cdots \tag{13.4}$$

Here, g_0 is free energy of the paraelectric phase, $A = a(T - T_c)$, B, C are Landau coefficients. As in Eq. (13.5) there is no any derivative, the conditions for the free energy minimum are given by the simplest Euler equation $\partial g/\partial P_s = 0$ and stability condition $\partial^2 g/\partial P_s^2 > 0$:

$$AP_s + BP_s^3 + CP_s^5 = 0 \quad \text{and} \quad A + 3BP_s^2 + 5CP_s^4 > 0 \tag{13.5}$$

Consider the case of small P_s. Then, the sixth order term is ignored and $g = g_0 + \tfrac{1}{2} AP_s^2 + \tfrac{1}{4} BP_s^4 + \cdots$ The plot of this function is very similar to that in Fig. 6.10b for the free energy close to the SmA-nematic transition discussed in Section 6.3. The phase transition occurs at $A = 0$. For $A > 0$ there are two minima corresponding to finite values of the spontaneous polarisation in the ferroelectric phase (curve 1 in the figure); for $A < 0$ only one minimum at zero P_s corresponds to the paraelectric phase (curve 3). Totally, we have only three solutions of Eq. (13.5):

$P_s = 0$ (for the paraelectric phase) and $P_s = \pm(-A/B)^{1/2} = \pm[(a/B)(T_c - T)]^{1/2}$ (for the ferroelectric phase). Signs ($\pm$) mean that P_s can look in two opposite directions and correspond to the two minima in the free energy. The square root dependence of P_s on temperature near the phase transition is a continuous function characteristic of the second order transition like SmA-nematic transition, see Fig. 6.10a or SmC-SmA transition. Such dependence is in accordance with many experiments on ferroelectrics. When P_s is not small we should return back to the initial free energy expansion (13.5) and keep the sixth order term. A similar situation has been already discussed in Section 6.2 for the isotropic – nematic phase transition. Now Eq. (13.5) has five solutions and can explain a jump-like growth of P_s with decreasing temperature, (as in Fig. 6.5), hysteresis of $P_s(T)$ close to the transition temperature and specific features of other thermodynamic properties.

To discuss the electric field switching we add the field term $g_E = -PE$ to (Eq. (13.4)) and make minimisation of free energy with respect to the total polarization $P = P_s + P_{in}$ that includes the spontaneous and the field induced terms $P = P_s + P_{in}$. Then we obtain $\partial g_E/\partial P = -E$ or

$$E = AP + BP^3 + CP^5 \tag{13.6}$$

This equation implicitly represents the dependence of polarization on the applied electric field. Usually, the function $P(E)$ can be found numerically with temperature dependent coefficient A and constant B and C.

From Eq. (13.6) we can easily derive the Curie law for dielectric permittivity ε or susceptibility $\chi = (\varepsilon - 1)/4\pi$. For small fields, we can leave only the first term of the expansion $E = AP$. In the paraelectric phase $P = P_{in}$ and $P_{in} = \chi_{para}E = E/a(T - T_c)$. In the ferroelectric phase, for small fields, $P_s >> P_{in}$, therefore $P^2 \approx P_s^2 + 2P_sP_{in} + \cdots$ and $(A + BP_s^2 + 2BP_sP_{in})(P_s + P_{in}) = E$. From here, using formula for $(P_s)^2 = -A/B$ found above and leaving only linear terms in P_{in}, we obtain $E = -2AP_{in}$.

Therefore, the Curie law is given by

$$\chi_{para} = 1/a(T - T_c) (\text{for } T > T_c \text{ in paraelectric phase}) \tag{13.7}$$

$$\chi_{para} = 1/2a(T - T_c) (\text{for } T < T_c \text{ in ferroelectric phase}) \tag{13.8}$$

The inverse susceptibility follows a linear dependence on temperature in both the paraelectric and ferroelectric phases; a sign of the slope of function $1/\chi(T)$ in the two phases is opposite and the magnitude of the slope is twice larger in the ferroelectric phase in agreement with experiment. Note that the Curie law is valid for both second and first order transitions, but the critical temperatures T_c and T_c* the two cases may not coincide, like in Fig. 6.8b.

Now, going back to Eq. (13.6) we may discuss the $P(E)$ dependence even for strong fields. An example of such dependence is pictured qualitatively in Fig. 13.2. The values of P at $E = 0$ on the vertical axis corresponds to $\pm P_s$. In the field range

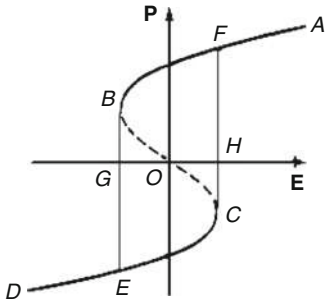

Fig. 13.2 Hysteresis type dependence of total polarization **P** on electric field **E** for a typical crystalline ferroelectric

between points G and H the function $P(E)$ has three values. In reality, a hysteresis is observed. With increasing field the curve follows the route DECFA, but, due to a memory of state A, the back route AFBED does not coincide with the forward one. As a result, a ferroelectric loop forms with width G-H. A half of the width is called "coercive field". We see that, upon application of the electric field, the spontaneous polarization of the ferroelectric can be switched between two states $\pm P_s$ corresponding to the two equivalent minima in the free energy. Therefore, the ferroelectric demonstrates a bistability again in agreement with experiment. It is very surprising how many experimental results on ferroelectricity can be explained using such a simple theoretical consideration!

13.1.2 Ferroelectric Cells with Non-ferroelectric Liquid Crystal

13.1.2.1 Meyer's Discovery

Year 1975 has been marked off by an outstanding publication of R. Meyer and his French co-workers [4]. As has been discussed in Section 4.9, chirality of molecules removes the mirror symmetry of any phase. The idea of Meyer was to apply this principle to the SmC phase by making it chiral. He believed that if chiral molecules formed a tilted smectic phase, its point group symmetry would reduce from C_{2h} to C_2 and the new phase would belong to pyroelectric class with a specific polar axis [5].

The chemists from Orsay have synthesised chiral compound *p*-decyloxybenzylidene-*p*′-amino-2methylbutylcinnamate (DOBAMBC), Fig. 13.3. Indeed, in the temperature range 95–117°C, this substance showed a linear electro-optical effect characteristic of a pyroelectric phase. The effect was observed in thick homeotropically oriented layers. Due to chiral structure of DOBAMBC molecules, the SmC* phase had a spiral structure with the helical axis perpendicular to the limiting glasses, Fig. 13.4a. Under a microscope the preparation showed a conoscopic cross typical of a uniaxial phase, and, upon application of the in-plane electric field E_x,

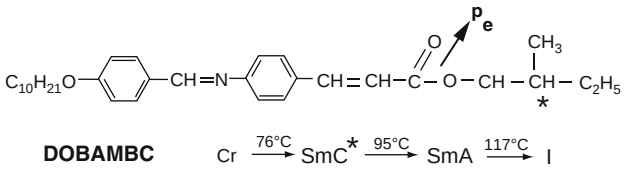

Fig. 13.3 Chemical formula of DOBAMBC molecule which is chiral due to asymmetric carbon C* and has a dipole moment $\mathbf{p}_e$. Below is a sequence of transition temperatures between crystal (Cr), SmC*, SmA and isotropic (I) phases

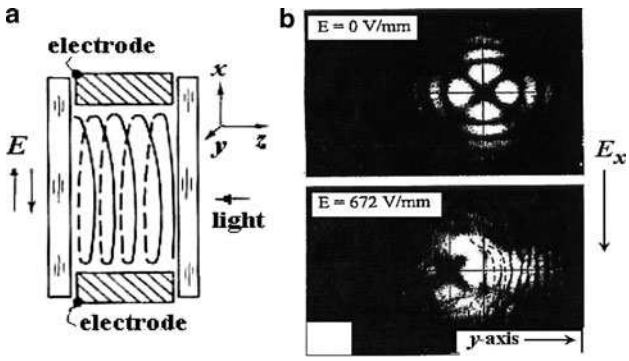

Fig. 13.4 Meyer's experiment. Geometry of the cell with helical structure of DOBAMBC (**a**) and two conoscopic images (**b**), one in the absence of the field (*top*) and the other at $E_x = 672$ V/mm showing a shift of the conoscopic cross perpendicular to E_x

the cross moved perpendicular to the field along the *y*-axis, Fig. 13.4b. The direction of the cross shift changed with a change of the field polarity. The effect was clearly related to the pyroelectric nature of the SmC* phase and existence of the spontaneous polarisation interacting with the external field. Therefore, in 1975 for the first time, a *polar liquid phase* (of course, anisotropic) with finite spontaneous polarisation was reported.

The value of P_s in DOBAMBC was very small, about 18 CGSQ/cm^2 (or 60 μC/m^2). It is 2,500 times less than P_s in $BaTiO_3$ (150 mC/m^2). However, nowadays there are SmC* materials with $P_s \approx 5$ mC/m^2. The magnitude of P_s depends on the molecular structure. A molecule should have a large transverse dipole moment located close to the chiral moiety; otherwise the intra-molecular rotation of chiral moiety with respect to the dipolar part would prevent, at least, partial orientation of dipoles along the polar axis. For the same reason, a rotation of molecules about their long molecular axes should be hindered. In DOBAMBC, the smallness of P_s is explained by rather free rotation of the chiral tail about the –O–CH- bridge connecting the asymmetric carbon C* with the –C=O dipolar group shown by an arrow in Fig. 13.3.

13.1.2.2 Goldstone Mode and Helicity of the Structure

As we discussed in Section 4.9, on a large scale, the SmC* phase acquires a helical structure. This is not surprising, because, in the achiral SmC phase, the *c*-director of the infinite stack of layers may look over any direction. The rotation of the SmC* director about the smectic layer normal does not cost any energy. We meet the same situation in nematics: when there is no external field and limiting surfaces, the direction of the director **n** is not fixed and one can rotate it without spending any energy. It is an elastic mode, the so-called *Goldstone mode***,** trying to restore the continuous symmetry $D_{\infty h} \rightarrow K_h$ of the phase existing above the corresponding transition (isotropic phase in case of nematics) [6]. Due to this non-energy demanding rotation, any small amount of a chiral additive (considered as a perturbation) would easily twist the nematic structure into the cholesteric.

The Goldstone mode in an *achiral* SmC tries to restore the symmetry of the smectic A phase $C_{\infty h} \rightarrow D_{\infty h}$ by free rotation of the director along the conical surface with the smectic layer normal as a rotation axis. Thus, like chiral molecules convert a nematic into a cholesteric, they convert an achiral SmC into chiral SmC* without any phase transition. In addition, mixing left (L)- and right (R)-handed additives results in a partial or complete compensation of the helical pitch both in cholesterics and chiral smectic C*. For example, the L- and R- isomers of the same molecule taken in the equal amounts would give us a racemic mixture, that is achiral SmC without helicity and polarity.

What has been said above shows that the macroscopic helicity as such has no direct relation to the polarity of the SmC* phase. One can select chiral molecules without dipoles and construct a helical SmC* that will have a polar axis without polarisation. But, is it possible to have finite polarisation without helical structure in the bulk? Can we make a uniform polar phase with infinite helical pitch? The answer is "Yes". To this effect we should prepare a mixture of left-handed and right-handed molecules *of different chemical structure*. An example is shown in Fig. 13.5 [7]. In this case, R-DOBAMBC is mixed with L-HOBACPC (*p*-hexyloxybenzylidene - *p*′-amino-chloropropyl-cinnamate). The sample is rather thick, $d = 200$ μm. With a

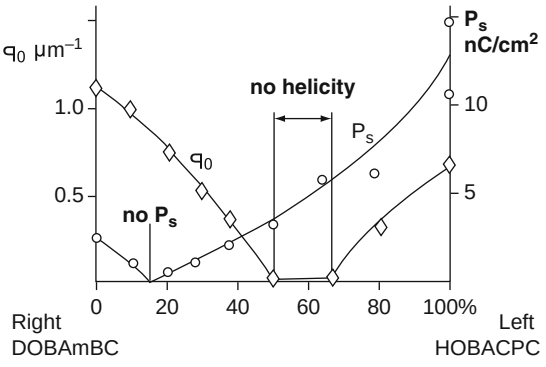

Fig. 13.5 Phase diagram for the mixture of two chemically different left- and right-handed compounds. Note that at a certain concentration of HOBACPC ($c \approx 15\%$) the spontaneous polarization P_s vanishes in the helical structure (wavevector $q_0 \approx 0.8\ \mu m^{-1}$); on the contrary, at $c = 50$–70%, the helicity is compensated ($q_0 = 0$) but P_s remains finite ($\approx 5\ nC/cm^2$)

change in composition we observe two magic points: in one of them the helical pitch is compensated and the helical vector $q = 0$ (no helicity), in the other the spontaneous polarisation vanishes (no polarity). The two points do not degenerate into one because molecular interactions responsible for polarity and chirality are different. This result is very interesting from the practical point of view: it shows how to get rid of the undesirable helical structure in liquid crystals electrooptical cells. It is also significant from the theoretical point of view because it proves a possibility to have a uniform polar liquid crystalline structure without any limiting substrates.

Such a polar phase would manifest the same Goldstone mode as an achiral SmC does. The origin of the Goldstone mode in SmC* is not a helical structure, as often stated in literature. On the contrary, the helicity originates from the Goldstone mode due to its gapless nature (the absence of any energy gap for the **c**-director rotation from one orientational state to the other). What is true that the same mode in the SmC* phase is much better seen in the low frequency dielectric spectrum due to the coupling of the director to the spontaneous electric polarisation of the chiral polar phase. Particularly, in the helical structure, the Goldstone mode has a characteristic (hydrodynamic) dependence of the relaxation frequency on the wavevector of the helix, $\omega \approx Kq^2$, exactly like in cholesterics.

13.1.2.3 Smectic C* Phase and Criteria for Ferroelectricity

Is the SmC* phase ferroelectric? To answer this question we should look more carefully at the criteria formulated for crystalline ferroelectrics:

1. All crystalline ferroelectrics without exceptions belong to one of the pyroelectric classes and possess *spontaneous polarisation* (polar class).
2. Sometimes, a formation of *domains* with different direction of P_s is also taken as a pre-requisite of the ferroelectricity.
3. There is a distinct *phase transition* between the ferroelectric and the paraelectric phase (there would be no exception from this rule if we consider even melting to the liquid phase as such a transition).
4. There are two equivalent stable states (*bistability*) differed by the spontaneous polarisation direction, between which we can switch the direction of P_s. It seems there is no exception from this criterion among the crystalline ferroelectrics.

As we have seen, locally the smectic C* layers are polar, belonging to pyroelectric class C_2. Macroscopically SmC* either forms a helical structure or does not. So, we can discuss a structure without helicity. In a sense, the formation of a helix is equivalent to formation of ferroelectric domains which would reduce overall macroscopic polarisation. Thus we can consider the (1) (very important) and (2) (additional) requirements fulfilled. As to the phase transition (3), we know that in the smectic A* phase, even chiral, there is no polar axis, therefore that phase can be considered as a paraelectric phase. The two-component order parameter of the A*–C* transition is the same as the parameter of the A–C transition in an achiral substance, namely $\vartheta \exp(i\varphi)$, where we recognise the tilt ϑ and azimuth φ angles. The spontaneous

polarisation is not considered as an order parameter, but this is not a limitation for, at least, improper ferroelectricity. We just deal with a transition to improper pyroelectric phase. Thus, the third criterion for ferroelectricity is also fulfilled.

The last criterion (4) is bistability. In the non-helical structure the direction of the polar axis is fixed in the sense that the three vectors, the polar axis $\mathbf{P_s}$, the director $\mathbf{n}$ and the smectic normal $\mathbf{h}$ form either right or left vector triple. This depends on molecular handedness and cannot be changed. In this sense there is no bistability. On the other hand, the Goldstone mode allows the thresholdless rotation of $\mathbf{P_s}$ together with $\mathbf{n}$ about $\mathbf{h}$ through any angle by an infinitesimally low electric field. So, a number of possible states is infinite.

The situation can be well modelled by a magnetic arrow, placed in a viscous liquid: by realignment of an external magnetic field the arrow will follow the field and eventually it takes the field direction (the time depends on liquid viscosity). Our case can also be modelled by a pyroelectric crystal installed on the needle like the magnetic arrow. Now the arrow is not magnetic but electric and follows an electric field E. If the electrodes are fixed in the smectic layer plane, we can switch the polarisation between two angular states, controlled by the positive and negative field. Since the polarisation direction is rigidly coupled to the director (and the optical axis) we would observe a linear electrooptical effect. The switching is faster if we have stronger E, higher P_s and lower viscosity and this is in agreement with experiment. However, the two field controlled states are not intrinsically stable states and, in the absence of the field, they can easily be destroyed by thermal fluctuations or even by very weak chirality.

Therefore, in conclusion, we may say that the *bulk smectic C* phase* is, in principle, a *liquid pyroelectric*, which, due to its fluidity, allows a thresholdless realignment of its polarisation (and the director) by an external field. Strictly speaking, it is not a ferroelectric in both the uniform and helical states. It may be called a *helielectric* [8] to distinguish it from the conventional pyroelectric, however, this does not change anything. But why a large class of smectic C* materials is called ferroelectric and under this name is widely used in modern technology?

13.1.2.4 Surface Stabilised Ferroelectric Cells

We can answer the last question if consider a construction of the so-called "surface stabilised ferroelectric liquid crystal cell" or simply SSFLC cell [9]. Such SSFLC cell is only few micrometers thin and, due to anchoring of the director at the surfaces, the intrinsic helical structure of the SmC* is unwound by boundaries but a high value of the spontaneous polarisation is conserved. The cell is constructed in a way to realise two stable states of the smectic C* liquid crystal using its interaction with the surfaces of electrodes, see Fig. 13.6a. First of all, in the SSFLC cell, the so-called bookshelf geometry is assumed: the smectic layers are vertical (like books) with their normal $\mathbf{h}_s$ parallel the z-axis. Then the director is free to rotate along the conical surface about the $\mathbf{h}_s$ axis as shown in Fig. 13.6b (Goldstone mode). It is important that, to have a bistability, the director should be properly

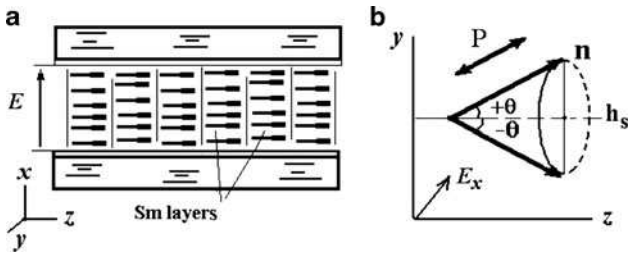

Fig. 13.6 SSFLC cell. The structure of the cell with bookshelf alignment of smectic layers (**a**) and the cone of the director **n** motion with two stable states $\pm\vartheta$ in the electrode plane *yz* (**b**). Note that in sketch (**a**) the director in the cell plane *yz* is turned to the reader through angle $+\vartheta$ (shown by *thicker right parts of the rod-like molecules*) in agreement with sketch (**b**). The *double-head arrow* shows the optimum angular position of polarizer P

anchored at the electrodes. In the ideal case, the zenithal anchoring energy W_z should be relatively strong, but the azimuthal one W_a should be zero. Thus, in the absence of the external field, to have minimum W_z the director **n** must be located parallel to electrodes that is in plane *yz* intersecting the surface of the cone. Therefore, there are only two stable positions for **n**, either angle $+\vartheta$ or $-\vartheta$. Consequently, the spontaneous polarization P_s will be directed along the $\pm x$-axis, i.e. either up or down in sketch (a).

In experiments, very often spatial domains appear in the initial field-off state of approximately equal total area with the director oriented at $+\vartheta$ or $-\vartheta$. Under a microscope, with a polariser P oriented, say, along the $+\vartheta$ direction, as shown in Fig. 13.6b, and analyser A$\perp$P, the $+\vartheta$ domains look black and $-\vartheta$ domains bright. When a sufficiently strong, square-wave electric field $\pm E_x$ is applied to electrodes, P_s is switched along the *x*-axis and, since the director is rigidly fixed to both the P_s and the conical surface, its projection on the *yz*-plane will oscillate between $\pm\vartheta$ positions through total angle 2ϑ. Usually it sticks in one of the two stable positions (memory states) as soon as the field is switched off. This process results in a *true bistable switching* of P_s like in solid state ferroelectrics and, due to director switching, a fast electrooptical effect with a good contrast is observed.

SSFLC cells are very convenient for measurements of the magnitude of P_s. Indeed, upon switching the polarization by external voltage, a change of the surface charge at the electrodes of area A creates an electric current $i = dQ/dt = A\, dP/dt$. Therefore, applying a step voltage of sufficient amplitude to switch the polarization from $-P_s$ (at $t = -\infty$) to $+P_s$ (at $t = +\infty$) and measuring the time dependence of the current $i(t)$ we find P_s by integrating the area under the $i(t)$ function.

$$2P_s = A^{-1} \int_{-\infty}^{\infty} i(t)dt$$

Unfortunately, the ideal bookshelf structure is difficult to make. Usually the electrodes are covered by polymer layers and rubbed unidirectionally. This provides a good alignment of the director along the electrodes and the "bookshelf"

structure of the SmA* phase. Upon cooling the cell from the SmA* to SmC* phase the director keeps its in-plane direction. Although the rubbing is appropriate for strong zenithal anchoring it is incompatible with the requirement of zero azimuthal anchoring of the director necessary for the genuine bistability. Moreover, upon the passage of the SmA* – SmC* transition, the smectic layers become tilted or acquire a chevron structure. The chevrons and accompanying zigzag defects have been discussed in Section 8.5.4, see Figs. 8.33 and 8.34. These factors reduce the performance of the SSFLC cells. Nevertheless, the principle of the bistable switching of the pyroelectric SmC* phase is realised in the SSFLC cells and such cells can be considered as *genuine ferroelectric cells*.

13.1.3 Phase Transition SmA–SmC**

13.1.3.1 Simplification

Due to low symmetry (C_2) of the chiral smectic C* phase, its theoretical description is very complicated. Even description of the achiral smectic C phase is not at all simple. In the chiral SmC* phase two new aspects are very important, the spatially modulated (helical) structure and the presence of spontaneous polarisation. The strict theory of the SmA*–SmC* transition developed by Pikin [10] is based on consideration of the two-component order parameter, represented by the **c**-director whose projections $(\xi_1, \xi_2) = (n_z n_x, n_z n_y)$ are combinations of the director components $n_x = \sin\vartheta\cos\varphi$, $n_y = \sin\vartheta\sin\varphi$, and $n_z = \cos\vartheta$:

$$\xi_1 = n_z n_x = \tfrac{1}{2}\sin 2\vartheta\cos\varphi, \quad \xi_2 = n_z n_y = \tfrac{1}{2}\sin 2\vartheta\sin\varphi \tag{13.9a}$$

or

$$\mathbf{c} = \tfrac{1}{2}\sin 2\vartheta(\mathbf{i}\cos\varphi + \mathbf{j}\sin\varphi). \tag{13.9b}$$

Here, ϑ is the tilt angle of the director with respect to the smectic layer normal (and the helical axis z) and φ is the azymuthal angle counted from the x-axis. The free energy of the SmC* includes both the helicity and polarization. Then, assuming constant orientational order parameter Q, a linear relationship between the tilt and polarisation and leaving only the lowest order terms in ξ_1, ξ_2 and gradients $\partial\xi_1/\partial z$, $\partial\xi_2/\partial z$, one has fifteen terms in the equation for the free energy [11].

However, many interesting effects in ferroelectric cells may be described without account of the helicity, in the approximation of a uniform SmC* structure (e.g., unwound by limiting surfaces or formed by mixtures with compensated helicity). So, in this paragraph, we ignore all the space dependent terms i.e. consider a SmC* structure with azimuthal angle $\varphi \to 0$. Going back to Fig. 13.5 this approximation may correspond to a ferroelectric mixture with $q_0 \approx 0$. Then the free energy is:

$$g_{SmC*} = g_0 + \frac{1}{2}A\vartheta^2 + \frac{1}{4}B\vartheta^4 + \frac{P^2}{2\chi_\perp} - \mu P\vartheta - PE \tag{13.10}$$

where ϑ [in rad] is the tilt of the director, $A = a(T - T_0)$ [in erg/cm^{3}K] describes the elasticity for ϑ-changes, P [in CGSQ/cm^2 or statV/cm] is polarization, μ [in statV/cm] is the *polarization-tilt coupling constant* (or piezocoefficient), E is an external electric field [statV/cm] applied perpendicular to the tilt plane, g_0 and $\chi_\perp = (\varepsilon_\perp - 1)/4\pi$ are the background energy of the SmA* phase and dielectric susceptibility of the SmA* phase well above the A*–C* transition.

Equation (13.10) is principally different from the equation (13.4) for the free energy of a solid ferroelectric. Here, the leading term of the expansion is related to the tilt angle, but the appearance of the spontaneous polarisation (the secondary effect) is taken into account by coupling term $\mu P\vartheta$. Term $P^2/2\chi_\perp$ describes the energy of the polarised dielectric. For a racemic phase, with spontaneous polarization $P_s = 0$ and without coupling of the tilt to total polarisation P we would put total polarization $P = 0$ in Eq. (13.10) because there is no additional contribution to the *field energy* in the SmC phase above the background (SmA) term $g_{0.}$ Therefore, for the achiral SmC phase, minimisation of Eq. (13.10) with respect to the tilt angle would provide the result obtained in Section 6.4.

$$\frac{\partial g}{\partial \vartheta} = A\vartheta + B\vartheta^3 \text{and } \vartheta_s = (a/B)^{1/2}(T_0 - T)^{1/2}$$

13.1.3.2 Soft Mode for Smectic A*–Smectic C* Transition

Low field limit. Minimising Eq. (13.10) with respect to polarization P we find the relation between the tilt and polarization:

$$P = \chi_\perp \mu\vartheta + \chi_\perp E \tag{13.11}$$

For discussion of the soft mode close to the phase transition we can assume small ϑ angles, and a weak field $E << \mu\vartheta$. Then, substituting $P \approx \chi_\perp \mu\vartheta$ in Eq. (13.10) and ignoring term $B\vartheta^4$ we exclude P from the free energy difference between the SmC* and SmA* phases:

$$\Delta g = \frac{1}{2}\left(A - \chi_\perp \mu^2\right)\vartheta^2 - \chi_\perp \mu E\vartheta \tag{13.12}$$

Note that the fourth and fifth terms in expansion (13.10) merge with the second term and this results in renormalisation of the transition temperature.

Now we minimise the free energy with respect to the tilt angle

$$\frac{\partial \Delta g}{\partial \vartheta} = \left(A - \chi_{\perp}\mu^2\right)\vartheta - \chi_{\perp}\mu E = 0$$

and arrive at the expression for the tilt angle linearly dependent on the field:

$$\vartheta = \frac{\chi_{\perp}\mu E}{A - \chi_{\perp}\mu^2} = \frac{\chi_{\perp}\mu E}{a(T - T_c)} = e_c E \tag{13.13}$$

where

$$T_c = T_0 + \chi_{\perp}\mu^2 / a$$

We see, that the phase transition temperature increases, because the dipole–dipole interactions (P^2-term) stabilise the smectic C* phase. Note that the field induced tilt angle (or *electroclinic coefficient* e_c) diverges at a temperature T_c. This means, that at T_c even infinitesimally low field would create a finite tilt. This is the *soft mode* of the director motion: any small force (not necessary electric) would cause the tilt of the director, because, at the transition, the medium becomes *soft with respect to the tilt*. The corresponding dielectric susceptibility shows the Curie–Weiss law:

$$\chi_{sm} = \frac{P}{E} = \frac{\chi_{\perp}^2 \mu^2}{a(T - T_c)} \tag{13.14}$$

In reality, a growth of the induced tilt at the phase transition is limited by two factors. In a strictly compensated non-helical ferroelectrics only $B\vartheta^4$ term in expansion (13.10) is limiting. In the most practical cases, the helix cannot be precisely compensated over the whole range of the smectic C* phase and a finite wavevector $q_o = 2\pi/P_0$ remains. Thus, in a more advanced theory, the space dependent, chiral terms must be added to expansion (13.10). They renormalize the transition temperature for the second time, and put a limit for the divergence of the induced tilt:

$$\vartheta = \frac{\chi_{\perp}\mu E}{a(T - T_{ch}) + K_{\varphi} q_0^2} \text{ with } T_{ch} = T_0 + \frac{\chi_{\perp}\mu^2}{a} + \frac{K_{\varphi} q_0^2}{a} \tag{13.15}$$

Here, K_{φ} is an effective elastic modulus for the azimuthal motion of the director in the SmC* phase that includes factor $\sin^2\vartheta$ [11]. Due to this factor, in the one-constant approximation, which will be used below, $K_{\varphi} \approx 10^{-7}$ dyn is roughly one order of magnitude smaller than $<K_{ii}>$ for nematics. The third term in the equation for T_{ch} determins the difference in the transition temperatures for a helical and unwound ferroelectric.

With the chiral term in the expansion, the Curie type temperature dependence of the low field soft-mode susceptibility in the smectic A phase becomes somewhat smoothed:

$$\chi_{sm} = \frac{\chi_{\perp}^2 \mu^2}{a(T - T_{ch}) + K_{\varphi} q_0^2}. \tag{13.16}$$

At a low field with ignored term $B\vartheta^4$ in Eq. (13.10), the dynamics of the director soft mode can be investigated using the Landau–Khalatnikov equation, see Section 6.5.1. The corresponding equation describing the balance of the viscous and elastic torques reads:

$$\gamma_{\vartheta} \frac{\partial \vartheta}{\partial t} = -a(T - T_{ch})\vartheta \tag{13.17}$$

Here, γ_{ϑ} is the rotational viscosity for the ϑ-angle change. From this equation is clear, that the inverse relaxation time of the soft mode $(\tau_{sm})^{-1}$ diverges at T_{ch} (on the SmA* side of the transition):

$$\tau_{sm}(SmA*) = \frac{\gamma_{\vartheta}}{a(T - T_{ch})} \tag{13.18}$$

Indeed, the Curie-type behaviour is in agreement with the experimental data [12] obtained by the pyroelectric technique on a SmC* mixture with $P_s \approx 600$ statV/cm or 2 mC/m^2, see Fig. 13.7. However, the maximum time at T_{ch} is limited by the value of $\tau_{sm} \approx 13\mu s$. To account for this saturation the fourth order term $B\vartheta^4$ in the free energy has to be taken into account.

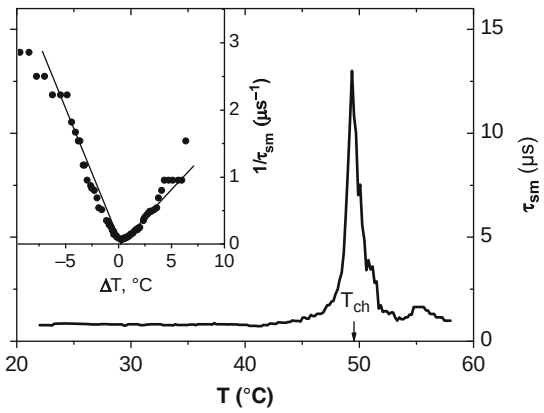

Fig. 13.7 Experimental temperature dependence of the soft-mode relaxation time (main plot), and demonstration of the Curie type behaviour of the inverse relaxation time on both sides of the phase transition (*inset*) in accordance with Eqs. (13.18) and (13.19) depicted by *solid lines*. Experimental parameters: chiral mixture with $P_s \approx 2$ mC/m^2, $a = 5{\cdot}10^4$ J m^{-3} K^{-1}, $T_{ch} = 49°$C, cell thickness 10 μm, the rotational viscosity found is $\gamma_{\vartheta} = 0.36$ Pa·s or 3.6 P

Strong field limit. For a very strong field, the helical structure is always unwound, the $B\vartheta^4$ term in expansion (13.10) dominates over $A\vartheta^2$ term, and the temperature dependencies of the induced tilt and susceptibility disappear:

$$\vartheta = \left(\frac{\chi_\perp \mu E}{B}\right)^{1/3} \text{ and } \quad \chi = \frac{\partial P}{\partial E} = \frac{1}{3}\left(\frac{\chi_\perp^4 \mu^4}{B}\right)^{1/3} E^{-2/3}$$

In fact, a strong field smears the soft mode behaviour and the phase transition vanishes. All these results are in agreement with experiments on dielectric and electrooptical properties owed to the soft mode in the chiral SmA* phase.

It is worth to mention that, in the higher symmetry SmA* phase, the soft mode is the only one elastic mode for the director. It is related to the short-range elastic excitations of the director tilt i.e. to the amplitude of the two-component order parameter of the less symmetric phase SmC*. Therefore, the soft mode may be called the amplitude mode and the corresponding excitation amplitudons [6, 13]. On the transition to the SmC* phase the continuous symmetry group D_∞ is broken and the reduced symmetry C_2 of the SmC* phase allows the Goldstone mode. The latter is related to the long-range excitations of the director azimuth i.e. the phase of the SmC* order parameter. Such excitations may be called phasons. Note that in the SmC* phase the soft and Goldstone modes coexist and have very different relaxation times.

13.1.3.3 Goldstone and Soft Modes in Sm C* Phase

In the SmC* phase the tilt is $\vartheta = \vartheta_s + \delta\vartheta$ where ϑ_s and $\delta\vartheta$ are spontaneous and the field induced tilt. In the absence of the field, ϑ_s is constant and minimisation of Eq. (13.10) with respect to P relates the spontaneous polarization to the tilt angle:

$$P_s = \chi_\perp \mu \vartheta_s$$

Then we exclude $P = \chi_\perp \mu \vartheta$ from Eq. (13.10) and minimize that equation with respect to ϑ:

$$\left(A - \chi_\perp \mu^2 + B\vartheta^2\right)\vartheta = \chi_\perp \mu E$$

In the low field limit, expanding $(\vartheta_s + \delta\vartheta)^2$ we shall find the soft mode susceptibility of the SmC* phase using exactly the same procedure as for crystalline ferroelectrics, see Eq. (13.8):

$$\chi_{sm} = \frac{\chi_\perp^2 \mu^2}{2a(T_{ch} - T)}$$

By analogy, instead of Eq. (13.18) for the soft-mode relaxation times on the SmC* side of the A*–C* transition we have

$$\tau_{sm}(SmC*) = \frac{\gamma_\vartheta}{2a(T - T_{ch})} \tag{13.19}$$

If we take into account the chiral terms, the low field susceptibility would consists of two parts (the soft and Goldstone modes):

$$\chi = \chi_{sm} + \chi_G = \frac{(1/2)\chi_\perp^2 \mu^2}{2a(T_{ch} - T) + K_\varphi q_0^2} + \frac{(1/2)\chi_\perp^2 \mu^2}{K_\varphi q_0^2} \tag{13.20}$$

The Goldstone mode does not show the explicit temperature dependence (in reality, parameters K_φ, q_0, μ depend on temperature but not critically) and the total susceptibility manifests a quasi Curie type behaviour at temperature T_{ch} with a cusp of amplitude

$$\chi_{sm}^m = \chi_\perp^2 \mu^2 / K_\varphi q_0^2 \tag{13.21}$$

qualitatively depicted in Fig. 13.8.

13.1.3.4 Measurements of Landau Expansion Coefficients

We can use Eqs. (13.13) and (13.14) and find parameters a, $\chi_\perp$ and μ in the SmA* phase. For this we need slow, automatically made temperature scans through the A* → C* phase transition with simultaneous measurements of SSFLC cell capacitance, i.e. $\chi_{sm}(T)$ and the electrooptical response i.e., field induced angle $\vartheta(T)$ at frequency 0.1–1 kHz. Then the asymptotic behaviour of capacitance at temperature $T > T_c$ provides us the value of dielectric constant and susceptibility $\chi_\perp = (\varepsilon_\perp - 1)/4\pi$, and the ratio $\chi_{sm}/e_c = \mu\chi_\perp$ gives us the coupling constant μ in the vicinity of the transition. After this we can substitute the μ value into any of the two Eqs. (13.13) and (13.14) and find the Landau coefficient a, e.g., from the slope $de^{-1}/dT = a/\chi_\perp$. Finally, with known coefficient a we can find coefficient B from the temperature dependence of the spontaneous tilt angle measured by the electrooptical switching technique $\vartheta_s = (a/B)^{1/2}(T_0 - T)^{1/2}$ in the SmC* phase.

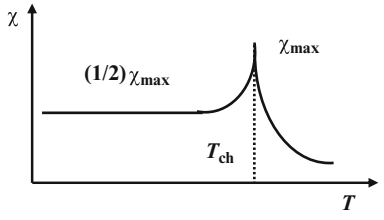

Fig. 13.8 Qualitative temperature dependence of dielectric susceptibility in the SmC* phase with the Goldstone mode plateau and the soft mode cusp

13.1.4 Electro-Optic Effects in Ferroelectric Cells

In principle, the Pikin's free energy [11] may be used for interpretation of almost all electro-optic effects at any temperature of the SmC* phase including the phase transition domain. However, for simplicity, it is more convenient to use different variables for different effects. For discussion of the pre-transitional electroclinic effect in the SmA* phase, one takes as a variable the tilt angle $\vartheta(T,\mathbf{E})$ assuming helical vector $q_0 = 0$ i.e. constant azimuthal angle φ. On the contrary, when discussing the Deformed Helix Ferroelectric (DHF) and Clark–Lagerwall effects observed in the SmC* phase well below the A*–C* transition, one assumes a tilt angle ϑ to be constant and operates with the director projection on the plane perpendicular to the helical axis, the **c-**director. The latter may be represented by a single variable, the azimuthal angle φ (T, **E**, **r**).

13.1.4.1 Electroclinic Effect in SmA

This electro-optical effect is related to the soft elastic mode just discussed [14]. For observation of the electroclinic effect one should use a proper chiral material in a standard planar cell with its normal along the x-axis and homogeneous alignment of the director in the SmA* phase (e.g., by rubbing polymer layers on both transparent electrodes in one direction, e.g., along the z-axis). In such a bookshelf structure the smectic layer normal is also parallel to the z-axis and the layers themselves are located in the x,y-plane, see Fig.13.9a. The electrooptical effect is observed in polarised light of a laser or using a polarising microscope with crossed polarisers. As discussed in the previous paragraph, the electric voltage applied to the electrodes (along the x-axis) induces a tilt ϑ_y of the director from the smectic normal according to Eq. (13.13). The electroclinic coefficient is field independent,

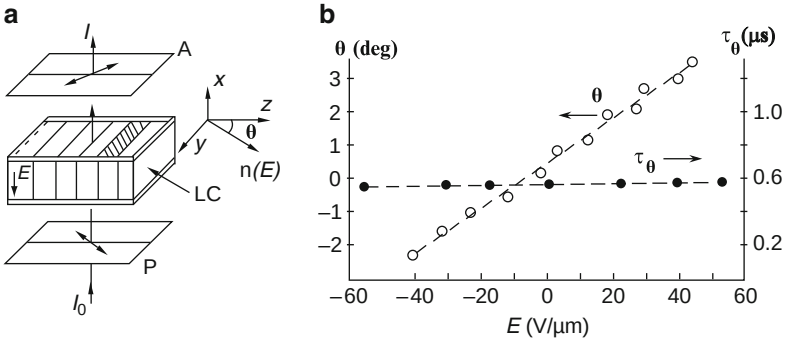

Fig. 13.9 Electroclinic effect in SmA* phase. The geometry of a bookshelf cell placed between polarizer (P) and analyser (A); ϑ is field controlled tilt angle of the director (**a**). Typical linear field dependence of angle $\vartheta(E)$ and characteristic soft-mode relaxation time independent of the field (**b**)

proportional to the tilt-polarisation coupling constant $\mu = P_s/\vartheta\chi_\perp$ and critically dependent on temperature

$$e_c = \frac{\chi_\perp \mu}{a(T - T_{ch})} = \frac{P_s/\vartheta}{a(T - T_{ch})} \tag{13.22}$$

The optical appearance of the electroclinic effect corresponds to a rotation of a birefringent plate in the *zy*-plane through angle $\pm\vartheta$ counted from the *z*-axis. Therefore, the optical transmission depends on orientation of the polariser with respect to the director (induced optical axis) and on the birefringence of a cell. As seen from Fig.13.9a, the maximal switched transmission (and optical contrast) is observed when the polariser is oriented along one of the $\pm\vartheta$ positions (-ϑ in the figure). In this case, the switching angle is 2ϑ and the transmission (see Section 11.1.1) is given by:

$$T = I/I_0 = \sin^2 4\vartheta \cdot \sin^2 \delta/2$$

For proper selected birefringence Δn at a given wavelength λ and cell thickness d, $\delta/2 = \pi\Delta nd/\lambda = \pi/2$ and the transmission is $T = \sin^2 4\vartheta$. In the ideal case, when there are neither light scattering nor reflections and the induced angle reaches $\vartheta = 22.5°$, the transmission is complete, $T = 1$. Such wide induced angles $\vartheta(E)$ can, in principle, be reached very close to the phase transition (from the SmA* side), but, in this case, its time characteristics are not very attractive. The reason is in the properties of the soft mode.

The dynamics of the electroclinic effect is, in fact, the dynamics of the elastic soft mode. From Eqs. (13.18) and (13.19) follows that the switching time of the effect is defined only by viscosity γ_ϑ and the term $a(T - T_c)$ and is independent of any characteristic size q^{-1} of the cell or material. It means that the relaxation of the order parameter amplitude is not of the hydrodynamic type controlled by term Kq^2 (K is elastic coefficient). For the same reason τ_ϑ is independent of the electric field in agreement with the experimental data, shown in Fig.13.9b. At present, the electroclinic effect is the fastest one among the other electro-optical effects in liquid crystals.

The coefficient γ_ϑ is rotational viscosity of the director similar to coefficient γ_1 for nematics. In fact, it does not include a factor of $\sin^2\varphi$ and, in the same temperature range, can be considerably larger than the viscosity γ_φ for the Goldstone mode. This may be illustrated by Fig. 13.10: the temperature dependence of viscosities γ_ϑ and γ_φ have been measured for a chiral mixture that shows the nematic, smectic A* and smectic C* phases [15]. The pyroelectric and electro-optic techniques were the most appropriate, respectively, for the measurements of γ_ϑ and γ_φ describing the viscous relaxation of the amplitude and phase of the SmC order parameter. The result of measurements clearly shows that γ_ϑ is much larger than γ_π and, in fact, corresponds to nematic viscosity γ_1.

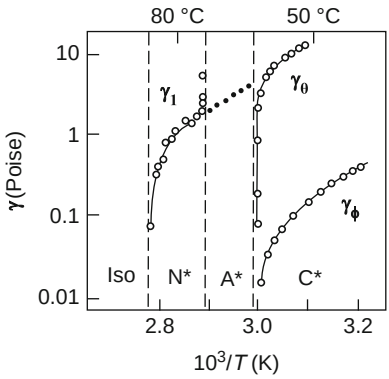

Fig. 13.10 Comparison of the temperature dependencies of viscosity coefficients γ_1 (nematic), γ_ϑ (soft mode) and γ_φ (Goldstone mode) of the same chiral mixture within the ranges of the N* and SmC* phases [15]. Note that γ_1 and γ_ϑ curves may be bridged through the SmA* phase (*black points*) where measurement have not been made

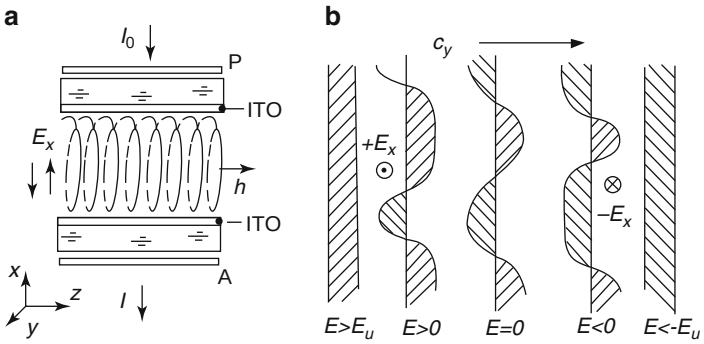

Fig. 13.11 Deformed Helix Ferroelectric effect. Scheme of observation of the effect (**a**) and the picture of distortion of the helical structure (**b**) in the zero, positive and negative field. P and A are polarizers and analyser, ITO means indium–tin oxide electrodes, I_0 and I are intensities of incoming and outgoing beams. Note that at $E = 0$ the helix is harmonic, for $0 < |E| < |E_u|$ anharmonic and for $|E| > |E_u|$ unwound

13.1.4.2 Helix Distortion and Deformed Helix Ferroelectric effect

To consider this effect we should leave our discussion of the phase transition and consider the field interaction with the helical structure deeply in the SmC* phase. Now the amplitude of the two-dimensional order parameter ϑ is considered constant, but the variation of the azimuthal angle φ is essential. The helical structure under discussion has the axis of the helix $\mathbf{h} \| z$, the electric field E_x is applied perpendicular to the helical axis and the boundary conditions are not taken into account. This corresponds to a thick cell with the geometry shown in Fig. 13.11a.

In the absence of field, the azimuth of the **c**-director is changed along the z-axis as $\varphi(z) = q_0 z$ and the polarization vector has projections onto the x,y-plane, $P_x = \sin q_0 z$ and $P_y = \cos q_0 z$. Therefore, for $E = 0$ the projections of the **c**-director and

$\mathbf{P}_s$-vector follow the harmonic law. This is shown for the $c_y(z)$-component in the middle of Fig. 13.11b. When the electric field is applied along the x-axis, it interacts with the spontaneous polarisation tending to install the $\mathbf{P}_s$-vector parallel to the field. The distortion begins at an infinitesimally small field, then develops as shown in the figure. Now the form of the helix has no longer a sine-form and, with increasing field, the probability for the **c**-director to be aligned along $+y$ becomes larger than along $-y$; it is shown by wider and narrower dashed areas, respectively. Then, the narrow areas transform into peaks called π-solitons [13]. In fact, the latter are defects (walls) that, finally, at a certain critical field disappear, the helix unwinds and the structure becomes uniform. Like in cholesterics, due to similar topological problems, the helix unwinding has to be assisted by other structural defects or thermal fluctuations.

In the stationary regime, for the balance of the elastic and electric torques we have a sine-Gordon equation [16]:

$$K_\varphi \frac{\partial^2 \varphi(z)}{\partial z^2} + P_s E \sin \varphi(z) = 0 \tag{13.23}$$

We guess, that *in the low field regime* the solution should have a form $\varphi(z) = q_0 z + \delta\varphi(z)$ with $\delta\varphi << q_0 z$. Substituting this in Eq. (13.23) we find

$$\xi^2 \frac{\partial^2 \delta\varphi(z)}{\partial z^2} + \sin(q_0 z + \delta\varphi(z)) = 0 \tag{13.24}$$

with field coherence length ξ given by

$$\xi^2 = \frac{K_\varphi}{P_s E} \tag{13.25}$$

Neglecting $\delta\varphi$ in the second term of Eq. (13.24) and substituting solution of the form $\delta\varphi = A \sin q_o z$ therein we get

$$-A q_0^2 \xi^2 \sin q_0 z + \sin q_0 z = 0$$

and obtain the amplitude A of the φ-angle modulation by electric field: $A = q_0^{-2} \xi^{-2}$.

Finally the field dependence of the twist angle is given by:

$$\varphi = q_0 z + \frac{P_s E}{K_\varphi q_0^2} \sin q_0 z \tag{13.26}$$

According to this result, for $E \to 0$, there is a small modulation of the helical structure that is a deflection from the harmonic low without a change in the structure period. With *increasing field*, the helix becomes distorted stronger and the soliton structure appears. Now a solution of Eq. (13.23) may be found in the

form of the elliptic functions or numerically. However, the critical field for the complete helix unwinding can be estimated just from comparison of the electric energy $-P_sE$ gained and the elastic energy $K_\varphi q_0^2$ lost due to unwinding,

$$E_u \approx K_\varphi q_0^2 / P_s. \tag{13.27a}$$

The exact solution of the same equation would give us a slightly lower critical field:

$$E_u = \frac{\pi^2 K_\varphi q_0^2}{16 P_s} \tag{13.27b}$$

For typical parameters $K_\varphi = 10^{-7}$ dyn (10^{-12} N), pitch ≈ 0.3 μm, i.e. $q_0 = 2 \times 10^4$ cm^{-1} $= 2 \times 10^6$ m^{-1}, $P_s = 300$ statC/cm^2 ($\approx$1 mC/m^2) the threshold field for helix unwinding is about $E_u = 9$ statV/cm (≈ 0.28 V/μm).

The Deformed Helix Ferroelectric (DHF) electrooptical effect [17] is observed in short pitch materials. It is a particular case of a more general phenomenon of the field induced helix distortion discussed above. The geometry of the cell showing DHF-effect is the same as presented in Fig. 13.11a; the helical axis $\mathbf{h} \| z$ is in the cell plane and smectic layers are perpendicular to the substrates. To study the new regime, the equilibrium pitch of the helix should be shorter than the visible light wavelength $P_0 < \lambda$ and the layer thickness d is much larger than P_0. A light beam with aperture $a >> P_0$ and wavelength λ passes through the cell along x. Due to the shortness of the pitch, the helical structure is not seen under a microscope and the cell behaves as a uniaxial plate with its optical axis directed along z in the absence of field.

In an electric field $\pm E$ the helical structure becomes strongly deformed, and cosφ(z) function oscillates between the two situations pictured in the sketches for $E > 0$ and $E < 0$ in Fig. 13.11b. These oscillations cause variation of the local refractive index which, being averaged over the entire cell, results in either clock- or anticlockwise *deviation of the optical axis* from the z-axis in the plane of the cell zy. The axis rotation angle α is proportional to $P_sE/K_\varphi {q_0}^2$. As usual, the cell is placed between two crossed polarisers and the first of them (P) is installed at the same angle α to the z-axis. As the optical transmission is proportional to $\sin^2\alpha$ and the helix distortion has no threshold, the DFH effect provides a smooth variation of the angle α and transmission T that is the so-called *grey scale*. The effect takes place up to the fields of helix unwinding E_u. The characteristic response times of the effect in low fields $E/E_u << 1$ are independent of spontaneous polarization and field strength and determined only by the rotational viscosity γ_φ and helix pitch P_0:

$$\tau_c = \frac{\gamma_\varphi}{K_\varphi q_0^2} = \frac{\gamma_\varphi P_0^2}{4\pi^2 K_\varphi} \tag{13.28}$$

Therefore at relatively low field a fast and reversible switching could be obtained in the DHF mode. Note that the optics of the DHF effect is almost the same as that of

the linear electro-optical effect in cholesterics described in Section 12.4. Moreover, formula (13.28) is identical to Eq. (12.44). However, as the rotational viscosity of SmC* phase $\sin^2\vartheta$ times less than the rotational nematic viscosity [8, 15], the DHF effect is faster than flexoelectric switching of cholesterics.

13.1.4.3 Frederiks Transition and Clark–Lagerwall Bistability

The switching of the director in the surface stabilised ferroelectric liquid crystal cells (SSFLC) [8] has briefly been discussed in Section 13.1.2. Due to its importance for ferroelectric liquid crystal displays we shall discuss this effect in more detail. The geometry of a planar cell of thickness d is shown in Fig.13.1.2. Now, the helical structure is considered to be unwound. We are interested in the field and time behaviour of the director or **c**-director given by angle $\varphi(x)$, and this process is considered to be independent of z and y- coordinates. The smectic C* equilibrium tilt angle ϑ is assumed constant.

(i) Case of infinitely strong zenithal anchoring (Frederiks transition). First we shall explain why, for the infinite zenithal anchoring of SmC* liquid crystal at the boundaries of a SSFLC cell, the bistability is absent. Let define an easy axis parallel to z fixed, for instance, by a rubbing procedure. Consider rather an artificial but simple case of the infinitely strong zenithal anchoring strength $W_z \to \infty$ and extremely weak (hardly possible!) azimuthal strength $W_a \to 0$. In the zero field, due to strong zenithal anchoring, the director **n** ought to be in one of the two stable states, left or right in the zy-plane. Hence, angle φ is either 0 or π for the **c**-director coincides with either $+y$ or $-y$. Then the **n** director forms either $+\vartheta$ or $-\vartheta$ angle counted from the z-axis and the polarisation vector $\mathbf{P}_s \perp \mathbf{n}$ is looking either up or down.

Assume that $\varphi = 0$, $\vartheta = +\vartheta$ and $\mathbf{P}_s$ is looking up. Then, with the electric field directed down, the situation becomes unstable and, at a certain threshold field, due to some φ-fluctuation in the bulk and $\mathbf{P}_s\mathbf{E} = P_s E\cos\varphi$ interaction energy, a torque appears, which drives the director along the conical surface with apex angle 2ϑ.

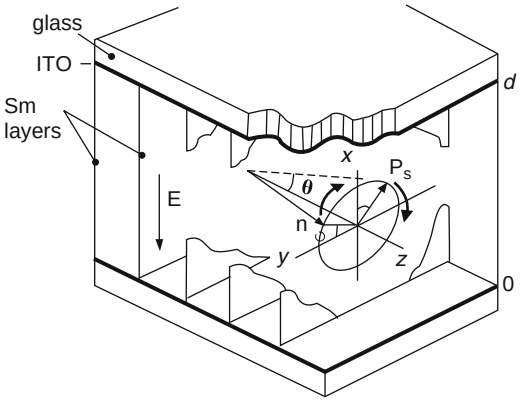

Fig. 13.12 Clark–Lagerwall effect in thin SSFLC cell. Application of the electric field E between the ITO electrodes causes up-down switching of spontaneous polarization P_s accompanied by conical motion of the director **n**. The projection of the **n**-vector on plane xy is **c**-director forming an angle φ with respect to y. ϑ is the tilt angle between **n** and the smectic layer normal z

The beginning of this motion is shown in Fig. 13.12 by curved arrows. In the strong enough field, everywhere except surfaces, the final situation will correspond to $\varphi = \pi$, $\vartheta = -\vartheta$, $\mathbf{P}_s$ directed down. Then, with a change in the field polarity, the process reverses.

The balance of the volume torques is expressed by the same sine-Gordon equation (13.23) rewritten here for convenience:

$$K_\varphi \frac{\partial^2 \varphi(x)}{\partial x^2} + P_s E \sin \varphi(x) = 0 \tag{13.29}$$

However the physics of the two phenomena is different. Now, there is no helix and the elastic term $K_\varphi \partial^2 \varphi / \partial x^2$ corresponds to the uniform rotation of the **c**-director in the bulk with fixed φ_s angles at the boundaries. Thus, we deal with a kind of the Frederiks transition, like in nematics, however, with another electrical torque and the confinement for the director motion along the cone surface. The first integral of Eq. (13.29) is given by:

$$\frac{\xi^2}{2}\left(\frac{\partial \varphi}{\partial x}\right)^2 = \cos \varphi + C \tag{13.30}$$

where coherence length ξ is defined by Eq.(13.25). The range of the field-induced $\varphi(x)$-variation is 0-π. Due to the symmetry of our cell with respect to the middle plane yz at $d/2$, the maximal **c**-director deviation from the z-axis is $\varphi(d/2) = \varphi_m$. Therefore,

$$\frac{\partial \varphi}{\partial x}|_{d/2} = 0,\ C = -\cos \varphi_m$$

and Eq.(13.30) takes the form: $\partial \varphi / \partial x = \left(\sqrt{2}/\xi\right)(\cos \varphi - \cos \varphi_m)^{1/2}$. The corresponding integral

$$\int_0^\varphi \frac{d\varphi}{(\cos \varphi - \cos \varphi_m)^{1/2}} = \frac{d\sqrt{2}}{\xi} \tag{13.31}$$

may be reduced to the Legendre form of the 1st kind elliptic integral. Its solution may be found in the form of elliptic functions, which would give us the angle φ as a function of $d\sqrt{2}/\xi$ and φ_m.

From Eq. (13.29) is seen that, at $\varphi = 0$, there is no electric torque exerted on the director. Thus, there should be a threshold for the distortion as in the case of the Frederiks transition in nematics. We can find the threshold field E_c, considering a small distortion $\varphi \to 0$. The equation

$$\xi^2 \frac{\partial^2 \varphi}{\partial x^2} + \varphi = 0 \tag{13.32}$$

has solutions $\varphi(x) = \varphi_m \sin qx + C$ where constant $C = 0$ is found from the boundary condition: $\varphi = 0$ for $d = 0$. Substituting $\varphi(x)$ into (13.32) we find $-\xi^2 q^2 + 1 = 0$. As minimum value of q is fixed by rigid boundary conditions, $q_{\min} = \pi/d$ we arrived at the threshold condition $1/\xi_c = q_{\min}$. Hence, the threshold field for the "quasi-Frederiks" transition is:

$$E_F^* = \frac{\pi^2 K_\varphi}{P_s d^2} \tag{13.33}$$

For instance, for $K_\varphi = 10^{-7}$ dyn, $d = 2 \times 10^{-4}$ cm, $P_s = 300$ statC/cm^2 (1 mC/m^2), the threshold field is $E_F^* \approx 0.1$ statV/cm, i.e. 3 kV/m. Due to a high value of P_s, the Frederiks type distortion in SmC* can be observed at extremely low voltage across the cell ($U_c = dE_c \approx 30$ mV for 10 μm thick cell). However, independently of the field magnitude, after switching the field off, the distortion relaxes to the initial uniform structure, $\varphi(x) = 0$. The relaxation time of the distorted structure is owed to pure elastic, nematic-like torque and for small distortion only fundamental Fourier harmonic is important,

$$\tau_F^* = \gamma_\varphi / K_\varphi q_{min}^2 = \gamma_\varphi d^2 / K_\varphi \boldsymbol{\pi}^2. \tag{13.34}$$

For larger distortions, the relaxation rate will be determined by the sum of the rates m/τ_F^* of each harmonic with number m. Evidently, there is *no bistability* in this case.

(ii) Case of finite anchoring energy (Clark-Lagerwall bistability). In reality, both the zenithal and azimuthal anchoring strengths are always finite, therefore the surface terms should be added to the balance of torques. But what is the anchoring energy for the smectic C* phase? In Section 10.2.3 we introduced the zenithal and azimuthal anchoring energies W_z and W_a for the director **n** in both nematics and cholesterics. But in this paragraph we operate with another variable, the **c**-director or angle φ and should reconsider the problem. In Fig. 13.13 the easy axis z is situated in the substrate plane xy and the end of the director $\mathbf{n} = 1$ is confined to move along the semicircle (dot line). The conical angle ϑ between **n** and the easy axis z is assumed to be fixed. The projection of the director on the substrate plane

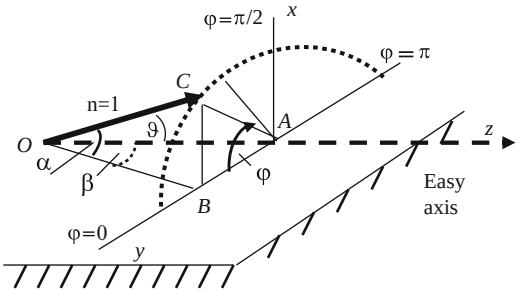

Fig. 13.13 Geometry for discussion of the anchoring energies for the **c**-director. α and β are the angles the director **n** forms with the easy axis z coinciding with the normal to smectic layers; ϑ is the director tilt angle and AC is the c-director forming angle φ with y-axis

OB forms angles α and β with respect to **n** and easy axis z, respectively. Each arbitrary point C on the semicircle is characterised by the only variable φ used in Eq. (13.29). Now we would like to make find the strength of anchoring for the **c**-director in the SmC phase, no matter chiral or achiral.

In the Rapini approximation, the zenithal and azimuthal anchoring energies are defined for the director **n** in terms of angles α and β:

$$W_z = \tfrac{1}{2}W_z^0 \sin^2\alpha \quad \text{and} \quad W_a = \tfrac{1}{2}W_a^0 \sin^2\beta \tag{13.35}$$

Let express the same energies using angles ϑ and φ, which describe the motion of the director in the smectic C* (or C) phase. Using the elementary geometry and the fact that all angles OAC, OAB, OBC and CBA are equal to π/2, we find

$$W_z = \tfrac{1}{2}W_z^0 \sin^2\vartheta \cdot \sin^2\varphi \quad \text{and} \quad W_a = \tfrac{1}{2}W_a^0 \frac{\sin^2\vartheta\cdot\cos^2\varphi}{1-\sin^2\vartheta\cdot\sin^2\varphi} \tag{13.36}$$

Typically $\vartheta \approx 0.5$ or less, and the φ-angles for the anchored director at the surface are even smaller (the case of the break of anchoring is discussed below). Then the denominator of W_a is close to unity and we can approximately write

$$W_z \approx \tfrac{1}{2}W_z^0 \sin^2\vartheta \cdot \sin^2\varphi = \tfrac{1}{2}W_z^\varphi \sin^2\varphi \tag{13.37a}$$

and

$$W_a \approx \tfrac{1}{2}W_a^0 \sin^2\vartheta \cdot \cos^2\varphi = \tfrac{1}{2}W_a^\varphi \cos^2\varphi. \tag{13.37b}$$

Note that the amplitudes of the anchoring energy W_z^φ and W_a^φ defined for the azimuthal angle φ include factor $\sin^2\vartheta \approx 0.1$, which, unfortunately, is often forgotten in the literature. This is very important for our discussion of bistability. For simplicity and just to begin with, let assume that the azimuthal anchoring energy is negligible.

If we are only interested in the Frederiks-type threshold we should add the surface term $\pm W_z^\varphi \varphi$ to Eq. (13.32). Then, a finite anchoring only increases the apparent cell thickness by two extrapolation lengths b^φ: $d_{\text{app}} = d + 2b^\varphi$ where $b^\varphi = K_\varphi / W_z^\varphi$. For realistic values of $K_\varphi = 10^{-7}$ dyn and W_z (measured for nematics) ≈ 0.1 erg/cm^2 ($W_z^\varphi \approx 0.01$ erg/cm^2), the value of $b^\varphi \approx 2 \times 10^{-5}$ cm (0.2 μm) is considerably less than a typical cell thickness (few micrometers) and the second term in d_{app} is of minor importance.

To discuss a bistability, we should leave the small − φ approximation and go back to the equation (13.29) with the Rapini surface energy added.

$$K_\varphi \frac{\partial^2\varphi(x)}{\partial x^2} + P_s E \sin\varphi(x) \pm \tfrac{1}{2}W_z^\varphi \sin^2\varphi = 0 \tag{13.38}$$

Now we are interested in the strong field case when distortion has a specific form. Like in nematics, well above the Frederiks transition, the director alignment is uniform throughout the SSFLC cell thickness except two layers of thickness b^{φ} adjacent to electrodes. To have a bistability we should break the initial zenithal anchoring, that is reach the second critical field E_c, whose coherence length becomes comparable with the surface extrapolation length, $\xi_c = b^{\varphi}$, see Section 11.2.4. Using the coherence length from Eq. (13.25) the condition for the break of anchoring is given by

$$\left(\frac{K_{\varphi}}{P_s E_c}\right)^{1/2} = \frac{K_{\varphi}}{W_z^{\varphi}} \text{ or } E_c = \frac{\left(W_z^{\varphi}\right)^2}{P_s K_{\varphi}} \tag{13.39}$$

Hence, for typical values of $K_{\varphi} = 10^{-7}$ dyn, $P_s = 300$ statC/cm^2, $W_z^{\varphi} = 0.01$ erg/cm^2, the break of anchoring occurs at $E_c = 3$ statV/cm (or 0.1 V/μm).

Thus, we see, that for a typical value of $W_z^{\varphi} \approx 0.01$ erg/cm^2 (corresponding to nematic anchoring as high as $W_z \approx 0.1$ erg/cm^2) we only need a voltage as low as $U = 0.2$ V to break the zenithal anchoring in 2 μm thick cells. As soon as the initial anchoring is broken, the director is driven by the same electric field into the new stable position at $\varphi = \pi$. When the field is switched off the director is still held in the new position by the zenithal anchoring until the field of the opposite polarity switches it back to $\varphi = 0$. Thus, in SSFLC cells, we have real bistable switching at rather low fields [18]. Such cells are unequivocally ferroelectric!

13.1.5 Criteria for Bistability and Hysteresis-Free Switching

13.1.5.1 Cells with No Insulating Layers

In real SmC* cells both $W_z^{\varphi}$and W_a^{φ} are finite. A finite azimuthal strength would create an additional surface torque trying to move the director from its angular positions at $\varphi = 0$ or $\varphi = \pi$ to the easy axis z, Fig.13.13. On the cone surface, the minimum anchoring energy W_a^{φ} corresponds to director position at $\varphi = \pi/2$ and the minima of W_z^{φ} are at $\varphi = 0$ and $\varphi = \pi$. But what will happen if $W_z^{\varphi} = W_a^{\varphi}$? It follows from Eqs. (13.37) that the sum W^{φ} of the two anchoring energies with equal amplitudes W

$$W^{\varphi} = W\sin^2\vartheta\left(\sin^2\varphi + \cos^2\varphi\right) = W\sin^2\vartheta$$

becomes independent of φ and the director is free to take any position on the cone as though there were no anchoring at the substrates. Thus, due to a competition between equal $W_z^{\varphi}$and W_a^{φ}, there is no stable states at $\varphi = 0$ and $\varphi = \pi$, and, of course, no bistable switching. In fact, what does control the bistability is the difference W_{za}^{φ} between W_z^{φ} and W_a^{φ}! Hence, the *criterion for bistability* is very simple:

$$\infty > W_{za}^{\varphi} = W_z^{\varphi} - W_a^{\varphi} > 0 \tag{13.40}$$

As to dynamics of the response of a SSFLC cell to the alternating field, it is controlled by Eq. (13.38) with the viscous $\gamma_\varphi d\varphi/dt$ torque added. When the helical structure of the SmC* is unwound in a thin cell (a typical case) one can neglect the elastic torque $\partial^2\varphi/\partial x^2$. If, in addition, the anchoring energies W_z^{φ} and W_a^{φ} are reasonably weak, the electric field torque would solely be balanced by the viscous torque:

$$\gamma_\varphi \frac{d\varphi}{dt} = P_s E \sin\varphi \tag{13.41}$$

Here, the viscosity coefficient γ_φ corresponds to the azimuthal motion of the director. From this equation, for small distortions, we immediately find the time of the response to an external field.

$$\tau_\varphi = \frac{\gamma_\varphi}{P_S E} \tag{13.42}$$

For larger φ the response is not exponential, however, controlled by the same physical parameters with a numerical factor of 1–2. The viscosity γ_φ can be found from the measurements of kinetics of the optical transmission.

13.1.5.2 Role of Aligning Layers in Bistability

If one were capable to align a SmC* without insulating layers, e.g., by rubbing uncovered electrodes or by smectic layer shearing, then, in a cell with W_{za}^{φ} not exceeding 0.01 erg/cm^2, the bistable switching would be observed at voltages less than 1V for P_s as low as 20 nC/cm^2. However, as a rule, there are insulating alignment layers covering the electrodes, which have their own capacitance. For a given a.c. voltage U across the electrodes, such layers may dramatically change both the amplitude and phase of field E_{LC} on the liquid crystal layer. Field E_{LC} may even have the opposite sign with respect to voltage applied! Thus, the criterion for the bistability (13.20) should also change.

Consider a two layer SSFLC cell, Fig.13.14, consisting of a liquid crystal layer (white) and a single alignment insulating layer (grey); the latter mimics two alignment layers of a typical experimental cell. For simplicity, both the liquid crystal and aligning layers are assumed to be nonconductive and having constant dielectric permittivities. The x-component of the dielectric displacement D_x and the total potential difference along the close contour (the Maxwell and Kirchhof equations, respectively) are given by:

$$\begin{aligned} \varepsilon_{IL} E_{IL} &= \varepsilon_{LC} E_{LC} + 4\pi P_x \equiv D_x \\ d_{IL} E_{IL} &+ d_{LC} E_{LC} = U, \end{aligned} \tag{13.43}$$

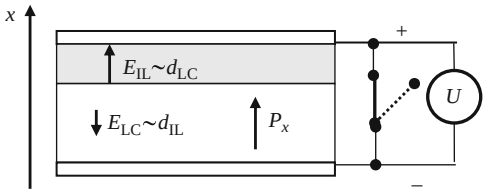

Fig. 13.14 A model showing distribution of the electric field strength over an aligning insulating layer (E_{IL}) and a ferroelectric liquid crystal layer (E_{LC}) in a SSFLC cell. The electric voltage U is switched ON with polarity shown by (+) and (−) signs

Here, suffices (IL) and (LC) mark insulating and liquid crystal layers, d is their thickness, P_x is x-component of spontaneous polarization parallel to the cell normal. From this set we immediately find the electric field in each layer,

$$E_{LC} = \frac{\varepsilon_{IL}U - 4\pi P_x d_{IL}}{(\varepsilon_{LC}d_{IL} + \varepsilon_{IL}d_{LC})} \quad \text{and} \quad E_{IL} = \frac{\varepsilon_{LC}U + 4\pi P_x d_{LC}}{(\varepsilon_{LC}d_{IL} + \varepsilon_{IL}d_{LC})}. \tag{13.44}$$

For $P_x \neq 0$, even without an applied voltage ($U = 0$, short circuited electrodes), there are "built-in" electric fields in both liquid crystal and aligning layers and these fields are opposite to each other.

Now, consider a switching process. Let, in the beginning, the director is close to $\varphi = 0$ and polarization $\mathbf{P}$ is almost parallel to the electrodes i.e. P_x component is small). When the voltage is switched ON along positive x, at first, the field E_{LC} drives the polarization vector into the $+$ x-direction along the field, as shown in Fig.13.14. Then the counteracting polarization term in Eqs. (13.44) reduces the E_{LC} field and increases field E_{IL} and a charge on the insulating capacitor. This effect is detrimental for devices because it increases the total voltage necessary to switch the director completely from $\varphi = 0$ to $\varphi = \pi$. With sufficient voltage the state $\varphi = \pi$ is achieved and the director is temporary anchored at the new position. Let us see now whether this state is stable or not.

When the voltage is switched OFF then, according to Eq. (13.44), the field E_{LC} changes its sign and drives the P_{s} vector in the opposite direction. Now, if P_{s} is large and the torque $\mathbf{P}_{\mathrm{s}} \times \mathbf{E}_{\mathrm{LC}}$ exerted on the polarization (and, consequently on the director) in the OFF state is high enough, it would break anchoring at $\varphi = \pi$ and, under the influence of E_{LC}, the director leaves the $\varphi = \pi$ position and moves back to $\varphi = 0$. The cycle is over and we are in the initial situation. It means that there is no bistability for high enough P_{s}.

Therefore, if we would like to work in the bistable regime, we should avoid the action of the reversed field. According to the first of the last two equations, it means the condition of $\varepsilon_{IL}U >> 4\pi P_x d_{IL}$ to be fulfilled, that is the alignment layers must be as thin as possible, their dielectric constant (ε_{IL}) large and P_{s} of the SmC* small. The latter would be in contradiction with a low threshold field for the bistability given by Eq. (13.39). Indeed, in experiments, the genuine bistable switching is always observed for liquid crystals with intermediate values of $P_{\mathrm{s}} \approx$ 20–40 nC/cm^2.

There is, however, another way to fight with the inverse field. Both the alignment and liquid crystal materials can be made conductive. The conductivity σ would screen the built-in field E_{IL} and accelerate its relaxation. Then, for a voltage pulse of

duration exceeding τ_φ given by Eq. (13.42), the built-in field would not prevent bistable switching if

$$\varepsilon_{LC}/\sigma_{LC} > \varepsilon_{IL}/\sigma_{IL} \tag{13.45}$$

This is an additional criterion for bistability valid for conductive ($\sigma > 0$) materials [19]. In experiments with very conductive alignment layers the bistability is much easier to observe.

13.1.5.3 V-Shape Effect

In some applications the hysteresis and the threshold character of the director switching are undesirable because they do not allow a grey scale to be realised. The hysteresis-free switching means the zero coercive field for the director switching and the absence of bistability. Then one can observe the hysteresis-free V-shape switching. In this case, the curve of the optical transmission as a function of the total voltage on the cell $T(U)$ acquires a shape of the letter "V" (no hysteresis) instead of letter "W" characteristic of hysteresis. For the first time the hysteresis-like switching was observed in a chiral material having both SmC* and antiferroelectric SmC*$_A$ phase at temperatures close to the phase transition between them [20] and explained by a kind of frustration between the two phases having very low energy barrier between them. However, the absence of hysteresis is also a characteristic feature of the SmC* phase well below the phase transition temperature when a special condition of $W_z^\varphi = W_a^\varphi$ discussed above is fulfilled, although this case is rather incident. Numerous experiments and modelling have unequivocally shown that the hysteresis-free switching with a clear V-shape of the $T(U)$ transmission curve in the SmC* phase may always be achieved when one uses relatively thick alignment layers and selects proper parameters for a liquid crystal and the layers [21].

13.2 Introduction to Antiferroelectrics

13.2.1 Background: Crystalline Antiferroelectrics and Ferrielectrics

Liquid crystal ferri and antiferroelectrics have many features discovered for years of comprehensive studies of corresponding crystalline substances. Thus, it would be convenient and instructive to begin with a short introduction in the structure and properties of antiferroelectric crystals. A difference between ferro-, ferri and antiferroelectrics is schematically shown in Fig. 13.15, where the three very simplified

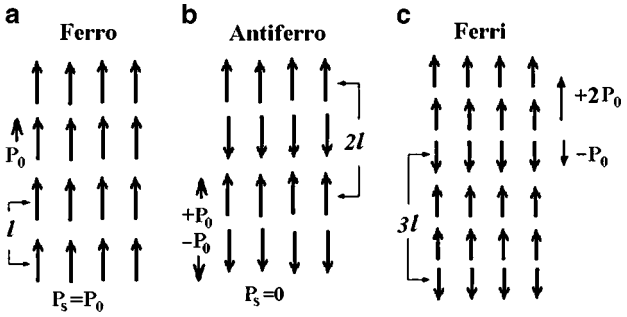

Fig. 13.15 Schematic structure of a ferroelectric (**a**), an antiferroelectric (**b**) and a ferrielectric (**c**). Note that period of each structure is different: l, $2l$ and $3l$, respectively

structures are depicted. In ferroelectrics, the dipoles are oriented parallel to each other everywhere, the period of the lattice is l, and, if each layer has spontaneous polarization $\mathbf{P}_0$ then the resulting spontaneous polarization of such a ferroelectric structure, $\mathbf{P}_s = \mathbf{P}_0$. An antiferroelectric may be represented as a combination of two dipolar sublattices built in each other, as shown in Fig. 13.15b. The periods of each sublattice and the entire structure are equal to $2l$. An antiferroelectric has a higher translational symmetry than a ferroelectric. In sketch (b), we can recognise the additional planes of reflection situated exactly in the middle between any pair of dipolar layers. Therefore, despite each layer is polar and have finite local polarization $\mathbf{P}_0 \neq 0$, the macroscopic spontaneous polarization is absent $\mathbf{P}_s = 0$.

In some crystals the location of dipole moments can even be more complicated. For example, in Fig. 13.15c, one layer with the dipoles looking down alternates with two layers where the dipoles are looking up. Therefore we have three-layer periodicity $3l$ with two antiparallel layers and one extra polar layer. Such a structure may be considered as a mixture of the ferroelectric and antiferroelectric structures and is called ferrielectric. In case (c), the ferroelectric fraction is one part per period, $q_F = 1/3$ and the spontaneous polarization is finite, $\mathbf{P}_s = (1/3)\mathbf{P}_0$. For pure antiferroelectric phase $q_F = 0/2$ and for pure ferroelectric one $q_F = 1/1 = 1$. More generally, for different ferrielectric structures $q_F = n/m$, where m is the number of layers in the unit cell (period) and $n < m$ is the ferroelectric layer fracture per unit cell, both being integers. Then, for both n and $m \to \infty$, $n/m \to 1$, the difference between n and m become smaller and smaller and the so-called *Devil's staircase* forms.

With increasing temperature the order of dipoles in each sublattice decreases and, at a certain temperature, a phase transition into the paraelectric phase occurs. It may be either second or first order transition. In the paraelectric phase local polarization P_0 vanishes. The nature of the spontaneous polarization is similar in solid ferro- and antiferroelectrics. In both cases, the dipole-dipole interactions are dominant. For example, if dipoles are situated in the points of the body-centred cubic lattice, they preferably orient parallel to each other and such a structure is ferroelectric. However, the same dipoles placed into the points of a simple cubic

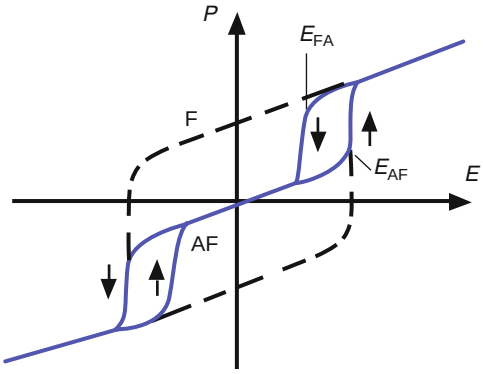

Fig. 13.16 Typical hysteresis-type dependence of the total (spontaneous and induced) polarization P as a function of the external field for a ferroelectric (*dashed curve*) and antiferroelectric (*solid curve*). *Arrows* show the direction of the field cycling

lattice prefer to align anti-parallel to each other and form an antiferroelectric structure. Very often the difference in electrostatic energy between the parallel and anti-parallel dipolar structures is small and the phase transitions occur between ferro- and antiferroelectric phases.

Such a transition of an antiferroelectric into a ferroelectric state can also be observed in an electric field E exceeding a certain threshold E_{AF}, Fig. 13.16, because in the presence of the field the ferroelectric structure becomes more favourable. When the polarity of the field changes, all dipoles are realigned following the field. At large fields $\pm E$ the two opposite ferroelectric states are energetically equivalent. If the switching between $\pm E$ is fast enough the polarization follows the dashed curve with the hysteresis characteristic of typical ferroelectrics (like in Fig. 13.2). For slow field cycling, the antiferroelectric state has enough time to recover at $E < E_{FA}$ and one observes a double hysteresis loop indicative of the antiferroelectric nature of the ground state. The solid line in Fig. 13.16 shows this type of tri-stable switching. Note that in low fields between $\pm E_{FA}$ the antiferroelectric behaves as a conventional linear unpolar dielectric.

A difference between ferro- and antiferroelectrics may also be discussed in terms of the soft elastic mode [3]. In the infinite ferroelectric crystal, there is no spatial modulation of the spontaneous polarization (only dipole density is periodic). Therefore, at the transition from a paraelectric to the ferroelectric phase, both the wavevector q for oscillations of ions responsible for polarization and the correspondent oscillation frequency $\omega = Kq^2$ tend to zero. We may say that the soft elastic mode in ferroelectrics condenses at $q \to 0$. In antiferroelectrics, the sign of the local polarization P_0 alternates in space with wavevector $q_0 = 2\pi/2l = \pi/l$ and the corresponding ion oscillation frequency is finite, $\omega = Kq_0{}^2 = K\pi^2/l^2$. It means that in antiferroelectrics the soft mode condenses at a finite wavevector π/l and rather high frequency. As a result, in the temperature dependence of the dielectric permittivity at low frequencies, the Curie law at the phase transition between a paraelectric and antiferroelectric phases is not well pronounced.

13.2.2 Chiral Liquid Crystalline Antiferroelectrics

13.2.2.1 Discovery and Polymorphism

The very first observation of antiferroelectric properties in a chiral liquid crystalline mixture was reported in 1982 [22]. The pyroelectric technique clearly showed the absence of spontaneous polarization in the zero field and a growth of pyroelectric coefficient γ with characteristic saturation at the field strength of about 0.5 V/μm. In addition, the value of γ was two orders of magnitude higher than the value of γ for the electroclinic effect in the SmA* phase. The original picture presented in that paper is reproduced here without any changes, Fig. 13.17. We can see that, in the field absence (ground state), the tilt of molecules alternates from layer to layer, however, in the strong field, the tilt within the smectic layers is uniform. Nowadays such pictures are called *anticlinic* and *synclinic*, respectively. The local polarization is always perpendicular to the tilt plane and also alternates in the zero field as shown by symbols • and ⊕.

More impressive results, particularly, the tristable switching, were demonstrated by Fukuda group [23]. In Fig. 13.18 we can see the chemical formula and the phase diagram of MHPOBC. Different antiferroelectric and ferrielectric phases in single compound 4-(L-methylheptyloxy-carbonyl)-4′-octylbiphenyl-4-carboxylate (MHPOBC) were unequivocally shown to exist by optical and electrooptical techniques, dielectric spectroscopy, X-ray analysis, etc. In this compound, additionally to the known SmA* and SmC* (SmC_β* in the figure) phases, new phases have been revealed: antiferroelectric SmC_A* and SmC_α* and ferrielectric SmC_γ* phase. This work stimulated fast development of investigations in this area, see review articles [24, 25]. As we see, MHPOBC reveals rich polymorphism and becomes a model compound for further studies. Other liquid crystals made up of chiral molecules that include three-benzene-ring cores and long tails with asymmetric carbon atoms and dipole moments also show a variety of similar phases (often called subphases). It has taken about 20 years to understand the structure of these subphases although many subtle details are still under question.

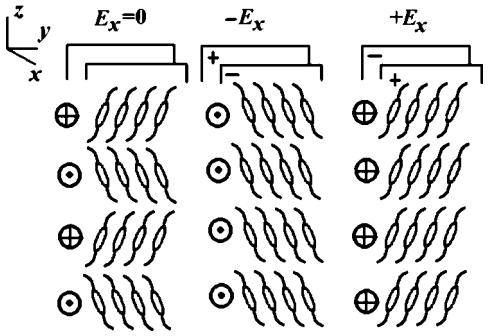

Fig. 13.17 Field induced switching between the antiferroelectric structure (*left sketch*) and two ferroelectric structures with opposite tilt and spontaneous polarization $\mathbf{P}_s$. The directions of $\pm\mathbf{P}_s$ coincides with the field $\pm E_x$ directions [22]

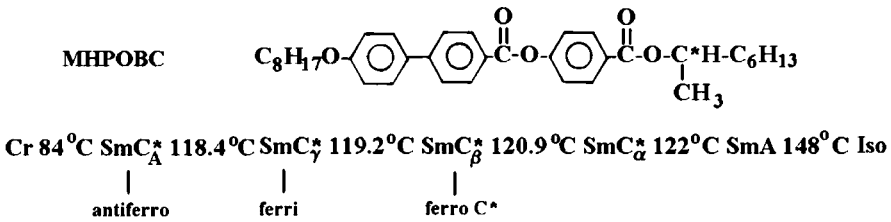

Fig. 13.18 Chemical formula and the phase sequence of the compound MHPOBC demonstrating a variety of transitions between ferro-, ferri- and antiferroelectric phases

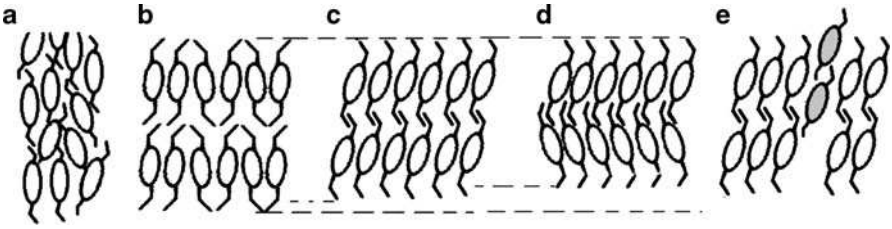

Fig. 13.19 Intermolecular interactions responsible for formation of different liquid crystal phases: attractive anisotropic van der Waals and repulsive steric interactions for nematics (**a**), van der Waals (bifilic) and steric for SmA* (**b**), steric quadrupolar interaction for SmC* (**c**) and SmC*$_A$ (**d**) owed to molecular biaxiality. The density is increasing in a sequence: orthogonal (**b**), synclinic (**c**) and anticlinic (**d**) phases. An interlayer steric correlations in SmC* (**e**) are shown by displacements of "grey molecules". Note that the displacement of "gray molecules" may influence the next to nearest layer via a kind of relay race mechanism

On account of the new experimental data and theoretical works, the same phase sequence for (L)-MHPOBC well purified from the right-handed (D)-enantiomer may be re-written as follows (for decreasing temperature) [26]:

$$\text{Iso} \rightarrow \text{SmA}* \rightarrow \text{SmC}*_{\alpha} \rightarrow \text{SmC}* \rightarrow \text{SmC}*_{FI2} \rightarrow \text{SmC}*_{FI1} \rightarrow \text{SmC}*_{A} \quad (13.46)$$

Here, ferrielectric SmC*$_{FI1}$ and SmC*$_{FI2}$ phases replace SmC*$_{\gamma}$ and SmC*$_{\beta}$ phases. Further on we shall repeatedly refer to this phase sequence.

13.2.2.2 Molecular Interactions

A variety of different phases emerging in narrow temperature interval and also easily converted into each other by electric field (see below) testifies that different inter-layer interactions have comparable energy. Moreover, molecules in one layer may interact even with next-to-nearest layers. Figure 13.19 may help to understand some hierarchy of interactions beginning from the nematics and going down with temperature. It is instructive to assume that our molecules are elongated, biaxial,

chiral with relatively long tails and having transverse dipole moments. At relatively high temperature of the nematic phase they rotate free and may be represented by ellipsoids with tails showing translational invariance, sketch (a). Between such ellipsoids the most important are the attractive anisotropic Van der Waals interactions (of Maier-Saupe type, decaying with distance as r^{-6}) and repulsive steric ones. In the SmA* phase (b), due to decreasing thermal motion, the molecule form layers because the specific core-to-core and tail-to-tail Wan-der-Waals interactions may be more preferable, as very often observed in lyotropic systems (biphilic effect). However, molecular rotation about the layer normal is still free and, for a moment, the chirality may be ignored.

Remember now that our molecules are biaxial i.e. they have either a lath-like form or a special form of the tails anti-symmetrically bent in the figure plane. Then, with decreasing temperature, mostly due to steric reasons, they may acquire a collective tilt and form a SmC* phase (c). Now, due to chiral symmetry C_2 and transverse molecular dipoles each smectic layer acquires spontaneous polarization P_s and the helical arrangement of the layers on a micrometer scale. At even lower temperature, specific packing of molecular tails can stabilise the antiferroelectric phase. Indeed, the anticlinic arrangement of cores emerges (d) that increases density and reduces entropy. The steric forces can also provide the molecular interaction not only within the smectic layers but also between near neighbour (*NN*) layers as qualitatively pictured in Fig. 13.19e. Moreover, it is also seen how the distorted part is advanced up beyond the boundary of a neighbour layer. It means that the steric correlations may also be installed between next-to-nearest neighbours (*NNN*).

Similarly, the electrostatic correlations may be installed between *NN* and *NNN* layers. Note that P_0 is a large collective dipole moment lying, due to chirality, in the layer plane, perpendicularly to the tilt plane. The energy between permanent molecular dipoles decay with distance as r^{-3} (see Section 3.2). It seems that the negative repulsive forces between parallel permanent dipoles may provide the long-range interaction necessary for the antiparallel dipole packing i.e. antiferroelectric order of the layers. However, it is known from electrodynamics, that the same molecular dipoles oriented even in the same direction within a thin, infinitely wide (smectic) layer do not create an electric field outside the layer (due to complete compensation of the fields of individual dipoles). Therefore dipolar smectic layers cannot interact directly with each other. Nevertheless, there is a long-range interaction owed to fluctuations of P_0 coupled to the director fluctuations. The latter are long-wave Goldstone excitations requiring very low energy (Kq^2) in the limit of wavevectors $q \to 0$ as any hydrodynamic mode. It is that long-range coherent polarization wave that, according to [27], installs necessary correlations responsible for antiferroelectricity. There are other electrostatic interactions such as quadrupole–quadrupole or flexoelectric ones. The latter emerges due to spatial modulation of the tilt of molecules in the layered structure. Consider briefly few interesting models that have been suggested for understanding polymorphism of tilted antiferroelectric smectics.

13.2.2.3 Models

Continuous models. With discovery of antiferroelectrics a question has arised about the possible structures and order parameters describing the new phases. Since all the structures are based on the single tilted SmC* layers of the same C_2 symmetry, it was suggested to use the same **c**-director to characterised each pair of neighbour layers (bilayer model [28]). Taking two neighbour layers i and $i + 1$, one writes two order parameters, ferroelectric and antiferroelectric, both in terms of the director components $\xi(n_x n_z, n_y n_z)$, see Eqs. (13.9a, b) where z is the normal to smectic layers:

$$\xi_F = \frac{1}{2}\left(\xi_i + \xi_{i+1}\right) \quad \text{and} \quad \xi_{AF} = \frac{1}{2}\left(\xi_i - \xi_{i+1}\right) \tag{13.47}$$

Then, for paraelectric SmA phase both $\xi_F = 0$ and $\xi_{AF} = 0$, for ferroelectric SmC* phase $\xi_F \neq 0$ but $\xi_{AF} = 0$ as discussed in Section 13.1, for antiferroelectric SmC^*_A phase $\xi_F = 0$ but $\xi_{AF} \neq 0$, and for ferrielectric phases SmC^*_{FI} both $\xi_F \neq 0$ and $\xi_{AF} \neq 0$. Now the Landau expansion of the free energy in the vicinity of transitions between the paraelectric, ferroelectric and antiferroelectric phases will operate with two order parameters and both coefficients at the ξ^2 terms in the free energy are considered to be dependent on temperature:

$$\frac{1}{2}a_F\xi_F^2 = \frac{1}{2}\alpha_F(T - T_F)\xi_F^2 \quad \text{and} \quad \frac{1}{2}a_{AF}\xi_{AF}^2 = \frac{1}{2}\alpha_{AF}(T - T_{AF})\xi_{AF}^2$$

The two polarizations P_F and P_{AF} may be taken as secondary order parameters coupled with the genuine order parameters. As a result, depending of the model, the theory predicts transitions from the smectic A phase into either the synclinic ferroelectric phase at temperature T_F or into an anticlinic antiferroelectric phase at T_{AF}. One intermediate ferrielectric phase is also predicted that has a tilt plane in the $i + 1$ layer turned through some angle φ with respect to the tilt plane in the i layer. The models based on the two order parameters are of *continuous nature* (φ may take any values) and, although conceptually are very important, cannot explain a variety of intermediate phases and their basic properties.

Discrete models. The most advanced are discrete models that explicitly take into account the interactions between nearest neighbour (NN) layers and even next to nearest neighbour (NNN) layers. Among those approaches the most successful are *Ising models* [24] and the XY models, particularly, the so-called *clock model* [6, 26].

Consider one of the most successive Ising models. From the electrooptic study it was clear that between ferroelectric and antiferroelectric phases there are intermediate "subphases" of the mixed type. Thus, from the very beginning it was tempting to classify the new phases using analogy with their crystalline counterparts. Such an analogy is based on the assumption (even counter-intuitive) that there are SmC-like (achiral) correlations of the type shown in Fig.13.19c, d. For certain molecular parameters synclinic and anticlinic order may compete but the in-plane tilt configuration

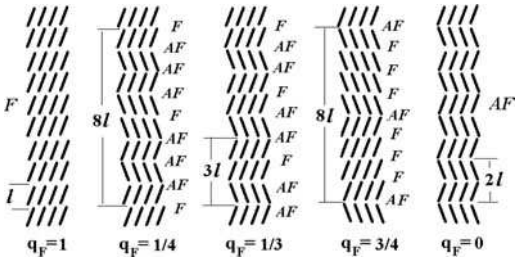

Fig. 13.20 Ising model. Sequence of ferroelectric ($q_F = 1$), ferrielectric ($q_F = n/m = 2/8 = 1/4$, 1/3 and 3/4) and antiferroelectric ($q_F = 0$) phases

always remains. As mentioned above, such structures may be described in terms of ferroelectric fraction q_F, in analogy with the microscopic Ising model describing the interaction energy of the up and down (or $\pm$) spins in one-dimensional lattice. In Fig. 13.20, the "ferroelectric states" marked off by letter F have the same sign of the molecular tilt in the neighbour smectic layers whereas the "antiferroelectric states" with opposite tilt in neighbour layers marked by AF (here tilt angles $\pm\vartheta$ play the role of up and down spins). Microscopically, the interaction between nearest and next to nearest layers is taken into account. The genuine ferroelectric F/F/F/F and antiferroelectric AF/AF/AF/AF. . . .phases correspond to $q_F = 1$ and $q_F = 0/1$. The sequences AF/AF/F/AF/AF/F. . . , AF/F/AF/F/AF/F. . . and AF/F/F/F/AF/FFF mean ferrielectric phases with $q_F = 1/3$, 1/2, and 3/4, respectively. As in the case of crystalline antiferroelectrics, for both n and m increasing the difference between q_F values becomes step-by-step smaller down to zero and the Devil staircase forms. Note that in the limit of $n/m \rightarrow 1$ a ferrielectric becomes a ferroelectric.

In the Ising model, all the molecules are in the tilt plane but, despite such a severe simplification, the electrooptic measurements and resonant X-ray scattering [29] have confirmed the sequence of ferro- ferri- and antiferroelectric phases. However, the same X-ray experiments clearly showed that the tilt planes in different layers are not at all parallel. Moreover, in frameworks of the Ising models the structure of the SmC^*_α phase could not be understood. Therefore, another approach has been developed.

In the discrete clock model [26], one operates with the **c**-director lying in the XY plane and the tilt plane in layer $i + 1$ is allowed to be at a discrete angle φ with respect to the neighbour layer i. Therefore, for a ferroelectric structure $\varphi = 0$, for antiferroelectric $\varphi = \pi$, for ferrielectric structure it could be $2\pi/3$ or $\pi/2$ (by analogy with a clock hand in the x, y plane). Correspondingly, SmC*, SmC^*_A, SmC^*_{FI1} and SmC^*_{FI2} phases have unit cells of one, two, three or four smectic layers and the order parameter is abruptly changed from layer to layer. Note that in any *continuous model* a number of order parameters corresponds to a great number of layers in a unit cell and even phenomenological theory becomes very complicated. Alternatively, in the discrete clock model the interlayer interactions can be separated from the molecular interactions within the smectic layer. Due to complexity of both types of interactions they are modelled by phenomenological approximations based on the symmetry arguments. The *intra-layer* interactions were considered most important: they induce both smectic order and tilt. *Inter-layer* interactions between nearest layers

responsible for ferro- or antiferroelectricity are usually weak because transitions between synclinic and anticlinic structures easily occur. Due to this, long range interactions between next to nearest layers especially electrostatic and chiral ones become very important.

All these interactions are taken into account in the discrete phenomenological model. The chiral interaction is also included although its contribution is considered small. As the primary and secondary order parameters, the tilt vector ξ_i and polarization vector P_i for a single smectic layer i are taken into account. Both parameters may vary from layer to layer, the tilt magnitude being constant and only directions of ξ_i and P_i change. Then Landau expansion for the free energy is written as a sum of different energy terms for N layers, where N is a number of layers in a unit cell. Further on, the polarization perpendicular to the tilt plane is excluded due to weakness of the chiral interaction within a smectic layer and possible stable structures have been found by minimisation of the free energy with respect to all tilt order parameters ξ_i.

As a result of numerical calculations [30], five phases shown in Fig. 13.21 have been found. In the first two rows we find the symbols and types of the phases whereas the third column represents the corresponding unit cells for the first four phases in terms of smectic layer numbers (m) per one period of the structure. The SmC*$_\alpha$ phase is incommensurate in the sense that it has a short-pitch helical structure with a period not coinciding with integer number of the smectic layers. In the fourth column, a top view of the dielectric ellipsoid is presented for different layers within each unit cell. All these phases are in agreement with sequence

Symbol	Type	Unit cell	Top view
SmC*	Ferro	1l	
SmC*$_A$	Antiferro	2l	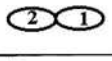
SmC*$_{FI1}$	Ferri 1	3l	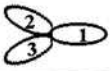
SmC*$_{FI2}$	Ferri 2	4l	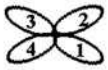
SmC*$_\alpha$	Short-pitch helical (IC)	none	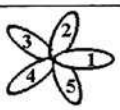

Fig. 13.21 Classification and structure of ferro-, ferri and antiferroelectric phases. The third column represents the number (m) of the smectic layers l in a unit cell (for SmC*$_\alpha$ abbreviation IC means incommensurate). In the right column the orientation of the dielectric ellipsoid is presented for different layers within the unit cell viewed along the z-axis. The long-pitch helical structure due to the molecular chirality is ignored for clarity, although it slightly influences the value of angle φ for the ellipsoids in the xy plane for each structure, see the next figure

(13.46). Note that in our simplified picture the molecular chirality is ignored and its role in the formation of long-pitch helix will be discussed below. The structure and properties of the phases pictured in Fig. 13.21 may be summarised in order of increasing temperature:

1. SmC*$_A$: optically uniaxial antiferroelectric phase with period of $2l$ and zero spontaneous polarization P_s. It manifests Bragg diffraction and optical rotatory power (ORP). *NN* interactions prevail. The helical structure is shown in Fig. 13.22: it is similar to that of SmC*, but the sign of helicity may be opposite.
2. SmC*$_{FI1}$: biaxial ferrielectric phase with $3l$ periodicity and finite P_s. It manifests ORP, which may change sign at a certain temperature.
3. SmC*$_{FI2}$: uniaxial antiferroelectric phase with $4l$ periodicity and zero P_s. However, on account of chirality the phase acquires small P_s and ferrielectric properties.
4. SmC*: the helical, optically uniaxial phase, with period $P_0 >> l$ and finite P_s. It manifests Bragg diffraction and ORP and familiar to us from Sections 4.9 and 13.1. The near-neighbour (*NN*) interactions prevail.
5. SmC*$_\alpha$: It is the most symmetric, antiferroelectric-type phase ($P_s = 0$) that borders SmA phase. It is helical but the helicity originates not from the molecular chirality but is due to specific *NNN* interactions. The pitch is short and incommensurate to the layer periodicity. In Fig. 13.21 the top view on the first five layers is shown and one may conclude that the helical pitch may be as short as $5l$, but it vary with temperature. Due to short helical pitch the phase does not show ORP.

Figure 13.21 presents the picture of the dielectric ellipsoid orientation within each unit cell that is at the nanometer scale. The weak molecular chirality results in additional weak twisting of all structures with characteristic pitch of about $P_0 \approx 0.1$–1 μm. An example of a such twisted structure is shown in Fig. 13.22; it is an antiferroelectric double-layer cell describing two geared helices upon rotation about z-axis. The helices are shifted in phase by $\varphi = \pi$ and have the same handedness. On the molecular scale, due to molecular chirality, the **c**-director turns from layer to layer by a small angle $\delta\varphi = 2\pi l/P_0$, therefore, for $l \approx 1$nm,

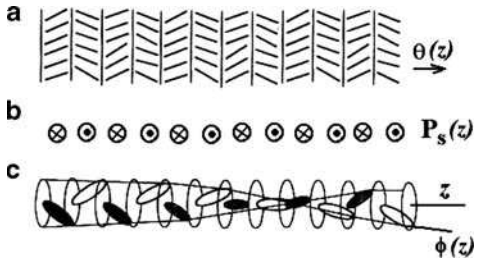

Fig. 13.22 Chiral antiferroelectric SmC*$_A$ phase. Alternating tilt plane (**a**) and layer polarization (**b**) and the long-pitch helical structure (**c**). Note that the unit cell consisting of two layers rotates as a whole forming two geared helices of the same handedness. This type of rotation is controlled by molecular chirality inherent in all phases shown in Fig. 13.21

$\delta\varphi \approx 1^\circ$. Consequently, to have a more correct structures in Fig. 13.21 one should present each ellipsoid configurations in the forth column as an overlapping stack of the same configurations. Such stuck will consist of the same sketches turned m-times through angle $\delta\varphi$ about the z-axis according to the number of layers (m) in a unit cell [30, 31]. More recent publications confirm the picture presented here, see [32] and references therein.

13.2.2.4 Electric Field Switching

Experimental data. Upon application of the external electric field, the transition temperatures between different phases change [33]. It is seen in the field–temperature phase diagram Fig. 13.23. First, we notice that all transition temperatures are shifted considerably that confirms a subtle difference between the interactions responsible for antiferroelectricity. In addition, the temperature range of the polar SmC* phase becomes wider at the cost of the antiferroelectric SmC_A* and unpolar SmC_α* phases. The range of ferrielectric SmC_{FI2}* phase remains unchanged. It can be understood as follows. As the smectic C* phase has high spontaneous polarization, due to the $-P_sE$ term, its free energy is reduced by the electric field. Therefore, the field stabilised the smectic C* phase and expands it temperature range. To some extent, the ferrielectric phases with lower spontaneous polarization are also stabilised by the field but not the antiferroelectric ones.

In the field-off state the macroscopic polarization of the antiferroelectric phase is zero. With increasing field, the induced polarization, at first, increases linearly with field and then, at a certain threshold, the antiferroelectric (AF) structure with alternating molecular tilt transforms in the ferroelectric one (F) with a uniform tilt, see Fig. 13.24a. Correspondingly, the macroscopic polarization jumps from a low value to the level of the local polarization P_0 [34]. The process is quite similar to that observed in crystalline antiferroelectrics. With a certain precaution we can speak about a field-induced AF-F non-equilibrium "phase transition". The magnitude of the switched polarization in some antiferroelectric materials can be quite

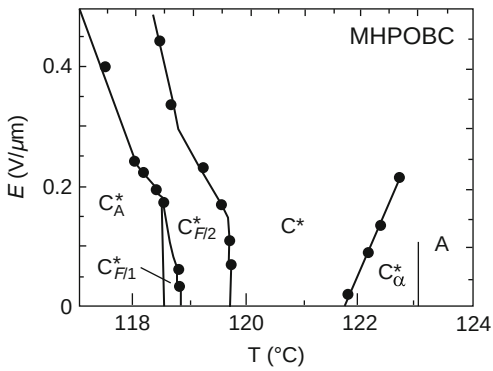

Fig. 13.23 Electric field–temperature phase diagram of MHPOBC (Adapted from [33])

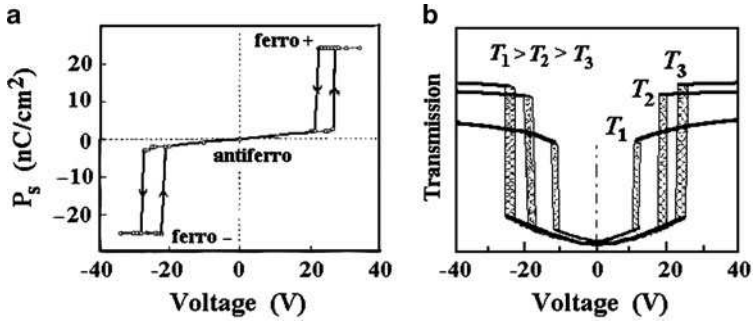

Fig. 13.24 Tri-stable switching of an antiferroelectric liquid crystal. Typical hysteresis-type dependence [34] of the total polarization P as a function of the external field (**a**) and optical transmission-voltage curves [35] measured at three different temperatures ($T_1 > T_2 > T_3$) in the same SmC*$_A$ phase (**b**)

large, of about several hundred of nC/cm^2. Upon a change in the field polarity, the process reverses. Therefore, we have three distinct states, one stable antiferroelectric state and two (plus and minus) ferroelectric states with a certain memory. It should be noted that, in some materials, such a switching process between the antiferroelectric and ferroelectric states could proceed via intermediate ferrielectric states.

By a proper treatment of the electrodes, one can obtain a texture with a uniform orientation of the smectic normal in one direction within the cell plane. Between the crossed polarizers such a cell will be black if a polarizer is installed parallel to the smectic normal. Upon application of the electric field, the antiferroelectric structure becomes distorted. At low voltages of any polarity, the electrooptic response is proportional to E^2: the bottom part of the curves has symmetric parabolic form [35] shown in Fig. 13.24b. Above the AF-F transition, the director acquires one of the two symmetric angular positions ($\pm\vartheta$ on the conical surface) typical of the SmC* phase. At these two extreme positions the transmission is maximum. With increasing temperature from T_3 to T_1 the AF–F threshold decreases due to a decrease of the potential barrier separating structures with alternating and uniform tilt. It is natural because within the SmC*$_A$ phase T_1 is closer to the range of the SmC* phase than T_2 or T_3.

At high frequencies of the a.c. field, the total polarisation of the entire sample is switched very fast and the ground, antiferroelectric state may be bypassed. Then the switching occurs between the two ferroelectric states as in an SSFLC cell. With increasing frequency (for example, from 100 Hz to 10 kHz) the double hysteresis loop is substituted by a single loop typical of ferroelectrics as shown in Fig. 13.16 by the solid and the dashed curves.

Theoretical consideration. We shall consider a simple and instructive theory of the switching of a helix free antiferroelectric phase [36]. The smectic layers normal h is aligned along the rubbing direction z in the plane of the cell (bookshelf geometry in Fig. 13.25). The tilt has the amplitude $\pm\ \vartheta$ and its phase Φ changes

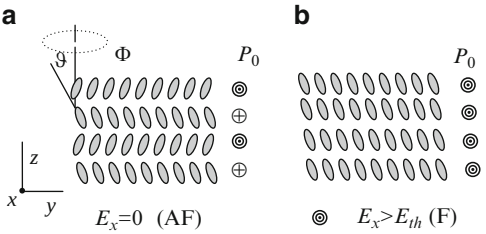

Fig. 13.25 Geometry for discussion of the electric field-induced ferroelectric–antiferroelectric transition. Antiferroelectric structure (**a**) in the zero field and ferroelectric structure at the field exceeding the F–AF transition threshold (**b**)

by π in each subsequent layer. An applied electric field is within the smectic layer plane parallel to the x-axis. Due to chirality, each layer possesses polarization $\mathbf{P}_0$ perpendicular to the tilt plane. The total polarization in the ground state is zero, sketch (a). With increasing external filed a transition is observed from the antiferroelectric (AF) ground state to the ferroelectric (F) field-induced state, sketch (b). After transition, all vectors $\mathbf{P}_0$ are oriented along the field and the director azimuth is the same in all smectic layers, $\Phi = 0$.

For simplicity we disregard a change in the ϑ angle and focus our attention only on azimuthal motion of the director. The density of the bulk free energy can be taken in the form:

$$F = \frac{1}{2}K\left[\left(\frac{\partial\Phi_i}{\partial y}\right)^2 + \left(\frac{\partial\Phi_i}{\partial x}\right)^2\right] + W\cos(\Phi_{i+1} - \Phi_i) - P_0 E\cos\Phi_i \qquad (13.48)$$

Here, the first term describes the nematic-like elastic energy in one constant approximation ($K \approx K_N \sin^2\vartheta$). This term allows a discussion of distortions below the AF-F threshold (a kind of the Frederiks transition as in nematics in a sample of a finite size). In fact, the most important specific properties of the antiferroelectric are taken into account by the interaction potential W between molecules in neighbour layers: the second term in the equation corresponds to interaction of only the nearest layers (i) and ($i + 1$). Let count layers from the top of our sketch (a); then for odd layers i, $i + 2$, etc. the director azimuth is 0, and for even layers $i + 1$, $i + 3$, etc. the director azimuth is π. The third term describes interaction of the external field E_x with the layer polarization P_0 of the layer i as in the case of ferroelectric cells. Although for substances with high P_0 the dielectric anisotropy can be neglected, the quadratic-in-field effects are implicitly accounted for by the highest order terms proportional to P^2.

The solution of Eq. (13.48) depends on further simplifications. If we assume that the director in the odd layers with $\Phi_i = 0$ is unaffected by an external field and only the azimuth in the even layers Φ_{i+1} is changed from π to 0, then, for an infinitely thick sample ($x \to \infty$), the free energy is independent of both x and Φ_i. The corresponding torque balance equation reduces to the form with index ($i + 1$) omitted:

$$K\frac{\partial^2\Phi}{\partial y^2} + (2W - P_0E)\sin\Phi = 0 \tag{13.49}$$

If we disregard the elastic, nematic-like term we would see that the distortion has a threshold character with the threshold field $E_{th} = 2W/P_0$. It is easy to understand: the AF–F threshold is achieved when the field energy is sufficient for the director in even layers to overcome potential barrier W and change its azimuth from π to 0. Above the threshold, $E_x > E_{\text{th}}$ the uniform ferroelectric structure is installed.

At fields below E_{A-F}, the macroscopic polarization is absent due to alternating $\pm P_0$, the first order term in polarization is absent and the distortion is controlled by a higher order term proportional to ${P_0}^2E^2$. This explains the parabolic form of the electrooptical response at the fields below AF–F threshold.

To describe the dynamics of Φ at constant ϑ, the viscous torque with viscosity coefficient γ_φ should be added to the balance equation

$$\gamma_\varphi\frac{\partial\Phi}{\partial t} = K\frac{\partial^2\Phi}{\partial y^2} + (2W - P_0E)\sin\Phi. \tag{13.50}$$

Assuming small field-induced Φ angles, sinΦ → Φ, the inverse switching time can be found in the vicinity of the AF–F transition. $\tau_{AF}^{-1} = \gamma_\varphi^{-1}(P_0E - 2W)$. It shows a divergence of the switching time at the threshold field, as observed in experiments. When the field is switched off ($E_x = 0$), the inverse time for the back relaxation from the ferroelectric to the antiferroelectric state is controlled solely by the interlayer potential $\tau_{FA}^{-1} = 2W/\gamma_\varphi$. Surprisingly, this simple theory [36] explains the most important experimental facts and can be applied to both chiral and achiral (banana-type) antiferroelectrics.

13.2.3 Polar Achiral Systems

13.2.3.1 The Problem

As we know, chiral tilted mesophases, manifest ferroelectric (C*, F*, I* and other less symmetric phases), antiferroelectric (SmC_A*, SmC_α*) and ferrielectric (SmC_{FI}*) properties. These properties owe to a tilt of elongated chiral molecules, and polar ordering of the molecular short axes (and transverse dipole moments) perpendicular to the tilt plane. The head-to-tail symmetry $\mathbf{n} = -\mathbf{n}$ is conserved. The $\mathbf{P}_S$ vector lies in the plane of a smectic layer perpendicularly to the tilt plane. Such materials belong to improper ferro-, ferri and antiferroelectrics.

Since discovery of chiral ferroelectrics in 1975, a search for the *achiral* analogues of liquid crystal ferro- and antiferroelectrics was a challenge to researchers, both theoreticians and experimentalists and recently there was a great progress in this area. The idea was to find a way to break non-polar symmetry $D_{\infty h}$ or C_{2h} of

achiral compounds and conserve a liquid crystalline state. For example, in materials belonging to point group $C_{\infty v}$ the axis C_∞ is polar axis and polarization vector is parallel to C_∞. In biaxial smectics of C_{2v} symmetry the polar axis and polarization vector is parallel to rotation axis C_2. There were many theoretical suggestions to use such a reduced symmetry reviewed in [37], however, only in 1992 the first polar smectic liquid crystal showing all polar properties was synthesised [38]).

13.2.3.2 Achiral Ferroelectrics

It was an achiral lamellar mesophase formed by polyphilic compounds. The basic chemical idea to form "building elements" of a polar phase was quite remarkable: the so-called polyphilic effect has been realised. The word "polyphilic" is a generalisation of the well-known term "biphilic" or "amphiphilic". According to this concept, chemically different moieties of a molecule tend to segregate to form polar aggregates, lamellas or smectic layers. The latter can form a polar phase. As shown in Fig.13.26a, a compound studied was made up of three distinct parts: perfluoroalkyl and alkyl chains and a biphenyl rigid core. A fluorinated chains does not like hydrocarbon chains and prefers to have another fluorinated chain as a neighbour. The same is also true for the hydrocarbon chains preferring to be close to each other. To some extent such a tendency is also characteristic of biphenyl moieties. In this way the head-to-tail symmetry is broken at the molecular scale and a polar smectic layer forms according to sketches (b) and (c) in the same figure. In principle, such polar layers may be stacked either in a ferro- or antiferroelectric structure.

Indeed, upon cooling from the isotropic through the smectic A phase, a metastable polar phase forms at temperature 82°C, which existed down to the room temperature before the next heating cycle. The phase manifests all polar properties, namely, pyroelectric and piezoelectric effects, repolarization current and optical

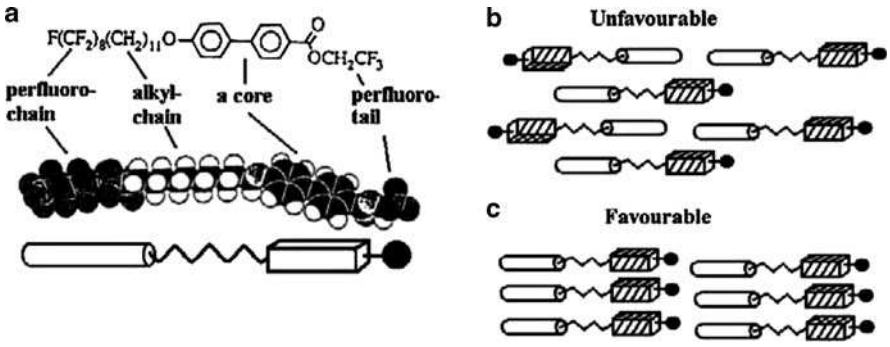

Fig. 13.26 Polyphilic effect. (**a**) An appropriate molecule having well-defined moieties hardly compatible with each other: hydrophobic perfluoro- and alkyl- chains and a hydrophilic biphenyl core. Below are shown a steric model and its schematic version used in sketches (**b**) and (**c**). The latter illustrate unfavourable (**b**) and favourable (**c**) packing of molecules in aggregates or layers

second harmonic generations. Ferroelectricity was demonstrated by the measurements of the hysteresis in the acoustically induced piezo-electric response. The subsequent X-ray investigations an infra-red spectroscopy have shown that the phase consists of polar liquid-like layers having some blurred disordered structure. The phase consists of mesoscopic domains with high spontaneous polarization within each of those domains but almost averaged over a macroscopic sample. Due to smallness of the overall $\mathbf{P}_s$ value and difficulties in the chemical synthesis the polyphilic polar materials have not found practical applications. However, their investigations stimulated activity in the search of new polar achiral liquid crystals, especially based on bent-core molecules. In particular, the ferroelectric phase was reported in an achiral compound [39]. Later, it has been understood that, in such a compound, the conglomerates of left and right chiral domains emerged as a result of spontaneous break of the mirror symmetry discussed in Section 4.11.

13.2.3.3 Achiral Antiferroelectrics

Achiral smectic materials with anticlinic molecular packing are very rare [40] and their antiferroelectric properties have unequivocally been demonstrated only in 1996 [41]. The antiferroelectric properties have been observed in mixtures of two achiral components, although no one of the two manifested this behaviour. In different mixtures of a rod like mesogenic compound (monomer) with the polymer comprised by chemically same rod-like mesogenic molecules a characteristic antiferroelectric hysteresis of the pyroelectric coefficient proportional to the spontaneous polarization value has been observed; for an example see Fig.13.27a. Upon application of a low voltage the response is linear, at a higher field a field-induced AF–F transition occurs.

The absolute value of the P_s has been measured by the pyroelectric technique as explained in Section 11.3.1 but with an applied d.c. electric field, exceeding the AF–F transition threshold. The value of the observed polarization dramatically

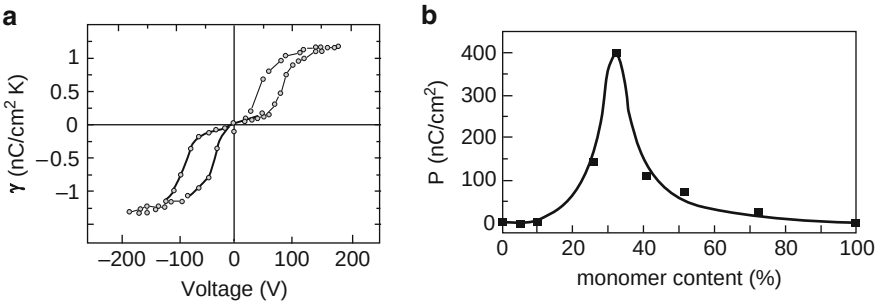

Fig. 13.27 Achiral antiferroelectric. Voltage dependence of pyroelectric coefficient describing the double hysteresis loop (**a**) and dependence of the field-induced polarization on the content of a monomer in the polymer–monomer mixtures (**b**)

depends on the mixture composition: there is a very sharp maximum for the polymer/monomer ratio 70:30 as shown in Fig.13.27b. The macroscopic polarization measured in the mesophase reaches the value of about 400 nC/cm^2, that requires a dipole moment projection onto the smectic plane of about 1 D per mesogenic unit. Indeed, polar intermolecular hydrogen bonds provide such dipole moments located at a small angle to the long axes of the tilted mesogenic groups. The arrows in Fig.13.28 picture schematically the dipolar parts of the mesogenic groups.

As shown by the X-ray diffraction, polymer-monomer mixture consists of SmC bilayers. A bilayer is the principal unit cell having either non-polar C_{2h} (*a*) or polar C_{2v} (*b*) symmetry. The former is incompatible with both ferroelectricity or antiferroelectricity, because such a structure has an inversion centre. On the contrary, in sketch (b) each bilayer is polar with $\mathbf{P}_0$ vector located in the tilt plane along the *y*-axis. In a stack of such layers the direction of $\mathbf{P}_0$ alternates and the structure (b) is antiferroelectric in its ground state. Only strong electric field E_y causes the transition to the ferroelectric structure shown in sketch (c) as observed in experiment. Note that both the $\mathbf{P}_0$ and $\mathbf{P}_s = \Sigma\, \mathbf{P}_0$ vectors are always lying in the tilt plane.

The suggested bilayer antiferroelectric structure is compatible with the X-ray diffraction data and the optical observation of the influence of a rather weak electric field (below the AF–F transition) on freely suspended films of the same mixture [42]. Only the structures with odd number of bilayers appeared to be field-sensitive due to a finite polarization $\mathbf{P}_0$ of single bilayers. Therefore, the antiferroelectricity of the polymer-monomer mixtures is confirmed by all possible experiments. The role of the monomer admixture is explained as follows. As X-ray analysis shows, pure polymer has only the bilayer smectic C phase shown in Fig.13.28a, which is too symmetric to manifest polar properties. From the polarization and electrooptical measurements it is evident that the monomer additive changes the packing of the mesogenic groups and provokes the alternating tilt structure (b) in side-chain polymer bilayers. This results in antiferroelectricity, although the molecular mechanism of such polymer–monomer interaction is not clear.

At the optimum concentration of the mixture the pyroelectric coefficient reaches the value of 4 nC/cm^{2}K exceeding that observed in the famous ferroelectric crystalline copolymers PVDF-TrFE. On cooling down to the glassy state and

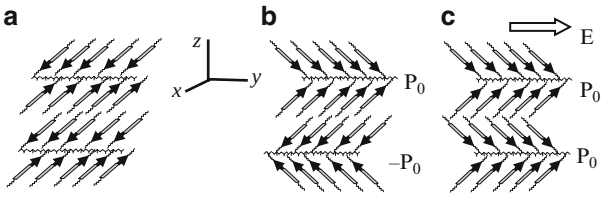

Fig. 13.28 Non-polar dipolar structure of a bilayer and a lamellar phase (**a**) and antiferroelectric phase (**b**) formed by polar bilayers. A strong electric field **E** applied along the *y*-axis converts the antiferroelectric phase (**b**) into polar ferroelectric phase (**c**)

subsequent removing the field, the pyroelectric coefficient may be kept stable for years, and this material may be very useful as an easily formed pyroelectric glass.

13.2.3.4 Ferro- and Antiferroelectric Compounds Based on the Bent-Shape Molecules

As discussed in Section 4.11, achiral molecules of the bent or banana shape may form locally chiral phases in the form of the left- and right-handed domains. This is a result of spontaneous break of the mirror symmetry [43].

Assuming the head-to-tail symmetry of a bent-shape molecule, the highest symmetry of a uniaxial non-tilted smectic A layer is $D_{\infty h}$. Then, according to molecular packing presented in Fig.13.29a, the highest symmetry of the biaxial polar layer is C_{2v}: there is a rotation axis C_2 parallel to *x,* and two symmetry planes *xz* and *xy*. The layer polarization is possible along the C_2 axis. Had the layer consisted of the rod-like molecules tilted within the *xz* plane the symmetry would be C_{2h} as in SmC. However, when the bent-core molecules are tilted in the *y*-direction (forward

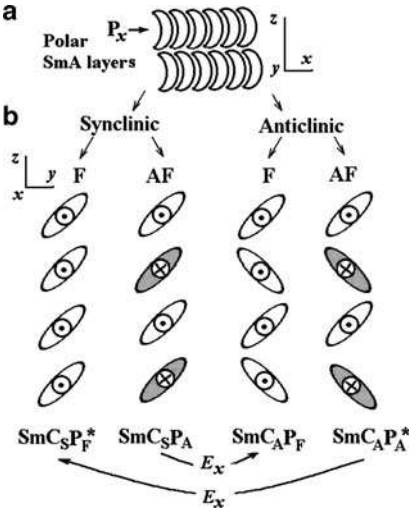

Fig. 13.29 Bent-shape molecules form polar smectic layers in the polar plane *xz* with polarization P_x (**a**). Upon cooling, the molecules can spontaneously acquire a tilt forward or back within the tilt plane *yz*. The stack of the layers may be either synclinic SmC_S or anticlinic SmC_A (**b**). Additionally, depending on the direction of polarization P_x, both the synclinic and anticlinic structure may have uniform (ferroelectric P_F) or alternating (antiferroelectric P_A) distribution of polarization within the stack. In the field absence there are four structures marked by symbols below. Note that the leftmost structure is chiral SmC* and rightmost structure is also chiral because, for any pair of neighbours, the directions of the tilt and polarization change together leaving the same handedness of the vector triple. In the electric field, the phase transitions from chiral SmC_AP_A* to chiral SmC_SP_F* and from racemic SmC_SP_A to racemic SmC_AP_F structures are possible (shown by *ark arrows*)

or backward with respect to the drawing plane), both the reflection planes are lost. Now each smectic monolayer becomes chiral, either left- or right-handed with symmetry C_2. In the right Cartesian frame forward (or backward) deviation corresponds to the right (or left) sign of chirality because we have three non-coplanar vectors, the smectic layer normal **h**, the director **n** (along the molecular long axis) and polarization $\mathbf{P}_0$ (along x) that form a left or right triples.

In a stack of subsequent layers the tilt may be constant (synclinic structure) or alternating (anticlinic structure). Both synclinic and anticlinic multilayer stacks can further be subdivided into ferroelectric and antiferroelectric structures. The molecular projections onto the tilt plane zy are shown in Fig. 13.29b. In ferroelectric (symbol F) phases spontaneous polarization has the same direction in each layer (synclinic chiral SmC_sP_F* and anticlinic achiral SmC_AP_F phases). In the antiferroelectric (symbol A) phases the direction of polarization alternates (achiral synclinic SmC_sP_A and chiral anticlinic SmC_AP_A* phases). In fact we have a conglomerate of chiral and achiral phases both in either synclinic or anticlinic form.

As was said, each smectic layer is chiral, left or right, but the pair of layers might be homogeneously chiral or racemic. The leftmost structure is typical chiral SmC* structure and the rightmost structure is also chiral because in any pair of neighbours the direction of the tilt and polarization change together leaving the same handedness of the vector triple. The two middle stacks are racemic because left and right vector triples alternate from layer to layer. As usual, the asterisks are added to the symbols of each homogeneously chiral subphase. The electric field exceeding some threshold ($E > E_{tr}$) causes transitions between different structures: it transforms SmC_AP_A* into SmC_sP_F* (both are homogeneously chiral) and the direction of the tilt is controlled by the sign of E. The racemic SmC_sP_A phase may be transformed into SmC_AP_F. As the field interacts with polarization, the final state is always ferroelectric (P_F) be it synclinic or anticlinic.

At present, eight different phases are known in banana compounds dependent on particular in-plane packing symmetry and they usually labelled as B_1, B_2, ...B_8, etc., counted from the isotropic phase [44]. Among them the B_2 phase is especially interesting, because it has low viscosity and can easily be switched by an electric field with rather short switching times [45]. In fact, the B_2 phase is basically a conglomerate of chiral and achiral antiferroelectric structures SmC_AP_A* and SmC_AP_A mixed with some percentage of the two ferroelectric structures.

Since the discovery of spontaneous break of mirror symmetry [39, 43], many new, so-called banana-form compounds have been synthesised and hundreds of papers published on that subject [44]. It became a hot topic in modern physics and chemistry of liquid crystals. In the present book there is no space for discussion of different aspects of this fascinating phenomenon and I have decided to finish my narration here. I believe very soon the books shall appear devoted solely to this important subject related not only to liquid crystals, but to the general problems of chirality of the matter.

In conclusion of this chapter it should be stated that bistable and tristable switching of ferro- and antiferroelectric liquid crystals is very fast and provides long memory states. The latter allows one to design displays without semiconductor

thin-film transistors used in each small pixels of a matrix with thousands rows and columns. Such displays have been constructed and their feasibility demonstrated. The beautiful pictures may be seen in references [8] (black and white) and [24] (in colour). However, some disadvantages, such as not enough tolerance of smectic structures to mechanical shots and temperature variations are still to be overcome. Today smectic materials are indispensable for temperature stabilised optical space modulators, image processors or image projectors and, in nearest future, will be very useful as electronic paper.

References

1. Smolensky, G.A., Krainik, N.N.: Ferroelectrics and Antiferroelectrics. Nauka, Moscow (1968) (in Russian)
2. Kittel, Ch: Introduction to Solid State Physics, 4th edn. Wiley, New York (1971)
3. Lines, M.E., Glass, A.M.: Principles and Applications of Ferroelectrics and Related materials. Clarendon Press, Oxford (1977)
4. Meyer, R.B., Liebert, L., Strzelecki, L., Keller, P.J.: Ferroelectric liquid crystals. J. Phys. (Paris) Lett. **36**, L69–L71 (1975)
5. Meyer, R.B.: Ferroelectric liquid crystals. Mol. Cryst. Liq. Cryst. **40**, 33–48 (1977)
6. Muševič, I., Blinc, R., Žekš, B.: The Physics of Ferroelectric and Antiferroelectric Liquid Crystals. World Scientific, Singapore (2000)
7. Blinov, L.M., Beresnev, L.A.: Ferroelectric liquid crystals, Usp. Fiz. Nauk 143, 391–428 (1984) (Sov. Phys.Uspekhi, 27, 7 (1984))
8. Lagerwall, S.T.: Ferroelectric and Antiferroelectric Liquid Crystals. Wiley-VCH, New York (1999)
9. Clark, N.A., Lagerwall, S.T.: Submicrosecond bistable electro-optic switching in liquid crystals. Appl. Phys. Lett. **36**, 899–901 (1980)
10. Pikin, S.A., Indenbom, V.L.: Thermodynamic states and symmetry of liquid crystals. Usp. Fiz. Nauk **125**, 251–277 (1984)
11. Pikin, S.A.: Structural Transformations in Liquid Crystals. Gordon & Breach, New York (1991)
12. Blinov, L.M.: Pyroelectric studies of polar and ferroelectric mesophases. In: Vij, J. (ed.) Advances in Chemical Physics. Advances in Liquid Crystals, vol. 113, pp. 77–158. Wiley, New York (2000)
13. Muševič, I., Žekš, B., Blinc, R., Rasing, Th: Ferroelectric liquid crystals: From the plane wave to the multisoliton limit. In: Kumar, S. (ed.) Liquid Crystals in the Nineties and Beyond, pp. 183–224. World Scientific, Singapore (1995)
14. Garoff, S., Meyer, R.B.: Electroclinic effect at the A-C phase change in a chiral liquid crystal. Phys. Rev. Lett. **38**, 848–851 (1977)
15. Pozhidayev, E.P., Blinov, L.M., Beresnev, L.A., Belyayev, V.V.: The dielectric anomaly near the transition from the smectic A* to smectic C* phase and visco-elastic properties of ferroelectric liquid crystals. Mol. Cryst. Liq. Cryst. **124**, 359–377 (1985)
16. Ostrovski, B.I., Pikin, S.A. Chigrinov, V.G.: Flexoelectric effect and polarization properties of chiral smectic C liquid crystals, Zh. Eksp. Teor. Fiz. 77, 1615–1625 (1979) (Sov. Phys. JETP 50, 811–815 (1979))
17. Beresnev, L.A., Blinov, L.M., Dergachev, D.I., Kondrat'yev, S.B.: Electro-optical effect in a ferroelectric liquid crystal with a small helical pitch and high value of spontaneous polarization. Pis'ma Zh. Eksp. Teor. Fiz. **46**, 328–330 (1987)

18. Blinov, L.M., Palto, S.P.: A new insight on the bistability and relevant phenomena in ferroelectric smectic C* liquid crystals. Mol. Cryst. Liq. Cryst. **429**, 31–53 (2005)
19. Palto, S.P., Geivandov, A.R., Barnik, M.I., Blinov, L.M.: The new role of alignment layers in bistable switching of ferroelectric liquid crystals. Numerical simulations and experimental results. Ferroelectrics **310**, 95–109 (2004)
20. Inui, S., Iimura, N., Suzuki, T., Iwane, H., Miyachi, K., Takanishi, Y., Ishikawa, K., Fukuda, A.: Thresholdless antiferroelectricity in liquid crystals and its application to displays. J. Mater. Chem. **6**, 671–673 (1996)
21. Blinov, L.M., Palto, S.P., Pozhidaev, E.P., Bobylev, Yu.P., Shoshin, V.M., Andreev, A., Podgornov, F., Haase, W.: High frequency hysteresis-free switching in thin layers of smectic C* ferroelectric liquid crystals. Phys. Rev. E 71: 051715-1-10 (2005)
22. Beresnev, L.A., Blinov, L.M., Baikalov, V.A., Pozhidayev, E.P., Purvanetskas, G.V., Pavluchenko, A.I.: Ferroelectricity in tilted smectics doped with optically active additives. Mol. Cryst. Liq. Cryst. **89**, 327–338 (1982)
23. Chandani, A.D.L., Gorecka, E., Ouchi, Y., Takezoe, H., Fukuda, A.: Novel phases exhibiting tristable switching. Jpn. J. Appl. Phys. **28**, L1261–L1264 (1989)
24. Fukuda, A., Takanishi, Y., Izosaki, T., Ishikawa, K., Takezoe, H.: Antiferroelectric chiral smectic liquid crystals. J. Mater. Chem. **4**, 997–1016 (1994)
25. Matsumoto, T., Fukuda, A., Johno, M., Motoyama, Y., Yui, T., Seomun, A.-S., Yamashita, M.: A novel property caused by frustration between ferroelectricity and antiferroelectricity and its application to liquid crystal displays: Ferroelectricity and V-shape switching. J. Mater. Chem. **9**, 2051–2080 (1999)
26. Žekš, B., Čepič, M.: Modeling of ferroelectric and antiferroelectric liquid crystals. In: Haase, W., Wrobel, S. (eds.) Relaxation Phenomena, pp. 257–274. Springer, Berlin (2003)
27. Bruinsma, R., Prost, J.: Fluctuation forces and the Devil's staircase in ferroelectric smectic C*s. J Phys. II France **4**, 1209–1219 (1994)
28. Orihara, H., Ishibashi, Y.: Electro-optic effect and third order nonlinear response in antiferroelectric liquid crystals. J. Phys. Soc. Jpn. **64**, 3775–3786 (1995)
29. Mach, P., Pindak, R., Levelut, A.M., Barois, P., Nguen, N.T., Huang, C.C., Furenlid, L.: Structural characterization of various chiral Smectic-C phases by resonant X-ray scattering. Phys. Rev. Lett. **81**, 1015–1018 (1998)
30. Čepič, M., Gorecka, E., Pociecha, D., Vaupotič, V.: Systems with competing synclinic-anticlinic interactions. In: Haase, W., Wrobel, S. (eds.) Relaxation Phenomena, pp. 332–361. Springer, Berlin (2003)
31. Hirst, L.S., Watson, S.J., Gleeson, H.F., Cluzeau, P., Barois, P., Pindak, R., Pitney, J., Cady, A., Johnson, P.M., Huang, C.C., Levelut, A.-M., Srajer, G., Pollmann, J., Caliebe, W., Seed, A., Herbert, M.R., Goodby, J.W., Hird, M.: Interlayer structures of chiral smectic liquid crystal phases revealed by resonant x-ray scattering. Phys. Rev. E, 65: 041705-1-10 (2000)
32. Liu, Z.Q., McCoy, B.K., Wang, S.T., Pindak, R., Caliebe, W., Barois, P., Fernandes, P., Nguen, H.N., Hsu, C.S., Wang, Sh, Huang, C.C.: Unique pitch evolution in the smectic C^*_α phase. Phys. Rev. Lett. **99**, 0778021–4 (2007)
33. Isozaki, T., Fujikawa, T., Takezoe, H., Fukuda, A., Hagiwara, T., Suzuki, Y., Kawamura, I.: Competition between ferroelectric and antiferroelectric interactions stabilizing varieties of phases in binary mixtures of smectic liquid crystals. Jpn. J. Appl. Phys. **31**, L1435–L1438 (1992)
34. Johno, M., Chandani, A.D.L., Ouchi, Y., Takezoe, H., Fukuda, A., Ichihashi, M., Furukawa, K.: Smectic layer switching by an electric field in ferroelectric liquid crystal cell. Jpn. J. Appl. Phys. **28**, L119–L120 (1989)
35. Johno, M., Itoh, K., Lee, J., Ouchi, Y., Takezoe, H., Fukuda, A., Kitazume, T.: Temporal and spatial behaviour of the field-induced transition between antiferroelectric and ferroelectric phases in chiral smectics. Jpn. J. Appl. Phys. **29**, L107–L110 (1990)
36. Qian, T., Taylor, P.L.: Field-induced phase transitions in antiferroelectric liquid crystals. Phys. Rev. E **60**, 2978–2984 (1999)

37. Blinov, L.M.: On the way to polar achiral liquid crystals. Liq. Cryst. **24**, 143–152 (1998)
38. Tournilhac, F., Blinov, L.M., Simon, J., Yablonsky, S.V.: Ferroelectric liquid crystals from achiral molecules. Nature **359**, 621–623 (1992)
39. Niori, T., Sekine, T., Watanabe, J., Furukava, T., Takezoe, H.: Distinct ferroelectric smectic liquid crystals consisting of banana shape achiral molecules. J. Mater. Chem. **6**, 1231–1233 (1996)
40. Nishiyama, I., Goodby, J.: A nonchiral swallow-tailed liquid crystal exhibiting a smectic C structure that has an antiferroelectric structure. J. Mater. Chem. **2**, 1015–1023 (1992)
41. Soto Bustamante, E.A., Yablonskii, S.V., Ostrovskii, B.I., Beresnev, L.A., Blinov, L.M., Haase, W.: Antiferroelectric behaviour of achiral mesogenic polymer mixtures. Liq. Cryst. **21**, 829–839 (1996)
42. Link, D.R., Clark, N.A., Ostrovskii, B.I., Soto Bustamante, E.A.: Bilayer-by-bilayer antiferroelectric ordering in freely suspended films of an achiral polymer-monomer liquid crystal mixture. Phys. Rev. E **61**, R37–R39 (2000)
43. Link, D.R., Natale, G., Shao, R., Maclennan, J.E., Clark, N.A., Korblova, E., Walba, D.M.: Spontaneous formation of macroscopic chiral domains in a fluid smectic phase of achiral molecules. Science **278**, 1924–1927 (1997)
44. Takezoe, H.: Bent-core liquid crystals: Their mysterious and attractive world. Jpn. J. Appl. Phys. **45**, 597–625 (2006)
45. Blinov, L.M., Barnik, M., Soto Bustamante, E., Pelzl, G., Weissflog, W.: Dynamics of electro-optical switching in the antiferroelectric B_2 phase of an achiral bent-core shape compound. Phys. Rev. E **67**, 1217061–8 (2003)

Index